Volume 3/3

C.E. Coleman

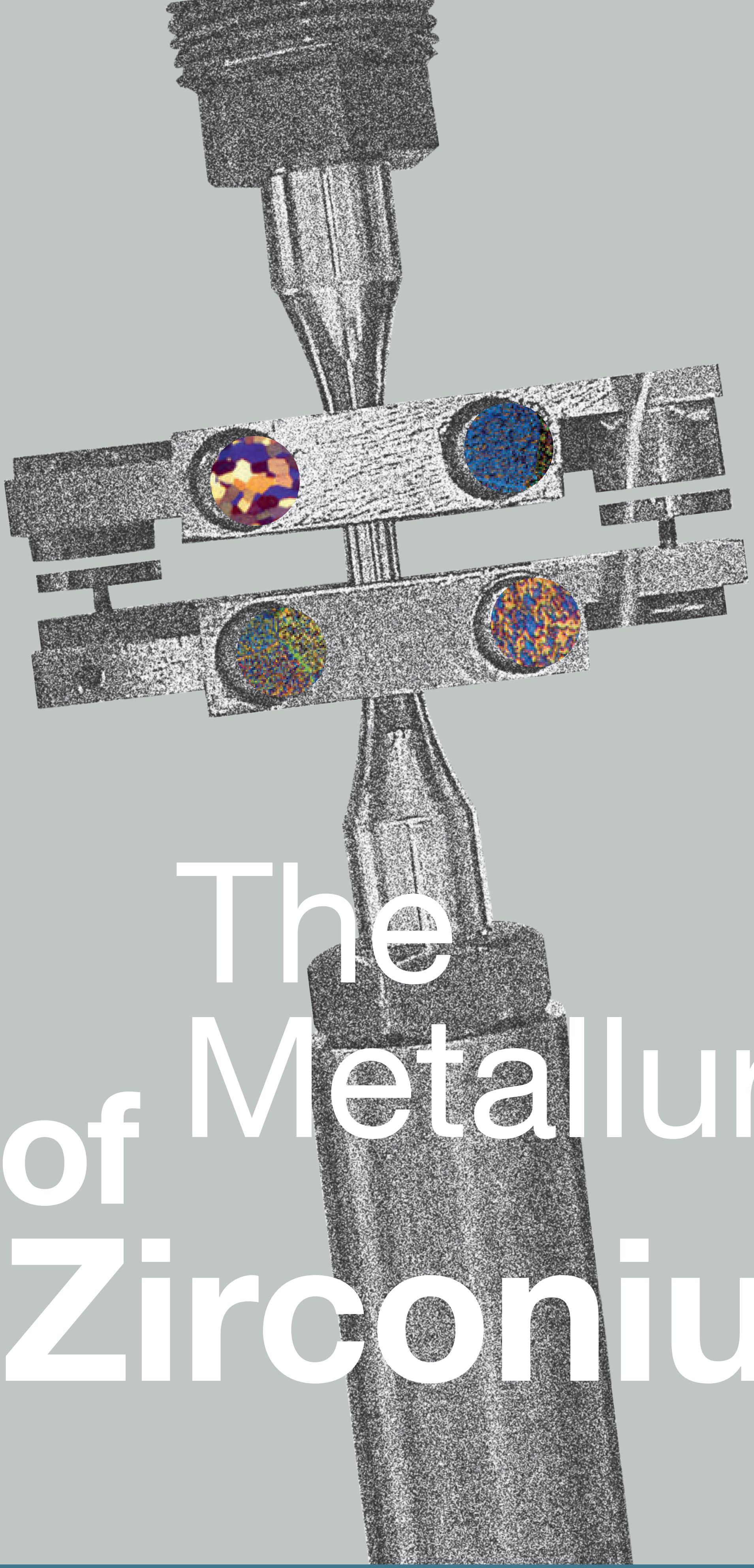

The Metallurgy of Zirconium

IAEA
International Atomic Energy Agency

The Metallurgy of Zirconium

The following States are Members of the International Atomic Energy Agency:

AFGHANISTAN
ALBANIA
ALGERIA
ANGOLA
ANTIGUA AND BARBUDA
ARGENTINA
ARMENIA
AUSTRALIA
AUSTRIA
AZERBAIJAN
BAHAMAS
BAHRAIN
BANGLADESH
BARBADOS
BELARUS
BELGIUM
BELIZE
BENIN
BOLIVIA, PLURINATIONAL STATE OF
BOSNIA AND HERZEGOVINA
BOTSWANA
BRAZIL
BRUNEI DARUSSALAM
BULGARIA
BURKINA FASO
BURUNDI
CAMBODIA
CAMEROON
CANADA
CENTRAL AFRICAN REPUBLIC
CHAD
CHILE
CHINA
COLOMBIA
COMOROS
CONGO
COSTA RICA
CÔTE D’IVOIRE
CROATIA
CUBA
CYPRUS
CZECH REPUBLIC
DEMOCRATIC REPUBLIC OF THE CONGO
DENMARK
DJIBOUTI
DOMINICA
DOMINICAN REPUBLIC
ECUADOR
EGYPT
EL SALVADOR
ERITREA
ESTONIA
ESWATINI
ETHIOPIA
FIJI
FINLAND
FRANCE
GABON
GEORGIA
GERMANY
GHANA
GREECE
GRENADA
GUATEMALA
GUYANA
HAITI
HOLY SEE
HONDURAS
HUNGARY
ICELAND
INDIA
INDONESIA
IRAN, ISLAMIC REPUBLIC OF
IRAQ
IRELAND
ISRAEL
ITALY
JAMAICA
JAPAN
JORDAN
KAZAKHSTAN
KENYA
KOREA, REPUBLIC OF
KUWAIT
KYRGYZSTAN
LAO PEOPLE’S DEMOCRATIC REPUBLIC
LATVIA
LEBANON
LESOTHO
LIBERIA
LIBYA
LIECHTENSTEIN
LITHUANIA
LUXEMBOURG
MADAGASCAR
MALAWI
MALAYSIA
MALI
MALTA
MARSHALL ISLANDS
MAURITANIA
MAURITIUS
MEXICO
MONACO
MONGOLIA
MONTENEGRO
MOROCCO
MOZAMBIQUE
MYANMAR
NAMIBIA
NEPAL
NETHERLANDS
NEW ZEALAND
NICARAGUA
NIGER
NIGERIA
NORTH MACEDONIA
NORWAY
OMAN
PAKISTAN
PALAU
PANAMA
PAPUA NEW GUINEA
PARAGUAY
PERU
PHILIPPINES
POLAND
PORTUGAL
QATAR
REPUBLIC OF MOLDOVA
ROMANIA
RUSSIAN FEDERATION
RWANDA
SAINT KITTS AND NEVIS
SAINT LUCIA
SAINT VINCENT AND THE GRENADINES
SAMOA
SAN MARINO
SAUDI ARABIA
SENEGAL
SERBIA
SEYCHELLES
SIERRA LEONE
SINGAPORE
SLOVAKIA
SLOVENIA
SOUTH AFRICA
SPAIN
SRI LANKA
SUDAN
SWEDEN
SWITZERLAND
SYRIAN ARAB REPUBLIC
TAJIKISTAN
THAILAND
TOGO
TONGA
TRINIDAD AND TOBAGO
TUNISIA
TÜRKİYE
TURKMENISTAN
UGANDA
UKRAINE
UNITED ARAB EMIRATES
UNITED KINGDOM OF GREAT BRITAIN AND NORTHERN IRELAND
UNITED REPUBLIC OF TANZANIA
UNITED STATES OF AMERICA
URUGUAY
UZBEKISTAN
VANUATU
VENEZUELA, BOLIVARIAN REPUBLIC OF
VIET NAM
YEMEN
ZAMBIA
ZIMBABWE

The Agency’s Statute was approved on 23 October 1956 by the Conference on the Statute of the IAEA held at United Nations Headquarters, New York; it entered into force on 29 July 1957. The Headquarters of the Agency are situated in Vienna. Its principal objective is “to accelerate and enlarge the contribution of atomic energy to peace, health and prosperity throughout the world”.

The Metallurgy of Zirconium

C.E. Coleman

Volume 3

INTERNATIONAL ATOMIC ENERGY AGENCY
VIENNA, 2022

COPYRIGHT NOTICE

Marketing and Sales Unit, Publishing Section
International Atomic Energy Agency
Vienna International Centre PO Box 100
1400 Vienna, Austria
fax: +43 1 26007 22529
tel.: +43 1 2600 22417
email: sales.publications@iaea.org
www.iaea.org/publications

Printed by the IAEA in Austria
November 2022
STI/PUB/1943

IAEA Library Cataloguing in Publication Data

Names: International Atomic Energy Agency.
Title: The metallurgy of zirconium / International Atomic Energy Agency.
Description: Vienna : International Atomic Energy Agency, 2022. | Includes bibliographical references.
Identifiers: IAEAL 22-01496 | ISBN 978-92-0-109221-2 (paperback : alk. paper) |
ISBN 978-92-0-109321-9 (pdf) | ISBN 978-92-0-109421-6 (epub)
Subjects: LCSH: Zirconium — Metallurgy. | Zirconium — Properties. | Zirconium — Ductility. | Zirconium alloys.
Classification: UDC 661.883.1 | STI/PUB/1943

FOREWORD

The future of the nuclear industry worldwide depends primarily on the ability of the nuclear community to further improve our understanding of the materials used in the industry. Material science and metallurgy play an important role in reactor performance and safety.

This is the first time in nearly five decades that the International Atomic Energy Agency has gathered and updated information on the scientific and technological application of zirconium in the nuclear industry. The IAEA initiated a comprehensive project on The Metallurgy of Zirconium in 2005, at the request of Member States through the Technical Working Group on Fuel Performance and Technology.

For the greatest convenience of the users of this publication, it has been divided into three volumes. Chapters on fabrication are contained in Volume 1, chapters on the important properties of zirconium relating to its use in nuclear reactors in Volume 2, and information on ductility and fracture is presented in Volume 3.

The contributors to drafting and review were drawn from several countries — Canada, France, Germany, India, the Russian Federation, the United Kingdom and the United States of America. Each chapter was assigned to a leading expert in the field. The publication aims to provide the nuclear industry with a picture of the overall state of development and understanding of zirconium over the years. The first drafts were reviewed by five to seven reviewers, and contributions and appendices from additional authors were added to round out the perspective.

The IAEA wishes to express its gratitude to all the experts who contributed to this publication. Particularly, the IAEA appreciates the support of the main authors of the chapters and C.E. Coleman (Canada), who guided this project to its completion.

The IAEA officer responsible for this publication was M. Veshchunov of the Division of Nuclear Fuel Cycle and Waste Technology.

CONTENTS

Chapter 9

DUCTILITY AND FRACTURE

C.E. COLEMAN
Chalk River Laboratories, Ontario, Canada

With R.B. Adamson, B. Cox and G.A. McRae

9.1. INTRODUCTION

The fracture of components during service in a nuclear reactor may lead to the dispersion of fission products, the loss of heat transport fluids and impaired structural integrity and is thus very undesirable. This chapter describes the various ways zirconium alloys may neck or crack and eventually rupture. The key to good performance is to prevent the initiation of a neck or crack.

In some cases, components have failed during service. The circumstances of these failures have been studied in detail and lessons have been learned so that the particular failure will not recur. Understanding such failures has led to methods for improving the components, although care must be taken that solving one problem does not create another. Tensile stresses drive unstable deformation and cracks, and the sources of these stresses need to be identified. Examples of each of these points will be given where appropriate.

The important quantities for evaluating the risk of fracture are represented by the three stages in the life of a crack. These quantities are:

(1) An estimate of the threshold conditions for cracks to initiate or flaws to extend by the suspected cracking mechanism.
(2) The rate of any stable crack propagation.
(3) The point at which the structure can no longer sustain the load on the crack. The crack grows independent of any stable cracking mechanism, becoming unstable.

The formalism of fracture mechanics provides a useful guide to the significance of cracking. The thickness of the usual components (e.g. 0.6 mm for fuel cladding and 4 mm for pressure tubes) often limits the strict validity of tests, so care has to be exercised in interpreting the results. During testing of specimens for valid linear elastic fracture mechanics (LEFM) the specimen thickness and crack length must exceed $2.5(K_I/\sigma_y)^2$, where K_I is the applied stress intensity factor and σ_y is the yield stress [9.1]. The LEFM approach is often appropriate close to the threshold and during the early stages of crack propagation. In tests at 573 K (300°C) on fuel cladding with a yield stress of 250 MPa, K_I is valid at values of 3.9 MPa$\sqrt{}$m or less whereas with pressure tubes with a yield stress of 500 MPa, K_I is valid up to 20 MPa$\sqrt{}$m. Crack initiation from nominally smooth surfaces or blunt flaws requires other criteria, such as critical stresses. Beyond the validity range of LEFM, especially with long cracks at high loads, the methods of elastic-plastic fracture mechanics, invoking the J integral, may be used. Again, care has to be taken with validity criteria. A size independent measure of the fracture toughness at crack initiation, J_{IC}, can be determined if both specimen thickness and remaining ligament are greater than 25 J_{IC}/σ_y [9.2]. For thin-walled components with high toughness the criteria for specimen independent J is often invalid. When testing is done on full size specimens, application to actual components may be appropriate even if the fracture mechanics are not strictly valid. Alternatively, if a test on a component provides valid LEFM in the presence of a possible crack at operating loads and temperatures, then the material is unsuitable for service and any component with material in that condition should be replaced.

A wide range of specimen designs has been used for testing in several stressing modes. Usually variations on ‘dog-bone’ specimens are used for tensile testing while cracking tests have been done on notched bars in tension or bending and on compact tension and double cantilever beam specimens in bending. Slits in tubing have been extended by internal pressure or bending. Machined notches and slits are often sharpened by fatigue. Full size tubes representing fuel cladding, pressure and calandria tubes have been subjected to a wide range of temperatures, pressures and chemical environments. Special specimens have been used for simulations of reactor situations and in some environmental cracking tests. The effects of service life are simulated by irradiating well-characterized specimens in both power and research reactors and evaluating them either in or out of the reactor. Properties can also be determined directly by evaluating components both within or removed from power reactors; often test specimens are machined from these components.

Tensile behaviour is described in Section 9.2 to provide background information. Subsequent sections describe the relevance to reactor components of fracture under sustained load (Section 9.3), oxygen embrittlement (Section 9.4), the effects of oscillating load (Section 9.5), environmental cracking from fission products (Section 9.6) and hydrogen embrittlement (Section 9.7). The ability of the materials to resist crack growth is evaluated in Section 9.8.

9.2. DUCTILE FRACTURE: UNIAXIAL TENSILE TESTING BELOW 770 K (500 °C)

Without intervention by other mechanisms, zirconium alloys fracture in a ductile manner when specimens or components are highly stressed in tension. During normal reactor operation, failure of components by ductile fracture is unlikely because large safety margins are included by design. For load bearing structures, the specification requires that the material has a certain strength that is several times that of the design stress. For example, pressure retaining components may follow the principles of Section VIII of the American Society of Mechanical Engineers (ASME) Boiler and Pressure Vessel Code [9.3]; at the maximum operating temperature the imposed stress must not exceed the lowest of:

- One third of the ultimate tensile strength (UTS);
- Two thirds of the yield strength;
- Three fifths of the stress to produce rupture within 100 000 hours;
- The stress to provide a creep rate of 10^{-7} per hour.

The creep strain is sometimes restricted to 1%.

Figure 2.8 shows schematically the temperature regimes where short term and long term mechanical properties control the design stress. If cracks initiate and propagate by stable mechanisms or the component is heated to a high temperature during some hypothetical accident, the final rupture is usually by ductile fracture.

Uniaxial tensile testing has many uses: to confirm that the material meets a specification, to evaluate new alloys or modifications to old ones, to assess the effects of reactor operation and to elucidate mechanisms of strengthening or embrittlement. Often a standard test method is used, for example, the ASTM Methods E8 [9.4] and E21 [9.5]. The outcomes are measurements of strength such as 0.2% yield strength and UTS, and measurements of ductility, such as uniform and total elongation, and reduction in area at fracture. The factors that control elongation and reduction in area may be different and the comparison of each measure of ductility may provide a contradictory evaluation.

9.2.1. Behaviour of unirradiated material

Before irradiation, zirconium alloys behave similarly to other ductile metals in a tensile test. In a load elongation curve, an initial linear elastic rise in load is followed by yielding when the rate of rise in load declines during plastic deformation until a maximum value is reached — the UTS —

followed by a gradual decrease in load to fracture. Occasionally test specimens exhibit a definite yield point instead of a gradual deviation from elastic behaviour; for example, in pure zirconium with small grains (<8 μm) [9.6–9.8] or large grains — 910 μm [9.9] in Zircaloy-2 [9.10] and in Zr-1Nb [9.11]. A rise in load during plastic deformation indicates work hardening. When the elongation rate is varied, strain rate hardening is also observed. The relationship of true flow stress, σ_T, to true strain, ε_T, to true strain rate, $\dot{\varepsilon}_T$, can be described by several methods. As examples, work hardening may be fitted to power functions [9.12–9.14] or exponential functions [9.15]. Including strain rate effects in the power functions leads to Eq. (9.1) [9.16]:

$$\sigma_T = H\varepsilon_T^h\dot{\varepsilon}_T^m \tag{9.1}$$

where

H is the strength constant,
h is the work hardening coefficient,

and m is the strain rate sensitivity.

Such a simple representation has been criticized because it does not necessarily capture full load elongation curves. The exponential version is sometimes found to be superior to the power law representation [9.17]. The power law approach is poor at describing variable loading history whereas an approach using differential constitutive relations can deal with changing conditions [9.18]. Despite these reservations, in this section the parameters of Eq. (9.1) are used to illustrate and compare the effect of test and metallurgical variables on work and strain rate hardening because historically most reports of tensile properties do not include the full load elongation curve that would be required to derive the exponential function or the differential description. Equation (9.1) is used by the United States Nuclear Regulatory Commission (NRC) in their codes for calculating stress and plastic deformation in fuel cladding, especially for accident analysis [9.19].

The values of constant h vary from zero, perfect plasticity, to 0.5, representing maximum dislocation generation [9.20]. The values of m vary from close to zero up to 1.0; they depend on the thermally activated mechanisms represented by the activation volume, v^*, for a particular barrier to dislocation motion at temperature T [9.21, 9.22]:

$$m \propto k_B T/v^*\sigma_T \tag{9.2}$$

where k_B is Boltzmann's constant and T is the test temperature (K).

The shape of the load elongation curve depends on specimen geometry and rates of work hardening and strain rate hardening. A tensile test on a bar of uniform cross-section at a constant cross-head rate would exhibit a maximum load because the loss of cross-sectional area and decrease in strain rate cannot be completely compensated by work hardening. The true strain to maximum load, ε_{ml}, is given by [9.23]:

$$\varepsilon_{ml} = h/(1+m) \tag{9.3}$$

Necks form in real specimens, which are allowed by the standards to have a central taper on cross-sectional area of up to 2%. The development of a neck also depends on work hardening and strain rate hardening [9.23–9.29]. Using a general stability criterion [9.23], the strain to the start of necking, ε_n, is given by:

$$\varepsilon_n = h/(1-m) \tag{9.4}$$

Thus, the strain to maximum load is smaller than the strain to the onset of necking but when m is small the two strains will be similar. Note that the attainment of a maximum load has nothing to do with the formation of a neck, although the elongation to maximum load is often called uniform strain; the strain to maximum load (in a perfect specimen) and the strain to the start of detectable necking (in a real specimen) simply almost coincide when values of m are low, and especially when the load elongation curve is almost flat after yield. The relation between the two strains was indicated by plotting $d(\ln P)/d(\ln \varepsilon_T)$ against ε_T, where P is the applied load; $d(\ln P)/d(\ln \varepsilon_T) = 0$ is the maximum load and necking starts when $d(\ln P)/d(\ln \varepsilon_T)$ deviates from linearity with ε_T. Figure 9.1 is such a plot for annealed Zircaloy-2 tested at room temperature showing that $\varepsilon_n > \varepsilon_{ml}$ by 0.05 [9.30]. With cold worked material the two strains are much closer together.

Total elongation is the sum of uniform elongation and elongation during necking up to final rupture, which is initiated by cavity or pore formation. Total elongation depends on specimen length because, although uniform elongation is independent of specimen length for unirradiated materials, necking localizes deformation and forms a higher proportion of a short specimen than of a long specimen; using total elongation as the measure of ductility, a short specimen will appear more ductile than a long specimen. To aid comparison between materials, in the standards the ratio of the gauge length to diameter is specified to be 5 in the European Standards (or 4 in the ASME codes). For flat specimens the ratio of gauge length, ℓ, to specimen width, w, is set at 4 in both versions. In thin material the ratio of specimen width to thickness, t, can also affect measurements of ductility based on original length, ε_ℓ, width, ε_w, or thickness, ε_t [9.31]. For example, in tensile tests on Zircaloy-2 at room temperature with t = 1.5 mm, the strains to fracture varied with w/t, as shown in Fig. 9.2. At ℓ/w = 4, for this material w/t = 8.3, and ductility appears to become independent of w/t. The shape and dimensions of the specimen should always be noted because circumstances, such as sampling components from power reactors [9.32], may force the use of specimens that do not meet the standard.

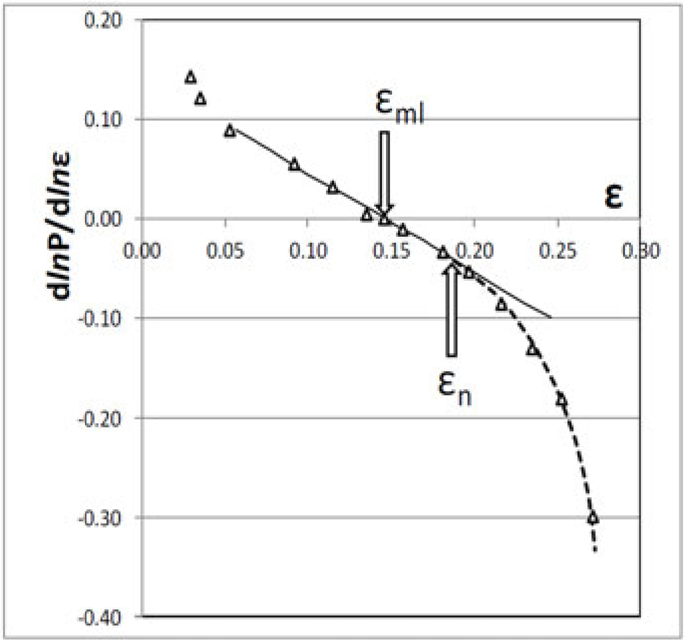

FIG. 9.1. *Proximity of strains to maximum load and start of necking in uniaxial tensile test on annealed Zircaloy-2 tested at room temperature:* ε_{ml} *= 0.145 and* ε_n *= 0.197 [9.30].*

Necking is very sensitive to geometry and strain rate hardening; a high value of m suppresses neck development. The value of m is determined by $d(\log \sigma)/d(\log \dot{\varepsilon})$. Defining $\sigma = P/A$, where P is the load imposed on a cross-section of area A and assuming no work hardening, because at any point along a specimen in tension $\dot{\varepsilon} = -1/A(dA/dt)$, it follows that $-(dA/dt) = (P/A)^{1/m} [A^{(m-1)/m}]$. With $m \ll 1$, smaller cross-sections reduce more rapidly than larger cross-sections and necking follows. As m approaches 1.0, the shape of an incipient neck is preserved and large elongations can be expected. Consequently, a large variation of ductility is possible, depending on h and m. Figure 9.3 compares the data from many samples [9.33] with the calculations of the effects of wide ranges of h and m on total elongation for a tensile specimen with a taper of 2% [9.25]. As a practical example, in Section 4.11.1.3 in Volume 1 of this publication, wall thickness variation was indicated as an issue for some fuel cladding. When h and m are small, the calculations predict that the ductility should be sensitive to wall thickness variation; this conclusion is confirmed by measurements of total elongation from burst tests on zirconium alloy fuel cladding, as shown in Fig. 9.4.

Ductility, indicated as either elongation or reduction in area, depends on several interacting factors such as testing variables, temperature, strain rate and stress state, and alloy composition and microstructure, including texture and irradiation. Since much research has included some tensile

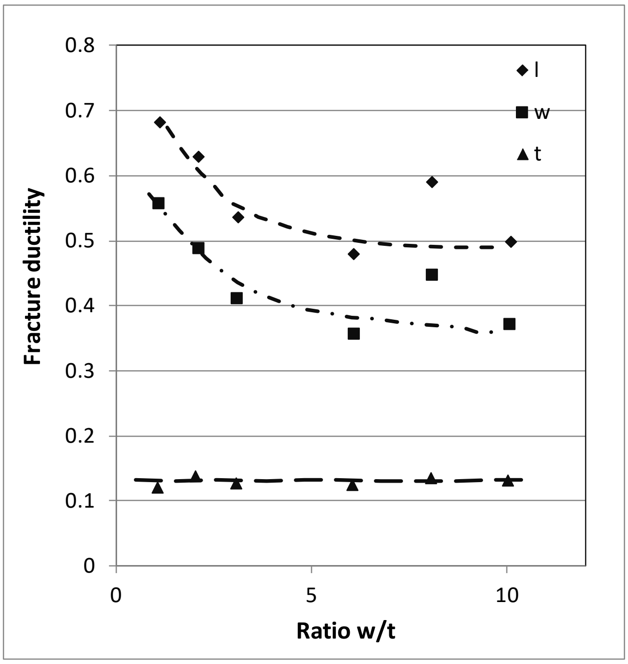

FIG. 9.2. Fracture ductility, based on length, ε_ℓ, width, ε_w, or thickness, ε_t, at room temperature of cold worked Zircaloy-2 as a function of w/t. *With* t = *1.5 mm, to meet ASTM Standard* w/t *should be 8.3 [9.31].*

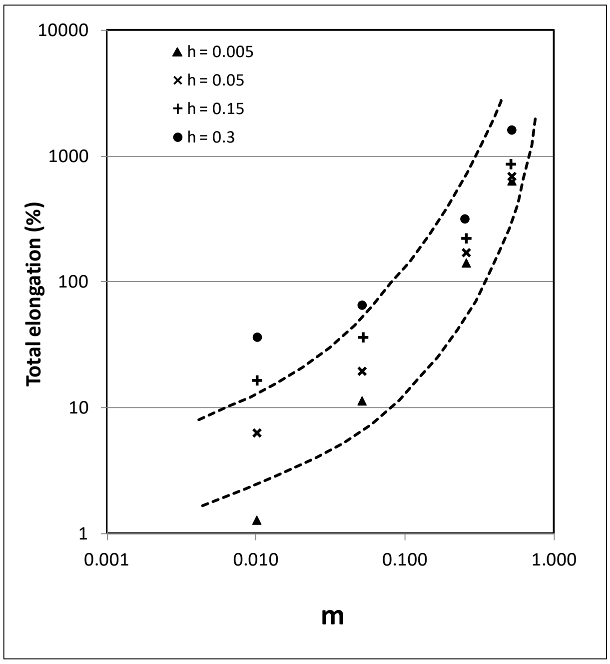

FIG. 9.3. Dependence of total elongation on h *and* m *for tensile specimen with 2% taper. Dotted line represents range of values for many materials [9.25, 9.33].*

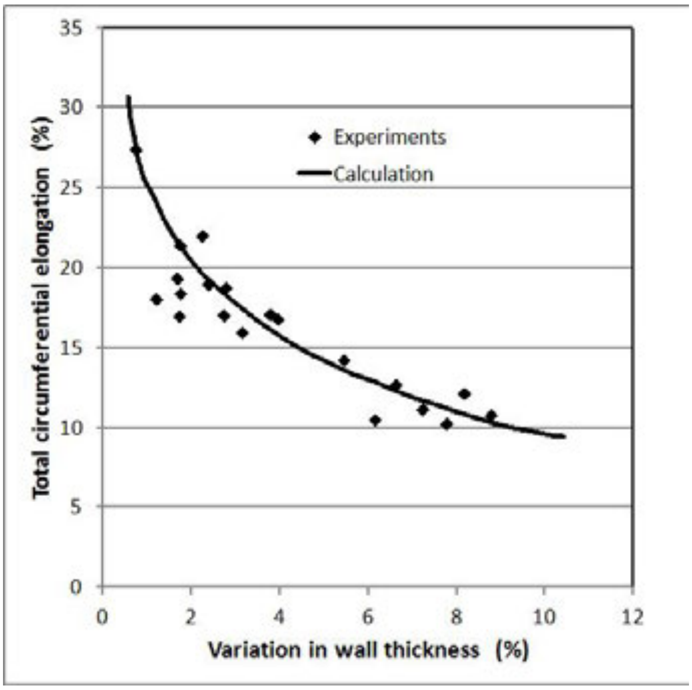

FIG. 9.4. Effect of wall thickness variation on total elongation for burst tests at room temperature on zirconium alloy fuel cladding with h = *0.065 and* m = *0.05 [9.25].*

properties, only a small proportion of the literature is mentioned below to illustrate where the phenomenology of ductility outlined above is valid and where it breaks down.

Pure zirconium has moderate strength and ductility. In the temperature regime for the normal operation of a power reactor, the parameters *h* and *m* are low so the expectation is for low strains to maximum load and low resistance to neck formation; because of the latter, elongation is dominated by *h*. Values for crystal bar zirconium are summarized in Table 9.1 [9.6]. When the material is cold worked 97%, as the test temperature is increased, the strength and value of *h* decreases but elongation increases because *m* increases. When the cold worked material is annealed, *h* and elongation at room temperature start to increase with annealing temperatures of between 673 and 773 K (400 and 500°C), as shown in Fig. 9.5. Compared with cold worked material, as shown in Table 9.1, in material annealed at 872 K (600°C), *h* increases by about 3 to 6 times over the test temperature range. The total elongation remains approximately constant because *h* and *m* are approximately test temperature independent. The values of *h* are not sensitive to grain size [9.6, 9.7].

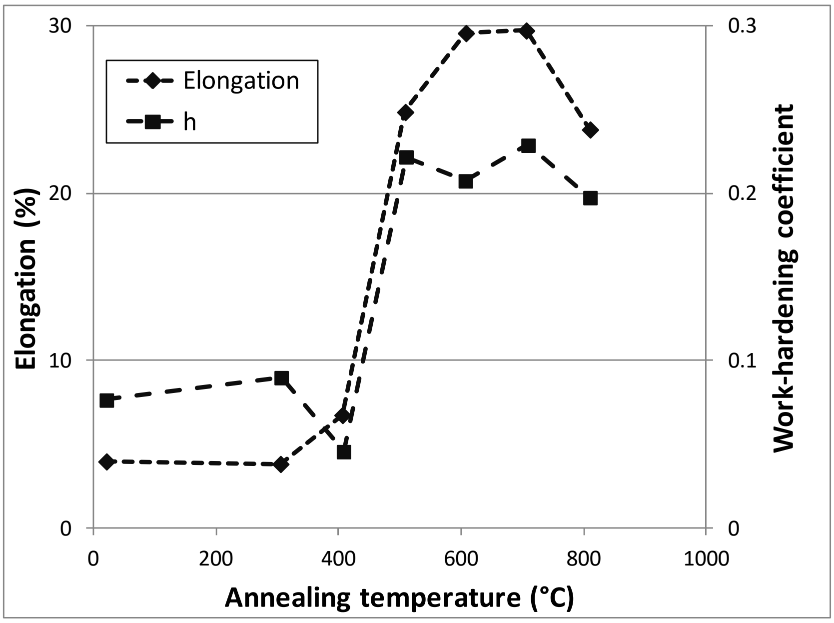

FIG. 9.5. Increase in elongation and h *with annealing temperature of cold worked pure zirconium [9.6].*

The basic phenomenology for elongation is followed by the alloys because they too have low values of *h* and *m*. In the following examples, when *h* was not quoted directly, it was derived as d(log σ)/d(log ε) using values of the 0.2% yield stress, UTS and strain to maximum load (uniform elongation). In the examples, the values and ranges of values of *h* and *m* are small, and the effects of variables can be contradictory.

TABLE 9.1. RELATIONSHIP BETWEEN DUCTILITY OF CRYSTAL BAR ZIRCONIUM AND STRAIN HARDENING COEFFICIENT AND STRAIN RATE SENSITIVITY [9.6]

Material	Test temperature (°C)	0.2% yield strength (MPa)	Total elongation (%)	Reduction of area (%)	*h*	*m*
Cold worked	−195	658	7	35	0.06	0.004
97% reduction	30	488	4	60	0.08	0.010
	200	292	12	85	0.045	0.048
	300	255	14	82	0.04	0.070
	370	241	16	84	0.04	–
Annealed	−195	143	33	56	0.25	0.0083
1800 s at 600 °C	25	123	30	56	0.21	0.016
	200	92	26	75	0.25	0.017
	300	89	24	86	0.25	0.014
	370	87	27	86	0.26	0.013

A sampling of the effects of common variables on h in unirradiated material follows:

— Sometimes the stress–strain curves do not follow Eq. (9.1) throughout the whole test; at low strains, usually between 0.01 and 0.02, values of h are different, usually higher, than those at higher strains [9.7, 9.9]. A dramatic example of a change in work hardening at a strain of 0.015 is reported for Zircaloy-4 when quenched from the (α + β) phase [9.34]; in this material the work hardening rate, $d\sigma/d\varepsilon$, decreases suddenly by a factor of about seven to that of annealed material in which h is 0.10. The values of h at strains greater than the critical value are the most relevant for ductility.

— When Zircaloy-4 is water quenched or air cooled from the β phase, stress–strain curves can be interpreted by Eq. (9.1) with h between 0.10 and 0.17 at room temperature [9.35, 9.36]. In Zr-2.5Nb, h is consistently 0.064 ± 0.015 when the material is quenched from the β phase or (α + β) phase region, either as-quenched, or after tempering at 770 K (500°C) [9.37, 9.38] or after intermediate cold work followed by tempering [9.39, 9.40]; when slowly cooled from the β phase or (α + β) phase region h is increased to 0.11. As indicated with pure zirconium, the value of h in Zircaloy is reduced by a factor of between 2 and 4 with cold work, starting as early as 10%, as shown in Fig. 9.6 [9.30, 9.36]. In Zr-2.5Nb pressure tubes h is also reduced by 20 to 30% cold work to about 0.09 in the axial direction and 0.04 in the transverse direction [9.41].

— The role of texture may be interpreted from an idealized picture [9.42], as shown in Fig. 9.7.
  - When the [0002] is perpendicular to the specimen surface and the tensile direction, as shown in Fig. 9.7 (a), the material deforms by slip and h will be as high as the grain microstructure allows. The main deformations are in the specimen length and width. Specimens of plate material with this texture will have similar values of h when tested in the rolling and transverse directions; for example, h_{RD}/h_{TD} is close to 1.0 in Zircaloy

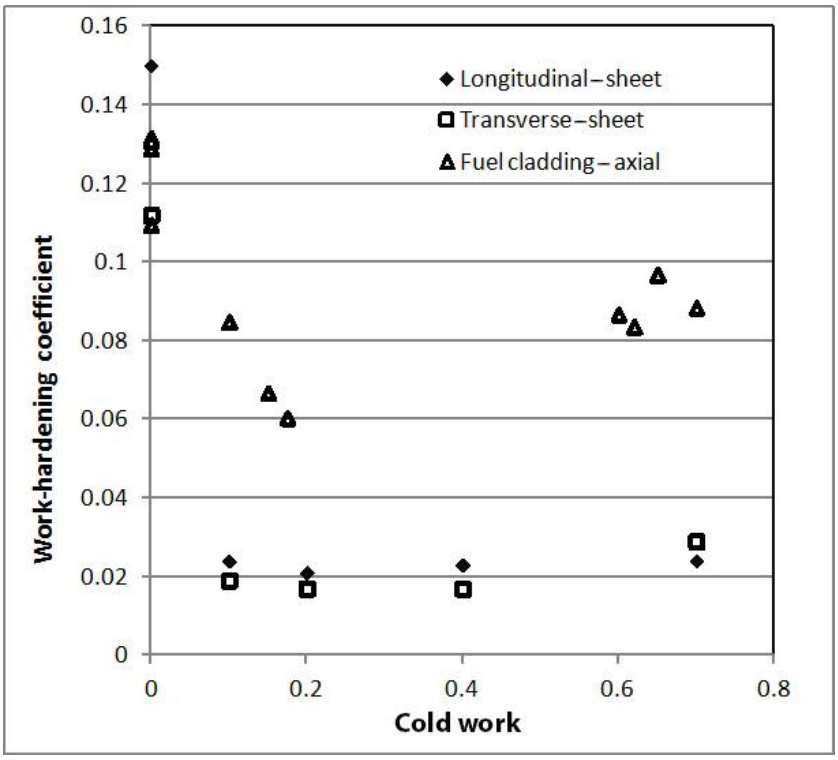

FIG. 9.6. Effect of cold work on the work-hardening coefficient of Zircaloy-2 at room temperature in sheet material [9.30] and fuel cladding [9.36].

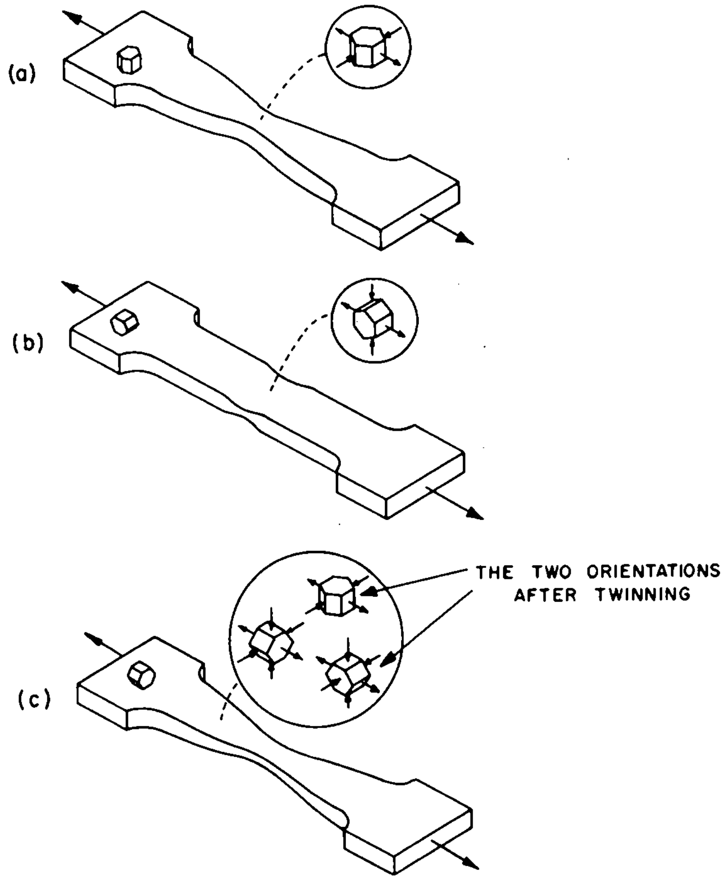

FIG. 9.7. Schematic illustration of strains developed by tensile testing of sheets with hexagonal closed packed crystals oriented in three principal directions (after [9.42]).

plate material [9.30]. In tensile specimens with a circular cross-section, at large strains, the cross-section becomes elliptical, with the major axis corresponding with the thickness of the component. In fuel cladding with a strong radial texture, axial and ring tensile specimens will strain mostly by slip in the circumferential or axial direction, respectively, with little wall thinning.

- When the [0002] is parallel to the specimen surface and perpendicular to the tensile direction, as shown in Fig. 9.7(b), again the material deforms by slip and *h* will be as high as the grain microstructure allows. The main deformations are in the specimen length and thickness. In pressure tubes with a strong transverse texture, tensile tests in the axial direction will strain mostly by slip in the axial direction with little thinning of the specimen width; in specimens with a circular cross-section, at large strains, the cross-section becomes elliptical, with the minor axis corresponding with the thickness of the component.
- When the [0002] is parallel to the specimen surface and the tensile direction, as shown in Fig. 9.7(c), the material deforms by twinning followed by slip in the crystals with a new orientation. Consequently, *h* will appear low because twinning contributes a change in orientation but only a small amount of strain (see Chapter 5 in Volume 1 of this publication). In tests on a thick plate with basal plane normals in the thickness direction, *h* in the rolling direction was twice that in the thickness direction [9.43]. In pressure tubes with a strong transverse texture, *h* in the axial direction was 2.3 times that in the transverse direction [9.41]. At large strains, the specimen deforms in all

three principal directions and in tensile specimens with a circular cross-section, the cross-section remains approximately circular.

- The effect of temperature on *h* is variable, depending on the microstructure and alloy, as shown in Fig. 9.8. Up to 770 K (500°C), *h* may exhibit a maximum value around 570 K (300°C), which has been demonstrated in annealed, unalloyed Zr [9.6, 9.44], annealed Zr-1Nb [9.11] and Zr-1.14Cr-0.1Fe [9.45]; this behaviour has been attributed to strain ageing. The value of *h* has very little temperature dependence in Zircaloy-2 from calandria tubes [9.46], cold worked Zr-2.5Nb from pressure tubes [9.41, 9.47], and stress relieved Zr-2.5Nb from fuel cladding [9.48].
- Similarly, the effect of strain rate on *h* is variable, as shown in Fig. 9.9. In annealed Zircaloy-4 tested between 555 and 588 K (282 and 315°C), *h* declines as the strain rate is increased [9.49], whereas in Zircaloy-2 tested at 623 K (350°C), *h* seems to have a maximum value of about 10^{-3}/s [9.10]. Any effect of strain rate on *h* in stress relieved Zircaloy-4 appears small over a narrow strain rate range at 298 and 673 K (25 and 400°C) [9.50].

The value of *m* can be determined from the yield strength at different strain rates; from changes in strength with change in strain rate during a tensile test, both using $d(\log \sigma)/d(\log \dot{\varepsilon})$; or from stress relaxation at a fixed load [9.51]. Because *m* is small under 773 K (500°C) and there is variation in yield strength between specimens, the first method is unreliable. For example, in tests on annealed Zircaloy-4 at 555 and 588 K (282 and 315°C) at various strain rates in the range 1.1×10^{-8} to 8×10^{-4}/s [9.49], sometimes the yield strength at the lower strain rate was higher than that at a higher strain rate, resulting in a negative value of *m*. Taking the extremes of the data still only gave low values of *m*, between 0.01 and 0.03, in line with the data for pure zirconium, as shown in Table 9.1.

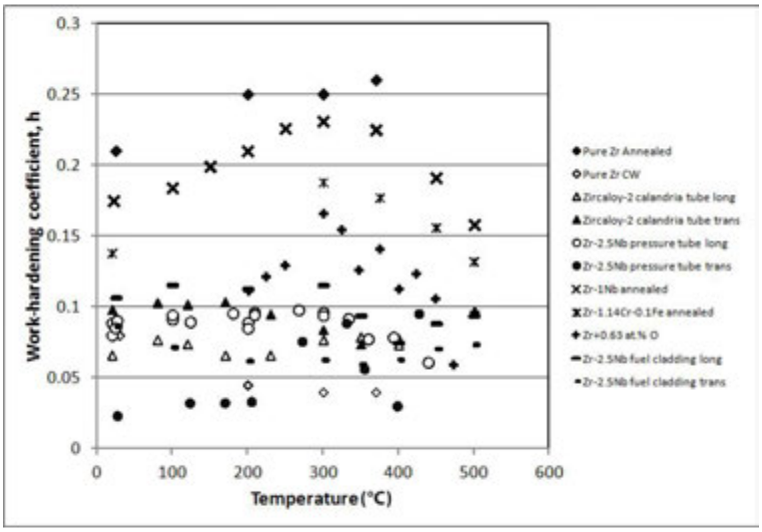

FIG. 9.8. Effect of temperature on work-hardening coefficient of pure Zr [9.6], Zr-1Nb [9.11], Zr-2.5Nb pressure tubes Zr-O [9.44], Zr-1.14Cr-0.1Fe [9.45], Zircaloy-2 [9.46], [9.41, 9.47], Zr-2.5Nb fuel cladding [9.48].

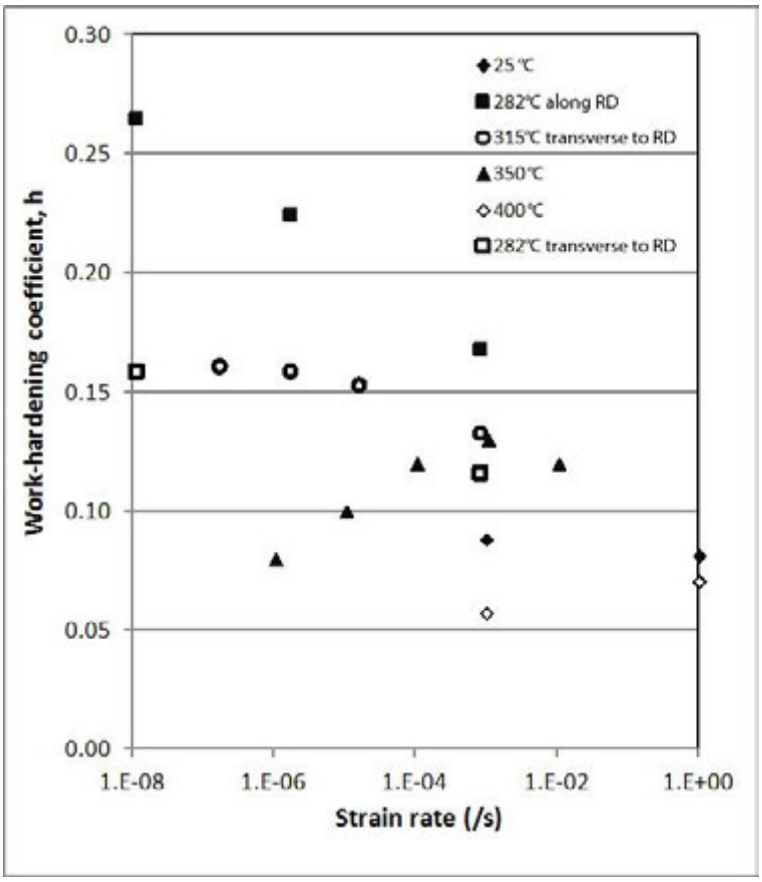

FIG. 9.9. Effect of strain rate on h *in Zircaloy at room temperature and 673 K (400°C) [9.10, 9.49, 9.50]. RD — radial direction.*

The effects of strain rate and test temperature on *m* in unirradiated material intermingle, for example, in annealed Zircaloy-2, as shown in Fig. 9.10 [9.10]. At room temperature *m* is low and independent of strain rate, passes through a minimum between 10^{-5} and 10^{-3}/s at 623 and 673 K (350 and 400°C) and at 773 K (500°C) and steadily declines with increasing strain rate over the testing range from a modest value compared with those found at the lower temperatures. Tests on Zircaloy-2 calandria tube material at 343 K (70°C) over the strain rate range 10^{-4} to 300/s provided values of *m* between 0.03 and 0.05 [9.52]. The value of *m* has a complicated temperature dependence in the strain rate range between 10^{-6} and 10^{-3}/s, as shown in Fig. 9.11, in commercial grade zirconium [9.53], Zircaloy-2 [9.10], Zircaloy-4 [9.54], Zr-1Nb [9.11, 9.54], and Zr-2.5Nb [9.53]. The value of *m* passes through a maximum at about 420 K (150°C) then declines to a minimum value in the temperature range 523 to 673 K (250 to 400°C), and rises as the test temperature is increased to 773 K (500°C); the maximum and minimum in Zr-2.5Nb are much less marked than in the other materials. The minimum in *m* is attributed to strain ageing, with oxygen thought to be the species responsible for the impedance of dislocation motion [9.10, 9.11, 9.44, 9.53, 9.55–9.58], although other elements (e.g. Sn and Fe) may contribute through complex interactions between substitutional and interstitial atoms [9.59, 9.60]. A plateau in the temperature dependence of the yield strength of main alloys between about 523 and 673 K (250 and 400°C), as shown in Fig. 9.12, is also interpreted as a manifestation of strain ageing, [9.11, 9.48, 9.54]. At higher temperatures around 730°C (1000 K) Fe is thought to be responsible for strain ageing [9.61].

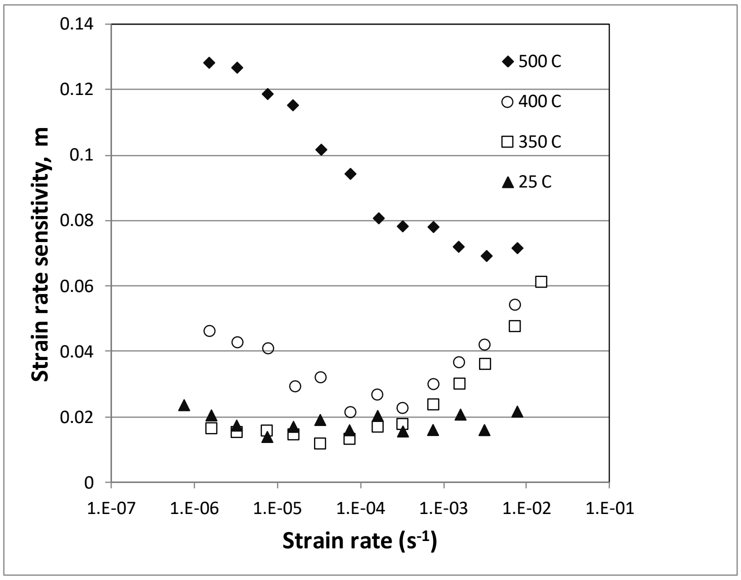

FIG. 9.10. Effect of strain rate and test temperature on m *in annealed Zircaloy-2 [9.10].*

The strain to maximum load (uniform elongation) follows Eq. (9.3), as shown by the dotted line in Fig. 9.13, for several versions of Zircaloy and for two other α alloys; in this plot the effect of *m* was ignored because it is small compared with unity. An exception was found with some data on Zircaloy-4 [9.49] in which the strain to maximum load declined with an increase in *h*. This behaviour was attributed to strain ageing, but since the results of other α alloys follow Eq. (9.3), although the temperature dependence of both *h* and *m* was linked to strain ageing, this exception needs further explanation. The benefit of work hardening is not always realized in Zr-2.5Nb [9.41, 9.47, 9.62] or Zr-1.3Sn-1Nb-0.4Fe [9.62], as shown in Fig. 9.14. The crystallographic texture may promote twinning that changes the local orientation and the deformation mode to slip during early straining leading to a loss in load, or flaws may develop at the ends of twins. In the alloy Zr-1.3Sn-1Nb-0.4Fe,

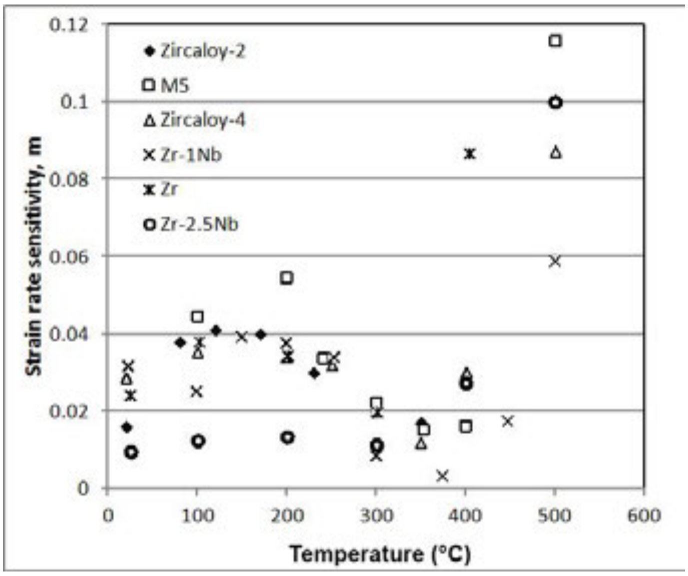

FIG. 9.11. Effect of temperature on m *in the strain rate range 10–6 and 10–3/s in commercial grade zirconium [9.53], Zircaloy-2 [9.10], Zircaloy-4 [9.54], Zr-1Nb [9.11, 9.54], Zr-2.5Nb [9.53].*

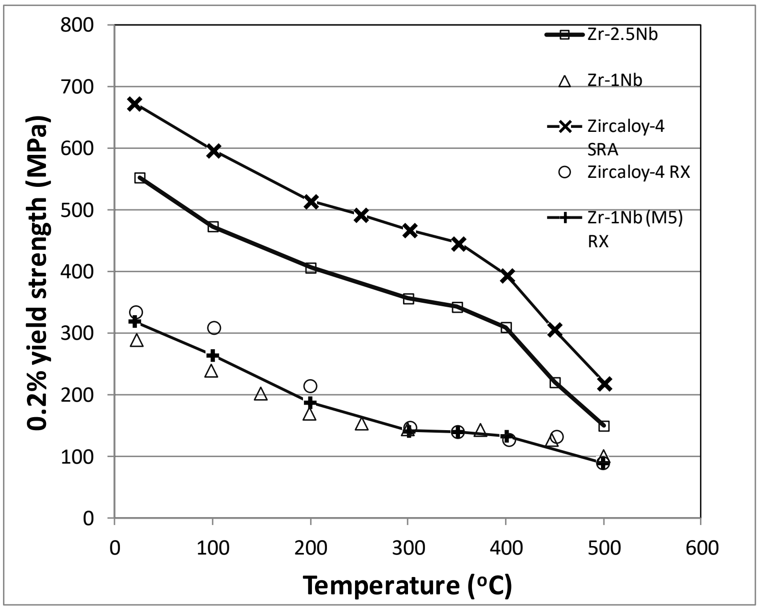

FIG. 9.12. Temperature dependence of the 0.2% yield strength of Zircaloy-4 (stress relieved (SRA), recrystallized (RX)), Zr-1Nb [9.54] and Zr-2.5Nb [9.48], showing plateau between about 523 and 673 K (250 and 400°C).

premature cracking at large intermetallic particles, with diameters up to 1.2 µm, reduces plastic stability compared with material containing small particles, with diameters of less than 0.3 µm [9.62].

Total elongation is also linearly related to *h* when *m* does not vary with the test variables, because *m* dominates the development of necking. When *m* varies with temperature, as shown in Fig. 9.11, the total elongation follows the same temperature dependence as *m*. This effect is seen, for example, in Zircaloy-4, in the both annealed condition [9.57], as shown in Fig. 9.15, and the stress relieved condition [9.58], and in Zr-2.5Nb in the stress relieved condition, as shown in Fig. 9.16 [9.48, 9.53]. When *h* and *m* vary with either temperature, as shown in Table 9.1, or strain rate, Table 9.2 [9.10], the examples indicate that both factors contribute to this measure of ductility.

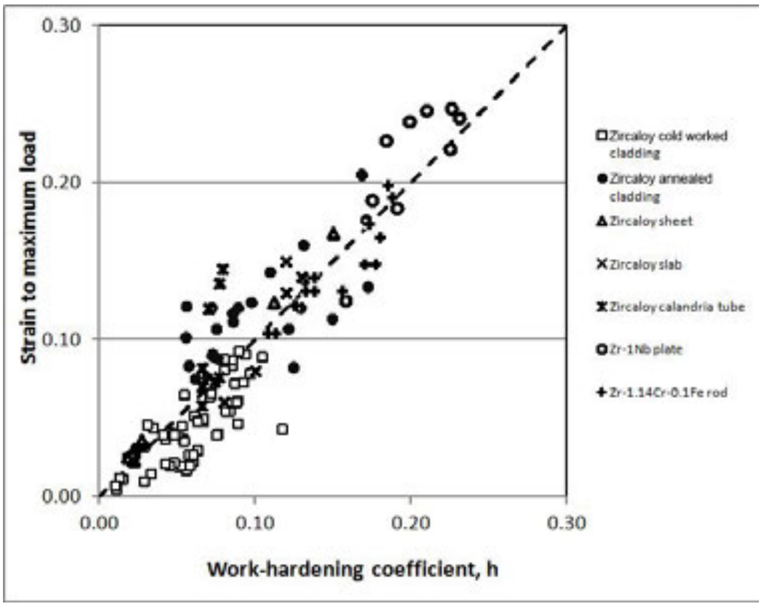

FIG. 9.13. The correlation between the strain to maximum load and work-hardening coefficient in tensile tests on Zircaloy [9.10, 9.30, 9.36, 9.46], Zr-1Nb [9.11] and Zr-1.14Cr-0.1Fe [9.45]. Dotted line is Eq. (9.3) with m *= 0.*

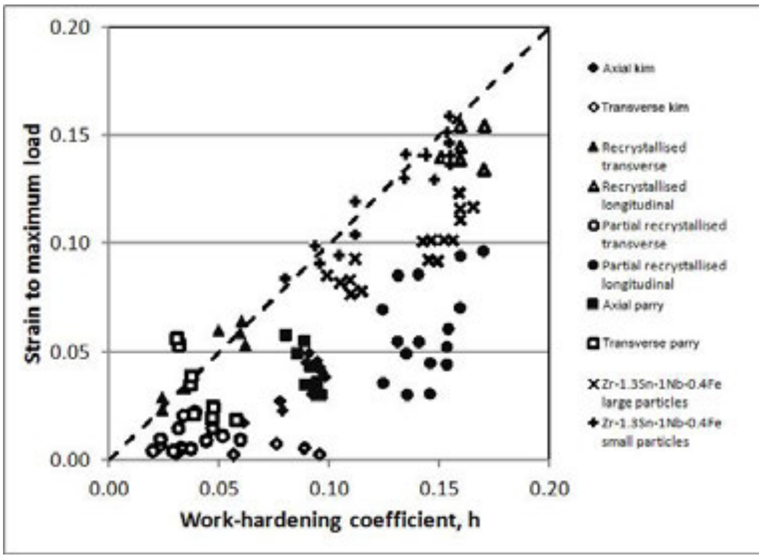

FIG. 9.14. The correlation between the strain to maximum load and work-hardening coefficient in tensile tests on Zr-2.5Nb [9.41, 9.47, 9.62] and Zr-1.3Sn-1Nb-0.4Fe [9.62]. Dotted line is Eq. (9.3) with m *= 0.*

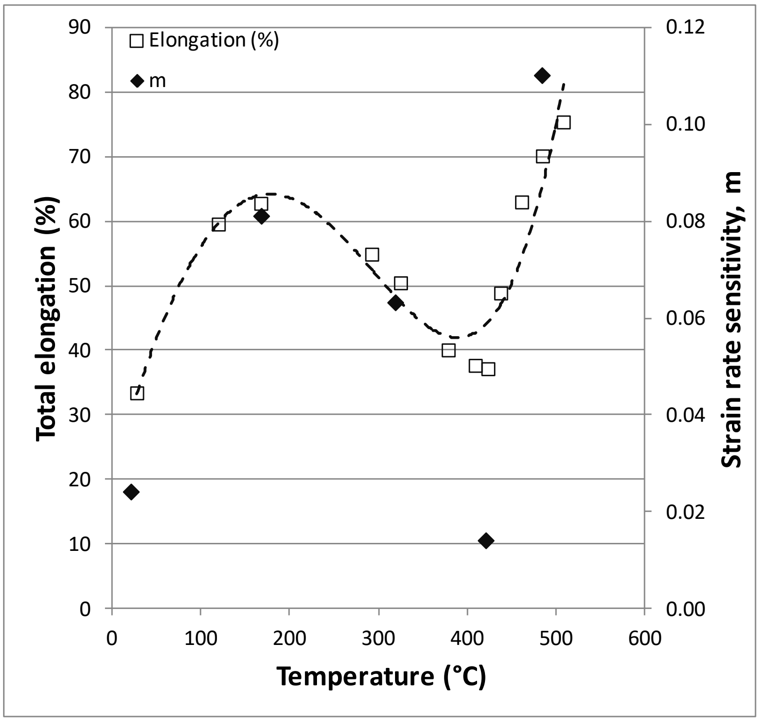

FIG. 9.15. Correlation between total elongation and m *in annealed Zircaloy-4 [9.57].*

As a neck develops, the strain is concentrated in the region of reduced cross-sectional area. Cavities, voids or pores form, usually at inclusions and second phase particles [9.63] or at triple points [9.64], in the centre of the neck because of the buildup of hydrostatic tensile stress. The material between the cavities shows necking down close to 100% and the cavities coalesce.

The development of cavities as a function of strain has been studied by following density changes and directly by metallography. A 38 mm diameter rod of pure zirconium was pulled to

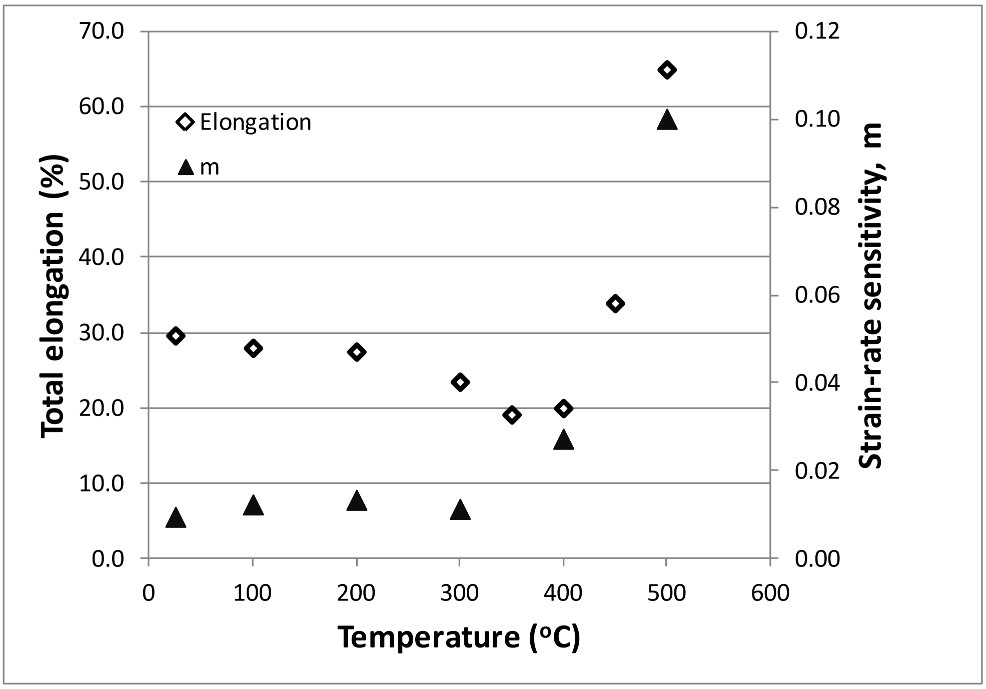

FIG. 9.16. Correlation between total elongation and m *in stress-relieved Zr-2.5Nb [9.48, 9.53].*

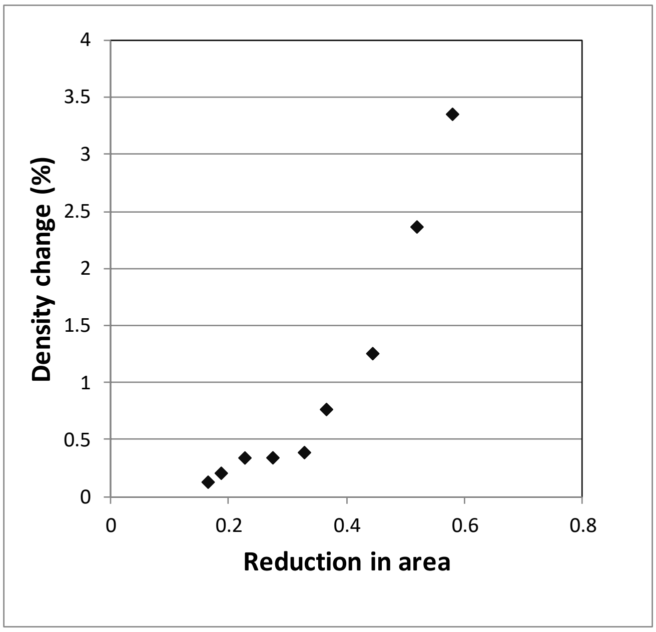

FIG. 9.17. Reduction in density as a function of strain in the neck of a tensile specimen of pure zirconium tested at room temperature (based on [9.65]).

rupture at room temperature and the development of pores was estimated from the density on discs machined at intervals from the fracture surface; the reduction in area at rupture was about 60% [9.65]. The density started to decline at a strain around 0.17, as shown in Fig. 9.17, and the maximum change in density and porosity volume close to the fracture was about 3.5%. Similar observations were made of Zircaloy-2 [9.30]. Cavities formed at intermetallic particles but well after necking had started, as

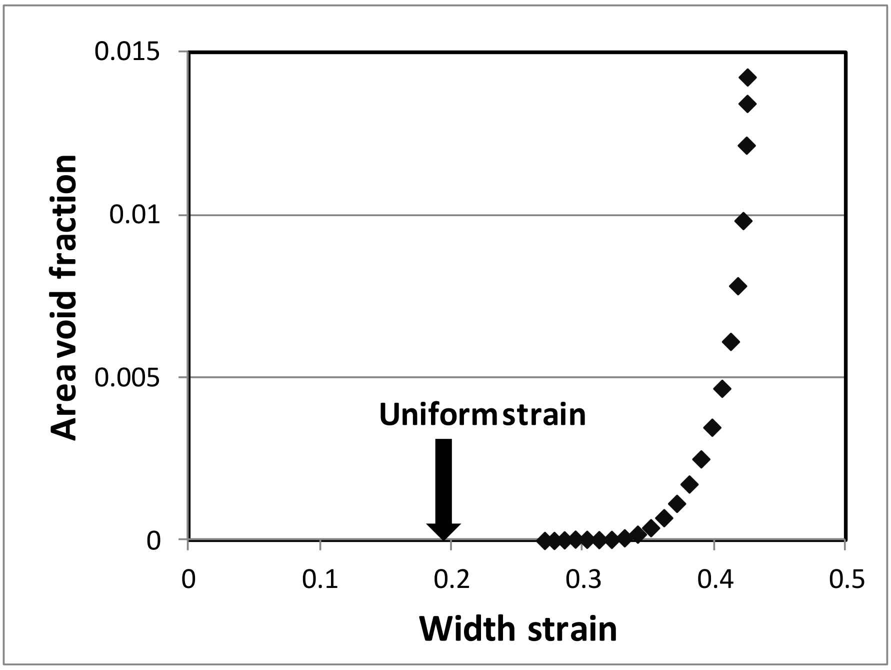

FIG. 9.18. Development of cavities in annealed Zircaloy-2 at room temperature at strains greater than uniform strain (based on [9.30]).

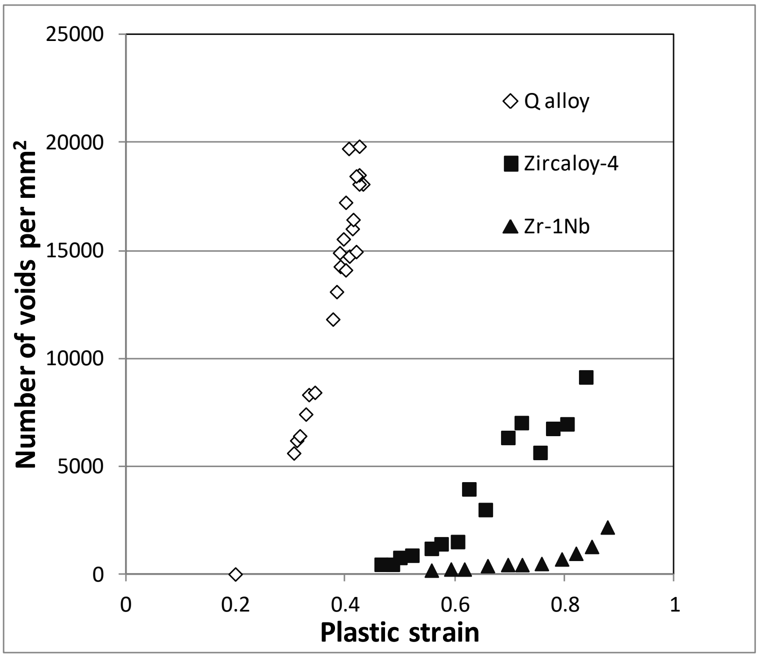

FIG. 9.19. Increase in number of cavities as a function of plastic strain in as-extruded Q-alloy, Zircaloy-4 and Zr-1Nb at room temperature (after [9.66]).

shown in Fig. 9.18. The contribution to the volume fraction of cavities can be separated into nucleation and growth. These quantities were compared in Zircaloy-4, Zr-1Nb (M5) and Zr-1Nb-0.35Fe-0.25Sn (known as Q-alloy) after hot extrusion by following the change as a function of plastic strain at room temperature [9.66]. The volume fraction followed the same form, as seen in Figs 9.17 and 9.18, with voids only being observed after necking had started; the highest values reported were

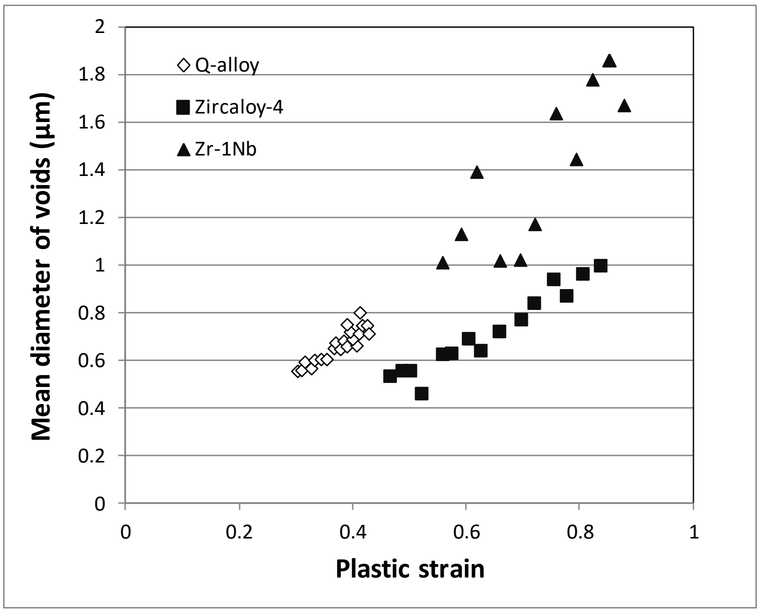

FIG. 9.20. Growth of voids as a function of plastic strain in as-extruded Q-alloy, Zircaloy-4 and Zr-1Nb at room temperature (after [9.66]).

about 0.85% before rupture — about four times less than for pure zirconium. The number of cavities depends on the number of nucleation sites, as shown in Fig. 9.19. The Q-alloy contained a mixture of $Zr(NbFe)_2$ and $(ZrNb)_4Fe_2$ particles, as well as β-Zr, with a volume fraction of 2%. Fracture started at these particles at a low strain, about 0.2, and the number of sites increased rapidly with strain until rupture at a strain of 0.42, with a reduction in area of 42%. Compared with the Q-alloy, Zircaloy-4 had a lower volume fraction of $Zr(Fe,Cr)_2$ intermetallic particles, 0.5%, and fracture started at a higher strain, about 0.45; the number of crack initiation sites increased more slowly with strain until rupture

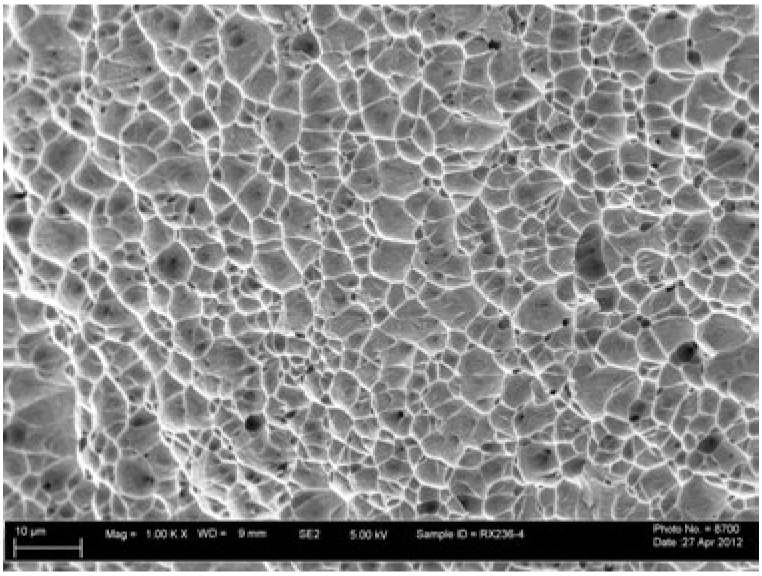

FIG. 9.21. Fracture surface of cold worked Zr-2.5Nb tested in tension at room temperature, showing uniform ductile dimples (C. Mayhew, AECL).

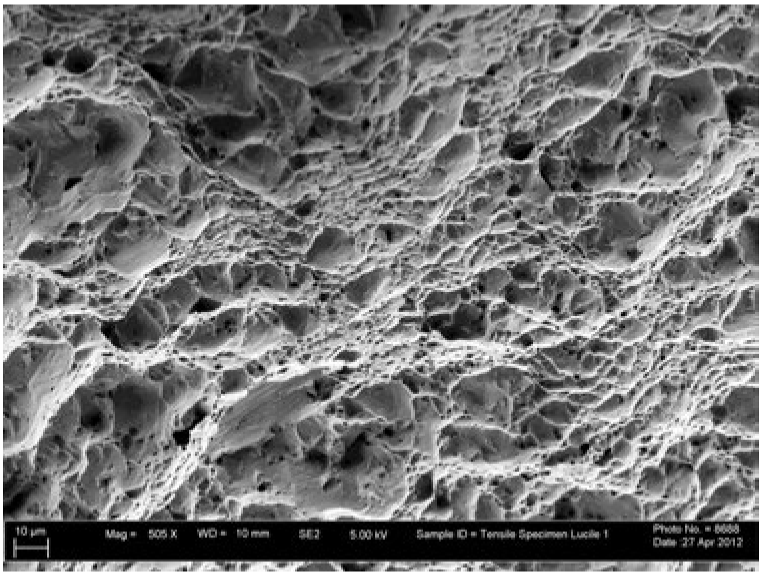

FIG. 9.22. Fracture surface of cold worked Ziracloy-2 tested in tension at room temperature, showing uneven distribution of ductile dimples (C. Mayhew, AECL).

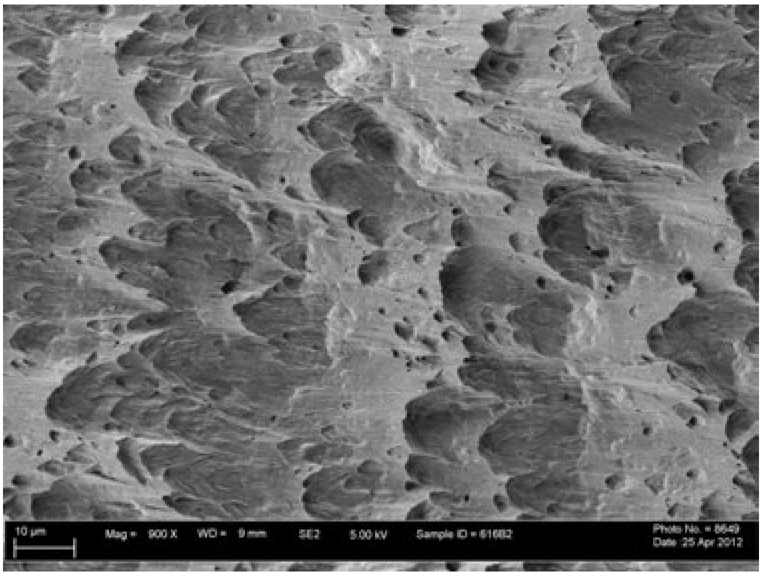

FIG. 9.23. Fracture surface of cold worked Zr-2.5Nb tested as compact tension specimen at room temperature, showing ductile tear dimples (C. Mayhew, AECL).

at a strain of 0.84, with a reduction in area of 84%. The Zr-1Nb alloy had very few intermetallic particles but contained β-Zr and β-Nb phases. In this alloy fewer cavities are nucleated and their rate of nucleation with strain is lower than in the other two alloys. These cavities are nucleated at grain-to-grain misorientations rather than at intermetallic particles, starting with a strain of over 0.5; rupture was at a strain of 0.88, with a reduction in area of 88%. The rate of void growth is also different in the three alloys, as shown in Fig. 9.20. The cavities grow faster in Zr-1Nb than in Zircaloy-4 and Q-alloy; their size in Q-alloy is limited because they coalesce at low strain because of their high number density. Although extrapolation back to zero void size seems to indicate nucleation at lower strains than those presented in Fig. 9.19, the observations suggest that the initial void diameter, d_0, is controlled by the size and shape of the initiation site at the intermetallic particles or grain boundaries. Rupture takes place when the cavities coalesce, that is, when a critical size, d_c, and a critical distance, ℓ_c, between them is attained. For these alloys the cavities coalesce when $\ell_c/d_c \approx 6$.

The fractographic features representing the coalesced cavities associated with the fracture initiation sites are termed ductile dimples. A typical uniform array of ductile dimples observed on Zr-2.5Nb tested in tension is depicted in Fig. 9.21 while Fig. 9.22 illustrates a non-uniform distribution of dimples in Zircaloy after tensile testing. The final rupture is often by shear on the annular rim of the specimen and shear dimples form, which are similar to the tear dimples shown in Fig. 9.23, which can be observed on ductile crack surfaces. (Shearing and tearing can only be distinguished if both fracture surfaces are examined; shear dimples progress in opposite directions on each face whereas tear dimples point away from the crack direction on both fracture surfaces.) Under high stress triaxiality, for example with notched specimens, tubular dimples with hexagonal section are observed [9.66], as shown in Fig. 9.24. This observation is consistent with the void growth mechanism proposed by Crépin et al. [9.67], which is based on the activation of the three prismatic slip planes, but seems to be active only at high stress triaxiality.

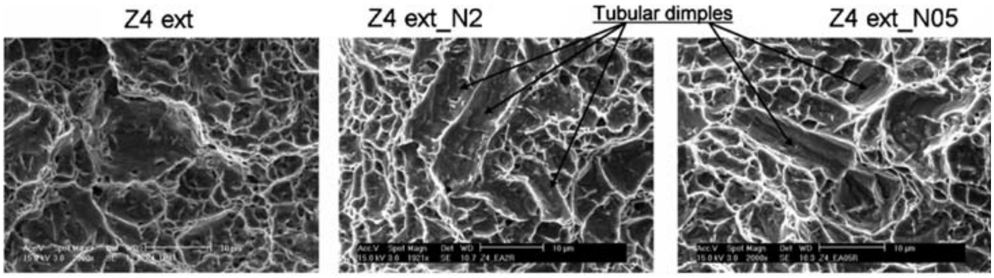

FIG. 9.24. Voids on the fracture surface of tensile specimens made from Zircaloy-4 tested at room temperature showing tubular dimples [9.66].

One might expect that the reduction in area at fracture would depend on a combination of the amount of uniform strain, how the neck develops and the efficacy of the cavity nucleation sites. The first factor depends mostly on work hardening, the second factor will depend mostly on the strain rate sensitivity while the last factor depends on alloy and impurity content and grain structure. As illustrated in Table 9.1, the plasticity factors *h* and *m* are responsible for the difference in total elongation between annealed and cold worked pure zirconium but the values of reduction in area and their temperature dependence are similar for both materials. Since the composition of the two materials was identical, this observation suggests that sources of cavity nucleation control area strain at rupture. Similarly, in Zircaloy-2 tested over a range of strain rates, as shown in Table 9.2, the total elongation is controlled by the plasticity factors while the reduction in area is not substantially affected. Other variables affecting reduction in area include the following:

(a) Composition: Figures 9.19 and 9.20 depict the importance of composition for cavity formation and the consequences for reduction in area at room temperature. As indicated in Chapter 2 in Volume 1 of this publication, many of the potential alloying elements have low solubility limits and the resulting second phase particles provide sites for cavity formation with a subsequent reduction in ductility from that of pure material as the concentration of alloying element is increased, as shown in Fig. 2.5. As suggested above, when few intermetallic particles are present, the β phase in Nb alloys does not promote cavity formation, as indicated by the insensitivity of the reduction in area to Nb concentration, as shown in Fig. 9.25 [9.43].

(b) Texture: Some of the results at room temperature in Fig. 9.25 suggest that loading parallel to [0002] may lead to a high ductility because the material deforms in all three principal directions. Tensile tests on cold worked Zr-2.5Nb pressure tubes with a strong transverse texture confirm this result [9.41], as shown in Fig. 9.26, with specimens tested in the transverse direction having a higher reduction in area than those tested in the axial direction. Tests on Zircaloy-2 calandria tubes, which have a strong radial texture, show little difference in reduction in area when loaded in the same two directions [9.46], as shown in Fig. 9.27.

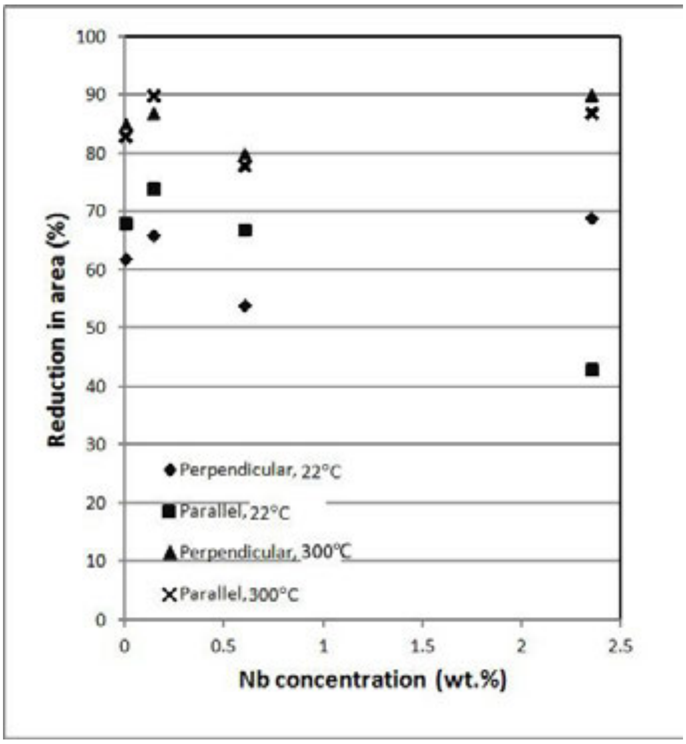

FIG. 9.25. Insensitivity of reduction in area to Nb concentration at two temperatures and tested perpendicular and parallel with [0002] (based on [9.43]).

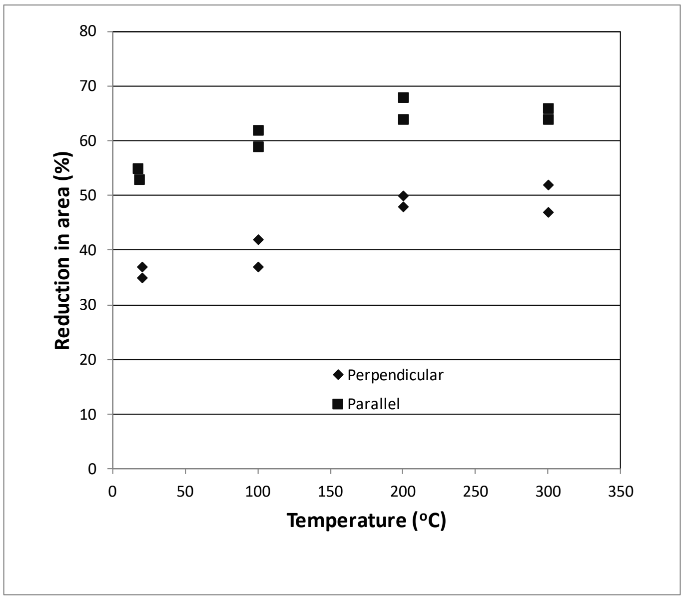

FIG. 9.26. Reduction in area from tensile tests of cold worked Zr-2.5Nb loaded in the axial (perpendicular to the [0002]) and transverse (parallel with the [0002]) directions [9.41].

(c) Test temperature: The results presented in Table 9.1 and Figs 9.25 to 9.27 show that reduction in area increases with test temperature, although the contributions of void nucleation and growth to the temperature dependence are unknown. In Zircaloy-2 the temperature dependence of elongation and reduction in area are similar up to about 273 K (200°C) but subsequently deviate at higher temperatures, as shown in Fig. 9.27, with elongation declining following the temperature dependence of *m*, as shown in Figures 9.11 and 9.15.

(d) Grain size: Reduction in area increased with a decrease in recrystallized α grain size in pure zirconium reflecting the smaller stress intensification available to initiate cavities with small grains; a $d^{-1/2}$ dependence fits the data, as shown in Fig. 9.28 [9.6, 9.7]. A similar correlation is found with prior β grain size when Zr-2.5Nb is quenched from the β phase, as shown in Fig. 9.29 [9.38, 9.68, 9.69]. When the β grain size is limited by α grains by quenching from the (α + β) phase region, the reduction in area is independent of β grain size once it is smaller than about 28 μm ($d^{-1/2}$ of about 6 $mm^{-1/2}$).

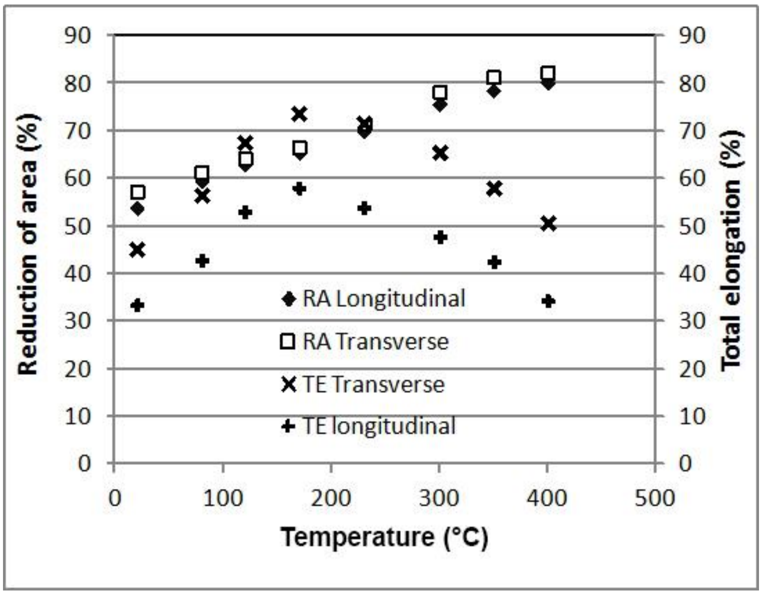

FIG. 9.27. Dependence on test temperature and testing direction of reduction in area (RA) and total elongation (TE) of Zircaloy-2 calandria tubes (after [9.46]).

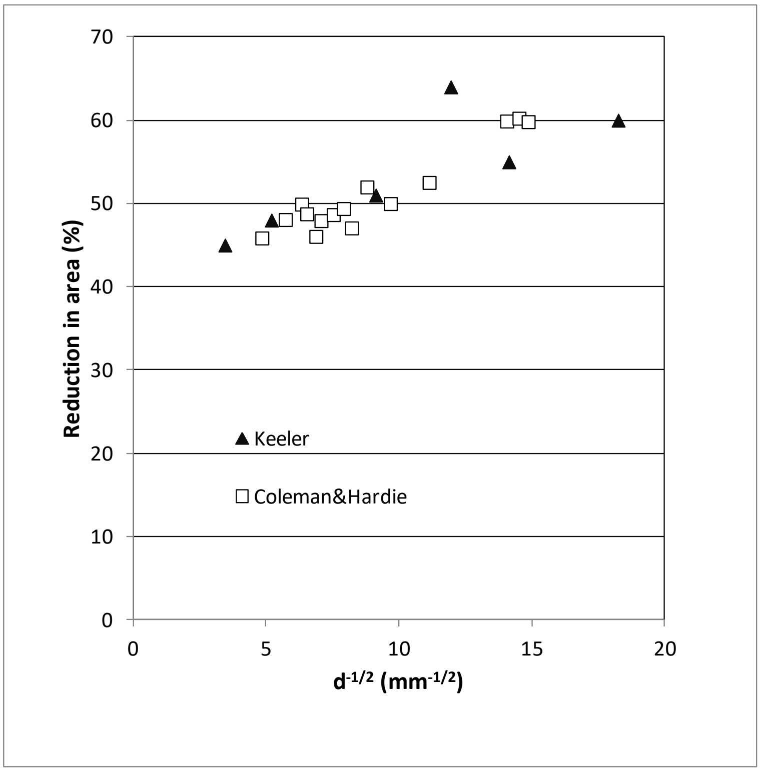

FIG. 9.28. Grain size dependence of reduction in area in pure zirconium at room temperature [9.6, 9.7].

TABLE 9.2. EFFECT OF STRAIN RATE ON THE TENSILE BEHAVIOUR OF ANNEALED ZIRCALOY-2 TESTED AT 623 K (350°C) [9.10]

Strain rate (s^{-1})	Elongation to maximum load	h	Elongation during necking	m	Total elongation	Reduction in area (%)
1.05E-02	0.15	0.12	0.34	0.052	0.49	81
1.05E-03	0.14	0.13	0.32	0.028	0.46	81
1.05E-04	0.13	0.12	0.25	0.015	0.38	79
1.05E-05	0.08	0.10	0.22	0.014	0.30	77
1.05E-06	0.06	0.08	0.24	0.018	0.30	77

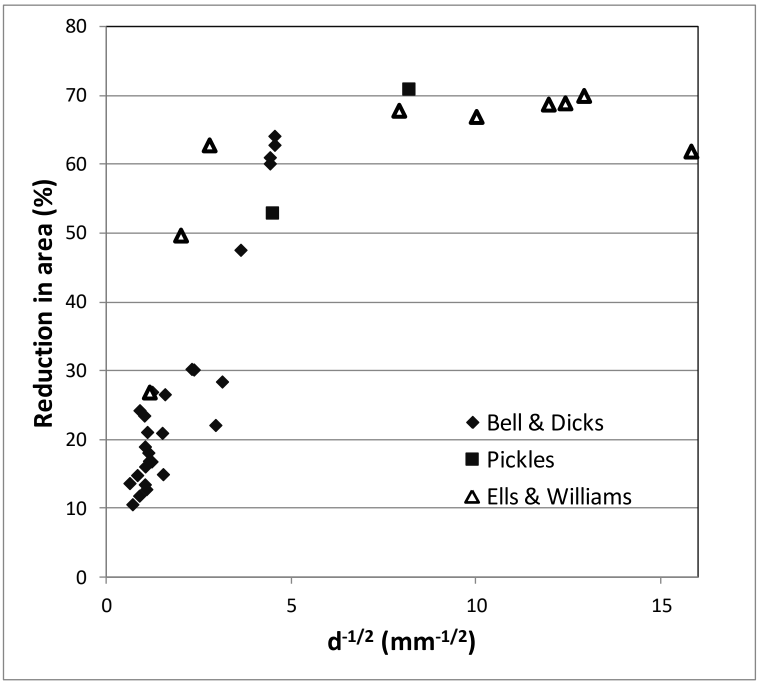

FIG. 9.29. Dependence of reduction in area on β grain size in quenched Zr-2.5Nb (based on [9.38, 9.68, 9.69]).

9.2.2. Behaviour of irradiated material

The effects of irradiation on the mechanical properties of zirconium alloys are described in Chapter 6, Volume 2 of this publication. A wide response of these properties to irradiation has been reported that depends on the starting microstructure and the conditions of irradiation and testing. At reactor operating temperatures (520–630 K (250–360°C)), the strength increases between 10 and 80% up to a fluence of about 3 × 10^{24} n/m^2; in general the larger proportional increase is obtained with weak starting materials and vice versa. The transient is followed by a gradual increase in strength with neutron fluence, as shown in Figs. 6.35 and 6.36. As a further example, compared with unirradiated material, the proportional response of annealed Zircaloy to irradiation temperature is illustrated in Fig. 9.30 for uniaxial tensile tests in the ranges 300 to 500 K (27–227°C) and 520–680 K (250–410°C) [9.30, 9.36, 9.43, 9.70–9.83]. The values represent a wide range of neutron flux and maximum fluence in each study and show that the increase in strength could be close to 300%. Despite the similarity of the starting materials, the data are very scattered, which is attributed to flux effects at high temperatures and fluences not always exceeding 3 × 10^{24} n/m^2. Test temperature only seems to affect the strength after irradiation in the range 520 to 630 K (250–360°C), where much irradiation hardening can be attained. A maximum in the hardening with the higher test temperatures seems to be associated with this range in irradiation temperatures. As the irradiation temperature is increased beyond 630 K (360°C), the irradiation damage starts to anneal out as fast as it is produced and the hardening diminishes. This high temperature response is strongly affected by neutron flux, with a high flux raising the temperature at which no hardening is produced.

Dislocation loops developed during irradiation are responsible for strengthening. During tensile testing, mobile dislocations can annihilate the loops in narrow bands (or channels or swaths), as shown in Fig. 6.42. Softening is observed that is associated with this loss of the strengthening agents, and the maximum load is attained at low strains, as shown in Fig. 6.34. This phenomenon is an example of the development of plastic instability in strengthened metals through strain softening [9.84]. When ductility is measured by total elongation, it is mostly affected through the loss in uniform strain. The mode of fracture is by cavity coalescence and the fracture surface consists of ductile dimples because, although the second phases may change, the underlying grain structure and composition (apart from a minor amount of transmutation (discussed in Appendices I and II of Volume 2)) are not affected by irradiation. Thus reduction in area is not always impaired by irradiation to the same extent as elongation. Some examples are given below.

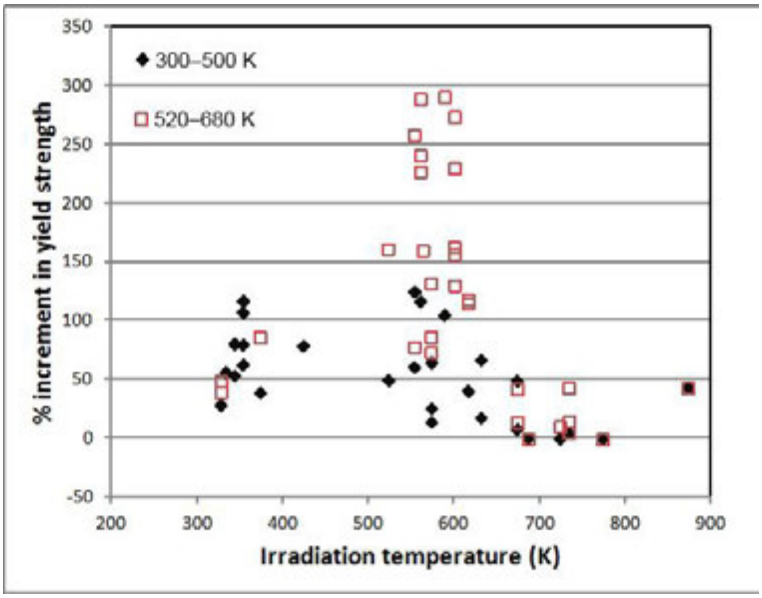

FIG. 9.30. Effect of irradiation temperature on increment of yield strength of annealed Zircaloy tested in the ranges 300–500 K (27–227°C) and 520–680 K (247–407°C) [9.30, 9.36, 9.43, 9.70–9.83].

The clearing out of irradiation damage depends on irradiation conditions, amount of strain, test temperature and material texture, composition and microstructure. Irradiation damage locks the sources of mobile dislocations and a high stress is required to activate them — hence irradiation strengthening. Once activated, avalanches of dislocations sweep away the irradiation barriers and create a softened zone that ends at a grain boundary or is restricted by other microstructural features, such as dislocation cell structures in cold worked material [9.72, 9.85]. The tendency to form channels increases as the yield strength of the material rises with the amount of irradiation leading to a threshold fluence. For example, a threshold fluence for the formation of channels was indicated in annealed Zircaloy-2 irradiated between 423 and 473 K (150 and 200°C); after deformation at 593 K (320°C) material irradiated to 3.0×10^{24} n/m^2 contained channels whereas material irradiated to 3.2×10^{23} n/m^2 did not [9.86]. Also, in annealed Zircaloy-4 irradiated at ≤ 373 K (100°C) and tested at room temperature, channels were only observed in material irradiated to a fluence $\geq 6.7 \times 10^{22}$ n/m^2 (0.01 dpa); these channels were observed on prism planes [9.87]. Channels free of irradiation damage are observed before their effect is manifest on a macroscale as a load drop [9.88–9.90]. Since less force is required to maintain further deformation after the initial channels are formed, new sources of dislocations are difficult to activate in the surrounding strong material in the original grain and the increase in the number of channels declines. The deformation is heterogeneous; in annealed alloys tested at 623 K (350°C), between 40 and 60% of the grains contained narrow channels. The width of the channels, as shown in Fig. 9.31, and their spacing seems to have a weak dependence on the irradiation fluence, but none on test temperature or plane of the channel, as shown in Table 9.3 [9.72, 9.79, 9.87–9.93]. The volume fraction of basal plane channels was saturated by 0.5% plastic strain [9.90]. The confined strain within the channels can be very high, over 100% [9.91], producing high stresses at the grain boundaries that may lead to new channels in the adjacent grains [9.88, 9.90], and displacement at the boundaries [9.91, 9.92] or surfaces [9.89]. As the material is deformed, the original channels work harden and dislocation cells form in material free of irradiation damage [9.72, 9.89, 9.93]. Subsequent deformation continues to be restricted and appears as shear bands that are visible to the naked eye on the surface [9.71, 9.72, 9.89], as shown in Fig. 6.39.

When pure zirconium is unirradiated, the critical resolved shear stress (CRSS) for prism slip is usually much lower than for basal slip, as shown in Fig. 9.32 [9.94]. When the Schmid factor (given by Eq. (5.19 in Chapter 5, Volume 1 of this publication) is applied to individual grains in irradiated material, high values for basal slip lead to channels on basal planes whereas high values on prism planes do not always lead to channels on prism planes. In irradiated material the basal CRSS tends to be lower than that for prism slip — for example, 84 to 140 MPa for basal slip compared with 105 to 175 MPa for prism slip at 623 K (350°C) [9.90] — and prism channels tend to be observed only when Schmid factors for basal planes are low and for prism planes are high [9.90, 9.95]. This difference in the response of each slip plane is explained as follows: in the hexagonal close packed structure, the junctions created between an <a> dislocation loop and an <a> dislocation gliding in the basal plane are glissile whereas the junction created between an <a> dislocation gliding on the prismatic plane interacting with an <a> loop is sessile in two out of three possible configurations, leading to more difficult channelling and therefore a higher CRSS [9.89, 9.90, 9.93].

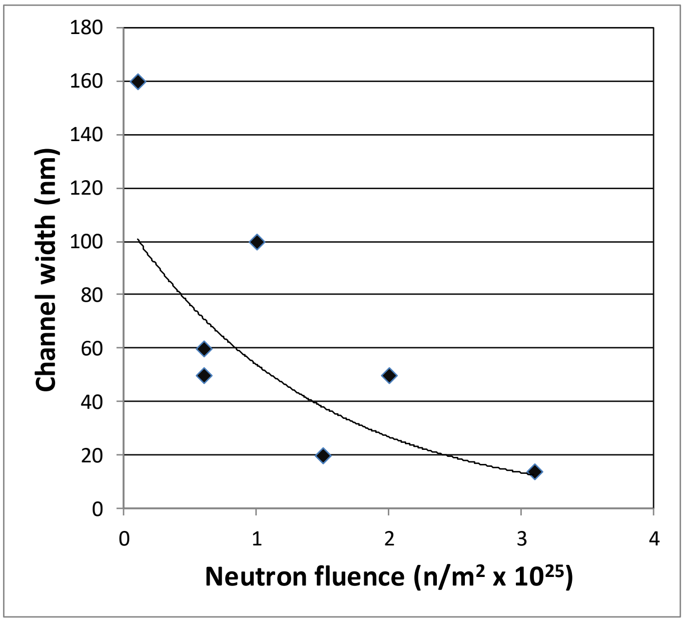

FIG. 9.31. Decrease in width of channels cleared of irradiation with irradiation fluence; irradiation temperatures between 560 and 610 K (290 and 340°C) (see Table 9.3).

TABLE 9.3. VALUES OF WIDTH AND SPACING OF CHANNELS CLEARED OF IRRADIATION DAMAGE IN ZIRCALOY

Material	Irradiation conditions		Test conditions		Channels			Source
	Temperature °C	Fluence n/m^2 (× 10^{25})	Temperature °C	Orientation	Width nm	Spacing nm	Plane	
Annealed Zircaloy-4 sheet	280	0.6	350	Transverse	50–70	650	Basal	[9.90]
Annealed Zircaloy-4 sheet	280	0.6	350	Transverse	30–70	600	Basal	[9.93]
Annealed Zircaloy-4 cladding	380	3.1	350	Transverse	14	120	Basal	[9.93]
Annealed Zircaloy-4 sheet	<100	0.55	25	Longitudinal	40–75	400–1100	Prism	[9.87]
Annealed Zircaloy-2 rod	290	1		From hydrides during cooling	≈100	—	Prism	[9.91]
Annealed Zircaloy-4 cladding	290	0.1	300	Longitudinal	160	—	—	[9.72]
Annealed Zircaloy-2 sheet	150	0.032	25	Transverse	40	—	—	[9.88]
Annealed Zircaloy-2 sheet	150	0.032	300	Transverse	100	—	—	[9.88]
Annealed Zircaloy-2 sheet								
Low oxygen	327	1.5	327	Transverse	≈20	—	Basal	[9.79]
Annealed Zircaloy-2 sheet								
High oxygen	327	1.5	327	Transverse	≈ 20	—	Prism	[9.79]

Although slip is sometimes observed on pyramidal planes, the difference in the propensity for deformation on the two main planes, basal and prism, leads to texture, test temperature and compositional effects. The following are examples:

— When annealed and irradiated Zr-1Nb fuel cladding, with a basal texture 20° from the radial direction, was stressed at 623 K (350°C) in the transverse direction only basal channels were observed whereas prism and some pyramidal channels were observed after stressing in the longitudinal direction [9.90]. When transverse specimens of similar material were tested at room temperature, both prism and basal channels were observed. Between 293 and 523 K (20 and 250°C) the strength of both irradiated and unirradiated materials decreases with test temperature at about the same rate, as shown in Fig. 9.30, showing that test temperature may have little influence on the irradiation induced hardening in this test temperature range. If the increment with irradiation in the CRSS of both the basal and prismatic slip consists of a constant increment independent of the test temperature, and the increment of CRSS is much higher for prismatic slip than for basal slip, the possible consequence for deformation can be illustrated schematically, as shown in Fig. 9.33 [9.95]. As an example, a reversal of the prismatic and basal CRSS with irradiation is observed at 623K (350°C), leading to a change of the easy glide slip system from the prism plane to the basal plane. When the temperature is about 293 K (20°C), CRSS on each plane is close so small differences in the Schmid factor will allow clearing out of damage on either plane.

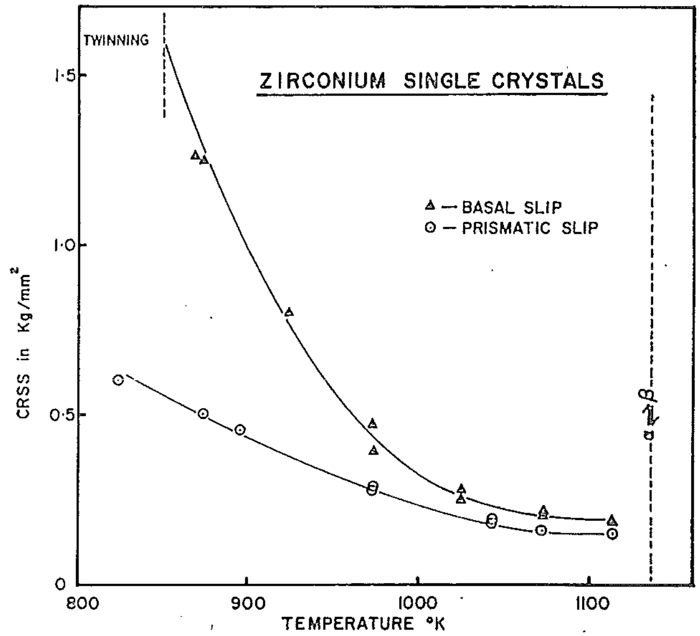

FIG. 9.32. Effect of temperature on critical resolved shear stress in single crystals of pure zirconium [9.94].

— The change with irradiation in the anisotropy in Zircaloy-2 calandria tubing with Kearns' factors of F_R between 0.6 to 0.8, F_T between 0.2 to 0.3 and F_L of about 0.1 can be interpreted similarly [9.82]. Before irradiation, the strength in the transverse direction is greater than that in the longitudinal direction whereas after irradiation close to 20 × 10^{25} n/m², little difference in strength is detected in the two directions. The increase in strength is less for the transverse direction (oriented favourably for basal slip) than for the longitudinal direction (oriented favourably for prism slip).

— After irradiation and testing at 600 K (327°C), Zircaloy containing low (44 ppm (0.025 at.%)) and high (1500 ppm (0.85 at.%)) concentrations of oxygen had similar strengths [9.79]. The specimens were transverse to the rolling direction of sheets with basal pole maxima about 20° to the sheet plane normal in the through-thickness-transverse plane. The specimens containing low oxygen concentration exhibited small serrations in their load elongation curves after maximum load and the irradiation damage was cleared out on basal planes and

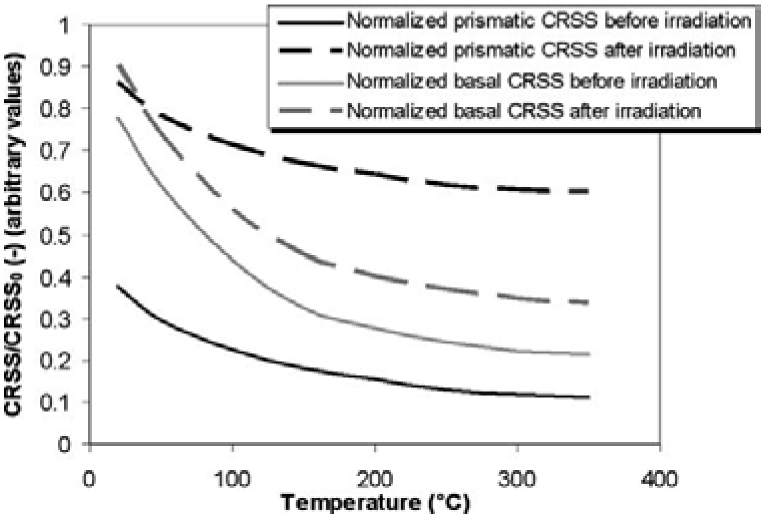

FIG. 9.33. Schematic diagram of the temperature dependence of the critical resolved shear stress (CRSS) of prism and basal slip before and after irradiation [9.95].

planes containing a basal component leading to strain in the thickness direction of the specimen. The load elongation curve of the specimens containing high oxygen concentration had a few large load drops and the irradiation damage was cleared out mostly on prism planes with little strain in the thickness direction. The change in mode of deformation is attributed to the interaction of the oxygen atoms with the irradiation damage and possible high stacking fault energy with low oxygen concentration aiding cross-slip from prism to basal planes.

Most of the observations on clearing out irradiation damage are on annealed Zircaloy. Irradiation damage is also annihilated in cold worked materials during deformation but the channels are much less obvious and the original dense dislocation structure both impedes their development and obscures their observation [9.72, 9.85]. Channelling in β quenched or welded Zircaloy is also obstructed by the Thomson–Widmanstätten structure, or grain-to-grain variation in texture or both [9.91]. Irradiation damage inhibits twinning at low test temperatures. Tests at room temperature on annealed zirconium showed that a small dose of irradiation can raise the stress to nucleate twins by nearly 50% [9.77, 9.96]. In highly textured, cold worked Zr-2.5Nb tested, as shown in Fig. 9.7(c), after irradiation, twinning contributed up to 25% of the strain. At about 420 K (150°C) and higher, the twinning stress was similar to the yield stress. Twin planes $\{10\bar{1}2\}$ and $\{10\bar{1}1\}$ are expected (see Chapter 5, Volume 1 of this publication) and they have been observed in irradiated Zircaloy cladding deformed at 600 K (327°C) [9.97] and in Zr-2.5Nb [9.85]. Deformation twins have been observed to contain dislocation loops, even after much plastic strain, indicating that twins are less effective than slip dislocations in removing irradiation damage [9.43, 9.77, 9.85]. Subsequent slip in the material reoriented by twinning can be effective in removing irradiation damage.

The consequence of the destruction of irradiation strengthening by strain leads to a large reduction in strain to maximum load and *h*. Despite some reservations [9.20], the phenomenological link between *h* and strain to maximum load is often maintained. Some examples are given below:

- Tests at room temperature after a low temperature irradiation lead to a consistent reduction in *h* in annealed and cold worked Zircaloy-2 [9.30], as shown in Fig. 9.34. The initial directional difference caused by texture is much diminished.
- A similar reduction was observed in pressure tubes of the N reactor made from cold worked Zircaloy-2 [9.98], as shown in Fig. 9.35. The maximum operating temperature was 555 K (282°C) and specimens were machined in the longitudinal direction and tested at 305 K (32°C) and 561 K (288°C). The strain to maximum load and *h* followed the same fluence dependence as with low temperature irradiation and testing.
- After irradiation at 588 K (315°C), annealed Zircaloy-4 strip exhibited a similar loss in work hardening ability, but *h* passed through a minimum at a neutron fluence of about 1×10^{24} n/m^2 [9.80], as shown in Fig. 9.36. A similar minimum was detected in Zircaloy-2 sheet prepared with three different annealing parameters, ranging from 1.45×10^{-19} *h* to 3.46×10^{-21} *h*, and irradiated at 561 K (288°C) to three fluences [9.99], as shown in Fig. 9.37. Tensile tests at room temperature on α annealed and β heat treated Zircaloys irradiated at 631 K (358°C) also exhibited minima in uniform and total elongations at neutron fluences between 5 and 10×10^{24} n/m^2 [9.83]. Garde et al. [9.100] have suggested this effect may be caused by the development of irradiation induced <c>type dislocation defects acting as impediments to channelling and providing some strain hardening, although the fluence may be too low for such dislocations [9.101].
- Tensile tests on Zircaloy-4 fuel cladding in several metallurgical conditions and tested at 293 K (20°C) and 573 K (300°C) as axial and ring specimens continue to follow Eq. (9.3) after irradiation at 523 K (250°C), even though the work hardening is much reduced [9.36], as shown in Fig. 9.38.

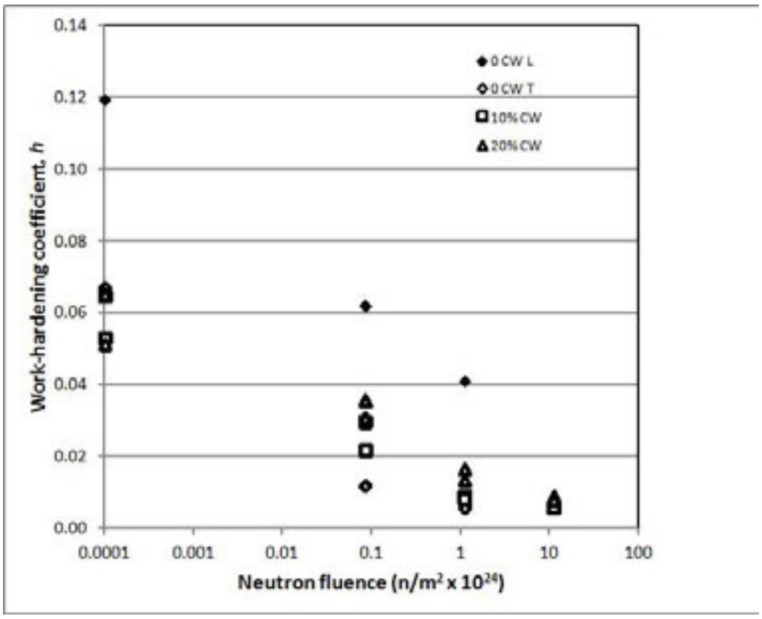

FIG. 9.34. Reduction at room temperature in work-hardening of Zircaloy-2 sheet material with low temperature irradiation. L — longitudinal; T — transverse; CW — amount of cold work. Note: for plotting zero fluence is represented by 0.0001 [9.30].

— Similar behaviour was observed in annealed Zr-1.14Cr-0.1Fe rod material after irradiation at 573 K (300°C) and testing at room temperature and 573 K (300°C) [9.45]. Again, both strain to maximum load and work hardening were much reduced by irradiation, as shown in Fig. 9.39.

Measurements of *m* in irradiated material in the temperature range 298–623 K (25–350°C) have been made using either stress relaxation or variation in yield stress and the values are summarized in Table 9.4. Some values indicate that the starting low value may be reduced further [9.72, 9.77, 9.81, 9.102], others show an increase in *m* with irradiation [9.103, 9.104], while a few data show no difference [9.52, 9.102]. The increase in *m* by irradiation has been attributed to the change in slip plane from prism to basal plane [9.104]. Values pre- and post-channelling hint that some recovery towards the initial value may be possible [9.72].

The examples in Figs 9.35 to 9.39 illustrate the large decrease in uniform elongation caused when irradiation damage is annihilated, especially in material that starts out in the annealed condition. The subsequent amount of elongation before rupture, the necking strain, is decreased because the effective gauge length of specimens is reduced by the localization of the deformation, which may be exacerbated if *m* is also reduced by irradiation. The total elongation is thus much reduced. A representative example is provided in Table 9.5 where cold worked and stress relieved (CWSR) and annealed Zircaloy-4 are compared [9.80]. The reduction in the uniform strain by irradiation is not much affected by the test temperature but the remnants of cold work ameliorate the severity of the loss of the ability to hold a load. This effect reflects channelling being obstructed by the forest dislocations. The necking strain is also much reduced by irradiation in annealed material but less so in the CWSR material.

The possible suppression of channelling in β treated microstructures may be expected to reduce the loss in uniform elongation by irradiation. Table 9.6 [9.36, 9.80, 9.91] lists some values of uniform strain before and after the irradiation of annealed material and the same material that has been heated into the β phase for a short time then cooled rapidly to room temperature to simulate welding or brazing. With one exception, the α annealed material suffered the expected large reduction in uniform ductility when irradiated. The results for the β treated material were inconsistent. The β treatment itself may reduce the initial ductility. In some samples, but not all, the value of uniform elongation was larger and its percentage drop after irradiation was smaller for the β treated material than for the α annealed material.

TABLE 9.4. EFFECT OF NEUTRON IRRADIATION ON STRAIN-RATE SENSITIVITY

Material	Condition	Method	Test temperature (°C)	m		Source
				Unirradiated	Irradiated	
Zircaloy-2	α annealed plate	Stress relaxation	25	0.02–0.027	0.02–0.023	[9.102]
Zircaloy-2	β annealed plate	Stress relaxation	25	0.02–0.023	0.015–0.018	
Zircaloy-2	Annealed calandria tube	Rate dependence of YS	70	0.028–0.048	0.025–0.037	[9.52]
Zircaloy-4	Annealed cladding	Rate dependence of YS	290	0.03	0.03–0.034	[9.103]
Zircaloy-4	Annealed cladding	Stress relaxation <0.3% strain	300	0.094–0.12	0.016–0.020	[9.72]
		>1% strain		0.052–0.071	0.036–0.044	
Zircaloy-4	Cold worked cladding	Stress relaxation <0.3% strain	300	0.045–0.060	0.008–0.017	[9.72]
		>1% strain		0.045–0.060	0.021–0.033	
Zr-1Nb	Annealed cladding	Rate change of YS and stress relaxation	350	0.013–0.005	0.032–0.034	[9.104]
Zirconium	Annealed sheet	Rate dependence of YS	25	0.087	0.033	[9.77]

Note: YS — yield stress.

TABLE 9.5. TYPICAL LOSS IN DUCTILITY IN ZIRCALOY-4 CAUSED BY NEUTRON IRRADIATION [9.80]

Material	Test temperature (°C)	Irradiated	Uniform strain	% reduction with irradiation	Necking strain	% reduction with irradiation
CWSR	20	Yes	0.007-0.018	59-84	0.053-0.045	58-64
Annealed	20	No	0.0113		0.277	
Annealed	20	Yes	0.002-0.011	90-98	0.027-0.043	84-90
CWSR	315	No	0.027		0.093	
CWSR	315	Yes	0.003-0.014	48-89	0.071-0.085	9-24
Annealed	315	No	0.182		0.168	
Annealed	315	Yes	0.003-0.006	97-98	0.047-0.056	67-72

Fractography of broken irradiated specimens shows the presence of ductile dimples, indicating cavity formation and coalescence. Yasuda et al. [9.81] reported that in tests at room temperature the number density of dimples increased by nearly three times when annealed Zircaloy-2 cladding was irradiated to 1.1 × 10^{25} n/m^2 while the average diameter decreased from 2.2 µm down to 1.6 µm. Other examples of ductile fracture in Zircaloy are listed in Table 9.7 [9.72, 9.91, 9.100, 9.103, 9.105–9.107]. The ranges of dimple sizes are estimated from the published photographs. The wide dispersion of sizes prevents further reliable conclusions on the effects of irradiation and test temperature other than these observations showing that irradiation does not qualitatively affect the fracture processes and lead to an embrittlement. Its role is to strengthen and produce inhomogeneous plastic instability and strain localization.

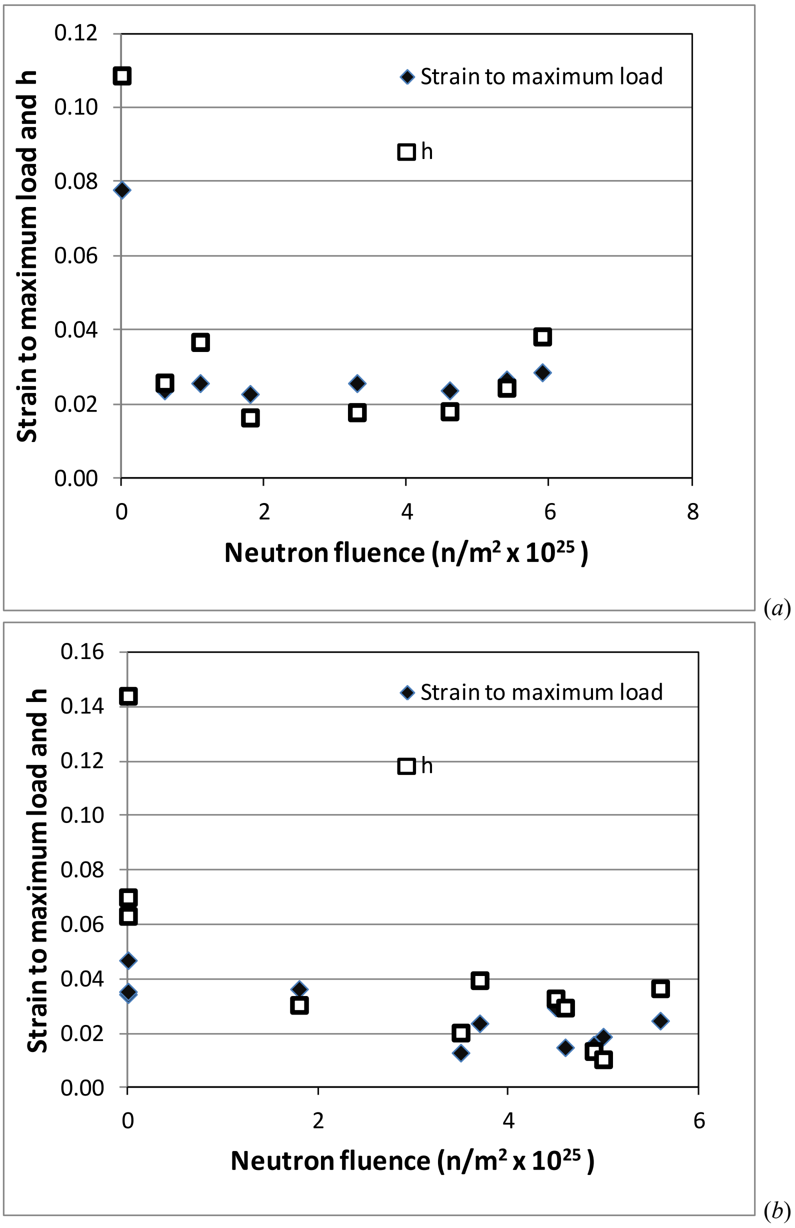

FIG. 9.35. Effect of neutron fluence on values of work-hardening and strain to maximum load in Zircaloy-2 pressure tubes operating in the N-reactor with a maximum temperature of 555 K (282°C) and tested at (a) 305 K (32°C) and (b) 561 K (288°C) [9.98].

TABLE 9.6. EFFECT OF β HEAT TREATMENT AND IRRADIATION ON DUCTILITY OF ZIRCALOY [9.36, 9.91, 9.80]

Material	Neutron fluence × 10^{25} (n/m^2)	Test temperature (°C)	Annealed Uniform strain	% drop with irradiation	β heat treatment		Source
					Uniform strain	% drop with irradiation	
Zircaloy fuel cladding	0	20	0.14		0.107		[9.36]
Axial tensile tests	0.2	20	0.042	70	0.018	83	
	0	300	0.16		0.094		
	0.2	300	0.002	99	0.009	90	
Zircaloy-2 strip					Weld		[9.91]
Transverse	0	288	0.145		0.043		
	1.5	288	0.007	95	0.011	74	
Longitudinal	0	288	0.11				
	1.5	288	0.008	92			
β-quench	0	342			0.024		
	1.0	342			0.012	50	
Zircaloy-4 strip longitudinal	0	20	0.113		0.122		[9.80]
	10	20	0.011	90	0.031	75	
	0	315	0.182		0.118		
	10	315	0.006	97	0.005	96	

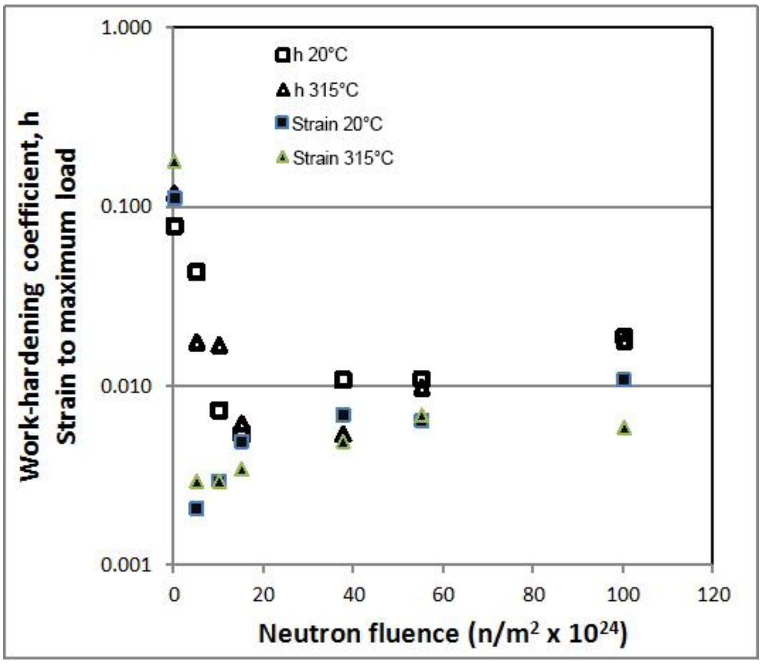

FIG. 9.36. Effect of irradiation at 588 K (315°C) on work-hardening and strain to maximum load of annealed Zircaloy-4 tested at 293 and 588 K (20 and 315°C) [9.80].

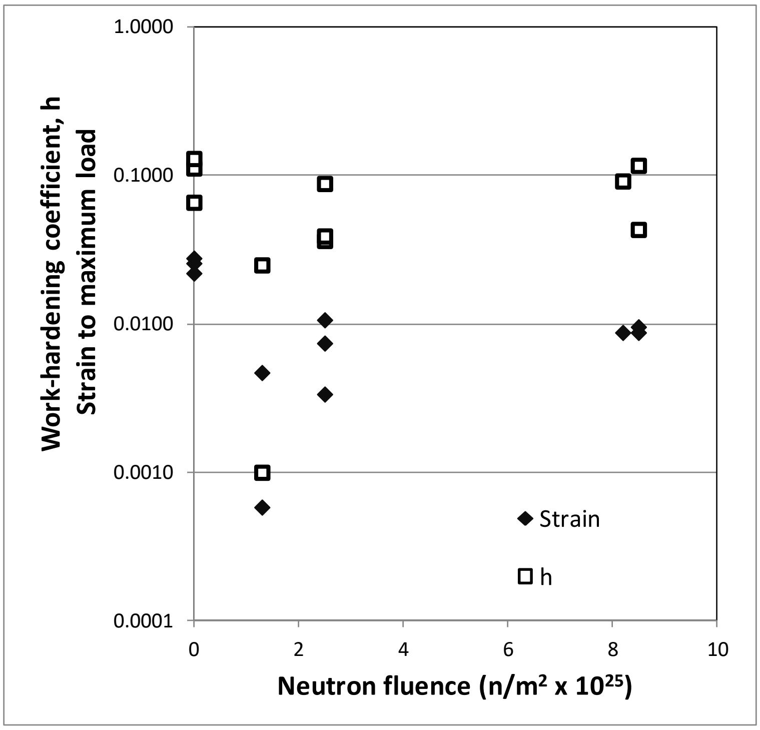

FIG. 9.37. Effect of irradiation at 561 K (288°C) on work-hardening and strain to maximum load of Zircaloy-2 fabricated by three routes and tested at 561 K (288°C) [9.99].

TABLE 9.7. EXAMPLES OF DUCTILE FRACTURE IN IRRADIATED ZIRCALOY

Material	Irradiation conditions		Testing conditions		Dimple size mean (range) μm	Source
	Fluence 10^{25} n/m^2	Temperature °C	Type	Temperature °C		
Annealed Zircaloy fuel cladding	0.1	290	Tensile	300	3 (1–10)	[9.72]
Zircaloy-2 sheet (low oxygen)	2.8	327	Tensile	327	(1–7)	[9.91]
Zircaloy-4 guide tube	9.0 (E>0.82 MeV)	298	Tensile	25	(2–4) & (10–15)	[9.100]
Zircaloy-4 fuel cladding, CWSR	5 cycles in PWR	350	Tube tensile	300	4 (1–14)	[9.106]
Zircaloy-2 annealed cladding	0	—	Tube tensile	25	2.7	[9.81]
	0.14	287	Tube tensile	25	1.7	
	1.1	287	Tube tensile	25	1.6	
Zircaloy tubes	0.41	285	Burst	300	(4–18)	[9.103]
Zircaloy-2 annealed, water rod	7	288	LDA	332	(6–7)	[9.107]
Zircaloy	1.4	327	LDA	350	11 (3–24)	[9.105]

The confinement of the deformation to a limited region tends to augment the hydrostatic stresses in the neck and restricts the reduction in area. Since the fracture mechanism is not changed from that of unirradiated material, any decrease in the values of reduction in area is caused by the strain localization, perhaps quantitatively affecting the nucleation and growth of cavities, as indicated in [9.81]. Figure 9.40 depicts the reduction in area as a function of irradiation fluence in both cold worked and annealed Zircaloy materials irradiated between 555 and 600 K (282 and 327°C) and tested between 523 and 605 K (250 and 332°C) [9.43, 9.73, 9.79, 9.91, 9.98, 9.107–9.109]. The decline in reduction in area seems to halt in both materials at about 2 × 10^{25} n/m^2 and thereafter remains steady at about 30%. The great difference induced by irradiation, between the start of strain localization, characterized by uniform strain, and the final ductility, characterized by reduction in area, is illustrated by comparing the change of each measure relative to that of unirradiated material, as shown in Fig. 9.41. The big decrease in the strain to maximum load by irradiation is apparent at very low fluences. With higher fluences, the relative decreases indicated by each measure seem to converge because the loss in uniform strain may be smaller at very high fluences than at low to intermediate fluences, as discussed above.

Any model of the stress–strain history of irradiated zirconium alloys should try to include the following:

- Strengthening;
- Clearing of irradiation damage before any effect on the load-carrying capacity is detected;

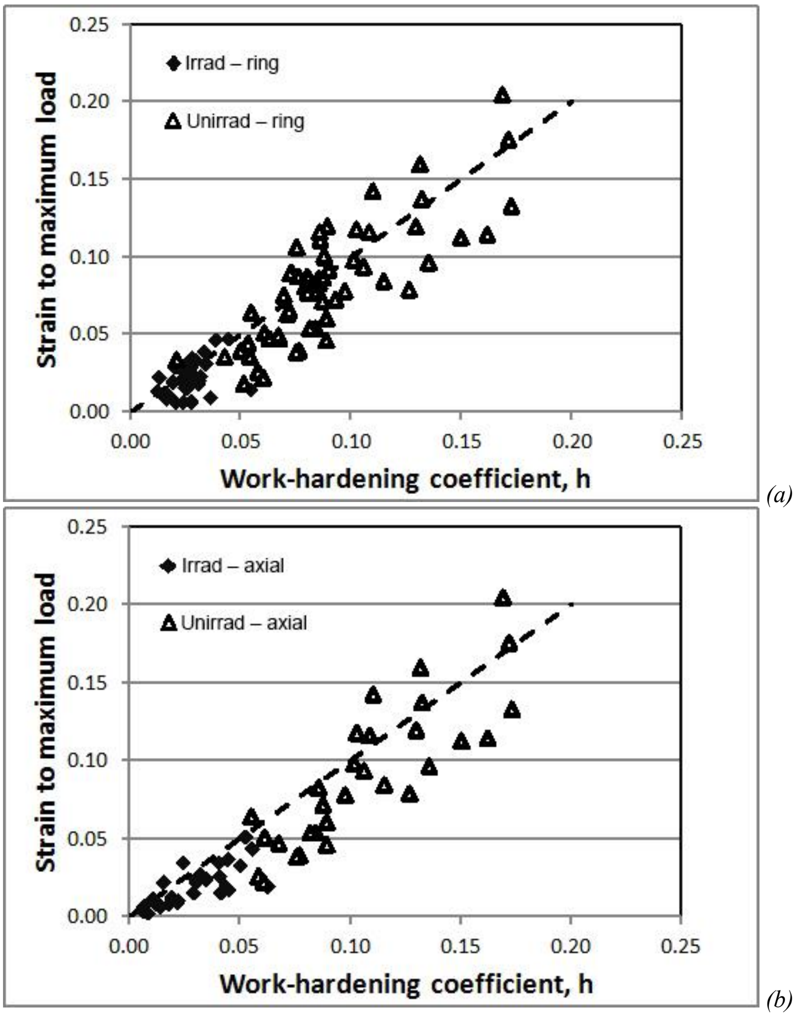

FIG. 9.38. Relationship between h *and strain to maximum load from tensile tests on Zircaloy-4 fuel cladding in several metallurgical conditions and tested at 293 K (20°C) and 573 K (300°C) as (a) ring and (b) axial specimens after irradiation at 523 K (250°C) [9.36].*

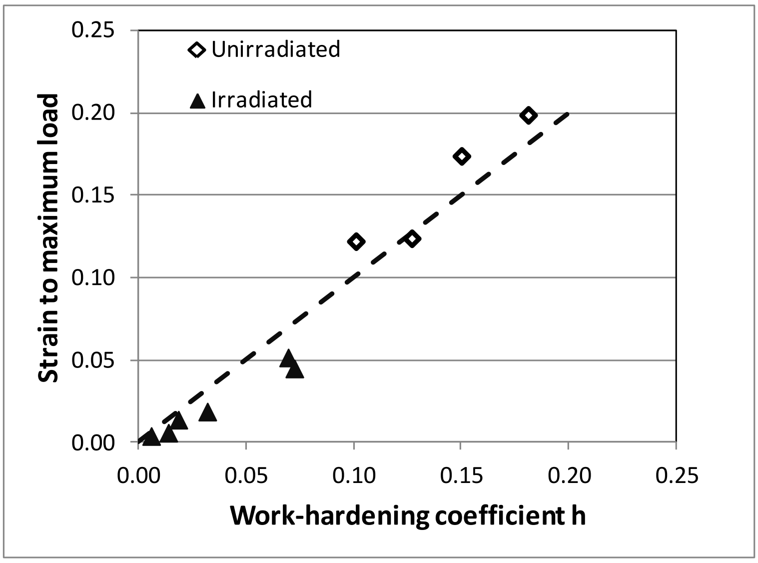

FIG. 9.39. Reduction in work-hardening and strain to maximum load in annealed Zr-1.14Cr-0.1Fe rod material after irradiation at 573 K (300°C) [9.45].

— Clearing of irradiation damage in several grains, perhaps forming a dominant slip region, leading to a loss in load-carrying capacity;
— Dislocation accumulation and work hardening of the zones cleared of irradiation damage;
— A loss in elongation.

Four examples are discussed below:

(1) Lee and Adamson [9.92] modelled the local strain developed by a softening and hardening sequence applying Hill's plasticity theory [9.110] to a zone about 55° to the tensile axis, as found

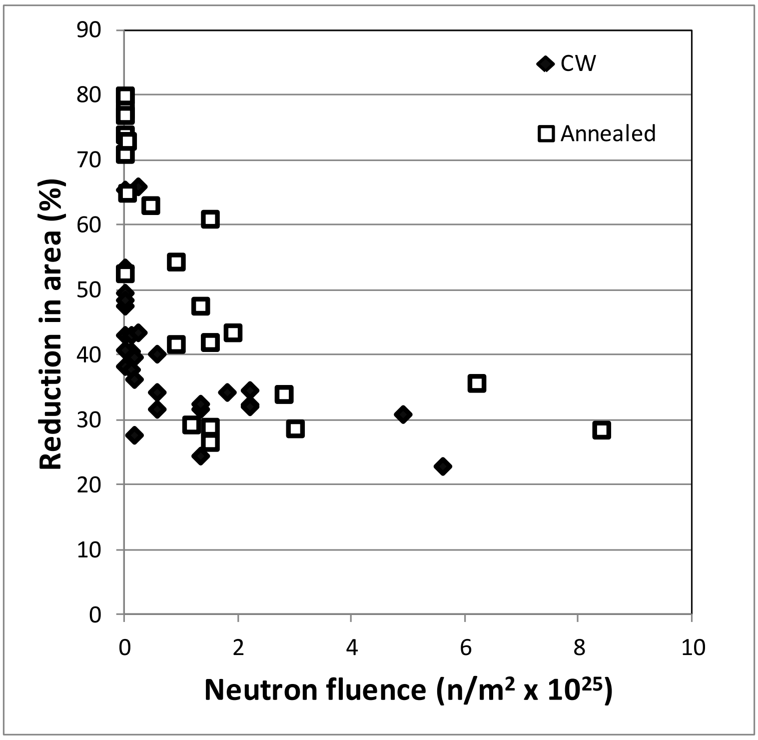

FIG. 9.40. Change in reduction in area of Zircaloy materials in the cold worked (CW) and recrystallized (annealed) conditions when irradiated between 555 and 600 K (282 and 327°C) and tested between 523 and 605 K (250 and 332°C) [9.43, 9.73, 9.79, 9.91, 9.98, 9.107–9.109].

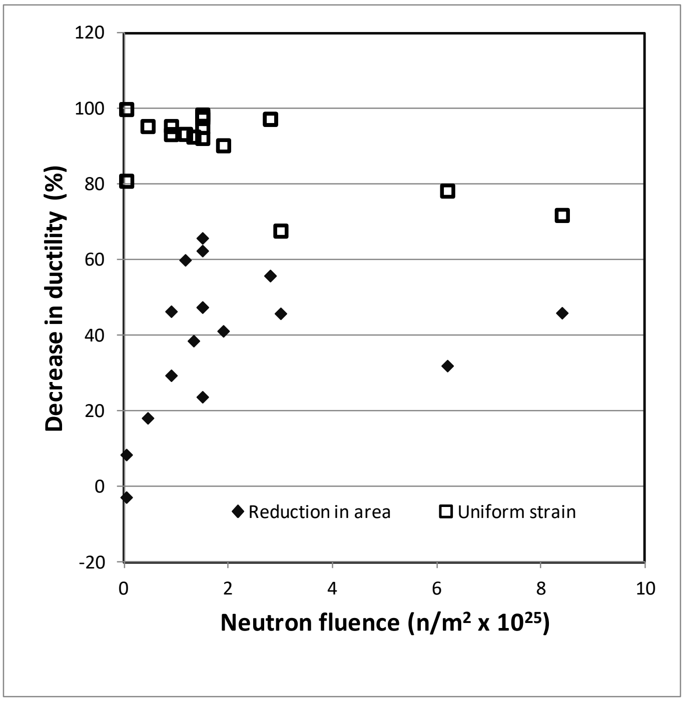

(a)

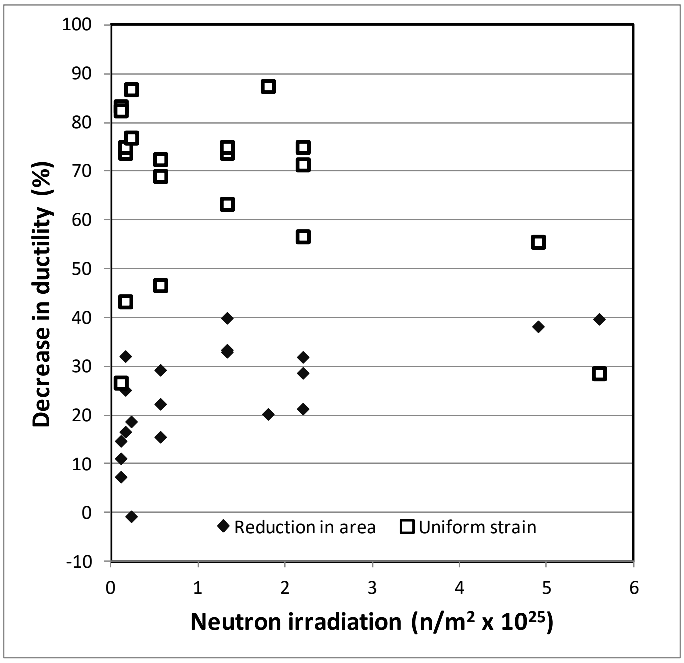

(b)

FIG. 9.41. (a) Relative change in ductility in annealed Zircaloy with irradiation between 555 and 600 K (282 and 327°C) and tested between 523 and 605 K (250 and 332°C) — comparison of strain to maximum load and reduction in area; (b) relative change in ductility in cold worked Zircaloy with irradiation between 555 and 600 K (282 and 327°C) and tested between 523 and 605 K (250 and 332°C) — comparison of strain to maximum load and reduction in area.

in the experiments [9.73]. Using the empirical strain hardening and drop in engineering stress the local strain was estimated to be 0.035.

(2) In a simple phenomenological approach, Hosbons et al. [9.111] simulated the strengthening and low strain to maximum load in a tensile test by manipulating the constants in Eq. (9.1) and adding an elastic strain term. In the example, if the irradiation damage had a diameter 20 times the slip plane spacing, only 1/20 of the slip planes have to be swept to remove all the damage. The deformation is inhomogeneous and only a small fraction of slip planes need to be activated to

cause softening. Assuming this fraction is 1/5 then after 1% strain the clearing process is complete. During a tensile test, although the engineering stress goes through a maximum with strain, the true stress also passes through a maximum but then recovers to increase by normal work hardening [9.45, 9.72]. To introduce the effect of irradiation in the model, the value of H was changed to characterize irradiation hardening with the removal of damage by strain being normally distributed up to a limiting strain that in this example is 0.01:

$$H = H_0 + \Delta H[1 - \exp\{-(0.01 - \varepsilon_p)^2/C\}]^{1/2} \qquad (9.5)$$

where

ΔH is the increment in H from irradiation;
C is the empirical constant;
ε_p is plastic strain;

and when $\varepsilon_p > 0.01$, $H = H_0$, the strength constant for unirradiated material.

The underlying material work hardening and strain rate hardening were unchanged from their values in unirradiated material, as indicated by the deformed region developing a cell structure typical of normal work hardening once the irradiation damage was cleared [9.72]. The simulation used the previous method for unirradiated material [9.25], in which the load required to extend perfect and tapered model specimens was calculated at intervals to provide load extension, true-stress–true-strain and stress relaxation curves that described the behaviour of irradiated zirconium alloys. This method satisfied the five target criteria for a model of the stress–strain history of irradiated zirconium alloys and was included in an early operating fuel code [9.112].

(3) An analogous approach used finite element analysis and plastic stress–strain hardening on a model specimen containing a small defect to stimulate necking [9.113]:

$$\sigma_{\mathrm{fl}} = \sigma_y + K(\varepsilon/\varepsilon_y)^{h} \qquad (9.6)$$

where

σ_{fl} is the true flow stress at a true plastic strain ε;
σ_y is the yield stress at the yield strain ε_y;
K is the strength constant;

and h is the strain hardening coefficient.

This model contains no elastic strain or strain rate sensitivity. Softening is modelled by replacing the $K(\varepsilon/\varepsilon_y)^h$ term by ($-$ constant $\cdot\ \varepsilon_p$) and yielding is modelled by setting σ_{fl} to σ_y for a small plastic strain. With the choice of suitable values of the constants, the engineering load elongation curves were modelled, including those for irradiated V-4Cr-4Ti.

(4) Onimus et al. [9.104, 9.114, 9.115] also followed a similar method but with more details in the clearing process on basal planes and its consequences for mechanical behaviour. In Ref. [9.114], the model is built up on three scales.

The first is dislocations interacting with irradiation damage causing strengthening then softening in channels. The second is grains with channels modelled as an ellipsoidal inclusion within a spherical grain. The stress within the channel, σ_{ch}, was related to the strain within the channel, $\varepsilon_{\mathrm{ch}}$, through:

$$\sigma_{ch} = \Sigma_a - E\xi\,\varepsilon_{ch} \qquad (9.7)$$

where

Σ_a is the applied stress;
E is the elastic modulus;

and ξ is a scaling tensor.

The third is when there is no deformation outside the channels and the plastic strain in the grains, ε_g, is related to ε_{ch} through the product with the volume fraction of channels per grain, f_{ch},

$$\varepsilon_g = f_{ch}\cdot\,\varepsilon_{ch} \qquad (9.8)$$

and

$$f_{ch} = n_{ch}d_{ch}/d_g \qquad (9.9)$$

where

n_{ch} is the number of channels per grain;
d_{ch} is the width of the channels;

and d_g is the grain size.

The plastic strain rate inside the channels can be related to the shear strain rate on each slip system by knowing the crystallographic texture, from which the plastic strain rate in the grain can be deduced. When a critical internal stress is attained, the channel stops deforming and a new channel forms; the volume fraction of channels is expressed as a function of the total plastic strain from all the channels.

The macroscopic behaviour at the polycrystal scale was incorporated into a modified plasticity model [9.116] in four stages. The macroscopic stress is calculated from the applied load; then the stress inside the channel is obtained from Eq. (9.7). The derivation of the plastic strain rate within the channels is then used to compute the macroscopic strain rate. The appropriate coefficients for unirradiated material are first fitted then the information from the mechanical behaviour and microstructural changes in irradiated material are included. Three empirical fitting parameters, related to the plastic accommodation of surrounding grains, are required for a complete simulation of internal pressure and stress relaxation testing.

In summary, good ductility is promoted by:

- High values of work hardening, represented by h, to postpone reaching maximum load or uniform elongation;
- High values of strain rate sensitivity, represented by m, to slow the growth of necks;
- Few inclusions to minimize the initiation of cavities.

Usually for zirconium alloys only some ductility values are reported but not the supporting plasticity empiricism or microstructure. The value of h may be deduced from the yield stress, UTS and uniform elongation, if provided; rarely is m evaluated. For expedience's sake, the description of plasticity by h and m may be adequate as a guide for the ductility of unirradiated material. Below 770 K (500°C) the values of h and m are low in zirconium alloys and consequently the ductility of unirradiated materials is quite modest. During irradiation, dislocation loops are formed that provide strengthening. The dislocation loops can be annihilated by strain leading to softening and strain localization, and subsequent loss of ductility, especially strain to maximum load. The mechanism of fracture, nucleation and growth of cavities is not changed by irradiation. Much of the early development work on zirconium alloys was aimed at producing materials with good corrosion resistance in hot water and steam; modest ductility was considered sufficient. In specifications, total elongation on a gauge length of 50 mm is the usual measure of ductility; at room temperature and 573 K (300°C) tubes made from recrystallized Zircaloy and Zr-2.5Nb must have a total elongation $\geq 20\%$ while those made from CWSR Zr-2.5Nb must have an elongation $\geq 12\%$ [9.117, 9.118]. Reduction in area is not a requirement and neither is any evaluation of work hardening or strain rate hardening.

9.3. CREEP DUCTILITY

9.3.1. Phenomenology

Components may deform by creep when loaded in tension for long periods. The time dependence of creep is shown in Fig. 7.18, in Volume 2 of this publication. The three main stages include:

- Stage I or primary creep where the initial high rate of deformation gradually diminishes towards Stage II;
- Stage II, or secondary or steady state creep where the rate of deformation is approximately constant (also called the minimum creep rate (MCR) when it is followed by Stage III);
- Stage III or tertiary creep where the deformation rate starts to increase and leads to rupture.

Low creep strains and their consequences for component viability are discussed in Chapter 7, in Volume 2 of this publication. Now the residual capacity for strain and the potential for creep rupture are evaluated during normal reactor operation as well as during storage after service and during a hypothetical loss of coolant accident.

Fracture by creep is caused by the onset of the inability of the specimen or component to carry the applied load. If no external chemical reaction interferes (e.g. oxidation), two categories of how the load bearing cross-section is lost are:

(1) In the absence of cavities, when volume is conserved, the cross-section simply decreases as the specimen deforms in response to the applied stress.
(2) If cavities form, they also contribute to the loss in cross-section. The area, A_1, of a cross-section containing a uniform array of spherical cavities with radius r and spacing λ is related to an area A_0 that is cavity-free through:

$$A_1 = A_0 [1 - \pi(r/\lambda)^2] \tag{9.10}$$

When r/λ is 0.05 the area loss is < 1%, it increases to 10% when r/λ is 0.18 and reaches 50% when r/λ approaches 0.4.

The consequence of the concomitant increase in tensile stress, σ, depends on how the rate of plastic flow, $\dot{\varepsilon}$, changes with stress. With a simple power law, $\dot{\varepsilon} \propto \sigma^n$, an increase in creep rate is expected. Rupture follows either when the cross-section is so reduced that the UTS is exceeded or the ratio of the initial creep rate to the final creep rate reaches infinity. If the initial creep rate is represented by MCR, then the time to rupture, t_f, is given by Eq. (9.11) [9.119]:

$$(\mathrm{MCR})\cdot n t_f = 1 \tag{9.11}$$

Earlier, Grant and Monkman [9.120] represented creep rupture data of many materials by:

$$\log t_{\mathrm{f}} + \zeta \cdot \log (\mathrm{MCR}) = \psi \qquad (9.12)$$

When $\zeta = 1$, Eq. (9.12) becomes Eq. (9.13) with the same form as Eq. (9.11):

$$(\mathrm{MCR}) \cdot t_{\mathrm{f}} = \text{constant} \qquad (9.13)$$

The constant found by Eq. (9.13) has the units of strain and has a value of $1/n$ in uniaxial loading and $1/2n$ with internal pressurization of a tube.

When values of t_{f} and MCR for zirconium alloys are plotted as indicated (see Fig. 9.42), $\zeta \approx 1$. These results are from a wide array of materials and test conditions, as shown in Table 9.8 [9.121–9.125]. The results suggest that the same phenomenology applies to different alloys, both α and β phases, different loading conditions and whether the material is irradiated or not, and therefore can be applied to several practical situations.

TABLE 9.8. CORRELATION BETWEEN MINIMUM CREEP RATE AND TIME TO RUPTURE FOR ZIRCONIUM ALLOYS

Material	Test details	Test temperatures (°C)	Stress (MPa)	χ	MCR×t_{f}	Source
CW Zircaloy-2, pressure tube	Uniaxial specimen, axial direction	350	290–355	1.018	0.045	[9.121]
CW Zircaloy-2, pressure tube	Uniaxial specimen, axial direction	300–450	140–380	1.025	0.052	[9.122]
CW Zircaloy-2.5Nb, pressure tube	Uniaxial specimen, axial direction	300–450	140–380	0.991	0.064	[9.122]
CWSR & RX Zircaloy-2 fuel cladding	Tube specimen, internal pressure	700–800	13–66	0.994	0.131	[9.123]
RX Zircaloy-4 strip; α-phase	Uniaxial specimen	700–800	10–50	1.012	0.287	[9.124]
Zircaloy-4 wire; β-phase, bamboo structure	Uniaxial specimen	1050–1150	0.5–1.7	1.008	0.118	[9.124]
CWSR Zircaloy-4 fuel cladding	Tube specimen, internal pressure	350–470	100–550	0.824	0.065	[9.125]
CWSR Zircaloy-4 fuel cladding irradiated between 0.4 and 9.5×10^{25} n/m^2	Tube specimen, internal pressure	350–470	100–550	1.164	0.043	[9.125]

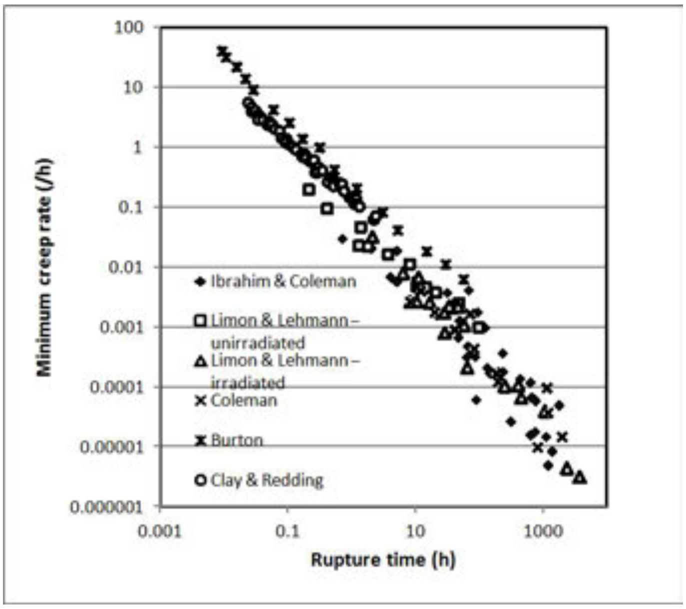

FIG. 9.42. Relationship between minimum creep rate and rupture time in zirconium alloys [9.121 to 9.125].

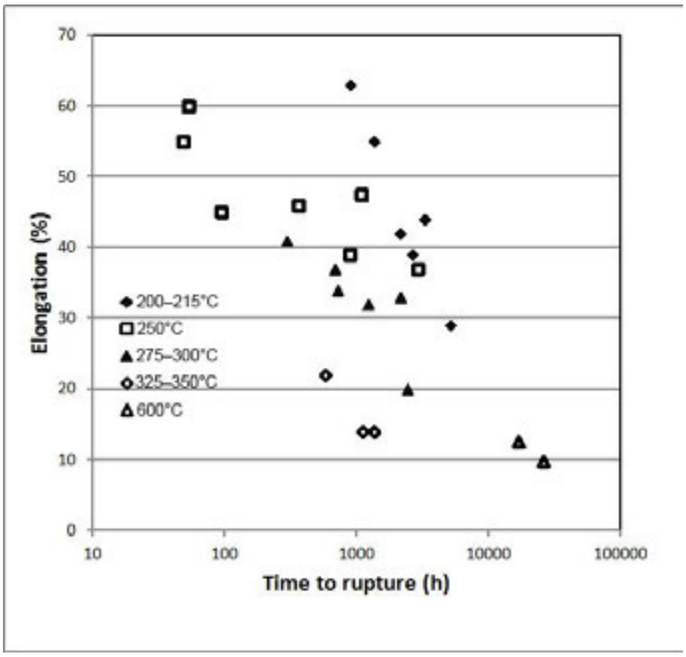

FIG. 9.43. Decrease in elongation with increase in rupture time in phosphorus-doped oxygen-free copper tested between 473 and 873 K (200 and 600°C) [9.127].

In many materials, cavities may be formed throughout the component or specimen during creep [9.126]. As a consequence, the elongation at rupture decreases as the time to rupture increases; Fig. 9.43 shows the behaviour of phosphorus-doped oxygen-free copper tested over a range of temperatures, 473 to 873 K (200 to 600°C) [9.127]; at each temperature the creep ductility declines as the rupture time increases. In out-reactor tests on zirconium alloys, the same pattern is not observed as elongation tends to increase with rupture time [9.122, 9.125, 9.128] (e.g. in tests on material from fuel cladding, as shown in Fig. 9.44(a), and pressure tubes, as shown in Fig. 9.44(b), at temperatures between 573 and 673 K (300 and 400°C)). Zirconium is very resistant to forming cavities from deformation or voids from irradiation [9.129, 9.130]; see also Section 6.3.1.1, in Volume 2 of this publication. Metallography and density measurements after creep testing of Zircaloy-2 indicate that cavities only form in the elevated hydrostatic tensile stress of a neck in uniaxial creep tests leading to ductile fracture, similar to the data shown in Figs 9.21 to 9.23 [9.121].

Contrary evidence that cavitation does contribute to area loss, and therefore creep rupture, has also been presented:

- A 0.76 mm thick specimen from an annealed Zircaloy-4 sheet was strained to 3% by creep at 648 K (375°C), notched to a depth of 0.01 mm then loaded to failure in tension at 623 K (350°C) [9.131]. The residual plastic elongation was about 3% for a total elongation of about 6%. The failure mode was reported to be transgranular, similar to that observed with stress corrosion cracking (see Section 9.6), with evidence of cavities on the grain boundaries. Since an uncrept specimen had a total elongation of about 12%, the difference in ductility between the two specimens was attributed to grain boundary cavities.
- Creep tests on an annealed Zircaloy-2 rod appeared to indicate cavity formation after deformation at 770 to 870 K (500 to 600°C) [9.132]. Unfortunately, the material started out containing detectable cavities, as indicated by metallography on the grip section of the specimens, and failed by ductile fracture at 623 K (350°C). Even if the formation of cavities was a dominating failure mechanism, the residual ductility was large, with true strains at failure >0.48 at the higher test temperatures.

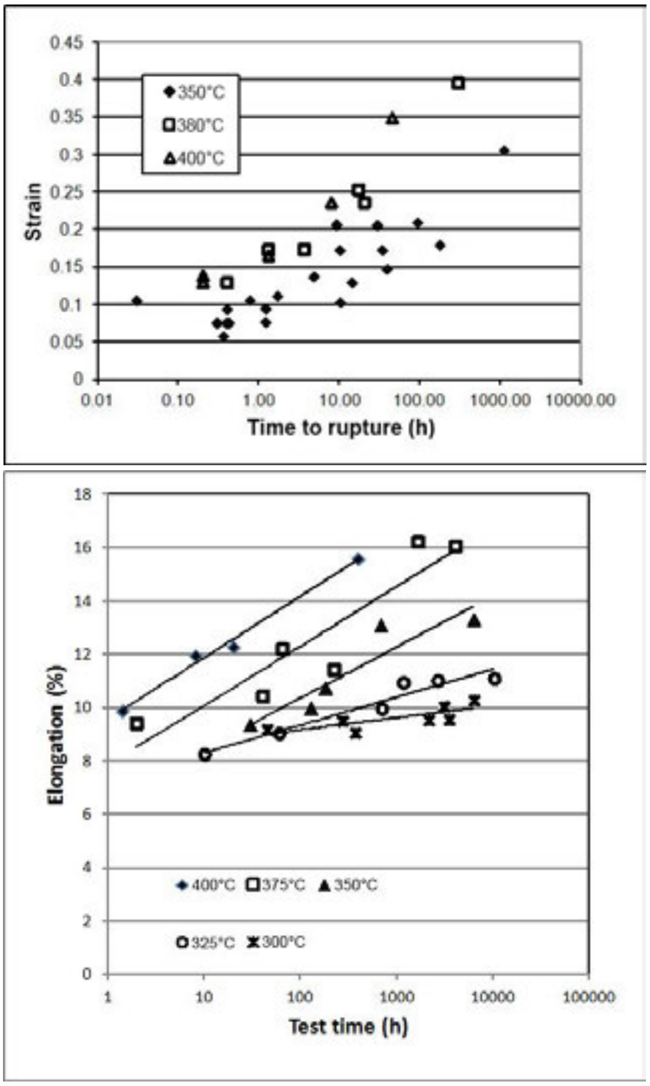

(a)

(b)

FIG. 9.44. (a) Increase in strain to rupture with increasing test time in unirradiated Zircaloy-4 fuel cladding [9.125]; (b) increase in strain to rupture with increasing test time in unirradiated Zircaloy-2 pressure tube [9.128].

Since most of the observations of high strain creep and rupture of zirconium alloys correspond with Category 1 (the case in which cavities are absent), this is taken to be the default case in the following sections.

9.3.2. Creep during irradiation — normal reactor service below about 620 K (350°C)

The operation of a pressure tube is used as an example because it is exposed to tensile stresses and a neutron flux throughout its lifetime of up to 30 years. With a few per cent creep strain, the pressure tube may interfere with the operation of other components or the thermohydraulic condition of the heat transport system may be compromised. If these operational issues are resolved, the question becomes: what is the prospect of tertiary creep followed by rupture at the limiting strain? The hoop stress is the largest principal stress and therefore hoop strain leading to an increase in diameter is the focus of attention. The national and international codes provide guidelines but are inadequate to deal with strains much above 1%. The current approach is to base the defence on phenomenological arguments and time to reach the limiting strain. This time should be much less than time to rupture; for tubes in steam generating heavy water reactors (SGHWRs) the time to reach the limit strain was proposed to be less than half the rupture time [9.128, 9.133]. In non-nuclear applications, accelerated tests are often possible and the results can be extrapolated to the required operating conditions, using suitable parameters. For example, data from stress rupture tests on unirradiated Zircaloy-2 [9.122, 9.125, 9.133] and Zr-2.5Nb [9.122] illustrate the Larson–Miller [9.134] method, as shown in Figs 9.45 and 9.46. At a given stress, the parameter Λ_R is derived as $T(20 + \log_{10}t_f)$, where t_f is the time to rupture in hours and T is the test temperature in K. A similar parameter, $\Lambda\dot{\varepsilon}$, is used for the MCR, $\dot{\varepsilon}_m$, namely $T(20 - \log_{10} \dot{\varepsilon}_m)$. The parameters are assumed to be a function of stress only. For a rupture time of twice the scheduled reactor life of 30 years, assuming 90% capacity factor, Λ_R is 14 710 at 573 K (300°C), permitting stresses of about 300 MPa for Zr-2.5Nb and 260 MPa for Zircaloy-2. Similar values of permitted stress are obtained using the MCR; $\Lambda\dot{\varepsilon}$ is 15 500 for 5% creep strain in 30 years (a creep rate of about 2×10^{-7} h^{-1}). Using the ASME criterion for stress rupture (see Section 9.2) with the reactor lifetime, which is 2.6 greater than 100 000 hours, the allowed stresses are 180 MPa and 156 MPa for these alloys. The actual design stresses for Canada deuterium uranium (CANDU) reactors of 160 MPa for Zr-2.5Nb and 110 MPa for Zircaloy-2 provide rupture times of over 10^9 hours — more than 100 000 years — or creep rates of about 10^{-10} h^{-1}. These values are unrealistically optimistic for in-reactor behaviour, and an alternate approach is required.

Except at reactor shutdowns, the pressure in the heat transport system is kept constant. As discussed in Section 9.3.1, the creep rate may increase because:

(a) The stress increases by the reduction in wall thickness and increase in diameter;
(b) Internal voids and cracks may develop;
(c) A local reduction in thickness or neck may develop;
(d) The microstructure may recover and reduce the material’s strength;
(e) The cross-section may be reduced by chemical attack.

During irradiation, once an initial transient increase in strength is passed, the short term strength of pressure tubes during service remains almost constant for long times (see Section 6.4.3, in Volume 2 of this publication, and Section 9.2) because an approximately constant microstructure is developed. Various materials retain much local ductility after small amounts of irradiation creep, as indicated by measurements of reduction in area, as shown in Table 9.9 [9.135]. (It should be noted that the values of elongation for the post-creep specimens were based on specimens twice as long as for the pre-creep specimens so direct comparison is not strictly valid.) Full recovery of fracture toughness with heat treatment also indicates that long term service does not induce underlying embrittlement [9.136]. Since items (b), (d) and (e) do not apply to creep at normal reactor operating

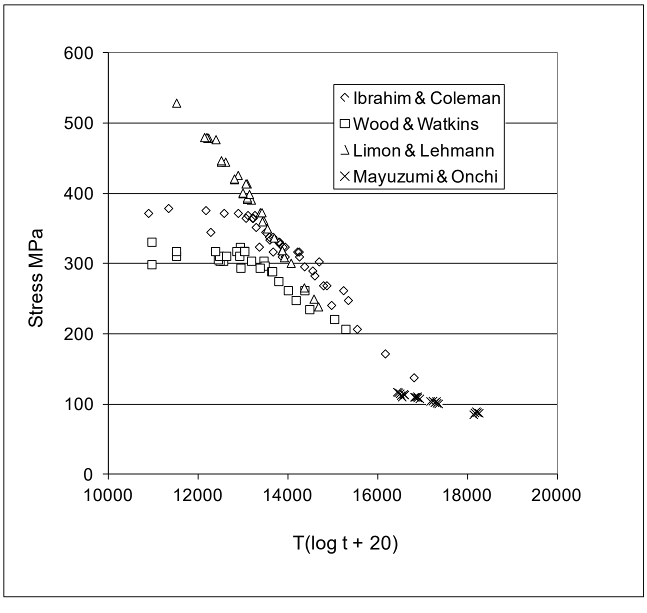

FIG. 9.45. Larson–Miller parameter for Zircaloy based on stress rupture time [9.122, 9.125, 9.133, 9.134].

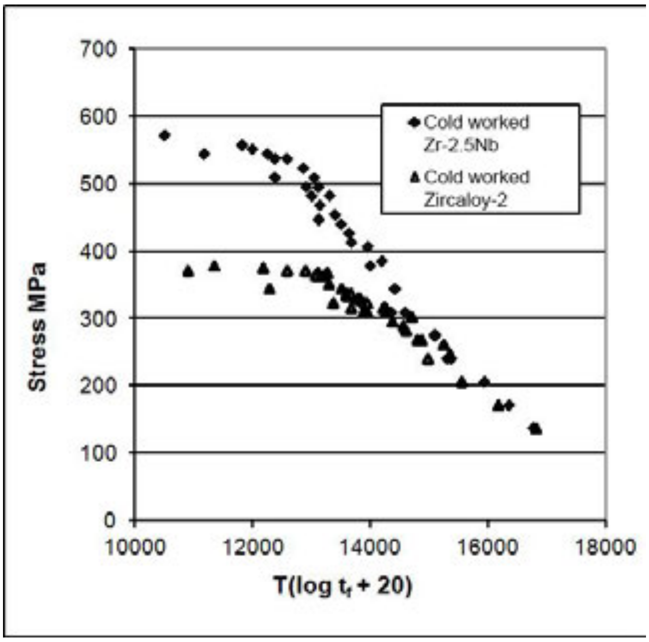

FIG. 9.46. Comparison of Larson–Miller parameters for cold worked Zircaloy and Zr-2.5Nb based on stress rupture time [9.122].

temperatures, a similar approach to that for tensile behaviour may be taken in the absence of intrinsic fracture mechanisms or departures from a stable microstructure.

Calculated creep curves for specimens of uniform cross-section (e.g. perfect cylinders) under constant load indicate accelerating creep based purely on the geometry of the deforming specimen [9.121, 9.137, 9.138]. Using Eq. (9.14) to describe primary and secondary creep of cold worked Zircaloy-2, the strain for tertiary creep was less than 3% when the minimum strain rates were about 1.5×10^{-4} /h at temperatures up to 450°C [9.121].

$$\varepsilon = \mathrm{B}\sigma^{\mathrm{p}}t^{\mathrm{q}} + \mathrm{A}\sigma^{\mathrm{n}}t \qquad (9.14)$$

where A, B, n, p, and q are constants.

The deformation of imperfect specimens that formed a neck could also be accurately calculated using the same formalism. At high strains and long times the second term in Eq. (9.14) dominates. As applied stress is reduced and test temperature is increased, the stress sensitivity, *n*, is reduced. Consequently, accelerating creep is postponed and neck development is retarded. This phenomenology explains the increase in elongation with long test times. When *n* approaches 1, very large strains are obtained before rupture. To a first approximation, $n = 1/m$, where *m* is the strain rate sensitivity in Eq. (9.1). Values of *n* and *m* should be compared at the same strain and strain rate, that is, at constant structure [9.139]. In practice, such a procedure is usually not followed and care must be taken to interpret the data. A strong empirical correlation exists between *m* (Eq. (9.1) for tensile behaviour) and total elongation for many materials [9.33]. Stress rupture tests on Zircaloy-2 and Zr-2.5Nb can be similarly interpreted by correlating *n*, from MCRs in constant load tests, with total elongation at rupture, as shown in Fig. 9.47 [9.122]; these results fit with the band of data from the tensile tests on different materials, as shown in Fig. 9.3.

TABLE 9.9. TENSILE PROPERTIES AFTER A PERIOD OF IN-REACTOR CREEP [9.135]

Material	In-reactor creep conditions				Pre-creep tensile properties (Gauge length = 25 mm)			Post-creep tensile properties (Gauge length = 50 mm)		
	Stress (MPa)	Temperature (°C)	Test time (h)	Total strain (%)	0.2% yield stress (MPa)	Elongation (%)	Reduction in area (%)	0.2% yield stress (MPa)	Elongation (%)	Reduction in area (%)
Pure zirconium; annealed	68–140	200–300	4360	1.12	125	50	72	189	6.3	61
Zircaloy-2; 20% CWSR	310–207	350	382	2.58	614	18	39	583	4.5	58
Zircaloy-2; 16% CWSR	138	300–400	2576	0.55	489	13	34	505	7.7	34
Zircaloy-2; 16% CWSR	310	300	1655	1.95	489	13	34	586	4	34
Zircaloy-2; 19% CWSR	207	220–400	4985	0.095	559	14	36	649	6	32
Zr-2.5Nb; (α+β) quench, 24 h 500°C	207	300	2650	0.3	559	14	36	649	6	32
Zr-2.5Nb; (α+β) quench, CW 5%, 24 h 500°C	110	300	2100	0.3	662	19	52	905	6.5	64
Zr-2.5Nb; (α+β) quench, CW 5%, 24 h 500°C	414	300	930	0.8	676	18	55	493	2.9	36
Zr-2.5Nb; (α+β) quench, CW 22%, 24 h 500°C	250–110	300	5540	0.36	593	23	54	823	3.5	38
Zr-2.5Nb; 21% CWSR	159	300	3200	0.16	537	14	44	641	8	23
Zr-2.5Nb; 21% CWSR	114	300	2800	0.42	537	14	44	634	7.6	59

Note: Fast fluence in range from 3×10^{23} to 4.3×10^{24} n/m^2.

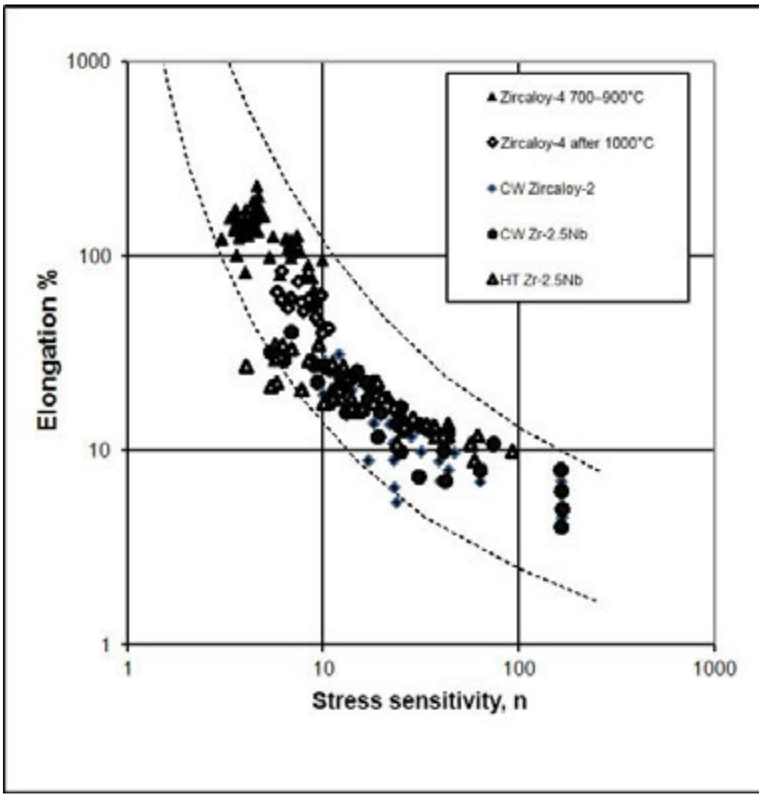

FIG. 9.47. Variation of creep rupture ductility with stress sensitivity of the minimum creep rate for cold worked Zircaloy-2 and Zr-2.5Nb, and heat treated Zr-2.5Nb in out-reactor tests between 573 and 723 K (300 and 450°C) [9.122]. Tests at 973 to 1173 K (700 to 900°C) on Zircaloy-4 cladding with or without excursions to 1273 K (1000°C) into β-phase [9.255]. Dotted lines include tests on many alloys [9.139].

At stresses close to those of reactor operation, creep strain follows the second term in Eq. (9.14) (see Chapter 7, in Volume 2 of this publication). Since creep ductility increases with reduction in n, and during neutron irradiation the value of n approaches 1 at low stress [9.133, 9.135, 9.140–9.142], the expectation is that plastic instability would be suppressed and high creep ductilities would be attained during reactor operation [9.143–9.145]. For nuclear applications of zirconium alloys, satisfactory techniques for accelerating creep to demonstrate enhanced creep ductility are difficult to achieve because inappropriate deformation mechanisms may occur at stresses and temperatures higher than those for normal operation. Using fast neutron fluxes higher than those in the power reactors would be the preferred method for accelerating the deformation but such tests still require several years to attain the neutron fluence expected at the desired lifetime of pressure tubes. Another problem is that measurements in-reactor are prone to error and post-irradiation values of dimensions are needed to provide confidence in the values of strain. Despite these difficulties, several results from both uniaxial and biaxial loadings have been obtained that support the phenomenology outlined above, even though the stresses during the tests were at least twice those used during reactor operation and are thus conservative. Both test times and estimated fluence of fast neutrons are indicated where appropriate.

Specimens for uniaxial tests were machined from pressure tubes. Tests on cold worked Zircaloy-2 at temperatures between 548 and 598 K (275 and 325°C) and stresses in the range 240 to 318 MPa have attained strains of 8.7% in 15 200 hours (0.16×10^{26} n/m^2) without indications of tertiary creep [9.133]. The duration of one test was 49 000 h and the creep strain was reported to be 28% [9.145]. No necking was detected with an elongation of 7% in a test at 310 MPa at 598 K (325°C) that lasted 5675 hours (0.013×10^{26} n/m^2) [9.121].

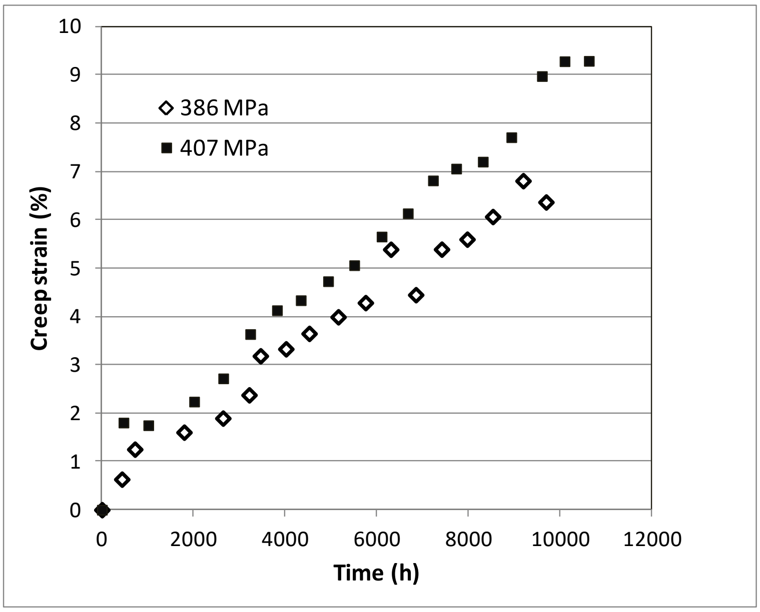

FIG. 9.48. High creep strains in Zircaloy-2 tubes at 548 K (275°C) with no acceleration [9.146].

Similar tests on Zr-2.5Nb were less successful because of experimental difficulties, but strains of at least 4.5% were attained in 5600 h (0.056×10^{26} n/m^2) at 573 K (300°C) and 448 MPa without the creep rate accelerating [9.142].

Many of the attempts to demonstrate high in-reactor creep ductility in biaxial loading used sealed capsules. These specimens provided tests close to constant stress rather than constant load so the results may appear optimistic; they apply to nuclear fuel, especially during storage when no new fission gases are being generated. Also, in test specimens the diameters were smaller and the microstructures different from pressure tubes used in power reactors so the application of the results requires care. In the United Kingdom (UK) programme [9.146], the initial phase consisted of small prepressurized capsules whose dimensions were measured after irradiation at 548 ± 10 K (275 ± 10°C). Strains of up to 7.0% were attained in cold worked Zircaloy-2 at a stress of 352 MPa. Similar tests were carried out at 573 K (300°C) in Canada [9.147], with dimensions being measured during reactor shutdowns. With a hoop stress of 389 MPa for 16 500 hours (0.13×10^{26} n/m^2) a cold worked Zr-2.5Nb specimen strained over 10% without the strain rate increasing. Some of these tests were continued for up to 36 430 h and attained a maximum creep strain of 17.6% [9.145]. (During the UK irradiation, a cold worked Zr-2.5Nb specimen failed at 1.8% strain with a brittle crack; although this failure was attributed to stress rupture, a possible failure mechanism could have been delayed hydride cracking initiated at a sealing weld (see Section 9.7). (This mechanism was invoked for some of the Canadian specimens that ruptured at room temperature while awaiting measurement.) The Japanese used similar methods on heat treated Zr-2.5Nb [9.148]. At their highest hoop stress of 400 MPa at 553 K (280°C) a strain of 5.5% was attained in about 4.8 years (0.45×10^{26} n/m^2) with no sign of accelerating creep [9.149].

In an extension of the UK programme constant pressure tests were carried out at 548 ± 20 K (275 ± 20°C) with diameters being measured by neutron radiography of the displacement of dysprosium markers [9.146]. In one test at 407 MPa, after some primary creep, the deformation of cold worked Zircaloy-2 progressed at a steady rate with no increase for 11 150 hours (0.16×10^{26} n/m^2) up to a strain of 9.2%, as shown in Fig. 9.48. Similar tests exhibited steady deformation, but to lower strains. In Canada, small tubes of cold worked Zr-2.5Nb subjected to constant pressure at 573 K (300°C) deformed at a constant rate in flux and at the maximum hoop stress of 311 MPa attained a hoop strain of 2.4% after 7 years (0.36×10^{26} n/m^2), with no indication of acceleration [9.150]. Pressurized full size high-power channel-type reactor (RBMK) tubes made from annealed Zr-2.5Nb tested at 613 K (340°C) exhibited strains up to 4.8% after 11 000 hours (0.21×10^{26} n/m^2) at a hoop stress of 100 MPa with no sign of rupture [9.151].

Examination of pressure tubes from power reactors, either in situ or after their removal, indicates that either the strains were small and therefore rupture was not an issue, or else the phenomenology is correct and high ductility is expected in-reactor when n is about 1 at stresses well below those of the test programmes. Pressure tubes were analysed in the following cases:

- Gauging the cold worked Zircaloy-2 pressure tubes of SGHWRs showed that the fluence dependence of diametral strain was either linear, after a period of primary creep, or followed a power law, (fluence)$^{0.6}$ [9.152]. These tubes operated at 561 K (288°C) with a hoop stress of 84.5 MPa. Close to the retirement of the reactor, a central channel had a maximum diametral strain of 1.17% after a fast fluence of 1.05×10^{26} n/m^2 [9.153]. The predicted strain for the fluence was either 1.43% (linear) or 0.96% (power law), spanning that observed and not representing a threat of imminent rupture.
- Extrapolation of early gaugings of heat treated Zr-2.5Nb pressure tubes [9.148] provides average strains of about 1.0% in Fugen up to its retirement after a similar fluence [9.149]. These tubes were stressed to 96 MPa at 553 K (280°C).
- The diametral expansion of cold worked Zr-2.5Nb pressure tubes in Pickering was at a constant rate and after a fluence of 0.8×10^{26} n/m^2 at a hoop stress of 120 MPa and at 565 K (292°C) the maximum strain was 1.1% [9.154].
- The flux in the Nuclear Power Demonstration (NPD) reactor was much smaller than in large power reactors. After about 25 years of operation the maximum diametral strain at about 538 K (265°C) in cold worked Zircaloy-2 stressed at 80 MPa was 0.4% after a maximum fluence of about 0.6×10^{26} n/m^2 (140 200 hours) [9.155]. The strain was linear in time after a short period of primary creep; a power law, similar to that proposed for SGHWRs, could represent the data but the correlation was not as good as for the linear law. In heat treated Zr-2.5Nb stressed at 132 MPa the hoop strain was about 0.6% after a maximum fluence of 0.43×10^{26} n/m^2 (124 300 hours) [9.156].
- Measurements of the dimensions of several cold worked Zr-2.5Nb pressure tubes in various CANDU 6 reactors with hoop stress of about 125 MPa at 583 K (310°C) show that the diametral strain is increasing linearly with time and after nearly 18 years of full power operation (and a fluence of about 2×10^{26} n/m^2) has attained a value of 3.6%, as shown in Fig. 9.49 [9.157]. Forcing the intercept of the trend line through zero provided a worse

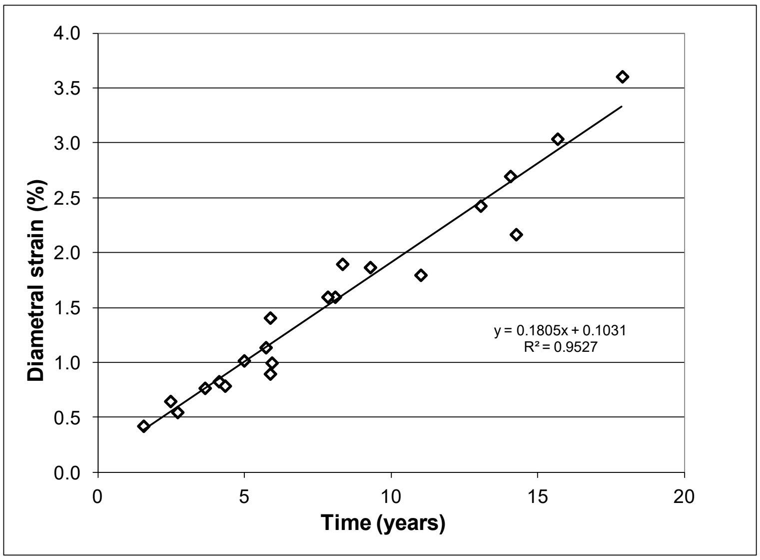

FIG. 9.49. Change in diameter of cold worked Zr-2.5Nb pressure tubes in several CANDU reactors [9.157].

correlation than without doing so, indicating a small amount of primary creep. These tubes also elongate, and because the volume is conserved, the wall thickness decreases linearly with time. Consequently, the hoop stress has increased by about 8.7% thus further emphasizing the resistance to accelerating creep.

- The diameter of annealed Zr-2.5Nb pressure tubes operating at a hoop stress of 86 MPa and 561 K (288°C) in RBMK-1000 reactors also increases linearly with fluence. After a fluence of 0.62×10^{26} n/m^2 the maximum strain was about 2% [9.158]. After a similar fluence in RBMK-1500 reactors, the maximum strain in tubes with the thermomechanical treatment in water (TMT-1) (Fig. 4.89) was about 1% whereas in tubes with the thermomechanical treatment in gas (TMT-2) (Fig. 4.89), the maximum strain was about 0.5% [9.159].

In summary, this survey shows that at the operating conditions of pressure tube reactors, diametral strain increases linearly with the dose of fast neutrons, usually after a period of primary creep. The tubes operate in a stress range where stress sensitivity is very low and high ductility would be expected. Although superplasticity has not been demonstrated, the strains attained to date suggest that fracture from creep is not a problem for pressure tubes in their normal operating environments. As operating temperatures and neutron fluxes are increased in advanced reactors, and alloys and their fabrication are modified, this mode of failure will require review.

9.3.3. Post-irradiation creep behaviour — storage of spent nuclear fuel

Once nuclear fuel has provided its energy and the absorption rate of neutrons approaches their production rate, the fuel is discharged from the reactor. The next stage in the life of the fuel depends on the choice of final disposition — whether interim storage before reprocessing or several stages of storage before final disposal, probably in geological repositories.

When fuel is removed from the reactor, the decay of radioisotopes generates heat. This heat raises the temperature of the cladding and concomitantly increases the inside pressure from the filler and fission product gases. The temperature must be controlled if the fuel is to remain intact and not suffer mechanical damage. Two sources of heat have different time constants — fission products and actinides. The heat from the decay of fission products depends on the makeup of the fissile isotopes, the fuel burnup and the final power. For UO_2 [9.160]:

$$P/P_0 = 6.1 \times 10^{-3}\,[(T_t - T_s)^{-0.2} - T_t^{-0.2}] \tag{9.15}$$

where

P_0 is the power at fuel discharge;
P is the power at total time, including storage;
T_s is the time in reactor (days);

and T_t is the total time since start of irradiation (days).

The decline in the decay heat is summarized in Table 9.10. For the first 60 years, this source of heat will dominate. Subsequently, thermal power from the transuranic elements, notably ^{241}Am, will control the decay heat. The contribution of each source up to 10 000 years is illustrated in Fig. 9.50 [9.161].

The decay heat and radiation field of the spent fuel can be very high when it is first discharged from the reactor. The spent fuel must be stored for several years in water filled pools until the decay heat declines sufficiently to employ dry storage. During pool storage, the circulating pool water disperses the decay heat and provides radiation shielding. Pool storage typically lasts at least five years, depending on the burnup of the fuel; by this time the heat will be less than 0.02% of the heat at discharge, as shown in Table 9.10. The pools are designed to withstand severe geological events, such as the earthquake and tsunami that devastated Fukushima, and the ambient conditions in a pool are benign, with low cladding temperatures, about 313 K (40°C), and low hydrostatic pressures of water in the pool. No evidence for degradation has been found for storage times in pools exceeding 20 years [9.162, 9.163]. On cooling from service conditions to pool conditions, since the coefficient in thermal expansion of UO_2 [9.164] is over 60% larger than that of the diametral change in the cladding [9.165] (assuming a radial texture), the fuel will shrink away from the cladding and will only maintain loose contact. Thus, the main stressing agent will be internal pressure from the initial helium and internally generated gases. The resulting pressure at 313 K (40°C) is too low to result in any mechanical degradation of the cladding during pool storage. Although there will be some heat flux, the temperature gradient will be small enough to ignore. Storage in pools is costly and space is limited so the more cost and space efficient dry storage is used when space in the spent fuel pool is exhausted or as soon as practicable. The vessels for dry storage are called by various names: container, canister, caisson, cask or silo, with the latter two being the most common. They are used for both transport and storage. They have to provide criticality control, shielding, mechanical support, chemical and radiological protection and be able to dissipate heat from the spent fuel; the latter is achieved with a helium atmosphere that also provides an inert environment. They are constructed from steel or concrete or both and are usually very large and require specialized handling. Dry storage systems are designed to withstand the most severe credible conditions. For example, the dry storage casks at Fukushima withstood the earthquake and tsunami with little damage, perhaps suggesting a further reason for minimizing time in pool storage. Safe dry storage before either final disposal or reprocessing is being accomplished in Argentina, Armenia, Belgium, Canada, Czech Republic, France, Germany, India, Japan, Republic of Korea, and the United States of America (USA) [9.163].

TABLE 9.10. REDUCTION IN DECAY HEAT FROM FISSION PRODUCTS IN SPENT FUEL WITH TIME AFTER DISCHARGE

Time after shutdown	Initial thermal power (%)
1 second	5.8
1 minute	2.4
1 hour	1
1 day	0.48
1 week	0.28
1 month	0.18
1 year	0.059
5 years	0.019
10 years	0.01
100 years	0.0008
1000 years	0.00005

The circumstances for dry storage are quite different from those during residence in the reactor, for which the fuel was designed. These differences include the following:

- No extra irradiation damage from neutrons; because the temperature during dry storage may be greater than the reactor operating temperature, some irradiation damage may anneal out and result in the recovery of cladding ductility and decreased strength.
- An external gas environment, usually an inert gas such as helium, with a pressure around atmospheric pressure and heat transfer that is less efficient than in water.
- No extra corrosion or hydrogen pick-up expected.

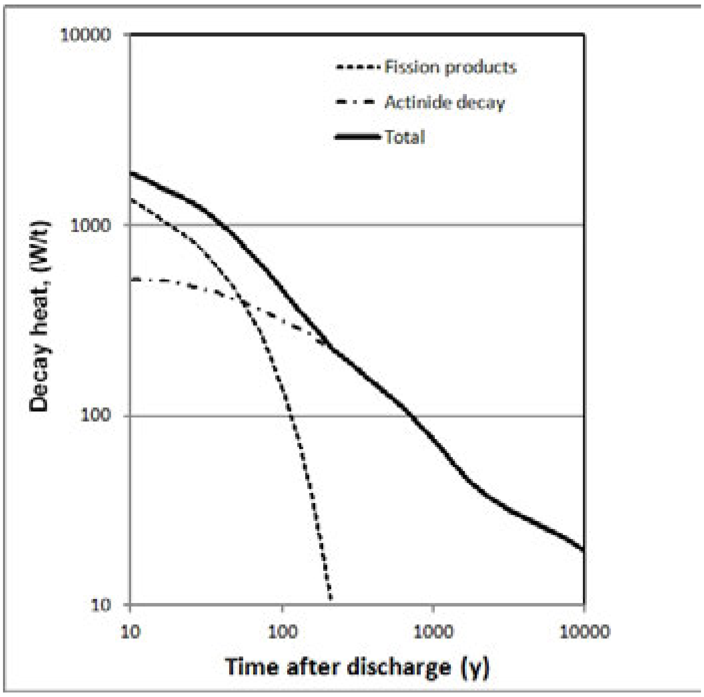

FIG. 9.50. Decay heat during time in storage. Burn-up in pressurized water reactor of 50 MWd/kgU [9.161].

- The internal gas pressure from the original filler gas and fission products is greater than the ambient gas pressure, leading to tensile hoop stresses; these stresses may result in creep.
- Very long residence times, with targets between 40 and 300 years.
- Heating from radioactive decay that declines with time; because of the limited heat transfer, the cladding temperature is raised from the pool temperature by several hundred degrees celcius, but it decreases with time as the decay heat is reduced. The heat flux is about 1% of that during residence in the reactor, therefore the temperature gradient through the cladding wall is very low, <1 K (1°C)/mm.
- The ambient temperature of the container may vary depending on whether it is indoors or outdoors. If the latter, the variation in ambient temperature depends on the geographical location; for example, in central North America the seasonal range of temperature could be as high as 343 K (70°C) [9.166] with daily cycles as large as 18°C [9.167]. Measurements of temperature variation confirm that seasonal changes can affect the temperatures of stored fuel [9.168]. After a CANDU fuel bundle received a modest burnup of 7.3 MWd/kgU and was stored in a pool for 34 months, it was held outdoors in Manitoba, Canada, in a concrete canister lined with steel. Temperature variation was determined from thermocouples inserted between elements in the bundle. The values followed the outside temperatures; in July when the average temperature was 293 K (20°C) the temperature of the bundle averaged 330 K (57°C), a 37°C difference between the bundle temperature and the outside temperature. In January when the mean temperature was 239 K (−34°C), the temperature of the bundle decreased to 289 K (16°C) but the temperature difference increased to 50°C. The fuel had a 41°C variation in temperature between summer and winter. The thermal lag was too great to pick up daily temperature fluctuations. Calculations for pressurized water reactor (PWR) fuel irradiated up to 44 MWd/kgU in Calvert Cliffs, Maryland (USA) and stored outside after pool storage for about 15 years, support the seasonal variation in cladding temperature [9.169]. In the summer with an average temperature of 298 K (25°C), the highest burnup material was predicted to be at 479 K (206°C) while during the winter with an average temperature of 275 K (2°C) the fuel temperature reduced to 454 K (181°C). The temperature difference between the fuel and the outside temperature in both summer and winter was calculated to be

about 180°C — the fuel temperature varied by 25°C, almost exactly following the yearly change.

The initial conditions for dry storage will depend on the following factors:

- The fuel composition: for example, in mixed oxide (MOX) fuel, α decay leads to the generation of He, amounts of which can be large after very long storage times, >100 years [9.170]; He may be produced from transmutations of B if it is used as a burnable absorber. The low diffusivity of He in ceramic fuel may postpone its release to the fuel rod plenum at fuel storage temperatures.
- The in-reactor creep strength of the cladding: during reactor operation, weaker cladding creeps down and contacts the fuel earlier than strong cladding, resulting in a lower fuel temperature and less fission gas release and thus lower pressure at the start of dry storage after the same burnup.
- Fuel burnup: higher values provide more decay heat and fission gases.
- Residence time in pool storage: longer times allow for greater decay and lower temperatures for subsequent dry storage.

The temperature is highest at the start of storage; consequently, the pressure and the hoop stresses are highest then, too. The pressure decreases as the temperature is reduced. If the cladding creeps, the internal fuel rod pressure also decreases because of the increased volume. To prevent excess creep and potential rupture, regulators have set limits on the normal conditions of storage. For example, the NRC requires that cladding temperature not exceed 673 K (400°C) and that cladding hoop stress be <90 MPa [9.171, 9.172]. This cladding stress has to be based on the cladding thickness reduced by any hydride layer and the thickness of the oxide; the maximum corrosion allowance is 120 μm, corresponding to a metal loss of 80 μm ([120/1.5] μm, where 1.5 is the Pilling–Bedworth ratio for the oxide). One of the in-reactor operating limits for PWR fuel is for the internal gas pressure to be lower than the coolant water pressure, 15.5 MPa at 623 K (350°C).[1] An upper-bound stress at the start of storage can be estimated using these values. At the limiting temperature of 673 K (400°C) the limiting internal pressure is raised to 16.7 MPa. In typical cladding the outside diameter is 9.5 mm and the wall thickness is 0.57 mm; the thickness is reduced to 0.49 mm by corrosion. The upper-bound hoop stress at 673 K (400°C) is therefore about 150 MPa (based on PD/2t or 16.7 × 8.85/2 × 0.49), which is 60 MPa greater than the NRC limitation. (During pool storage with this gas pressure at 313 K (40°C) and ignoring the pressure from the pool water, the hoop stress would be 70 MPa, insufficient to produce creep strain.) In other examples, German regulators allow the hoop stress limit to be 120 MPa, while in France the stress limit may be as high as 300 MPa, based on creep rupture behaviour for very short times [9.173]. During loading of the fuel for storage, not more than ten thermal cycles of less than 65°C are allowed by the NRC; these stress and thermal cycle restrictions are designed to minimize reorienting hydrides to a radial, and therefore embrittling, configuration (see Section 9.7). Transients up to 743 K (470°C) may be allowed for a few days by the NRC; for example, during transportation. Seasonal temperature cycles of up to 40°C are not included. For abnormal conditions temperatures up to 843 K (570°C) are allowed as long as the hoop stress does not exceed 90 MPa [9.174]. Note that the burnup in CANDU fuel is 4 to 10 times lower than in light water reactors (LWRs); consequently the temperatures at the start of dry storage are very low, often about 423 K (150°C) [9.175], and stress induced failures are not an issue. Spent fuels from these power reactors have been stored in air or dry helium for many years with no problem.

Since measurement of the temperature and pressures inside spent fuel are not available for very long periods, analyses are used to estimate the conditions for fuel storage. For example, at the start of dry storage after a burnup of 55 MWd/kgU and about 6 years in pool storage, typical predicted

---

[1] In some cases, the internal fuel rod pressure is allowed to exceed the coolant system pressure as long as the cladding does not creep outward faster than the fuel swells. This exception is intended to result in no increase in the gap between the fuel and the cladding.

temperatures were 623 to 633 K (350 to 360°C), declining to 503 to 513 K (230 to 240°C) after ten years [9.176]. The calculated hoop stresses at the start of storage were 60 to 80 MPa, which declined, owing to both the drop in temperature and the less than 1% creep strain, to 45 to 60 MPa. Similar calculations using the regulatory limit of 673 K (400°C) were performed and are depicted in Fig. 9.51 [9.177]. An end-of-life internal pressure was used to calculate the hoop stress at the start of storage. Using, for illustration, a value of hoop stress of 90 MPa, the temperature and stress decline so that after 40 years the temperature is predicted to be about 493 K (220°C) while the hoop stress will have decreased to 62 MPa.

Maintaining the integrity of the cladding is required to minimize spread of radioactivity and ease further handling. The issue is whether any potential failure modes compromise safe storage. The potential failure mechanisms are the following:

(a) Oxidation (see Chapter 8, in Volume 2 of this publication): In an inert atmosphere, post-transition linear rates of oxidation, integrated over the first 20 years of storage, provide a maximum loss of clad thickness of <15% [9.178]. Little further oxidation is expected during subsequent time in storage because the temperatures are low. Oxidation is not considered a primary failure mechanism during dry storage.

(b) Stress corrosion cracking from fission products (see Section 9.6): This mechanism is considered unlikely to crack the clad because during dry storage the hoop stresses are not ramped upwards quickly and are insufficient to initiate cracks [9.179], and the central fuel temperatures are too low for the fission products to migrate to the inside surface of the clad [9.180].

(c) Hydrogen effects: Hydrogen pick-up by fuel cladding is discussed in Chapter 8, in Volume 2 of this publication; the deleterious effects of hydrogen that are associated with fracturing hydrides will be discussed in Section 9.7, below. Application of the results is debatable, with some regulators wishing to limit the allowed initial stress to 90 MPa to avoid an embrittling reorientation of hydride precipitates into the radial direction in cladding of fuel that has reached a burnup of 62 MWd/kgU [9.174]. The imposed stresses are thought to be too low for time dependent cracking, such as delayed hydride cracking. The configuration of hydrides could be important for the handling and transportation of spent fuel — both these topics will be covered in Section 9.7. Hydrogen in solution or as hydrides can affect deformation — see (d) below.

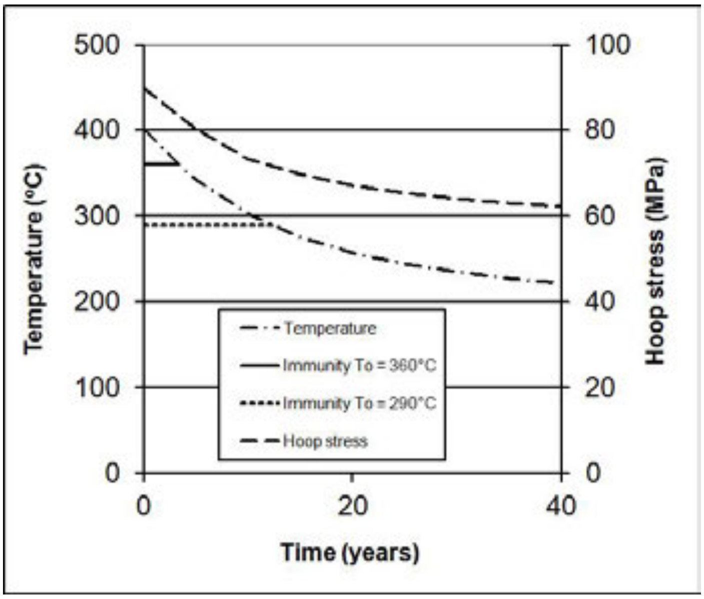

Fig. 9.51. Calculated decline in temperature and hoop stress from internal pressure during the first 40 y of storage [9.177]. Temperatures for immunity from delayed hydrogen cracking, T_0, are described in Section 9.7.

(d) Creep rupture: If failure mechanisms (a) and (b) are unlikely and (c) can be controlled, the remaining mechanism to guard against is creep rupture. The formation and growth of cavities leading to low strain failures do not seem likely in light of the evidence presented in Section 9.3.1. A common approach is to set a limit on the allowable strain from creep, usually with a target of <2%. The strain restriction consequently limits the allowable temperature, which depends on the burnup of the fuel, residence time in the spent fuel pool after reactor discharge, the heat removal capability of the dry storage system and stress, which is a function of the gas pressure, the dimensions of the clad and the degree of any mechanical damage. The metallurgical factors to consider are the effect of hydrogen in solution or as hydrides on creep rate and strain at rupture, and neutron irradiation fluence and annealing of irradiation damage. As a first step, each of the factors has been evaluated separately.

The main effects of hydrogen are on the creep rates rather than on creep ductility and fracture. In unirradiated Zircaloy-4, hydrogen, when precipitated as hydrides, suppresses creep in short term tests for up to 250 hours. In uniaxial tests at 673 K (400°C) on CWSR material with a stress of 350 MPa, 215 ppm (1.92 at.%) hydrogen in solution slowed the secondary creep rate by two times [9.181]. When the hydrogen concentration was raised to 360 ppm (3.18 at.%), so that about 150 ppm (1.26 at.%) hydrogen was present as hydride precipitates, the creep rate decreased by 3.5 times. The time to failure increased by about 4 times and the total elongation nearly doubled. Tests on tubes biaxially loaded between 623 and 743 K (350°C and 470°C) [9.182] confirmed the suppression of creep; ductility was not affected, even with 1040 ppm (8.67 at.%) hydrogen.

Steady state creep may be considered a competition between strain hardening and recovery of that strain. Delay of recrystallization of CWSR material at 743 to 793 K (470 to 520°C) by between 105 and 330 ppm (0.95 to 2.92 at.%) hydrogen in solution was taken as an indication of the importance of the recovery part of the competition [9.181]. Tensile testing at room temperature after a creep test at 743 K (470°C) with a stress of 80 MPa supports this conclusion. A specimen containing 720 ppm (6.17 at.%) hydrogen and strained 3% in 240 hours had a yield strength of about 600 MPa, similar to that of as-received material, while a specimen containing little hydrogen and strained 5% in 120 hours had a post-test yield stress of 450 MPa, showing that much of the creep strain and original cold work was recovered. In fully annealed Zircaloy-4, hydrogen in solution causes a softening, especially in the strain ageing temperature regime of 503 to 703 K (230 to 430°C) [9.183]. This decrease in creep resistance was attributed to trapping of hydrogen at dislocations that increased their mobility by reducing lattice friction. Hydrides overcome this softening and suppress creep, as in CWSR material, probably by providing obstacles to dislocation glide at low strains.

TABLE 9.11. EFFECT OF TEMPERATURE AND STRESS ON SUPPRESSION OF CREEP BY IRRADIATION [9.184]

Temperature (°C)	Stress (MPa)	Secondary creep rate: Irradiated material/unirradiated material	
		RX Zircaloy-2	CW SR Zircaloy-4
330	95	—	0.5
330	170	0.13	0.3
390	92	0.13	0.21
420	35	—	0.36
420	60	0.055	0.21
420	90	0.04	0.1
330	95	—	0.5
330	170	0.13	0.3
390	92	0.13	0.21
420	35	—	0.36

The hardening of zirconium alloys by irradiation observed in tensile tests also slows post-irradiation creep. The reduction in creep rate mirrors the increase in strength with neutron fluence, with the rate slowly decreasing after an initial sharp drop with small fluences [9.184], as shown in Fig. 9.52. The effect of high neutron fluence on creep may be illustrated with the ratio of the creep rate in irradiated material compared with that for unirradiated material. The results in Table 9.11 are from internally pressurized fuel cladding after service in both a PWR and a boiling water reactor (BWR). The effect of irradiation is greatest at high stress and temperature and with starting material that has been annealed [9.185]. The effect of irradiation appears to be greater than the effect of hydrides since the creep rates of specimens with hydrides were indistinguishable from those where the hydrogen was all in solution. Post-irradiation behaviour also depends on the stress imposed during irradiation. Residual stress retained in the cladding from external or internal pressure during irradiation contributes to deformation; if the residual stress is compressive, positive strain is observed only after a delay time in the post-irradiation test while if the residual stress is tensile, the cladding deforms without an applied stress [9.186]. As may be inferred from the tensile properties, irradiation reduces the strain to the onset of tertiary creep, from about 10% down to about 1% [9.125, 9.184, 9.187], and reduces the strain to creep rupture. Calculations of the onset of tertiary creep based on the increase of stress, with strain leading to plastic instability (similar to the approach described in Section 9.3.1), are in good agreement with observations at high stress and give approximately 200 MPa [9.125]. Thereafter, the creep rate is faster than that calculated. Although this acceleration was attributable to the annealing of irradiation damage, clearing of the damage from the deformation could be another explanation (see Section 9.2.2). With unirradiated material, the strain to rupture decreases with an increase in applied stress, as expected from the phenomenology described in Section 9.3.1. At high stress in the temperature range 623 to 673 K (350 to 400°C) irradiation much reduces the strain to failure, in some examples being less than 1%. The strains to failure appear to be much greater than 1% at stresses expected for dry storage, as shown in Fig. 9.53. The time to rupture depends on the strain to rupture and the creep rate. The data from rupture tests on internally pressurized, unirradiated and irradiated CWSR Zircaloy-4 cladding [9.125] were fitted to the Monkman and Grant

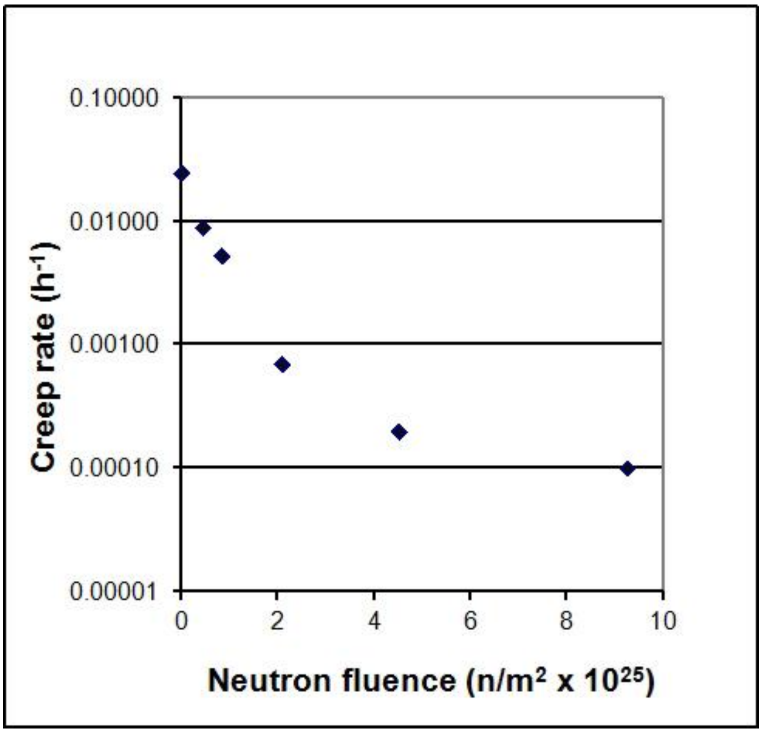

Fig. 9.52. Effect of fluence of fast neutrons (E > 1 MeV) on post-irradiation creep rate of cold worked and stress relieved Zircaloy-4 fuel cladding at 623 K (350°C) with a hoop stress of 445 MPa (based on data from [9.184]).

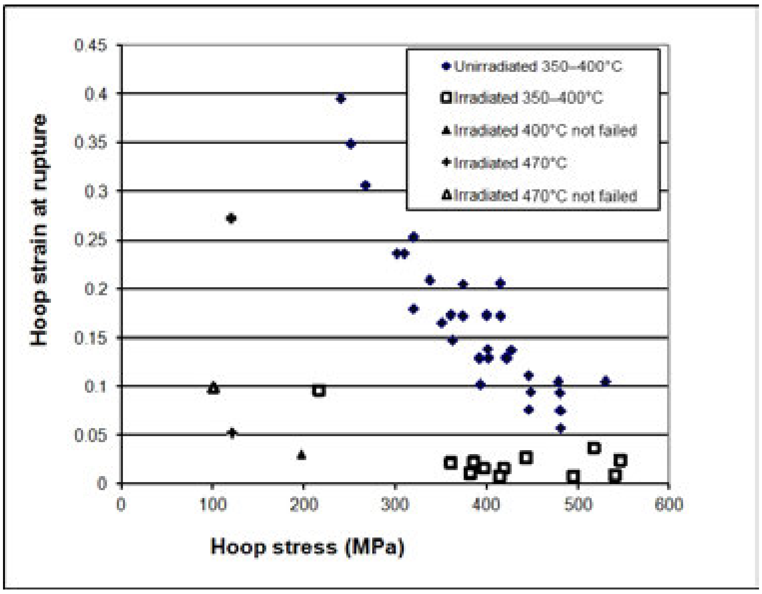

Fig. 9.53. Dependence of hoop strain on hoop stress during stress rupture tests on cold worked and stress relieved Zircaloy-4 fuel cladding both before and after irradiation to fluences between 2 and 9 × 10^{25} n/m^2 (based on data from [9.125]).

formulation in which the product of the MCR and rupture time is a constant, 0.056. When the same data were interpreted through the Larson–Miller approach, the increase in rupture time with irradiation was clear, as shown in Fig. 9.54, showing that despite the loss in ductility, the simultaneous increase in creep resistance dominated time to rupture.

Irradiation damage starts to anneal out at temperatures above the irradiation temperature. When specimens of CWSR Zircaloy-4 were creep tested at 673 K (400°C) with a stress of 150 MPa after a pre-test at 743 K (470°C) for ten days with stresses between zero and 120 MPa, the creep rate was higher than in as-irradiated material [9.186]. The irradiation damage had started to recover during the residence at the higher temperature; these results suggest that stress during annealing had no effect on the amount of recovery. The microstructure was completely recrystallized after annealing for ten days at 793 K (520°C) and all the irradiation damage was removed.

To apply these observations to dry storage a suitable description of the creep behaviour, how it is accommodated by the decline in temperature and stress with time, and the evolution of the microstructure is needed. With no reduction in temperature and stress and initial values at the NRC recommended limits of 673 K (400°C) and 90 MPa, rupture is predicted in about 15 years using the data from irradiated material, as shown in Fig. 9.54, thus providing some margin for the decline of temperature and pressure. Similarly, the data from tests on unirradiated material predict no rupture for close to 90 years for an initial temperature of 633 K (360°C) and stress of 80 MPa [9.176]. An allowed initial temperature for dry storage of about 673 K (400°C) with a stress of about 70 MPa was developed using a theoretical creep fracture map and a life fraction rule [9.188]. The life fraction rule assumes that fracture damage may be accumulated additively; the component is assumed to have failed when the sum of the times at a temperature and stress divided by the rupture time at those test conditions reaches unity. In this analysis diffusion-controlled cavitation and triple point cracking were assumed to be the dominating creep fracture mechanisms for zirconium alloys in the temperature regime appropriate for dry storage. Since these mechanisms do not apply at these temperatures, more appropriate rules should be based on strain accumulation and recovery of irradiation damage. Results from tests on stress relieved Zircaloy-2 plate followed a strain hardening rule rather than a time hardening rule [9.189]; that is, after a change in stress or temperature, subsequent deformation followed creep behaviour as though the previous strain was accumulated at the new conditions (see Section 7.4.3.2, in Volume 2 of this publication). Unirradiated Zircaloy-4 fuel cladding stressed by internal pressure confirmed the strain hardening rule after large changes in both stress and

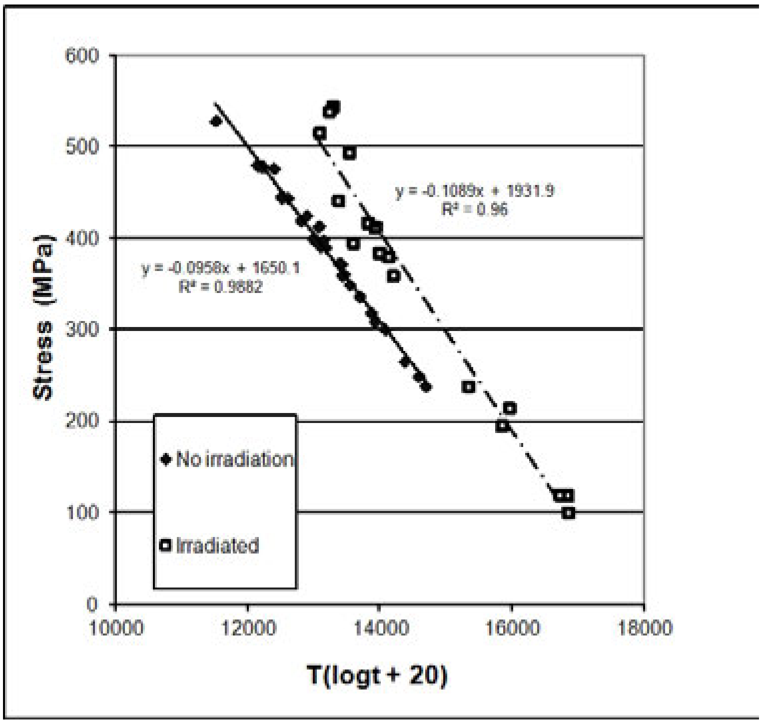

Fig. 9.54. Larson–Miller representation of stress rupture tests on cold worked and stress relieved Zircaloy-4 fuel cladding both before and after irradiation to fluences between 2 and 9 × 1025 n/m^2 (based on data from [9.125]).

temperature [9.190]. With a test temperature of 673 K (400°C) the hoop stress was raised from about 75 MPa to about 150 MPa or the reverse. With a stress of 118 MPa the temperature was raised from 633 to 663 K (360 to 390°C) or the reverse with a stress of 196 MPa. In each experiment the creep rate of the second step was predicted accurately from results at constant conditions but applied at the strain attained during the first step. Internally pressurized sections of recrystallized Zircaloy-2 irradiated to a fluence of about 9 × 10^{25} n/m^2 (E > 1MeV) confirmed the strain hardening rule for irradiated material with tests in which the temperature and stress were changed between 633 to 663 K (360 and 390°C) and stresses between 124 MPa and 137 MPa [9.184]. For fuel stored outdoors, any effects of seasonal temperature variation should be calculated with a strain hardening rule with the stress from the gas pressure declining with the drop in temperature in the winter and increasing with temperature rise in the summer. Detailed evaluation of this effect needs more attention.

Since the results from short tests have to describe creep behaviour during long term storage, various creep formulations have been proposed with the objective of confining the deformation to primary and early secondary creep; tertiary creep is avoided by keeping the strain close to 1%. In Germany, the suppression of creep by irradiation was acknowledged but the behaviour of unirradiated material was considered to provide a conservative description. Data from creep tests on unirradiated CWSR Zircaloy-4 cladding in the temperature range 523 to 673 K (250 to 400°C) and with stresses between 80 MPa to 150 MPa were fitted to a description of primary creep, $\varepsilon = At^{b}$. The expected strain was estimated by an iterative calculation using this equation with temperature and pressure histories similar to those shown in Fig. 9.51. Strains of between 0.37% and 0.77% were predicted within two years of the start of dry storage, with little change thereafter [9.176]. These results suggest that for these cases creep rupture is not a significant risk and confirms the conclusion based on interpolating the results from stress rupture tests. Creep laws for irradiated material have also been developed in France. One description for cold worked stress relieved Zircaloy-4 uses a single term expression [9.191], $\dot{\varepsilon} = (f(\varepsilon))^{-p} \cdot \sinh(f(\sigma)) \cdot \exp(-\,\mathrm{constant}/T)$, with $p = 0.9$. An alternative method is to separate the terms for primary and secondary creep, then multiply each term by a function describing the effect of irradiation [9.192]. This formulation assumes that the stress sensitivity and thermal activation energies are not affected by irradiation damage.

Another method is to apply the Larson–Miller approach to the reported creep data. Fuel from several reactors was removed from fuel rods and the cladding was internally pressurized at a range of temperatures from 573 to 693 K (300 to 420°C). The starting materials were CWSR Zircaloy-4 [9.184, 9.193–9.195] and ZIRLO [9.196] and the fuel burnups were in the range 34 to 68 MWd/kgU. The minimum or secondary creep rates were converted to Larson–Miller parameters through T(20 log $\dot{\varepsilon}$), where T is in K and $\dot{\varepsilon}$ is in h^{-1}. The results are pooled in Fig. 9.55. Using the mean value of the parameter, if a strain of 1% is acceptable, at a constant temperature of 673 K (400°C), a hoop stress of 101 MPa could be tolerated for one year; for 2% strain the tolerable hoop stress would increase to 125 MPa. Since the temperature and pressure will decrease with time, these results suggest there is some margin on deformation for storage starting conditions with a hoop stress of 90 MPa at 673 K (400°C). When the creep strain is integrated over 40 years using the temperature and stress histories of Fig. 9.51 and the equation fitted to the Larson–Miller description of the creep rate, as shown in Fig. 9.55, the calculated total strain is small, as shown in Fig. 9.56. Less than 0.5% strain is accumulated in the first year and a total of less than 0.7% strain is attained in ten years, with little subsequent change. Although this approach ignores primary creep and uses the average value of the Larson–Miller parameter so that the dispersion of the results erodes the margin, in the tests much capacity for straining was observed. For example, after a burnup of 67 MWd/kgU, the Zircaloy-4 cladding sustained a strain of over 5% with test conditions of 673 K (400°C) and 190 MPa for 2427 h [9.194]. After a similar burnup, peak strains of 13% and 17% were attained in ZIRLO for similar test conditions [9.195]. Combining this approach with the Monkman and Grant constant of 0.056 provides a rupture time of nearly 7 years with constant conditions of hoop stress of 90 MPa at 673 K (400°C).

Surveillance of spent fuel after periods of dry storage have confirmed that creep deformation is small. PWR fuel was discharged after a burnup of 35.7 MWd/kgU in the Surry Nuclear Power Station. After residence in a water pool for 3.7 years, it was stored in a dry, inert atmosphere for 14.8 years. After some thermal benchmark tests, in which the maximum temperature reached 688 K (415°C), but for less than 72 h, the fuel rods were stored in a Castor cask. The temperature at the start

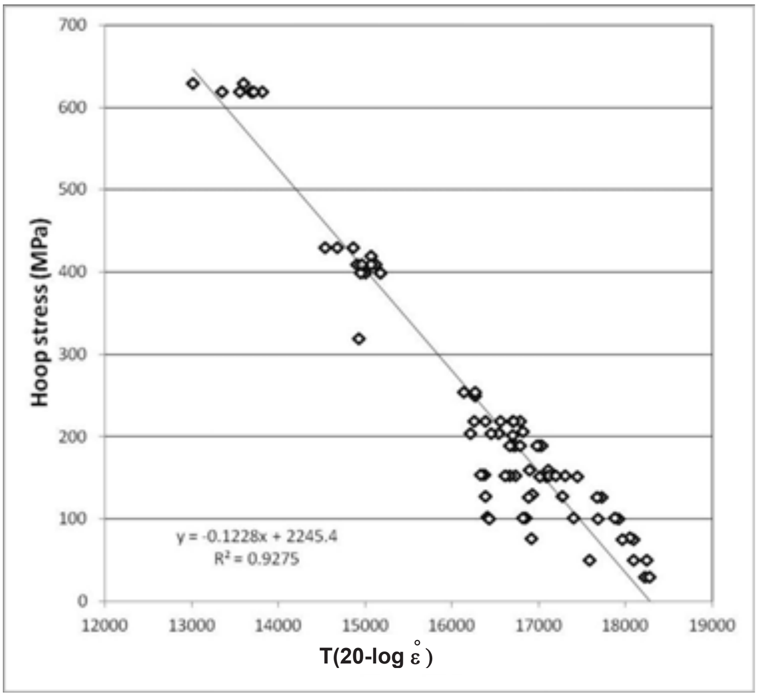

FIG. 9.55. Larson–Miller representation of creep rates from thermal creep tests on Zircaloy-4 and Zirlo fuel cladding irradiated in power reactors [9.185, 9.193–9.196].

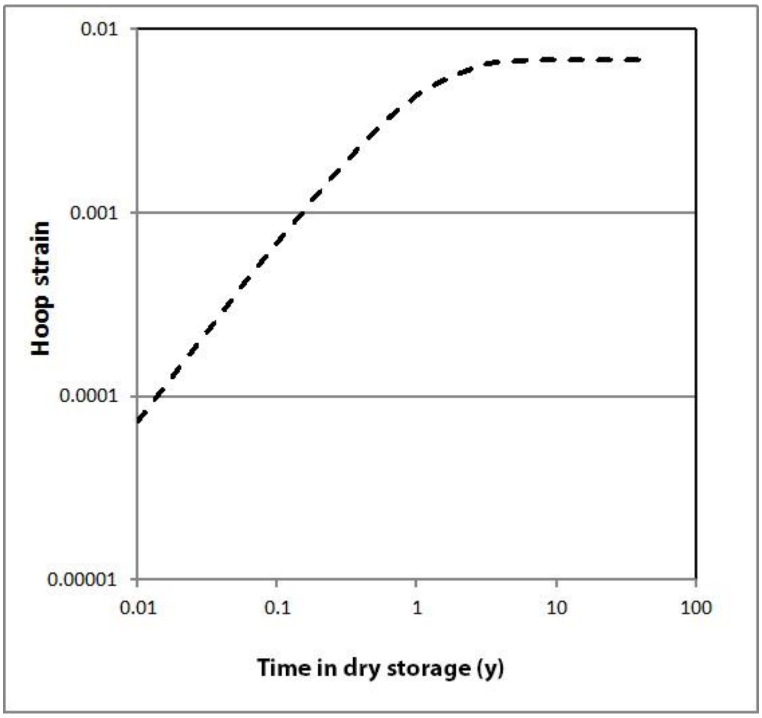

FIG. 9.56. Creep strain accumulated in Zircaloy fuel cladding during dry storage of spent fuel with initial temperature of 673 K (400°C) and hoop stress of 90 MPa, using temperature and stress history described by FIG. 9.51 and the creep properties depicted in FIG. 9.55.

of dry storage was 617 K (344°C); this temperature declined to about 428 K (155°C) after 14.2 years. To examine the health of the spent nuclear fuel after storage some of the fuel rods were destructively examined [9.197]. The contribution to the internal pressure from the fission gases was 0.75 MPa for a total pressure of 3.61 MPa. At 688 K (415°C) this pressure would impose a hoop stress of 72 MPa, but at the start of dry storage, 617 K (344°C), the value would be 64 MPa. Based on hardness tests, no irradiation damage had been annealed out during dry storage. In the absence of prestorage rod profiles, the creep was estimated by three methods:

(1) Applying the Yucca Mountain Project creep code [9.198] using estimates of the storage temperature history.
(2) Comparing tube diameters after storage with those from a similar reactor before dry storage.
(3) Comparing the poststorage profile with the minimum diameter estimated for in-reactor creep down.

The maximum value of creep strain was estimated at 0.2%, most of which probably occurred during the performance testing phase.

No gross diameter change was reported when 20 rods of similar PWR fuel with a burnup of 58 MWd/kgU were stored dry for 20 years after 3 years of pool storage [9.199]. The fission gas release after dry storage was similar to that after initial discharge indicating that no extra fission gas was released during storage. The inner pressure was estimated from puncture tests to be 4.58 MPa, which would impose a hoop stress of 88 MPa if the highest temperature was the NRC limit of 673 K (400°C). No temperature measurements were reported; they likely did not exceed 673 K (400°C) because the poststorage tensile properties were similar to those measured immediately after discharge from the reactor indicating no removal of irradiation damage. Under these storage conditions, no creep rupture was observed.

To summarize, creep rupture is a potential failure mechanism of spent fuel during dry storage in which decay heat provides a high temperature and internal gas pressure provides a hoop tensile stress. Irradiation damage suppresses creep but promotes plastic instability. Invoking the creep properties of unirradiated material may offer adequate ductility as a defence against excess deformation that may lead to fracture. The early part of storage imparts the most onerous conditions for creep but once withstood, creep should not present a problem. Starting dry storage after the decay heat has dissipated sufficiently to induce an initial hoop stress of 90 MPa or less, at a temperature of 673 K (400°C) or less, should provide protection from creep rupture. Further confirmation is required with more surveillance, especially thermometry and profilometry of high burnup fuel after several years of dry storage and attention being paid to the role of seasonal temperature variation.

9.3.4. High temperature behaviour — loss of coolant accident

If a large pipe carrying heat transport fluid to the reactor core should break, the fuel and its containers would be without cooling and would reach very high temperatures. This situation is called a loss of coolant accident (LOCA). Regulators require assurance that the reactor is designed so that during a LOCA the damage to the systems, the structure and components can withstand the conditions sufficiently to assure public health and safety; it is a design basis accident. The next two sections are concerned with the evidence that enables the designer to provide this assurance through knowledge of how the fuel cladding responds to rapid changes in temperature and pressure.

In PWRs a LOCA from a break in an inlet pipe is postulated to pursue a course similar to the following:

- Before an accident, the average temperature of the UO_2 fuel would be about 1370 K (1100°C) with a peak greater than 2470 K (2200°C). The temperature of the cladding would typically be about 610 K (340°C).
- Early in an accident, the pressure in the heat transport water is reduced as it escapes through the break and the water becomes steam. Heating from the nuclear reaction is much reduced, because moderation decreases as the density of the water decreases and because control rods are automatically inserted into the reactor core, but much heat remains stored in the fuel and in the steam generators. The cooling of the cladding diminishes. The temperature gradient across the fuel and cladding tends to even out, increasing the temperature of the cladding at a rate of 10 to 100°C/s [9.200]. The initial temperature rise of the cladding is limited because much of the stored heat is removed by the escaping steam and water; this stage of the accident is called blowdown.
- The fuel will continue to contribute heat from the radioactive decay of fission products and actinide elements such as plutonium produced during reactor operation. Another potential source of heat is oxidation once the clad temperature exceeds 1250 K (980°C). These heat sources cause the temperature of the cladding to rise again once the cooling effect of the blowdown stops.
- In the design of a reactor, several precautions are taken to mitigate damage to protect both the reactor and people. For example, cold water can be automatically injected into the bottom of the reactor core to remove the excess heat by what is called an emergency core cooling system (ECCS).
- Initially, the ECCS water is converted to steam to provide cooling. This steam is gradually displaced by water as the reactor core refloods and the accident is contained.

The expected temperature history is complicated. In an example, shown in Fig. 9.57 [9.201], initially the temperature spikes in a few seconds to about 1200 K (930°C), followed by cooling during blowdown, indicated by point (1), reheating at point (2) from decay heat as the steam in blowdown is exhausted, then slowing of the heat-up rate as the ECCS imposes film boiling, indicated by points (3) and (4), then more effective cooling by nucleate boiling after 110 to 150 s, indicated by point (5). In laboratory experiments the transition from film to nucleate boiling — the Leidenfrost temperature —

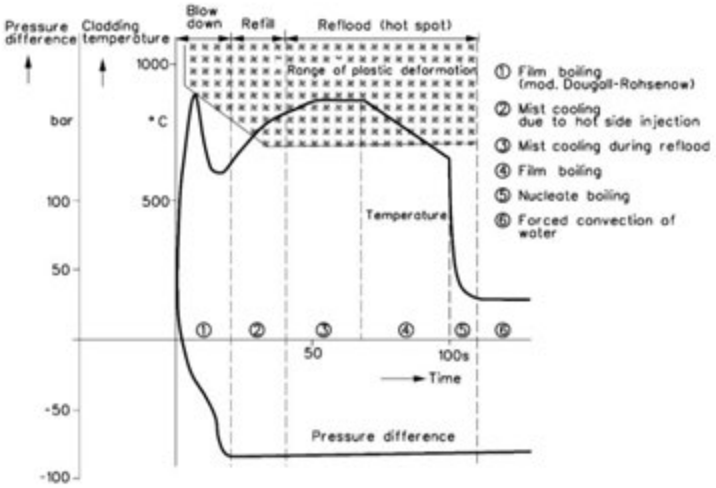

FIG. 9.57. Schematic diagram of possible temperature and pressure response in a PWR after a LOCA with application of an ECCS (based on [9.201]).

is in the range 530 to 900 K (265 to 630°C)[2] independent of the maximum temperature attained during heating [9.202]. As the heat transport water is dispersed, the pressure difference across the cladding wall will decrease and, in this example, will be represented by internal pressure of about 7 MPa from initial filler gas and fission gases. During the heat-up to the first cladding temperature peak, in the blowdown phase, indicated by point (1) in Fig. 9.57, coolant pressure is still relatively high, so that internal overpressure does not occur. At the end of the blowdown phase, when the rod internal pressure exceeds the coolant pressure, the cladding temperature is relatively low. The cladding may deform and swell, but the probability of fuel rod failure is much lower during the blowdown phase than during the subsequent second heat-up phase, indicated by points (2) and (3) in Fig. 9.57. At that point the pressure inside the fuel can produce a positive hoop stress in the cladding and the internal temperatures will be high. The cladding will balloon and may rupture, and if the deformation is large, may cause blockages that prevent the heat transport fluid from cooling the fuel. The cladding will also oxidize and pick up hydrogen sufficiently to embrittle the tube at low temperatures and may also cause problems with blockage and fuel dispersal.

In BWRs the equivalent accident would be a break in the intake line to a recirculation pump. Initially, nucleate boiling would continue to cool the core until the pump on the intact line stops. As the flow of water declines, the core temperature rises. The water flows through the break and blowdown follows when the level outside the shroud surrounding the core reaches the break. Steam also escapes from the vessel and the pressure falls rapidly resulting in the water at the bottom of the reactor flashing to steam. Some of this water and steam mixture rises through the core and cools it. Indications of problems prompt the ECCS to provide cooling water, which at first is a steam-water mixture flowing through the core followed by eventual reflooding. Figure 9.58 shows a postulated temperature and pressure history in a jet pump BWR schematically [9.203].

A CANDU-type pressurized heavy water reactor (PHWR) provides a third example. Although the cladding is subjected to similar high temperatures should a large pipe in the heat transport system break, the sequence of temperatures and pressures is different from that in an LWR. As the coolant voids in the pressure tubes, the reactivity and therefore the fuel power increases initially. This spike in power lasts less than 2 s and is terminated by one of two independent shutdown systems. Thereafter the fuel power decreases to decay power values. In the absence of full cooling, the stored heat in the fuel redistributes rapidly and the cladding heats up quickly. Simultaneously the UO_2 fuel may expand and may interact with the cladding. A few seconds after the break, the fuel

---

[2] Sometimes the lower limit is quoted as 748 K (475°C) although fig. 12 in Ref. [9.26] indicates the lower value.

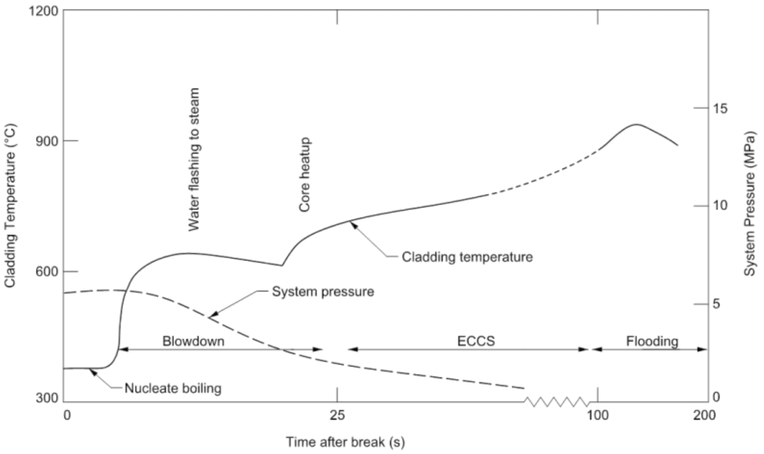

FIG. 9.58. Schematic diagram of temperature and pressure history during a postulated LOCA in a jet pump BWR [9.203].

element temperatures are influenced by the balance between the decay heat and the heat losses to the surroundings and the remaining coolant. The heat-up rate of the cladding is rapid, with maximum initial rates up to 200°C/s, and it reaches a plateau temperature for a few seconds. The transient is then terminated by the injection of the ECCS. An example of the predicted pressure and temperature transients for a fuel element are shown in Figs 9.59(a) and (b) [9.204]. The temperature of the cladding reaches about 1470 K (1200°C) after about 20 s while the pressure of the heat transport heavy water declines from 10.5 MPa to less than 1 MPa in 30 s. The internal pressure in the fuel element is initially about 8 MPa but declines rapidly during the transient. The differential pressure between the inside and outside of the fuel element starts out negative but gradually increases to be slightly positive. The reason for the low differential pressure is that the gas volume within a fuel element is small — <1 cm^3 at power — and a small strain is sufficient to reduce the pressure greatly by increasing the volume. For example, a 1% increase in tube diameter increases the gas volume to 2.2 cm^3.

The postulated accidents described above are caused by a single event, with the initial stages over in a time scale of seconds. Accidents may also be a series of several events taking place over a time scale of hours. The initiating event may be as small as a sticking valve, as in the accident at Unit 2 of Three Mile Island in 1979 [9.205], or as large as a major geological upheaval. After the earthquake in 2011 that caused the accident at the Fukushima Daiichi nuclear power plant, its reactors were shut down in good order but the subsequent tsunami destroyed the power to the pumps for the heat transport system and ECCS, the reactors could no longer be cooled and meltdown followed [9.206]. The very hot Zircaloy-2 fuel cladding reacted with steam to produce hydrogen (see Section 8.7.1, in Volume 2 of this publication) that led to explosions [9.207]. This event, and that at Chornobyl in 1986 [9.208], were beyond design basis accidents and are not considered in this publication. They do, however, emphasize the need for robust infrastructure, and clear and well rehearsed operating procedures as well as a forgiving design using materials with high structural integrity.

Since the possible accidents in the different types of reactors are many and varied, a description of each one is beyond the scope of this chapter. To mitigate the consequences of such accidents, designers and operators of reactors must demonstrate, through their computer codes describing the behaviour during normal reactor operation and accidents, that the criteria to assure safety set up by the regulators are fulfilled during all the postulated accidents. A common theme is the demonstration of the ability to cool the fuel by providing a continuous supply of water before its access is blocked. One approach is prescriptive: the maximum temperature is restricted and the applicable models for calculation are mandated. In the USA, the NRC requires the following during a postulated LOCA of the sudden type in a PWR [9.209, 9.210]:

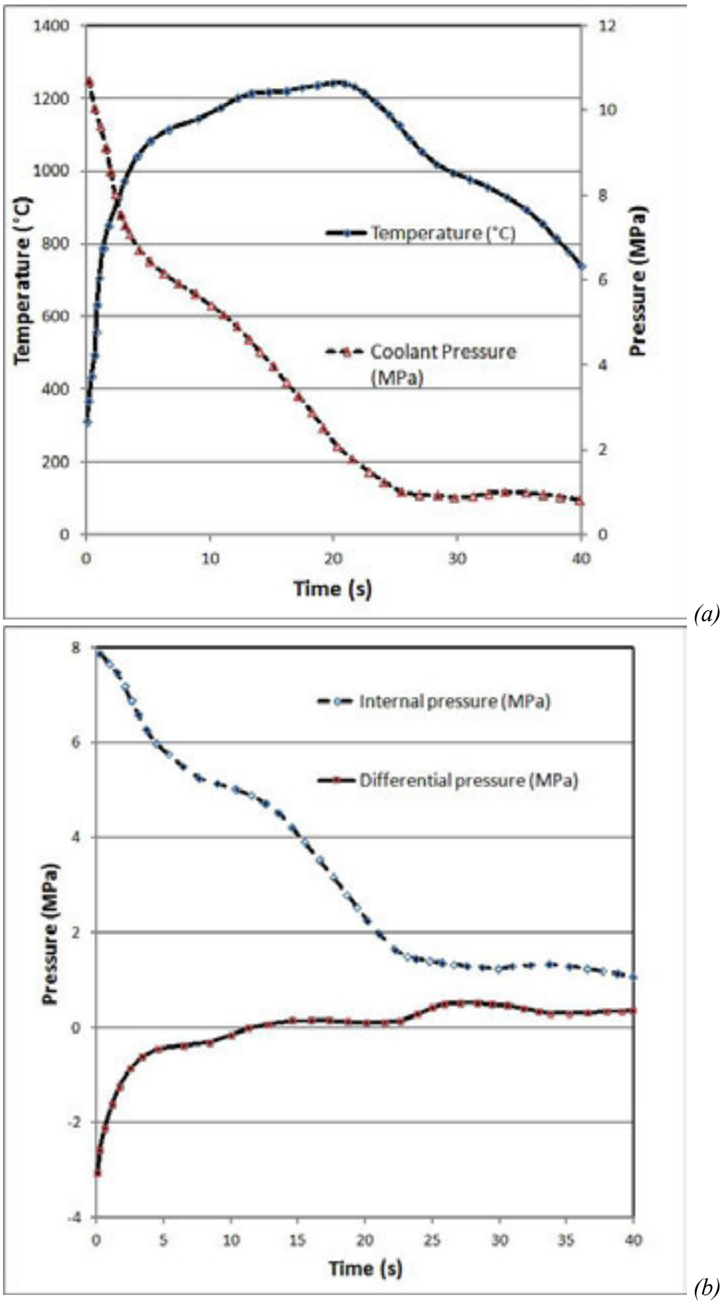

FIG. 9.59. Predicted histories of cladding temperature and pressures during a LOCA in a CANDU reactor; (a) coolant pressure; (b) internal and differential pressures in the fuel element [9.204].

(a) The fuel should remain coolable; the implication is that spaces between individual fuel rods should not be blocked. This criterion places a limit on cladding deformation; the cladding will tend to balloon, driven by the internal gas pressure and high temperatures, and may burst to release fission and filler gases. Full rupture that may allow the dispersal of irradiated fuel and fission products has to be dispositioned.

(b) The reactor core should remain acceptably cooled once the accident has been contained (i.e. the decay heat from long lived radioactivity should be removed for a time sufficient to maintain an acceptably low temperature). This criterion implies that the fuel assemblies should stay essentially intact.

(c) The thickness of the cladding affected by oxygen (the oxide and oxygen enriched layer) should not exceed 0.17 times the initial cladding thickness.

(d) The total amount of hydrogen generated should not exceed 0.01 times the amount that would be generated if all the metal in the cladding were reacted with the steam.

Criteria (c) and (d) are to minimize embrittlement and loss in shape at low temperatures after the quench by the ECCS. Their values depend on the time at the temperatures reached in stages (1) and (3) shown in Fig. 9.57. Consequently, the cladding temperature should not exceed 1477 K (1204°C). The source of this value is described in Section 9.4, but for this section on deformation it is sufficient to note this limiting high temperature.

Initially these criteria applied to Zircaloy-2, Zircaloy-4 and ZIRLO, with cases being made for burnups of about 45 MWd/kgU. With more information and understanding, burnups of 62 MWd/kgU were allowed and fuel clad in alloys other than Zircaloy and ZIRLO (e.g. various versions of Zr-1Nb) were shown to meet the NRC criteria and were permitted.

The models that must be used to calculate the above criteria are described in appendix K to 10 CFR Part 50 [9.211]. The models include initial stored energy in the fuel, decay heat, heat transfer in the structure, ballooning and rupture of the fuel cladding and metal–water reaction rates. Alternatively, a less conservative, realistic evaluation model may be used for the same phenomena [9.212]. These evaluation models must include sufficient supporting justification to demonstrate that the analytic techniques employed realistically describe the behaviour of the reactor system during a postulated LOCA. Other countries use similar criteria, for example, Germany [9.213, 9.214]. They are considered to be conservative, based on the models of the accident required by the regulators [9.210].

The same principles apply in a PHWR but the approach of the Canadian Nuclear Safety Commission is to state basic safety objectives for protecting the public [9.215] with qualitative acceptance criteria [9.216]. The licensee sets up and demonstrates quantitative criteria to meet the safety objectives and regulatory qualitative criteria, then gains agreement from the regulator as to their efficacy. With the added complication of maintaining the integrity of the pressure tube and the calandria tube, the following criteria must be met:

(a) No significant fuel sheath (cladding) oxidation and bundle deformation such that:
    (i) All fuel assemblies and components in the reactor shall be kept in a configuration that maintains continuous removal of the residual heat produced by the fuel; in practice the strain in the fuel cladding is limited to 5 to 6%.
    (ii) Cooling flow shall be supplied to prevent further damage to the fuel after adequate cooling of the fuel is re-established by the ECCS.
(b) To maintain integrity of the fuel channel, including the pressure tube and the calandria tube:
    (i) Fuel string expansion caused by fuel bundle and element deformation shall not cause excessive localized strain of the pressure tube;
    (ii) Sufficient moderator subcooling must be maintained to prevent sustained calandria tube dryout as a result of the pressure tube ballooning into contact.
(c) No fuel or fuel cladding melting, which could challenge the integrity of the fuel channels.

For CANDU, there is no explicit sheath temperature limit such as 1470 K (1200°C), but in the new designs, this temperature limit is used as a design target.

For all reactors, the analyses and computer programs depicting accidents and demonstrating that the above criteria are met partly rely on data describing the response of the zirconium alloy components to the accident. Two main modes of deformation need to be considered to maintain a coolable reactor core — ductile behaviour at high temperatures and brittle behaviour at low temperatures. The properties to consider are deformation and fracture and pick-ups of oxygen and hydrogen at high temperatures [9.217]; the latter two are discussed in Chapter 8, in Volume 2 of this publication, and their effect on fracture properties at temperatures below 570 K (300°C) are described in Sections 9.4 and 9.7. The focus of the experimentation is to elucidate the important metallurgical processes and effect of experimental conditions and to evaluate the size of any conservatism in the criteria through the simulation of postulated accidents. This section focuses on the deformation properties of fuel cladding and structural materials at high temperatures to determine whether the fuel cladding and structure maintain a high degree of coolability through the absence of flow blockage and efficient heat transfer. The examples show how the experiments evolved from straightforward mechanical testing to experiments of increasing complexity in attempts to model in-reactor behaviour. Detailed and comprehensive reviews of the testing and analyses are available [9.199, 9.202, 9.218–9.220] so only the metallurgical highlights are presented here. The objectives of the testing are to evaluate the deformation of the cladding and structural components during temperature ramps to high temperatures and to validate computer codes. Variables include geometrical and thermal gradients; phase transformations; interactions with neighbouring fuel and components; in-reactor effects, including irradiation damage and burnup; changes in chemistry during service; heat transfer and coolability and new alloys. It is acknowledged that some cladding will rupture during a LOCA; to limit the release of fission products, in Germany and Finland the fraction of burst elements or rods is restricted to 10% [9.213].

9.3.4.1. Simple testing.

The deformation rates between 920 and 1870 K (650 and 1600°C) in Zircaloy and dilute tin alloys have been evaluated in creep and compression tests. In Zircaloy the formation of a mixture of the α and β phases starts at about 1080 K (810°C) and the two phase region extends to 1250 K (980°C) above which the material is completely in the β phase [9.221]. The behaviour in the three phase regions is quite distinct. In the α phase and β phase, the dependence of strain rate, $\dot{\varepsilon}$, on stress, σ, and temperature, T, is well represented by:

$$\dot{\varepsilon} = \mathrm{A}\sigma^n \exp(-Q/\mathrm{R}T) \tag{9.16}$$

where

A is a constant;
n is the stress sensitivity;
Q is the activation energy for the deformation;

and R is the gas constant.

In the α phase, n is in the range 4.5 to 7.5 with a mean value of 5.4 ± 0.52; the activation energy, Q, is in the range 213 to 418 kJ/mol with a mean value of 297 ± 41 kJ/mol; and in the β phase, n is in the range 3.2 to 4.4, with a mean value of 3.8 ± 0.33; and Q is in the range 123 to 238 kJ/mol, with a mean value of 156 ± 32 kJ/mol. These values are in good agreement with results from internally pressurized Zircaloy-2 cladding [9.222]. In the α phase, the value of Q is similar to that for self-diffusion, suggesting that diffusion is involved with deformation while the value of n suggests that dislocation climb is important. The data from several sources merge as the test temperature increases because effects of the various fabrication processes are removed by annealing. The rate in the β phase is also controlled by self-diffusion. No single equation describes the deformation in the (α + β) phase region because of differences in the starting microstructure. With creep rates of less than 10^{-3}/s, n is equal to 1.8 and Q is equal to 56.6 kJ/mol, indicating that grain boundary sliding is important.

Deformation at high temperatures may produce large strains. Based on the phenomenology described in Sections 9.2.1 and 9.3.1, as the strain rate sensitivity of the flow stress, m, or the stress sensitivity of the strain rate, n, approach 1.0, superplasticity is predicted. Such behaviour has been demonstrated in tensile tests on Zircaloy-4 [9.220, 9.223, 9.224]. As the test temperature was raised, the value of m increased from below 0.1 up to 770 K (500°C) to 0.35 to 0.8 between 1120 and 1170 K (850 and 900°C), declined to a minimum value then increased again at higher temperatures, as shown in Fig. 9.60. The elongation tracks m up to about 1470 K (1200°C), as shown in Fig. 9.60. As the

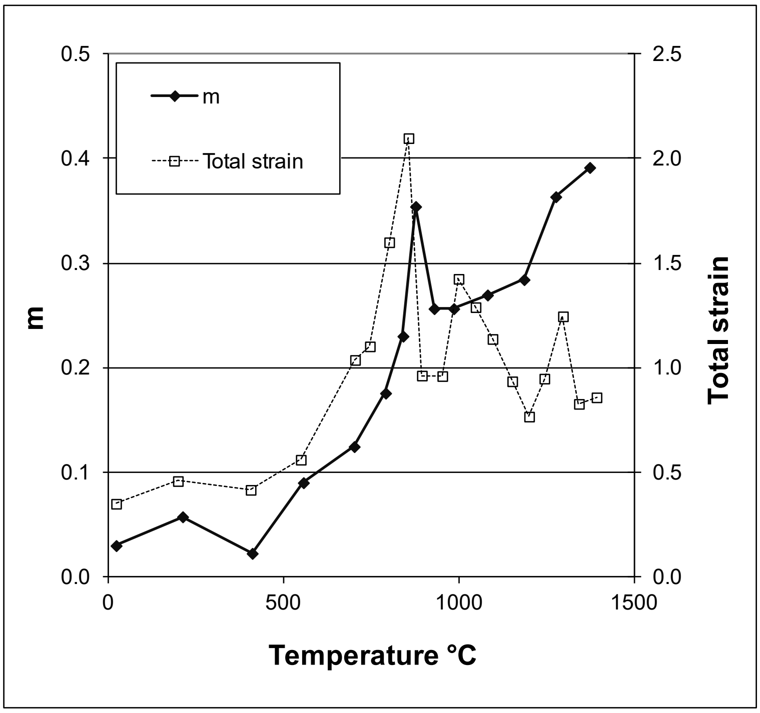

FIG. 9.60. Temperature dependence of strain rate sensitivity, m, *and total strain of Zircaloy-4; grain size 11µm, oxygen concentration 0.11 wt%, strain rate 3.3 ×* 10^{-3} s^{-1} *[9.221].*

grain size diminishes the maximum value of *m* increases — at 1170 K (900°C) *m* is 0.35 with a grain size of 11 µm and increases to 0.57 when the grain size is 5 µm — and the elongation follows the same trend, as at 1120 K (850°C) the total strain at rupture increases from about 1.8 to 2.4 as the grain size is reduced from 11 to 5 µm. The maximum values of *m* and ductility were associated with the low temperature part of the (α + β) phase. Scanning electron microscopy and measurement of the shape of the grains showed that grain boundary sliding of primary α grains in a continuous matrix of β phase was an important deformation mechanism that is accommodated by dislocation creep in both α and β grains to maintain material continuity. A small α grain size promoted high *m* values while Widmanstätten α grains formed by cooling from the β phase halved *m* at low strain rates and decreased the total elongation. As the oxygen concentration is increased, the peak in elongation diminishes, because the α phase becomes less ductile, and the peak moves to higher temperatures, because the α/(α + β) boundary and the critical volume fraction of β phase are shifted to higher temperatures [9.225]. At temperatures beyond the peak in *m*, the contribution of grain boundary sliding declines as the volume fraction of β phase increases and the α–β interface area diminishes. A second peak in *m* appears just above 1270 K (1000°C) in the β phase and is possibly associated with small, newly formed β grains. Tensile and stress relaxation testing in the temperature range 1005 to 1061 K (732 to 788°C) in the α, (α + β) and β phase fields was accomplished by adding up to 20 at.% hydrogen [9.226]. At strain rates greater than 10^{-6}/s, the strength of the β phase was about 30% that of the α phase, while the (α + β) phase material had intermediate strength that was strain rate dependent. The value of *m* was in the range 0.2 to 0.3 in both single phase regions, but up to 0.5 in the mixed phase region. With this condition, using a gauge length of 16 mm, with a value of *m* of 0.33, an elongation of 450% was measured.

In Zr-2.5Nb the α/(α + β) phase transformation takes place at a temperature about 100°C lower than in Zircaloy but the phenomenology is similar. At 1070 K (800°C), where the volume fraction of each phase is approximately equal, with small grain size and interphase spacing, 5 µm, the value of *m* was 0.45, providing an elongation of 450% with a gauge length of 12.5 mm [9.227]. The retention of grain size and shape during deformation indicates α grain rotation in the β matrix, as in Zircaloy.

9.3.4.2. Less simple tests

Unlike in most applications for which the goal is to maximize ductility before failure (however it is defined), during a LOCA the goal is to limit deformation, preferably without rupture. Only small expansions are required for the cladding of adjacent rods in a fuel assembly to touch; in LWRs expansions of about 30 to 40% are required [9.228], in CANDUs this strain is about 10% [9.229], while in SGHWRs the strain is only about 5% [9.221]. Experiments to study the consequences of LOCAs aimed at confirming that, despite this limitation, adequate cooling from the ECCS would be available. Most of the testing representing the early parts of the accident, indicated by points (1) to (3) in Fig. 9.57, consisted of temperature ramps on internally pressurized fuel cladding, with varying degrees of complexity in efforts to simulate a postulated accident and understand the dynamic metallurgical changes taking place over a wide range of temperatures; these changes include recovery and recrystallization, removal of irradiation damage by annealing, phase transformations and oxidation, and ingress of oxygen and concomitant hydrogen into the substrate. The important test parameters are heating rate, internal pressure, environment and non-uniformities; the mode of heating and thermometry can be crucial for the latter. The critical outcome is strain, usually at bursting.

For single rod behaviour, lengths of Zircaloy fuel cladding were internally pressurized with an inert gas and heated rapidly to either rupture or a limit of strain, from either room temperature or about 610 K (340°C), using direct resistance, induction, external shroud or internal heaters. Various specimen lengths were tested. The external atmosphere may be vacuum, air, inert gas, steam or heat transport water. The internal volume of the specimen may be reduced, for example, with alumina cylinders, and the ends of the tubing may be restrained to prevent shortening. Despite this wide array of test conditions and methods, as shown in Table 9.12, the qualitative trends were consistent, although the values of strains and temperature of rupture depend on the details of the experiments.

During a test, if the gas is not vented, the pressure increases a few per cent with temperature until the specimen deforms, then the pressure declines a few per cent as the specimen balloons to rupture. These variations in pressure are small compared with the size of the initial pressure. Deformation starts at a temperature at which the yield stress is exceeded and progresses rapidly to rupture [9.230], as shown in Fig. 9.61. Since most of the deformation takes place in the latter part of a ramp test, the times to failure, and therefore the temperature at burst, are not sensitive to the burst strain. The placement and number of thermocouples are critical because the location of final rupture may be remote from a thermocouple and the burst temperature may be in error. The deformation is retarded if, during the ramp, the temperature exceeds the (α + β)/β boundary [9.231], as shown in

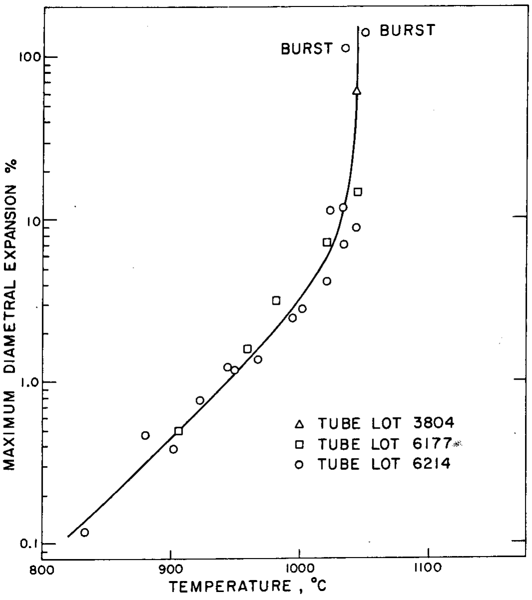

FIG. 9.61. Diametral expansion of Zircaloy-4 fuel cladding with temperature for a heating rate of 25°C/s and internal pressure of 0.7 MPa (imposing an initial hoop stress of about 14 MPa) [9.230].

TABLE 9.12. CONDITIONS FOR TEMPERATURE RAMPING EXPERIMENTS (ZIRCALOY EXCEPT WHERE NOTED)

Specimen length (mm)	Heating method	Internal atmosphere	Space filler	Axial restraint	External atmosphere	Irradiated material	Temperature ramp rate (°C/s)	Temperature measurement	Internal pressure (Mpa)	Comments	Source
50.8	Induction	He	No	No	Ar & steam	No	0.1–240	Spot welded & optical pyrometer	0.34–1.38	Limit to 34% strain. Maximum T = 1720°C	[9.228]
533	Internal heater & outer shroud	Ar	Heater	No	Ar then vacuum	No	14–42	Chromel/Alumel thermocouples spot welded to Ta pads	2.5–10	Thermographic camera confirmed temperatures	[9.234]
152	Direct resistance	Ar	Alumina cylinders	Yes	Vacuum	No	5, 55, 115	Pt/Pt-10Rh thermocouples spot welded	0.35–14	High-speed camera recorded dimensions. Three strain maxima. Axial restraint reduces elongation in alpha phase	[9.235]
915	Internal heater	He	Heater	No	Steam	No	28	Pt/Pt-10Rh thermocouples spot welded	0.8–20.5	Two strain peaks. Ductility sensitive to temperature uniformity	[9.236]
60	External heater	Ar + I	No	No	Inert gas or vacuum	No	4.0–7.0	Thermocouples	0.4–18	Ductility reduced by Iodine up to 850°C	[9.475, 9.476]
508 (380 heated)	Internal heater	He	Heater	Yes	Steam	Yes	28	Chromel/Alumel thermocouples spot welded to Ta pads	1–12.5	Irradiation damage annealed during tests	[9.248]
325	Internal heater	He	Heater	No	Steam	No	1.0–30	Pallaplat thermocouples spot welded	1.0–14	Two strain peaks associated with phase transformations	[9.237]
254	Internal heater & external radiant heat from neighbours	Ar	Heater	No	Ar	No	5.5–55	Chromel/Alumel thermocouples spot welded to Ta pads	0.85–6.9	Increase in wall thickness variation reduced strain to rupture	[9.233]
508–762	Induction	Ar (?)	No	No	Steam & Ar	Yes	5.0–23	Pt/Pt-Rh or Chromel/Alumel thermocouples spot welded	0.7–5.2	Little effect of irradiation; reduction in ductility from oxygen	[9.233]
178 (100 uniform)	Induction	He	Alumina cylinders	No	He	No	5.0–96	Remote pyrometers	1.4–17.2	Test to rupture or 30 s	[9.232]
500 (250 uniform)	Direct resistance	He	No	No	Vacuum	No	25, 100	W-26Re/W-5Re thermocouples spot welded	0.35–13.8	Strain history from many specimens	[9.230]

TABLE 9.12. CONDITIONS FOR TEMPERATURE RAMPING EXPERIMENTS (ZIRCALOY EXCEPT WHERE NOTED) (cont.)

Specimen length (mm)	Heating method	Internal atmosphere	Space filler	Axial restraint	External atmosphere	Irradiated material	Temperature ramp rate (°C/s)	Temperature measurement	Internal pressure (Mpa)	Comments	Source
460(less end caps)	Direct resistance	Air	Alumina cylinders	No	Air	No	5.0–200	Remote pyrometers	1-15		
280(less end caps)	Internal heater	Air	Alumina cylinders	No	Air	No	5.0–275	Remote pyrometers	1-15	Lower rupture strains than with direct heating	[9.201]
325	Internal heater	He	Alumina cylinders	No	Air	No	7–9	Pt/Pt-Rh thermocouples spot-welded	7.0–13	Strain from X ray cinematography	[9.213]
300	Direct resistance	Ar	No	No	Steam	No	2–100	Pt/Pt-Rh thermocouples spot welded; pyrometry	1.0–13	Kinetics of phase transformation counters lower transformation temperature in Zr-1Nb	[9.238]
760	Nuclear	He	Fuel	Fuel	Heat transport water	Yes	Dry out to 1200°C	Thermocouples in Zircaloy ‘pocket’ spot welded	0.3–2.6	Irradiation damage annealed during dry-out	[9.249]
300	Direct resistance	Ar	No	No	Steam	Yes	Ramp & hold	Pt/Pt-Rh thermocouples spot welded; pyrometry		H suppresses superplasticity. Irradiation damage annealed out during tests	[9.2471
500 (250 uniform)	Direct resistance	He	No	No	Vacuum	No	25	W-26Re/W-5Re thermocouples spot welded	0.07–0.34	Specimens of Zr-2.5Nb & Zircaloy-4. Strain history from many specimens	[9.230]
500	Direct resistance	He	No	No	Steam	No	25	W-26Re/W-5Re thermocouples spot welded	0.36–0.72	Creep and temperature ramp	[9.242]

Fig. 9.62. As the hoop stress from the initial internal pressure is increased, the temperature at which specimens burst decreases, as shown in Fig. 9.63; this Figure represents data derived from nine studies [9.200, 9.229, 9.232–9.238]. With low stresses the burst temperatures are very high — greater than 1470 K (1200°C) below about 5 MPa — and sensitive to pressure while in the β phase, below about 20 MPa. With intermediate and high stresses the burst temperatures are in the (α + β) and α phase region and decline approximately linearly with hoop stress. The effect of heating rate on burst temperature may be lost in the scatter of the data when they are pooled, as shown in Fig. 9.63. The trend is for the burst temperature to increase with heating rate at low hoop stress and be almost independent of heating rate at high stress. In individual studies that use very low heating rates, around 1°C/s, the increase in burst temperature is most sensitive to heating rate at low values and this effect is apparent over a wide range of hoop stresses, as shown in Fig. 9.64; the correlation between rupture temperature and heating rate is either logarithmic or a power law with exponents ranging from 0.03 to 0.07.

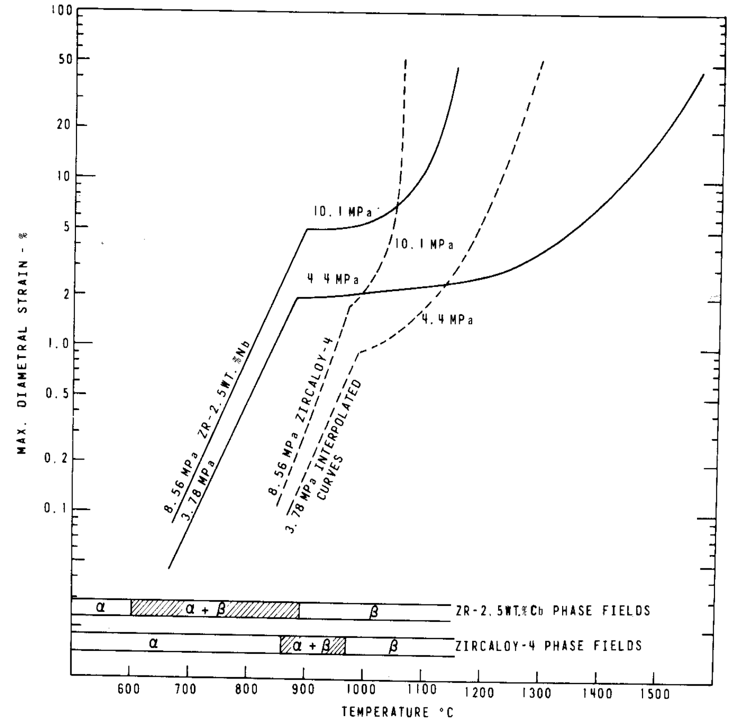

FIG. 9.62. Increase in diameter of Zircaloy-4 and Zr-2.5Nb fuel cladding with temperature ramp through the α+β/β phase boundary. Heating rate 25 °C/s [9.231].

The extent of the deformation and the ductility vary with the test conditions. Straining produces a wide range of specimen shapes [9.229, 9.232]: tight axial splits with little deformation; much bulging sometimes coupled with specimen shortening that can lead to bent specimens when constraint is absent; often localized deformation with flaps of the rupture area flattened out with high pressures and a roughened orange peel surface at high temperatures; and sometimes carrot-shaped specimens. The circumferential burst strain is a complicated function of burst temperature, having maxima associated with the upper part of the α phase and lower part of the (α + β) region, and the β phase, and a minimum in the centre of the (α + β) region, as shown in Fig. 9.65, which reflects the deformation described above and illustrated in Fig. 9.60. A third maximum may exist at very high

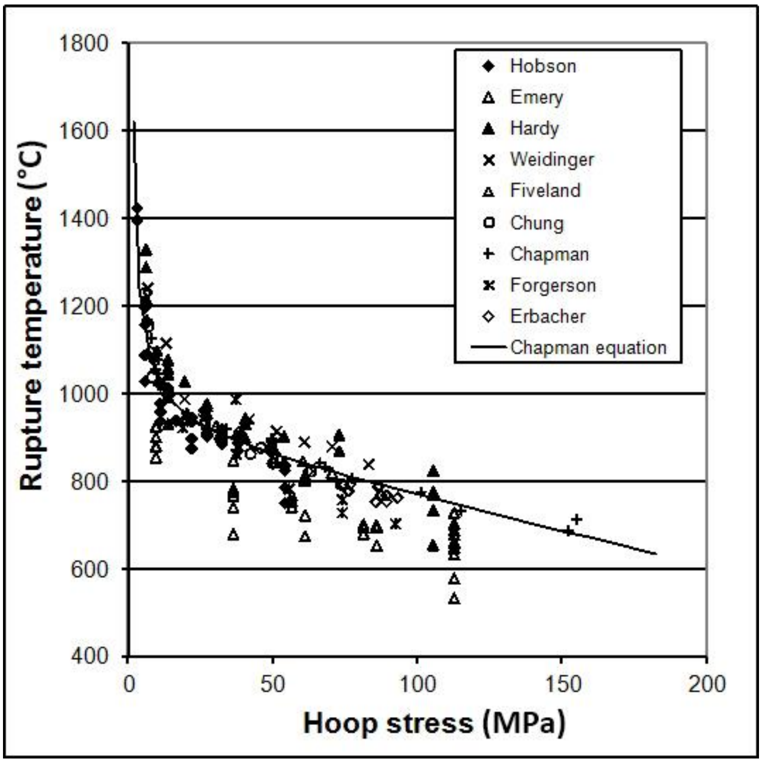

FIG. 9.63. Dependence of rupture temperature on hoop stress during ramp tests on Zircaloy and Zr-1Nb fuel cladding [9.201, 9.230, 9.232–9.238]; Chapman equation [9.236].

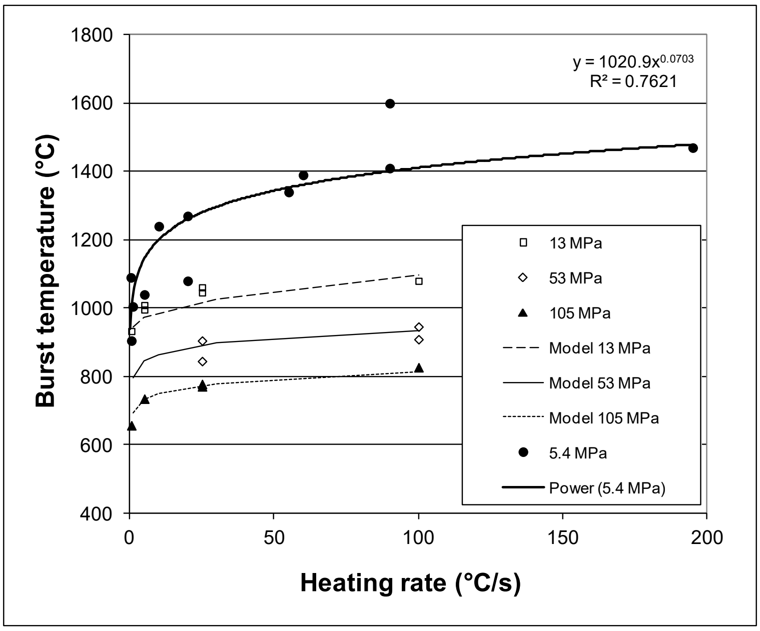

FIG. 9.64. Effect of heating rate on rupture temperature in ramp tests on Zircaloy cladding; data from [9.228, 9.230], model from [9.264].

temperatures. As the heating rate is increased, the start of the transformation into the ($\alpha + \beta$) phase is postponed to a higher temperature [9.237] and the strain maximum is also shifted to a higher burst temperature.

One consequence of Eq. (9.16) is that at high temperatures cladding deformation is extremely sensitive to temperature; for example, in the α phase, around 1070 K (800°C), an increase of 10°C increases the creep rate and reduces the time to burst by about 30%, while in the β phase, around 1270 K (1000°C), a similar increment changes the rate and time by about 10%. Azimuthal

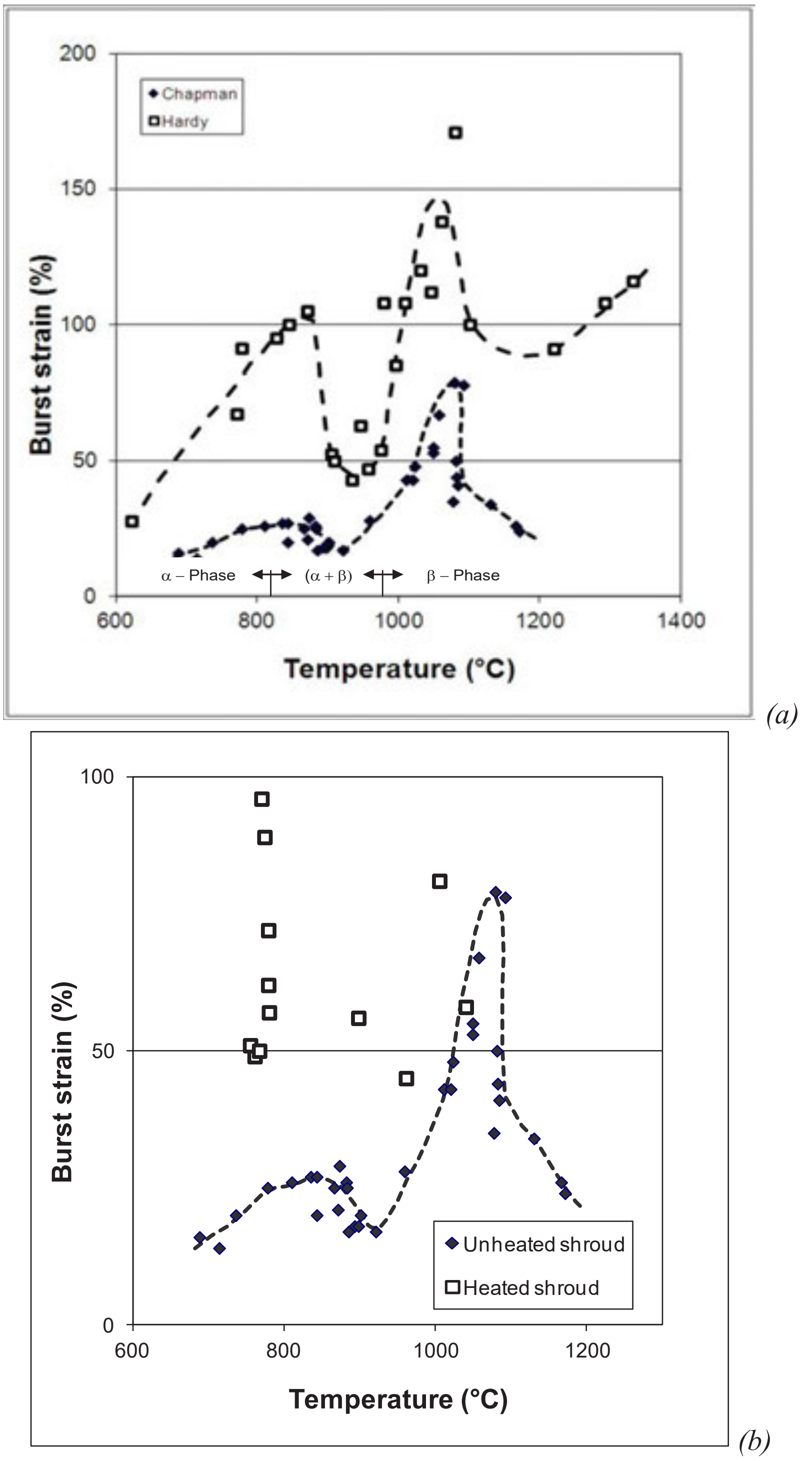

FIG. 9.65. (a) Dependence of burst strain on burst temperature in temperature ramp tests between 25 and 100°C/s on Zircaloy-4 — "Hardy" in vacuum and "Chapman" in steam [9.230, 9.236]; (b) dependence of burst strain on burst temperature in temperature ramp tests between 10 and 28°C/s on Zircaloy-4 using internal heaters with unheated or heated shrouds [9.236, 9.239].

temperature gradients that develop as the burst temperature is approached lead to preferred deformation at the hottest part of the cladding [9.212]; the higher the gradient, the less uniform the deformation and the lower the total strain to failure. Results of ramp tests at a pressure of 6.5 MPa and 1°C/s, providing burst temperatures of 1100 to 1118 K (827 to 845°C), illustrate the effect, as

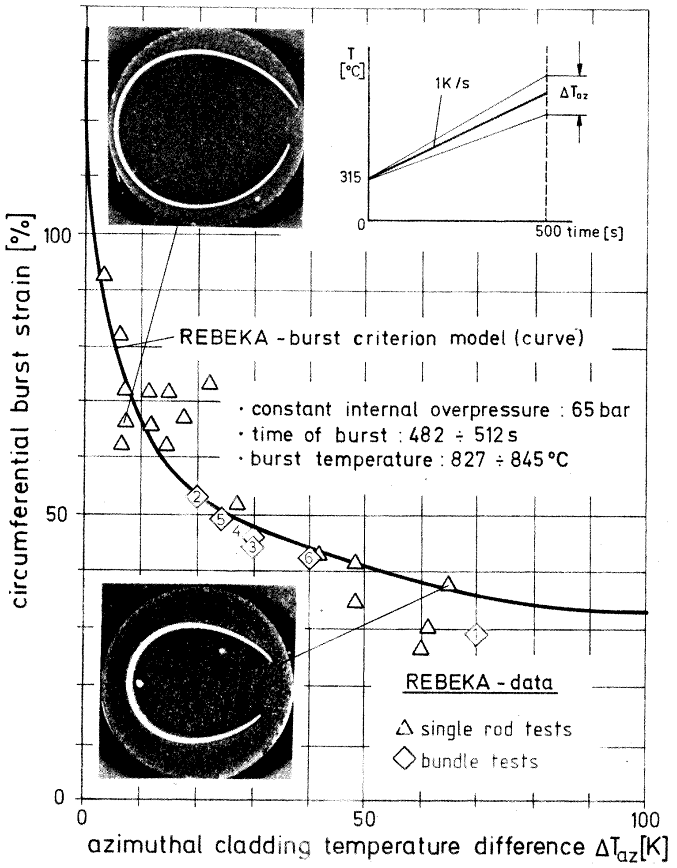

FIG. 9.66. Burst strain reduction by temperature gradient in ramp tests on Zircaloy-4 cladding [9.213].

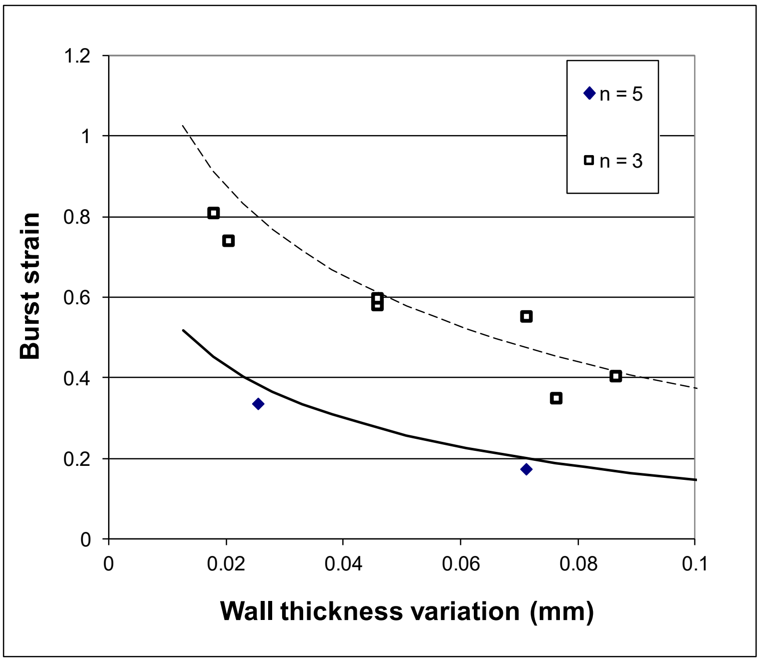

FIG. 9.67. Effect of wall thickness variation on burst strain in temperature ramp tests on Zircaloy-4; data from [9.233]; model [9.266] indicated by solid line for n = 5 and dotted line for n = 3.

shown in Fig. 9.66; a temperature difference of 25°C reduces the total strain from over 100% down to 50%. The method of heating is important for the development of severe azimuthal temperature gradients. With internal heaters, when in the α phase, a small temperature increase around the cladding provides extra circumferential strain that, because of anisotropy, leads to axial shortening on one side of the tube. Bending of the tube induces a hot spot where the heater comes into contact with the tube while the region where the gap between the heater and the tube has increased tends to be relatively cool. This intensification of the temperature gradient focuses the deformation at the hotter region, leading to early rupture and low total circumferential strain [9.235]. This effect is sometimes called the hot side straight effect and leads to non-concentric strain around the heater (and subsequently the fuel). When the material is completely in the β phase, the deformation is isotropic and the strain is concentric around the heater, and therefore the fuel. In the α phase, the difference in ductility between the two sets of data depicted in Fig. 9.65(a) is attributed to the sensitivity to temperature uniformity — direct resistance heating versus internal heating. Another factor is the immediate surroundings of the rod. When an internally heated rod is encased by an unheated shroud the ensuing temperature gradient results in low strains to failure [9.235] whereas when the shroud is heated similarly to the test rod, the temperature gradients are small, the rupture temperature is reduced — about 40°C at a pressure of 5 MPa — but the rupture strains are increased [9.239], as shown in Fig. 9.65(b), and similar to those obtained with direct resistance heating.

With direct resistance or induction heating, temperature gradients are set up at variations in wall thickness. Such non-uniformities in the tube wall thickness also induce mechanical localization of deformation, as described in Sections 9.2.1 and 9.3.1, leading to decreases in total elongation. In experiments where the temperature gradients were small, because of the use of both internal and external heaters, increasing the variation of wall thickness from 3% to 11% approximately halved the elongation, from 110% down to about 50%, and focused the location of rupture close to the thinnest section, as shown in Fig. 9.67 [9.232].

When the majority of the deformation is in the α phase, the usual crystallographic texture of cladding with basal poles in the radial direction restrains wall thinning and induces tube shortening as the tube bulges. The maximum value of shortening corresponds with the maximum in circumferential strain. Restricting axial deformation with an internal mandrel, simulating the fuel column, reduces the circumferential strain to rupture and shifts the maximum value to higher temperatures. During deformation the gap clearance between the ends of the specimen and the mandrel closes and the size of the axial constraint is determined by the size of the gap. The results of tests with no mandrel and clearances of 5.9 and 2.5 mm demonstrate these effects, as shown in Fig. 9.68 [9.234]. The effect of constraint is largest when much α phase is present, below 1143 K (870°C). When the cladding is in the β phase, the circumferential expansion can be accommodated

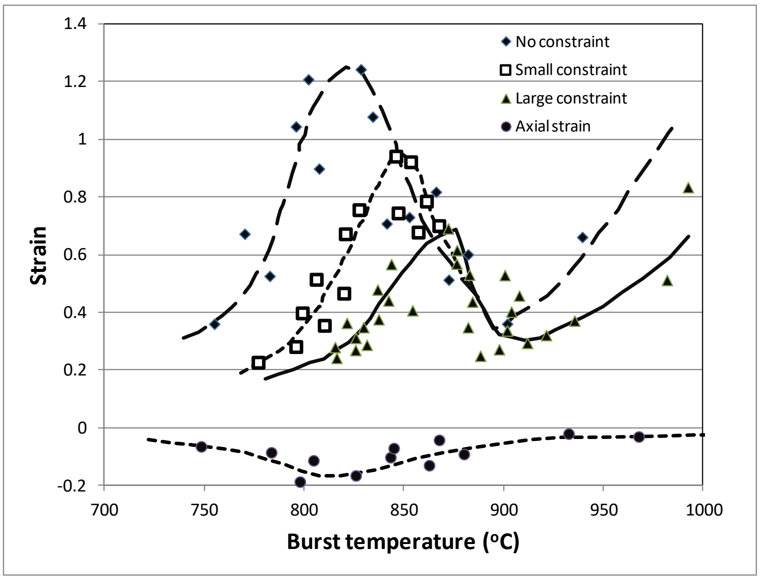

FIG. 9.68. Effect of axial constraint on hoop strain in burst tests on fuel cladding subjected to a temperature ramp of 115 °C/s; axial strain is shown when no constraint [9.235].

by wall thinning and the axial strain and the effect of axial constraint are small at temperatures above 1273 K (1000°C).

In tests on cladding from power reactors or tests in a steam atmosphere, the outer surface of the clad is oxidized. At temperatures above about 1070 K (800°C) some of the oxygen diffuses a short distance into the underlying metal where, depending on the temperature, it stabilizes the α phase or induces transformation of the β phase to the α phase. The clad may then comprise several layers: an oxide on the outside surface, oxygen enriched α and β phases, perhaps interspersed with a region of (α + β) phase, and β phase with initial concentration of oxygen. With time at high temperature, the oxide and α layer thicken and the oxygen concentration increases in the β phase with an increasing gradient towards the α phase. These layers affect the strength and fracture properties.

At temperatures above 1023 K (750°C), up to 6.6 at.% (12 360 ppm), oxygen in solution increases the strength of Zircaloy-2 in the α phase by about 6%/1000 ppm oxygen and by about 3.5%/1000 ppm oxygen in the β phase [9.240, 9.241]. In the (α + β) phase region the oxygen concentration determines the volume fraction of the much stronger α phase. The (α + β) phase strength can be described by a rule of mixtures, taking into account oxygen partitioning between the two phases. Extrapolation of creep results [9.221] into the (α + β) phase region suggests that the strength of the α phase dominates the high temperature strength; at 1173 K (900°C) with stresses between 50 and 100 MPa the α phase creeps about 55 to 30 times slower than the β phase.

Unpressurized tubes deform when exposed to steam; the oxide induces a tensile stress because it occupies a greater volume than the zirconium from which it is formed [9.221, 9.242, 9.243] and the lattice of the α layer is expanded by oxygen. The contribution to the stress from each source varies; with a thin oxide and little α layer, the oxide dominates while at high temperatures; when a significant α layer forms, the compressive stress from the oxygen in solution controls the deformation. Initial stresses up to 8 MPa have been calculated for oxidation at 1073 K (800°C); these stresses decline with increasing oxidizing temperature and with exposure time. The stresses produce creep strains up to 1% [9.244] in simulations of LOCA and up to 3% in sheet material.

During deformation the oxide cracks. In the high temperature region, cracks formed in the oxide from the steam environment led to premature necking and lower elongation [9.235] than in specimens heated in an inert atmosphere [9.229], as shown in Fig. 9.65(a). Two mechanisms for crack growth are (i) further penetration by oxidation — a crack that penetrates the oxide provides a path for oxygen to form fresh oxide that then cracks, and the sequence is repeated [9.245]; or (ii) cracking of the α phase [9.227] — an oxygen enriched layer of α phase from which the oxide has been removed cracks in a brittle manner at 1413 and 1513 K (1140 and 1240°C) and the crack stops at the α/β interface. The residual rupture strain at these test temperatures was much reduced by the presence of the oxygen enriched α layer, from 70 to 90% down to 5.5 to 7.4% [9.246]. With each mechanism, the support of the strong α phase is lost because either the α phase cracks or the rate of radial oxide cracking is greater than the radial movement of the front of α phase transformation, and cracking penetrates to the underlying β phase. This cracking induces a strain rate increase at small creep strains — about 2.3% at 1273 K (1000°C) [9.245]. Plastic instability follows in the remainder of the wall with one sided necks forming at the inside surface opposite cracks in the oxide [9.235, 9.241, 9.243]. Results of ramp tests at 25°C/s in vacuum and in steam, summarized in Table 9.13, illustrate the behaviour, based on Ref. [9.241]. With a short time at high temperature the oxide is thin and little oxygen diffuses. At a hoop stress of 12 MPa the rupture temperatures are similar in each environment with a small loss in ductility in steam. At 8.5 MPa, the test duration is longer and an embrittling oxide forms but no strengthening α phase layer. At 6 MPa in each environment, the strain paths coincide up to about 1273 K (1000°C), then diverge; in vacuum the tube ruptures at 1488 K (1215°C) with high elongation, but in steam sufficient time is available for oxygen diffusion and strengthening and rupture is postponed for over 100°C but the elongation is much reduced. Heating rates of 5 and 100°C/s produce similar results [9.243]. At high temperatures, rejection of β stabilizing elements from the newly formed α phase into the adjacent β phase leads to ageing and flow softening that enhance plastic instability [9.239].

TABLE 9.13. STRENGTHENING AND EMBRITTLEMENT OF ZIRCALOY IN STEAM WITH A TEMPERATURE RAMP OF 25°C/s [9.241]

Hoop stress MPa	Vacuum		Steam	
	Rupture temperature (°C)	Elongation (%)	Rupture temperature (%)	Elongation (%)
12	1040	110	1020	70
8.5	1050	100	1100	20
6	1215	90	1350	8

After long service, cladding may also contain much hydrogen — up to 1000 ppm (8.4 at.%). Hydrogen reduces creep resistance in recrystallized Zircaloy-4 [9.247] and lowers the α/(α + β) transformation temperature (see Section 2.4.4.10 on the Zr–H phase diagram). As a consequence of both these effects, during ramp tests deformation started and rupture ensued at lower temperatures as the hydrogen concentration increased. Hydrogen also reduced the ductility in high temperature creep tests, although the scatter was large; within this inconsistency, some specimens exhibited values of elongation around 100%, but in the middle rather than at the low temperature end of the (α + β) phase region, as expected. Values of 20% were also obtained with the same test conditions but no explanation was given for this erratic behaviour. The temperatures reached during the postulated accident are sufficiently high that, even with the rapid temperature rise, the irradiation damage is annealed out and deformation is unaffected by irradiation. Several test results confirm this conclusion for Zircaloy:

- Irradiated fuel rods (5–7 MWd/kgU), induction heated and pressurized with steam and argon, indicated little difference in rupture behaviour; the minimum in elongation was at the same stress and temperature as in unirradiated material, although a small drop in elongation was indicated [9.232]. Heating method, wall thickness variation and oxidation during irradiation could also have influenced the latter.
- With burnup increased to 30 MWd/kgU no effect of irradiation (and irradiation and constraint) is observed in the relationship between the rupture temperature and hoop stress or burst strain [9.248].
- Fuel irradiated up to 40 MWd/kgU was subject to several in-reactor dryouts of 10 to 15 s duration. Post-irradiation examination showed that a wide range of temperatures, up to 1470 K (1200°C), was attained. The tensile properties at 293 K (20°C) in the region of the cladding where the temperature had exceeded 823 K (550°C) in the α phase or reached the (α + β) phase indicated that the irradiation damage had recovered [9.249].
- After a burnup of 18 MWd/kgU, fuel was extracted from cladding containing a pure zirconium liner [9.250]. After cutting into 5 mm lengths, the rings were heated to temperatures between 773 and 973 K (500 and 700°C) at 40°C/s for various times then cooled at 30°C/s after heat treatment. The tensile properties at the in-reactor operating temperature of about 618 K (345°C) were similar to those of unirradiated material after 15 s at 873 K (600°C) and 5 s at 973 K (700°C).
- Ramp tests at 25 and 100°C/s using axial loading on fuel clad irradiated for three cycles in a PWR showed that this material behaved similarly to as-received material. With a load of 40 MPa, deformation started at about 923 K (650°C) and both types of material ruptured at about 1143 K (870°C) at an axial strain of about 25% [9.246].
- Results of creep tests between 1043 and 1073 K (770 and 800°C) on cladding irradiated to 10 MWd/kgU in SGHWR could not be distinguished from those on unirradiated cladding [9.221].
- In two sets of experiments, specimens were made from fuel irradiated in power reactors but the UO_2 was not removed. Fuel rods clad with Zircaloy-2 (with an inner liner) from a BWR (Limerick, USA) were cut to lengths of 300 mm, pressurized to 8 MPa in an argon or steam

atmosphere then temperature ramped at 5°C/s by radiant heating with the expectation of bursting in the α phase [9.251]. Specimens of unirradiated cladding containing a stack of zirconia pellets were tested using the same technique.

Similar experiments have been performed on fuel clad with ZIRLO [9.252]. The results are summarized in Table 9.14. The burst temperatures were all in the α phase and maximum diametral strains were close for all these tests, indicating that high burnup operation had little effect on cladding burst conditions and strains for both Zircaloy-2 and ZIRLO. The time was insufficient at too low a temperature for the steam to provide an embrittling oxide. In the burst region, fragmentation of the UO_2 was observed in the burst gap and by metallography of fuel cross-sections in the high strain region.

TABLE 9.14. BURST TESTS ON CLADDING CONTAINING UO_2 FUEL AFTER HIGH BURNUPS [9.251, 9.252]

Cladding and testing	Specimen	Burnup (MWd/kgU)	Atmosphere	Burst temperature (°C)	Burst stress (MPa)	Elongation (%)
Limerick BWR 9 × 9	ICL1	56	Argon	755	61	38
Zircaloy-2 liner	ICL2	56	Steam	750	57	39
Argonne	ICL3	56	Steam	730	61	43
	ICL4	56	Steam	790	57	36
	OCL5	0	Argon	733	59	44
	OCL11	0	Steam	753	56	43
ZIRLO	189	73	Steam	700	89	48
Studsvik	191	71	Steam	680	82	50
	192	73	Steam	700	60	56
	193	71	Steam	730	60	51
	196	55	Steam	686	54	29
	198	55	Steam	693	56	26

Although the α/(α + β) transformation starts at a lower temperature in Zr-1%Nb than in Zircaloy, the kinetics of the transformation dominate the mechanical behaviour during a temperature ramp. Under equilibrium conditions, the β phase fraction of 0.6 exists at 1138 K (865°C) in M5 and 1168 K (895°C) in Zircaloy containing 1.3% Sn whereas with heating at 10°C/s the transformation to the same phase fraction is postponed to 1222 K (949°C) and 1216 K (943°C), respectively [9.237]. Consequently, during a temperature ramp, the rupture temperature of M5 has a similar dependence on hoop stress as Zircaloy, as shown in Fig. 9.69. With more Nb the transformation temperature is lower still. For the same stress in ramp tests, deformation starts at lower temperatures in Zr-2.5Nb than in Zircaloy; if the β phase is attained, Nb provides more strengthening than Sn and the deformation is faster and rupture temperature lower in Zircaloy than in Zr-2.5%Nb [9.230], as shown in Fig. 9.62.

Cooling from the β phase can produce a range of microstructures (see Section 4.6.1, in Volume 1 of this publication). Two situations are considered for LOCA: joining by welding and brazing, and after the first stage of a LOCA.

In the heat affected zone (HAZ) adjacent to welds and braze zones in Zircaloy fuel cladding, the microstructure comprises a basketweave Thomson–Widmanstätten structure transformed from the β phase, a small region of recrystallized and partly recrystallized grains and then the initial

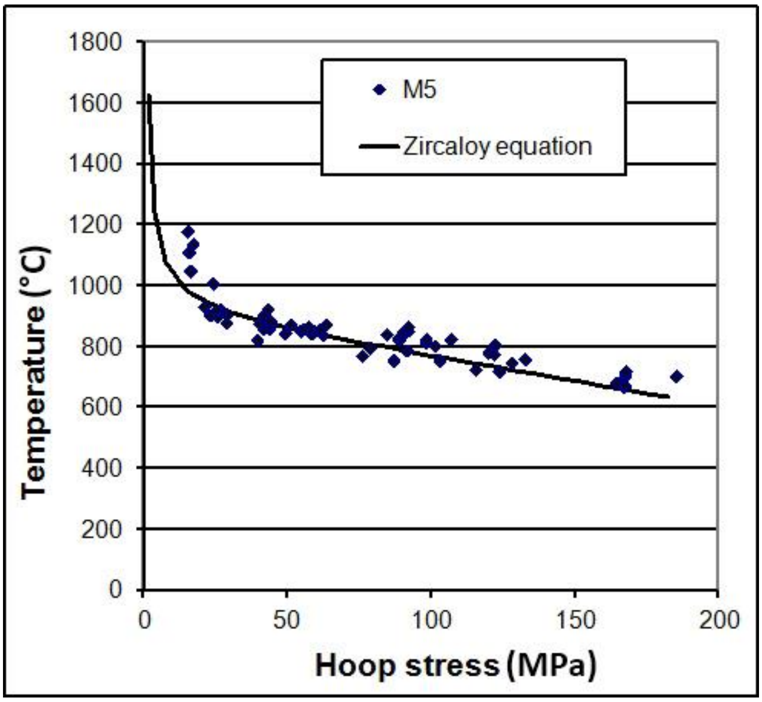

FIG. 9.69. Comparison of Zircaloy-4 and Zr-1Nb (M5) in temperature ramp tests (based on [9.238]).

microstructure, for example, CWSR. From room temperature up to normal operating temperatures the basketweave and recrystallized structures are 1.4 to 2.4 times weaker than a cold worked structure but the elongation of the recrystallized structure is about twice that of the other two, which are similar [9.35]. In a HAZ, during a temperature ramp of 25°C/s at high pressure (e.g. providing a hoop stress of 165 MPa) where the material deforms mostly at about 923 K (650°C), the strain concentrates in the recrystallized material [9.243, 9.253]. With lower pressures, providing a hoop stress of between 55 and 130 MPa, the majority of the deformation takes place high in the α phase, the initial microstructure recovers and starts to recrystallize and deform more than the basketweave structure [9.254]. At lower hoop stresses, 22 to 44 MPa, where much deformation is in the (α + β) phase, the strengths are reversed again. The basketweave microstructure increases the stress sensitivity, *n*, in both the α phase and (α + β) phase [9.253, 9.255]; as a result the ductility is reduced and in the latter phase the basketweave microstructure suppresses superplasticity [9.220, 9.224]. At 1073 K (800°C) with equiaxed α grains the total strain to rupture was over 2.0 whereas with a basketweave structure, produced by cooling through the two phase region from 1273 K (1000°C) to the test temperature, the total strain was 0.75.

A consequence for a LOCA is the effect of the temperature reached in the first stage of the event (shown as point (1) in Fig. 9.57) on the deformation in the second stage (shown as point (3) in Fig. 9.57) [9.254]. Heating into the β phase in point (1) followed by cooling into the α phase in point (2) produced a basketweave structure that has greater resistance to subsequent creep rupture in point (3) at 973, 1073 and 1173 K (700, 800 and 900°C) than material without this heat treatment. The ductility was also much reduced. To illustrate the effect, at a test temperature of 1073 K (800°C) with an initial hoop stress of 32 MPa and no residence in the β phase, the time to rupture was 164 s and the rupture strain was 202%, whereas if the creep at 1073 K (800°C) is preceded by 4 s at 1270 K (1000°C) and a rapid cool to 773 K (500°C) the time to rupture at 1073 K (800°C) was increased to 489 s but the rupture strain was reduced to 49%. The reduction in ductility was related to the stress sensitivity, *n*, that increased from about 4 up to 10, with hoop stresses greater than 20 MPa; the results fit into the empirical correlation between ductility and *n*, as shown in Fig. 9.47. Similarly, when the fuel cladding is cooled into region (5) in Fig. 9.57, the microstructure controls the mechanical response. In tests at 673 K (400°C) [9.224], when the α grains were equiaxed the UTS was 150 MPa and the total strain was 42%. A microstructure with about 10% transformed β phase was slightly stronger but less ductile, 160 MPa and 34%, and when fully transformed the strength increased to 190 MPa and the ductility dropped to 20%.

In summary, as an initial simulation of the early stages of a LOCA, single pressurized tubes have been subjected to a ramp in temperature. Knowledge of the strain attained during the ramp is important for evaluating blockage between fuel elements or rods and therefore coolability. As a consequence of the wide range in experimental variables — heating method and rate, initial pressure, environment, microstructure — the strain to rupture appears very variable but several experimental parameters contribute to the scatter:

- Maxima in rupture strain are observed in the temperature range encompassing high in the α phase and low in the (α + β) phase field as well as in the β phase whereas deformation at temperatures in the centre of the (α + β) phase field can produce a minimum in ductility.
- A basketweave microstructure can reduce rupture strain.
- Restricting axial deformation can decrease hoop strain.
- Gradients in temperature and thickness can focus deformation and reduce total elongation.
- Oxidation can lead to an embrittlement.
- Hydrogen lowers the α/(α + β) transformation temperature and can reduce rupture strain.

During a temperature ramp expected in a LOCA, damage from neutron irradiation is recovered before it can affect ductility.

9.3.4.3. Models

To help design and make regulatory cases, the properties of cladding and the responses to simulation of LOCA conditions are numerically evaluated in computer codes with the phenomenon described empirically or by mechanistic models. An example of the former is the fit to the data of rupture temperature, T_B, as a function of pressure, P, with a heating rate of 28°C/s through:

$$T_B = 3907 - 0.012P - 10^4P/(209 + 3.342P) \tag{9.17}$$

where P is in kPa [9.235]. The fitted line (converted to hoop stress) is included in Figs 9.63 and 9.69. To take account of the heating rate, Eq. (9.17) was modified to:

$$T_B = 3960 - 0.024P/(1 + H) - 10^4P/[100(1 + H) + 3.28P] \tag{9.18}$$

where H is a normalized heating rate (for 0°C/s, $H = 0$ and for 28°C/s, $H = 1$) [9.256]. This equation was used for early licensing standards by the NRC [9.257]. It is based on tests where the protective shroud was unheated. When the shroud is heated similarly to the test rod [9.238], Eq. (9.17) is modified between 1 and 10 MPa to:

$$T_B = 4026 - 0.02388P - 10^4P/(97.9 + 3.296P) \tag{9.19}$$

The results of ramp burst tests can be interpreted in terms of a deformation equation such as Eq. (9.16), providing values of n and Q [9.236]. Another method is to use a life fraction rule, although its application does not allow for microstructural processes that could influence the development of deformation damage [9.258]. The mechanistic foundation [9.259, 9.260, 9.261] for Eq. (9.16), based on dislocation creep and grain boundary sliding, along with descriptions of the kinetics of microstructural changes from heating, such as recrystallization and phase transformations, provide a total creep rate that is taken as the sum of separate components of creep rate. Anisotropy is accounted for by Hill’s plasticity theory [9.262]. The rates of change in conditions (temperature, differential pressure), microstructure and deformation rates form a set of differential equations that are solved by numerical integration. The constants in the equations are altered to reflect changes in microstructure and phase. The models describe the deformation that occurs during a temperature ramp, the increase in burst temperature with decrease in initial hoop stress at constant heating rate and the increase in burst temperature with increasing heating rate at constant hoop stress. In the α phase, T_B also depends on texture; for example, at a hoop stress of 100 MPa the range of T_B is predicted to be 60°C, low values being obtained with isotropic material and high values with anisotropic factors representing fuel cladding. In the curve relating T_B to hoop stress a slope change at the (α + β)/β boundary is predicted but the experimental scatter is too great to confirm this behaviour.

The strain at rupture can be estimated by invoking a further relation between T_B and the burst stress, σ_B [9.263]:

$$\sigma_B = \xi \exp(-\chi T_B) \tag{9.20}$$

where ξ and χ are empirical constants that depend on the metallurgical phase.

Assuming a constant cross-sectional area for the cladding and no tube shortening during deformation, during a temperature ramp the hoop stress, σ, changes with the hoop strain, ε, through:

$$\sigma = (1 + \varepsilon)^2 PR_0/w_0 \tag{9.21}$$

where

P is current pressure;
R_0 is initial mean radius;

and w_0 is initial wall thickness.

Combining these equations provides an estimate of the burst strain, ε_B, as shown in Eq. (9.22) [9.264]:

$$\varepsilon_B = [(w_0\, \xi/P_B R_0)\exp(-\chi T_B)]^{1/2} - 1 \tag{9.22}$$

The deformation of the tube is calculated using Eq. (9.21) to evaluate the hoop stress from the developing pressure differential across the tube wall and by numerically integrating the hoop strain rate, using Eq. (9.16) and the temperature history, to obtain the hoop strain as a function of time [9.265]. The integration continues in steps until the hoop stress reaches the burst stress, Eq. (9.20), where failure is assumed. This point defines the time, temperature, pressure and hoop strain. Instability or fracture criteria are not needed since the average burst strain does not depend on the local strain at rupture as long as it exceeds 1.5 [9.266]. In the α phase during ramp testing, tube shortening is expected and observed because of anisotropy. The values of the anisotropic factors [9.261], F, G and H, are assumed to be 0.5 in the β phase, indicating isotropic behaviour; sometimes tube lengthening is observed after deformation at high temperatures, also indicating anisotropy, presumably because of a texture developed during the transformation from the highly textured α phase. Fuel cladding is usually considered to be a thin-walled tube and during simulations of LOCA the loading is taken as being closed-end. Depending on the fuel design, in an assembly, adjacent rods may restrict each other's movement and the loading may approach fixed-end loading. This loading mode tends to provide reduced elongation and texture strengthening with the usual texture in fuel cladding — a high concentration of basal poles in the radial direction. Analysis of several variations of restraint, from none to axial or restriction in bending, with a range of anisotropy from isotropic to moderately textured material, showed that the failure strain was not sensitive to either restraints or anisotropy, even in the α phase [9.267]. So, despite the apparent inconsistency between invoking anisotropy but with no length change, the numerical integration provides a qualitative estimate of burst strain. In the α phase, the rupture strain decreases with increasing heating rate. A maximum value of strain is attained in the transition from α to (α + β) phase regions and a minimum value in the (α + β) region; with increasing heating rate the value of the maximum strain decreases and the temperature at which it is attained increases, in accordance with observations.

Experimental results show that temperature distribution in the cladding strongly influences burst strain, as shown in Fig. 9.66; a small circumferential variation in temperature leads to large strains and vice versa. A temperature variation, $T(t,\theta)$, was modelled either as a constant circumferential gradient [9.268] or by:

$$T(t,\theta) = T_0(t) - \Delta T((1 + \cos(\theta + \pi))/2)^{\mathrm{C}} \tag{9.23}$$

where

$T_0(t)$ is the maximum temperature at time t;
θ is the tangential angle;

and C is a constant.

For C = 1.0 there is a sinusoidal temperature distribution; a hot spot develops at values less than 1.0 while a more gradual gradient arises with higher values of C.

In the numerical calculations, the cladding was divided into circumferential elements and deformed in time steps. The cross-section was assumed to remain circular during ballooning; this assumption has been verified experimentally on Zr-2.5Nb pressure tubes [9.269], but even if wrong in fuel cladding, the underestimate of time to failure and burst strain would be small [9.270]. Failure was assumed when the hoop stress in one element (that with the highest temperature) attained the burst stress. The calculations confirm a very rapid decrease in burst strain with a few degrees difference in temperature followed by a more gradual decrease in strain with large temperature differences. This result applied to bursting in all three phase fields. The temperature distribution was important with a localized hot spot inducing the largest drop in burst strain. An azimuthal temperature gradient is predicted to suppress the effects of heating rate on burst strain. These results highlight the problem of thermometry; thermocouples may not be placed at the critical location and the size of the temperature gradient and the temperature of rupture may be underestimated.

Circumferential differences in wall thickness also contribute to the variation in burst strain; this effect is mostly important when there is little or no temperature gradient. Assuming failures at the thinnest cross-section, the hoop strain at burst, ε_{B}, is related to the wall thickness variation, Δw, through [9.271]:

$$\varepsilon_{\mathrm{B}} = -(1/n)\ln[1 - ((w_0 - \Delta w)/w_0)^{n}] \tag{9.24}$$

where n is the stress sensitivity and w_0 is the nominal wall thickness.

Values from ramp tests with small temperature gradients, assuming values for n of 3 and 5, illustrate the effect, as shown in Fig. 9.67 [9.232]. The thinnest part of the cladding wall will not necessarily coincide with the hottest part of the tube and the effects may be combined. Similarly, the temperature distribution may vary with time and such variation can be analysed numerically [9.266].

Modelling clad behaviour in steam when the alloy is heated into the β phase requires much information. Typical models contain some or all the following elements [9.272]:

Firstly, the kinetics of oxidation are described by a rate law obtained from isothermal experiments, for example, as in Eq. (9.25):

rate constant = 1.973 exp (−9222/T) (mm/s$^{1/2}$) (9.25)

Secondly, the kinetics of the development of the thickness and composition of the subsurface α layer are captured by a typical parabolic rate law such as Eq. (9.26):

rate constant = 12.56 exp (−11798/T) (mm/s$^{1/2}$) (9.26)

Thirdly, the oxygen concentration distribution, $c_O(x,t)$, is given by:

$$c_O(x,t) = \Theta + \Gamma\,\mathrm{erfc}\left(x/2\sqrt{D_O t}\right) \tag{9.27}$$

where

Θ and Γ are constants derived from the solubility limits at the α layer interfaces;
x is the distance from the original clad surface;

and D_O is the diffusion coefficient for oxygen in α zirconium and t is the time of exposure.

Fourthly, the mechanical properties of the three layers are represented. The oxide is represented by elasticity with a modulus of 4.6 × 10^4 MPa. The stress in the oxide depends on the relative size of the formation strain of the oxide and the strain in the deforming underlying clad; this stress may be compressive or tensile. Oxide cracking, based on observation, starts when the outer fibre strain reaches a critical value, for example, 1.8%. Further discrete increments of strain produce more cracks up to a maximum value, 300. The creep rate, $\dot{\varepsilon}$, of the α layer, as a function of temperature, T (K), and effective stress, σ (MPa), is described by steady state values [9.259], including hardening by oxygen concentration up to 1.5 wt% [9.273]:

$$\dot{\varepsilon} = [4092 \exp(-34726/T)\sigma^{5.3}]\exp(-3.42c_O) \tag{9.28}$$

The underlying β phase deforms as:

$$\dot{\varepsilon} = 7.1 \exp(-15702/T)\sigma^{3.6} \tag{9.29}$$

Additional strengthening of the β phase by oxygen is only required if it penetrates a significant amount, during long exposures at very high temperatures.

Fifthly, to evaluate the stress localizing effect in the clad of the oxide cracks a gauge length for deformation must be assumed. One possibility is to use the remaining clad wall thickness. The average strain, $\varepsilon_{\mathrm{av}}$, is then evaluated assuming that the α layer and β substrate creep at the same rate:

$$\varepsilon_{\mathrm{av}} = \ln(\exp \varepsilon_{\mathrm{s}} + N_{\mathrm{c}}w_{\mathrm{c}}/\pi D) \tag{9.30}$$

where

ε_{s} is the sheath strain remote from oxide cracks;
N_{c} is the number of cracks;
w_{c} is the width of the oxide cracks;

and D is the initial diameter of the clad.

The numerical application of such a model describes the main features of ramping experiments. An example of one code, called transient oxidation strain simulation [9.271, 9.274], is shown in Fig. 9.70, where the strain histories of tests in inert atmosphere and in steam are compared, with the latter being correctly modelled. Little effect of steam is predicted at high hoop stress because the oxide is thin and contains many cracks, so strain localization is small. Strengthening and loss in ductility are clearly apparent at lower stress, where more time is available for oxidation and oxygen ingress before rupture.

9.3.4.4. In-reactor tests on single LWR rods

Several experiments have been performed in-reactor to simulate a LOCA on cladding containing highly irradiated fuel. The main objectives were:

- To confirm (or otherwise) previous laboratory observations and provide confidence in the codes used to describe the consequences of a LOCA;
- To search for any new phenomena that the laboratory experiments do not imitate when heating is with nuclear fuel.

The challenge is to provide an accurate simulation of the temperature and pressure history without interference from the instrumentation that was required to provide the information to understand the test.

(a) Forschungsreaktor 2

Tests in Forschungsreaktor 2 [9.275, 9.276], a tank reactor cooled and moderated with heavy water, aimed at simulating stages (2) and (3), shown in Fig. 9.57, because for several tens of seconds the cladding is at a high temperature and the differential pressure is large. In the test section clad in Zircaloy-4, the length of nuclear fuel was 500 mm, the distance between spacer grids. The burnup received by the fuel before the tests ranged from 0 to 35 MWd/kgU with irradiation at 333 K (60°C) and low pressures — coolant 0.24 MPa and rod internal pressure 0.3 MPa. Typical starting conditions for the test were a linear power rate of 4 kW/m, loop water pressure of 6 MPa and flow of 100 kg/h and a steam temperature of about 573 K (300°C). The internal pressures were adjusted so that they ranged from 2.2 to 11.1 MPa at tube burst. The LOCA transient was simulated by cutting the coolant flow to zero, whereby the external pressure decreased to 0.01 MPa. The fuel and cladding were heated because the rod power was maintained. Once the target cladding temperature was attained the reactor power was shut down and the cladding was cooled by returning the coolant flow. A typical test history is depicted in Fig. 9.71. When the coolant flow was cut off, the temperature of the cladding rose at about 10°C/s. After about 45 s the internal pressure in the test rod dropped to a very small value indicating that the tube had burst; simultaneously the temperature fell, then recovered as heating continued. At about 80 s the reactor was shut down once the temperature reached about 1173 K (900°C) and after 160 s the coolant flow was returned to initiate a quench. In the experiments, the time to burst averaged 50 s with a range from 20 to 80 s.

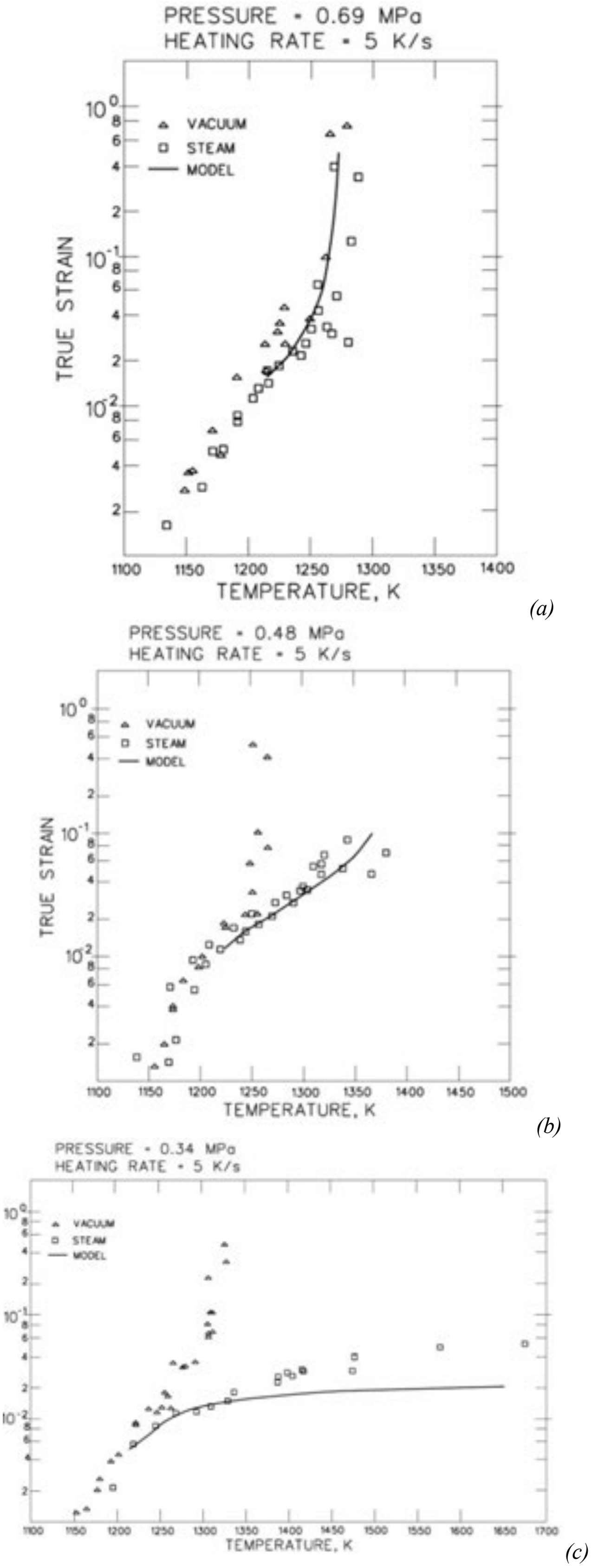

(a)

(b)

(c)

FIG. 9.70. Model and experimental values of strain increase in Zircaloy-4 cladding with ramped temperature, showing the effect of steam environment with different internal pressures: (a) 0.69 MPa; (b) 0.48 MPa; and (c) 0.34 MPa [9.272].

The burst temperature declined as the rod applied hoop stress increased. The values are compared with Eq. (9.17), representing the data for out-reactor tests, as shown in Fig. 9.72. In most tests the axial location of the maximum deformation and burst corresponded with the maximum power. When compared with a typical out-reactor set of data, the temperature dependence of the circumferential burst strain was scattered with values mostly in the high α phase and low (α + β) phase and some small strains in the centre of the (α + β) phase, as shown in Fig. 9.73. The expected reduction in strain with increase in temperature gradient and wall thickness variation was mostly masked by the

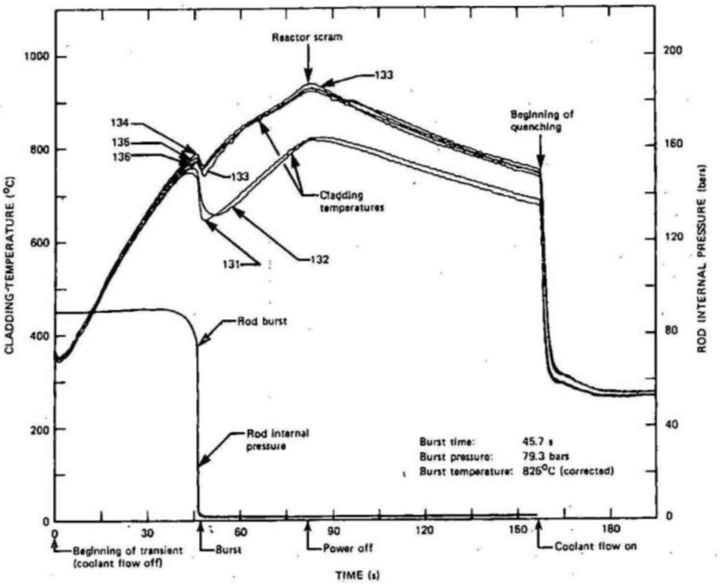

FIG. 9.71. Typical temperature and pressure histories during LOCA test in Forschungsreaktor 2 [9.275].

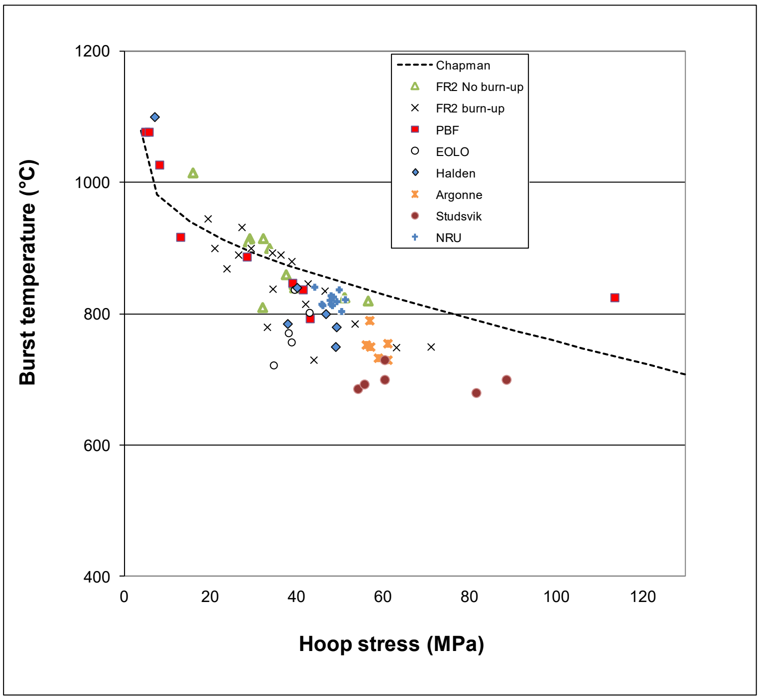

FIG. 9.72. Burst temperature as a function of burst stress for tests simulating LOCA in reactor. Comparison with tests on specimens containing highly irradiated UO_2 and a typical line representing out-reactor tests [9.236, 9.251, 9.252, 9.275–9.280, 9.283, 9.284, 9.302].

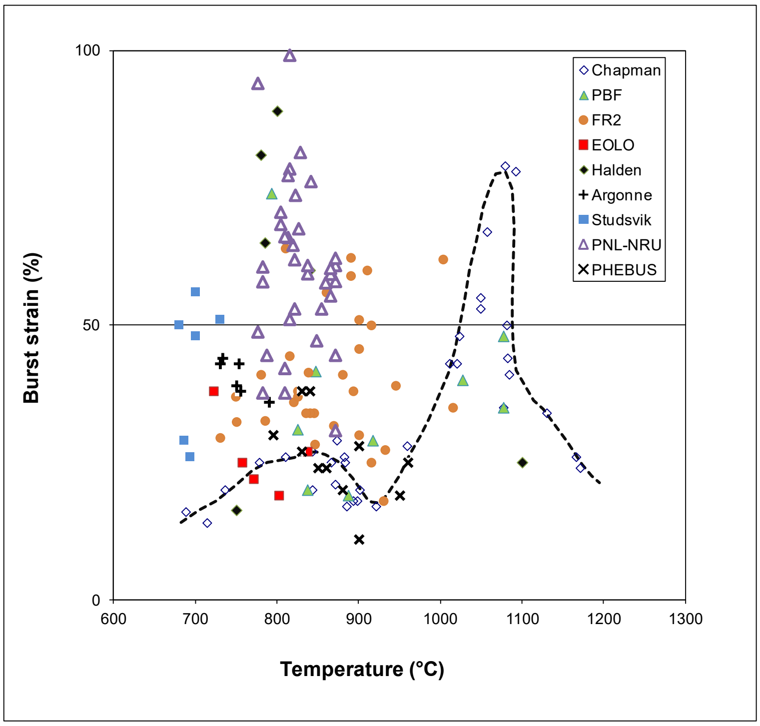

FIG. 9.73. Burst strain as a function of burst temperature for tests simulating LOCA in reactor. Comparison with tests on specimens containing highly irradiated UO_2 *and a typical line representing out-reactor tests [9.236, 9.251, 9.252, 9.275–9.280, 9.283, 9.284, 9.302, 9.305].*

scatter. No additional failure mechanisms were found. No effect of burnup, heating rate or fission products could be discerned. The tests with previously irradiated rods resulted in fragmented fuel pellets in the rod sections with major deformation. The pellet fragments relocated outward and downward, filling the space in the fuel rod created by the balloon. Fuel pellet fragmentation did not affect the cladding deformation process.

The preirradiations in Forschungsreaktor 2 were at lower coolant pressures and temperatures than in a PWR so the amount of cladding creep down onto the fuel would be smaller and the subsequent gas gap would be larger than in a power reactor. No effect of gas gap was observed in these experiments. These tests simulated the second heat-up phase of a LOCA without the preceding b1owdown.

(b) Power Burst Facility at Idaho National Engineering Laboratory

In experiments carried out at the Idaho National Engineering Laboratory, three test sections each contained four PWR rods clad with Zircaloy-4 with an active length of 0.91 m. These were held in an unheated shroud and submitted to similar thermohydraulic conditions in the Power Burst Facility [9.277, 9.278]. In the test sections two of the rods were preirradiated to a modest burnup, up to 16 MWd/kgU, and in each pair of rods the internal pressures represented either the start of life or after a high burnup. The tests started at constant irradiation of 45 to 48 kW/m, with a power profile flattened axially and with coolant at 593 K (320°C) and 15.2 MPa. The test section was isolated from the Power Burst Facility circuit and the pressure was released to simulate blowdown. Depending on the initial conditions, the heating rate of the rods varied between 4 and 100°C/s and the mean time to rupture was 10 s ranging from 3 to 18 s. The tests were terminated by water quenching.

Since the two types of fuel were irradiated under identical conditions, their behaviour can be compared directly. The burst temperature declined as the rod hoop stress increased and the values are included in Fig. 9.72; no distinction between fresh and preirradiated fuel could be made.

Although the temperature dependence of the rupture strain fits within the scatter of the data from other tests, as shown in Fig. 9.73, the two types of fuel can be distinguished. In one test section the claddings each ruptured in the high α phase and the preirradiated cladding failed after 74% strain whereas the cladding for the fresh fuel failed after only 31% strain. A similar result was obtained when the claddings failed low in the (α + β) phase with rupture strains of 42% and 20% for the preirradiated and fresh materials, respectively. This difference was attributed to the reduction in the pellet–clad gap during the preirradiation that homogenized the circumferential temperature distribution, leading to a uniform distribution of strain, whereas with the fresh fuel the strain was concentrated in one location, possibly because of the ‘hot side straight’ effect. The lack of such an effect in the tests in Forschungsreaktor 2 was explained by their preirradiation conditions being unsuitable for gap closure. The tests with previously irradiated rods resulted in fragmented fuel pellets in the rod sections with major deformation. The pellet fragments relocated outward and downward, filling the space in the fuel rod created by the balloon. Fuel pellet fragmentation did not affect the cladding deformation process.

(c) The EOLO-JR irradiation device at the ESSOR research reactor

Simulated LOCA tests were performed on 1 m lengths of fresh PWR Zircaloy-4 cladding containing natural UO_2 [9.279, 9.280]. The internal pressure was set at 4.8 MPa at room temperature. In EOLO-JR the external coolant was a mixture of He + 5%O_2 at 0.5 MPa. The tests were started by adjusting the reactor to supply a peak linear power in the rod of around 4 kW/m and external gas flow to provide a steady temperature of 823 K (550°C) for about 2 h. The gas flow was then decreased to induce a heating rate of 3°C/s to temperatures in the range 991 to 1103 K (718 to 830°C) where the cladding ballooned and failed, as indicated by a drop in internal pressure. The reactor was then shut down. The times to bursting varied from 130 to 540 s, although the specimen that reached the highest temperature failed after 10 s.

The burst temperatures tended to be on the low side of the values for other in-reactor tests, as shown in Fig. 9.72, while the strains to failure are in good agreement with values obtained in the laboratory on unirradiated materials, as shown in Fig. 9.73. Temperature differences around the circumference contributed to the variation in strain, as shown in Fig. 9.74, confirming the sensitivity of rupture strain to temperature gradients, in this example being halved when the gradient increased from about 2°C/mm to 8°C/mm.

(d) Siloé

PWR fuel rods with an active length of 300 mm containing either fresh fuel [9.281] or fuel from Fessenheim 2 with a burnup of 50.3 MWd/kgU [9.282] were irradiated to 1.4 to 3.3 MWd/kgU in the FLASH facility, a pressurized loop. To simulate a LOCA, the test section was depressurized and, after about 10 s, the rod temperature rose at an initial rate of 30 to 40°C/s to over 1373 K (1100°C), at which temperature it was held to obtain information on oxidation. The burst temperatures were in the range 1203 to 1268 K (930 to 995°C) as expected for a pressure of about 4.5 MPa. The strains were variable, ranging from 16 to 62%, the low values being attributed to large temperature gradients associated with rod bowing and an unheated shroud surrounding the test rod, as shown in Fig. 9.74. The fresh fuel cracked but did not relocate during the transient whereas, despite the low burst strain of 16%, the fuel of the high burnup material exhibited signs of fragmentation and relocation in the rupture plane.

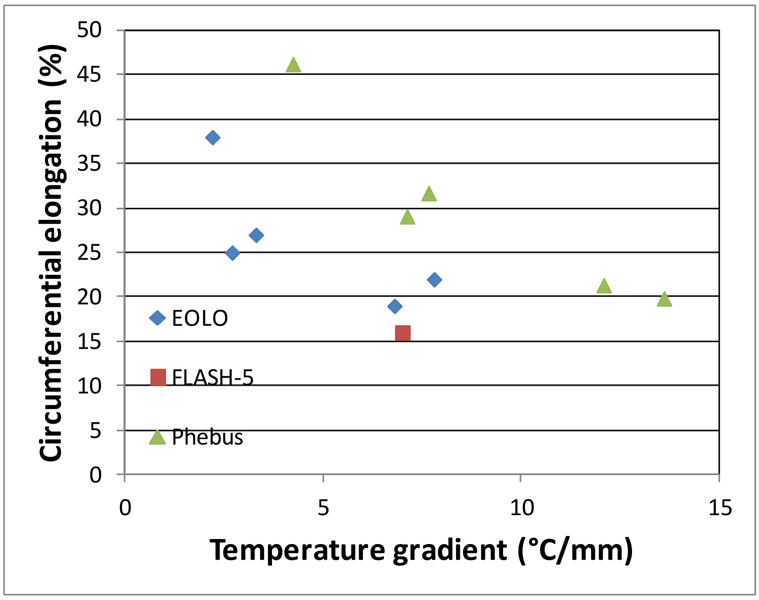

FIG. 9.74. Decline in ductility with temperature gradient estimated for in-reactor LOCA tests in EOLO, FLASH-5 and Phébus [9.279, 9.281, 9.305].

(e) Halden

Simulated LOCA tests have been carried out on 0.5 m lengths of highly irradiated fuel clad with various materials — PWR Zircaloy-4 with a low-Sn outside surface layer, water cooled water moderated power reactor (WWER) E110 Zr-1Nb and BWR Zircloy-2 in the LK3/L condition with an inner surface liner [9.283]. The fuel rod was surrounded by an electrically heated concentric tube within a high pressure flask connected to a heavy water loop in the Halden reactor. The heat-up and temperatures of the fuel during the LOCA were controlled by low nuclear power, simulating the residual heat, and by electric heating. After bursting, the cladding could be sprayed with water to supply steam to study oxidation and for additional temperature control. The apparatus was called an instrumented fuel assembly (IFA) because the instrumentation of the rod included thermocouples, internal pressure and elongation transducers, and a γ monitor, to indicate the release of radioactivity from the fuel. To initiate a LOCA, the flow of loop water to the test section was stopped and blowdown was achieved by depressurizing the flask. Heat-up was continued to beyond clad rupture followed by water quenching. Typical test histories, IFA-650.4 and IFA-650.5, are depicted in Figs 9.75 and 9.76 [9.284]. Each shows similar features but with quantitative differences. The temperature in both experiments rose steadily, but with a delay of about 60 s after initiating the LOCA. At burst, after a small decline, the temperature in IFA-650.4 fell steadily whereas that in IFA-650.5 continued to increase until the reactor was shut down. After an initial drop, the internal pressure in each rose with temperature; in IFA-650.4, with the increase in volume as the tube ballooned, the pressure decreased then dropped precipitously when the cladding burst, while in IFA-650.5, ballooning and rupture were only a few seconds apart but the pressure drop after tube burst was slow, taking about 100 s to fall to a background value. Rod IFA-650.4 gradually elongated up to burst where it had a sudden increase in length immediately followed by a steady decline in length. Rod IFA-650.5 had a gradual shortening up to burst and did not change length thereafter. The γ signal appeared about 20 s after burst in IFA-650.5 then oscillated three times before diminishing to a small value when the reactor was shut down. Post-irradiation examination revealed that the fuel was fragmented but, because the cladding had not deformed very much, the fuel was well contained and had not relocated. In IFA-650.4, about 60 s after bursting, a γ signal was detected that increased rapidly for about 60 s before gradually slowing; after the spray step, a large spike in activity was followed by a sharp decline. Post-irradiation examination revealed that about 40% of the original fuel

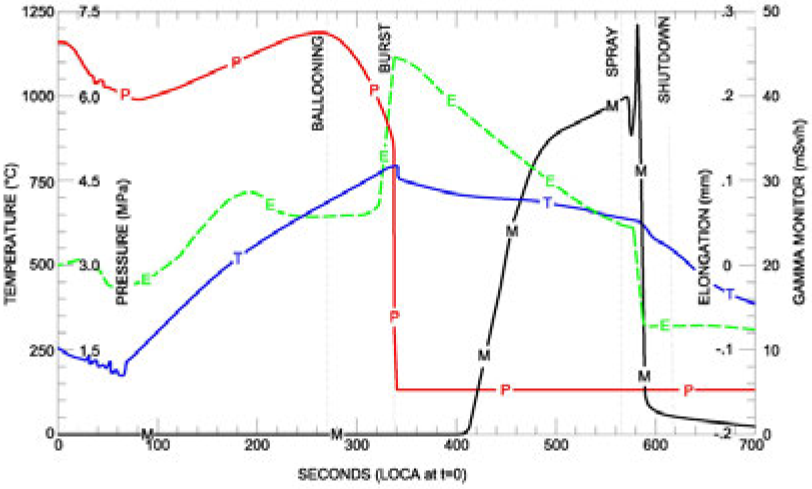

FIG. 9.75. History of temperature, T, pressure, P, and elongation, E, in Halden LOCA test IFA 650.4 showing changes at burst and subsequent detection of a γ-signal, M [9.284].

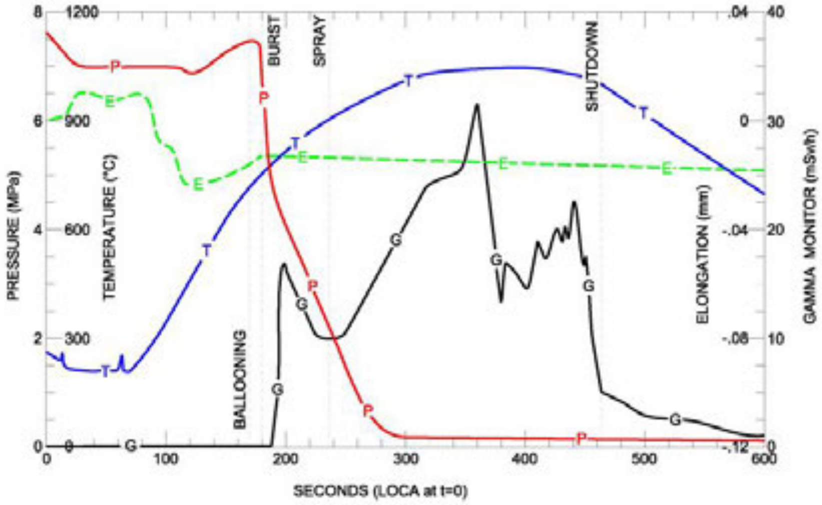

FIG. 9.76. History of temperature, T, pressure, P, and elongation, E, in Halden LOCA test IFA 650.5 showing changes at burst and subsequent detection of a γ-signal, G [9.284].

pellets had relocated into the ballooned volume and some fragments were found outside the fuel rod in the pressure flask. Those that remained within the cladding were highly fragmented.

The results of the early tests are summarized in Table 9.15. Despite the very high burnups, especially in IFA-650.3, 4 and 5, and the different materials, the temperature at burst fits with the other data from in-reactor tests, as shown in Fig. 9.72. The ductility was high in most of the cladding that burst in the high α phase or low (α + β) region, except for IFA-650.5, as shown in Fig. 9.73.

In summary, the results of the cladding behaviour in these five series of LOCA tests in-reactor fitted with expectations from tests in the laboratory. The temperature at rupture declined with increase in hoop stress, as indicated for unirradiated material. The scatter of the temperature dependence of strain at rupture was large and masked the expected trend of two maxima and a minimum in the upper (α + β) phase region. Contributions to the scatter, such as temperature gradients and axial constraints, were not always well controlled. Increased rod internal pressure generally resulted in shorter balloons but wider rupture openings [9.285]. No new phenomena, especially embrittlement of the cladding by high burnups, were observed. Cladding elongation values in LOCA experiments were independent of burnup, as indicated by several experiments in which UO_2 was clad with a zirconium alloy, usually Zircaloy-4, as shown in Fig. 9.77. Fuel breaks up after even a small burnup; breakup is caused by cracking in the brittle UO_2 because of large temperature gradients from fission and differential thermal expansion across the fuel pellet producing large stresses. The size of the fragments of fuel

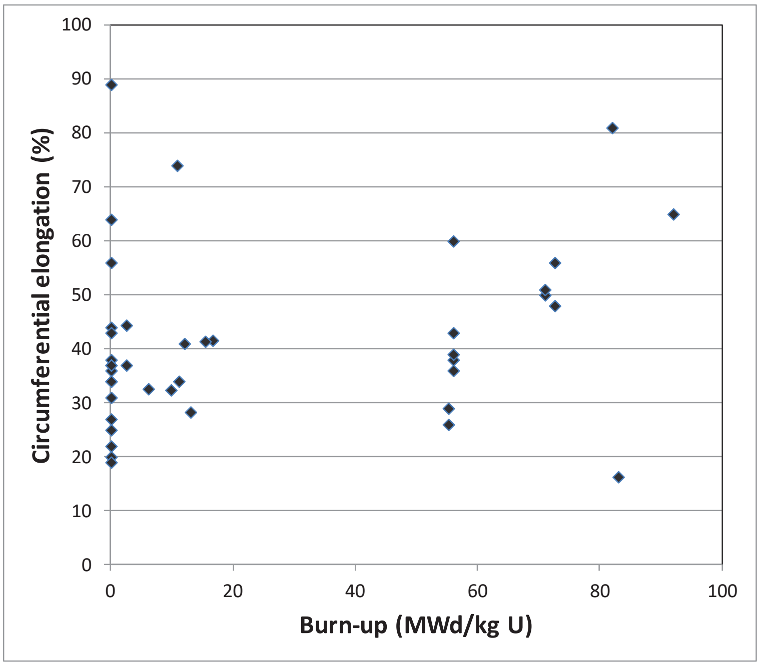

FIG. 9.77. Lack of dependence of ductility on burn-up in temperature ramp tests of UO2 clad in zirconium alloys (Argonne [9.251], Studsvik [9.252], FR2 [9.275, 9.276], EOLO [9.279], Halden [9.284]).

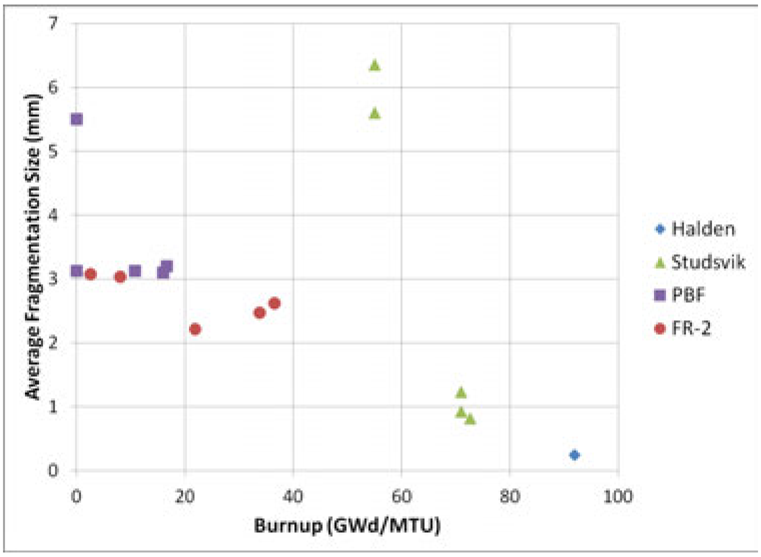

FIG. 9.78. Average fuel fragment cross-section as a function of burn-up, showing increased fragmentation with increasing burn-up [9.285].

appeared to decrease with burnup, as shown in Fig. 9.78 [9.284]. Axial relocation accompanying fragmentation is simultaneous with bursting of the cladding and is not its cause. Diametral strains resulting in fuel axial relocation were 8% in the Forschungsreaktor 2 tests [9.274, 9.275], 13 to 15% in the Halden LOCA IFA-650.X series [9.282, 9.283] and 5 to 12% in the Studsvik LOCA tests [9.251]. Some fuel dispersal was observed when the fuel fragments were small enough to pass through the rupture opening. The amount of fuel that was dispersed varied widely, from dust to pulverized particles to pieces with cross-sections of a few millimetres.

9.3.4.5. Assemblies and bundles

Using information gained from experiments on single rods (Section 9.3.4.2), tests have been carried out to simulate the behaviour of assemblies of fuel rods in a LOCA. The purpose of these tests was to evaluate coolant flow blockage and its effect on coolability by studying the deformation response of the cladding within the complex interaction between thermohydraulics and assemblies of fuel rods and to assess the effects of rod-to-rod contact and grid spacers. Total flow blockage, B, between n rods is estimated using Eq. (9.31) [9.255]:

$$B\% = 100/\mathrm{n}\ \sum_{1}^{\mathrm{n}} \frac{A_{\mathrm{f}} - A_0}{p^2 - A_0} \tag{9.31}$$

where

A_0 is the initial area of the fuel rod;
A_{f} is the final area of the fuel rod;

and p is the lattice pitch between rods.

TABLE 9.15. RESULTS OF SIMULATED LOCA IN HALDEN: TEST SERIES IFA-650.X [9.283]

Rod # Reactor type	Cladding	Burnup (MWd/kg)	Heating rate (°C/s)	Burst temperature (°C)	Elongation (%)	Burst stress (MPa)	Failure time (s)	H concentration (ppm)	Oxide (µm)
2-PWR	Zircaloy-4, low Sn	0	8.5	800	89	47	100	<25	<2
3-PWR	Zircaloy-4, low Sn outer layer	82	2.5	780	81	49	266	250	25
4-PWR	Zircaloy-4, low Sn outer layer	92	5–10	785	65	38	336	50	10
5-PWR	Zircaloy-4, low Sn outer layer	83	4	750	16.3	49	178	650/800	72
6-WWER	E110, Zr1Nb	56	1.5	840	60	40	526	N.a.	5
7-BWR	LK3/L inner liner	40	N.a.	1100	25	7	N.a.	1500	<10

As an example, in a test assembly simulating a PWR, the cladding diameter was 10.9 mm and the pitch was 14.4 mm. When the tubes are ballooned out to just touch each other, the circumferential strain is 31.9%. Based on Eq. (9.31), if all the tubes deformed identically and remained circular in the same plane, the blockage at contact would be 60.9%. In assemblies, if the axial temperature spread is similar along each rod, deformation will tend to be coplanar and lead to maximum blockage between rods. One of the results from experiments on single rods is that a large azimuthal temperature gradient can induce low strains at rupture but in assemblies, because the thermohydraulic conditions determine the temperature distributions and because of interactions between rods, the temperature distribution may be less uneven. Strain profiles, as well as B, can be measured on cross-sections of deformed assemblies that are fixed in position by epoxy resin then examined metallographically [9.286]. Three examples of tests on bundles follow.

In the REBEKA tests, 5 × 5 and 7 × 7 rod bundles were tested [9.212]. The simulated fuel rods were full length, 3.9 m, clad in Zircaloy-4 and held vertically in place by eight spacers. The high

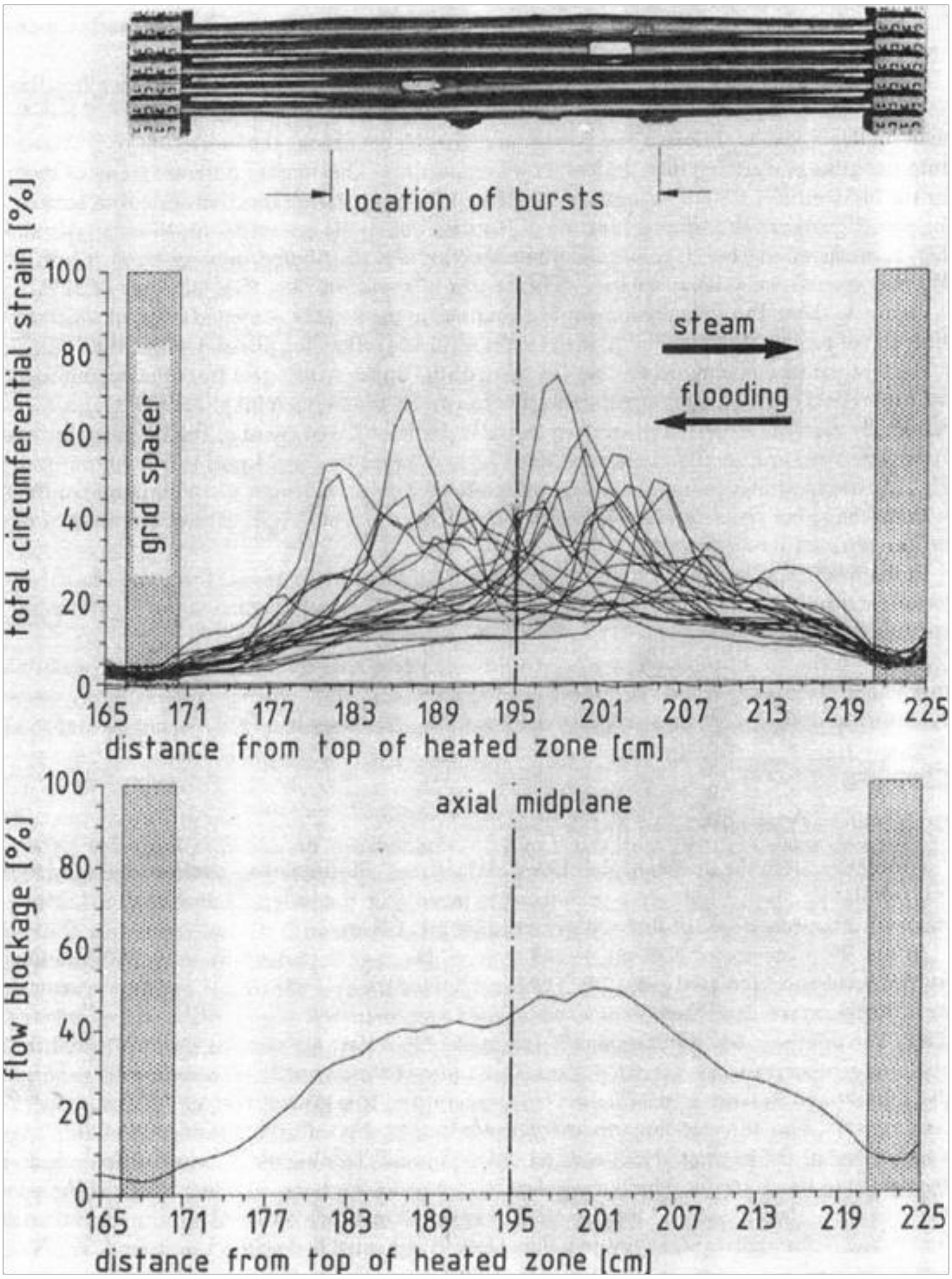

FIG. 9.79. REBEKA-5: Circumferential cladding strain and flow blockage between spacer grids in 7 × 7 assembly under reversed flow [9.213].

temperatures were attained by internal electrical heaters with maximum power in the centre of the rods. Two thermohydraulic schemes were used. Common to all tests was a first stage with heating at about 7°C/s with a downward flow of steam. Once a target temperature was reached, the test section was reflooded with either upward or downward flow.

In the 5 × 5 assemblies only the inner 3 × 3 rods were pressurized between 5 and 7 MPa; the outer rods were clad in Inconel, forming a non-deforming thermal shield. In three tests the temperature for the start of reversed flow reflooding was about 940 K (665°C). The average burst temperatures ranged from 1083 to 1003 K (810 to 830°C) and the average burst strain ranged from 28 to 46%. In REBEKA-3 (R-3) the axial spread of bursting between three spacer grids was 6 bursts over 230 mm and 3 bursts over 179 mm leading to a maximum flow blockage of 52%. In REBEKA-4 (R-4) the central rod in the assembly was replaced by a control rod guide tube. The expectation was that the

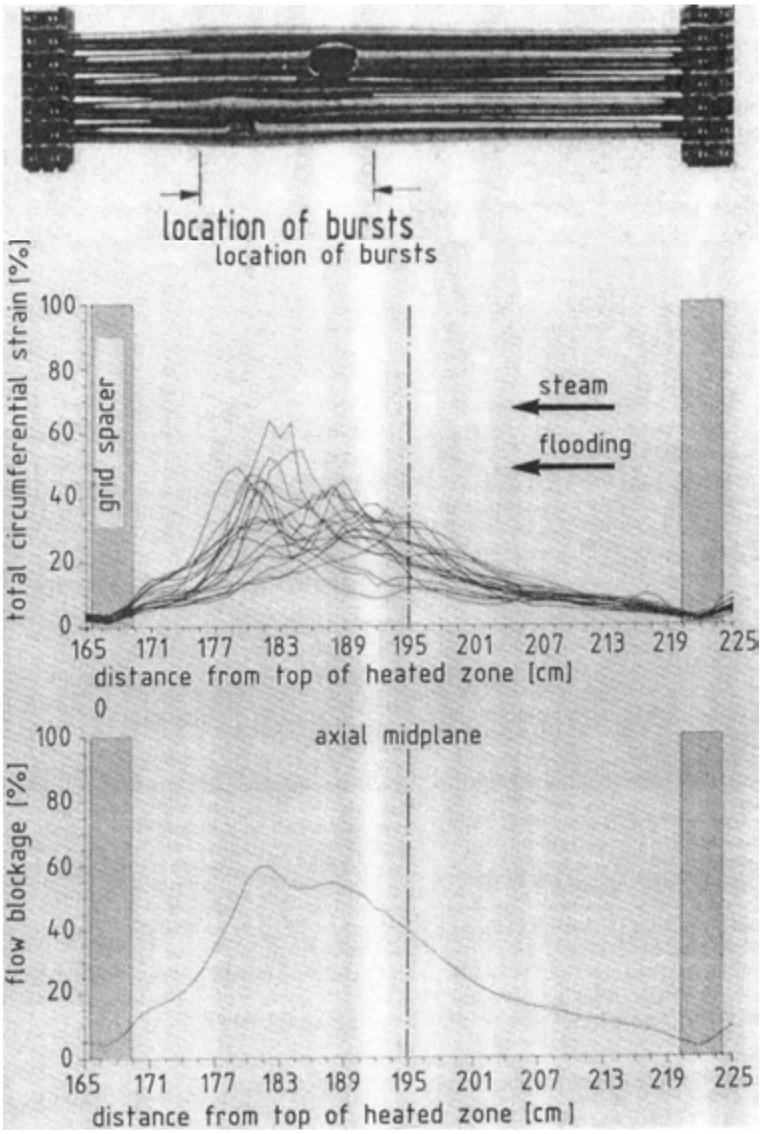

FIG. 9.80. REBEKA-6: Circumferential cladding strain and flow blockage between spacer grids in 7 × 7 assembly under unidirectional flow [9.213].

cooler tube would lead to a temperature gradient which in turn would result in strain localization. The reverse was observed. The maximum strain in R-3 was 64% whereas in R-4 the maximum strain was 79%; the axial spread was about 250 mm with the flow blockage being increased to 55%. This result was explained [9.287] by early contact with the guide tube, because of the ‘hot side straight effect’ stopping deformation on the now cool side and continuing on the remaining hot side. The subsequent lowering of the azimuthal temperature gradient led to higher strains before rupture. In REBEKA-2 (R-2) the burst temperature was 1123 K (850°C) and the deformation was completed in the heat-up phase before reflooding. The azimuthal temperature distribution was more homogeneous than in the tests where the clad burst during reflooding, so the deformation was more coplanar — maximum strains spread over about 100 mm between three spacer grids — and the maximum strain to rupture was 64% with maximum blockage of 60%.

With one exception, all 49 rods were pressurized in the 7 × 7 rod bundles, which were restrained by an unheated shroud. In REBEKA-5 (R-5) the test conditions were similar to those in R-3. The burst temperature was 1073 K (800°C) and the maximum strain was larger than in R-3, 75%, but because the deformation was spread over about 240 mm, the maximum flow blockage was similar, 52%, as shown in Fig. 9.79. In REBEKA-6 (R-6) the central position contained an instrumentation

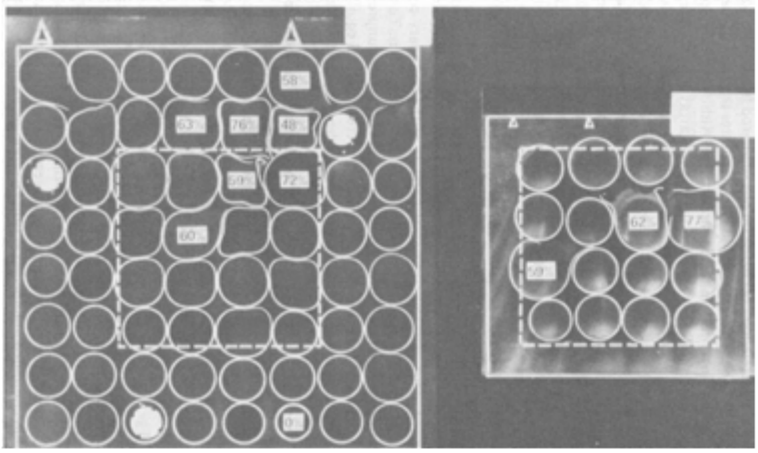

FIG 9.81. Sections through the highly deformed arrays tested in ORNL–MRBT: B5 (left) and B3 (right). The dotted lines outline the original 4 × 4 array. The numbers in some tubes indicate strain; note the 0% in B5, which was not pressurized but represents the initial diameter [9.286].

tube and two rods with a reduced pressure of 6 MPa. The steam and reflooding were in the same direction leading to axial uniformity in the temperature at burst of about 1063 K (790°C) and low axial spread of strain to rupture, about 140 mm, as shown in Fig. 9.80. The maximum strain was 65% and the flow blockage was 60%. REBEKA-7 (R-7) was a repeat of R-6 with all the rods pressurized. The maximum strain to rupture was 85% with an average value of 55% spread over 200 mm giving a maximum flow blockage of 66%.

In all the tests, the strain was low at the locations of the spacers because the grid generates turbulence and breakup of water droplets that improves the heat transfer and limits the temperature in the cladding. In these tests the thermohydraulic conditions were not conducive to mechanical interaction between rods so little effect of bundle size was observed.

Two arrays of assemblies clad in Zircaloy-4 were tested in the Oak Ridge National Laboratory–Multirod Burst Test (ORNL–MRBT) programme to evaluate the effect of bundle size: 4 × 4 as B1, B2 and B3, and 8 × 8 as B5 and B6. In these tests the steam atmosphere had a low downstream flow. The heat-up to simulate LOCA was achieved with internal heaters with uniform power over a length of 0.915 m. The initial pressures were imposed with helium. The rods were kept in place with spacers that were 560 mm apart in the heated section of the assembly.

The 4 × 4 rod assemblies were surrounded by a shroud that was sometimes heated to maintain a uniform radial profile but was sufficiently distant that it did not restrain deformation and bowing of the outer rods without contact, as shown in Fig. 9.81.

The first two tests used temperature ramp rates of about 30°C/s with burst pressures of about 6 MPa. Tubes burst in the temperature range 1123 to 1153 K (850 to 880°C). The burst strains in B1 were between 32 and 59% with blockage of about 49%. In B2 the shroud was not heated. The strains and blockage in B2 were similar to those in B1, but the bowing of the peripheral rods was greater because of the azimuthal temperature difference caused by the cool shroud. In B3 the heating rate was reduced to 9.5°C/s and the pressure was increased (burst pressure of 9.4 MPa) to cause rupture in the high α phase, around 1053 K (780°C). The circumferential strains of 42 to 77% were consistent with tests on single rods with heated shrouds. The maximum flow blockage was 77%.

The two 8 × 8 rod assemblies were tested with unheated closely fitted shrouds. The inner surface of these shrouds was highly polished Au plated stainless steel to minimize thermal losses by radiation. The test conditions for B5 were similar to those of B3. When the results of the two tests were compared [9.285], it was found that the outer rods in B5 had similar burst temperatures and pressures as B3 in reasonable agreement with results from single rod tests with heated shrouds. The inner rods of B5 burst at lower pressures but not because of higher burst temperatures. The shroud limited outward expansion, and after deforming into contact between the rods, rather than setting up a large temperature gradient the temperature distribution became more homogeneous in the centre of the array. Simultaneously, the volume expanded in both the radial and axial directions leading to lower pressure before eventual bursting. The central rods tended to an almost square cross-section, as shown in Fig. 9.81. The average circumferential strain in the inner rods of B5 was similar to that in B3 — compare 67% with 58% — but the volume increase was much larger — compare 59% with 42%. The high volume expansion in B5 led to a high maximum flow blockage of 90% over a wide axial extent, >70% over 230 mm, as shown in Fig. 9.82. Based on the results from single rod tests, a heating rate of about 3.5°C/s and initial pressure of about 3.2 MPa were chosen as test conditions for B6 aiming for burst at about 1200 K (927°C) — in the middle of the ($\alpha + \beta$) region where the strain at burst was minimized, as shown in Fig. 9.65. The rods in the central 4 × 4 array burst between 1190 to 1210 K (917 and 937°C) at pressures between 2.72 and 2.87 MPa. The burst strains were in the range 22 to 56%, with a mean value of 30% that is consistent with tests on single rods. The flow blockage was consequently modest, averaging 39% for the whole 8 × 8 array and 46% in the inner 4 × 4 array [9.238]. The results of the tests on the 8 × 8 array assemblies are summarized in Table 9.16.

In these tests the thermohydraulic conditions were conducive to mechanical interaction between rods. The results suggested that the behaviour in these simulations of LOCA depended on the size of the array and the complex interactions between central rods in large arrays were not properly modelled by small arrays. These differences can lead to underestimation of flow restriction. Again, the strains were low at the grid positions.

TABLE 9.16. SUMMARY OF BURST CONDITIONS AND RESULTS IN ORNL 8 × 8 ARRAY [9.238] AND JAERI 7 × 7 ARRAY [9.288]

Specimen	Heating rate (°C/s)	Initial pressure (MPa)	Burst pressure (MPa)	Burst temperature (°C)	Maximum strain (%)	Blockage (%)
ORNL B5	9.8	11.6	8.3	770	67	90
ORNL B6	3.5	3.2	2.8	930	56	46
JAERI 5	6.6–8.7	4.9	6.6	832	118	76.6
JAERI 6	7.3–9.0	2.0	2.7	895	45	40.3
JAERI 7	5.9–7.2	6.9	8.8	770	105	78.1
JAERI 8	5.9–7.9	3.4	4.5	875	60	51.4

Nineteen tests were performed on 7 × 7 arrays at the Japan Atomic Energy Research Institute (JAERI). These simulators had a heated length of 0.9 m, the rods were held in place by two spacers and the internal pressure was in the range 2 to 7 MPa. The external environment was similar to that

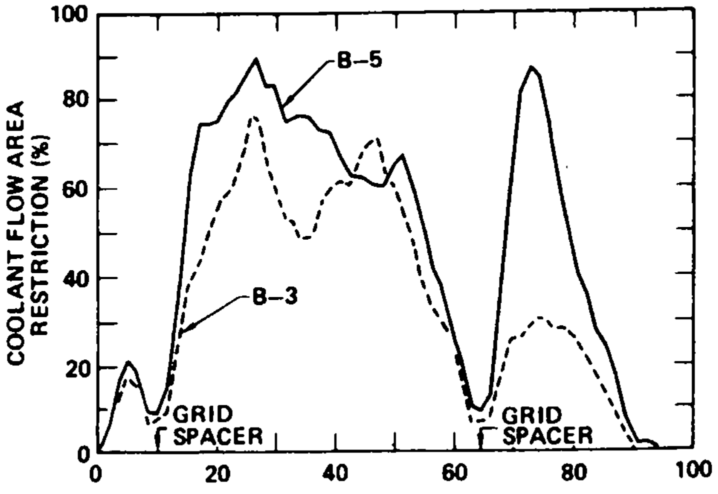

FIG. 9.82. Blockage in central 4 × 4 array in B5 compared with blockage in B3 [9.286].

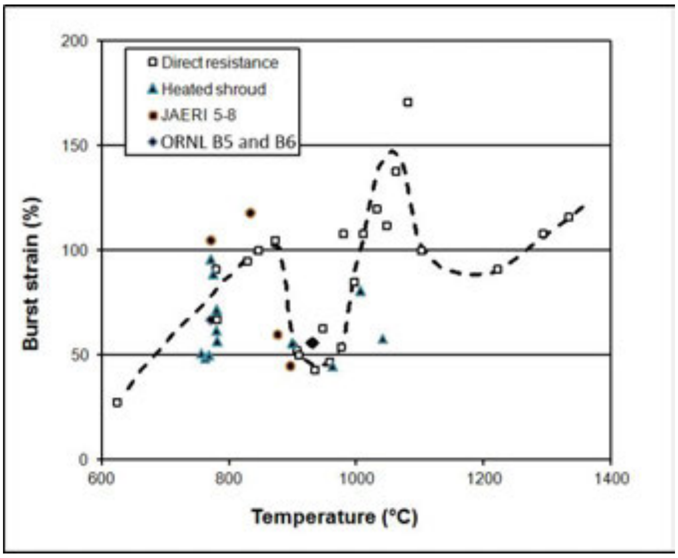

FIG. 9.83. Comparison of burst strains in single rods (direct resistance [9.230] or internal heater with heated shroud [9.239]) and the interior of 7 × 7 [9.288] and 8 × 8 [9.239, 9.256] arrays.

used in the ORNL–MRBT tests — a low flow of steam — with the expectation of large deformations. Three configurations were used: in tests 5 to 8 the assembly was surrounded with an unheated shroud; in tests 15 to 24 the shroud was heated; in tests 9 to 14 the assembly was surrounded by heater rods.

With initial pressures of 2.0 to 6.9 MPa and heating rates in the range 6 to 9°C/s, based on single rod tests, the expected burst temperatures for tests 5 to 8 were in the range 1010 to 1190 K (740 to 920°C), high in the α phase and in the (α + β) region. This expectation was exactly met; the circumferential strains in the central rods also agreed with expectations based on single rod tests [9.288]. In test 5, with one exception, the axial locations of the bursts were within a band 150 mm wide, and in agreement with B5 the axial extent of deformation was greater in the inner rods than in the peripheral rods. The blockage increased with maximum strain. The results of these tests are summarized in Table 9.16 where they are compared with those from B5 and B6. The temperature dependence of the maximum burst strain agrees with the data from the B5 and B6 assemblies and data on single rods heated by direct current or internally but with a heated shroud, as shown in Fig. 9.83.

In tests 9 to 14 the test conditions were similar to test 5. (One exception was test 13 where the ramp rate was <1°C/s. In this test, the tubes ruptured between 1040 and 1070 K (765 and 800°C) with coplanar deformation restricting the flow by 88%.) The external heaters reduced the temperature gradient between the centre and the periphery of the assemblies resulting in increased axial extension of the deformation. To simulate control rod guide tubes, the central tube in test 11 and four tubes in tests 12 and 14 were not heated [9.289]. Despite the temperature difference imposed by the unheated rods, the axial extent of the deformation was still large in adjacent rods — >34% over 200 mm — as observed in R-4.

This behaviour was confirmed in tests 15 to 24 where the assembly was surrounded by a heated shroud [9.290]. The initial pressure was 5 MPa and the heating rates were either 1°C/s or 7°C/s. In spite of the expected azimuthal temperature gradient, in tests where simulated guide tubes were used instead of heating rods, the ballooning behaviour of the rods neighbouring a guide tube was similar to that of other rods. The flow blockages were similar, with maximum values around 90%, and little effect from heating rate.

Although information on single tubes provides a useful guide to the relationships between burst temperature and strain, and internal pressure and heating rates, the behaviour of collections of single rods as bundles is governed by these relationships as well as the mechanical interaction between neighbouring rods that can critically alter the temperature distribution. Although a general trend relating flow blockage to the maximum burst strain in the assemblies can be discerned, as shown in

Fig. 9.84, such a relationship does not capture the axial extent of the deformation or the relative axial or clock positions of the maximum circumferential strain in each rod.

9.3.4.6. Coolability

The simulation of the early stages of a LOCA on assemblies indicates that sub-channels between rods become partially blocked, sometimes quite markedly, because the rods interact with each other. A series of experiments has been conducted in several countries to evaluate the consequence of this blockage on coolability. The results are summarized by Grandjean [9.291]. The outcome depends on the dimensions of the blockage and the coolant conditions. In the blowdown and initial reflood stages of a LOCA, the temperature of the cladding is controlled by heat transfer to a two phase mist, as shown in Fig. 9.57. The complex thermohydraulics in the blockage lead to opposing effects:

- A flow bypass effect, which tends to decrease the heat transfer in the blocked region because of the reduced mass flow. Flow rate is proportional to flow area. The consequence is heat-up of the cladding.
- A flow blockage effect, which tends to increase the heat transfer because of flow acceleration, turbulence and the development of new boundary layers, droplet breakup and improved mixing, and reduction in steam superheating. The consequence is cooling of the cladding.

Whether the cladding continues heating or starts cooling depends on the proportion of each of these effects. The heat transfer experiments simulated the temperature histories of arrays of fuel rods deformed in the assembly tests, with preshaping of the cladding to represent balloons of various diameters, lengths and positions.

In the USA, the programme of testing was called Full Length Emergency Cooling Heat Transfer–Separate Effects and System Effects Tests (FLECHT–SEASET) [9.292]. Arrays of 161 rods were exposed to a heating cycle representing a LOCA with reflooding from a simulated ECCS. The evaluation of 161 rod bundles with no blockage [9.293] provides information on the effect of relevant parameters on bundle quench rate, entrainment and heat transfer:

- Flooding rate: As the flooding rate of the ECCS increases, the bundle quench rate increases and the heat transfer above the quench front increases.

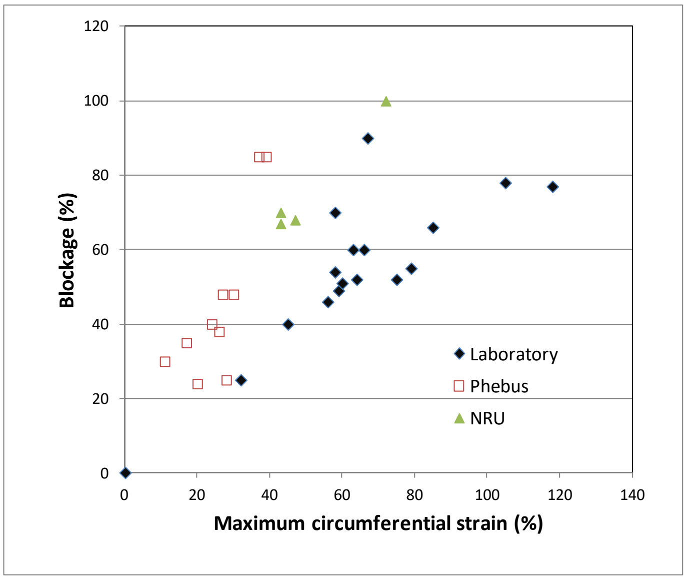

FIG 9.84. Relationship between area of blockage and circumferential strain based on burst tests on assemblies [9.213, 9.286, 9.287, 9.290, 9.302, 9.305].

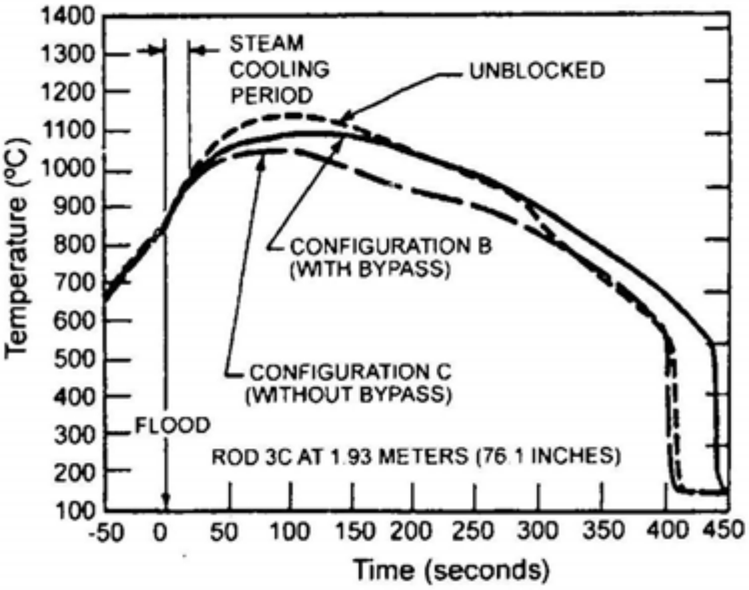

FIG. 9.85. Temperature history during simulation of injection of ECCS after deformation of fuel cladding in a LOCA. Array of 21 rods with no blockage, partial blockage (B) and 62% blockage with no bypass (C) in FLECHT–SEASET; blockage simulation clad in 304 stainless steel [9.292].

- Pressure: As the pressure inside the vessel increases, the rod bundle quench rate increases but the start of entrainment is delayed. Since the steam velocity is lower for the given mass flow of steam at higher pressures, lower system pressures result in earlier entrainment but later bundle quench times.
- Subcooling: The effect of the temperature of simulated ECCS water is weak; as the subcooling of the reflood water increases, the rod bundle quench rate increases since the fluid has the capability to absorb more energy. As the subcooling decreases, the quench rate decreases; there is earlier entrainment because of higher steam flows that can help to reduce the temperature rise early on.
- Initial temperature: The higher the initial temperature of the rod, the lower the temperature rise because the entrainment and steam flow increases with increased stored energy release. The quench times are longer with higher initial temperatures.
- Rod power: The effect is small, but for low flooding rates, increased power will delay bundle quench time but also leads to earlier entrainment.

In the 21 rod arrays, six distinct geometries of blockage were tested to simulate deformations found in the burst tests on the assemblies:

(1) Unblocked (configuration A), representing a reference.
(2) Concentric sleeve, 32.6% maximum strain, coplanar on 9 rods (configuration B), providing 62% blockage and bypass. Concentric blockage represents isotropic strain in the β phase during the LOCA.
(3) Concentric sleeve, 32.6% maximum strain, coplanar on all rods (configuration C), providing no bypass.
(4) Concentric sleeve, 32.6% maximum strain, non-coplanar on all rods (configuration D), providing blockage of about 30%.
(5) Non-concentric sleeve, 36% maximum strain, non-coplanar on all rods (configuration E). Non-concentric blockage represents anisotropic deformation when much α phase is present during the LOCA.
(6) Non-concentric sleeve, 44% maximum strain, non-coplanar on all rods (configuration F).

The ballooning was simulated with 304 stainless steel sleeves fitted over the heating rods. The concentric balloons in configurations B to D were short, 58 mm, while those used in E and F were 95 mm long. The heater rods in the test assemblies had heated lengths of 3.05 m and were held in place by eight spacer grids. The test parameters included a reflood rate range of 12.7 to 152 mm/s; a vessel pressure of 0.14 to 0.28 MPa; inlet fluid subcooling temperature of 295 and 351 K (22 and 78°C); and initial peak linear power of 0.89 to 2.57 kW/m, leading to clad temperatures around 1123 K (850°C) at reflood.

Typical temperature histories for configurations A, B and C are depicted in Fig. 9.85. The thermocouple in the blockage configurations was 50 mm downstream from the trailing edge of the blockage. This figure shows the early, nearly adiabatic heat-up period of approximately 15 s, when there was very little flow through the bundle and only small temperature differences between blocked and unblocked configurations. When the steam flow increased and liquid entrainment began, the rate of rod temperature rise decreased. Once entrained drops were present in the steam flow, a noticeable reduction was observed between the temperatures in the blocked region, with bypass (configuration B) and without bypass (configuration C), and the unblocked region (configuration A). The greatest temperature reduction occurred in the blockage configuration (C) without flow bypass; the difference in the maximum temperature between configurations A and C was about 100°C. The water droplets and all the steam had to pass through the blockage region where the droplets were broken up and the steam flow was accelerated. In the blockage configuration with flow bypass, some of the steam flow was redistributed around the blockage, and therefore the temperature reduction was smaller than when all the cladding was deformed. With these examples, full cooling was attained in less than 450 s. The results illustrate the importance of two phase flow for the heat transfer in the reflood stage of a LOCA. The expected penalty for cooling because of flow diversion at the blockage is overcome by the increase in heat transfer with the phase transformation in the water–steam mixture within the blockage.

The extra cooling at blockages was confirmed in similar tests simulating more severe blockages. In the THETIS experiments [9.294, 9.295] a 7 × 7 square array of heaters was held in place by 8 grids and the whole assembly was surrounded by a square shroud tube. The heaters were clad in Inconel, had a length of 3.6 m, an outside diameter of 12.2 mm and a chopped cosine power profile. A 4 × 4 array of rods within the 7 × 7 array contained a section about halfway up the bundle and within one grid interval simulating coplanar blockage with an Inconel balloon filled with nitrogen extending for 200 mm on each rod, with a 200 mm long entry taper and 50 mm long exit taper. Blockages of 80% and 90% were evaluated. The test parameters included a reflood rate[3] range of between 10 to 60 mm/s from the bottom of the array with an inlet fluid temperature of between 323 and 363 K (50 and 90°C); a vessel pressure of 0.13 to 0.4 MPa; and initial clad temperatures in the axial centre of the array of between 823 and 923 K (550 and 650°C) at reflood.

---

[3] In these experiments the area of the array was 7.61×10^{-3} m^2, so to support a reflood rate of 10 mm/s required an input of water of 0.076 kg/s.

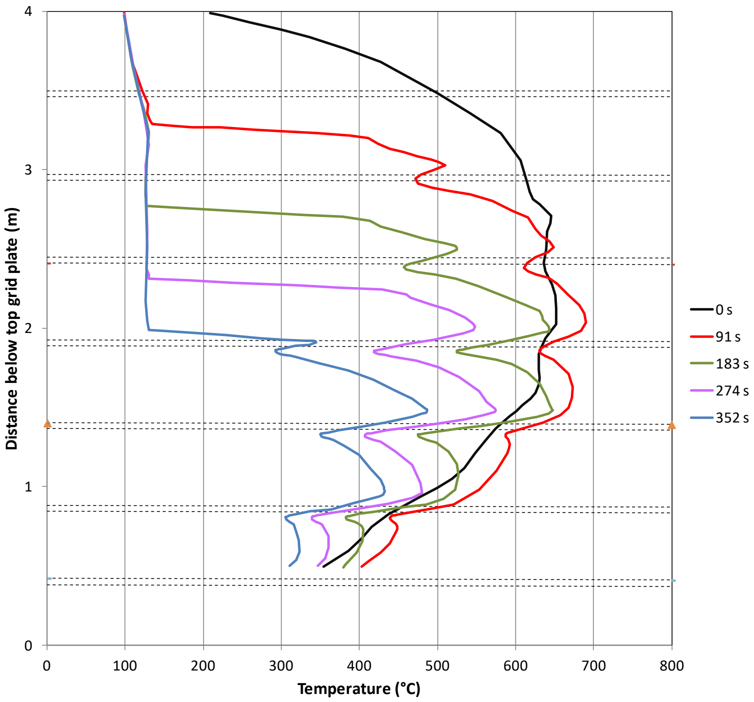

FIG. 9.86. Temperature distribution in THETIS bypass at various times showing the initial temperature profile (time = 0 s), the small temperature rise at short times, the movement of the quench front up the array (the reflood is from the top of the diagram) and the dip in temperature at the grids (dotted lines). Test conditions: reflood rate of 20 mm/s with water at 362 K (89°C), ambient pressure of 0.2 MPa and power of 101 kW (based on [9.295]).

The axial variation in temperature at successive times shows the progress of the rewetting front in a bypass region, as shown in Fig. 9.86. Although the reflooding rate was 20 mm/s, the average passage of rewetting was about 6 mm/s up to the centre of the assembly because the amounts of heat to be removed increased towards the axial centre of the array. The temperature passes through a maximum at the axial centre of the cluster of rods; during the reflooding the initial temperature may be exceeded because of superheating of the steam in the two phase coolant as it passes up the array. Sharp dips in temperature just downstream from the grids indicate the enhanced heat transfer from turbulence and reduction of steam superheating. The temperature histories in the blockage and bypass

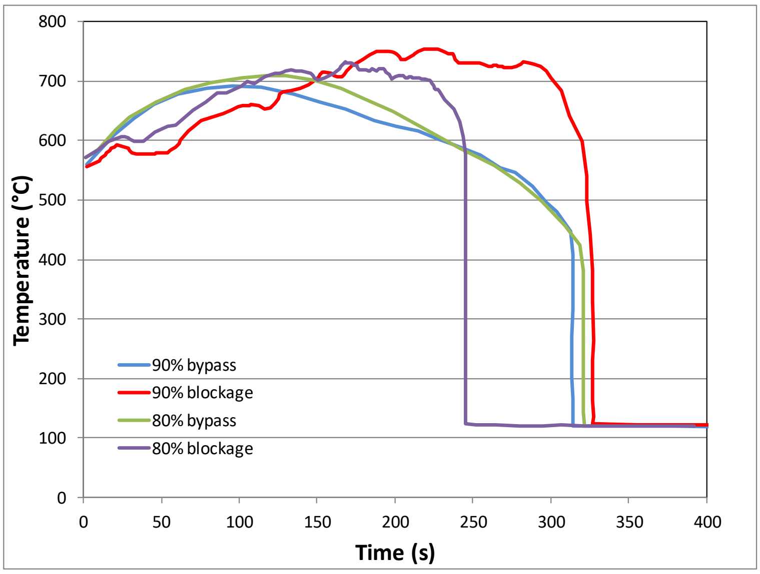

FIG. 9.87. Temperature histories of bypass and blockage regions in a heated array in THETIS with reflood rate of 30 mm/s (based on [9.295]).

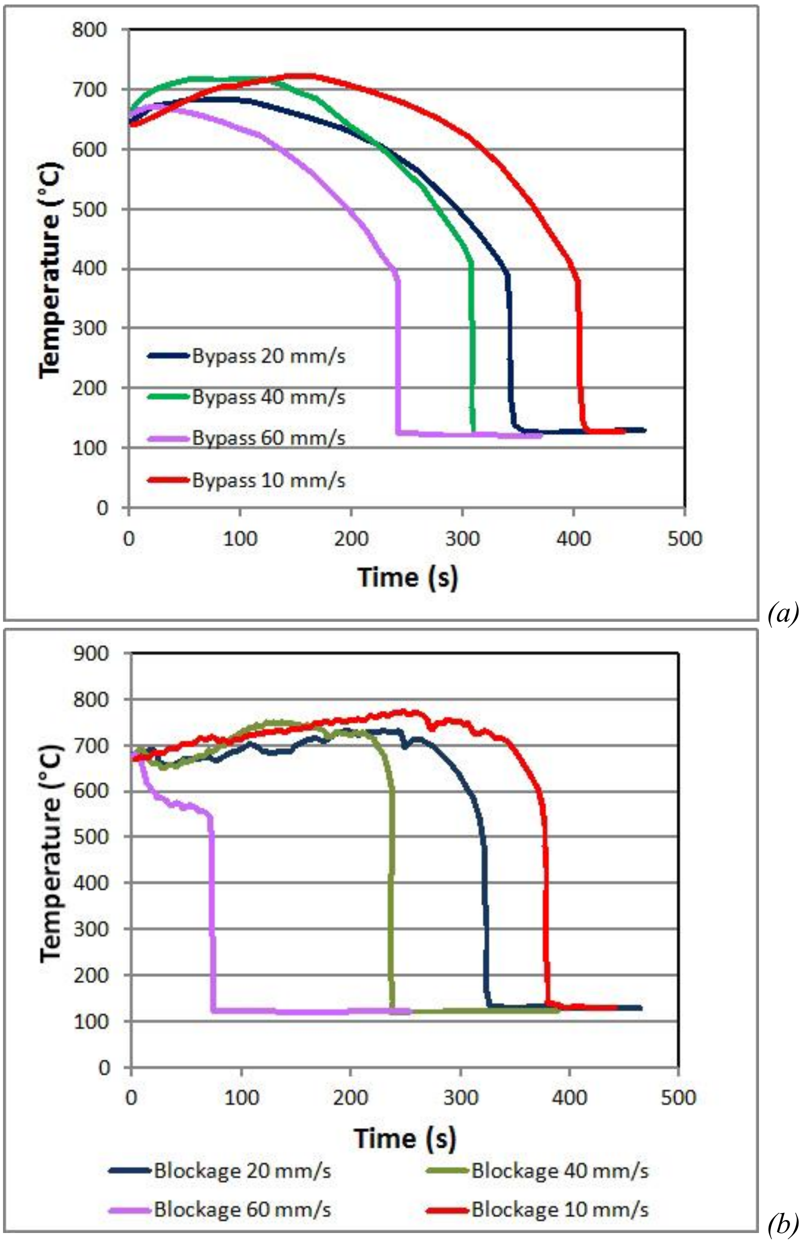

FIG. 9.88. Effect of reflood rate on temperature history in bypass region and in the blockage in a heated array in THETIS with 80% blockage: (a) bypass; (b) blockage (based on [9.295]).

region for 80% and 90% blockage with a reflood rate of 30 mm/s are illustrated in Fig. 9.87. Initially the temperature is lower in the blockage than in the bypass region, then the trend reverses. The temperature in the bypass region passes smoothly through a maximum value before rewetting. The different amounts of blockage have only a small effect on the temperature history in the bypass region because of the small difference in coolant flow. In the blockage region, intermittent periods of heating and cooling lead to variations in the temperature up to a maximum value before general cooling and rewet to close to the temperature of the reflood water. Early in the process, 90% blockage provides greater cooling than 80% blockage but later the rate of heat transfer is reversed. The maximum temperature and the time to quench are larger with a 90% blockage than with an 80% blockage. Similar results were obtained with a range of reflood rates for 80% blockage, as shown in Fig. 9.88(a) (bypass) and (b) (blockage). Again, the temperature history in the bypass region is smooth, passing through a maximum value before dropping rapidly once the temperature reaches about 670 K (400°C). In the blockage region, the temperature history is more complicated and erratic because of

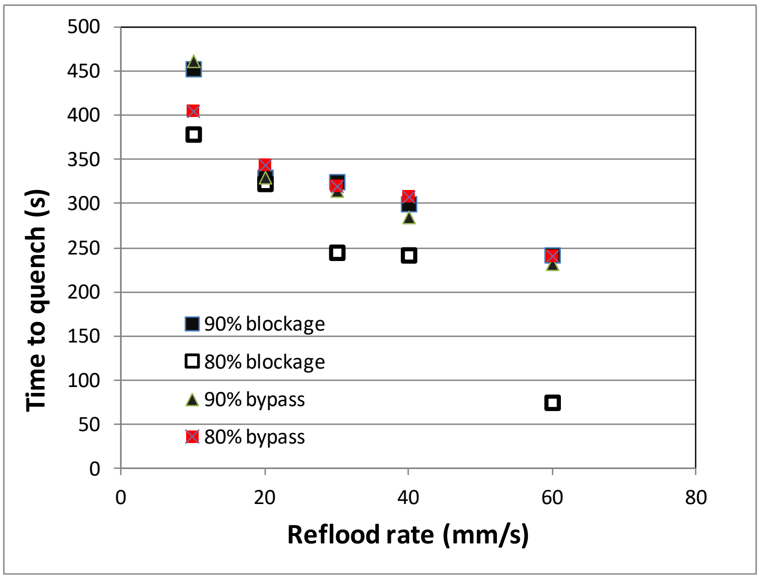

FIG. 9.89. Effect of reflood rate on time to quench cladding in a heated array in the THETIS experiment. The results show the effect of 80% and 90% blockage and the bypass around these blockages (based on [9.295]).

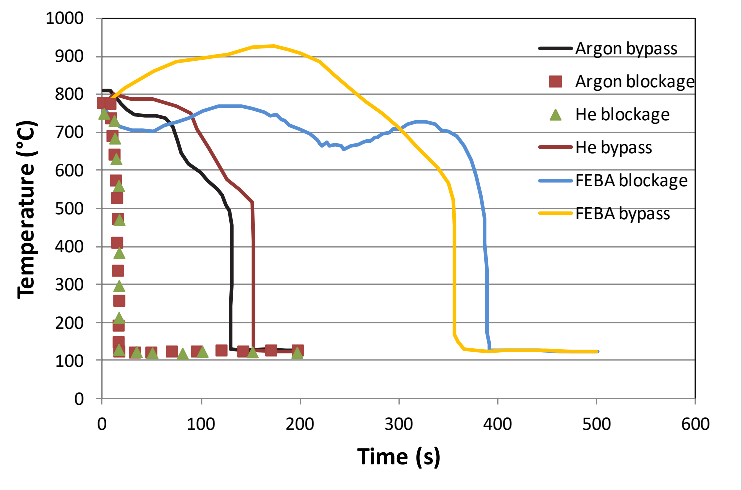

FIG. 9.90. Temperature history of Zircaloy cladding at 90% blockage and its bypass during reflood at 38 mm/s in simulated LOCA. Heater cladding gap filled with either helium or argon. FEBA rod clad in stainless steel with no gas gap between heater and cladding [9.296].

the competition between the surface-to-steam heat transfer and the steam-to-liquid heat transfer. The time to attain the quench temperature depends on the reflood rate. In the bypass region the effect of amount of blockage on the quenching time was small and the times were similar to those for 90% blockage whereas those for 80% blockage were much shorter, as shown in Fig. 9.89.

The thermohydraulic properties of the heater rods are expected to provide lower rewetting rates than actual fuel:

— Because no gap exists between the heater and the cladding;
— Because the simulators are clad in Inconel or stainless steel rather than a zirconium alloy;
— Because the simulator filler, often boron nitride, has higher thermal conductivity and heat capacity per unit volume than UO_2.

To overcome some of these shortcomings, experiments called Fuel Rod Simulator Effects in Flooding Experiments (SEFLEX) were set up [9.296]. These experiments contained REBEKA fuel rod heaters clad in Zircaloy, with a gap between the cladding and an insulating annulus of alumina pellets (simulating UO_2) that was filled with either helium, to simulate the starting internal atmosphere, or argon, to simulate the mixture of initial helium and end-of-life fission gas. (The thermal conductivity of helium is about ten times that of argon [9.297].) Gapless simulated heater rods clad in stainless steel, as used in the Flooding Experiments with Blocked Arrays (FEBA) [9.298], were used to show the difference in behaviour when the heater was clad in Zircaloy with a gas gap. The bundles contained a 5 × 5 array of rods with a heated length of 3.9 m in a cosine axial power distribution. The rods had a diameter of 10.75 mm and were separated by seven grid spacers. Within the main array, a 3 × 3 rod cluster contained cladding ballooned to represent 90% coplanar blockage over 65 mm. The reflooding rate was 38 mm/s and the system pressure was 0.21 MPa. The temperature histories are displayed in Fig. 9.90. In the short blockage region, the Zircaloy clad is quenched within 20 s with both helium and argon filler gas whereas in the bypass region the rewet time is slightly longer with helium than with argon — 150 s to 130 s. The times for quenching are much longer for the stainless steel cladding with no gas gap — 360 s to 400 s.

These experiments show that blockage (even 90%) between fuel rods formed during a LOCA can be cooled, the efficiency of the cooling depending on the geometry of the blockage, the reflood rate and the configuration and composition of the rod simulating fuel.

9.3.4.7. In-reactor tests on assemblies

(a) National Research Universal reactor tests

Four tests have been carried out on assemblies of full length PWR rods [9.299–9.302]. The experiments were performed on behalf of the Pacific Northwest Laboratory (PNL) in the National Research Universal (NRU) reactor at Chalk River Laboratories, Canada. The test train was about 9 m long and part of the fuelled section extended out of the neutron flux. The assembly consisted of 32 fuel rods formed into an array and held together with grids 533 mm apart; 11 or 12 pressurized test rods were arranged in a 2 × 4 × 4 × 2 cruciform surrounded by 20 unpressurized rods that reduced the heat transfer from the test rods to an encircling shroud, which protected the pressure tube of the reactor loop. The initial pressure of helium inside the test fuel was in the range 3.1 to 4.6 MPa at room temperature. The fuel was fresh UO_2, enriched 3%, clad with Zircaloy-4. The instrumentation included up to 143 thermocouples, 24 neutron detectors and 12 pressure transducers (MT-4). Before the LOCA transient test the fuel was preconditioned by power cycling that cracked the fuel. The LOCA simulation consisted of holding the assembly in flowing steam at 648 K (375°C) while the reactor power was set equivalent to decay heat. The transient started when the steam flow was cut off, allowing the assembly to heat up under adiabatic conditions at a rate between 8 to 11°C/s after a delay of about 10 s. In the first three tests, MT-1 to MT-3, at low pressure, two phase flow conditions existed before rupture whereas, possibly because of the high pressure, the cladding in MT-4 ruptured during the adiabatic heating phase, before reflooding was activated. After rupture, detected by pressure switches or pressure drop, the thermohydraulic conditions were stabilized to measure heat transfer characteristics of the deformed and ruptured fuel rods. Data on reflood rate, quench front propagation, liquid level, axial power, fuel rod temperature and heat transfer coefficients were obtained. Once the transient was judged to be complete, the tests were ended by shutting down the reactor.

The results are summarized in Table 9.17. During the transient, ballooning was followed by rupture. A typical axial distribution of strain is presented in Fig. 9.91. Often the strain had two peaks between grid locations. The grid spacers suppressed ballooning and prevented the strain from attaining very high values and spreading axially. This behaviour provided choke points for fuel relocation. The behaviour of the fuel was very variable, as observed in the opening of the ruptures — sometimes the fuel pellets appeared intact, in others large fragments were observed while in others no fuel remained. The length of the rupture openings had some scatter that may have contributed to the behaviour of the fuel; in test MT-4 the rupture opening had a mean length of 23.6 mm but had a range from 15.2 to 38.1 mm. The maximum strain and rupture were observed to be close to the same axial location in each bundle; for example, in MT-3 the axial location of the rupture in each rod was at 265 ± 4 cm from the top end of the bundle. The values of burst temperature for MT-4 agreed with those of the other investigations, as shown in Fig. 9.72, while the strains to failure for all four tests were highly variable but within the scatter of the other data, as shown in Fig. 9.73. A few of the pressurized tubes did not rupture; some had modest strains, MT-1, while others showed no indication of deformation, MT-2, suggesting that the rods had leaked. Because of the coplanar strains, the average flow blockage was between 70 and 100%, as shown in Fig. 9.84, although the temperatures in the blockage and in the bypass were similar, showing that cooling was not affected by the blockage. The measured heat transfer for ruptured and undeformed cladding in the MT-series and separate thermohydraulics tests was similar [9.303], indicating that the effect of flow reduction was balanced by the effect of turbulence, as discussed in Section 9.3.4.6.

(b) Phébus

A programme of testing for LOCA was performed by the French Institut de Radioprotection et de Sûreté Nucléaire in Phébus, a pool-type reactor [9.304, 9.305]. The test section consisted of a 5 × 5 bundle of PWR rods containing fresh UO_2 clad with Zircaloy-4. The rods were 1 m long with an active length of 0.8 m and could be internally pressurized; for the first four tests the fill pressure at room temperature was 4 MPa with values of 3.4 and 3 MPa for the subsequent two tests. The fuel bundle was surrounded by an unheated Zircaloy-2 shroud to link the square bundle to the circular containment tube. The temperature and pressure histories of the tests were designed to follow that illustrated in Fig. 9.57: a target initial temperature peak near 1190 K (920°C) (into the $(\alpha + \beta)$ phase region) followed by immediate cooling towards 1020 K (750°C) (to represent blowdown), then reheating to provide conditions for rupture at 1080 to 1169 K (810 to 890°C), then a plateau value (to

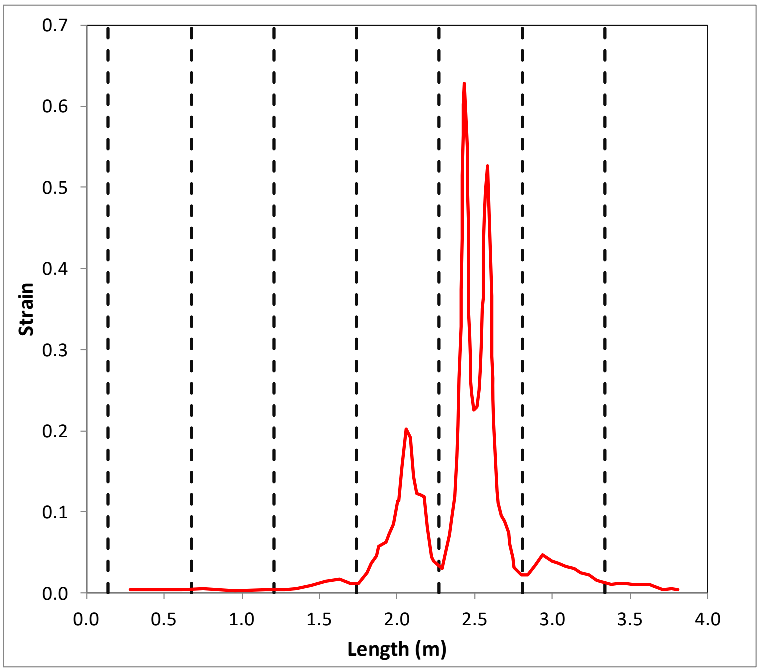

FIG. 9.91. Axial distribution of average diametral strain in the MT-4 PNL-NRU experiment. Dotted lines represent the locations of the grids [9.302].

provide information on oxidation), with termination by slow cooling (to preserve the structure of the rods) or quenching (to investigate embrittlement). The initial nuclear heating represented steady state conditions in a PWR with a temperature of (320°C) and a pressure of 15.5 MPa in the test section. LOCA blowdown was simulated by isolating the test section and emptying the loop of coolant while reducing the power to the reactor. The rate of emptying could be adjusted to simulate different transients. An ECCS was then simulated by injecting water after the blowdown and second heat-up phases were completed. Instrumentation enabled measurements of temperatures of cladding, gas plenum and fuel, rod internal pressure and nuclear power. Initial tests evaluated the thermohydraulic characteristics of the set-up, and were followed by the six thermomechanical tests.

The results are summarized in Table 9.18. The cladding of the inner 3 × 3 array of rods had a smaller temperature gradient than the outer 16 rods because of the influence of the shroud and this distinction is made in the table. In test 215P a flow malfunction caused temperature inhomogeneities that led to a large variation in rupture times in the outer rods and axial position of the burst. The bursts tended to be oriented towards the centre of the bundle. The temperature profile of test 215R followed the target history resulting in rupture times and temperatures close together in the second heat-up phase. The balloons were coplanar with the burst facing two hot rods that were not deformed. In test 216 the cladding burst during initial heating because the temperature was higher than required. After two false starts, the required temperature profile was attained in test 217; the tubes burst during the second temperature ramp. The temperature history approximately followed the target sequence in test 218. Even though the initial internal pressure was lowered to 3.35 MPa, the cladding of the central rods burst during the first temperature spike or subsequent dip in temperature whereas most of the bursts in the outer rod were during the second heat-up. The internal pressure was reduced further to 3 MPa for test 219. The tubes burst during the second temperature ramp.

In the Phébus experiments, the tendency for the ruptures to be oriented towards the centre of the bundle reflects the temperature gradient across the bundle with the hot side being determined by local radiant heat, as shown in Fig. 9.92. Within any single rod, the temperature gradient contributes to the value of strain, as observed in other tests; the results from test 219 are included in Fig. 9.74. The temperature dependence of the strains fit within the large scatter when rupture is in the α phase or low ($\alpha + \beta$) region, as shown in Fig. 9.73. When in the ($\alpha + \beta$) region, the strain is controlled by competing effects; the amount of β phase and its kinetics of transformation and the ramp rate may limit rupture strain. In several of the tests the ruptures were coplanar, being within 20 to 80 mm of each other. The subsequent blockage was modest, with some local high values, because the total strains were mostly low, as shown in Fig. 9.84; no problems with cooling were reported. Since the fuel was fresh and the amount of burnup during the tests was small, the consequence of the cracking of the UO_2 was that no small fragments were produced; a small amount of radial but no axial relocations were observed.

TABLE 9.17. RESULTS OF LOCA TRANSIENTS IN PNL–NRU TESTS [9.299–9.302]

Test number	Heat-up Rate (°C/s)	Time of Rupture (s)	Temperature of rupture (°C)	Initial Pressure (MPa)	Pressure at failure (MPa)	Number of failures	Rupture strain (%)		Average Blockage (%)
							Average	Maximum	
MT1	9	52–88	837–871	3.2		6	43	61	70
MT2	10	58–68	821–871	3.1		7	43	62	67
MT3	11	112–183	776–815	3.9	5.86–6.21	12	47	94	68
MT4	8	52–58	804–841	4.62	5.58–6.48	12	72	99	100
MT1	9	52–88	837–871	3.2		6	43	61	70
MT2	10	58–68	821–871	3.1		7	43	62	67
MT3	11	112–183	776–815	3.9	5.86–6.21	12	47	94	68

TABLE 9.18. RESULTS OF LOCA TRANSIENTS IN PHÉBUS [9.304, 9.305]

Test number	Inner rods Outer rods	Heat–up Rate (°C/s)	Initial Pressure (MPa)	Time of Rupture (s)	Temperature of rupture (°C)	Rupture strain (%)		Standard deviation	Average Blockage (%)
						Range	Mean		
215-P	Inner	7	4	50–66	840	20–54	38	13	48–85
	Outer			65–150	(?)–830	15–38	27	6	—
215-R	Inner	20	4	20–25	800–860	20–50	38	9	48–85
	Outer			25–30	760–830	15–35	30	5.5	—
216	Inner	15	4	15–17	920–1000	20(?)–30	—	—	—
	Outer			19–26	800–900	16–31	24	5	40
217	Inner	—	4	—	900	—	11	—	30
	Outer			—	—	—	17	—	35
218	Inner	12	3.4	11–13	900–1000	11–27	20	5	24
	Outer			15–26	820–900	12–36	26	6	38
219	Inner	6	3	24–36	850–950	19–46	28	9	25
	Outer			33–36	820?–880	14–26	20	4	—

9.3.4.8. PHWR issues

In PHWR (represented by CANDU) reactors, with two exceptions, the phenomenology describing the behaviour of fuel cladding is identical to that in LWRs but is quantitatively different because of the design of the fuel. These are the relevant differences between an LWR fuel rod and assembly and a CANDU fuel element and bundle:

- The LWR fuel is initially internally pressurized to about 2 MPa with inert gas, usually helium, while the inert gas in CANDU fuel is encapsulated at atmospheric pressure.
- When pressurized by the heat transport system, the cladding in LWR is freestanding because of its small outside diameter, typically about 10 mm, and thick wall, typically about 0.6 mm, supported by the high internal pressure, while CANDU cladding, which has an outside diameter of about 13 mm with a wall thickness of about 0.4, collapses onto the fuel to provide efficient heat transfer. Consequently, the average power ratings of CANDU fuel tend to be about two times higher than those in LWR fuel.
- The volume of an LWR rod is much larger than that of a CANDU element, mostly because of their differences in length, up to 4.4 m vs 0.5 m, and the presence of a plenum at the end of the fuel rod.

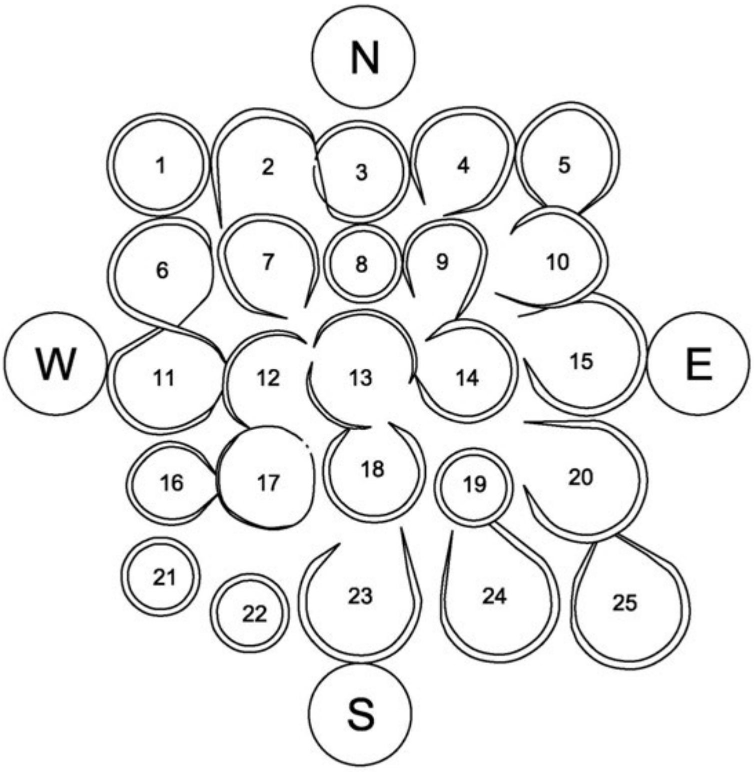

FIG. 9.92. Section through Phébus test 218 showing orientation of bursts and maximum strains towards centre of bundle [9.218].

In a LOCA, the time scale of the blowdown is similar in each type of reactor. In a CANDU bundle contact would be made between adjacent elements if the strain reached about 10%. Despite release of fission gases, a small outward strain in the clad results in a relatively large change in volume in a CANDU element, which results in only a small differential pressure, <1 MPa, when the heat transport fluid is evacuated. The resulting strains are a few percent compared with over 30% in LWRs.

For example, the strain history corresponding to the temperature and pressure sequence of Fig. 9.59 is depicted in Fig. 9.93 [9.204], with a predicted value <6%. In-reactor experiments simulating LOCA and application of an ECCS confirm the pressure drop with small strain, leading to low differential pressures, and final strains of less than 5% without failure, despite heating up to 1273 K (1000°C) at rates of 80°C/s [9.306, 9.307]. Much higher strains — 26% — were required to cause clad failure when the pretransient pressure was deliberately doubled. The computer code for the behaviour of fuel, ELOCA [9.308, 9.309], which includes the mechanical and corrosion properties of the cladding described above, accurately depicts the in-reactor behaviour, confirming the iteration between clad strain and fuel internal pressure, growth of the oxide and α phase layers and the lack of any effect of irradiation on the clad behaviour, as shown in Table 9.19. The two exceptions are the presence of spacers and bearing pads that are attached with a beryllium braze and the pressure vessel, which is a pressure tube.

Two consequences of brazing attachments to cladding are the Thomson–Widmanstätten microstructure of the HAZ, which is discussed in Section 9.3.4.2, and the presence of Zr-Be eutectic. If the temperature during a LOCA becomes high enough for long enough, the beryllium may penetrate into the clad and cause cracking. Isothermal tests on Zircaloy-4 cladding determined the dependence of the cracking on hoop stress, σ (MPa), and temperature, T (K) [9.243, 9.310]. Failure was by intergranular cracking following the prior β boundaries, as shown in Fig. 9.94. The penetration process comprises three stages, as shown in Fig. 9.95:

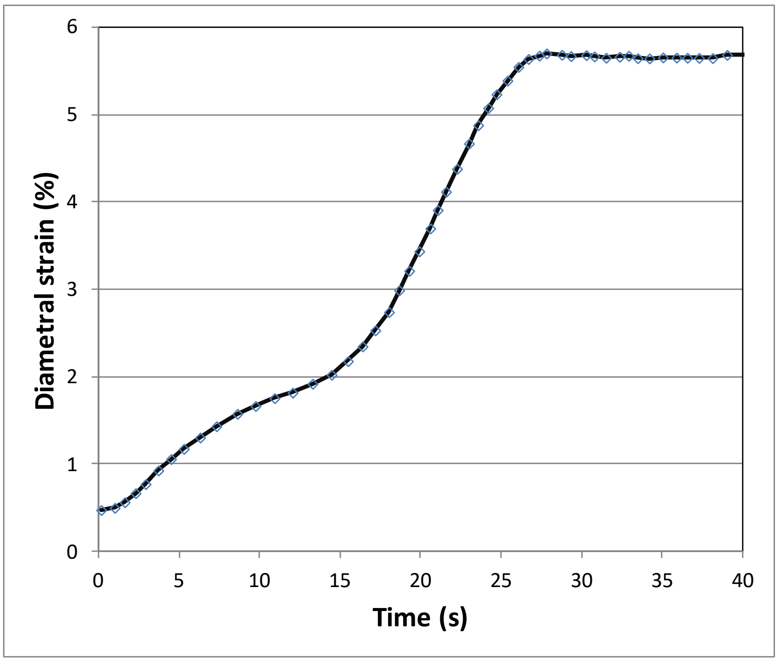

FIG. 9.93. Strain history of fuel cladding subjected to the temperature and pressure history described in Fig. 9.59 [9.204].

TABLE 9.19. IN-REACTOR LOCA EXPERIMENTS FOR ELOCA CODE VALIDATION [9.204]

Experiment	Burnup (MWd/kgU)	Pretest Pressure (MPa)	Maximum Temperature (°C)	Maximum Strain (%)	Average Strain (%)	Predicted average strain (%)	Oxide Thickness (μm)	Predicted oxide thickness (μm)	α-layer thickness (μm)	Predicted α-layer thickness (μm)
F10-130	1.46	3.5*	704	1.2	0.6	0.7	6	2	—	2
			970				12	8	18	9
F10-131	0.13	8*	690	5.3	2.2	3.2	2	2	…	2
			875				4–8	2	1–2	2
BA01	5	0.44	860	4.4	4.0	2.4	3–6	2–5	2–4	2–5
			1030				9–11	6–12	…	6–13
BA03	5	0.3	917	4.6	4.0	2.0	2–6	3–7	2–4	3–7
			988				6.5–10	5–10	6–8	5–11
BA05	5	1.09	942	26	15	10.7	3–4	4–7	…	3–7
			972				8–10	4–9	4–6	4–10
BA07	0.08	0.52	874	3.8	2.5	2.4	2–3	2–5	1–2	2–4
			931				4–6	4–8	2–4	4–8

* At full power before test

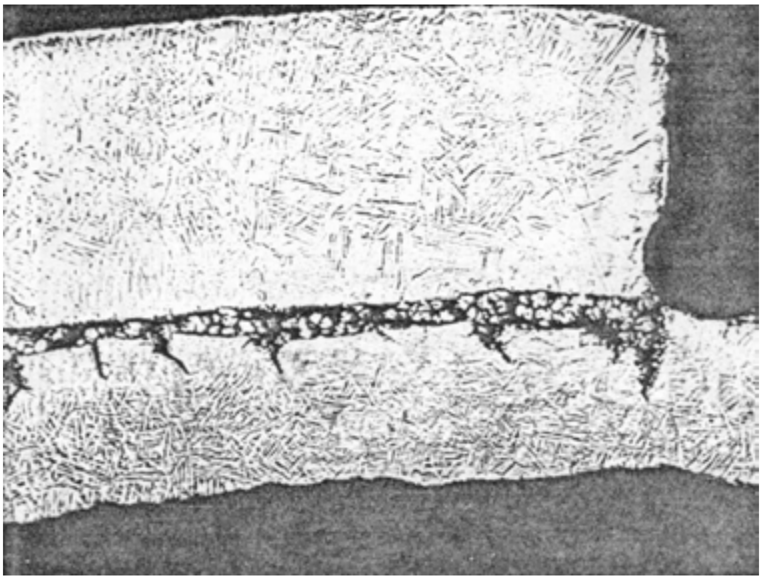

FIG. 9.94. Be-braze penetration at 1470 K (1200°C) at appendage (thickness 0.58 mm) on Zircaloy-4 fuel cladding (thickness 0.45 mm) stressed to 5.5 MPa [9.310].

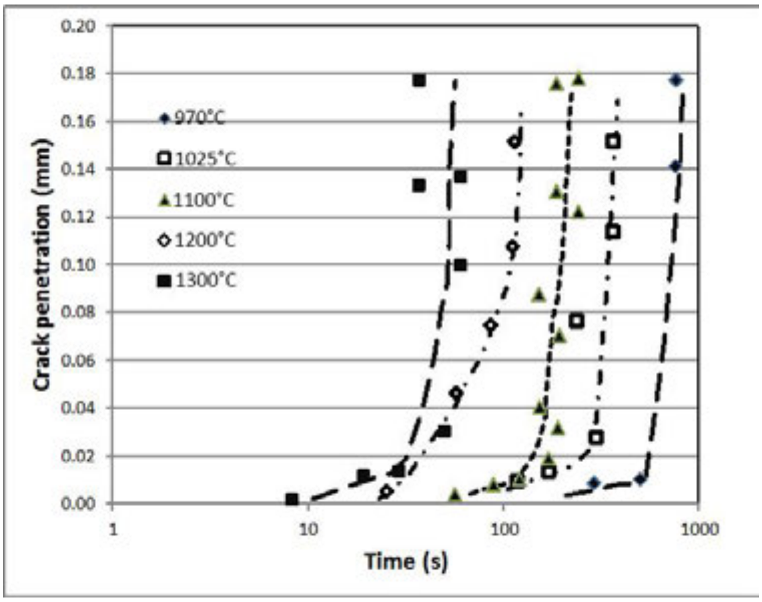

FIG. 9.95. Penetration of Zircaloy-4 by beryllium-assisted cracking above the melting point of the braze alloy with a hoop stress of 2.2 MPa (based on data from [9.310]).

- An incubation period, t_I (s), with no discernable cracking.
- A period of penetration at a constant rate, p_{Be} (μm/s).
- Rapid growth to rupture once the penetration reached a critical depth, dr (μm). This stage contributed little time to the total time.

The rupture time, t_r, is the sum of the incubation time and the time it takes to penetrate to d_r, that is:

$$t_r = t_I + d_r/p_{Be} \tag{9.32}$$

Two regimes of cracking kinetics are defined depending on whether the temperature is above or below the melting point of the eutectic, 970°C, as shown in Fig. 9.96. Note that this temperature is close to the (α + β)/β transus and material in tests done above the melting point is in the β phase:

$$t_r = 7.2 \times 10^{-3}\,\sigma^{-4.3}\exp(18000/T) + (75 + 15\sigma)/2.2 \times 10^{3}\sigma^{3.85}\exp(-15000/T) \qquad (9.33)$$

Below the melting point, with tests in the (α + β) phase region:

$$t_r = 640 \times 10^{-24}\,\sigma^{-4.2}\exp(72000/T) + 120/400 \times 10^{15}\sigma^{3.7}\exp(-57000/T) \qquad (9.34)$$

The stress dependencies and activation energies for the penetration closely resemble those for creep. In the β phase a suggested mechanism is stress-assisted corrosion with the dissolution rate at the penetration tips being augmented by local creep deformation, while in the (α + β) phase cracking of an intermediate phase formed by stress-assisted grain boundary diffusion of beryllium seems a likely mechanism.

The pressure tube may balloon and sag but should remain intact. To fully exploit the heat sink provided by the heavy water moderator, the temperature of the outside of the calandria tube when it is in contact with the pressure tube should be low enough for nucleate boiling in the moderator at the points of contact between the tubes.

In pressure tube reactors, moderated by heavy water, the moderator itself can be an effective supplementary heat sink even if the ECCS fails during a postulated LOCA. The fuel will heat the pressure tube, which creeps under the residual pressure; after a strain of about 18% the pressure tube contacts its surrounding calandria tube. If the moderator is cool enough, the excess heat is removed by nucleate boiling on the outside surface of the calandria tube and the whole fuel channel remains intact until the reactor can be shut down. The phenomenology of pressure tube ballooning is similar to that of fuel cladding. The model for ballooning is based on creep equations, such as Eq. (9.16), developed for Zr-2.5Nb from isothermal tests over a wide range of temperatures attained with a rapid ramp [9.311]. In the low α phase *n* is around 9.0, in the high α and low (α + β) phase *n* varies from about 7 at high stress down to 2 at low stress; in the middle of the (α + β) region, *n* is less than 2, while in the high (α + β) and β phases *n* increases towards a stable value of 3.4. Over the temperature

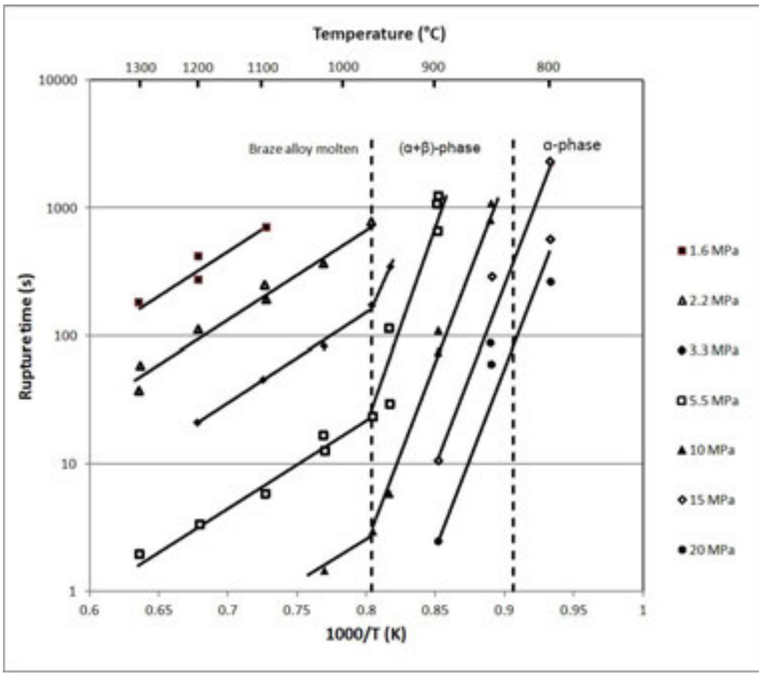

FIG. 9.96. Effect of temperature on the rupture time for beryllium-assisted cracking of Zircaloy-4 fuel cladding; note the change in temperature dependence close to the melting point of the braze alloy (based on [9.310]).

range of the tests, the activation energy, Q/R, decreases from 36 000 K to 19 600 K. To model strain during temperature ramps, the strain rate was described as the sum of two terms representing grain boundary sliding and power law creep in either the α or β phases. For temperatures high into the (α + β)/β region 720 to 1120 K (450 to 850°C):

$$\begin{aligned}\dot{\varepsilon} = {} & 1.3 \times 10^{-5}\sigma^{9}\exp(-29200/T) + \\ & 5.7 \times 10^{7}\sigma^{1.8}\exp(-29200/T)/[1 + 2 \times 10^{10}\textstyle\int_{t_1}^{t}\exp(-29200/T)dt]^{0.42}\end{aligned} \qquad (9.35)$$

where t_1 is the time when T = 973 K (700°C).

For temperatures into the β phase (1123 to 1473 K (850 to 1200 °C)):

$$\begin{aligned}\dot{\varepsilon} = {} & 10.4\sigma^{3.3}\exp(-19600/T) + \\ & 3.5 \times 10^{4}\sigma^{1.4}\exp(-19600/T)/[1 + 274\textstyle\int_{t_2}^{t}\exp(-19600/T)(T-1105)^{3.72}\,dt]\end{aligned} \qquad (9.36)$$

where t_2 is the time when T = 1123 K (850°C).

During a postulated LOCA, the horizontal configuration of the reactor introduces large temperature gradients that are modelled in the same way as during a temperature ramp in fuel cladding [9.268, 9.312, 9.313]; Fig. 9.97 shows a typical test result for a tube section containing a temperature gradient, with its companion calculation of total and local creep strains.

If the hot pressure tube contacts the cool calandria tube, the heat needs to be removed efficiently; bubbles, in nucleate boiling, accomplish this heat transfer. Both tubes will heat up to a high temperature and may fail if the heat cannot be removed efficiently because an insulating film of steam shrouds the calandria tube (called film boiling or dryout); in that case, the critical heat flux (CHF) has been exceeded. The border between the two modes of boiling were established in a simulation consisting of concentric sections of pressure tube and calandria tube, about 1 m in length, placed in a bath of warm water to simulate the moderator [9.314]. Passing a current through a central graphite rod simulates the overheated fuel and heats the pressure tube at up to 25°C/s. The inside of the pressure tube is pressurized with helium up to 6 MPa. The pressure tube starts to creep, as described previously, and comes into contact with the calandria tube. The temperature of the pressure tube at contact tends to be higher with lower pressures, for example, Table 9.20. The temperature

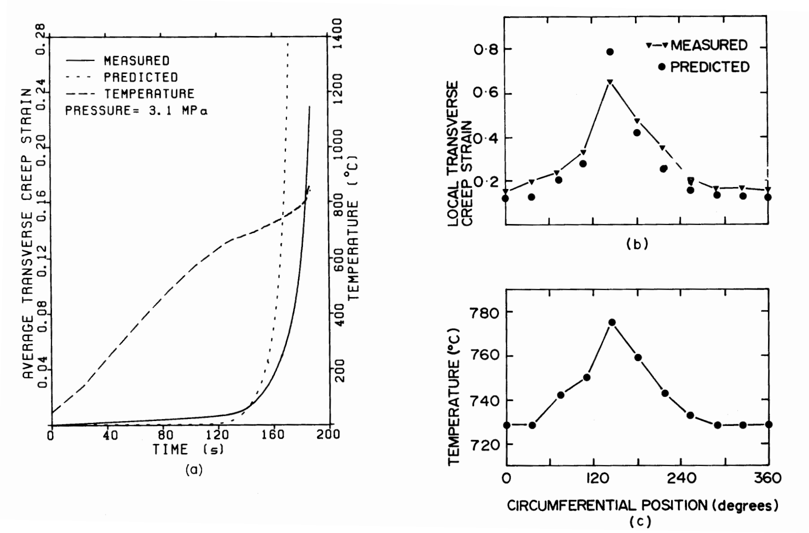

FIG. 9.97. Ramp test in Zr-2.5Nb pressure tube with temperature gradient with comparison between measurement and prediction. Test at 3.1 MPa: (a) measured and predicted average transverse creep strain; (b) measured and predicted local transverse creep strain at the end of the test; (c) circumferential temperature distribution at the end of the test [9.313].

history is measured using an array of thermocouples attached to the tubes and the type of boiling on the outside surface of the calandria tube is observed visually and videorecorded during the experiments and by examining oxidation after the experiment. Three modes of boiling were observed: fully nucleate, fully film, and a mixture of nucleate and film. The results in Fig. 9.98, based on Refs [9.313, 9.315], separate nucleate boiling and any form of film boiling and show that holding the moderator at 343 K (70°C) will prevent dryout.

The following two approaches increase the margins on moderator temperature:

(1) Increasing the temperature to the onset of film boiling (i.e. increasing the CHF);
(2) Reducing the rate at which the heat is passed from the pressure tube to the calandria tube.

TABLE 9.20. BEHAVIOUR OF MODIFIED CALANDRIA TUBE DURING CONTACT CONDUCTANCE TESTS [9.319]

Ridge Spacing (mm)	Outside surface of calandria tube	Pressure inside pressure tube (MPa)	Maximum Contact temperature (°C)	Mode of boiling
12	Smooth	1	1020	Nucleate
25	Smooth	1	1055	Film
12	Peened	1	1020	Nucleate
25	Peened	1	1055	Nucleate
12	Smooth	6	775	Film
25	Smooth	6	800	Film
12	Peened	6	820	Nucleate
25	Peened	6	820	Nucleate

Roughening the outside surface by peening with glass beads increases the temperature to the onset of film boiling by promoting bubble formation [9.316–9.318]. The CHF linearly increases with an increase in the fractal surface roughness. Beads with diameter in the range 90 to 125 µm increase

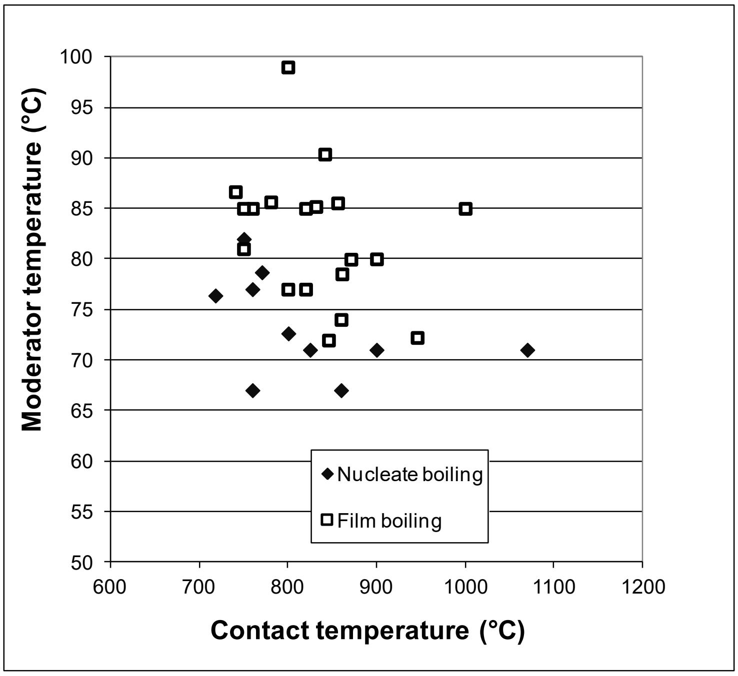

FIG. 9.98. Results of contact conductance tests showing the border between nucleate and patchy and complete film boiling (based on [9.314, 9.315]).

the CHF by about 50%, from 0.86 MW/m^2 to 1.35 MW/m^2, providing an extra 3 to 5°C in moderator temperature compared with untreated tubes.

An effective method to reduce the heat load on the calandria tube from contact with a hot pressure tube is to place a wire mesh between the two tubes [9.319]. The mesh forms a double barrier to heat conduction and reduces the area of heat transfer contact. The mesh used in simulation tests was made from 316 stainless steel with a spacing of either 1.3 mm or 10.0 mm and wire diameter of 0.38 mm. In half the test section containing the mesh, nucleate boiling was obtained, even with a moderator temperature of 373 K (100°C). The other half of the test section was unprotected and exhibited film boiling immediately on contact. The calandria tube remained at 398 K (125°C) in the protected section but was heated to 1198 K (925°C) in the unprotected section, where it ruptured about 65 s after contact between the tubes. Unfortunately, this method was considered too difficult to install; an alternative method for reducing the rate of heating was to reduce the contact area using small circumferential ridges on the inside surface of the calandria tube. The ridges can be formed by either masking and pickling or by radially oscillating the rollers during internal roll extrusion (Section 4.4.5, in Volume 1 of this publication). In the former method, painting a thin line on the inside surface — masking — sets the land and spacing and the height of the ridge depends on the time of pickling. In the latter method, the spacing of the ridge is controlled by the oscillating frequency, the height of the ridge depends on the radial displacement of the rollers and the shape of the land is determined by the time spent by the rollers in the withdrawn position. In simulation tests, the moderator could be warmer by 5 to 10°C with ridged tubes than with smooth tubes before dryout was observed [9.315].

Since the two methods of enhancing heat transfer — increasing CHF and reducing contact area — operate on different and independent principles, they can be used additively. The moderator would be able to operate 8 to 15°C warmer with the combination of roughening the outside surface and ridging the inside surface. Tests with the water tank at 358 K (85°C) confirm this behaviour and show efficient heat transfer at 15°C higher than the current specified moderator temperature, as shown in Table 9.20 [9.320]. The temperature histories of two sections of calandria tube in the same experiment demonstrate the principle, as shown in Fig. 9.99. The calandria tube has internal ridges, 75 µm high spaced 25 mm apart, but the outside surface is either smooth (a) or roughened (b). The pressure tube heats up and contacts the calandria tube at about 1173 K (900°C). In Fig. 9.99(a) the pressure tube cools about 350°C while the calandria tube heats up, reaching 1173 K (900°C) at the time of rupture of the assembly. This section was in film boiling and was oxidized. In Fig. 9.99 (b) where the outside surface is roughened, the pressure tube cools about 450°C and the calandria tube remains cool because it is able to disperse the heat by nucleate boiling; it is not oxidized.

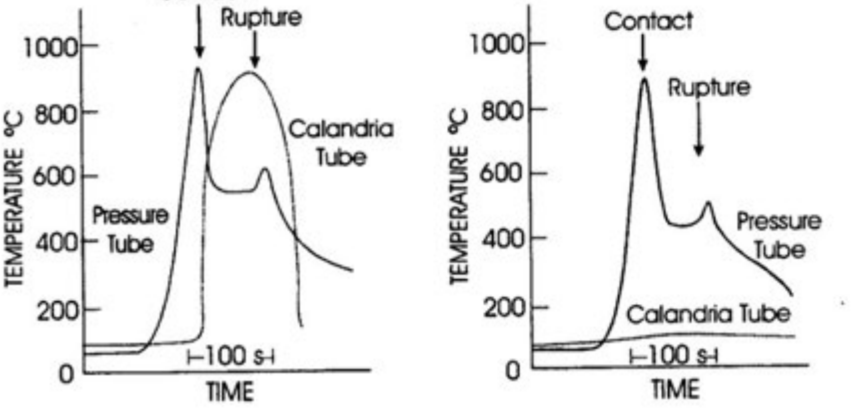

(a) *(b)*

FIG. 9.99. Temperature history of pressure and calandria tubes in contact conductance test: moderator temperature: 358 K (85°C), internal pressure: 1 MPa, heat-up rate 18°C/s, calandria tube with 75 µm-high ridges 25 mm apart on inside surface. In (a) outside surface was smooth and in (b) roughened [9.320].

If a pressure tube becomes very hot but does not touch the calandria tube, except where it may sag, the radiant heat transfer to the calandria tube can be augmented to extract heat to the moderator, thereby reducing the temperature reached by the pressure tube. For example, the temperature of the pressure tube is calculated to be reduced from 1773 K (1500°C) to 1373 K (1100°C) by increasing the absorptivity of the inside of the calandria tube from its unoxidized value of 0.16 [9.321] up to 0.7. This higher value of absorptivity (measured as emissivity) is attained by lightly peening the inside surface of the calandria tube and oxidizing in air for 3 h at 773 K (500°C) [9.315]. No adverse effects on strength, ductility or deformation were discerned.

Thus, in pressure tube reactors moderated by heavy water, this water provides a large heat sink should cooling of the fuel be interrupted. With natural UO_2 fuel and low fill pressures the expected cladding strains during a LOCA are small.

In summary, the initial responses of fuel cladding and structural components to pressure under very high temperatures are sufficiently understood for the design of both LWRs and PHWRs to meet the condition that the fuel and pressure vessels remain properly cooled by the ECCS during a LOCA. For analysis of LWRs, models of rupture are based on correlations such as those described in NUREG-0630 [9.322] that are translated into computer codes, such as FRAPTRAN [9.323]. The ductility and deformation of the alloys are sensitive to external factors such as heating rate and temperature gradients, and to metallurgical factors such as phase transformations. The effect of reactor operation is to oxidize and add hydrogen; any irradiation damage is annealed out at high temperature; thus, tests on unirradiated material can provide relevant information. Simulations with bundles of fuel rods, both in- and out-reactor, show that coplanar deformation can lead to high degrees of blockage, but that such blockage can be adequately cooled. Simultaneously with the cladding deformation, the UO_2 may fragment and, with large openings of the tube rupture, may be dispersed. The consequences for the low temperature part of a LOCA are considered in Section 9.4.

9.4. OXYGEN EMBRITTLEMENT

Oxygen is a powerful α phase stabilizer in zirconium and has much solubility in this phase, as shown in Figs 2.11 and 2.12, in Volume 1 of this publication. During reactor operation the majority of the material in cladding is in the α phase and the small amount of oxygen added to the cladding as a result of corrosion has little effect on the total amount of α phase. If the material is to tolerate a LOCA with a temperature history such as that shown in Fig. 9.57, depending on the temperature during the second period of heating, (2), (3) and (4), the cladding alloy matrix will be in either the (α + β) phase or the β phase. When exposed to steam at high temperature, the cladding surface oxidizes further and oxygen diffuses into the metal (see Section 8.9, in Volume 2 of this publication, and Section 9.3.4.2). The time at high temperature controls the thickness of the oxide and oxygen concentration in the metal, and the position on the alloy–oxygen phase diagram, as shown in Fig. 9.100 [9.324], determines what phases are present. If sufficient oxygen is absorbed, α phase may form at the metal–oxide interface, even though in the absence of oxygen the (α + β) phase or β phase would normally have been present. The temperatures and oxygen concentrations required to form α phase in Zircaloy-4 are listed in Table 9.21; the two numbers for the oxygen concentration represent the values where the (α + β) phase was still observed and where the α phase was formed [9.323]. At the end of the LOCA transient the fuel is cooled rapidly, represented by stage (5) of Fig. 9.57. Any β phase will transform to a Thomson–Widmanstätten α structure. As a result of the heat-up, oxidation and diffusion of oxygen into the cladding, and rapid cooling, the cladding consists of layers of different composition and crystal structure. Figure 9.101 shows the thick oxide on the outside surface of cladding formed in steam at 1566 K (1293°C), with an underlying oxygen enriched α phase and the core of α phase Thomson–Widmanstätten structure transformed from the prior high temperature β phase by rapid cooling. Since rupture likely occurs in the first part of a postulated LOCA, the inside surface of the clad close to the rupture may be exposed to steam and subsequently will also be oxidized, but to a lesser extent than the outside surface. The distribution of oxygen concentration through the cross-section is illustrated schematically in Fig. 9.102 [9.325, 9.326].

TABLE 9.21. FORMATION OF (α + β) PHASE AND α PHASE IN ZIRCALOY-4 AT HIGH TEMPERATURES WITH ADDITIONS OF OXYGEN [9.324]

Temperature (°C)	Oxygen concentration (wt%)			
	(α + β) phase limit	α phase start	β phase limit	(α + β) phase start
1400			1.04	1.07
1300	2.78	2.85	0.82	0.84
1200	2.45	2.54	0.59	0.62
1100	2.08	2.18	0.37	0.39
1000	1.63	1.75	0.14	0.16
900	1.05	1.18		
850	0.62	0.77		

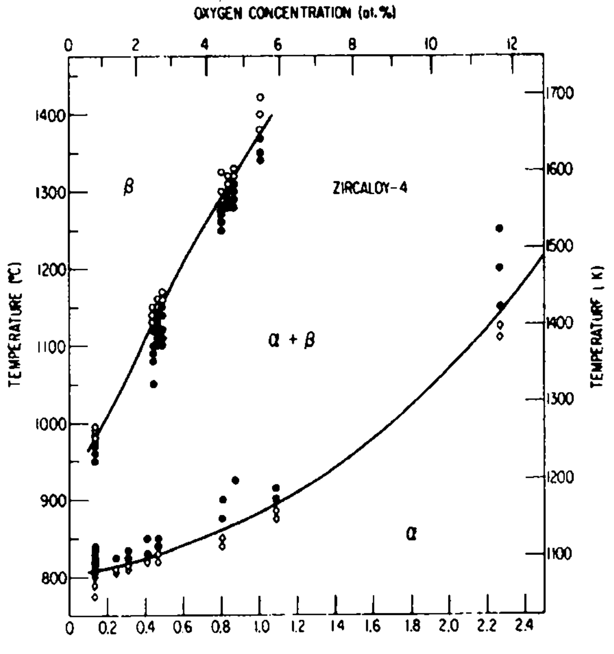

FIG. 9.100. The boundaries of α phase and β phase of the pseudobinary Zircaloy-4 — oxygen phase diagram [9.324].

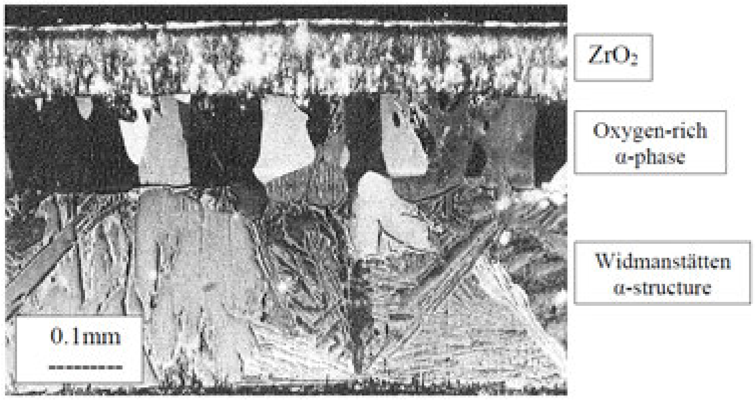

FIG. 9.101. Microstructure of Zircaloy-4 heated at 25°C/s to 1566 K (1293°C) in steam at 0.1 MPa and held 240 s under an internal pressure of helium at 0.35 MPa then cooled rapidly. Note the α grains enriched in oxygen under the oxide (S. Sagat and R. Dickson, AECL).

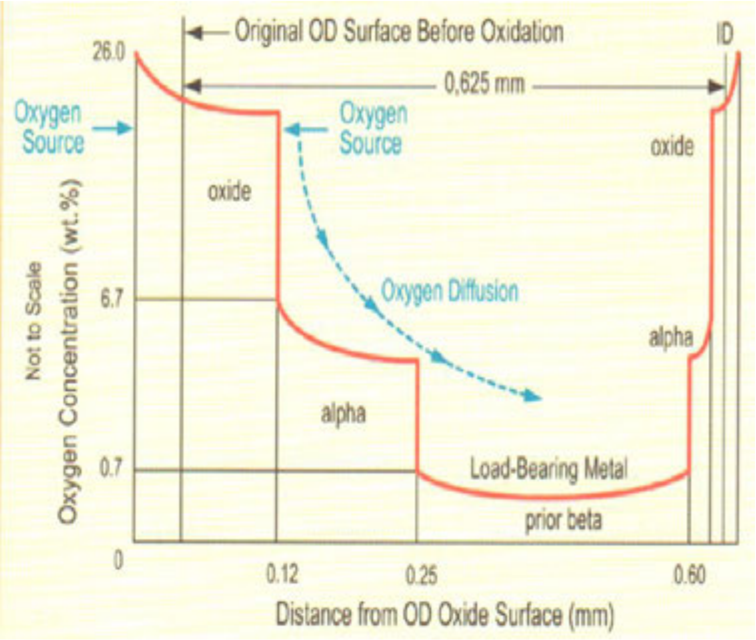

FIG. 9.102. Schematic diagram of through-wall oxygen concentration on fuel cladding ruptured during LOCA [9.325] (based on [9.326]).

In the early days of the development of zirconium, reducing the oxygen concentration to low values was found to be necessary to obtain ductile metal, but a small amount, usually specified at about 1000 ppm (0.1 wt%, 0.567 at.%) in alloys, is retained to provide strength. In pure zirconium, the ductility (represented by total elongation) at room temperature decreased monotonically by a factor of ten from about 25% down to 2.6% with increasing oxygen concentration up to 2.27 at.% (0.4 wt%) [9.327], as shown in Fig. 9.103. The elongation was less than 1% with 0.6 wt% (3.33 at.%) oxygen, based on exponential extrapolation. In Zircaloy-4, at room temperature a large drop in UTS [9.328] was observed at an oxygen concentration between 0.5 and 0.7 wt% (2.79 to 3.86 at.%), as

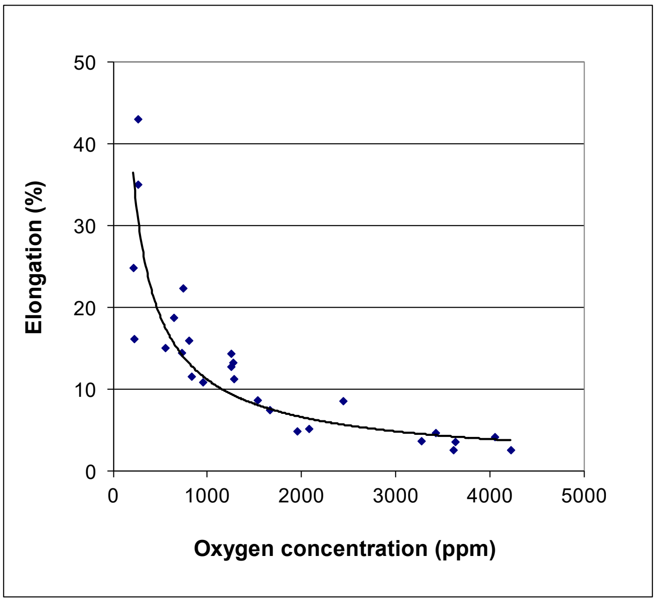

FIG. 9.103. Reduction in ductility of pure zirconium with increase in oxygen concentration [9.327].

shown in Fig. 9.104. For oxygen concentrations up to 0.03 wt% (0.17 at.%) as the test temperature was increased, the UTS declined. With higher oxygen concentrations the UTS passed through a maximum value with temperature and the maximum shifted to higher temperatures as the oxygen concentration was increased. Necking was not observed in material containing >0.9 wt% (4.92 at.%) oxygen. No effect of cooling rate or maximum homogenizing temperature up to 1873 K (1600°C) was observed. Similar strength maxima were observed in impact loading in Zircaloy-4 [9.329] and tensile strength of zirconium-copper alloys [9.330]. Fracture surfaces of specimens of pure zirconium containing 20 at.% (4.2 wt%) oxygen broken at room temperature were completely brittle [9.331]. The proportion of brittle and ductile fracture in Zircaloy-4 broken by impact at 473 K (200°C) depended on the oxygen concentration [9.328], showing a transition similar to that of UTS at between 0.5 and 0.7 wt% (2.79 and 3.86 at.%) oxygen, as shown in Fig. 9.104. Any α phase formed above 1120 K (850°C) during a LOCA will be brittle because its oxygen concentrations will have to exceed 0.7 wt% (2.79 at.%), otherwise it would not have formed, as shown in Fig. 9.100. When Zircaloy-4 or Zr-1Nb (M5) were oxidized between 1270 and 1470 K (1000 and 1200°C) and then quenched from either 1470 or 1570 K (1200 or 1300°C), material containing 0.5 to 0.7 wt% (2.79 to 3.86 at.%) oxygen had little to no ductility in tensile tests at room temperature [9.332]. These results show that Thomson–Widmanstätten α phase formed from prior β phase has the same sensitivity to oxygen concentration as α phase formed by slow cooling. This ductile to brittle behaviour is confirmed but at even lower oxygen concentration on quenched specimens broken by impact testing at room temperature [9.333]. Figure 9.105 illustrates the abrupt change in fracture mechanism in prior β material in Zr-1Nb (M5) after oxidizing for 110 s at 1523 K (1250°C) then being directly quenched at room temperature. At oxygen concentrations less than 0.3 to 0.4 wt% (1.69 at.%) the fracture surface consisted of ductile dimples whereas with greater oxygen concentrations the fracture was brittle cleavage. Zircaloy-4 specimens behaved in the same way.

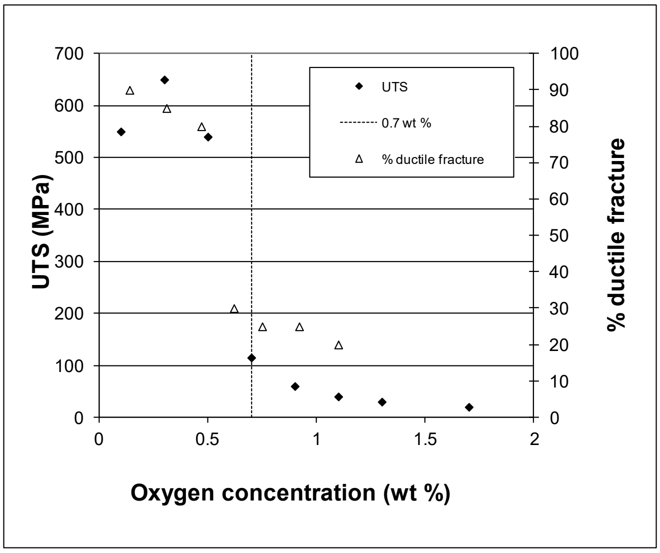

FIG. 9.104. Effect of oxygen concentration in Zircaloy-4 on UTS at room temperature and % ductile fracture after impact at about 473 K (200°C) [9.328, 9.329].

Zirconium oxides are ceramics and are brittle. An oxide layer on zirconium will crack when the underlying matrix is deformed. In the high temperature part of the LOCA, a hoop strain of 4 to 6% produced axial cracking in oxides thicker than 70 μm [9.241]. The consequence of the cracking can be an increase in the oxidation rate [9.244]. At room temperature a thick oxide formed at 1273 K (1000°C) cracked when the underlying substrate was deformed elastically [9.334]. The cracking was detected by acoustic emission, as shown in Fig. 9.106; the first maximum in acoustic count rate was related to cracks through the oxide and subsurface layer with a spacing of about 30 μm at A and 15 μm

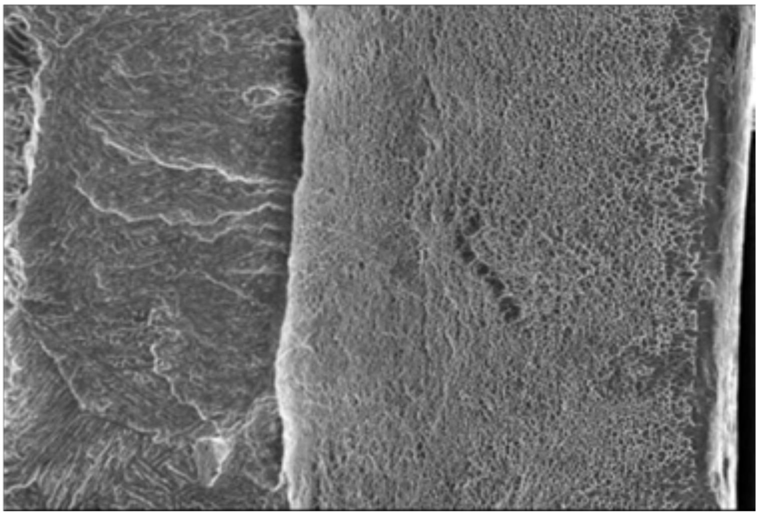

FIG. 9.105. Fractograph of prior β phase in M5 cladding oxidized for 110 s at 1523 K (1250°C), quenched to room temperature and broken by impact at room temperature showing change from ductile to brittle fracture as the oxygen concentration exceeds 0.3 wt% (1.69 at.%) [9.333].

at B. At the second maximum the oxide had started to spall. Because of this brittle behaviour, Zircaloy-4 cladding oxidized at high temperatures on both surfaces lost all ductility around room temperature when the oxide plus the α layer was thick enough — up to 25% of the wall thickness [9.244, 9.335, 9.336]. Sometimes the thermal shock from quenching was sufficient to fracture the cladding. In a series of 25 tests on single rods, 1 specimen had a thick enough oxide that it cracked when quenched from 1863 K (1590°C) [9.337].

Since the oxides and underlying α layers are brittle, the ductility and structural integrity of the cladding depend on the mechanical properties of the core material. To provide assurance that adequate ductility of the cladding is maintained when it is stressed at low temperatures, either mechanically or by thermal stresses, the following two approaches for assessment can be used:

- Determining the greatest thickness of oxide and oxygen-rich α phase that can be withstood.
- Determining the least amount of ductile prior β phase required. This material should contain less than some critical concentration of oxygen, likely about 0.7 wt% (3.86 at.%) oxygen.

To ensure continued coolability and containment at the end of a postulated LOCA, and provide a regulatory framework, it needs to be determined whether the cladding can withstand the loads induced during quenching by the ECCS water and by subsequent handling, thus preventing fracture with potential for blockages and release of fission products and fuel. The approach to evaluate this question is to measure the mechanical response of cladding after excursions into high temperatures in steam. The information needed is the temperature dependence of the oxide growth rate in high temperature steam, the diffusivity of oxygen in the zirconium alloy and the ductility of the oxidized cladding at low temperatures.

The test methodology used to judge the residual ductility after a LOCA has been reviewed [9.338]. For this testing, the clad is either freestanding, internally pressurized constrained or unconstrained or part of a fuel assembly. Various temperature histories have been evaluated varying from a direct quench from high temperatures to slow cooling to intermediate temperatures followed by a quench to simulate the transition from film to nucleate boiling during ECCS injection. Assessment is based on observation of the clad after the quench, or mechanical testing of sections of

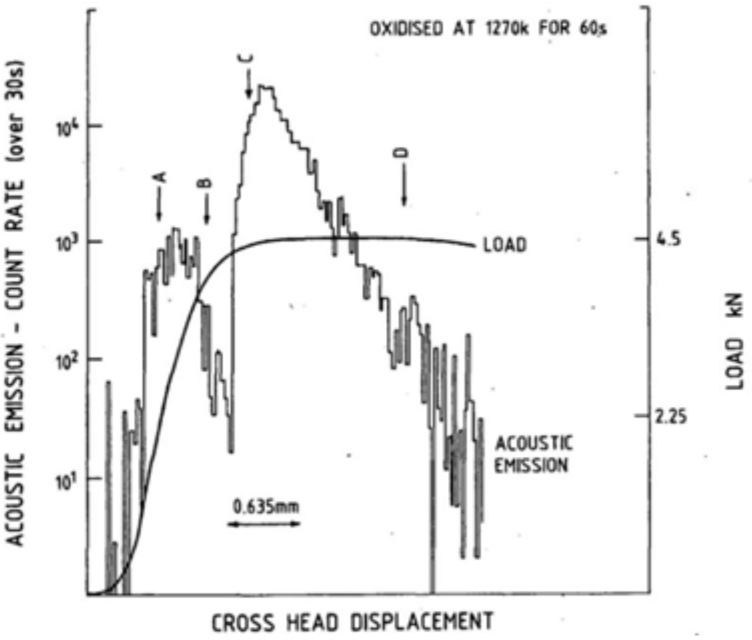

FIG. 9.106. Acoustic emission during tensile testing at room temperature of pre-oxidized rings of Zircaloy-4 fuel sheathing [9.334]. The outside surface was coated with an oxide, up to 8 μm thick, produced by holding in steam at 1273 K (1000°C) for times up to 120 s.

cladding that survive the quench; ring compression, bend and impact tests have been used. Evaluation of criteria for embrittlement, based on the thickness of the oxide and α layer and the concentration of oxygen in the prior β phase, require metallography and chemical analysis. Zircaloy has been the focus of the majority of studies. With the quest for higher burnups, other alloys have been compared with Zircaloy-4, although little difference was detected on embrittlement thresholds between Zircaloy-4, ZIRLO and Zr-1Nb (M5) [9.339].

When short oxidized sections of Zircaloy-4 cladding were compressed in the radial direction, the ring compression test, the dependence of the ductility on test temperature, was correlated with the fraction of wall thickness retained as transformed β phase, as shown in Fig. 9.107, or the sum of the thickness of the oxide and the brittle α phase, ξ [9.334, 9.335]. The data were separated into three regions: a region where the surface oxides and α phase cracked but the core region withstood 3.8 mm of deflection without cracking, an intermediate region where the central core fractured after some deformation and a third region of brittle fracture with no ductility — the rings broke into several pieces and could be fitted back into a ring with the original dimensions. The zero ductility temperature (*ZDT*) varied as:

$$ZDT\ (^\circ\mathrm{C}) = 0.555(A - B[1 - 2\xi/(w_0 + 0.252\xi)]) - 17.78 \qquad (9.37)$$

where

A is equal to 2727 for impact tests, and 2410 for slow strain rate tests;
B is equal to 3636 for impact tests, and 3660 for slow strain rate tests;
w_0 is equal to original wall thickness (cm);

and ξ is the thickness of oxide and oxygen stabilized α phase on one surface (cm).

Figure 9.108 summarizes the oxidation kinetics from this study. These data and those from Fig. 9.107 were combined to derive a family of curves for nil-ductility at different test temperatures

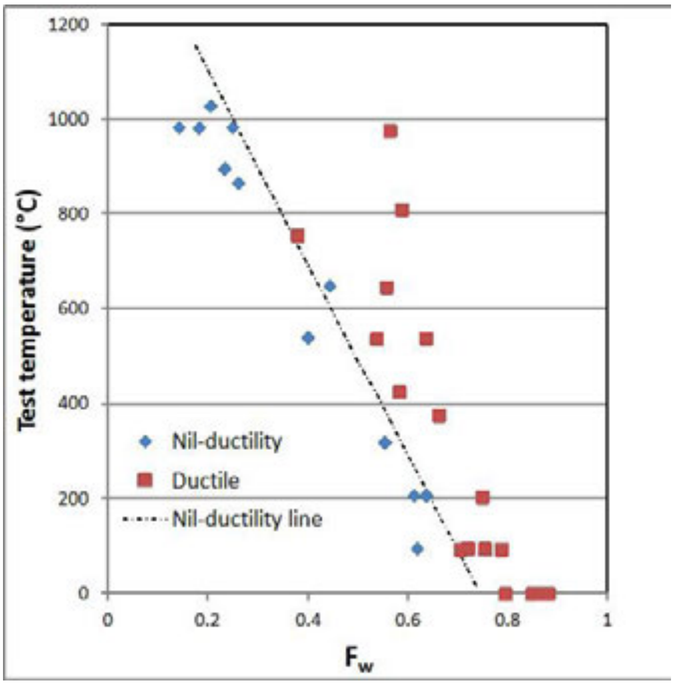

FIG. 9.107. Ductility of oxidized Zircaloy at high strain rate as a function of test temperature and F_w, the fraction of as-oxidized wall thickness consisting of transformed β phase (based on [9.336]).

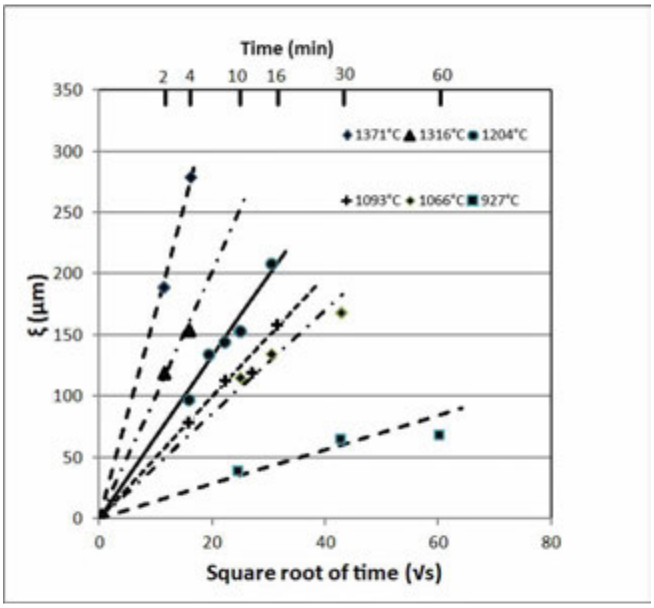

FIG. 9.108. Growth of the sum of oxide and α-phase layer on Zircaloy at high temperature as a function of exposure time [9.335].

responding to exposure times to steam at high temperatures for cladding with a thickness of 0.686 mm; Fig. 9.109 is a representative curve at a test temperature of 368 K (95°C). The exposure times at selected temperatures to induce zero ductility with this test temperature are summarized in Table 9.22. These results are for illustration only, but they set the scene for subsequent studies since they apply to a single cladding wall thickness and are based on isothermal exposures rather than representative variable temperatures. No account is taken of wall thinning from deformation at high temperatures; the latter would lead to shorter exposure times.

TABLE 9.22. TIME AT EXPOSURE TEMPERATURES IN STEAM TO INDUCE ZERO DUCTILITY IN ZIRCALOY-4 WHEN TESTED AT 368 K (95°C) [9.334]

Exposure temperature (°C)	Exposure time (s)
1300	130
1200	280
1100	490
1000	1460

These results were the foundation for the initial rules set up by the NRC to operate LWRs safely [9.208, 9.209] (see Section 9.3.4.). The reactor vendor and operator's computer codes must show that brittle behaviour will be avoided by controlling the time at high temperature so the cladding can survive quenching and subsequent handling. Hache and Chung [9.340] and Chung [9.341] described how five pieces of information were used to derive a maximum temperature and oxidation limit:

- The above results of mechanical testing [9.334, 9.335];
- Further ring compression tests after one sided oxidation;
- An oxidation equation based on experiments at the melting point of zirconium plus oxidation experiments at lower temperatures [9.342];
- Diffusivity of oxygen in β Zircaloy to determine the time and temperature to reach ξ_{critical} [9.343];
- Thermal shock experiments on tubes [9.344].

The length of time at high temperature was determined by the reactor system and regulated by a limit on the equivalent cladding reacted (ECR), defined as the fraction of total thickness of cladding that would be converted to stoichiometric ZrO_2 from all the oxygen contained in the fuel cladding as ZrO_2 and oxygen in solid solution in the remaining metal phase:

$$ECR = w/(\rho\tau) = 2.85w_g/(\rho\tau) \qquad (9.38)$$

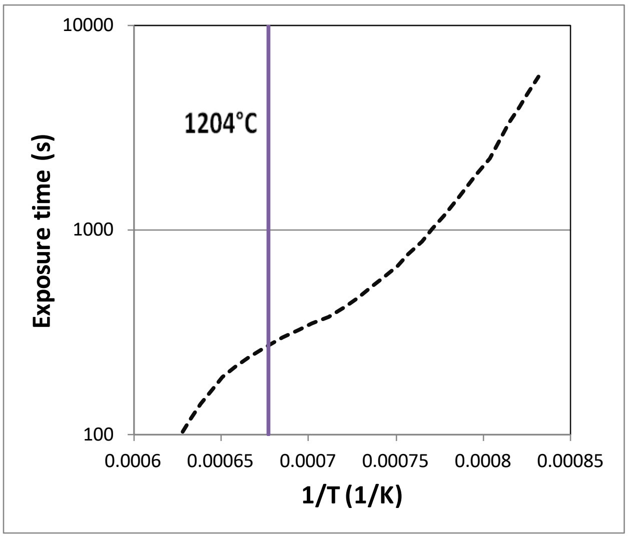

FIG. 9.109. Line above which ring specimens of Zircaloy oxidized for various times at various temperatures had no ductility at 200°F (368 K (95°C)), based on Figs 9.107 and 9.108 (based on [9.335]).

where

w is grams of zirconium reacted per cm^2 of surface area;
w_g is weight gain per surface area from oxygen pick-up during oxidation;
ρ is density of Zr;
τ is cladding wall thickness in cm;

and 2.85 is (91.2/32), a conversion factor for zirconium consumed during oxidation.

On the basis of the results of the mechanical tests, the NRC's ECR limit was set at 17%, calculated by the Baker–Just equation [9.341]:

$$w^2 = 33.3\, t \exp(-22\,900/T) \tag{9.39}$$

where t is time in seconds and T is temperature in K. This is converted to weight gain per surface area from oxygen pick-up during oxidation, w_g:

$$w_g = 2.0248 \sqrt{t} \cdot \exp(-11\,450/T) \tag{9.40}$$

Figure 9.110 [9.345] summarizes several other measurements of oxidation rates at high temperatures [9.346–9.359]. The broad band includes all these datasets, indicating that the Baker–Just equation bounds all the data with a large conservatism at high temperatures; the margin disappears at about 1370 K (1100°C). The Cathcart–Pawel [9.346] correlation is often chosen to represent a best estimate for calculating ECR and is accepted by the NRC for temperatures above 1310 K (1037°C) [9.211]:

$$w_g = 0.6018 \sqrt{t} \cdot \exp(-10\,050/T) \tag{9.41}$$

Typical calculations of ECR are summarized in Fig. 9.111 [9.344] comparing the Baker–Just and Cathcart–Pawel formulation for a cladding thickness of 0.57 mm at temperatures between 1300

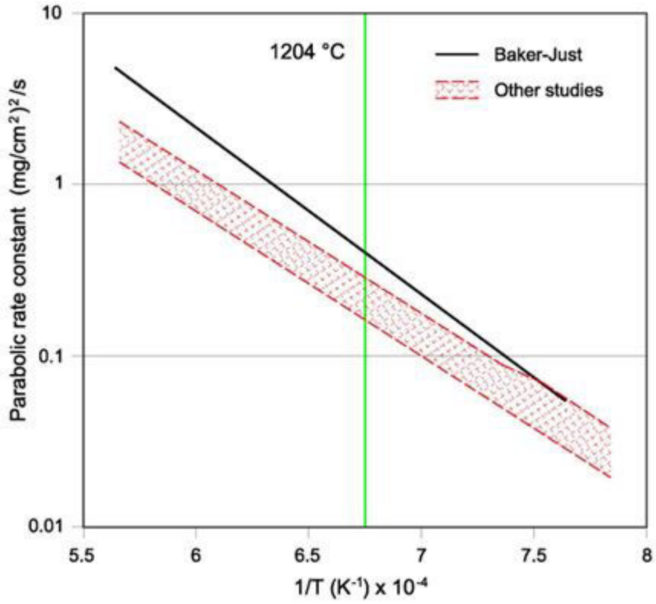

FIG. 9.110. Temperature dependence of the parabolic rate constant for the oxidation of Zircaloy at high temperatures — the area within the band includes data from 14 studies with the Baker–Just representation plotted separately [9.342, 9.345–9.359].

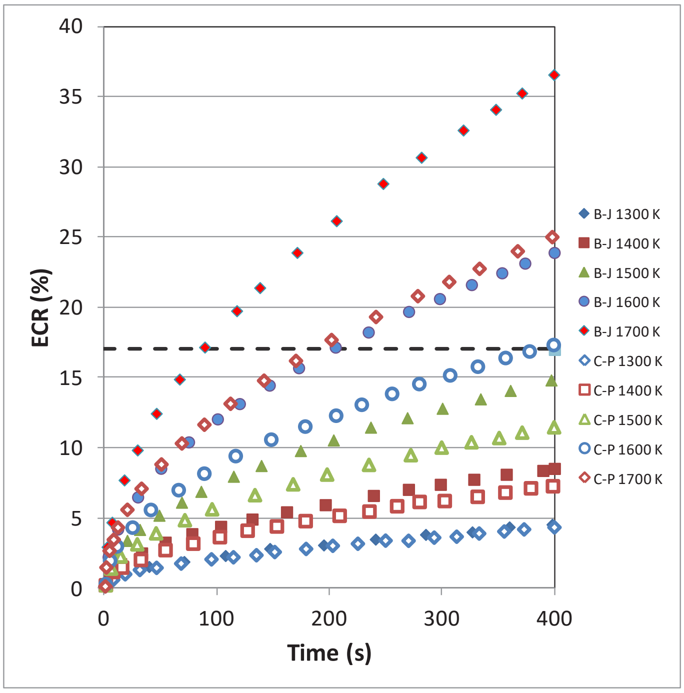

FIG. 9.111. Time dependence of equivalent cladding reacted (ECR) with time for cladding with wall thickness of 0.57 mm at five temperatures using the Baker–Just (B–J) and Cathcart–Pawel correlations (based on [9.345]).

and 1700 K (1030 and 1430°C). At the highest temperature the 17% limit is reached in about 72 s with the Baker–Just equation but is postponed until about 186 s using the Cathcart–Pawel correlation. Many studies use the Baker–Just equation to conservately apply test results where the cladding reaches a temperature of 1310 K (1037°C) or higher.

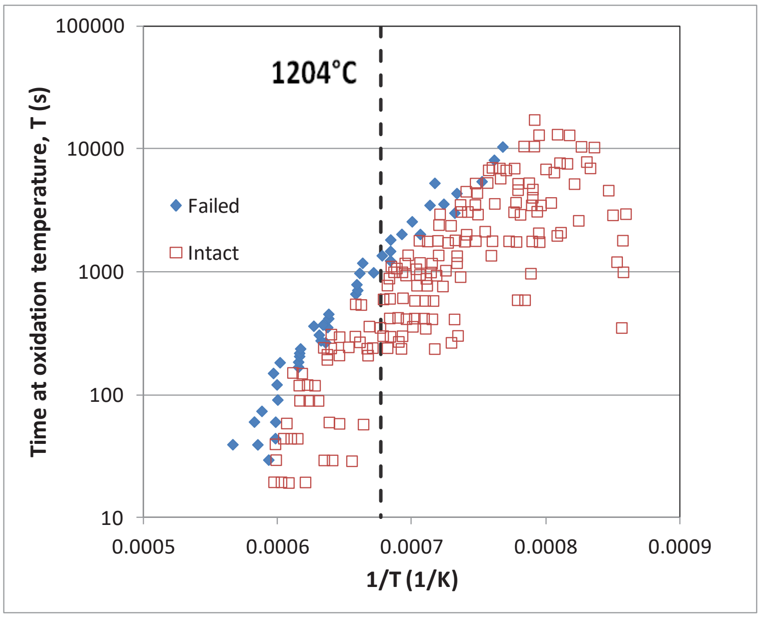

FIG. 9.112. Resistance of oxidized Zircaloy-4 to thermal shock in two-stage cooling from high temperature after oxidation at T [9.202].

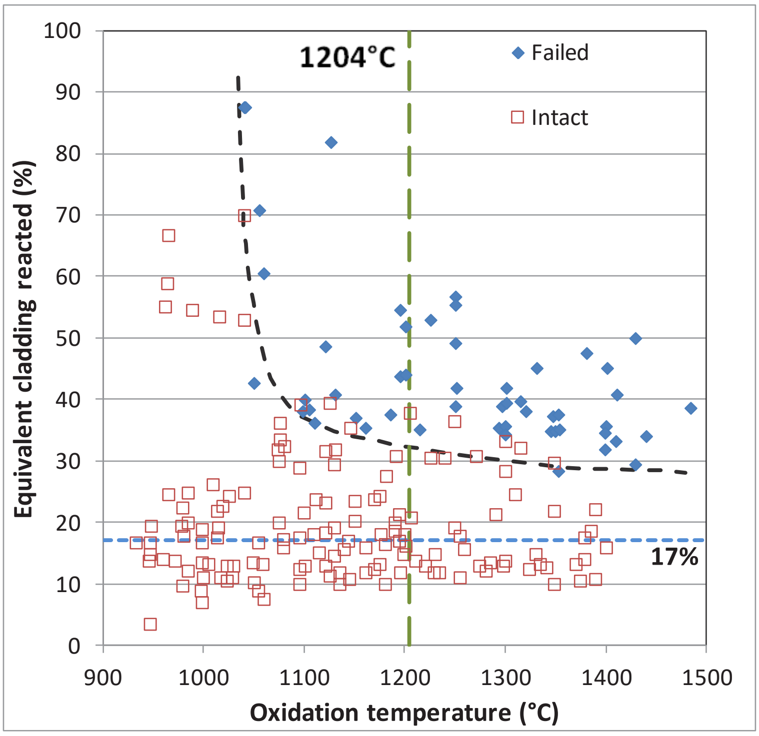

FIG. 9.113. Results in Fig. 9.112 showing response of oxidized Zircaloy-4 as a function of ECR. Black dotted line is estimated boundary between failure and survival after thermal shock (based on [9.202]).

The value of ECR varies with cladding wall thickness, described in Eq. (9.38), and has to take into account double sided oxidation, to accommodate tube bursting. The pre-LOCA oxidation from corrosion is not protective during high temperature oxidation [9.360] and should be subtracted from the 17% total limit. The saturation temperature during reflood, about 408 K (135°C), was recommended to be the upper temperature limit for mechanical testing for oxidized cladding.

When the mechanical test specimens were oxidized at temperatures above 1477 K (1204°C), incursions of α phase into the β phase were observed that exacerbated the embrittlement [9.335]. Also, above this temperature the oxygen concentration in the central core β phase can approach 0.7 to 0.9 wt% (3.86 to 4.92 at.%) oxygen, as indicated by the β phase/(α + β) boundary listed in Table 9.21, based on Fig. 9.100. On cooling, the transformed α phase will be brittle [9.342] in material containing concentrations of oxygen larger than 0.7 wt% (3.86 at.%). These observations set the high temperature limit and, combined with the limit on ECR, became an integrated criterion for assuring safety during a LOCA. Subsequent to setting the limits on upper temperature and the extent of oxidation, research focused on confirming their applicability to both Zircaloy and other alloys and evaluating the conservatism of the rules. Some examples are discussed below.

In the thermal shock tests [9.343] used to set the integrated criterion, the specimens were 305 mm long, and consisted of UO_2 pellets clad with Zircaloy-2 with an outside diameter of 14.4 mm and a wall thickness of 0.79 mm. They were held in a steam jacket and inductively heated to high temperature followed by quenching with water admitted either from the top or bottom of the steam jacket. When the ECR was 18% or greater the cladding failed on quenching; the peak temperature in several of the specimens exceeded 1477 K (1204°C) but the oxygen concentration in the prior β phase was 0.9 wt% or less because the heating time was insufficient for the oxygen to diffuse into the centre of the cladding to cause embrittlement [9.327].

In a more detailed study [9.201, 9.328], 200 mm long specimens of Zircaloy-4 cladding, with an outside diameter of 10.9 mm and a wall thickness of 0.635 mm, and containing alumina pellets, were pressurized with helium to 6.89 MPa and heated at about 10°C/s in steam. Rupture at about 1040 K (770°C) was accompanied by a strain between 0.65 and 1.0. The ruptured tube was then oxidized on the inner and outer surfaces for various times at various temperatures. The oxidized specimens were either cooled at about 5°C/s to between 983 and 1103 K (710 and 830°C) followed by quenching by bottom flooding at rates of about 50 mm/s with water at room temperature, or were quenched directly from the oxidation temperature at about 100°C/s. The resistance to thermal shock produced by two step cooling followed a similar pattern to that depicted in Fig. 9.109, with a boundary between the tubes that failed and those that survived the quench, as shown in Fig. 9.112. At 1477 K (1204°C) the critical oxidation time was about 1000 s. A failure map relating the failures to ECR, shown in Fig. 9.113, provides support for the large margin on the integrated criterion. No failures were close to the 17% ECR limit. The estimated boundary between the conditions for failure or survival indicated that the critical ECR declined with increase in oxidation temperature but at the temperature limit of 1477 K (1204°C) the critical ECR was about 32%. When similar specimens were quenched directly from the oxidation temperature, compared with the two step cooling, the required oxidation times to produce failure were lowered, sometimes by a factor of two, as shown in Fig. 9.114. The critical ECR was reduced, but still above 17% at 1477 K (1204°C), as shown in Fig. 9.115; the Figure includes results of similar tests by Scatena [9.337], Hesson et al. [9.344] and Grandjean et al. [9.360, 9.361].

The test sections of the fuel rods described in Ref. [9.201] were not axially restrained, whereas in practice, grids, other rods and pellet–clad bonding will exert some constraint during cooling. Single rod tests demonstrated the size of the effect. Specimens of pressurized cladding, 500 mm long with a wall thickness of 0.62 mm, were fixed at one end and allowed to expand in the

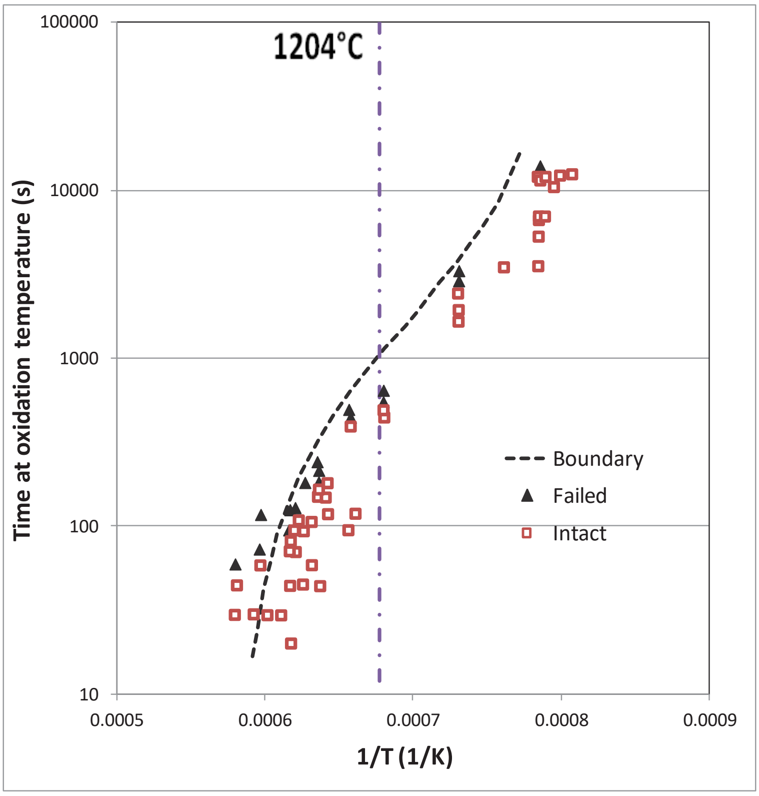

FIG. 9.114. Resistance of oxidized Zircaloy-4 to thermal shock by direct quenching from high temperature after oxidation at T. The dotted line represents the boundary between failure and survival in tests with two-stage cooling, Fig. 9.112 [9.202].

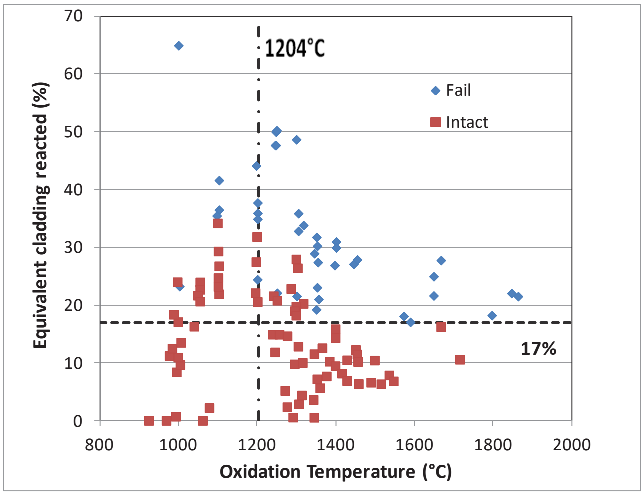

FIG. 9.115. Results in Fig. 9.114 [9.202] plus data from [9.337, 9.344, 9.360, 9.361] showing response of oxidized Zircaloy-4 to direct quenching from the oxidation temperature as a function of ECR.

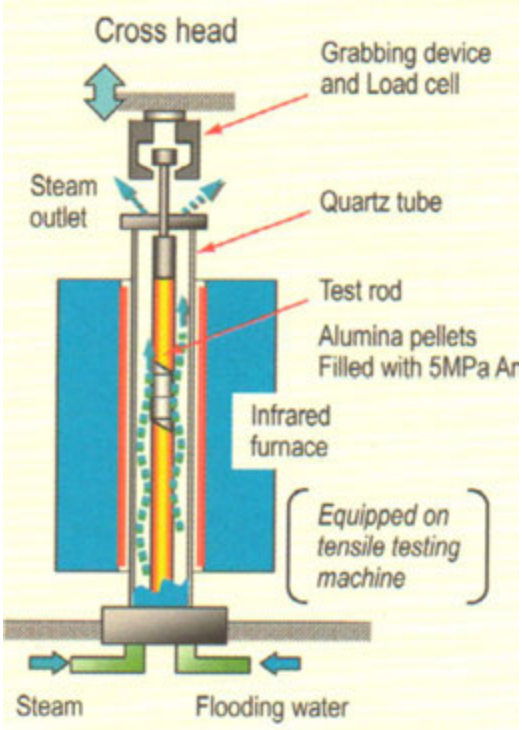

FIG. 116. Apparatus for integral thermal shock experiments [9.362].

axial direction during bursting, then during oxidation at high temperatures in the range 1193 to 1603 K (920 to 1330°C) [9.362]. The free end was fixed just before quenching at about 130°C/s by bottom flooding at rates of about 40 mm/s. The apparatus is depicted in Fig. 9.116. Unconstrained specimens failed from thermal shock with ECR in the range 35 to 38%, whereas specimens that were constrained failed with ECR in the range of 19 to 24%, as shown in Fig. 9.117. ECR was calculated with the Baker–Just equation [9.341]. The maximum axial load sustained by the specimens that failed was about 160 kg whereas the cladding with low oxide thickness withstood loads up to 430 kg. Results from subsequent tests using the same type of apparatus with similar temperature histories support the Japanese ECR limit of 15% [9.363–9.366]. Tests on thin-walled (0.57 mm) cladding made from low tin (1.3 wt% (1.0 at.%)) Zircaloy-4 containing up to 600 ppm (5.19 at.%) hydrogen provided results

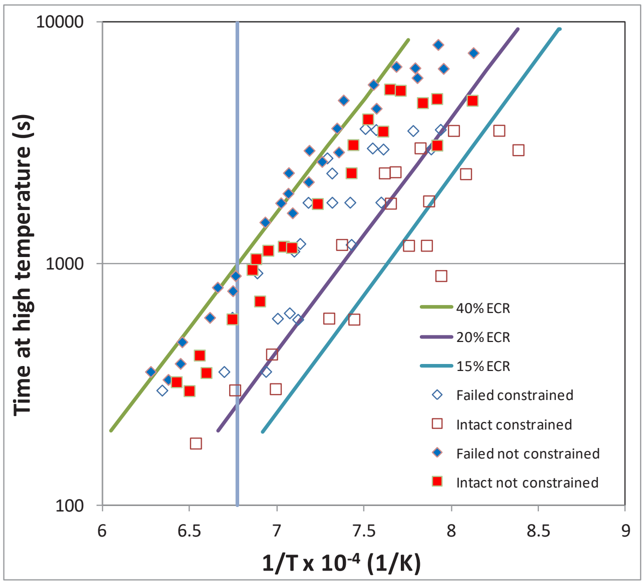

FIG. 9.117. Failure by thermal shock of oxidized Zircaloy-4 fuel cladding water quench from high temperatures. Axial constraint shifts the boundary between survival and failure to lower ECR [9.362].

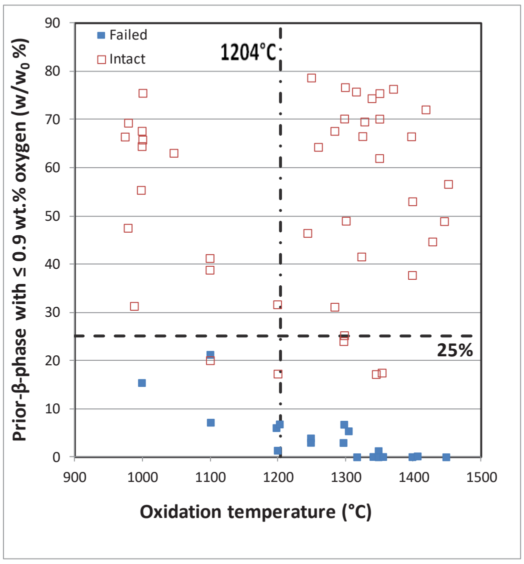

FIG. 9.118. Failure map for thermal shock of Zircaloy-4 cladding oxidized at high temperature and quenched at about 100°C/s with ≤0.9 wt% (4.92 at.%) oxygen in the prior β phase (based on [9.202]).

similar to those presented in Fig. 9.117 for no constraint. With full constraint, the critical ECR was reduced to 17% in the material containing low concentrations of hydrogen and declined further to 7% with high hydrogen concentrations [9.363]. A restraint that imposed an axial load of 390 to 735 N returned the critical ECR to 17% in material containing up to 800 ppm (6.8 at.%) hydrogen [9.364]. When the hydrogen concentration was in the range 120 to 210 ppm (1.0 to 1.9 at.%), irradiation had little effect on the response to thermal shock. After a burnup of 44 MWd/kgU, 2 specimens oxidized to ECRs of 26 and 29% fractured during the quench while 4 specimens oxidized to ECRs between 16 and 22% remained intact [9.365]. The lack of effect of irradiation because of annealing out of damage agrees with the discussion presented in Section 9.3.4.2.

In Ref. [9.201] the thickness of the prior β phase containing ≤0.9 wt% (4.92 at.%) oxygen, as shown in Fig. 9.118, indicated an alternate approach to the ECR criterion based on the residual strength and ductility of the core material. If there was over 25% of the central material containing

≤0.9 wt% (4.92 at.%) oxygen, the cladding survived the thermal shock. Material containing this oxygen concentration can be brittle, and according to the phase diagram, would have to have reached about 1603 K (1330°C) for the β phase to contain this concentration of oxygen at equilibrium if sufficient time had been allowed; in practice, a gradient in oxygen concentration will exist through the central core of material, as shown in Figs 9.102 and 9.105. The implication is that a criterion based on a lower concentration of oxygen may provide better protection. Both Pawel [9.343] and Sawatzky [9.328] proposed a criterion based on 0.7 wt% (3.86 at.%) — either <95% saturation of the average oxygen concentration in the prior β phase or an oxygen concentration in the β phase <0.7 wt% (3.86 at.%) over at least half the cladding thickness. These criteria are similar at temperatures >1553 K (1280°C) and less conservative than the original NRC criterion below 1477 K (1204°C). The time to reach the threshold values depends on the thickness of the cladding and whether both the inside and outside surfaces are oxidized. Direct thermal shock tests on CANDU cladding with a wall thickness of 0.42 mm [9.367] behaved in a similar way to those on LWR cladding with a wall thickness of 0.635 mm [9.201], as shown in Fig. 9.119. Apart from wall thickness, other differences between tests on CANDU and LWR cladding include the following:

- The outside diameter, 15.2 mm vs 10.9 mm;
- The starting filler pressure, 0.12 MPa vs 6.9 MPa;
- One surface oxidation vs two surface oxidation because the cladding burst during the high temperature phase in the LWR experiments but remained intact in the CANDU experiments.

The last factor probably dominated because the limit between survival and failure took less oxidation time in LWR cladding despite the thicker wall. The CANDU data fitted Sawatzky's failure criterion, as shown in Fig. 9.120; although 3 out of 42 failed specimens did not meet the criterion, they were within the experimental error of the theoretical line. The change in slope around 1533 K

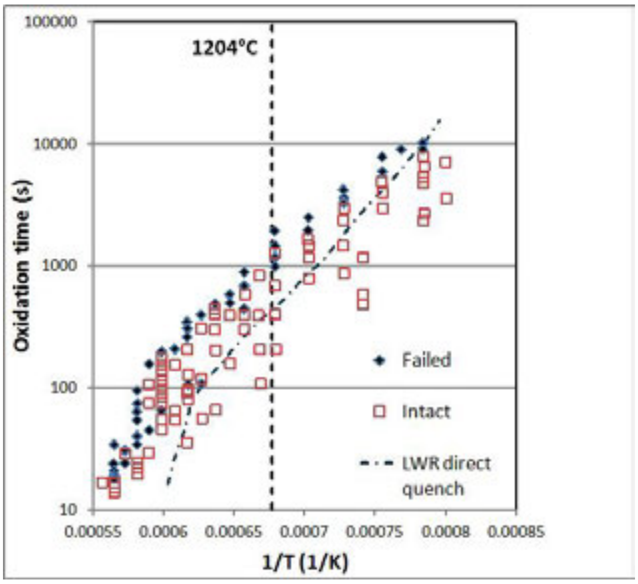

FIG. 9.119. Resistance of oxidized CANDU Zircaloy-4 cladding to thermal shock by direct quenching from high temperature after oxidation at T. The dotted line represents the boundary between failure and survival in direct quench tests on LWR cladding, Fig. 9.114 [9.202].

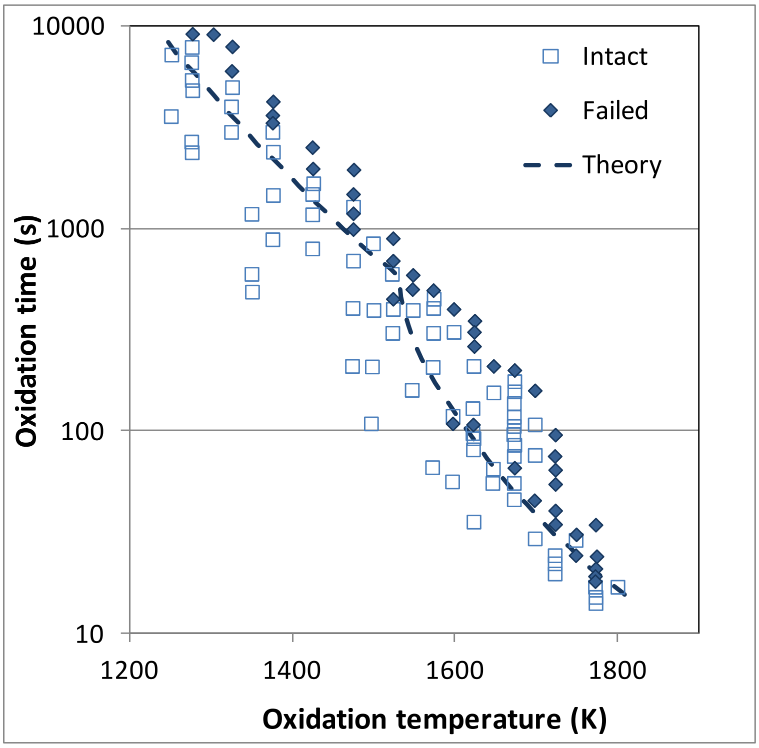

FIG. 9.120. Thermal shock failure map for CANDU cladding showing Sawatzky's failure criterion: to protect the cladding in a LOCA, more than half the cladding thickness should have an oxygen concentration of less than 0.7 wt% (3.86 at.%) oxygen [9.367].

(1260°C) is related to the phases present, as shown in Fig. 9.100. Above this temperature, the β phase can contain more than the critical oxygen concentration, 0.7 wt% (3.86 at.%), and the time at high temperature will determine whether the material is brittle; below this temperature, the mid-wall concentration exceeds 0.7 wt% (3.86 at.%) oxygen only if the (α + β)/β phase boundary has passed the cladding mid-point since it is the prior β phase thickness that determines brittleness. A clear demonstration of the criterion was the failure map of the oxidation temperature with the wall thickness where the failures were separated from the survivors at half thickness, as shown in Fig. 9.121. This criterion is used in safety cases for CANDU reactors. These results confirm that it is the central core of prior β phase material that provides protection against fracture. The thickness of this phase decreases and its oxygen concentration increases with oxidation temperature and time at oxidation temperature.

Another factor is hydrogen concentration. Hydrogen is picked up from corrosion (see Chapter 8, in Volume 2 of this publication) but does not affect the oxidation kinetics or the thicknesses of the oxide or α phase in Zircaloy-4 and M5 at LOCA temperatures [9.332]. When a tube is ruptured at high temperature, the local inside cavity is subjected to corrosion by stagnant steam that results in pick-up of large amounts of hydrogen [9.368]; embrittlement follows. Ring compression tests were done at 373 K (100°C) straddling the rupture opening of Zircaloy-4 cladding burst at 1332 K (1059°C) in steam, held for 240 s then quenched [9.369]. In the test, loss of ductility was assessed as the deflection at which the load, after reaching a maximum value, decreased to 80% of that value. The deflection in the mechanical test and the hydrogen concentration had a 'W' distribution about the rupture opening with the minimum in deflection being a mirror to the maximum in hydrogen concentration; the thickness of the inner oxide layer had a maximum at the rupture opening, as shown in Fig. 9.122. In this situation the oxide modestly reduced the ductility (compare the value at the rupture opening with those at ±60 mm from the rupture opening) whereas at the positions where the hydrogen pick-up was large, ±30 mm, the ductility was very low. Fracture surfaces of the prior β region in specimens containing 150 ppm (1.35 at.%) and 1027 ppm (8.57 at.%) hydrogen quenched

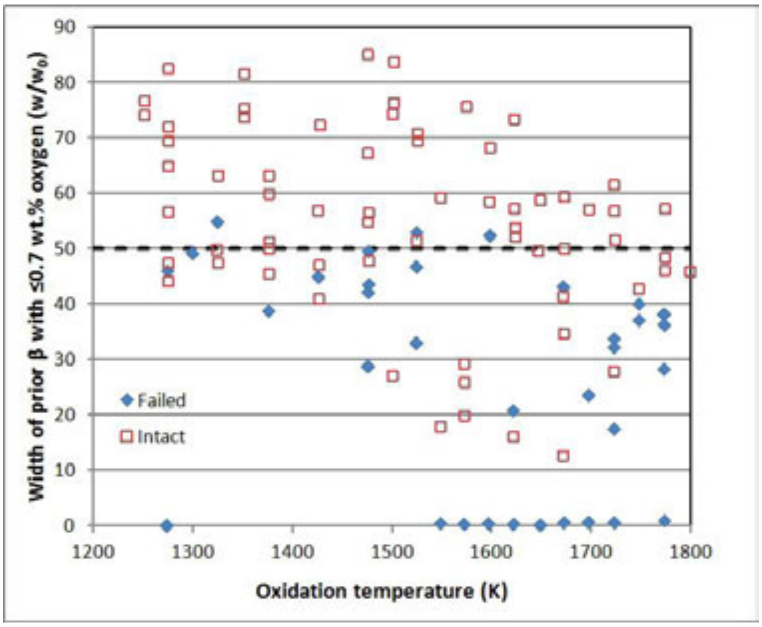

FIG. 9.121. Thermal shock failure map for CANDU cladding showing Sawatzky's failure criterion — dotted line at 50% — to protect the cladding in a LOCA; more than half the cladding thickness, w_0, should have an oxygen concentration less than 0.7 wt% (3.86 at.%) oxygen [9.367].

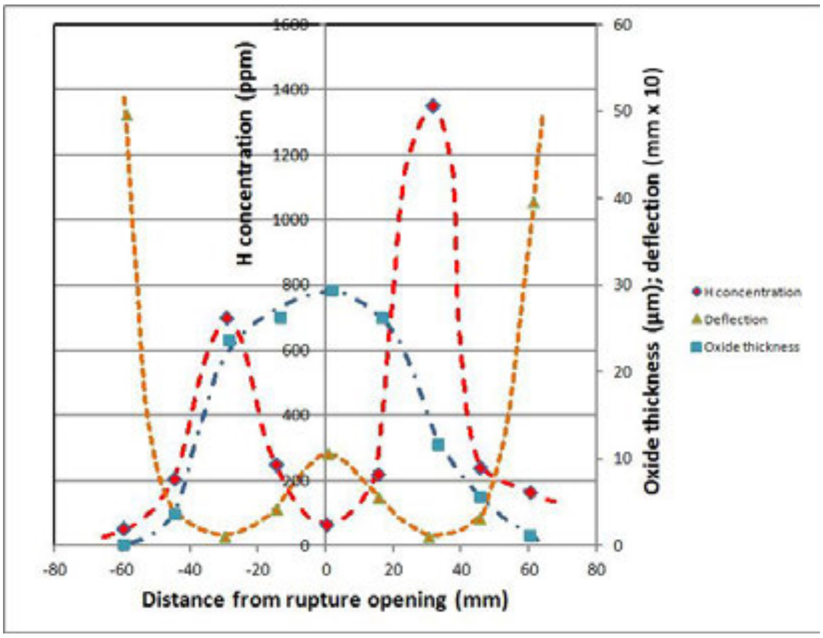

FIG. 9.122. Correlation between distributions of thickness of oxide layer on inner surface, hydrogen concentration and deflection of ring compression specimens tested at 372 K (100°C). Zircaloy-4 cladding burst at 1332 K (1059°C), oxidized in steam for 240 s then water quenched [9.369].

from about 1424 K (1151°C) with ECR of 23% exhibited brittle failure with little sign of ductile dimples, as shown in Fig. 9.123 ([9.364]). Ductility, as measured on M5 and Zircaloy-4 with impact tests and ring compression tests, declined with an increase in hydrogen concentration [9.332, 9.368] but specimens with the same hydrogen concentration but oxidized at different temperatures provided

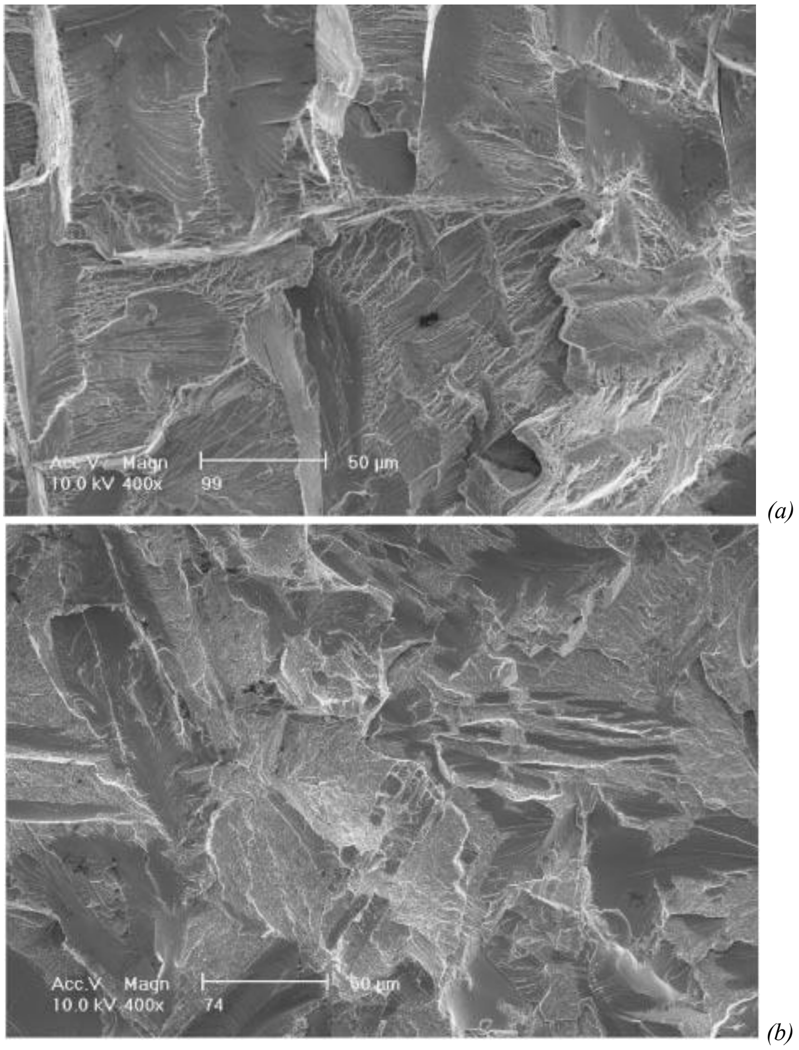

FIG. 9.123. Brittle fracture in the prior β phase in Zircaloy-4 containing (a) 150 ppm (1.35 at.%) and (b) 1027 ppm (8.5 at.%) hydrogen quenched from about 1424 K (1151°C) with an ECR of 23% [9.365].

different values of deflection — for example, specimens containing 250 ppm (2.23 at.%) hydrogen but oxidized at 1225 or 1357 K (952 or 1084°C) had deflections of 3 or 1 mm — indicating that the ductility loss is not caused by hydrogen alone [9.368]. Two mechanisms contribute to this decline: (i) embrittlement by precipitated hydrides formed at low temperatures after the quench [9.367] (to be discussed in Section 9.7), and (ii) since hydrogen is a β stabilizer, an increase in oxygen concentration in the prior β phase because the hydrogen shifts the β/(α + β) line of Fig. 9.100 to the right on the phase diagram, as shown in Fig. 9.124 [9.370, 9.371]. The consequence for the oxygen concentration in the prior β phase was measured in Zircaloy-4 and M5 containing up to 600 ppm (5.19 at.%) hydrogen. After oxidation at 1473 K (1200°C) for various times to ECR between 6 and 17% followed by direct quenching, the oxygen concentration in the prior β phase was measured by electron probe micro-analysis [9.332]. For a given weight gain or time at oxidation temperature, the oxygen concentration increased with increasing hydrogen concentration, as shown in Fig. 9.125. Consequently, as the hydrogen concentration increases the required oxidation time or temperature decreases for the oxygen concentration to reach its critical value for brittle failure.

In summary, the mechanical response of fuel cladding after the high temperature stages of a LOCA depends on the thicknesses of three layers: the oxide, the underlying oxygen-rich α phase and the remaining ligament of Thomson–Widmanstätten α phase transformed from the β phase at high

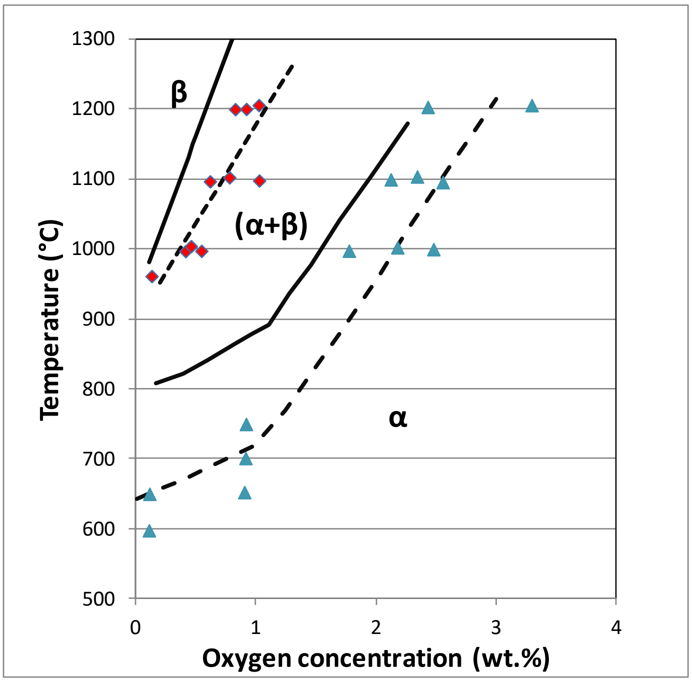

FIG. 9.124. Revision to Zircaloy-4-Oxygen phase diagram with addition of 600 ppm (5.19 at.%) hydrogen; note the shift in the β/(α+β) and (α+β)/α boundaries from those in Fig. 9.100 (full lines) [9.371].

temperature. Since the oxide and α layer are brittle, the integrity of the cladding depends on the oxygen concentration of the remaining ligament. For ductile behaviour the critical oxygen concentration in this ligament is variously reported as between 0.3 and 0.7 wt% (1.68 and 3.86 at.%). To remain below these concentrations in the β phase, an upper temperature of 1477 K (1204°C) was set to limit oxygen pick-up. A single parameter that captures the time at temperature of exposure is called the ECR. The reference limit is ≤17% of the total thickness of cladding that would be converted to stoichiometric ZrO_2 from all the oxygen contained in the fuel cladding. An alternate limit is based on the properties of the prior β layer; one example is that it should contain <0.7 wt% (3.86 at.%) oxygen for over 50% of the wall thickness to provide protection. Hydrogen reduces the temperature of the β/(α + β) transformation and contributes to diminishing the margin on protection by increasing the possible oxygen concentration in the Widmanstätten α phase.

9.5. FATIGUE

9.5.1. Introduction

Components of reactors and many other machines and structures are often subjected to alternating or cyclical loads. Utilities are sometimes required to monitor grid load and adjust the frequency under operating conditions, resulting in fuel temperature fluctuations caused by differential thermal expansion between pellets and cladding. In addition, complex thermohydraulics within the reactor create conditions of oscillating pressures and loads. The cyclical stresses and strains thus created and accumulated over a number of cycles can create microscopic damage in Zr alloys that leads to macroscopic cracking of components. These phenomena, due to cyclical stressing, which can occur at stresses considerably below the ultimate tensile stress, are called fatigue. The term itself originated in the mid-1800s, as engineers noted that parts such as rotating axles in wagons gradually lost their resistance to stresses, and after long operation failed suddenly.

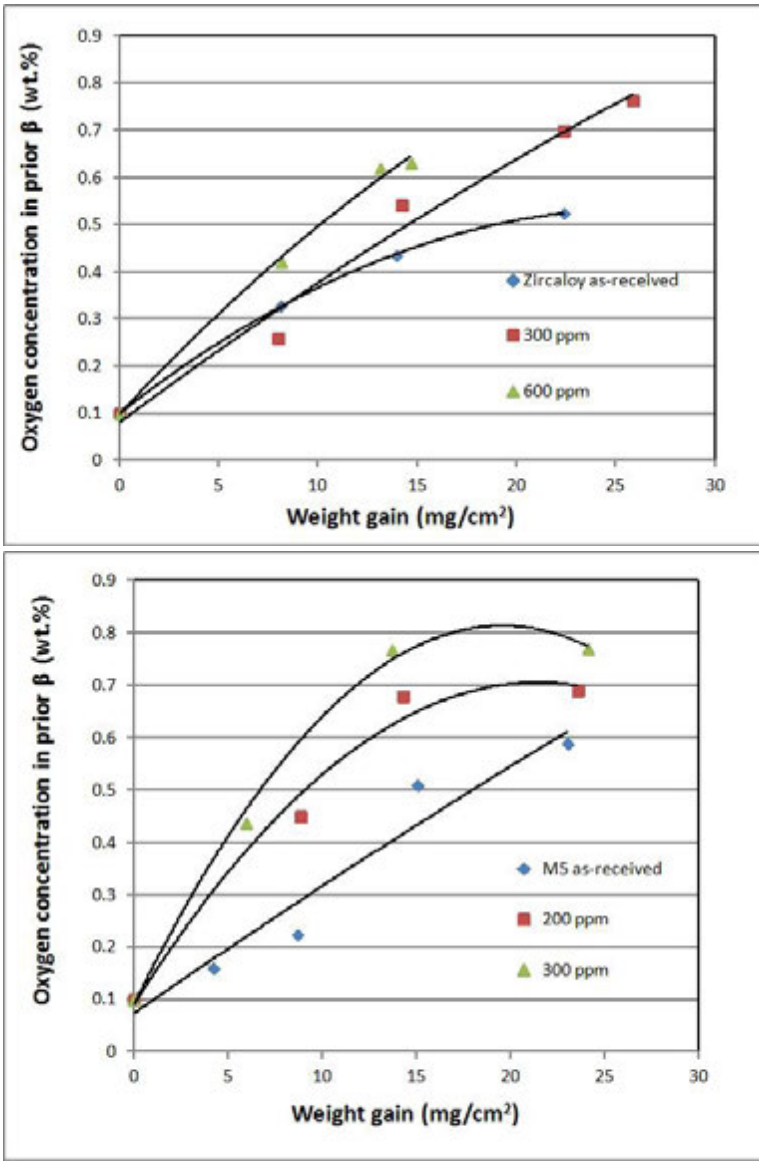

(a)

(b)

FIG. 9.125. Increase in oxygen concentration in prior β phase with oxidation at 1473 K (1200°C) showing further increase with added hydrogen for (a) Zircaloy-4 and (b) Zr-1Nb (M5) [9.333].

Unlike many other technologies where fatigue failures account for a large percentage of all mechanical failures, reactor components, with perhaps only one exception, are not susceptible to fatigue failures. For instance, in a testing programme, no negative effects on fuel rod performance were observed after extensive power cycling in a test reactor [9.372]. The margins between the operating conditions and failure by fatigue are usually large, which accounts for the observed good behaviour. As a typical institutional standard, the NRC Standard Review Plan [9.373] states that the cumulative number of strain fatigue cycles on structural members (grids, guide tubes, channels and fuel rods) should be significantly less than the design fatigue lifetime, which must be based on appropriate data and include a safety factor of two on stress amplitude or twenty on the number of cycles. ‘Appropriate data’ means either the data of O’Donnel and Langer [9.374] or other data justified and approved by the NRC. Testing is still required for new components and operating conditions to maintain safe performance, evaluate margins and confirm good tolerance to cyclical loading.

There are three major approaches to analysing fatigue. The traditional approach is based on analysis of the nominal or average stress in the component, as modified by the effects of stress raisers such as holes, fillets and interfaces — the stress based approach. The strain based approach involves a more detailed analysis of the plastic and elastic strains that develop in the component of interest [9.375]. The third approach uses fracture mechanics. Some useful terms for describing fatigue are included in Table 9.23. Much of the information in this section was developed within the ZIRAT Programme and is provided herein through the courtesy of ANT International. Information on the ZIRAT/IZNA Programmes can be obtained at [9.376].

TABLE 9.23. TERMS USED TO DESCRIBE FATIGUE

Term	Meaning and symbols
S–N	Number of cycles to failure, N_f, at stress S.
Stress range	$\Delta a = \sigma_{max} - \sigma_{min}$
Mean stress	$\sigma_m = (\sigma_{max} - \sigma_{min})/2$
Stress amplitude	$\sigma_a = \Delta\sigma/2$
Alternating stress	$\sigma_a = \Delta\sigma/2$
Stress ratio	$R = \sigma_{max}/\sigma_{min}$
Fatigue (endurance) limit	σ_e = stress below which fatigue failure does not occur
Fatigue strength	Stress amplitude value from *S–N* curve at a particular life of interest
High cycle fatigue	When fatigue life is greater than 10^6 cycles
Low cycle fatigue (LCF)	When fatigue life is below 10^5 cycles
Strain amplitude	$\varepsilon_a = \Delta\varepsilon/2$
Plastic strain	$\Delta\varepsilon_p$ = width of hysteresis loop
Plastic strain amplitude	$\Delta\varepsilon_p/2$

9.5.2. Stress based fatigue

Figure 9.126 illustrates typical stress based fatigue cycles. Figure 9.126(a) illustrates a completely reversed sinusoidal stress, such as could be produced by a rotating shaft. In this case the numerical value of the minimum and maximum stresses is equal. Figure 9.126(b) illustrates a case

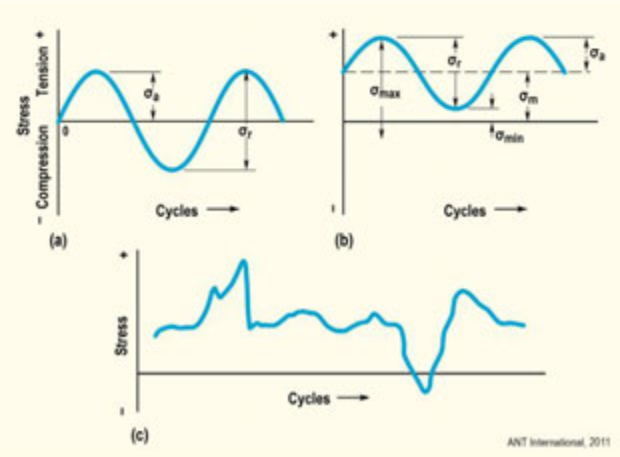

FIG. 9.126. Typical fatigue stress cycles: (a) reversed tensile and compressive stress; (b) alternating tensile stress; (c) irregular or random stress cycle (after [9.383]).

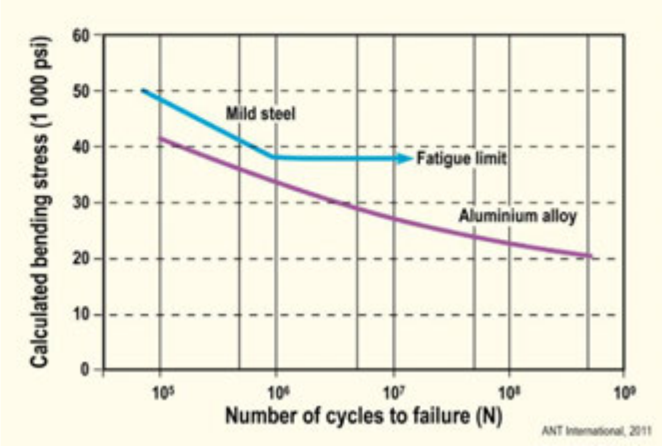

FIG 9.127. Typical fatigue curves for ferrous and nonferrous metals (after [9.383]).

where the values of the minimum and maximum stress are not equal. Both are examples of tension, but they could have opposite signs as well.

The stress ratio, *R*, is defined as the ratio of the minimum to maximum loads, $\sigma_{\min}/\sigma_{\max}$. With static loading, *R* is equal to 1; with tensile cycle loading, *R* is between 0 and 1 (as shown in Fig. 9.126(b)); with reversed load cycling, *R* is between −1 and 0; and with symmetrical load cycling, *R* is equal to −1 (Fig. 9.126(a)). Figure 9.126(c) illustrates a complicated stress cycle, which could be induced, for instance, in a component by thermohydraulic induced vibration.

The standard method of presenting stress based fatigue data is by the stress versus the number of cycles to failure (S–N) curve, illustrated in Fig. 9.127 for mild steel and an aluminum alloy. The axis of the number of cycles to failure, *N*, is usually in logarithmic form, while the stress axis is given either in linear or logarithmic form. Figure 9.127 illustrates that some materials have a definite fatigue limit; below a given stress they will not fail in fatigue. Interest in Zr alloys is mostly for less than a few million cycles, and there may be a fatigue limit in that range. As a rule of thumb, the fatigue limits of many ductile materials are less than half of the ultimate tensile stress. This observation is dependent on microstructure and does not hold for both unirradiated and irradiated Zr alloys. In general, S–N curves may be affected by material, microstructure, geometry (for example, notches), surface finish, chemical and thermal environment, frequency of cycling, residual stress and mean stress.

Since the mean stress in many practical applications to reactor components is not zero, this case is examined in more detail. The effect of a positive mean stress, as shown in Fig. 9.126(b), is to

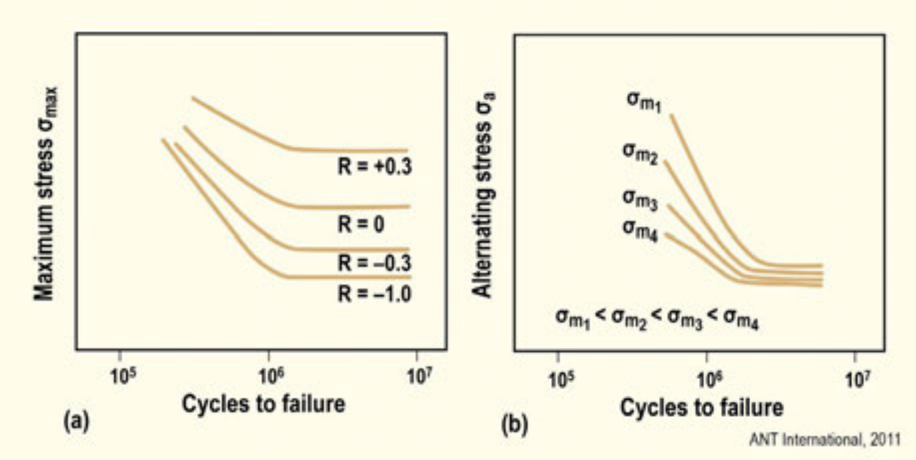

FIG. 9.128. Two methods of plotting fatigue data when the mean stress is not zero (after [9.383]).

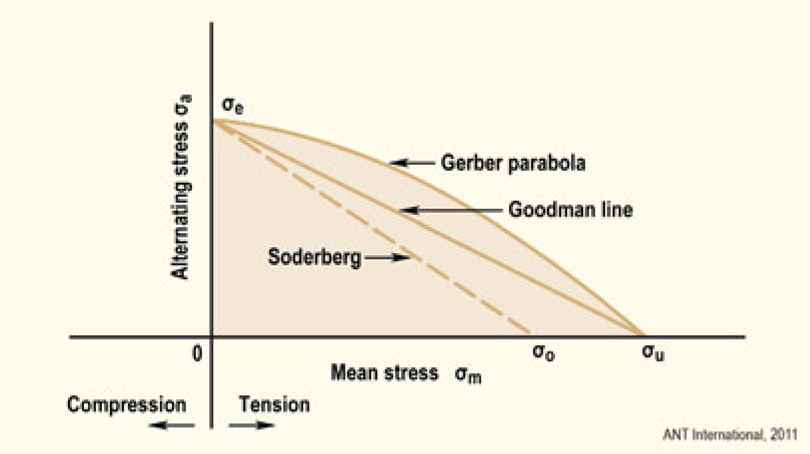

FIG. 9.129. *Alternative method of plotting the Goodman diagram (after [9.377]).*

lower the fatigue strength. Figure 9.128 illustrates two ways to represent that point. The Goodman diagram [9.377] and Haigh diagram [9.378] propose an approximate way to predict the effect of mean stress on the fatigue strength or endurance limit of a particular material. A form of the Goodman diagram is shown in Fig. 9.129 [9.374]. It is constructed by plotting σ_a, the alternating stress (or stress amplitude) at a given value of mean stress. At zero mean stress, the value of σ_a is the fatigue limit, σ_e, so it marks a point on the y-axis. When the alternating stress σ_a is zero — the stress is applied as in a uniaxial tensile test — the endurance limit σ_e is the UTS, σ_u, indicating when a specimen begins to fail in a tensile test (see Section 9.2), and marks a point on the x-axis. The Goodman line assumes the two marked points are connected by a straight line:

$$\sigma_a/\sigma_e + \sigma_m/\sigma_u = 1 \tag{9.42}$$

For ductile materials the line is close to a parabola (the Gerber line [9.379]) in which the σ_m/σ_u term in Eq. (9.42) is squared, and for brittle materials the yield strength is used rather than the UTS (the Soderberg line [9.380]). This approach has been variously modified since being first proposed in 1864 [9.381], but is still used in practical materials design [9.382, 9.383].

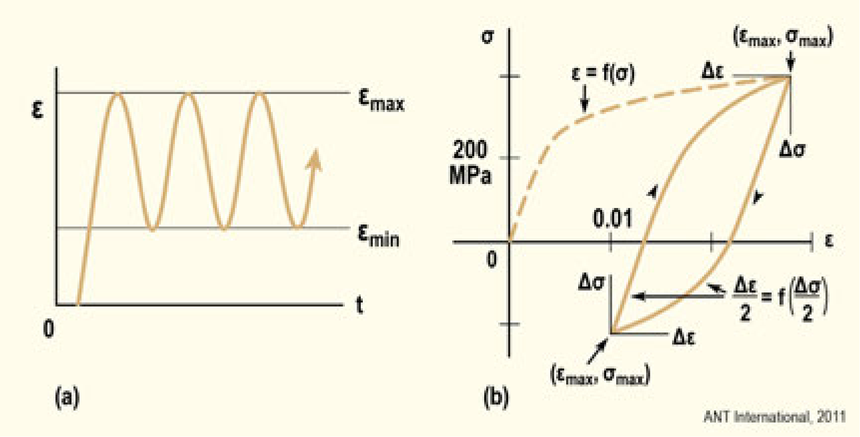

FIG. 9.130. *Stress–strain unloading and reloading behaviour consistent with a spring and slider theoretical model; (a) strain cycle; (b) stress versus strain behaviour.*

9.5.3. Strain based fatigue

To get insight into the strain based approach to fatigue, the plastic behaviour of deformation is examined. This approach is appropriate for ductile metals with short lives, such as when cyclical loading is due to thermal stresses. Use of the cyclical stress–strain curve is a feature of the strain based approach, as is the use of a strain versus life curve (as opposed to the stress versus number of cycles to failure (S–N) curve). When a strain cycle is imposed, as shown in Fig. 9.130(a), the stress versus strain behaviour of Fig. 9.130(b) results. The dashed line indicates the normal stress–strain behaviour for a tensile test. When the direction of straining is reversed at $\varepsilon_{\max}$, $\sigma_{\max}$, the initial reverse strain is elastic followed by compressive plastic strain to the point $\varepsilon_{\min}$, $\sigma_{\min}$. Another strain reversal is accomplished with tensile elastic and plastic strains. (The effect of a stress reversal on the yield stress, the Bauschinger effect, is not considered here.) For ideal behaviour, the stable hysteresis loop (solid lines in Fig. 9.130(b)) of Fig. 9.131 forms, although usually only after a large number of cycles. The width of the loop at zero stress is the cyclical plastic strain, $\Delta\varepsilon_p$, and the total strain is $\Delta\varepsilon_p$ + elastic strain.

When a metal is cycled in strain control between constant total strain limits, as illustrated in Fig. 9.132, some materials (such as unirradiated Zircaloy) undergo strain hardening and others (such as irradiated Zircaloy) undergo strain softening. In cyclical hardening (upper Fig. 9.132) the stress required to impose the strain increases at each cycle, the elastic strain increases and the plastic strain decreases. The width of the hysteresis loop therefore decreases. For cyclical softening, the opposite occurs. Construction of the cyclical stress–strain curve is illustrated in Fig. 9.133 for the case of cyclical hardening during three cycles. The cyclical stress–strain curve is defined by the locus of tips of the three hysteresis curves, O-A-B-C. When compared to a standard tensile stress–strain curve, the cyclical curve will lie above or below it, depending on whether the material hardens or softens, as illustrated in Fig. 9.134. In a detailed analysis of life estimates for structural components, the cyclical stress–strain curve is often used in place of a monotonic stress–strain curve [9.382].

Completely reversed cycling ($R = -1$) between constant strain limits of metals in the low cycle region often fits a simple relationship, shown graphically in Fig. 9.135. The equation is:

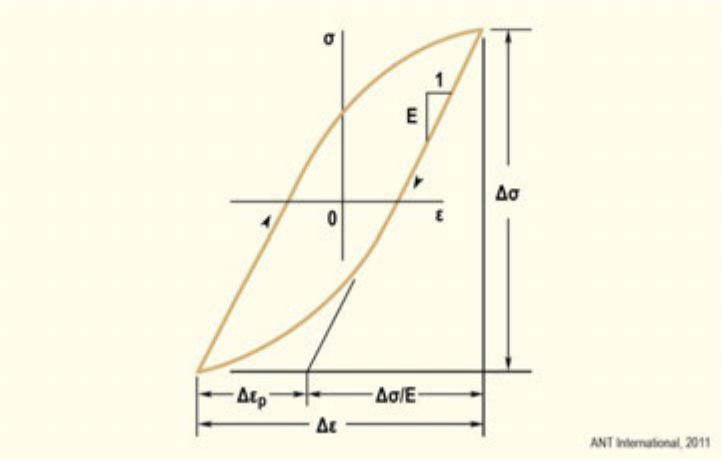

FIG. 9.131. Stable stress–strain hysteresis loop.

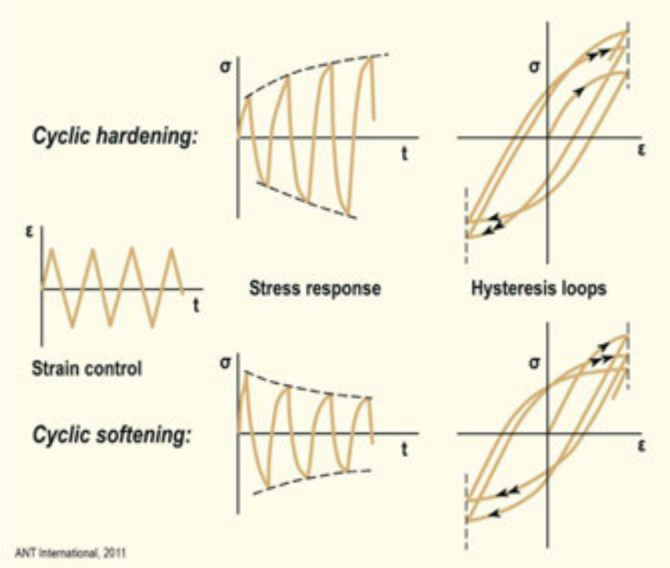

FIG. 9.132. Completely reversed strain controlled test and two possible stress responses, namely cycle-dependent hardening and softening (after [9.382]).

$$\varepsilon_{\mathrm{a}} = \frac{\sigma_f'}{E}\,(2N_{\mathrm{f}})^{\mathrm{b}} + \varepsilon_f^1\,(2N_{\mathrm{f}})^{\mathrm{c}} \qquad (9.43)$$

where ε_{a} is the total strain amplitude and ε_{f}, σ_{f}, b and c are constants, considered material properties.

Taking just the plastic strain part gives:

$$\varepsilon_{\mathrm{ap}} = \varepsilon_f^1\,(2N_{\mathrm{f}})^{\mathrm{c}} \qquad (9.44)$$

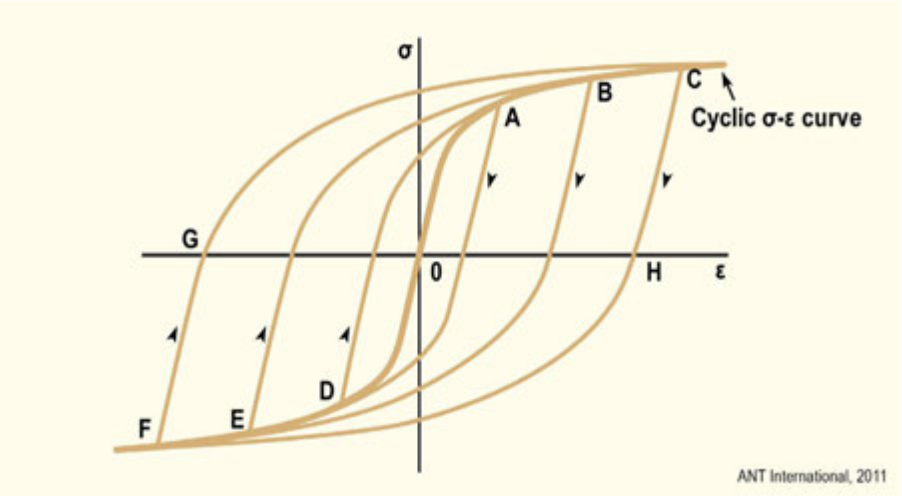

FIG. 9.133. Cyclic stress–strain curve defined as the locus of tips of hysteresis loops. Three loops are shown, A-D, B-E, and C-F. The tensile branch of the cyclic stress–strain curve is O-A-B-C, and the compressive branch is O-D-E-F.

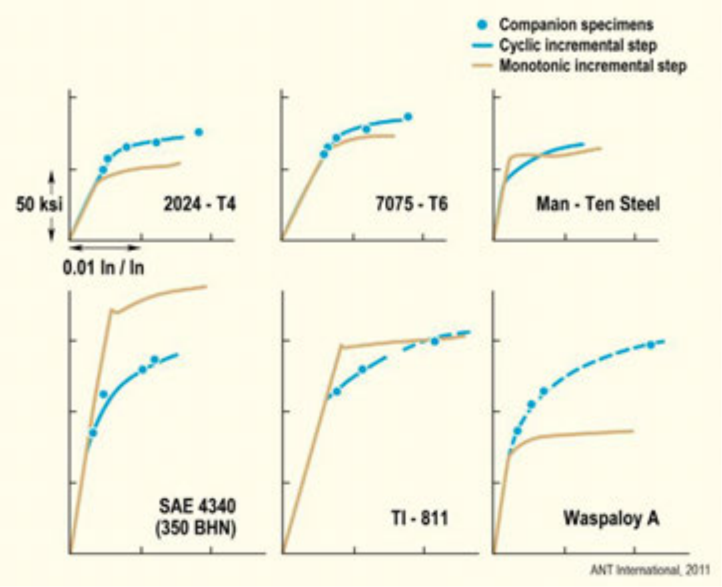

FIG. 9.134. Cyclic and monotonic stress–strain curves for several engineering metals (after [9.382]).

The convention that ε_f^1 is evaluated at one-half cycle ($N_f = 0.5$) allows one to obtain ε_f^1 as the uniform elongation of a tensile test. If the slope of the log–log curve is known for a material or class of materials, the entire strain versus failure curve can be approximated. The above equation is called the Coffin–Manson relationship and is analogous to the Goodwin diagram for stress based analysis.

9.5.4. Statistical nature of fatigue

For many materials the fatigue life and fatigue limit are statistical quantities and therefore considerable variations of data must be expected. For Zr alloys, no individual study has included sufficient data to derive statistical certainty of the results. An example of variation in a controlled experiment with steel is given in Fig. 9.136. This Figure summarizes Ref. [9.384], ten S–N curves determined in the conventional manner for the same bar of alloy steel, each curve being based on ten identical specimens. There are large differences in the indicated value of the fatigue limit because the individual curves were based on insufficient data. An example for an Al alloy is given in Fig. 9.137 where S–N data were obtained at eight different stress amplitudes [9.385]. The dashed lines indicate

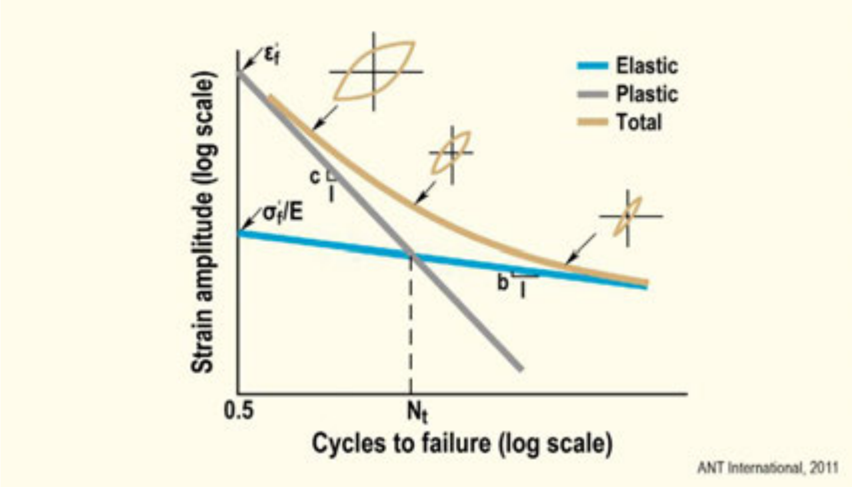

FIG. 9.135. Elastic, plastic and total strain versus fatigue life curves (after [9.382]).

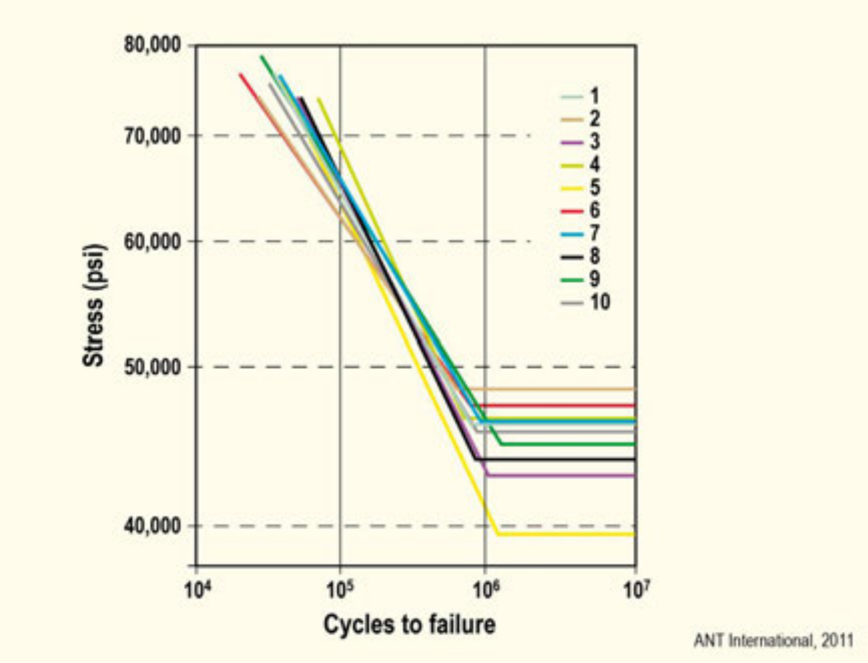

FIG. 9.136. Summary of S–N curves, each based on ten specimens, sampled from the same bar of steel (after [9.384]).

upper, mean and lower limit lines. When fatigue life is plotted against the number of cycles for failure, N_f, as in Fig. 9.138 [9.386], a log normal distribution is often indicated; if the logarithm of N_f is used, a reasonably symmetrical distribution (Fig. 9.138) is obtained that can be treated as a Gaussian or normal distribution.

As noted above, the available data for Zr alloys are insufficient to allow a statistical analysis to be constructed. This lack of data is the reason that in design, large safety factors on fatigue limit or life are appropriate. Many variables, such as heat treatment, surface condition, specimen design, mean stress and irradiation, could affect the fatigue limit.

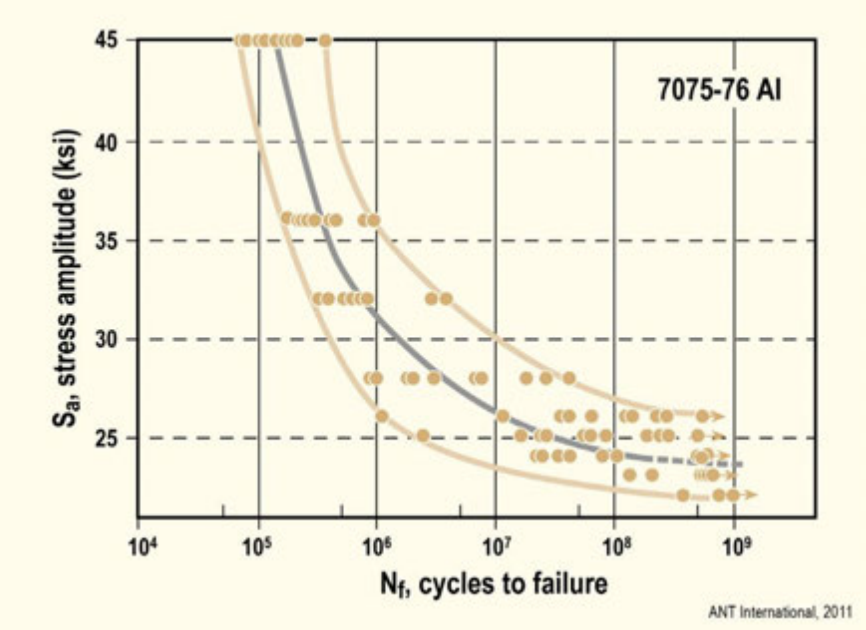

FIG. 9.137. Scatter in rotating bending S–N data for an unnotched aluminum alloy (after [9.385]).

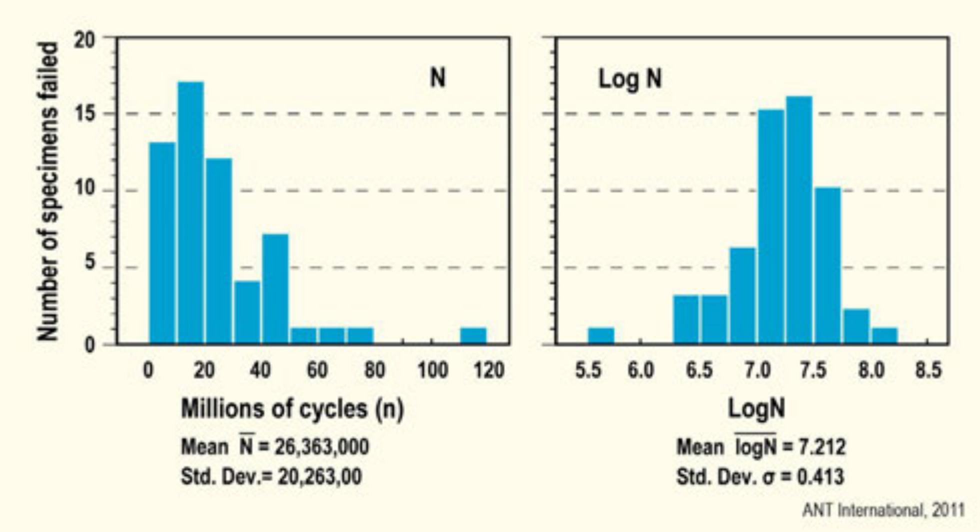

FIG. 9.138. Distribution of fatigue lives for 57 small specimens of 7075-T6 aluminum tested at a stress amplitude of 207 MPa in rotating bending (after [9.386]).

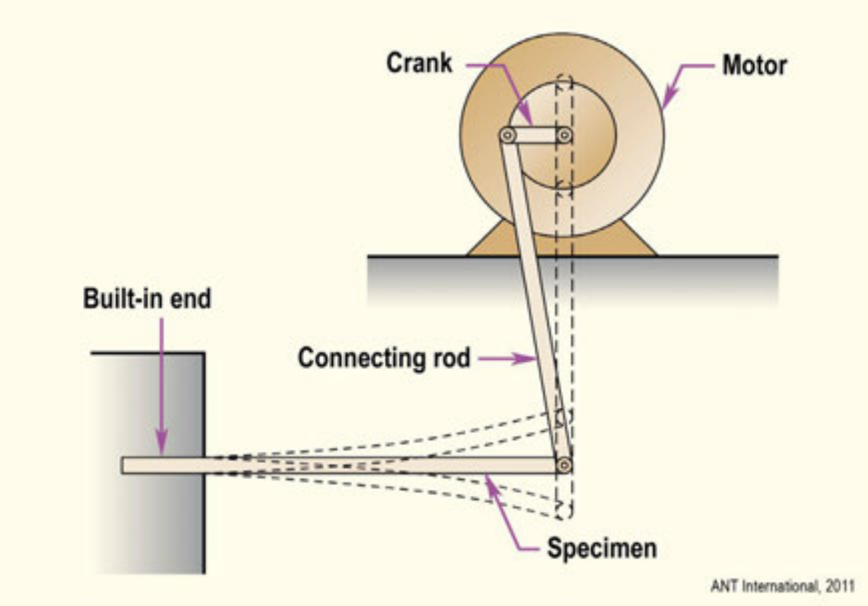

FIG. 9.139. A simple reciprocating cantilever bending fatigue testing machine based on controlled deflections from a rotating eccentric drum (after [9.387]).

9.5.5. Experimental

An understanding of specimen and testing technique is important since specimen geometry can affect fatigue behaviour. Fatigue testing requires an apparatus for stress (strain) reversal and measurement of the stress (strain) on a specimen and material having some relevance to the real component of interest. The most common testing mode is fully reversed bending, particularly in stress based fatigue analysis. A simple device for bending is illustrated in Fig. 9.139 [9.387]. If plastic yielding occurs in such testing, the load or specimen strain must be measured. Various types of standard fatigue test specimens are shown in Fig. 9.140 [9.388]. The bottom specimen is used for axial load testing while the others are suitable for bending tests.

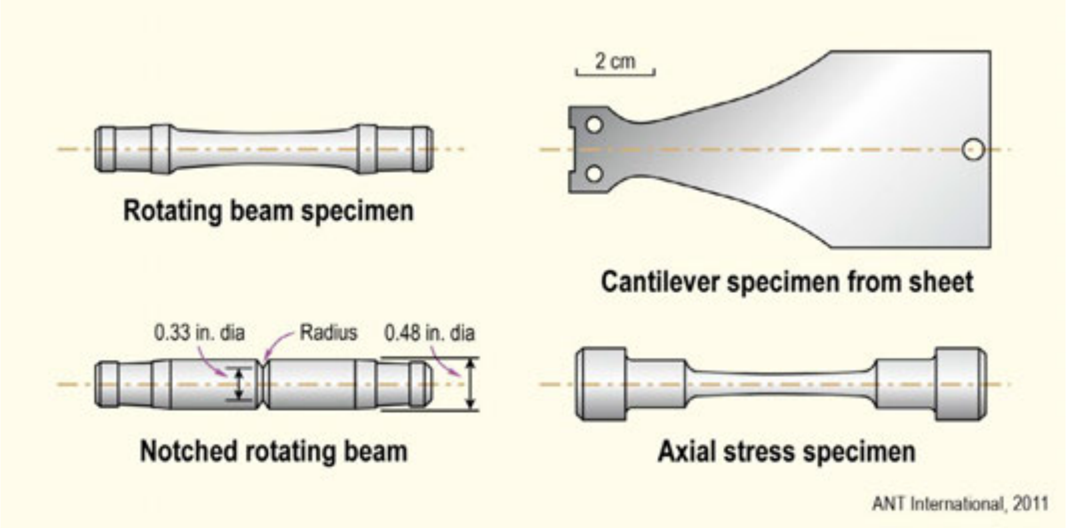

FIG. 9.140. Various fatigue test specimens, all shown to the same scale (after [9.388]).

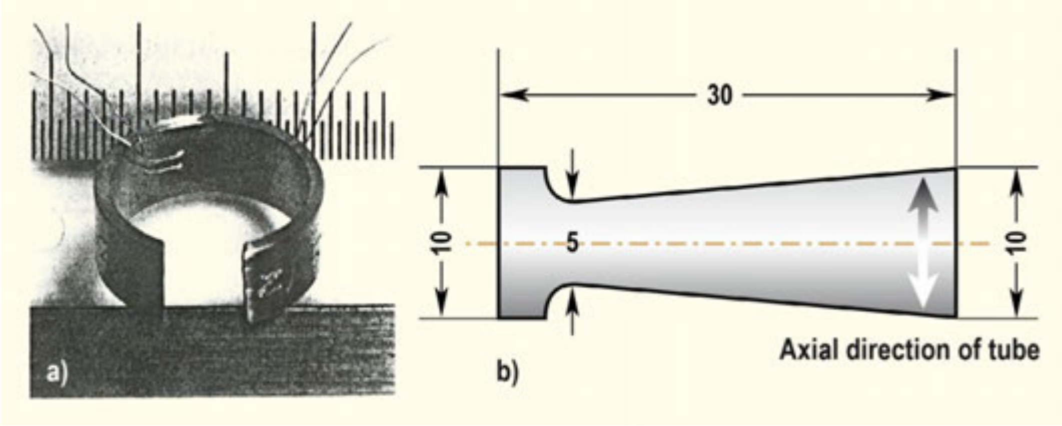

FIG. 9.141. Configuration of fatigue test specimens: (a) C shaped specimen with strain gauge for fuel cladding; (b) plate specimen from flattened cladding (after [9.389]).

For many materials it is necessary to conduct up to ten million cycles to cover the range of operation. For Zircaloy fuel tubes subjected to thermal stress loading the relevant number of cycles is in the range of one thousand to one million. At a cyclical frequency of 1 Hz the laboratory time required to reach 10^6 cycles is 11 days and 10^3 cycles is 16 mins. It has been shown that considerable time must be allocated for any extensive fatigue testing programme. Reference [9.389] reports fully reversed bending tests on the C shaped specimen obtained from a ring cut from fuel cladding tubes (Fig. 9.141). Testing was conducted either on the C specimen itself by attaching loading rods 180° apart from one another, or on the flat cantilever (plate) specimen obtained by flattening the C specimen. Strains were calculated by finite element analysis of the specimen and compared with measurements using strain gauges. The excellent agreement between the two shown in Fig. 9.142 allowed strain to be calculated from loading rod displacement and eliminated the need for strain gauge use at 623 K (350°C).

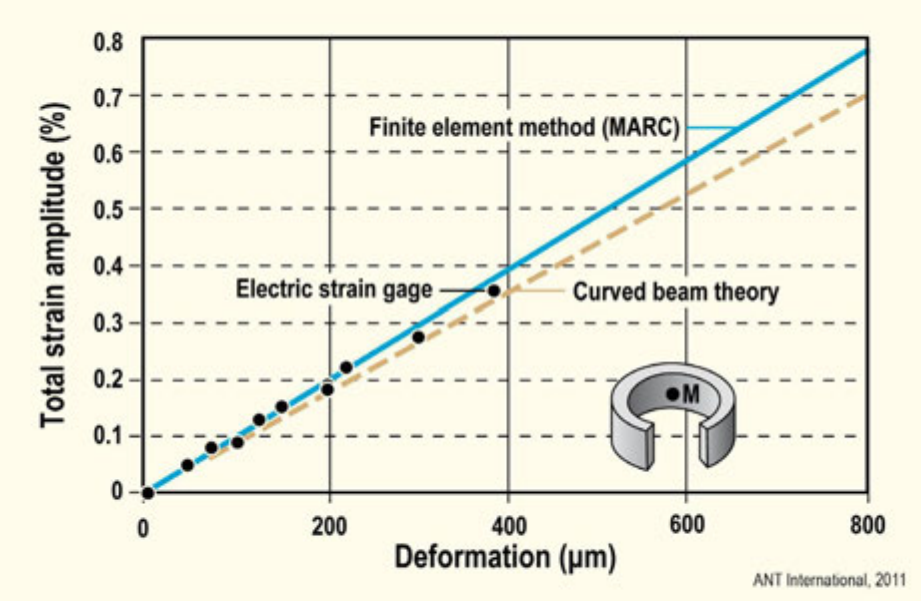

FIG. 9.142. Comparison of the measured and calculated relationship between total strain amplitude and diametral deformation of fuel cladding (after [9.389]).

Another approach to fully reversed, axial strain loading of Zircaloy used a thin plate specimen designed to resist buckling [9.390] (Fig. 9.143). It was cycled in tension and compression. Transverse strain across the gauge of the specimen was measured with an extensometer, and load measured by a standard load cell. Axial strain was then calculated from the transverse strain by use of the measured plastic contractile strain ratio of the specimen, using:

$$\varepsilon_t = L/A_0E + C\Delta W/W_0 \qquad (9.45)$$

where

ε_t	is equal to total strain (elastic and plastic);
L	is equal to uniaxial applied load;
A_0	is equal to specimen cross-sectional area;
W_0	is equal to gauge width;
ΔW	is equal to measured transverse strain;
C	is equal to measure contractile strain ratio;

and E is equal to elastic modules.

Another specimen, shown in Fig. 9.144, had a circular cross-section [9.391]. This type of specimen is excellent for obtaining basic fatigue data on Zircaloy but does not conform to any reactor component. Strain cyclical tests were made under total axial strain controlled by axial extensometers attached to the gauge length.

Kubo et al. [9.392] used a thin cantilever specimen cycled using the apparatus described in Fig. 9.145. A fatigue apparatus for testing conventional specimens in the strain controlled mode is included in Fig. 9.145 [9.393].

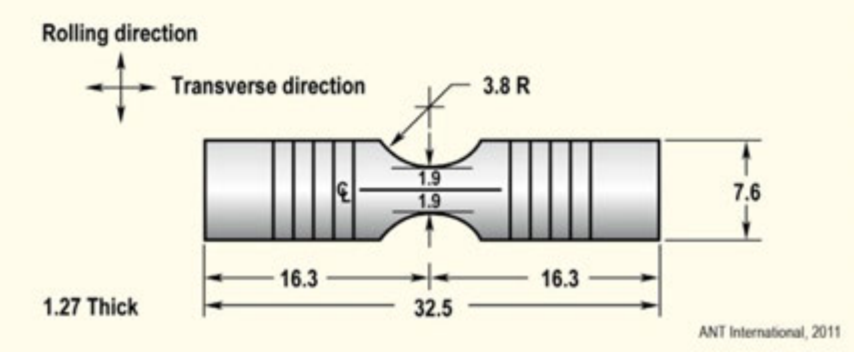

FIG. 9.143. Typical fatigue specimen [9.390].

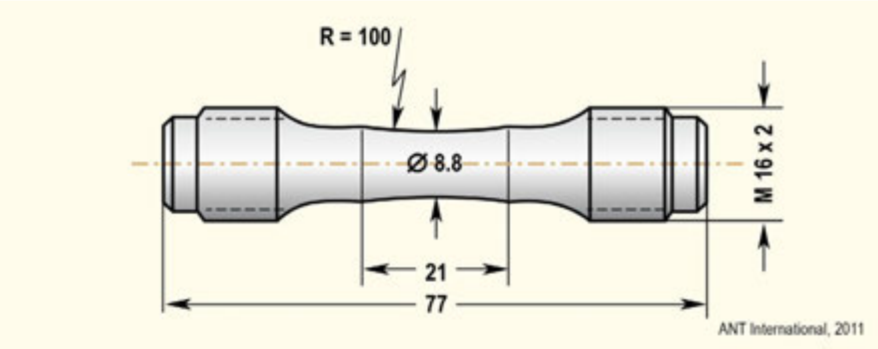

FIG. 9.144. Typical test specimen (measurements in mm) (after [9.391]).

9.5.6. Fractography

Fatigue cracks in ductile metals such as Zircaloy develop in three distinct stages: initiation, propagation and rupture. The initiation stage occurs early in life, at less than 20% of the total number of cycles to failure. It is influenced strongly by surface irregularities — stress concentration, notches, scratches — but for a smooth surface is characterized by the formation of slip bands, as shown in Figs 9.145 and 9.146, which are microscopic areas where the cyclical strain is concentrated [9.392]. The dark lines result from concentrated strain in the polycrystalline material. The existence of slip bands does not necessarily mean that the material will eventually fail, as slip bands are sometimes observed at stresses or strains lower than the endurance limit. In Fig. 9.146 it is seen that some of the slip bands have developed into a crack under the influence of an imposed tensile stress. The location of these cracks is likely where a fatigue crack would have eventually formed. In this example of Zircaloy, cracks initiated very early, at less than 10% of the fatigue life [9.392]. This time corresponds to about

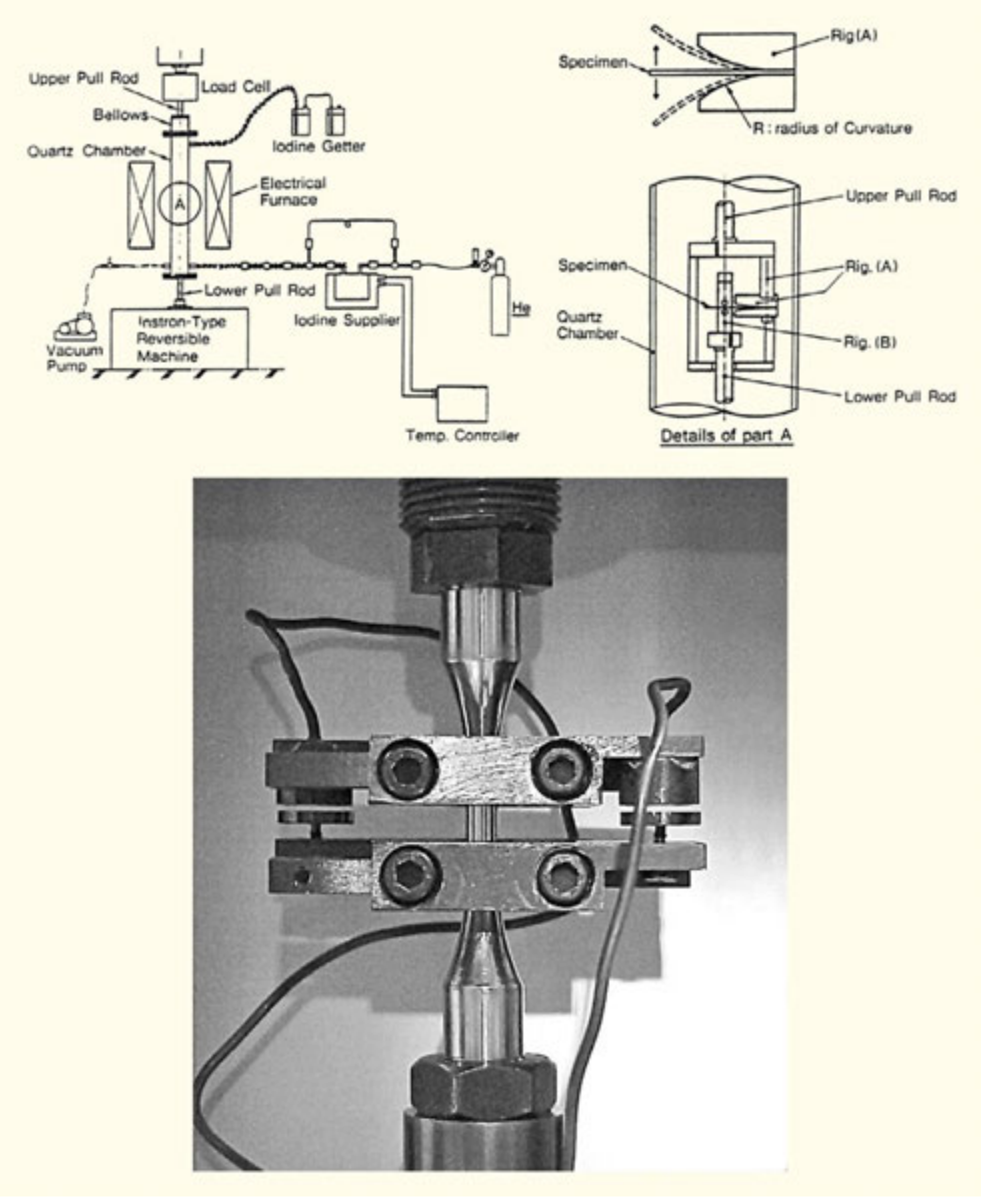

FIG. 9.145. Top: schematic diagram of test apparatus [9.392]; bottom: apparatus for testing conventional specimens in strain controlled mode (after [9.393]).

the same time as hysteresis loops become stable under plastic strain cycling [9.390, 9.392]. In irradiated material, slip bands are analogous to dislocation channels, discussed in Chapter 6, in Volume 2 of this publication, and in Section 9.2.2.

If the applied strain or stress is very high, crack propagation is rapid, resulting in a fracture surface similar in appearance to a tensile failure, as shown in Figs 9.21 to 9.24. At intermediate and low values of applied strain or stress, fatigue crack propagation occurs slowly, with the crack front advancing a small amount during each tensile portion of the cycle. This process results in telltale markings, called striations, on the fracture surface (Fig. 9.147). When viewed at high magnification in a scanning electron microscope (SEM) these striations mark the path of the crack, as shown for high strength steel in Fig. 9.148 [9.382, 9.394]. The crack path as viewed by light usually appears to

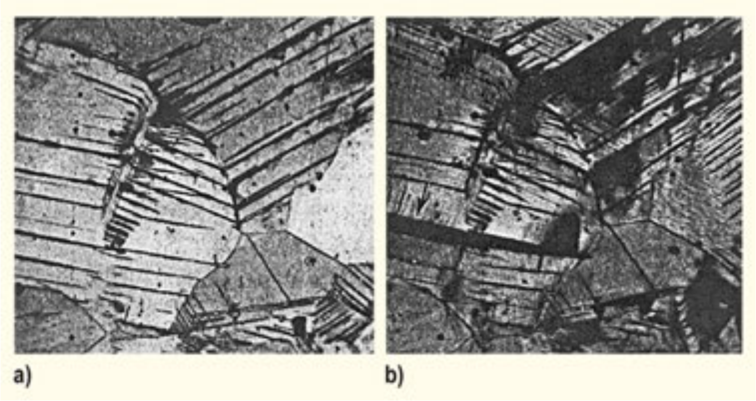

FIG. 9.146. The opening of cracks in fatigue slip bands by a tensile stress: (a) polycrystals showing slip bands caused by fatigue; (b) same specimen after the crack in a slip band has been opened by a tensile stress (after [9.392]).

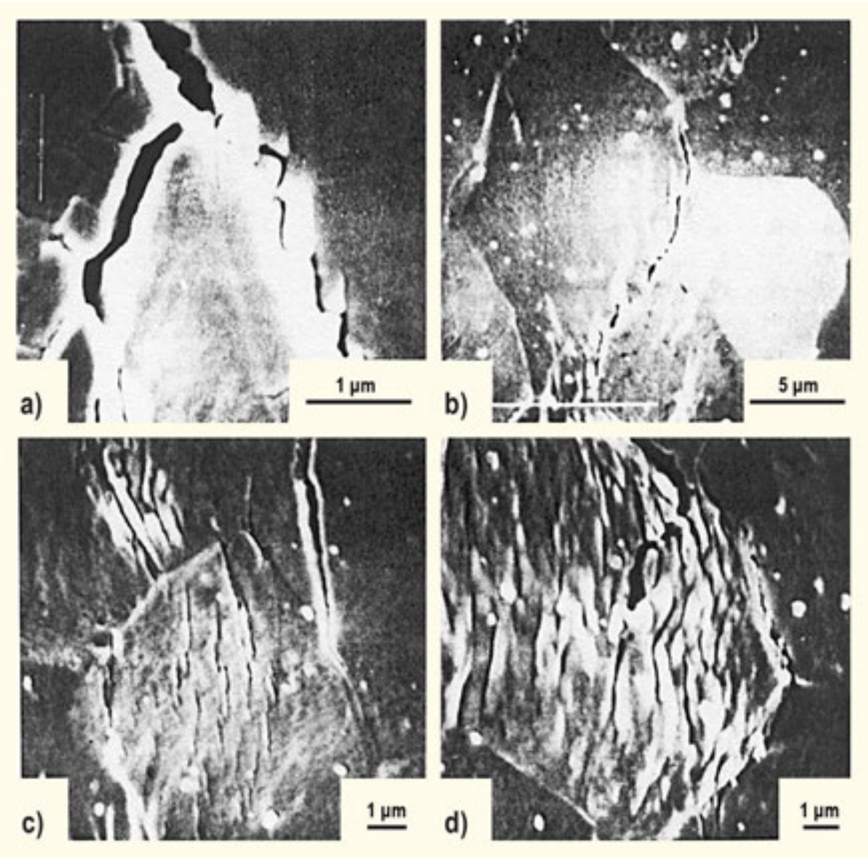

FIG. 9.147. Surface topography of fatigued specimens: (a) and (b) fatigue damage in the vicinity of grain boundaries; N = 200; (c) and (d) slip band extrusions and transgranular cracks extending along the extrusions; N = 500; $\varepsilon\rho \approx 1\%$ in an inert atmosphere (after [9.392]).

be flat, with curved markings, called beach marks or chevrons, normal to the crack path leading away from the crack initiation point. The failure of a component made from steel is illustrated in Fig. 9.149.

The fatigue fracture details for Zr alloys are sparse. Examples in Zircaloy-2 after testing at 623 K (350°C) are provided in Fig. 9.150, where some evidence of striations are indicated [9.389, 9.392]. For tests in which other forms of crack propagation are the main focus, for example, delayed hydride cracking and fracture toughness, fatigue at room temperature is often used to produce

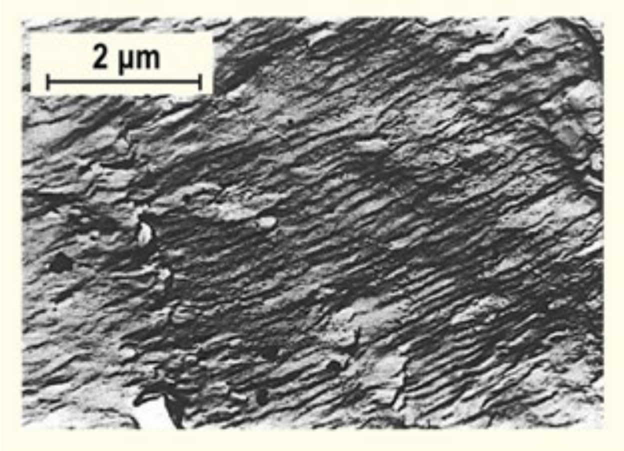

FIG. 9.148. Fatigue striations spaced about 0.12 µm apart, from the fracture surface of steel (after [9.382]).

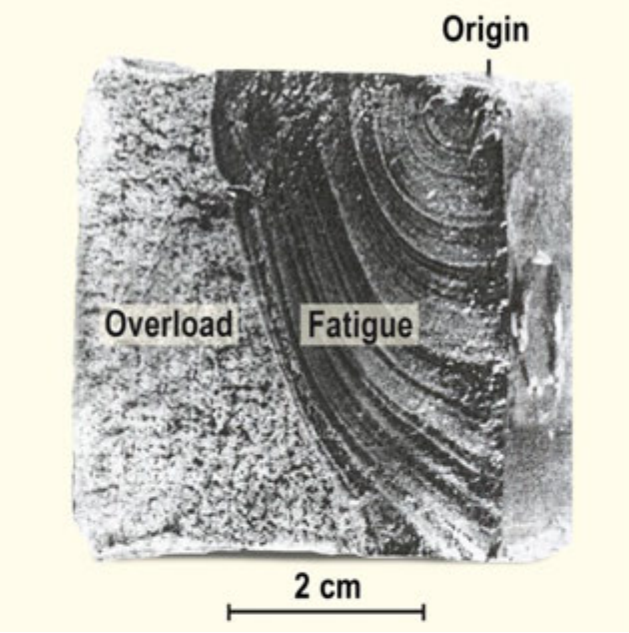

FIG. 9.149. Fracture surface for fatigue and final brittle fracture in a steel member (after [9.382]).

a sharp starter crack. The fatigue striations are not obscured by oxidation and are readily observed, as shown in Fig. 9.151. These examples are for CWSR Zircaloy-4, where the striation spacing is between 0.2 and 0.5 µm.

Macroscopically, the crack usually propagates normally to the applied tensile stress, but in a highly textured Zircaloy preferred slip planes such as $(10\bar{1}0)$ are favoured.

At some point the final failure occurs rapidly owing to a stress overload (where the local stress on the uncracked portion is greater than the ultimate tensile stress). In ductile materials such as Zr alloys this final failure is often by shear, and a shear lip at 45° to the surface can be expected.

Dislocation structures after fatigue have been observed [9.391, 9.392, 9.395] and are shown in Fig. 9.152. The dislocation arrangements after fatigue tend to be in tight clusters, which stabilize at about the time that the fatigue hysteresis loop becomes stable. More understanding in this area could lead to microstructures that are more resistant to fatigue damage if such work was justifiable for performance reasons.

9.5.7. Fatigue in irradiated and unirradiated Zircaloy

Table 9.24 lists published reports on fatigue of (mostly) Zircaloy, giving the topic studied and the year of publication [9.115, 9.372, 9.374, 9.389–9.430].

TABLE 9.24 STUDIES OF FATIGUE IN ZIRCONIUM ALLOYS WITH THE VARIABLES STUDIED

Authors	Year	Irradiated	Environment	Crack growth	Basic	Source
O'Donnell & Langer	1964	x				[9.374]
Mowbray	1965		x			[9.426]
James	1969		x	x		[9.396]
James	1970		x	x		[9.425]
Wanhill et al.	1972		x			[9.414]
Lee	1972				x	[9.397]
Hosbons	1973		x			[9.411]
Walker & Kass	1974	x		x		[9.398]
Pettersson	1975	x	x		x	[9.407]
Lee & Hill	1976				x	[9.399]
Snowden & Stathers	1977				x	[9.400]
Kuhlmann-Wilsdorf & Laird	1979				x	[9.420]
Pandarinathan & Vasudevaon	1980		x			[9.409]
MacEwen et al.	1981				x	[9.417]
Pickles & Picker	1981	x	x	x		[9.401]
Nakatsuka & Hayashi	1981		x			[9.410]
Pickles & Picker	1983	x	x	x		[9.428]
Gee	1984		x	x		[9.429]
Kubo et al.	1986		x			[9.392]
Armas & Alvarez-Armas	1987				x	[9.391]
Brun et al.	1987				x	[9.402]
Staal (review)	1987	x	x	x		[9.412]
Gee et al.	1989		x	x		[9.427]
Schuster & Lemaignan	1989		x		x	[9.413]
Christodoulou	1989				x	[9.418]
Rowland et al.	1991	x				[9.372]
Nakatsuka et al.	1991	x	x			[9.389]
Wisner et al.	1994	x	x	x	x	[9.390]
Soniak et al.	1994	x				[9.405]
Chow et al. (Zr2.5Nb)	1996	x				[9.404]
Xiao & Gu	1997				x	[9.421]
Prat et al.	1998		x		x	[9.416]

TABLE 9.24 STUDIES OF FATIGUE IN ZIRCONIUM ALLOYS WITH THE VARIABLES STUDIED

Authors	Year	Irradiated	Environment	Crack growth	Basic	Source
Lin & Haicheng	1999	x		x	x	[9.408]
Adamson	2000				x	[9.395]
Li et al.	2003				x	[9.419]
Ishimoto et al.	2003	x				[9.403]
Armas et al.	2004				x	[9.422]
Alvarez-Armas & Herenu	2004				x	[9.424]
Bolmaro et al.	2004				x	[9.423]
Tan et al. (Zr-Sn-Nb-Fe-Cr)	2006		x		x	[9.415]
Kim et al.	2007				x	[9.406]
Onimus & Béchade	2009				x	[9.115]
Garlea et al.	2010		x	x	x	[9.430]

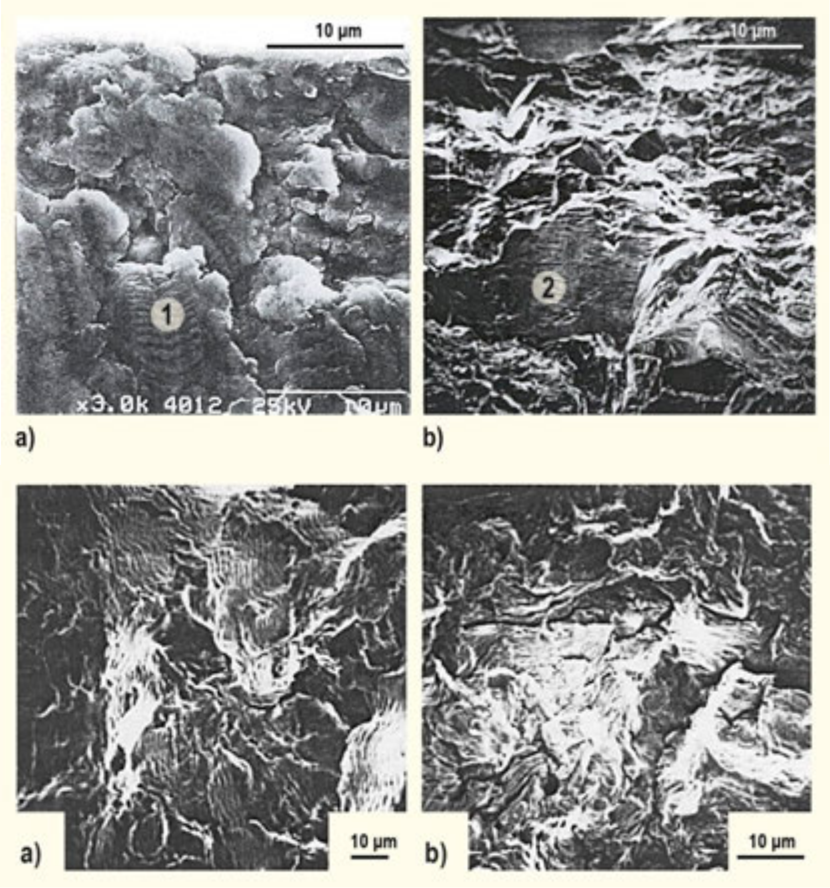

FIG. 150. Fracture surface after fatigue tests at 623 K (350°C): a) unirradiated; area 1; 'tyre' track; b) irradiated; area 2: quasi-striation patterns (after [9.389]). Surfaces of annealed Zircaloy-2 specimens fractured in an inert atmosphere at 623 K (350°C): (c) ductile striations at $\Delta\varepsilon p \approx 1.5\%$; (d) wrinkled patterns at $\Delta\varepsilon p \approx 0.33\%$ (after [9.392]).

The first article published by O'Donnell and Langer in 1964 [9.374] included data generated within the US Navy's nuclear programme that are not easily obtainable elsewhere. This article, entitled Fatigue Design Basis for Zircaloy Components, was used by the NRC [9.373], to set their

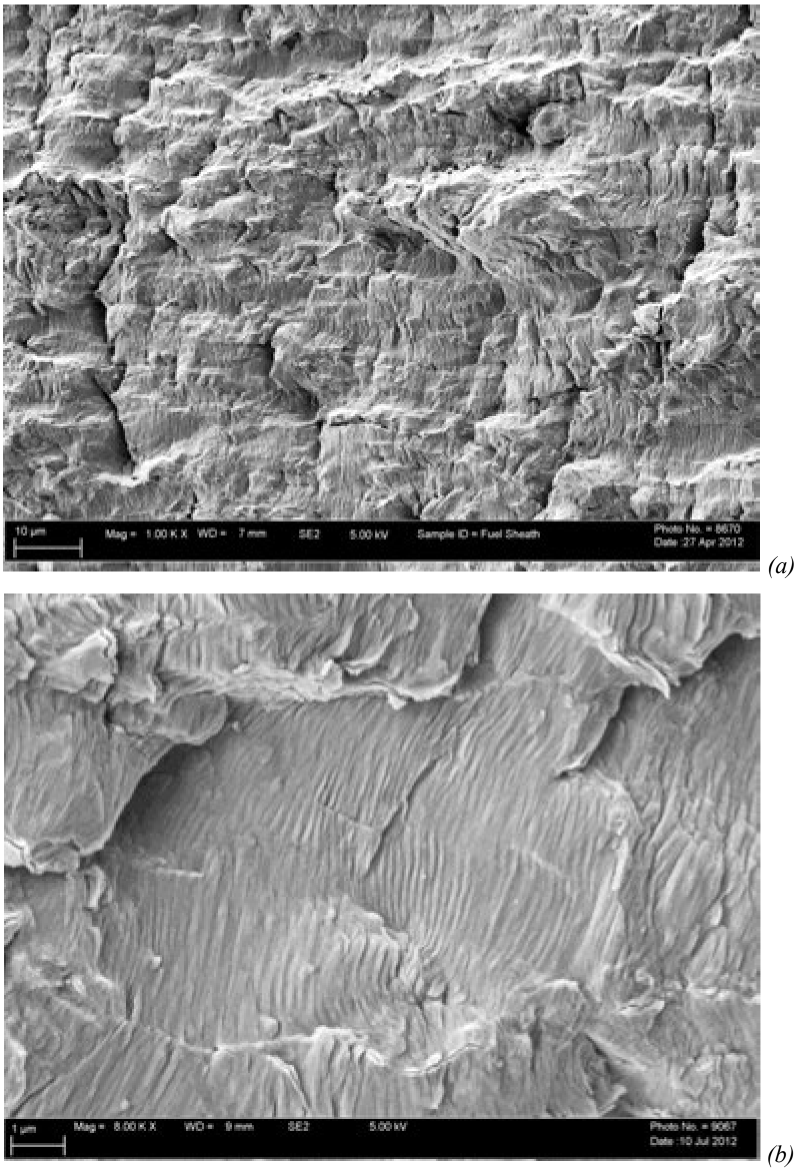

FIG. 9.151. (a) Low magnification photomicrograph of fatigue striations in Zircaloy-4 fuel cladding formed at room temperature (C. Mayhew, AECL); (b) high magnification photomicrograph of fatigue striations in Zircaloy-4 fuel cladding formed at room temperature (C. Mayhew, AECL).

fatigue guidelines. The results from this landmark article are reviewed along with subsequent work to show how later data supplement and add to its results. The emphasis is on irradiated material, but data for unirradiated Zircaloy are required for perspective. Very little information on Zr-Nb-type alloys is available with the exception of Zr-2.5Nb [9.404].

O'Donnell and Langer [9.374] were mainly interested in low cycle fatigue design ($<10^4$ cycles), although some limited data were obtained to greater than 10^6 cycles. A mixture of bending and axial fatigue was used, although the article does not describe the experimental procedures in detail. (Experimental techniques may be described in references given in Ref. [9.373], but those references are not readily available.) Although in most cases the data were apparently obtained by strain cycling, the S–N data are reported as a 'fictitious' stress obtained by multiplying the total strain amplitude ($\varepsilon_t/2$) by the elastic modulus (E).

The O'Donnell and Langer [9.374] S–N data at room temperature and 600°F (588 K (315°C)) for unirradiated Zircaloy-2 are shown in Fig. 9.153 and for irradiated Zircaloy-2 in Fig. 9.154. The

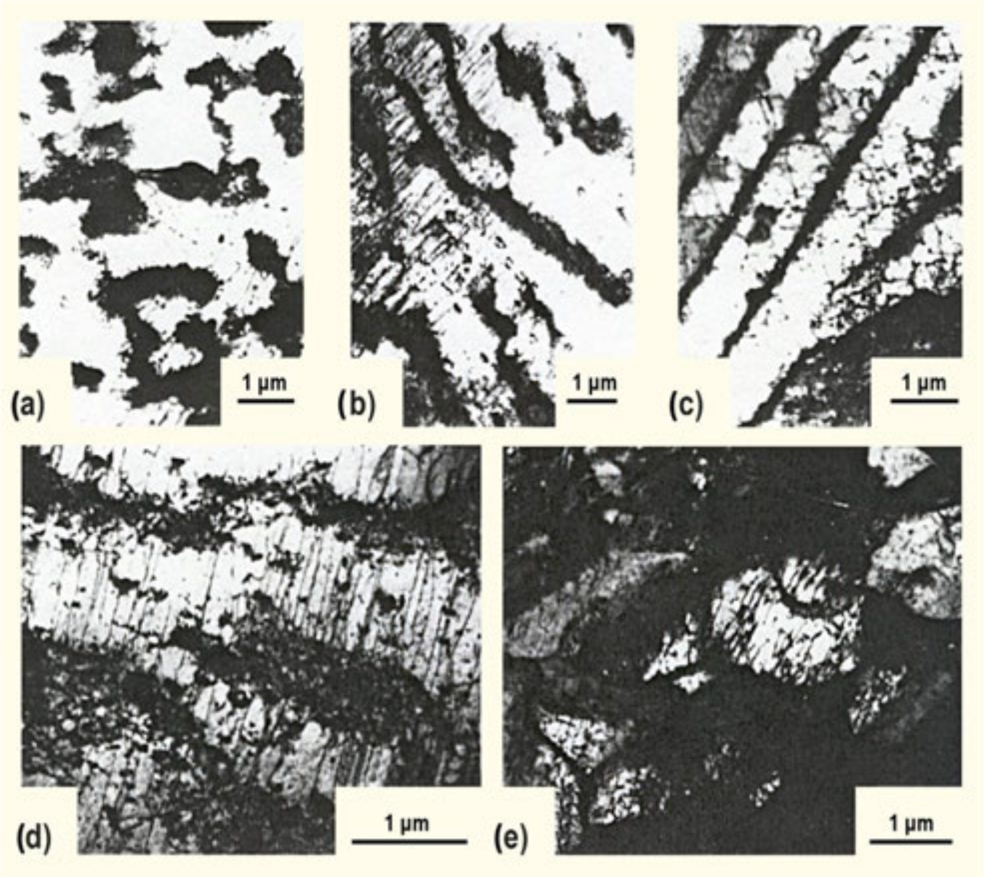

FIG. 9.152. Dislocation substructures produced at Δερ ≈1.0%: (a)–(d) wall structures, N = 500; (e) all structures, N = 200 (after [9.392]).

maximum neutron fast fluence for the data is about 5.5 × 10^{25} n/m^2 (E > 0.625 MeV), which is equivalent to the low burnup of 25 kWd/kg U. For reference, the dark lines under the data sets indicate the design line for irradiated material based on a safety factor of either 2 on the stress amplitude or a factor of 20 on cycles to failure. No effect of crystallographic texture or welding was observed.

Three major conclusions are drawn from these data:

(1) Zircaloy has a fatigue limit of 180 MPa at about 105 cycles.
(2) Irradiation slightly lowers the fatigue life in the low cycle range, below about 104 cycles.
(3) Irradiation has no effect on the fatigue life on the high cycle range, over about 105 cycles.

O'Donnell and Langer [9.374] also reported an effect of mean stress on fatigue life, as shown in Fig. 9.155. As expected, the fatigue life decreases under the influence of increasing mean stress. They also conducted constant total strain cycling and found that unirradiated material hardened during cycling, while irradiated material softened. The latter point is illustrated in Fig. 9.156, where it is seen that for each imposed ε_t, the load required decreased with cycles until a stable load value was reached. This load would be the point where the hysteresis loop became stable. Using these data to construct a modified Goodman diagram, the effect of the maximum mean stress was determined, and superimposed in Fig. 9.153 and Fig. 9.154.

The design curve for irradiated material, including the safety factors, is obtained by taking the most conservative best fit curves for unirradiated and irradiated material. This design curve, shown in Fig. 9.157 for 10^1–10^6 cycles based on the fictitious stress, is the approved NRC design curve and must be used in the USA unless other datasets can be justified. The fluence applicable to

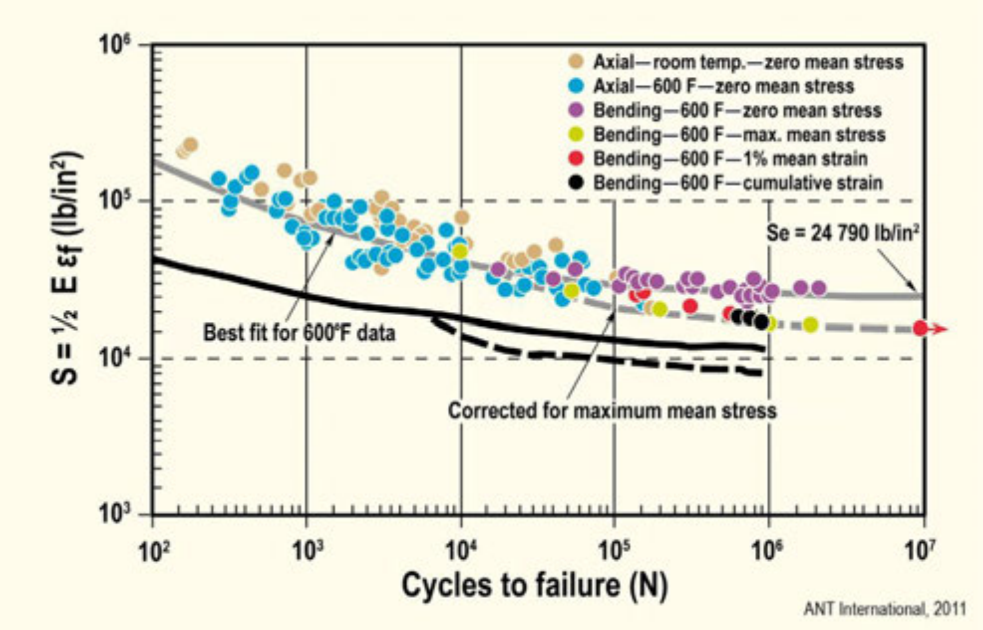

FIG. 9.153. Fatigue data for unirradiated Zircaloy-2 (after [9.374]).

this curve is up to 5.5 × 10^{25} n/m^2 (E > 0.625 MeV), which is equivalent to about 2 × 10^{25} n/m^2 (E > 1 MeV).

Since Ref. [9.374] was published in 1964, other fatigue data have been generated. A comparison of data to Ref. [9.374] is shown in Fig. 9.158 and Fig. 9.159. For unirradiated material (both Zircaloy-2 and -4, tested in a variety of ways), Fig. 9.158 indicates that Ref. [9.374] is a conservative, low fit to the data. Results for irradiated material (Fig. 9.159) [9.389], indicate a reasonable fit to the data, with the O'Donnell and Langer [9.374] design curve (dark line) being conservative. Another comparison for irradiated material is given in Fig. 9.160, for constant total strain cycling; again, Ref. [9.374] is conservative and low [9.390].

The effect of irradiation on fatigue life is summarized in Table 9.25. It can be seen that there is some controversy about this effect. In the low cycle region some results indicate a decrease in fatigue life [9.374, 9.390], while others suggest either an increase or no effect. Although there are fewer sets of data, the conclusion is similar with high cycle fatigue. It is likely that the differences are related to the method of testing and data reporting.

TABLE 9.25. EFFECT OF IRRADIATION ON FATIGUE LIFE NEAR 573 K (300°C)

Author	Year	Fluence, n/m^2 × 10^{25} (E > 1 MeV)	Effect of irradiation on fatigue life		Source
			Low cycle	High cycle	
O'Donnell and Langer	1964	2	Reduce	No effect	[9.374]
Wisner et al.	1994	1–7	Reduce	—	[9.390]
Pettersson	1975	0.3	Slight increase	—	[9.407]
Nakatsuka et al.	1991	6	Increase	Decrease	[9.389]
Soniak et al.	1994	4–8	No effect	Decrease	[9.405]
Chow et al.	1996	6	Slight increase	Slight increase	[9.404]
Ishimoto et al.	2003	15	increase	Increase	[9.403]

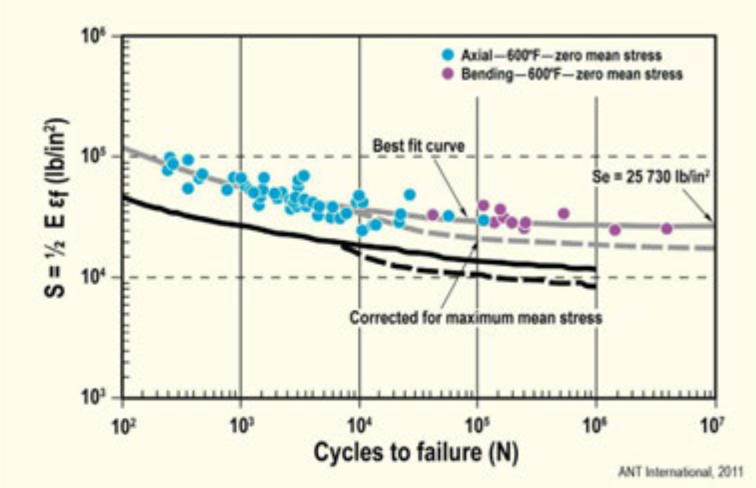

FIG. 9.154. Fatigue data for irradiated Zircaloy-2 (1.5 × 10^{25} to 5.5 × 10^{25} n/m²) [E > 0.625 MeV] (after [9.374]).

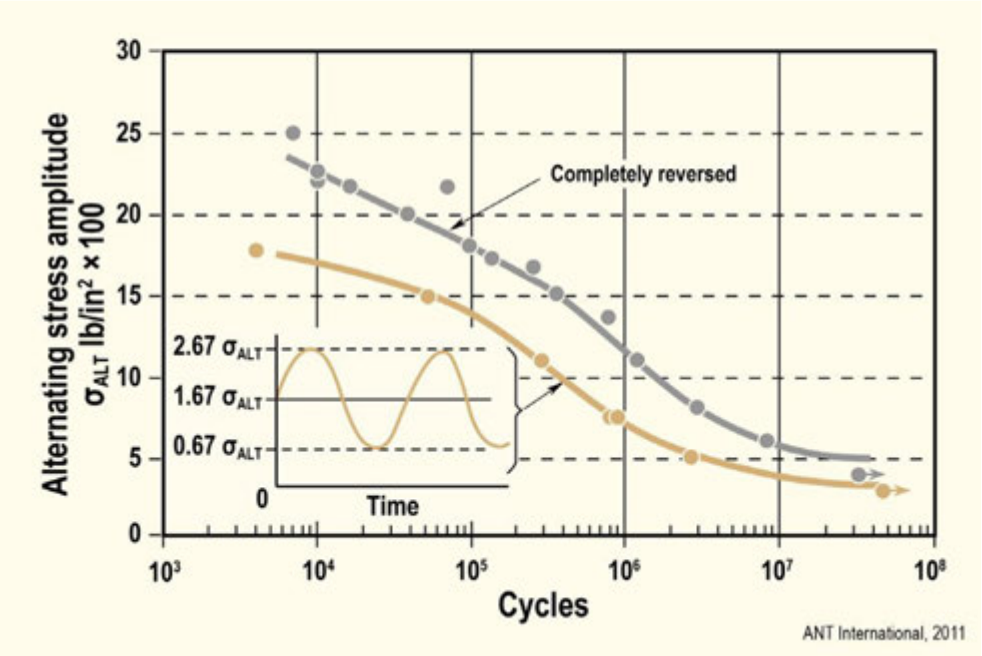

FIG. 9.155. Effect of mean stress on fatigue life of Zircaloy-2 (after [9.374]).

A comparison of two datasets is shown in Fig. 9.161 and Fig. 9.162. Irradiated material fluences for both, about 6 × 10^{25} n/m² ($E > 1$ MeV), are considerably higher than for Ref. [9.374]. Wisner et al. [9.390] conducted testing in constant total axial strain cycling and reported data as either total or plastic strain amplitude. They observed the expected cyclical hardening of unirradiated material and cyclical softening of irradiated material, with stable hysteresis loops developing (Fig. 9.163) after less than 10% of the fatigue life at any given strain. Nakatsuka et al. [9.389] conducted tests in constant total strain bending and reported data on total strain amplitude. They reported mainly softening for both unirradiated and irradiated material during testing, indicating that a stable plastic strain (hysteresis loop width) was not reached. It could be that both results are valid for the particular test method used; these results re-emphasize the importance of either closely simulating actual in-reactor operating conditions during laboratory testing or using conservative

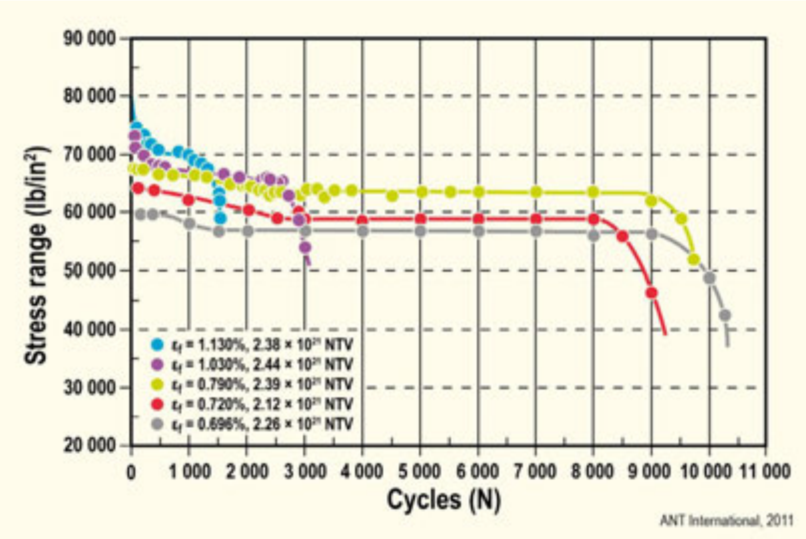

FIG. 9.156. Axial strain fatigue data for irradiated alpha-annealed Zircaloy-2 at 589 K (316°C) (longitudinal direction) (after [9.374]).

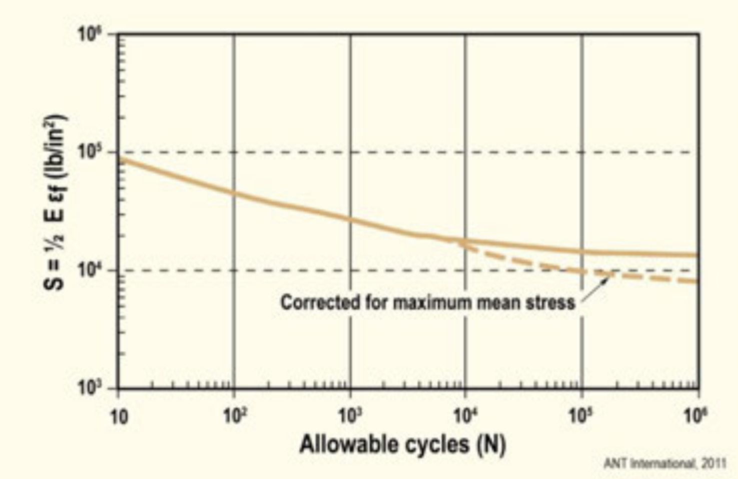

FIG. 9.157. Design curve for irradiated Zircaloy-2 or -4. Temperature 293–588 K (20–315°C). Total neutron fluence < 5.5 × 10^{25} n/m^2 (E > 0.625 MeV) (after [9.374]).

safety factors for design. (See Section 9.5.3 for a description of hardening and softening behaviour.) It is worth reiterating that the original fluences reported in Ref. [9.374] were low, and that the effect of high irradiation fluence was to reduce fatigue lifetime even further [9.390].

In the high cycle regions, some results [9.389, 9.405] disagree with Ref. [9.374]. Soniak et al. [9.405] performed fatigue tests at 623 K (350°C) at 1 Hz on irradiated tube portions cut from fuel cladding, using a device for tube fatigue by repeated internal pressurization. Data shown in Fig. 9.164 indicate that the fatigue (endurance) limit is significantly lowered by irradiation, from a maximum hoop stress of 350 MPa down to between 250 and 210 MPa. They also indicate that the effect saturates with fluence. Although the effect of irradiation is different from that reported by Ref. [9.374], comparison of the data with the O'Donnell and Langer [9.374] design curve for irradiated material (Fig. 9.157) indicates that Ref. [9.374] would still be conservative (i.e. the data fall to the right of the O'Donnell and Langer curve).

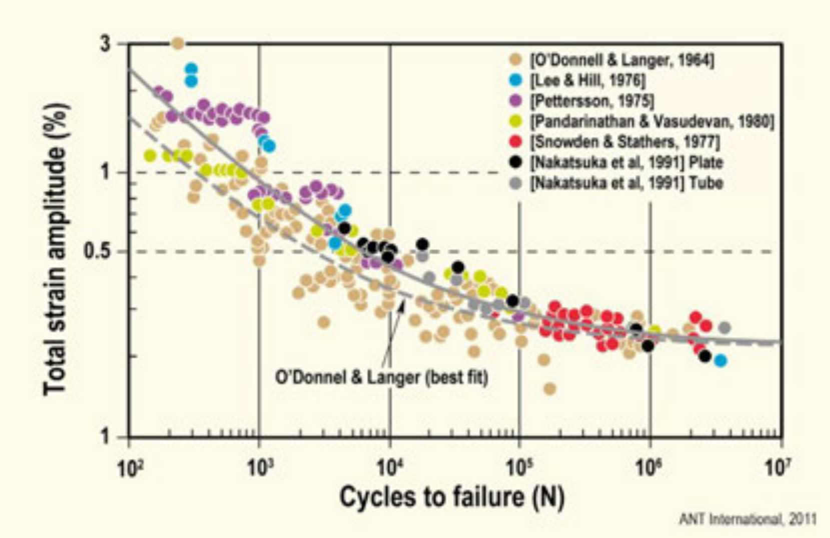

FIG. 9.158. Total strain amplitude vs. cycles to failure for unirradiated Zircaloy-2 tested between 293 and 673 K (20 and 400°C) (after [9.389]).

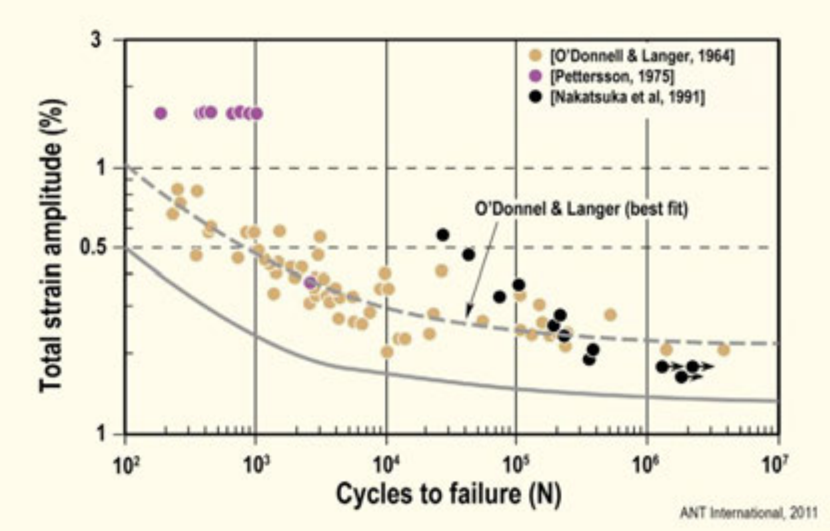

FIG. 9.159. Total strain amplitude vs. cycles to failure for irradiated Zircaloy-2 from 293 to 673 K (20 to 400°C). The lower curve is the O–L design curve (after [9.389]).

Zircaloy-2 fuel cladding with a zirconium liner was power cycled under simulated daily load following (175 cycles) and automatic frequency control modes (40 000 cycles) of operation [9.374]. No adverse effects were observed on the cladding. Hot cell fatigue tests were performed on cladding samples from the test rods to check the effect of load cycling on the fatigue strength of the Zr liner cladding. As shown in Fig. 9.165, the fatigue strength was equivalent to or higher than equivalently irradiated Zircaloy-2, which had not been previously power cycled [9.376].

In another test series designed to determine fatigue life under cyclical pressurization, Zircaloy-4 tubing was pressurized internally [9.406]. With a 1 Hz sawtoothed pressure cycle for unirradiated stress relieved tubing at 623 K (350°C), the stress-lifetime diagram fell slightly to the right of the O'Donnell and Langer [9.374] curve (Fig. 9.166). For this type of cycling, creep also contributed to the deformation.

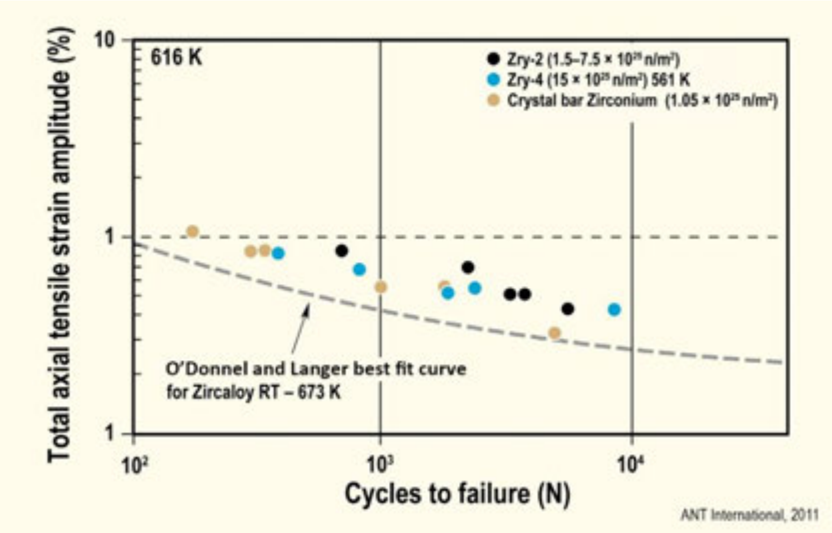

FIG. 9.160. Total axial tensile strain amplitude vs. cycles to failure for irradiated Zircaloy-2, Zircaloy-4 and crystal bar zirconium (after [9.390]).

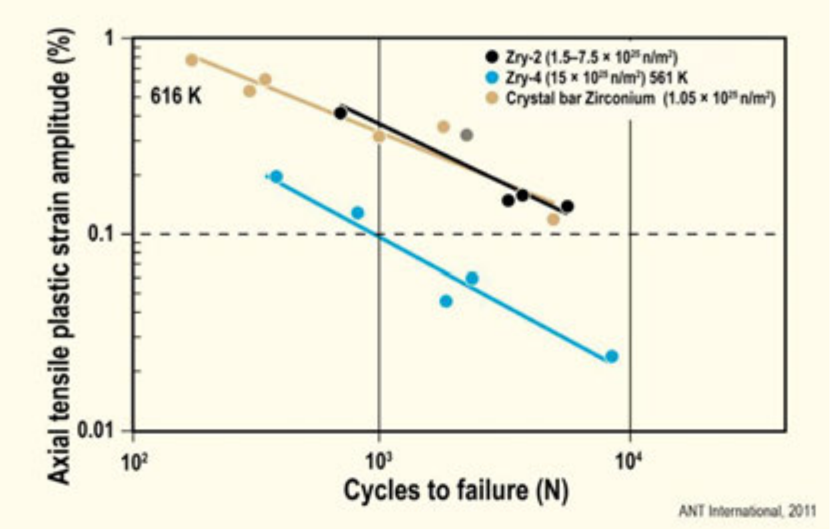

FIG. 9.161. Tensile plastic strain amplitude vs. cycles to failure for irradiated Zircaloy-2, Zircaloy-4 and crystal bar zirconium (after [9.390]).

9.5.8. Effects of temperature

The original data of O'Donnell and Langer [9.374] indicated a small fatigue life decrease when changing temperature from 295 to 573 K (22 to 300°C). Later studies present the opposite conclusion. A substantial increase in the fatigue life of Zircaloy-2 with plastic strain cycles of 1% was found in the same temperature range [9.407]; the fatigue life increased from 370 cycles at 293 K (20°C), through 620 cycles at 523 K (250°C) to 1200 cycles at 573 and 623 K (300 and 350°C), with a small drop-off at 673 K (400°C) to 950 cycles. Note there is a plateau in the 573–673 K (300–400°C) range, most likely related to the strain ageing phenomenon (see Section 9.2.1).

To check the difference in fatigue lives of recrystallized and stress relieved Zircaloy-4, uniaxial push-pull tests were conducted [9.408]. At both 298 K (25°C) and 673 K (400°C), the low cycle fatigue life was longer for the recrystallized material than for the stress relieved material (Fig. 9.167), reflecting the superior ductility at both temperatures. The fatigue lives were higher for both materials at the higher temperature (Fig. 9.168). A similar increase was found for Zircaloy-2

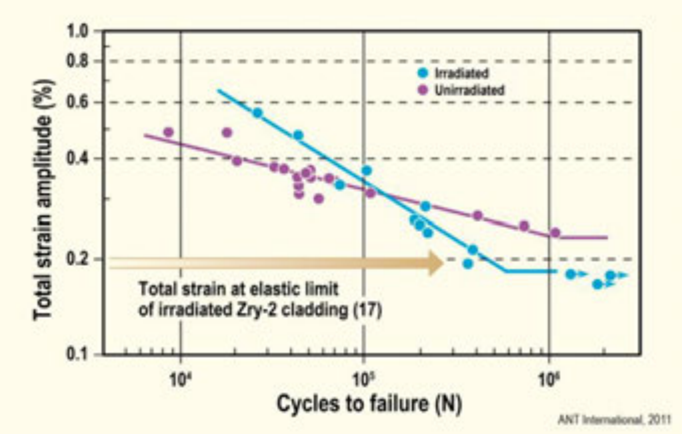

FIG. 9.162. Change in failure cycles in Zircaloy-2 due to neutron irradiation tested in inert gas environment at 623 K (350°C) (after [9.389]).

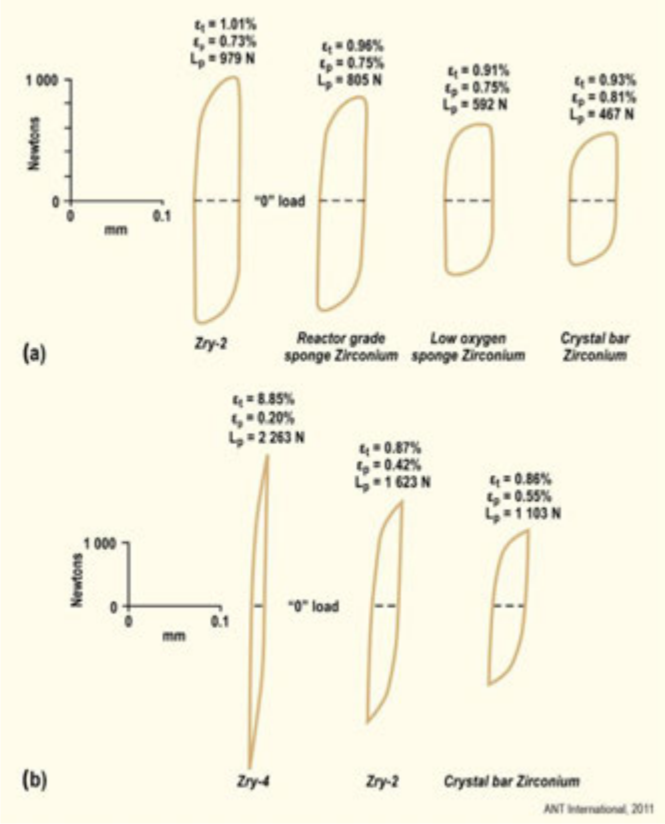

FIG 9.163. Mid-life stabilized hysteresis loops for (a) unirradiated and (b) irradiated Zircaloy and zirconium (after [9.390]).

tested by rotational bending at constant bending strain in the temperature range 293–573 K (20–300°C), as shown in Fig. 9.169 [9.409]. Although the temperature dependence should be similar for the various experiments, different techniques will produce variation in observed fatigue lives.

9.5.9. Effects of iodine

Iodine is implicated in failure by pellet–clad interactions and will be discussed in detail in Section 9.6. The observations of the effects of iodine on fatigue differ, in part because of technique

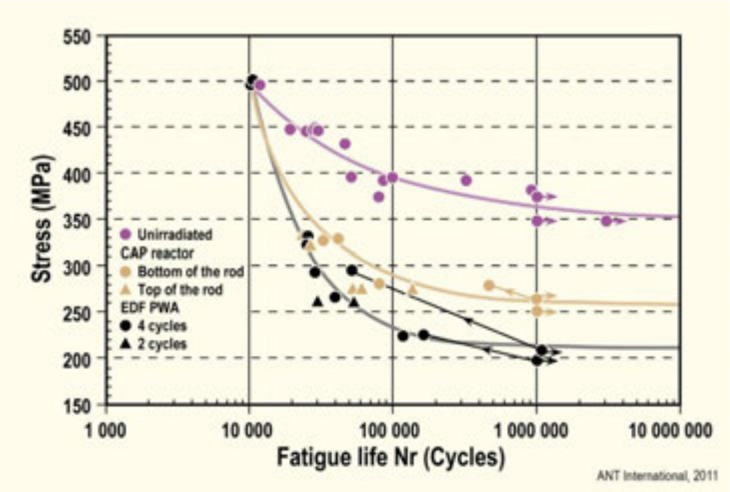

FIG. 9.164. Irradiation effect on the S–N curve (maximum stress vs. the number of cycles to rupture) at 623 K (350°C) and 1 Hz: "→" unfailed specimens and "↖" specimens tested at a σ_1 stress during 10^6 cycles then tested at a $\sigma_2 > \sigma_1$ stress up to rupture (after [9.405]).

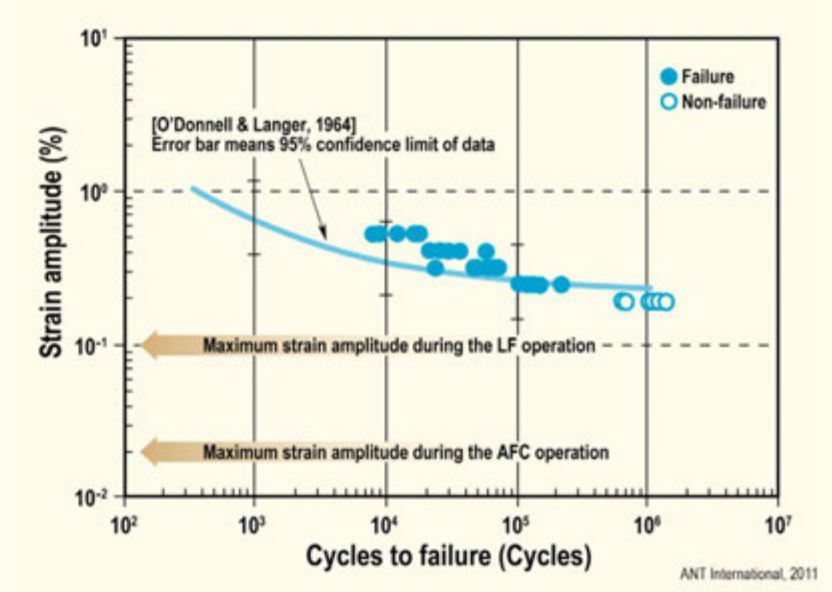

FIG. 9.165. Fatigue test results of Zircaloy-2 cladding with a Zr-liner after power cycling operation tests (after [9.372]). LF — load following; AFC — automatic frequency control.

differences. Although some results [9.410] indicate no effect of a concentration of 1 mg/cm^2 iodine at 623 K (350°C) on stress relieved Zircaloy-2, low cycle fatigue life can be reduced by iodine, with little effect on high cycle life. The earliest results [9.411], as reported in Ref. [9.412], show a reduction in cycles to failure by iodine in annealed Zircaloy-4 with 6% total applied strain at 573 K (300°C), where the lifetime was 212 cycles in air but was reduced to 136 cycles in air containing 30 g/m^3 iodine. This result was corroborated on annealed Zircaloy-2 plate in which the pressure of iodine was varied and a threshold pressure of about 27 Pa was observed in tests at 623 K (350°C), as shown in Fig. 9.170 [9.392]. No effect with 4 Pa iodine on cycles to failure was observed in tests at 623 K (350°C) on annealed Zircloy-2 cladding but a large effect was found in stress relieved Zircaloy-2 plate in which the threshold iodine pressure was about 0.1 Pa and the decline in fatigue life saturated around 30 Pa, as shown in Fig. 9.171 [9.389]. These tests indicated that cracks initiated very early in life (<10% of cycles to failure) in both iodine and air, but crack propagation was much faster in the presence of iodine. Fracture surface features were clearly delineated by environment, with

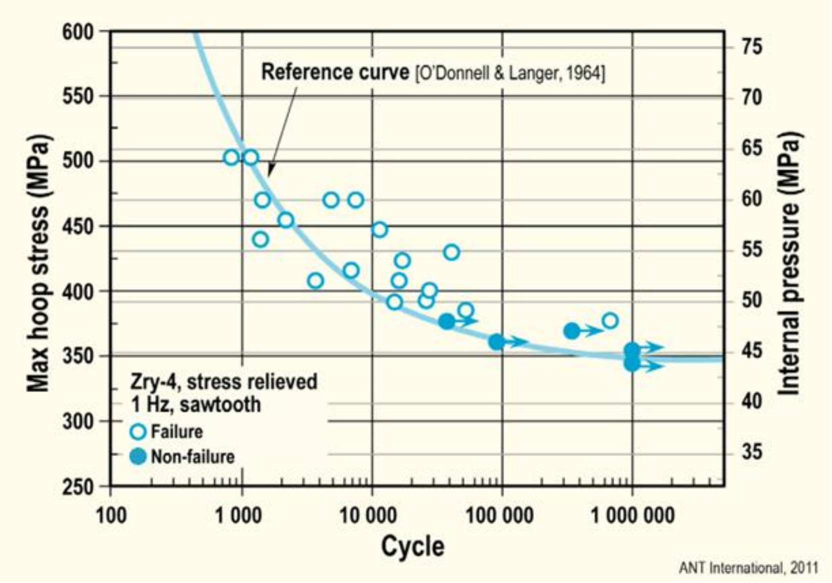

FIG. 9.166. Stress-life curve for Zircaloy-4 at 623 K (350°C) under internal pressure cycling (after [9.406]).

transgranular cleavage prominent in iodine. All the studies used iodine gas concentrations very far above those expected to be found inside fuel tubes, so it is not clear that the results are relevant to real fuel performance. Certainly, test conditions in addition to iodine concentration (material, material heat treatment, temperature, surface condition, fatigue technique) will affect the results.

Tests have also been conducted on Zircaloy in solutions of iodine in methyl alcohol at room temperature [9.413]. A decrease in fatigue life is shown for low cycles, but no decrease in fatigue strength for high cycles (Fig. 9.172). It was concluded that stress corrosion cracking (SCC) and corrosion fatigue in this environment occur simultaneously and almost independently. The fracture surface consists of grains fractured by pseudocleavage as seen during SCC crack growth, and other grains fractured by fatigue, with striation spacing similar to that obtained in dry air at the same ΔK_I.

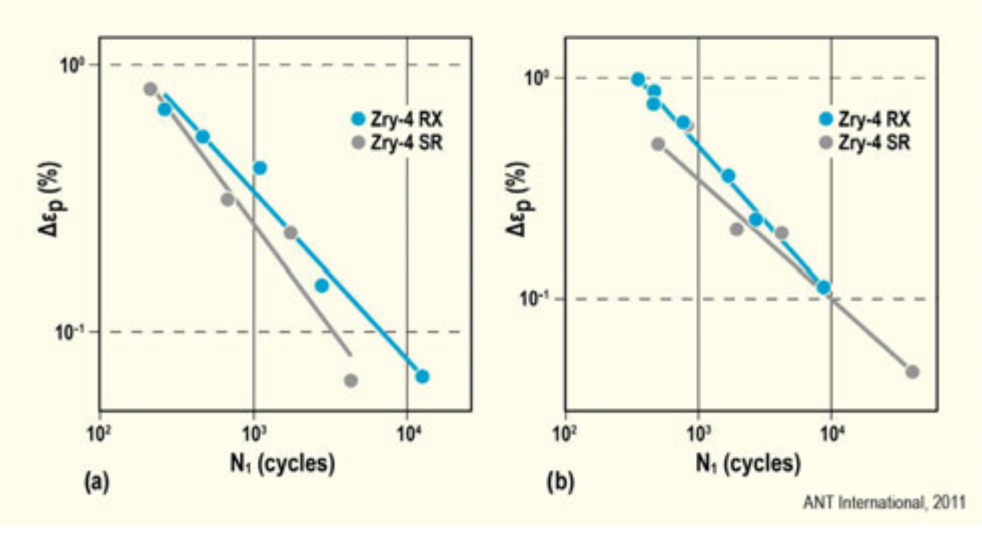

FIG. 9.167. Fatigue lives for recrystallized and stress relieved Zircaloy-4 at (a) 298 K (25°C) and (b) 673 K (400°C) (after [9.408]).

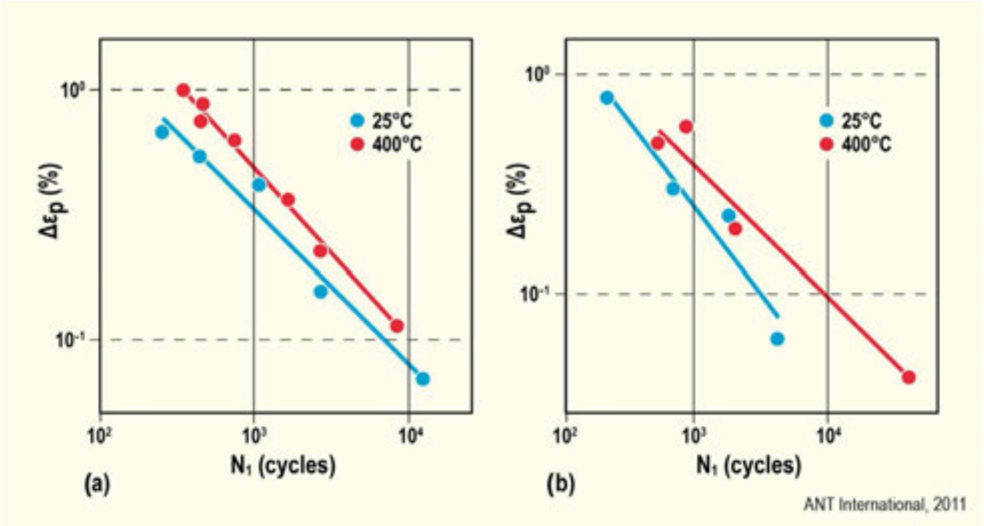

FIG. 9.168. Fatigue lives at 298 K and 673 K (25°C and 400°C) for (a) recrystallized and (b) stress relieved Zircaloy-4 (after [9.408]).

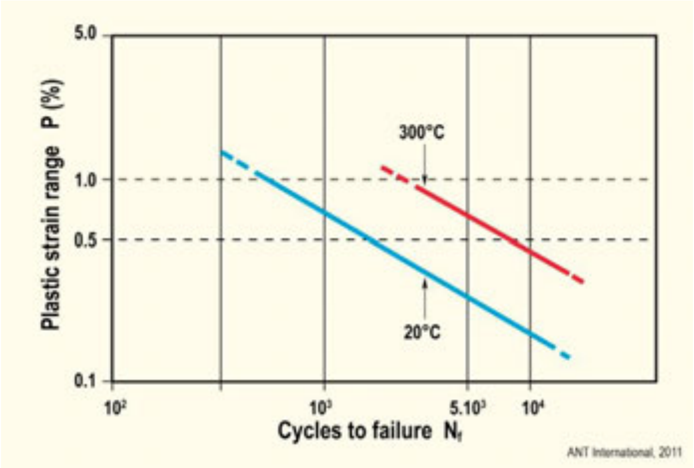

FIG. 9.169. Influence of temperature on fatigue life of Zry-2 (after [9.409], as reported by [9.412]).

For the initiation step, it was found that only intergranular cracking occurred at the free surface until the ΔK_I reached the threshold level for SCC or dry fatigue crack propagation, or both, at which point corrosion fatigue started [9.413]. Figure 9.173 depicts the fracture surface details as examined by SEM.

9.5.10. Effects of hydrogen

The effects of hydrogen on the fracture behaviour of Zr alloys will be discussed in detail in Section 9.7. Very little data exist on the effect of hydrides on fatigue life (see Section 9.5.12.1 for effects on crack propagation). No statistical difference between the fatigue lives of Zircaloy-2 for specimens containing about 20, 100, 300 or 600 ppm hydrogen was found in tests at both 293 K (22°C) and 573 K (300°C) [9.414]. The endurance limits at 107 cycles were 345 MPa at 295 K (22°C) and 264 MPa at 573 K (300°C). Similar to the behaviour during tensile testing at those temperatures, the fracture surfaces were brittle for 600 ppm hydrogen at 295 K (22°C) but exhibited normal fatigue and ductile fracture for all other conditions. A minor reduction by hydrogen in the fatigue life of a

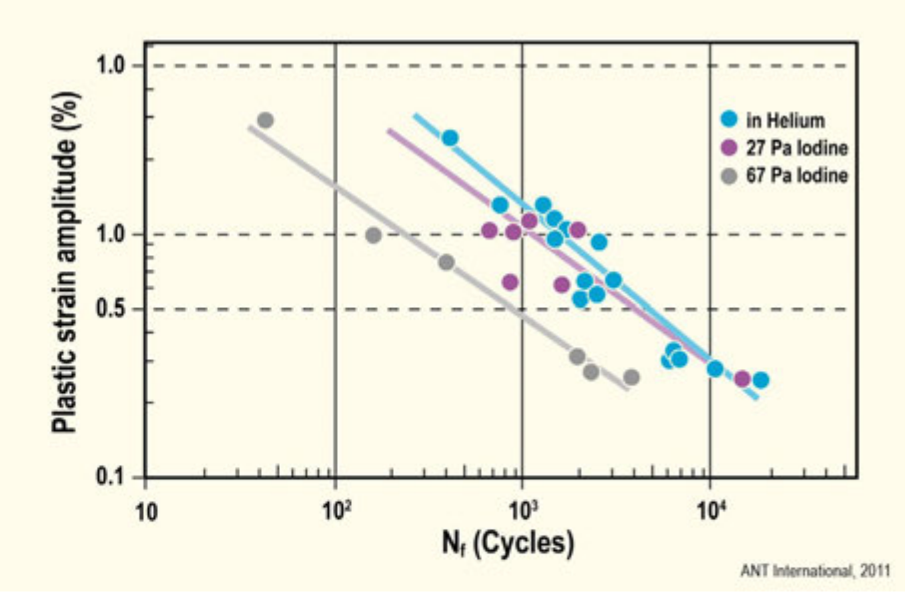

FIG. 9.170. *Low-cycle fatigue data for Ziracloy-2 in helium and iodine atmospheres at 623K (350°C) (after [9.392]).*

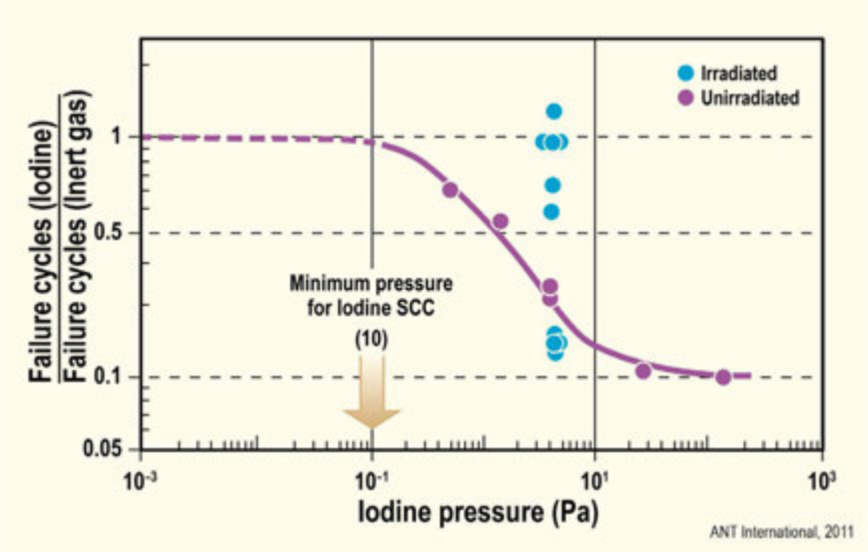

FIG. 9.171. *Effect of iodine pressure on cycles to failure at 623K (350°C) (after [9.389]).*

Zr-1Sn-25Nb-28Fe-09Cr alloy was found at room temperature, as shown in Fig. 9.174 [9.415]. The main conclusion was that cyclical softening was easier for hydrided (180 ppm) material than for material containing little hydrogen. This result is likely related to the observation that hydrides markedly increase the Bauschinger effect in Zircaloy-4, as shown in Fig. 9.175 [9.416]. The Bauschinger effect refers to the cyclical behaviour by which plastic yielding in the reverse or compression portion of the cycle begins at a lower absolute value of stress than in the initial tensile portion: “the flow stress of a metal in one direction is reduced by plastic flow in another direction” [9.417]. Figure 9.175 represents a tension-compression cycle with a strain amplitude $\Delta\varepsilon/2$ of 0.07%. If M is the maximum tensile stress during a cycle and R the stress at which plastic yielding starts during reverse loading, the Bauschinger effect can be characterized by β:

$$\beta = (M + R)/M \qquad (9.46)$$

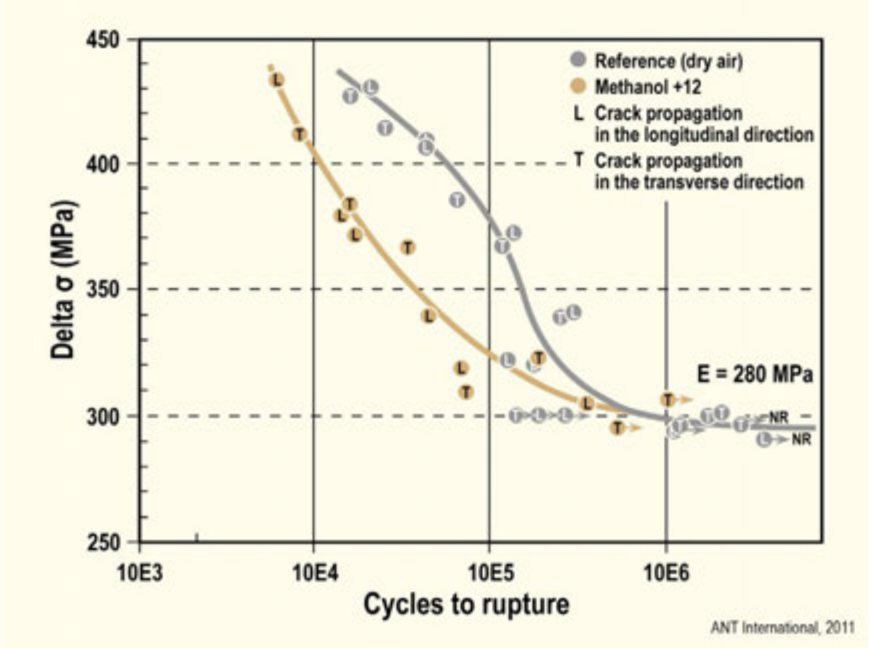

FIG. 9.172. Fatigue life curves in air and in iodine-methyl alcohol at 295K (22°C) (after [9.413]).

The results are summarized in Table 9.26. The material containing no hydrogen shows a strong Bauschinger effect and hydrogen amplifies the effect. With 1100 ppm hydrogen during unloading plastic yielding begins while the material is still in tension and β > 1.

TABLE 9.26. VALUES OF PARAMETER β FOR DIFFERENT HYDROGEN CONCENTRATIONS AND SIZE OF CYCLIC STRAINS (Δε/2) [9.412]

	$\Delta\varepsilon/2$		
C_H (ppm)	0.4	0.5	0.7
0	0.61	0.77	0.95
350	0.67	0.83	1.06
415	0.81	0.91	1.00
1120	0.93	1.18	1.25

9.5.11. Fundamental dislocation phenomena

In the case of zirconium alloys, the results discussed in Section 9.5.10 imply that hydrogen, hydrides or both are affecting dislocation motion in the zirconium lattice. A detailed analysis of hysteresis loops (see Section 9.5.3) such as those shown in Fig. 9.163 and Fig. 9.175, provides information about the Bauschinger effect, friction stress and back stress. The Bauschinger effect is discussed in [9.417–9.421]. The friction stress corresponds to the resistance dislocation must overcome to keep moving. The back stress depends on the density of long range impenetrable obstacles that are created by dislocation movement, such as pile-ups and the dislocation clusters shown in Fig. 9.152 and Fig. 9.176. Cyclical softening is related to the decrease in friction stress [9.422]. A dislocation interstitial mechanism is probably responsible, rather than any change in texture during cycling [9.423]. Dislocation dynamics can be used to explain the strain ageing observed

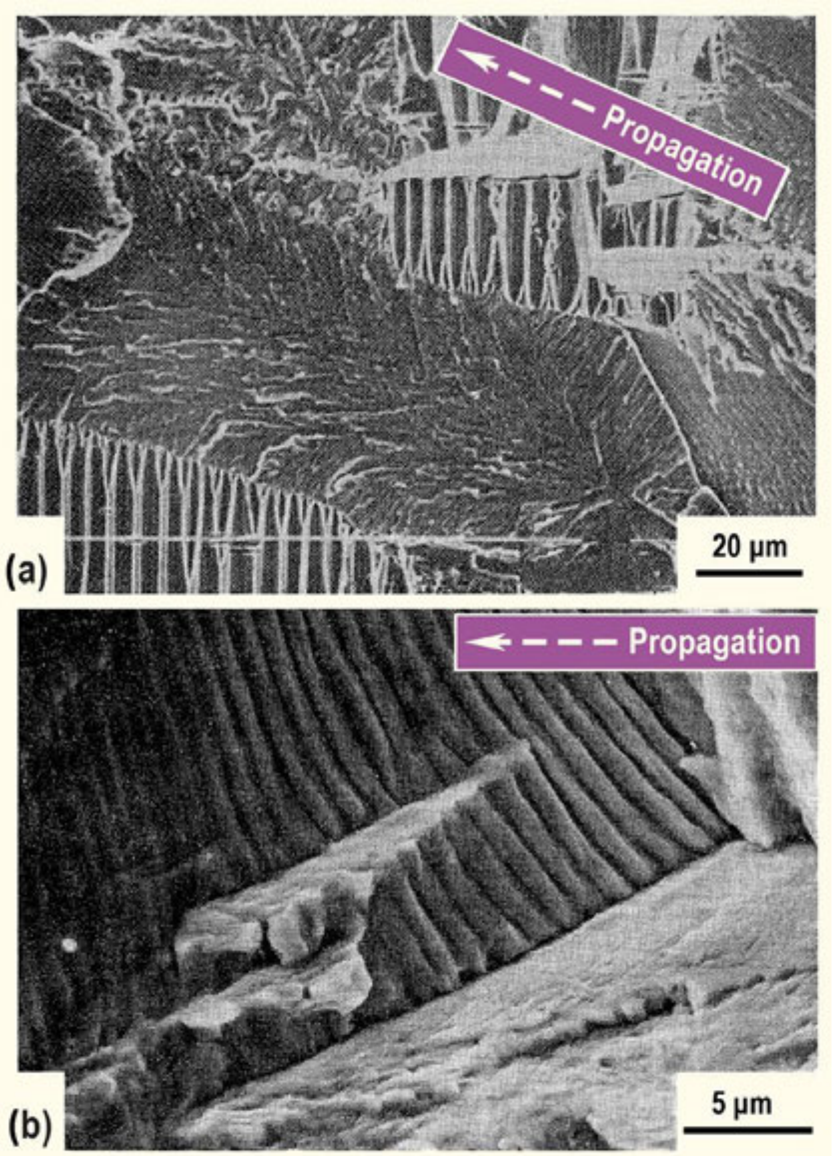

FIG. 9.173. Morphology of fracture surfaces: (a) by SCC and (b) by corrosion fatigue (after [9.413]).

in Zircaloy-4 during low cycle fatigue [9.424]. Invocation of friction and back stresses is used to explain the observed dislocation behaviour. An interaction with solute atoms alters the dislocation structure during fatigue by the process of dynamic strain ageing whereby in a certain temperature range (which depends on strain rate and applied strain range) oxygen (or other elements) diffuses to and inhibits the motion of dislocations (see Section 9.2.1). For conditions relevant to reactor components (applied plastic strain of ± 0.5% and strain rates near 10^{-3}/s) this temperature range has a threshold of about 573 K (300°C) but is pronounced at 623 K (350°C) and above. Figure 9.177 gives the peak tensile stress reached during constant plastic strain cycling; the plateau near 623 K (350°C) is indicative of dynamic strain ageing. In this temperature range a square shaped dislocation cell structure is developed (Fig. 9.176), and apparently dislocations are restricted to a single glide plane and progressively accumulate in the microstructure. It is not known how this dislocation arrangement might affect the microscopic or macroscopic behaviour of irradiated Zircaloys, but there is a possibility that it could affect the choice of dislocation channelling plane (see Section 9.2.2).

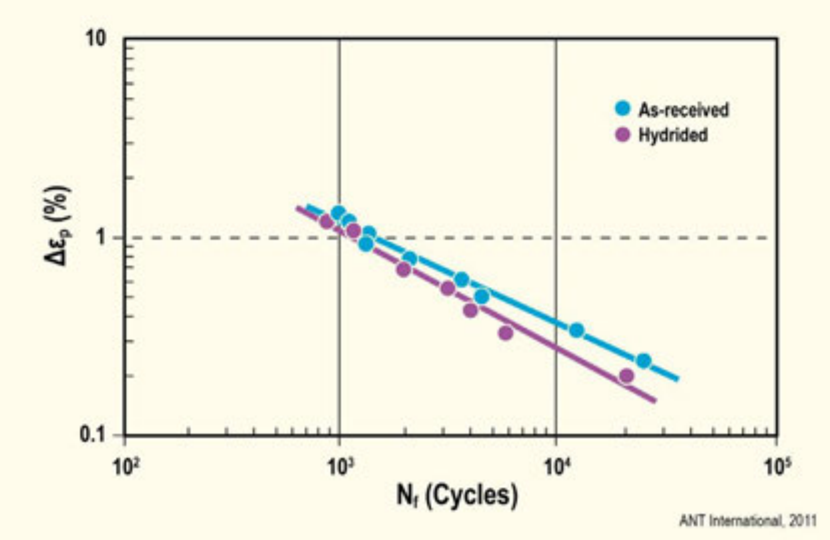

FIG. 9.174. Fatigue life curves (plastic strain range) at room temperature for as-received (~20 ppm H) and hydrided (180 ppm) Zr-Sn-Nb-alloy (after [9.415]).

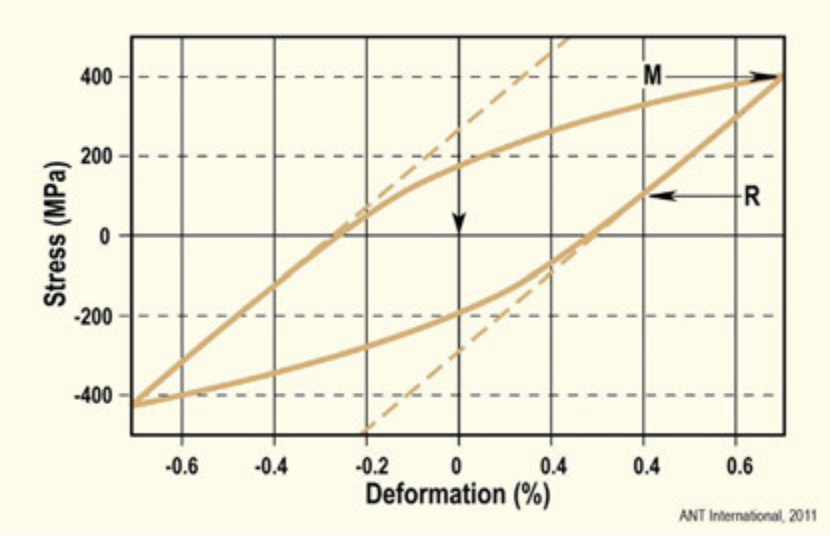

FIG. 9.175. Stabilized stress–strain cycle for Zircaloy-4 containing 1100 ppm H: $\Delta\varepsilon/2 = 0.7\%$. Bauschinger effect defined by $\beta = (M+R)/M$ *(after [9.416]).*

Knowledge of dislocation dynamics during cyclical deformation is required for the development of micromechanical models in irradiated zirconium alloys. A model that takes into account irradiation hardening during localized deformation in dislocation channels, Bauschinger effects and cyclical softening to simulate low cycle fatigue hysteresis loops in irradiated Zircaloy-4 [9.115] provides satisfactory description of some experimental results [9.390] and is shown in Fig. 9.178 and Fig. 9.179.

9.5.12. Fatigue crack growth rate

Fatigue crack growth data are generally obtained on a compact tension specimen of the general geometry shown in Fig. 9.180. The crack growth rate at the tip of the V-notch is measured either by light microscope on the surface of the specimen, electronically (e.g. using a direct current potential drop monitor) or by measurement of the specimen compliance. The measure of crack growth

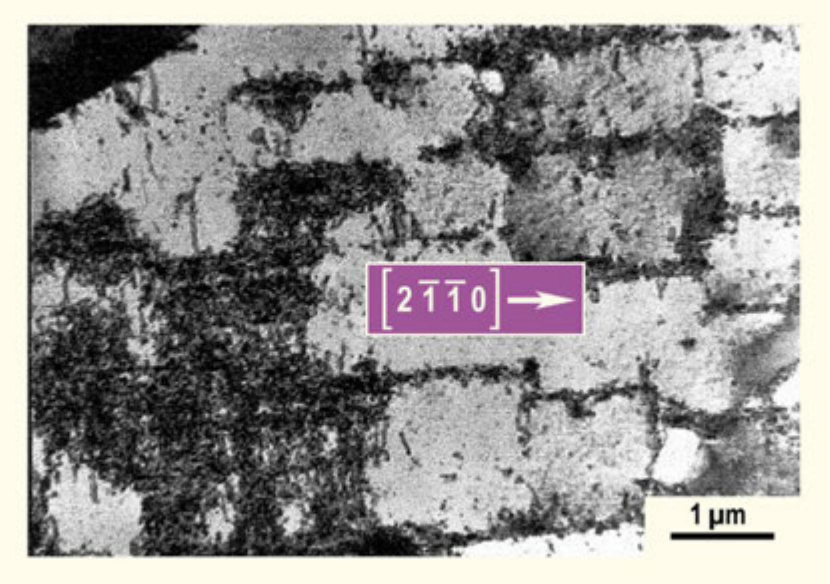

FIG. 9.176. Square-shaped cell structure developed in Zircaloy-4 at 713 K (440°C) after 500 cycles [9.424].

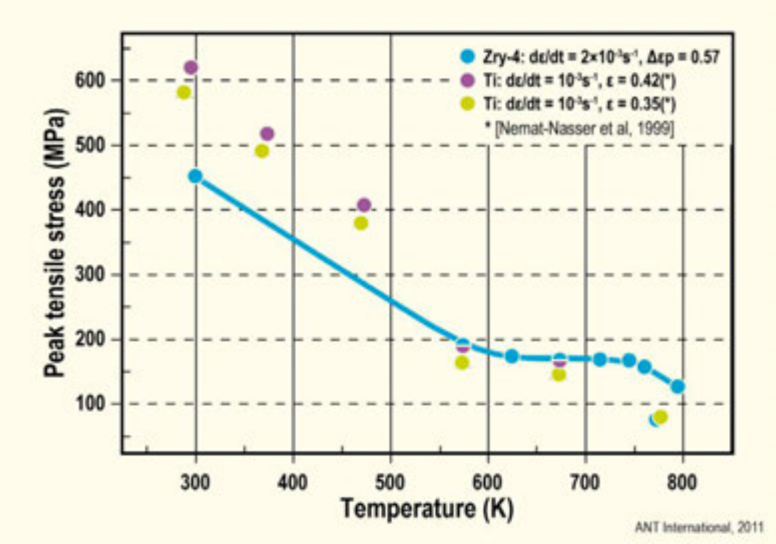

FIG. 9.177. Peak tensile stress versus test temperature for plastic strain range of ±0.57%, showing a plateau where DSA is activated (after [9.424]).

rate is the crack length increase, *da*, per fatigue cycle, *da*/*dN*, plotted against the range of applied stress intensity factor, ΔK_I. ΔK_I is a measure of the alternating stress amplitude corrected for the effects of the specific specimen and crack geometry.

An illustration of how to calculate *da*/*dN* is given in Fig. 9.181 and the general shape of the *da*/*dN* vs. ΔK_I curve is given in Fig. 9.182. Most often testing is done in the intermediate region, where $da/dN = C\,(\Delta K_I)^m$, or in the range where a threshold value of ΔK_I, below which the cracking rate is negligible, can be obtained. Usually, the tests are conducted with $R < 1$, meaning that the mean or average stress is greater than zero on the tension side.

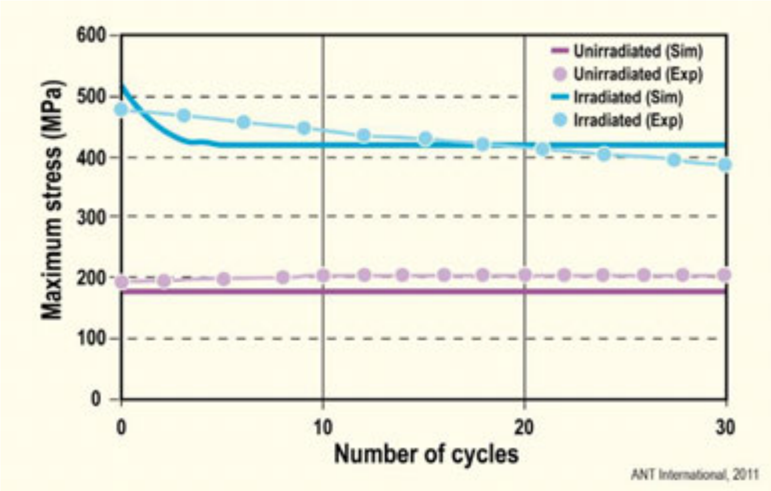

FIG. 9.178. Comparison of computed and experimentally observed cyclical strain softening of irradiated Zircaloy-2 (after [9.115]).

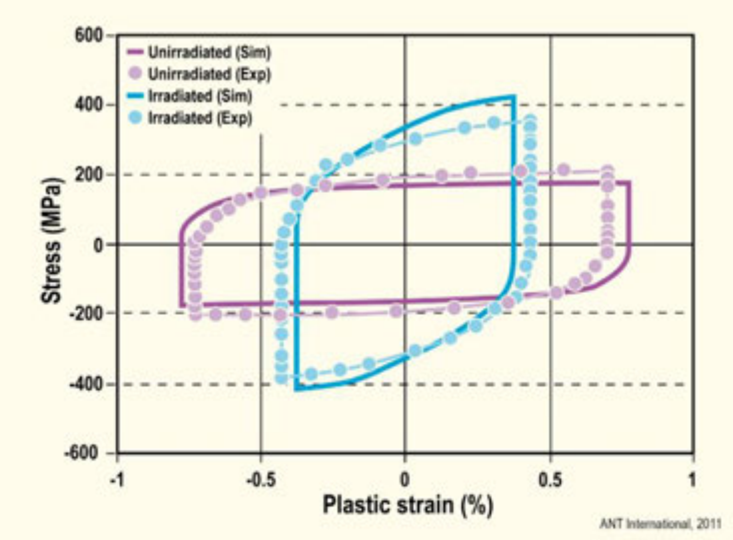

FIG. 9.179. Comparison of computed and experimentally observed stress-plastic strain hysteresis curves for irradiated Zircaloy-2 (after [9.115]).

Sources of fatigue crack growth rate data in Zircaloy are given in Table 9.27. Comparison of crack growth rates between different experiments is made difficult because of the possible effects of test variables. Crack growth thresholds, particularly at elevated temperature, can be affected by the load ratio, *R*, through effects of creep on the crack extension process. Increased temperature generally increases the crack growth rate, as shown by Refs [9.390] and [9.425] as reported in Ref. [9.412], making it advisable to test at temperatures relevant to the component of interest. For small temperature ranges, dividing the ΔK_I value by Young's modulus normalizes the crack growth rate for temperature [9.390]. For structural components (channels, water rods, guide tubes and assemblies) the relevant temperature is between 533 and 573 K (260 and 300°C) and for fuel cladding it is in the 573–623 K (300–370°C) range. Environmental effects are sensitive to surface conditions, load ratio and frequency. For example, Ref. [9.426] showed that fatigue life can be decreased by a thin oxide surface layer. In a water environment, decreased frequency or increased R increased the crack propagation rate [9.427].

TABLE 9.27. FATIGUE CRACK GROWTH RATES IN ZIRCALOY

Author	Year	Effect of irradiation on fatigue cracking		Effect of water	Source
Wisner et al.	1994	—	None	Increase	[9.390]
Pickles and Picker	1983	—	None	Increase	[9.428]
Walker and Kass	1974	Small increase	—	—	[9.398]
Chow et al. (Zr-2.5Nb)	1996	None	Small increase	—	[9.404]
Gee et al.	1989	—	—	Small increase	[9.427]
Gee	1984	—	—	Small increase	[9.429]

9.5.12.1. Effect of the environment

Preirradiation appears to have no effect on fatigue crack propagation, as shown in Table 9.28. Figure 9.183 gives an example for preirradiated Zircaloy-4 channel strips tested in 561 K (288°C) air [9.390]. For these test conditions $\Delta K_{I\ \mathrm{threshold}}$ was 1.2 MPa√m and $da/dN = (5.5 \times 10^{-11})\ \Delta K_I^{3.13}$. Picker and Pickles [9.427] demonstrated increased rates in water but also showed that testing in-reactor (in the presence of a neutron flux) had no additional effect.

TABLE 9.28. EFFECT OF WATER ON INCREASE OF FATIGUE CRACK GROWTH RATE

Author	Year	Temperature (°C)	R	Oxygen (ppb)	Factor increase (relative to air)	Source
James	1970	22	?	(low)	<2	[9.425]
Picker and Pickles*	1983	260	0.7	150	5–15	[9.427]
Gee	1984	260	0.2–0.7	7	<2	[9.429]
Gee et al.	1989	340	0.7	7	0– 2	[9.427]
		260	0.7	150	0–2	
		260	0.7	7	0–<2	
Wisner et al.	1994	288	0.7	150	2–4	[9.390]
		288	0.7	7000	4	

* Some tests done in-reactor showed no effects of a radiation environment.

Water appears to have an effect on crack growth rate, as illustrated in Fig. 9.184 [9.390]. Table 9.28 shows that rates were increased to varying degrees in different experiments. Very large increases can be produced, independent of whether the tests were conducted in- or out-of-reactor [9.428]. Oxygen appears to be an important variable. Figure 9.185 depicts rates in water with low oxygen (indicated in the Figure by ‘PWR’) and with high oxygen conditions (indicated in the Figure by ‘SGHWR’) and in air (indicated in the Figure by ‘UKAEA’) [9.427–9.429]; a clear difference is seen. When rates were compared between high (BWR) and low (PWR) oxygen concentrations in laboratory autoclave tests, almost no effect relative to air was discerned, as shown in Fig. 9.186

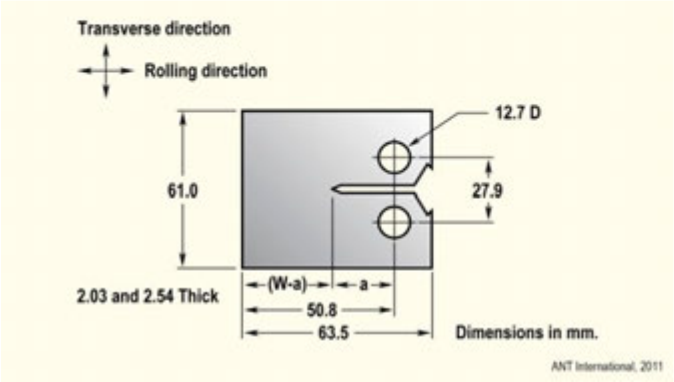

FIG. 9.180. Typical fatigue crack growth compact tension specimen design (after [9.390]).

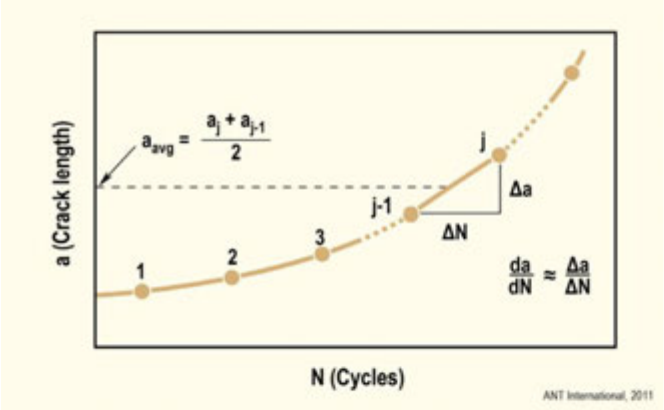

FIG. 9.181. Crack growth rates obtained from adjacent pairs of a *vs* N *data points (after [9.390]).*

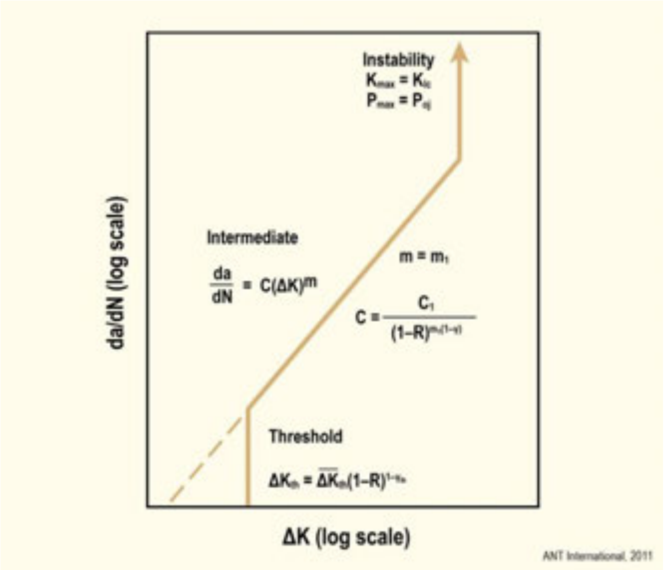

FIG. 9.182. Approximate representation of da/dN *vs.* ΔKI *behaviour with* R*-ratio effects included (after [9.382]).*

[9.427]. The mixed results for effects of water and oxygen require explanation. The hydrogen concentrations in all of the materials listed in Table 9.28 are expected to be low, about 20 ppm.

Prehydriding Zircaloy-2 to 300–1000 ppm hydrogen and testing in air at 533–613 K (260–340°C) does not change the rate of fatigue crack propagation relative to material containing

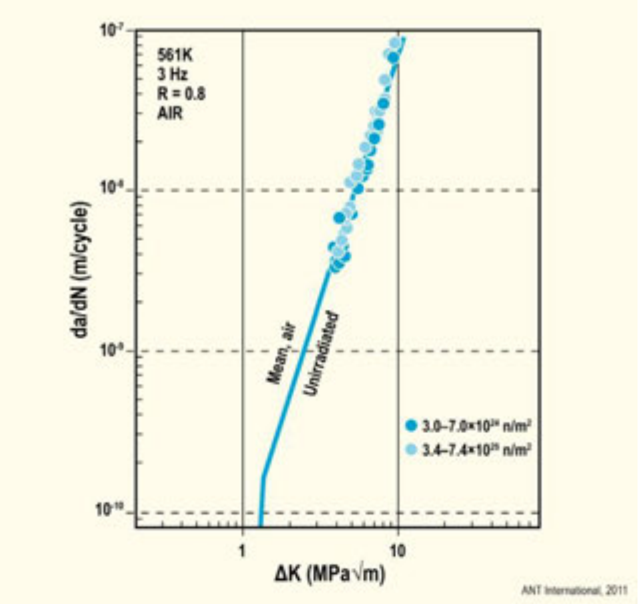

FIG. 9.183. Effect of neutron irradiation on normalized fatigue crack growth rates in Zircaloy-4 channel strip (after [9.390]).

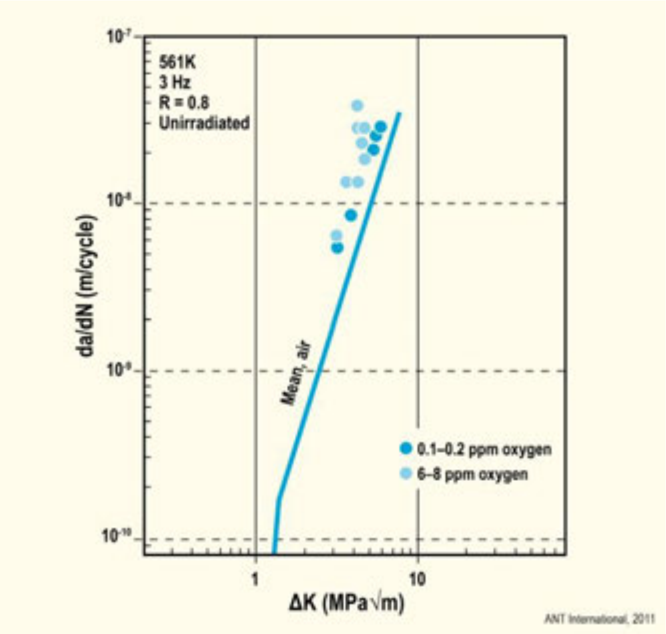

FIG. 9.184. Effect of water (561 K (288°C) 6.8 MPa) on fatigue crack growth rates in air for Zircaloy-4 channel strip (after [9.390]).

little hydrogen, as shown in Fig. 9.187 [9.427]. Testing hydrided material in water at 533 K (260°C) results in an increase in the crack propagation rate (Fig. 9.188).

Gee et al. [9.427] invoke a corrosion fatigue mechanism, perhaps delayed hydride cracking (DHC) related to hydrogen produced by corrosion at the crack tip (see Section 9.7), to explain why hydrides are effective in increasing crack propagation rates in water but not in air. Both corrosion fatigue and DHC are time and stress dependent phenomena and therefore effects on fatigue crack propagation are expected to be functions of both cyclical frequency and the loading ratio, *R*. The data shown in Fig. 9.188 demonstrate that such relationships exist, with decreased cyclical frequency

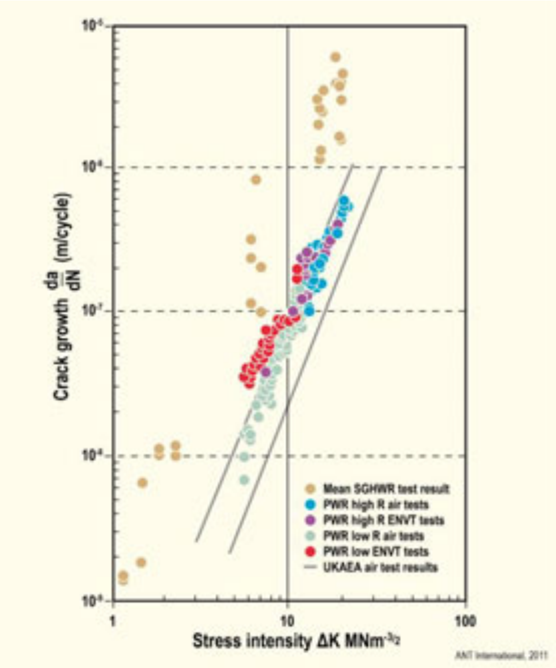

FIG. 9.185. Comparison of (high oxygen) SGHWR and (low oxygen) PWR water chemistry on the fatigue crack growth rate of Zircaloy-2, relative to tests in air (after [9.427]).

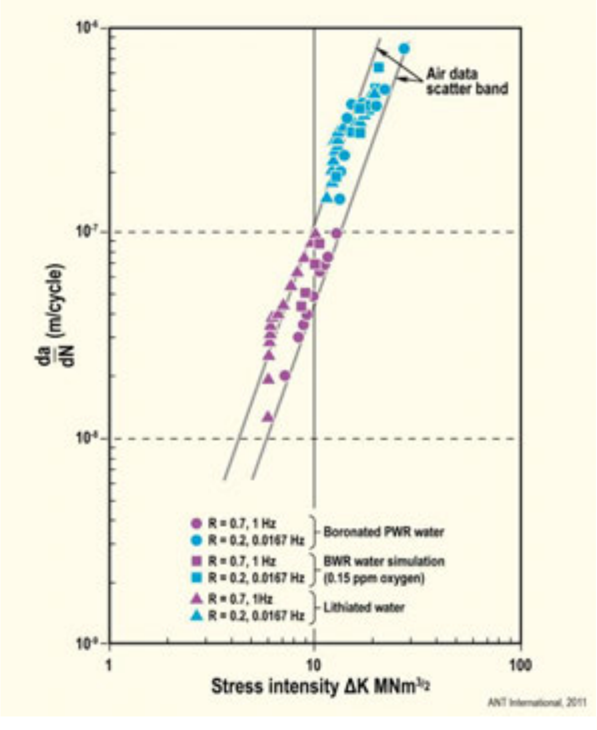

FIG. 9.186. Comparison of fatigue crack growth rates of Zircaloy-2 in air, high oxygen water (BWR), and low oxygen water (PWR, lithiated) (after [9.427]).

(more time for corrosion or hydrogen diffusion to occur) or increased *R* (higher net tensile stress) resulting in increased crack propagation rates.

Garlea et al. [9.430] explored the effect of hydrides on crack propagation in Zircaloy-4. Three conditions were studied: CT1, unhydrided and fatigued; CT2, hydrided and fatigued; and CT3, β quenched, hydrided and fatigued. Using standard compact tension specimens fatigued at room temperature, the fatigue cracks propagated through hydrides at the interlamellar grain boundaries.

Fracture toughness decreased and crack propagation rates increased in the order CT1, CT2, CT3. At a ΔK_{I} of 16.5 MPa√m the hydride material cracked nearly two times faster than the unhydrided material whereas the β quenched and hydrided material cracked nine times faster.

9.5.13. Practical applications

The main purpose of fatigue testing is to be armed with knowledge of the conditions for crack initiation and propagation so that these conditions can be avoided during service.

As the single exception, fatigue cracks have been observed in some CANDU fuel on the circumferential and radial arms of stress relieved Zircaloy-4 web-type end plates, adjacent to where they are welded to the end caps of the fuel elements, as shown in Fig. 4.97 (in Chapter 4, Volume 1 of this publication) [9.431]. In some reactors, the hydrodynamic load from a fuel string of 13 bundles is carried by a latch that bears on the outer periphery of the bundle elements closest to the flow outlet end of a fuel channel. Cracks were detected in both the radial and circumferential arms of the end plates, mostly initiating at the edge of the HAZ of the end cap to end plate weld and propagated through the end plate material. These failures were variable and occurred in groups in different fuel channels. Examination of the broken fuel bundles showed that the failures were not caused by manufacturing defects, embrittlement by corrosion products or gross overloading. The fracture surfaces near the initiation region were smooth and progressed into a region containing fatigue striations, 0.5 to 2.0 μm apart, and some band features called beach marks. In laboratory experiments, these marks were only observed when the stress amplitude was changed, close to the threshold stress; with constant stress amplitude, changes in frequency or temperature produced no marks. During reactor operation, the outlet end plate has a temperature of about 583 K (310°C) and deflects by creep into a slight dome shape indicting that the inner elements are displaced relative to the outer elements. With variations in pressure, axial oscillations of the inner elements with respect to the outer elements lead to cyclical bending stresses in the end plate arms at the boundary between the stronger weld zone and the as-manufactured end plate material. Stress analyses confirmed this region to be the likely failure point. Experiments simulating this configuration showed that the values of fatigue lifetime lie below the O'Donnell and Langer [9.374] line for smooth specimens, especially at high R ratio in the high cycle regime, as shown in Fig. 9.189 [9.432]. The fatigue properties were not affected by test temperature, plate orientation or manufacturer. In instrumented tests, fatigue growth started early in the tests, suggesting that the notch reduced the time of the crack initiation stage. This conclusion was confirmed from the timing of the in-reactor cracking, which was evaluated using Fourier transform infrared spectroscopy (Section 4.13.7.8, Volume 1 of this publication) to measure the oxide thickness on the outside surface of the end plate and on the fracture surface; the results showed that the fatigue cracking started soon after the reactor went to power [9.433]. The source of the stress was identified as a resonance that amplified a 150 Hz pressure pulse in the heat transport water that originated from the 5-vane pumps rotating at 30 Hz. Since the velocity of sound in water is temperature dependent, and the length of the feeders differed for different channels, the strength of the acoustic waves producing the resonance varied with power in individual fuel channels leading to the observed variation in cracking. When 7-vane impellors were installed, the resulting 210 Hz pressure pulse was not amplified by resonance and no further failures were observed.

Notches and machined flaws are often extended by fatigue at room temperature in experiments investigating fracture toughness or crack threshold conditions and crack growth rates of environmental cracking (e.g. SCC or DHC). This pre-cracking eliminates the variation of crack initiation from blunt flaws by providing a sharp crack from which the cracking being studied can start. Usually, the prefatigue is tension–tension and is started with high maximum stress that is gradually lowered so the maximum K_{I} during the cycles is much lower than the expected K_{I} to be applied in the test. This latter procedure is especially important when studying threshold K_{I} values.

9.5.14. Summary

Reactor components are often subjected to alternating or cyclical loading, which is termed fatigue loading or simply fatigue. With one exception, fatigue failures have not been a problem for reactor components because stresses in reactor components are well below the O'Donnell and Langer design curve, and laboratory generated data indicate that the governing curves are conservative. A clear consensus on the effect of neutron irradiation on the fatigue lifetime of zirconium alloys has not been reached. Irradiation has little or no effect on fatigue crack growth rates, but water, particularly with high oxygen concentration, increases the growth rate. The combination of hydrides and water, or hydrides forming during crack propagation, or hydrides forming after crack initiation has the potential to increase crack growth rates.

9.6. STRESS CORROSION CRACKING BY FISSION PRODUCTS

9.6.1. Background

Nuclear fission splits a heavy nucleus such as uranium or plutonium into two lighter nuclei, which are called fission products. The fission event causes the nucleus to split in an asymmetrical manner. The graph of the yield of immediate fission products against the atomic mass of the fragments has two peaks, one around mass 95 (in the range zirconium to palladium) and one around mass 140 (in the range xenon to neodymium), as shown in Fig. 9.190 (early discussions of this topic can be found in Refs. [9.434, 9.435]). Isotope and element yields will change as the fission products undergo beta decay. Three fission product elements — iodine, caesium and cadmium — have been identified as inducing SCC in zirconium alloys; this section describes the cracking behaviour in this environment.

Many structural metals undergo SCC in a wide range of chemical environments. In a susceptible material the combined effects of a localized stress and the right chemistry can generate cracks in conditions where neither the stress nor the chemistry alone would be capable of degrading the metallic component. The observations are often handled by a fracture mechanics approach where the crack growth rate, V, is plotted as a function of the applied stress intensity factor, K_I, as shown in Fig. 9.191. The two important properties of the alloy-environment combination are the fracture toughness at which the crack becomes unstable and the component fails in a purely mechanical fashion (K_{Ic}) and a threshold stress intensity factor to initiate cracking; for SCC, the threshold value is called K_{Iscc}. Often the crack growth rate has little dependence on K_I between these two limits.

In zirconium alloys, SCC falls into two distinct processes: transgranular and intergranular. In the transgranular cracking process, shown in Fig. 9.192, the fracture surface consists of a mixture of transgranular pseudocleavage planes interspersed with ductile tearing of residual uncracked webs. With the hexagonal crystal structure, the ductile features arise from the prism planes of the alloy and have a characteristic 'fluting' appearance if the grain size is sufficiently large for multiple, parallel prismatic flutes to be visible, as shown in Fig. 9.193 [9.436]. Fluting results from the mechanical slip of residual webs in the metal prism planes to produce a series of parallel flutes with hexagonal symmetry. Perfect fluting is seldom observed because of the small grain size typically present in reactor components. The intergranular cracking process results from chemical attack on the alloy grain boundaries, as shown in Fig. 9.194, and may occur simultaneously with transgranular cracking. This attack is usually in the form of a chemical dissolution process that results in a weight loss for the material unless reprecipitation of the dissolved material occurs elsewhere on the component. Intergranular cracking, because it is largely caused by chemical corrosion, is much less affected by fracture considerations, and may not follow the characteristic curve shown in Fig. 9.191.

Crack growth rates for intergranular cracking are often much slower than for transgranular cracking. When analysing in-reactor behaviour it is important to know whether intergranular, transgranular or a mixture of the two are being observed, and the respective rates of the different processes.

Not all reactor types are equally susceptible to these forms of SCC in their fuel. In general, the susceptibility to SCC failures is determined by whether or not the reactor design and operation permit large, sudden increases in the local fuel power. Such increases produce tensile stresses in the cladding when the fuel expands into contact with the cladding and may increase as the fuel expands further as an increase in power is accommodated. Two situations are identified, pellet–clad mechanical interaction, which does not necessarily involve SCC, and pellet–clad interaction (PCI), which implies a SCC component. In general, PWRs, including WWERs, are free of such conditions and so experience few or no SCC failures. The only major PCI failure in PWRs resulted from a large core flux tilt in Obrigheim [9.437]. Load following does not appear to cause rapid and sufficiently large power changes to induce PCI failures. Reactors such as BWRs and RBMKs, in which sudden control blade movements or movement of absorbers can cause large local power peaks, and reactors that refuel on-power, such as CANDU, where the fuel can go through a series of power peaks, are susceptible to PCI fuel failures.

9.6.2. Early indications of pellet–clad interactions

When the first through-wall PCI cracks in a high powered fuel pin were observed during the startup of a loop test in the General Electric Test Reactor [9.438], little published evidence on SCC of zirconium alloys was available [9.439, 9.440]. The cause of the failures was postulated to be SCC by fission products, possibly iodine, released from the UO_2. Atomic Energy of Canada Limited. observed failures of this type in 1965 [9.441] (Fig. 9.195), although there was some debate about the precise cause of these failures until 1969 [9.442]. In addition to the extensive studies aimed at elucidating the mechanism of PCI cracking of reactor fuel cladding [9.443], an extensive programme to study the SCC of Zr alloys in a wide range of chemical environments was inaugurated.

9.6.3. Stress corrosion cracking in organic chemical-halogen environments

Advantage was taken of the much further advanced state of SCC studies of titanium alloys for the aerospace industry [9.444]. Comparative studies of zirconium alloys in the same environments showed the similarity in the behaviour of the two metals, as seen in Table 9.29 [9.445–9.447].

Cracking of Zr alloys was generally a mixture of intergranular and transgranular cracking with 100% intergranular cracking in only a few environments (chlorinated hydrocarbons; I_2 in ethylene glycol). Most test specimens were of insufficient wall thickness for valid fracture toughness tests to be conducted. Precracked, double cantilever beam (DCB) specimens [9.448], with 25 mm square cross-section, did give valid fracture toughness measurements. In SCC tests with this type of specimen, the fracture surface was 100% TG, even in environments where complete intergranular, or mixed intergranular/TG, cracking was observed on thin-walled fuel cladding material. When DCB specimens are loaded to a constant crack opening displacement, the stress intensity factor decreases during crack growth; K_{Iscc} is evaluated when crack growth stops. When specimens were subsequently broken mechanically, to study the crack arrest fractography, no intergranular features were observed even in environments (e.g. methanol/I_2) where extensive intergranular cracking was observed during crack initiation in fuel cladding specimens. It has become common to argue that cracks grow intergranularly in Zircaloy in both I_2 and MeOH/I_2 until the stress intensity required to initiate a transgranular crack is attained, when the crack propagates through-wall in transgranular mode [9.449, 9.450]. The behaviour of the DCB specimens casts doubt on this conclusion.

TABLE 9.29. ENVIRONMENTS CAUSING CRACKING OF TITANIUM AND ZIRCONIUM ALLOYS[a]

Environment	Temperature (°C)	SCC in Ti	SCC in Zr alloys		
			Yes/no	Cracking mode[b]	First observed
Hydrogen					
Internal hydrogen	RT-350	Yes	Yes	TG	[9.17]
Hydrogen gas	RT-150	Yes	Yes	TG	[9.23]
Organic liquids					
Methanol and solutions with I_2, Br_2, NaCl, HC1	RT	Yes	Yes	IG initiation TG propagation	[9.7, 9.9]
Higher alcohols with similar additives	RT	Yes	Yes	Mixed IG/ TG	[9.9]
Iodine solutions in other organic liquids	300–800	Yes	NT		
Chlorinated hydrocarbons (e.g. CCl_4, $CHCl_3$)	RT	Yes	Yes	IG	[9.24]
Other halogenated hydrocarbons (e.g. freons, CH_3I)	RT	Yes	Yes	TG (DCB)	[9.24]
Ethylene glycol	RT	Yes	Only in I_2 solution	IG	[9.24]
Aqueous solutions					
HC1	25–150	Yes	Yes	IG	[9.12]
NaC1, KC1, etc.	25–290	Yes	Yes (needs polarization)	Mixed IG/TG	[9.25]
$FeC1_3$, $CuC1_2$	RT	Yes	Yes		[9.10, 9.11]
Hot and fused halides					
NaC1, KC1, CsC1	300–450	Yes	Yes	Mixed IG/TG	[9.7]
$KNO_3/NaNO_3$ + KBr/CsI	300–400	Yes	Yes	Mixed IG/TG	[9.26]
$KNO_3/NaNO_3$ + NaC1	300–400	Yes	Yes	IG	[9.27]
Halogen and halogen acid vapours	RT	NT	Yes	TG (DCB)	[9.24]
	250–500	Yes	Yes	Mixed IG/TG	[9.13]
Metals (solid, liquid, vapour)					

TABLE 9.29. ENVIRONMENTS CAUSING CRACKING OF TITANIUM AND ZIRCONIUM ALLOYS[a] (cont.)

Environment	Temperature (°C)	SCC in Ti	SCC in Zr alloys		
			Yes/no	Cracking mode[b]	First observed
Hg, Cd, Cs	RT-400	Yes	Yes	TG	[9.7]
Mg	700	NT	Yes	IG	[9.80]
Oxides and oxy acids of N_2					
N_2O_4	RT	Yes	NT		
Nitric acid	RT-100	Yes	Yes	TG	[9.28, 9.29]
Sulphuric acid	RT	Yes	NT		

Notes: For details of the references, see originals in Ref. [9.447]. IG — intergranular; NT — not tested; RT — room temperature; SCC — stress corrosion cracking; TG — trangranular.

[a] A more detailed description of the various environments causing cracking is given in ref. [9.447].

[b] DCB indicates fractures only in pre-cracked double cantilever beam specimens.

Zirconium alloys are also used in the chemical industry. The most frequent components are Zr-alloy-lined reaction vessels [9.451]. Here, the good corrosion resistance in inorganic acids [9.452] is the property of most concern; when mixed with organic chemicals, the potential for traces of halogen impurities can lead to cracking of the Zr-alloy-liner, and then to subsequent corrosion of the steel vessel [9.452, 9.453]. The results of iodine cracking in a wide range of iodine/organic solutions (characterized by optical absorption), detailed in Table 9.30, and in iodine/alcoholic solutions (characterized by viscosity), detailed in Table 9.31 [9.454], can probably be extrapolated to similar solutions containing chlorine or bromine. A series of tests in various iodine/organic solutions was designed to test the hypothesis that the stronger the I_2/organic complex bond, the lower the probability of SCC. The attempt to relate the severity of cracking to the strength of the I_2/organic complex was not successful [9.454], and neither were attempts to correlate the extent of intergranular corrosion in nuclear fuel cladding specimens with the measured transgranular and K_{1scc} from large DCB specimens. Thus, there is some doubt as to whether the change from intergranular to transgranular cracking in many types of specimens is solely related to the crack tip stress intensity, rather than to chemistry changes within incipient cracks.

TABLE 9.30. STRESS CORROSION CRACKING OF ZIRCALOY IN IODINE AND ORGANIC SOLUTIONS AT 298 K (25°C)

Solvent	Absorption Å Mellor	Max CRNL	DCB in 0.1% solution (K_{ISCC}/K_{IC}%)	Split rings (time to 0.1% solution)	Failure saturated solution
None (I_2 vapor)	5200	—	30.2	NF	NF
Trifluoroacetic acid	—	5150	100	NF	NF
Cyclohexane	(4900)	5150	34.4	NF	NF
Carbon disulphide	5185	5130	<36.5[a]	NF	NF
Carbon tetrachloride	5170	5120	<50	NF	NF
FREON 11	—	5110	<41.5	NF	NF
Chloroform	5110	5060	<50	NF	NF
Benzene	5000	4930	100	NF	NF
Toluene	4970	4910	45.9	NF	NF
O-xylene	—	4920	100	NF	NF
M-xylene	—	4920	<60	NF	NF
P-xylene	4960	4880	48.3	NF	NF
Nitrobenzene	—	4730	39.0	NF	NF
Pyridine	4800	—	100	NF	NF
Diethylether	(4560)	4630	46.3	NF	NF
Acetic acid	4780	4620	<50	NF (100 days)	3–50 h
Water	4700	4620	100[b]	[b]	[b]
1–4 dioxane	4515	4430	54.7	NF	NF
Ethanol	4470	4420	30.4	≈290 min	18–29 min
Methanol	4380	4380	27.9	4–7 min	2–3 min

[a] K_{IC} values for this batch and this type of specimen are 36.3 ± 2.7 ksi√ in (39.2 ± 2.9 MPa√m). Results are shown as < where crack propagation is continuing.

[b] See table 5 in Ref. [9.454] for details of experiments in aqueous solutions.

[c] NF — no failure. 'Absorption max' lists the optical absorption peaks for the various solutions obtained from the chemical literature, and those measured on the actual solutions tested at CRNL. The DCB results compare K_{ISCC} as a percentage of K_{IC} for each specimen tested.

TABLE 9.31. STRESS CORROSION CRACKING OF ZIRCALOY IN ALCOHOLIC IODINE SOLUTIONS AT 298 K (25°C) [9.454]

Solvent	Type	DCB in 0.1% solution K_{ISCC}/K_{IC}[a] (%)	Split-rings (time to failure)		Fracture, % transgranular	Viscosity (centipoises at 20°C)
			0.1% I_2	Saturated solution		
Methanol	Straight chain, aliphatic	27.9	4–7 min	2–3 min	≈90	0.597
Ethanol	Straight chain, aliphatic	30.4	290 min	18–29 min[b]	70–80	1.200
N-propanol	Straight chain, aliphatic	60	20–48 h	—	<5	2.256
N-amyl alcohol	Straight chain, aliphatic	60	5 days	69 h	<2	4.65 (15°C)
N-heptanol	Straight chain, aliphatic	43.2	≈13 days	7 days	30	8.5 (15°C)
N-decanol	Straight chain, aliphatic	31.7	NF (>30 days)	NF (>30 days)	—	10.1 (25°C)
2-propanol	Branched chain, aliphatic	≈30	15–24 h	—	>70	2.08 (25°C)
Ethylene glycol	Polyhydric, aliphatic	34.4	4–10 days	3–5 h	<1	19.9
Glycerol	Polyhydric, aliphatic	≈30	NF (150 days)	NF (150 days)	—	1490
O-cresol (40° C)	Nuclear, aromatic	≈60	NF (100 days)	Pitted	—	4.49 (40°C)
M-cresol (40° C)	Nuclear, aromatic	≈50	NF (100 days)	Pitted	—	6.18(40°C)
P-cresol (40° C)	Nuclear, aromatic	≈45	NF (100 days)	30–40 h	≈20	7.00(40°C)
Benzyl alcohol	Side-chain, aromatic	<60	9–11 days	Pitted	[c]	5.8
β-phenyl ethyl alcohol	Side-chain, aromatic	<34	Pitted	8 days	[c]	7.61 (25°C)
Cyclohexanol	Cyclical	<50	NF (100 days)	NF (100 days)	—	68

[a] K_{IC} values for this batch and this type of specimen are 36.3 ± 2.7 ksi√ in (39.2 ± 2.9 MPa√m). Results shown as < where crack propagation is continuing.

[b] One group of three specimens took 120–150 mins to fail. This experiment, during a period of high atmospheric humidity, may represent the influence of absorbed water on times to failure; as many instances where pitting rather than cracking occurred in other solvents.

[c] Duplicate specimens pitted rather than cracked. Fracture surfaces heavily pitted, visible features all intergranular.

Note: NF — no failure.

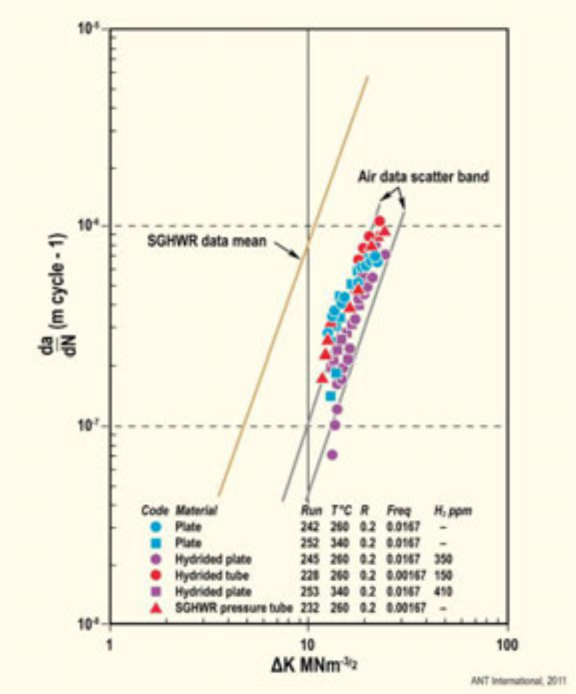

FIG. 9.187. Crack growth rate tests in air on hydrided and non-hydrided Zircaloy-2 [9.429]. Solid lines refer to data from [9.428].

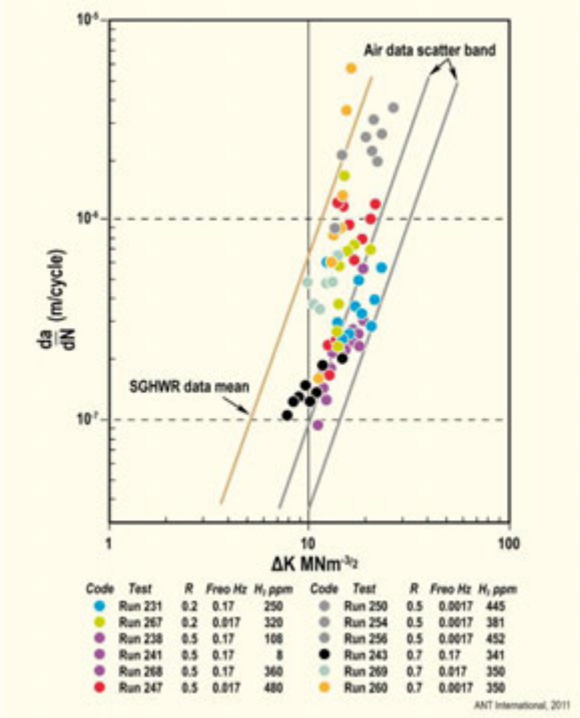

FIG. 9.188. Crack growth rate tests in water on hydrided Zircaloy-2 (after [9.427]). Comparison with tests in air indicates an increased crack growth rate.

Intergranular corrosion of Zircaloys involves a weight loss of the specimens [9.455]. In electrolyte solutions (whether aqueous or non-aqueous) the intergranular process is regarded as anodic dissolution at the crack tip, although other processes have been suggested. Galvele [9.456] has

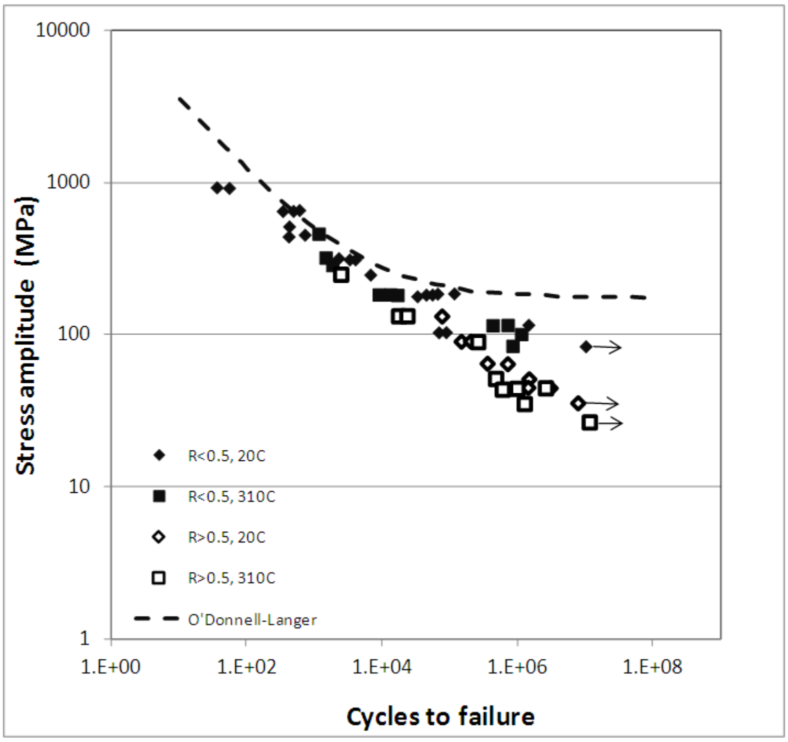

FIG. 9.189. Dependence of number of cycles to failure on stress amplitude in end plate — end cap welds made from Zircaloy-4 [9.432].

proposed several mechanisms for cracking in aqueous halide solutions. The transgranular cracking process in such environments is not well understood. Galvele's suggestion that it is caused by Zr tetrahalides cannot be supported because Zr tetrahalides are immediately hydrolyzed by water. In anhydrous organic/halide solutions, the action of the tetrahalides at the crack tip may be the propagation step; here, the tetrahalide may be removing Zr from the crack tip and depositing it on the crack walls as a lower Zr halide. Such a process could explain why organic solvents such as alcohols need to be carefully dried if the transgranular cracking process is to proceed. Even traces of water would hydrolyze the tetrahalides and prevent transgranular cracking.

Other processes leading to transgranular cracking include DHC (see Section 9.7) and liquid metal embrittlement (LME), which is commonly intergranular in other metals, but which is usually completely transgranular in Zr alloys [9.457, 9.458]. LME is important because of the possibility of Cs/Cd fission products causing cracking in-reactor and will be discussed in Section 9.6.4.

9.6.4. Pellet–clad interaction failures of nuclear fuel cladding

As indicated, the first clearly established case of PCI cracking of nuclear fuel occurred during the startup of a loop test in the General Electric Test Reactor on 17 June 1963. A highpowered pin, 12D, in assembly EPT-12C, was found to be leaking [9.438]. Some form of chemical attack, or SCC, by aggressive fission products released by the rapid rise in the UO_2 temperature was suspected. The choice of possible aggressive fission products was narrowed down to iodine or Cs/Cd mixtures. Stress corrosion tests using iodine were presented in 1966 [9.459] and data on embrittlement by Cs/Cd came later [9.460] following a survey of a large number of possible species; Grubb and Morgan [9.459] were unable to crack Zircaloy-2 in Cs in simple uniaxial tensile tests. Use of biaxial tests showed that cracking was possible in both Cs and CsI, although Cs/Cd mixtures were the most aggressive [9.461–9.463]. General Electric initiated a large series of ramp tests in 1967 [9.464] that showed mostly 'pin-hole' failures. Sometimes surface depressions formed by strain bands at the point of penetration left 'X' marks.

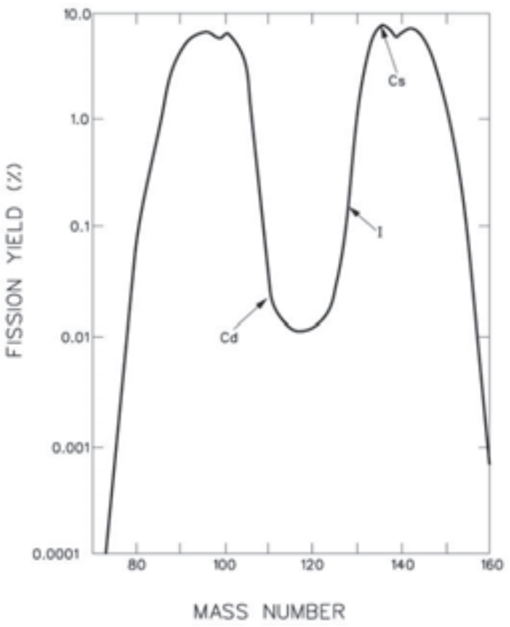

FIG. 9.190. Distribution of fission product yields from 235U (based on [9.434, 9.435]).

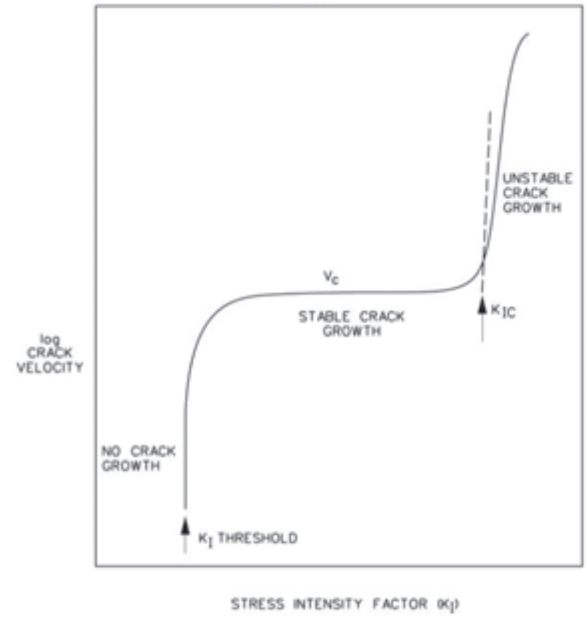

FIG. 9.191. Development of environmental cracking as a function of stress intensity factor, K_I. *With stress corrosion cracking the threshold is called* K_{ISCC}*; once exceeded, stable crack growth is almost independent of* K_I *until rupture at* K_{IC}.

Garlick et al. [9.465] identified similar cladding failures in fuel irradiated in loop tests in the Halden boiling water reactor, and suggested that similar failures had occurred in fuel pins in the NPD reactor, Canada, and in loop tests as early as 1965 [9.442, 9.466] (Fig. 9.195). These failures had occurred at low burnups (≤1000 MWd/tU) and available iodine was probably ≤1mg/kgU (Fig. 9.196) [9.465]. These failures were few, until an epidemic of such failures ensued following the start of on-power refuelling in the Douglas Point reactor, in 1969, and Pickering-1, in 1971 [9.466] (Fig. 9.197).

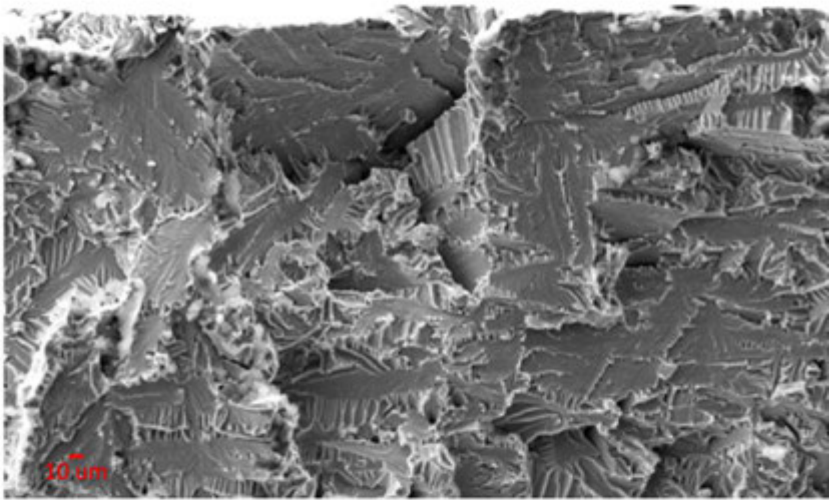

FIG. 9.192. Transgranular cleavage fracture and fluting in Zircaloy-4 (B. Surette, AECL).

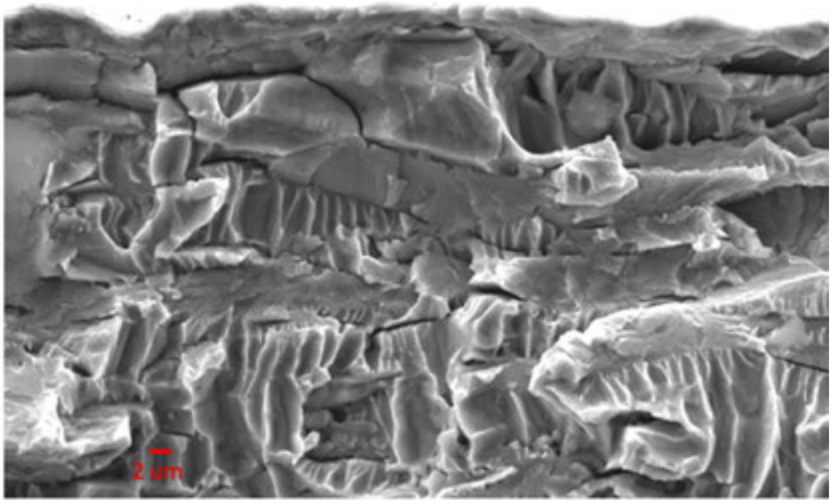

FIG. 9.193. Typical transgranular fracture and adjacent fluting in Zircaloy-4 at a higher magnification than Fig. 9.192 (B. Surette, AECL).

9.6.5. Lessons learned from early pellet–clad interaction failures

A large number of failures, about 200, between 1969 and 1973 in Douglas Point and Pickering, as shown in Fig. 9.197, allowed statistically significant data to be generated for the effect of change in power, ΔP, and final power, P_{max}, as shown in Fig. 9.198. These correlations were called Fuelograms. The probability of failure could be deduced from these data, showing the wide range of both maximum powers and ΔP required to transition from 2% probability of failure to 100% probability of failure (Fig. 9.199) [9.466]. The lines in Fig. 9.198 are based on the lowest combination of P_{max} and ΔP observed to cause failures. Figure 9.199 shows how the probability of failure increases as P_{max} and ΔP exceed this threshold.

From these data the following additional observations were made:

- There was an incubation time between the power increase and the appearance of a through-wall crack. Because the fuelling machines operated differently in Douglas Point and

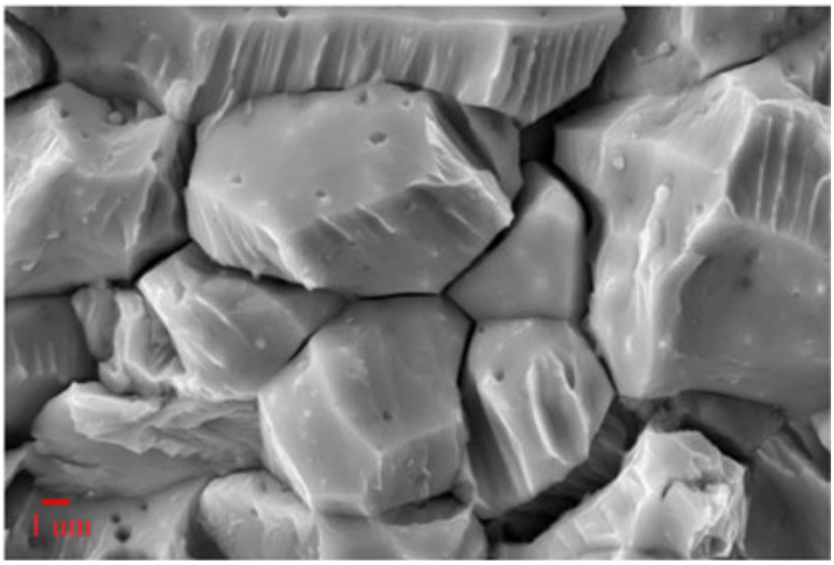

FIG. 9.194. Intergranular fracture in Zircaloy-4 (B. Surette, AECL).

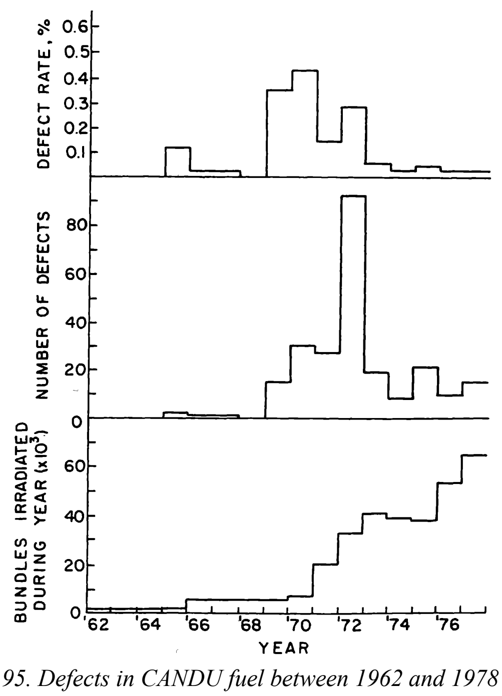

FIG. 9.195. Defects in CANDU fuel between 1962 and 1978 [9.441].

Pickering-1, and the power levels in the two reactors were different, there was a difference in these incubation times. If fuel in Douglas Point were left in a high flux position for <1800 s, or for <900 s in Pickering-1, there would be no PCI failure.

— There was a limited time range when the environment inside the fuel cladding was corrosive. If no failure occurred within 2 hours, then failure was unlikely, as shown in Fig. 9.199.

— Most of the CANDU failures during on-line refuelling were of the pin-hole type. Only failures resulting from incorrect movements of adjuster rods (where the ramp power persisted for a long time) suffered from secondary degradation cracking. Although the presence of delayed neutron monitors in the CANDU fuelling machines allowed rapid identification and rapid

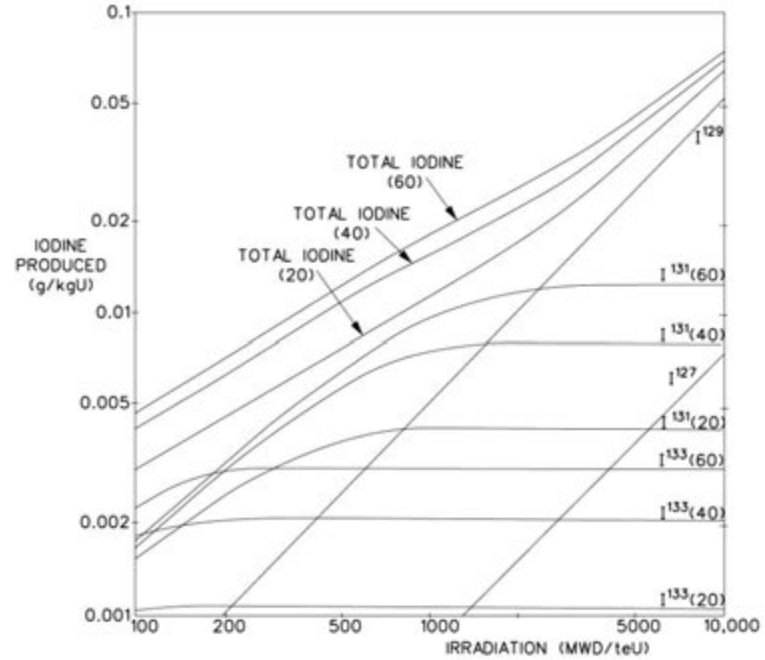

FIG. 9.196. Irradiation dependence of the amount of iodine formed as a fission product. Figures in brackets refer to power rating in MW/teU [9.445].

removal (<1 h) of failed bundles, most of the failures that were examined showed some secondary hydride (actually deuteride) blisters elsewhere in the failed fuel pin. Similar observations were made during Kraftwerke Union power ramps, as shown in Fig. 9.200. This Figure shows the failures that resulted from a major core flux tilt that occurred during Cycle 6 in the Obrigheim reactor [9.437].

— Because SCC cracking by iodine species stops once water gains access to the cladding's inside surface, anything other than a pin-hole defect in a water cooled reactor is impossible by PCI. All cracks observed are secondary effects resulting either from gross hydriding of the cladding, which usually (but not always) occurs at some distance from the primary defect, as shown in Fig. 9.200, or from ductile tearing. General Electric ramp test results [9.464] agree with this assessment. Small cracks adjacent to the primary failure are usually ductile mechanical tearing resulting from the presence of local thin webs of material adjacent to the primary pin-hole failure. The X marks are the result of local deformation adjacent to the pin-hole failure that is caused by the stress distribution producing a rabbit-ear distribution of strains at either end of the primary penetration [9.437]. If the high power (stress) persists these holes can tear mechanically, as shown in Fig. 9.201 [9.467].

— Because SCC cracking by iodine stops immediately once water is admitted, the PCI crack surfaces start to oxidize. The volume expansion from this oxidation may then 'reseal' the primary failure. It was observed in many CANDU-PCI failures that the delayed neutron signal vanished soon after it first appeared. Even so, CANDU bundles were quickly removed from the reactor core. In many BWR failures, where detection of small primary failures is often not possible, it is the later appearance of secondary defects that is the first intimation of a defect. Thus, 'times to failure' in most in-reactor and many test reactor ramp tests should be treated with a large degree of scepticism. In CANDU failures, the iodine atmosphere only remained aggressive for 2 to 3 hours, because of the conversion of ZrI_4 to lower iodides (ZrI_3, ZrI_2), which are non-aggressive. Any 'times to failure' significantly longer than 3 hours are probably 'times to secondary hydriding (deuteriding) failures'.

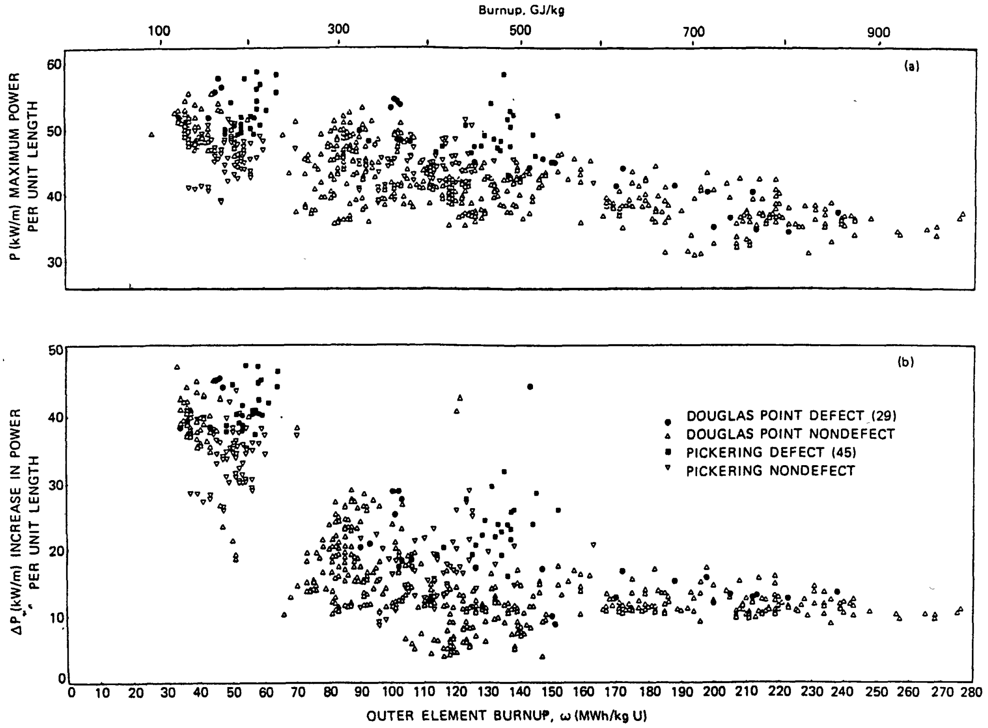

FIG. 9.197. Power ramp data showing distribution of defects and non-defects for the Douglas Point and Pickering reactors [9.466].

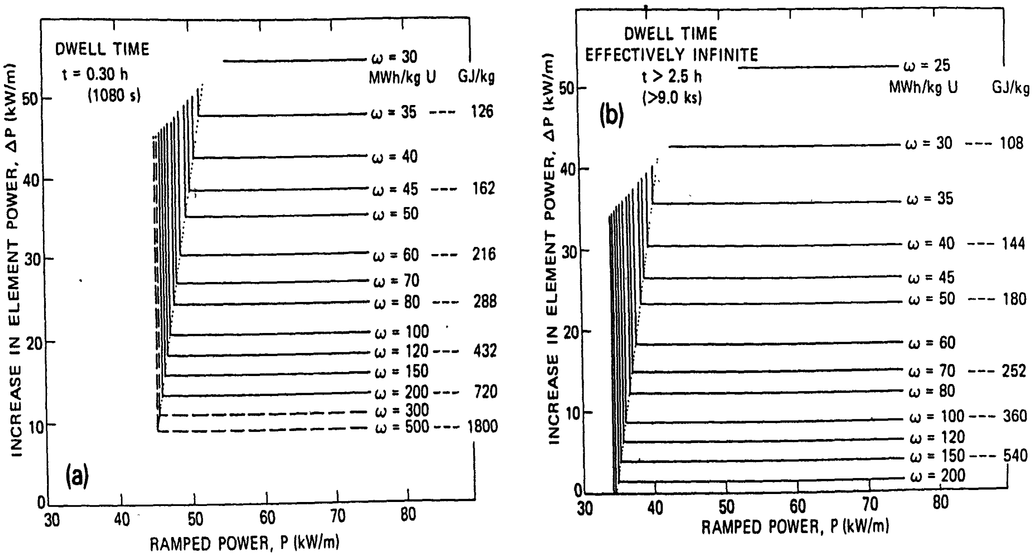

FIG. 9.198. Fuelogram for dwell times of (a) 1080 s and (b) >2.5 h [9.466].

9.6.6. Active species in pellet–clad interaction cracking

Studies of a large range of possible fission products that might cause PCI failures narrowed the possibilities to iodine or a mixture of caesium and cadmium [9.460]. It was unclear whether atomic or molecular iodine was the aggressive species. At high temperatures Hofmann and Spino [9.468] established that ZrI_4 was much more aggressive than I_2. This result was confirmed at reactor

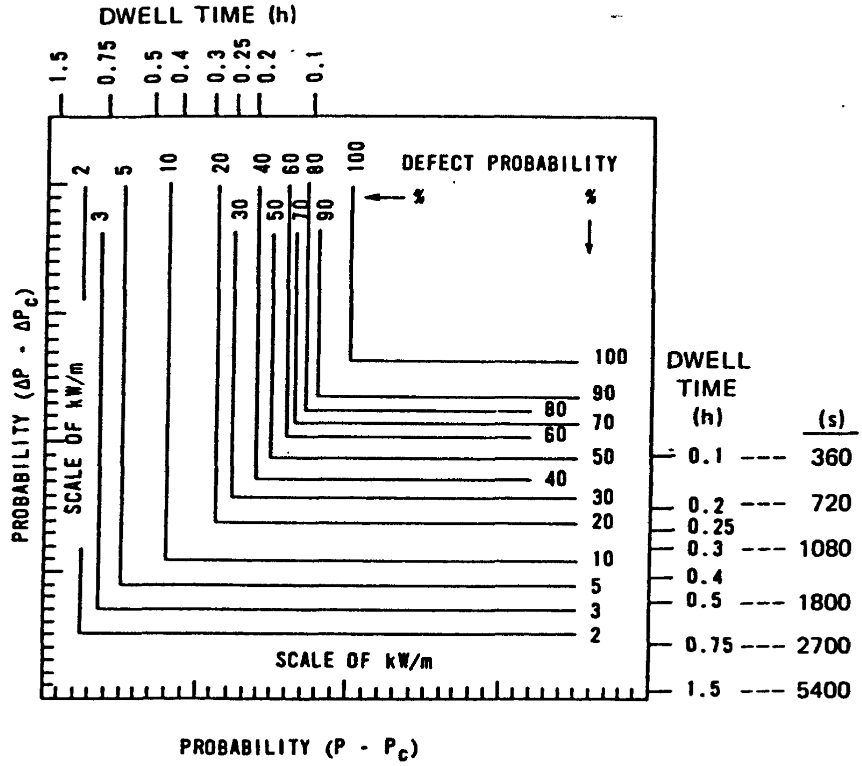

FIG. 9.199. Probability of a defect after power ramping of the fuel [9.466].

temperatures by Shimada et al. [9.469]. Zirconium forms a range of iodides (ZrI, ZrI_2, ZrI_3, ZrI_4) by reaction of iodine with an unoxidized zirconium surface. These iodides will grow in layers, as shown in Fig. 9.202 [9.470]. Tensile stress fractures both oxide and halide layers to allow access of ZrI_4. Of these, only ZrI_4 is sufficiently volatile to cause SCC. Hofmann and Spino [9.468] showed that the lower zirconium iodides were incapable of generating stress corrosion cracks.

Thus, it is concluded that the incubation times observed in CANDU refuelling failures and laboratory experiments reflect the time required for sufficient ZrI_4 to form in the cladding or the experimental equipment to allow a transgranular crack to initiate. The observed incubation times in in-reactor (typically about 15–20 minutes after movement to a high power position) and out-reactor split-ring tests, as shown in Fig. 9.203 [9.471], were remarkably similar and tended to confirm this hypothesis. Laboratory conditions are often less amenable to producing suitable chemistry for cracking (e.g. in uniaxial tensile tests where large reaction chambers surround the specimen and flowing I_2 inert gas mixtures are used [9.472]). The incubation times can be much longer than those observed in-reactor — often, no cracks initiate — probably because an acceptable ZrI_4 concentration is not achieved on the specimen surface. The apparent agreement between laboratory split-ring test incubation times, and those observed during CANDU refuelling failures, may be fortuitous because the split-ring test facilitates a reaction in a closed environment, which is a necessary condition, but other features (e.g. addition of steel wool [9.471]) were not intended to simulate the in-reactor environment.

The CANDU refuelling failures also conflicted with laboratory tests in terms of the critical iodine concentration required for cracking. In CANDU reactors, fuel failures were observed once a burnup of about 1000 MWd/tU was achieved, as shown in Fig. 9.204 [9.473]. This burnup is much less than the value of 8000 MWd/tU observed during LWR ramp tests [9.474]. Figures for the critical I_2 concentration obtained in out-reactor tests are very scattered at typical reactor temperatures and tend to be much higher than would be calculated from a reasonable estimate of the amount of fission

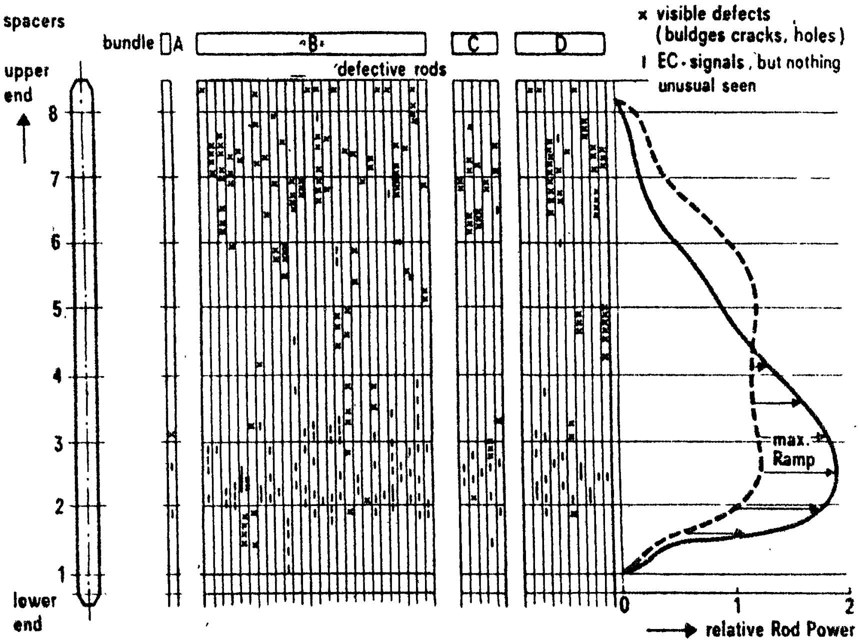

FIG. 9.200. Correlation between location of defects and a power ramp caused by a flux tilt in a PWR [9.437].

FIG. 9.201. Tear in fuel cladding, about 5 mm long, when the high power is maintained after initial wall penetration by SCC [9.467].

product iodine released during in-reactor power ramps (≤10%), as shown in Fig. 9.205 [9.475]. This observation also suggests that the problem of obtaining a suitable iodine chemistry may be a severe limitation on the success of both out-reactor tests and in-reactor ramp testing.

Hofmann and Spino [9.476] also estimated the critical amount of ZrI_4 required to cause cracking during their experiments and those of other investigators, as shown in Fig. 9.206. They comment that "the best results have clearly shown that iodine induced SCC failure of Zircaloy-4 cladding at elevated temperatures is caused only by gaseous ZrI_4. The condensed solid ZrI_x phases alone were not able to cause SCC failure". The results for ZrI_4 pressures needed to cause cracking,

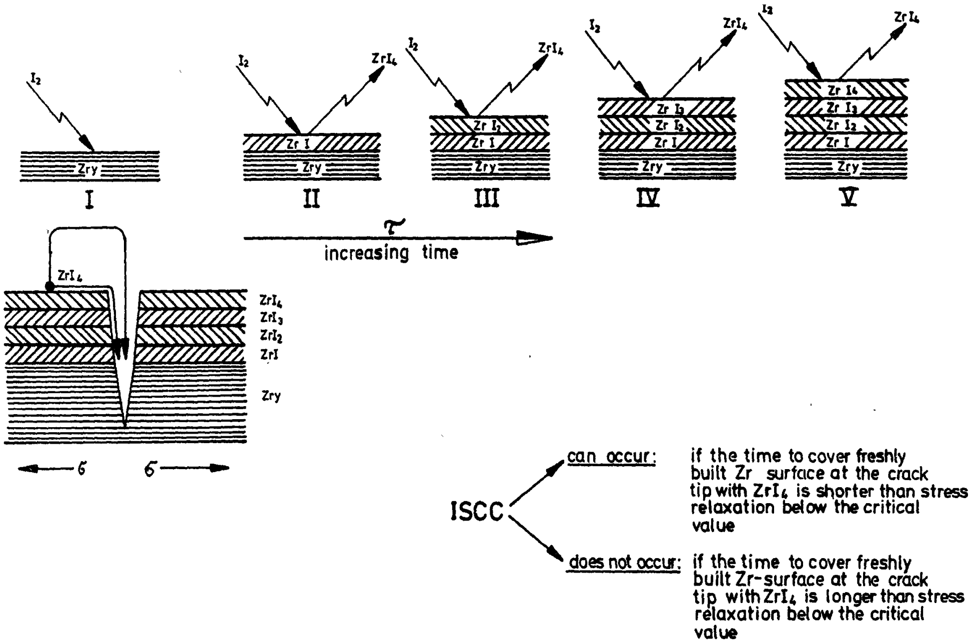

FIG. 9.202. Simplified model of the chemical formation steps of zirconium iodides [9.470].

shown in Fig. 9.206 suggest that at 573 K (300°C) only about 10^{-4} Pa are required for cracking. It is difficult to compare this value with the amount of iodine needed to cause an in-reactor failure because the free volume in fuel pins and the fractional release of the iodine generated are not well known.

9.6.7. The pellet–clad interaction process

In the light of the above observations, the overall PCI process appears to consist of five successive steps: an incubation time; a crack initiation process; a crack propagation process; a crack arrest step; and a secondary degradation stage. These steps will be considered individually, and initially in the context of laboratory tests.

9.6.7.1. Incubation time

Time is necessary after the rise in stress (either at the start of an in-reactor power ramp or when the stress is applied in the laboratory) to get the critical amount of ZrI_4 produced in proximity to a flaw in the surface oxide on the cladding inside surface. In laboratory tests, where large amounts of iodine may be added in a flowing system, this time can be long, and if gas flow rates are too high, the ZrI_4 may be swept away from the specimen surface and no crack will initiate. If the iodine is added when the Zr specimen is unstressed, the reaction of I_2 to form ZrI_4 and lower iodides appears to occur uniformly over the Zr surface. If stress, temperature and I_2 are applied simultaneously, the chemical reaction to form ZrI_4 appears to be localized at grain boundaries and triple points. If the experimental conditions are such that the ZrI_4 produced by this reaction is continuously swept away, then this process can continue, attacking more grain boundaries and producing progressively more intergranular corrosion [9.449].

This process may not produce a transgranular crack if the chemical conditions are unfavourable. Such situations, where a completely intergranular failure occurs, are typical of iodine solutions in some organic solvents (e.g. 0.1% iodine/ethylene glycol) [9.454]. Such a failure is shown in Fig. 9.194. Because intergranular attack is a much slower process than transgranular cracking [9.443], such complete intergranular failures take longer than transgranular failures (e.g. 3–5 days).

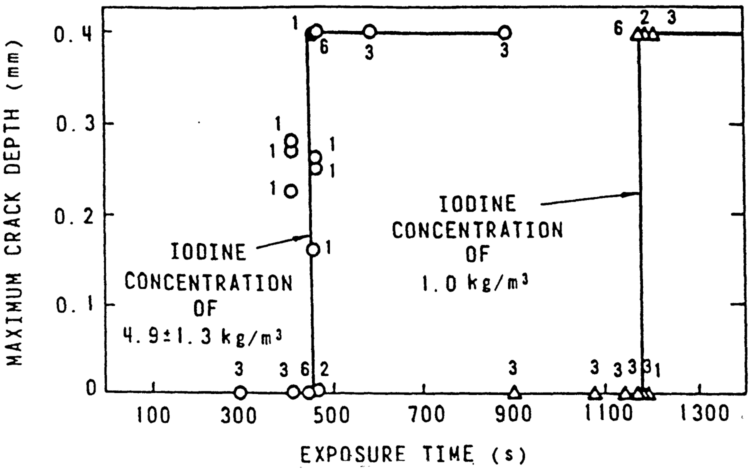

FIG. 9.203. *Exposure time dependence of iodine-vapour-induced SCC of stresses split rings of Zircaloy at 573 K (300°C) at two iodine concentrations (numbers beside data points indicate number of specimens tested) [9.471].*

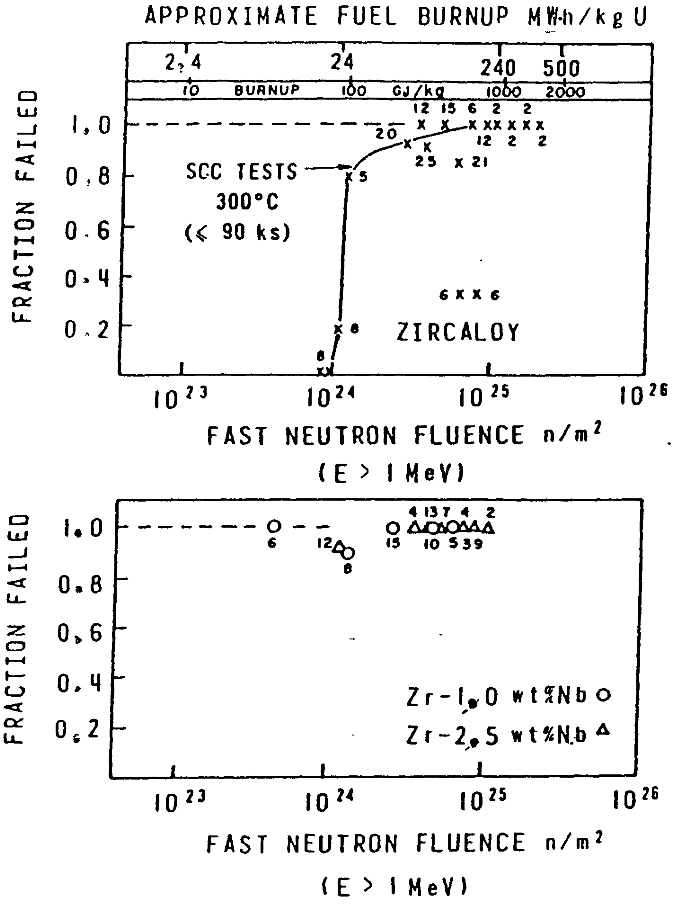

FIG. 9.204. *High susceptibility to iodine SCC in Zircaloy induced by neutron irradiation >8 × 10^{23} n/m^2 (upper graph) whereas Zr-Nb alloys are highly susceptible after a neutron fluence as low as 4 × 10^{23} n/m^2 (numbers beside data points indicate number of specimens tested) [9.473].*

If localized intergranular attack does not occur during the period when ZrI_4 production is occurring, then there will be no damage to the fuel cladding. This situation was common in CANDU refuelling incidents where fuel that did not remain in a high flux position longer than the critical

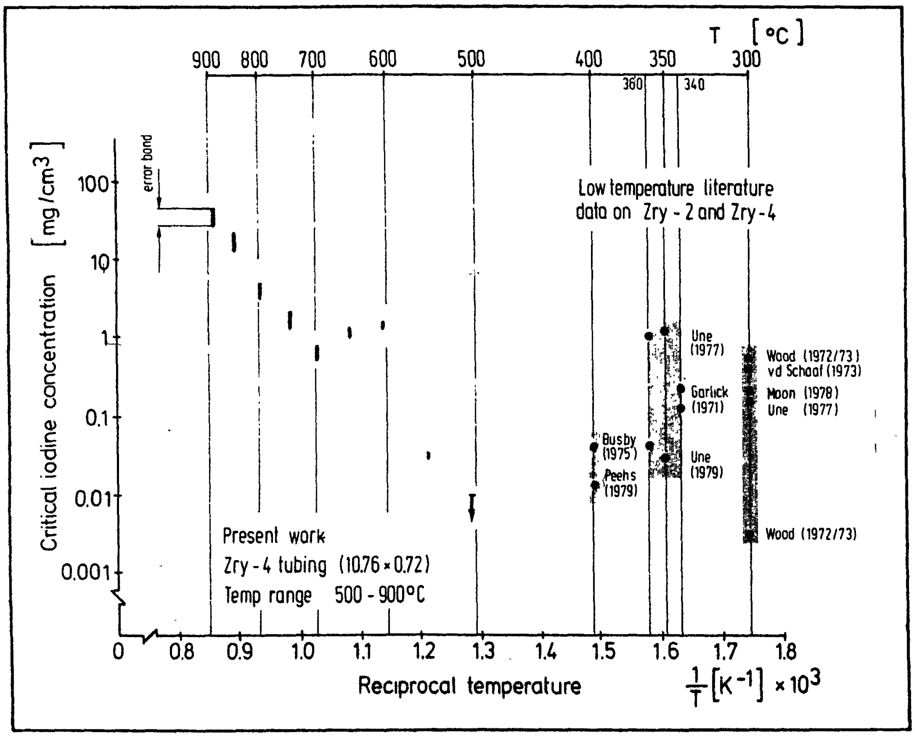

FIG. 9.205. Temperature dependence of critical iodine concentration for SCC in unirradiated Zircaloy-4 cladding ("present work" is [9.475]; other references provided in [9.475]).

(incubation) time, or survived the 2–3 h failure limit, remained intact and could undergo several more refuelling episodes without failure.

9.6.7.2. Crack initiation

Transgranular crack initiation apparently only requires stresses above the yield stress by an amount sufficient to crack the surface oxide film, and the presence of sufficient ZrI_4 in the vapour phase. If these conditions are met, then a transgranular crack will initiate, and propagate completely through the 0.4 mm thick wall of CANDU cladding in 20–30 s [9.462] or through the 0.6 mm thick wall of LWR cladding in 50–60 s [9.477].

If suitable ZrI_4 chemistry is not already present, but the material is under stress, then the iodine will attack the Zr grain boundaries and continue to generate intergranular corrosion until the chemical conditions for transgranular cracking are achieved. During this period the material will deform under the applied stress; this deformation is not a requirement for the cracking process to initiate, only evidence that a suitable chemistry was not present and that the material deformed mechanically under the applied dynamic stress [9.478].

It has been argued that the transition from intergranular to transgranular cracking occurs when the intergranular crack tip attains K_{Iscc} for transgranular cracking. A number of observations cast doubt on this hypothesis:

— Intergranular crack growth extends over a significant fraction of the wall thickness in BWR failures, but is almost completely absent in CANDU refuelling failures [9.443].

— If chemical equilibrium is attained before stressing the specimen, a completely transgranular crack is produced with no intergranular initiation.

— In some environments (e.g. I_2/ethylene glycol) intergranular cracking of statically loaded split-rings of fuel cladding is 100%. A 25 mm square cross-section DCB in the same environment cracks completely in a transgranular mode, and no intergranular features are observed where the cracks arrest at K_{1scc} [9.454].

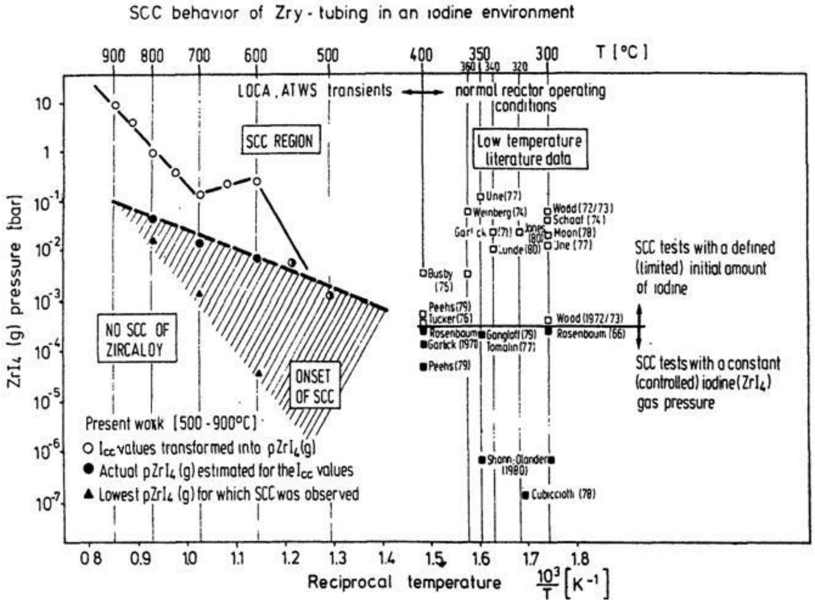

FIG. 9.206. Temperature dependence of critical concentration of ZrI_4 for SCC in unirradiated Zircaloy-4 cladding. ("Present work" is [9.476]; other references provided in [9.476]).

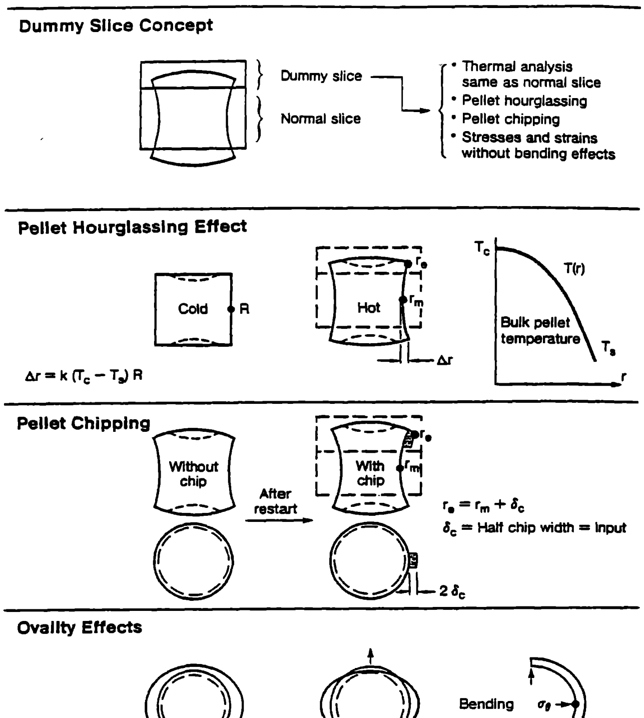

FIG. 9.207. Local shapes developed in fuel during operation [9.479].

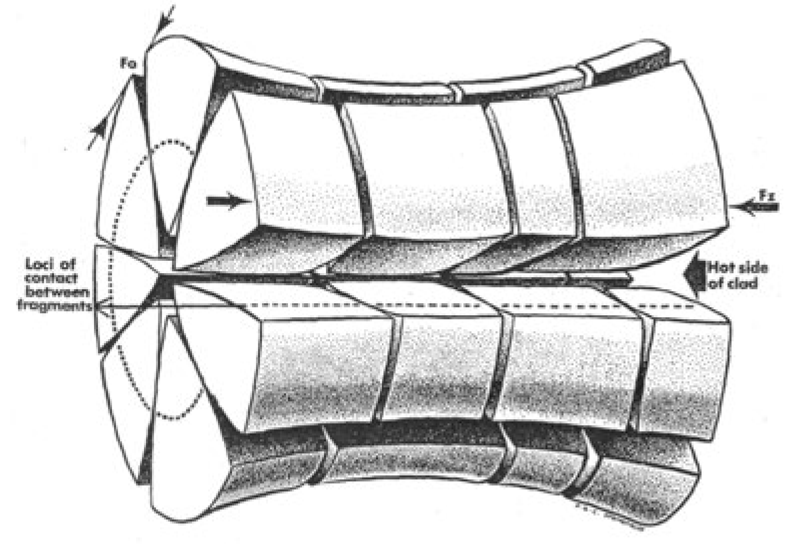

FIG. 9.208. Theoretical on-power shape of a UO_2 pellet [9.479].

— For identical split-rings (similarly stressed), the fraction of intergranular cracking varies widely in a range of iodine/organic solutions. For the same series of solutions the value of K_{1scc} measured for DCB specimens does not correlate with depth of intergranular cracking [9.451].

9.6.7.3. Source of stress

The stress applied to the cladding during a power ramp arises from the expansion of the UO_2 resulting from the increase in power and the corresponding increase in the UO_2 temperature. The UO_2 pellets do not expand symmetrically and tend to develop an hourglass shape [9.479], as shown in Fig. 9.207. Because of the temperature gradient across the UO_2 pellet it also develops a network of cracks [9.479] as shown in Fig. 9.208. As a result of these processes the maximum stress applied to the clad is at pellet interfaces and at major radial cracks in the UO_2 [9.480], as shown in Fig. 9.209. Stresses will reach a maximum once thermal equilibrium in the UO_2 is achieved and will then slowly relax as the UO_2 relaxes, provided fission gas release is not sufficient to significantly increase the gas pressure inside the fuel pin. Depending upon the size of the initial fuel/clad gap and the extent to which this gap has closed during the previous irradiation, a greater or lesser fraction of the stress generated by UO_2 expansion will be applied to the cladding. It now appears that the amount of strain in the cladding is less important than the rate of the chemical reactions (see below).

Other factors affecting the stress applied to the cladding include the following:

— The number of major radial cracks generated in the UO_2 [9.479]. If the ideal conditions outlined in Section 9.5.7.2 are not completely fulfilled, incipient failures may be observed as cracks in the cladding lined up with cracks in the periphery of the fuel. Fig. 9.210 shows an example.
— The coefficient of friction between the UO_2 and the cladding [9.479].
— Creep down of the UO_2 (soft pellets). The high speed of a PCI crack (<60 s to failure) does not allow much time for this relaxation to occur. Thus, it might be preferable to concentrate on increasing the number of radial cracks generated during the ramp.
— The presence of pellet chips, sometimes manifesting as missing pellet surface.
— Ovality in the cladding, affecting places of contact with the fuel.

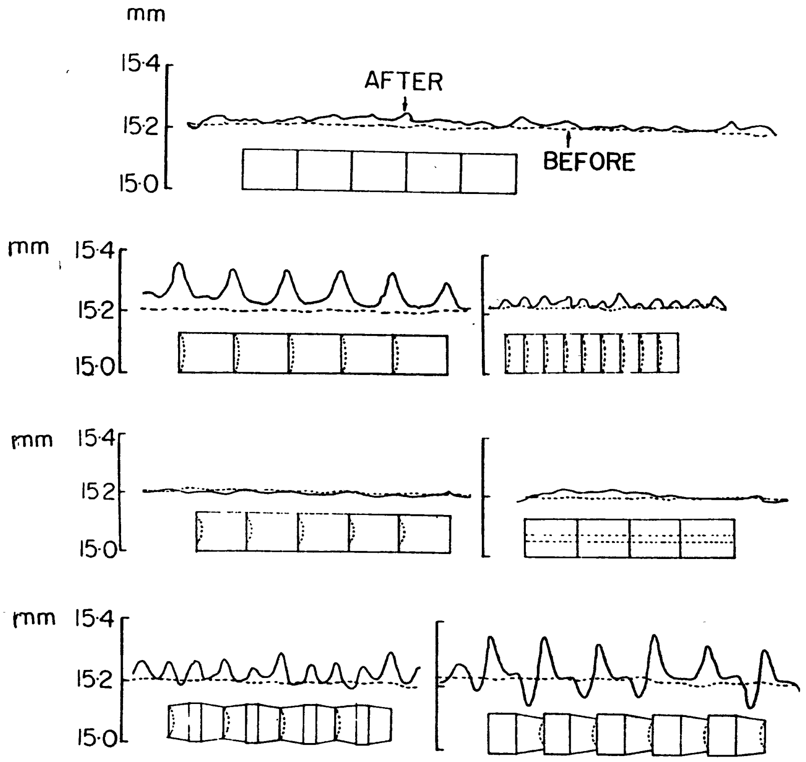

FIG. 9.209. Effect of pellet shape on the strain in CANDU fuel cladding caused by interaction with UO_2 fuel [9.480].

— Pellet shape (including length/diameter ratio and presence of chamfers and dishing) affects the extent of strain observed at pellet interfaces that result from a single thermal cycle [9.480]. The primary pin-hole failure will be almost radial and will barely penetrate the outer cladding surface before arresting, as shown in Fig. 9.211.

9.6.7.4. Strain to failure

The strain to failure parameter is something of a fiction resulting from a poor choice of test method. In all CANDU refuelling failures and most BWR ramp test failures, only pin-hole (or X mark) primary failures were observed, as shown in Fig. 9.211 [9.464, 9467]. Total strain in such failures is very small (<1%); local strains tend to be larger at arrested partial through-wall cracks (for reasons that will be discussed later). Since many primary pin-hole failures are not detected and a sufficiently strong fission product signal is not obtained until secondary degradation has started, much of the mechanical strain and all of the visible cracks will have been formed after the primary PCI crack has arrested. These secondary cracks may arise from mechanical (ductile) tearing of thin webs remaining adjacent to the primary pin-hole, as shown in Fig. 9.201 [9.467], or at an axial series of individual SCC cracks. Secondary cracking from regions of severe hydriding may also lead to fast fracture through the hydrides. Both these secondary degradation processes can be accompanied by significant local strain.

In laboratory tests using the creep rupture, or uniaxial tensile techniques, large strains to crack initiation and to failure are observed, as shown in Fig. 9.212 [9.449], because of unfavourable chemistry conditions. These strains are not a necessary part of the PCI process. Such measurements can be counterproductive, since they may mislead one into concluding that prior strain is a critical part of the cracking process, which it is not [9.481].

9.6.7.5. Pitfalls

PCI is a complex combination of mechanical and chemical phenomena. As such, several pitfalls may adversely affect the unwary experimentalist or modeller. The more frequent ones are discussed here.

PCI cracks generally nucleate at a few points on the cladding inside surface and propagate to form a roughly semi-elliptical crack. This crack will grow both radially and longitudinally until it penetrates the crack wall over a very small region (typically ≪1 mm long). In-reactor ingress of water immediately stops all PCI crack growth by hydrolyzing the active species (ZrI_4). At this time, all other PCI cracks that have initiated but not penetrated the tube wall will also be arrested. Unless a ramp test is deliberately stopped before the first through-wall penetration, the only source of partial through-wall cracks is when a primary failure has already occurred and all the SCC processes have been arrested. An example of partial through-wall cracks aligned in a defected fuel element is shown in Figs 9.210 and 9.211; the fuel in Fig. 9.211 was subjected to a power ramp of about 2 kW/m after a burnup of 4800 MWd/t U. If hot cell examination shows partial through-wall cracks, but apparently no through-wall crack then it is possible that either the primary through-wall pin-hole crack has been missed, or the hot cell metallographers have polished past the location of the through-wall crack without finding it. Otherwise, PCI cracks propagate so fast that it is unlikely that an in-reactor power excursion (as opposed to a deliberate short (<60 s) ramp test in an experimental reactor) will stop the crack before it penetrates the wall.

Because primary PCI failures are so small, arrest so quickly and oxidize rapidly to prevent the release of large fission product signals, most observed times to failure in power reactors are actually times to observe the formation of secondary degradation cracks. These secondary cracks, whether mechanical ductile tearing or secondary hydriding/deuteriding will not easily plug, and will provide detectable fission product signals. The advantage during CANDU refuelling failures was that the delayed neutron monitors on the fuelling machines produced better discrimination than a fission product monitor [9.481]. In addition, the presence of the fuelling machine already coupled onto the

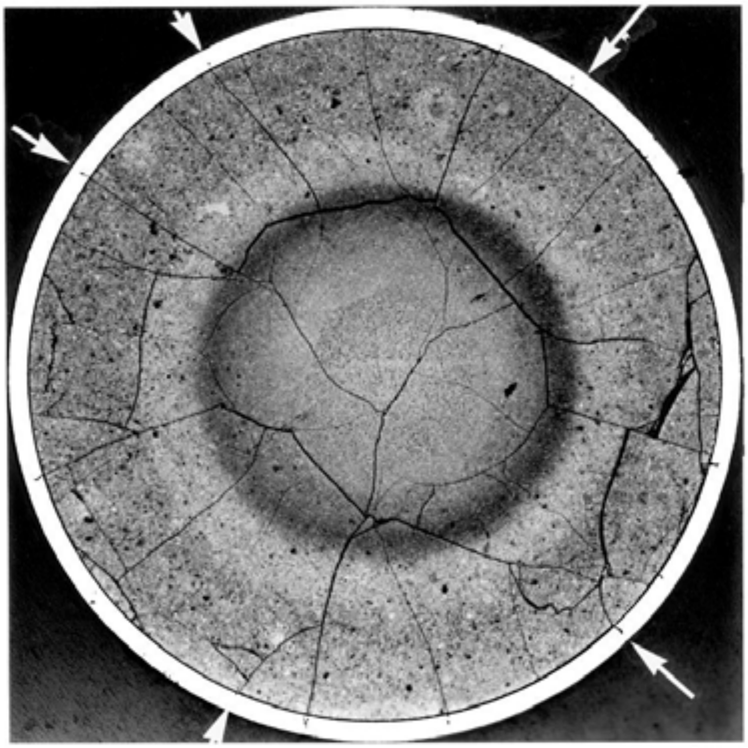

FIG. 9.210. Partial through-wall cracks in the cladding aligned with cracks in UO_2 fuel; through-wall defect elsewhere in fuel bundle after power ramp, early in the life of a CANDU reactor [9.466].

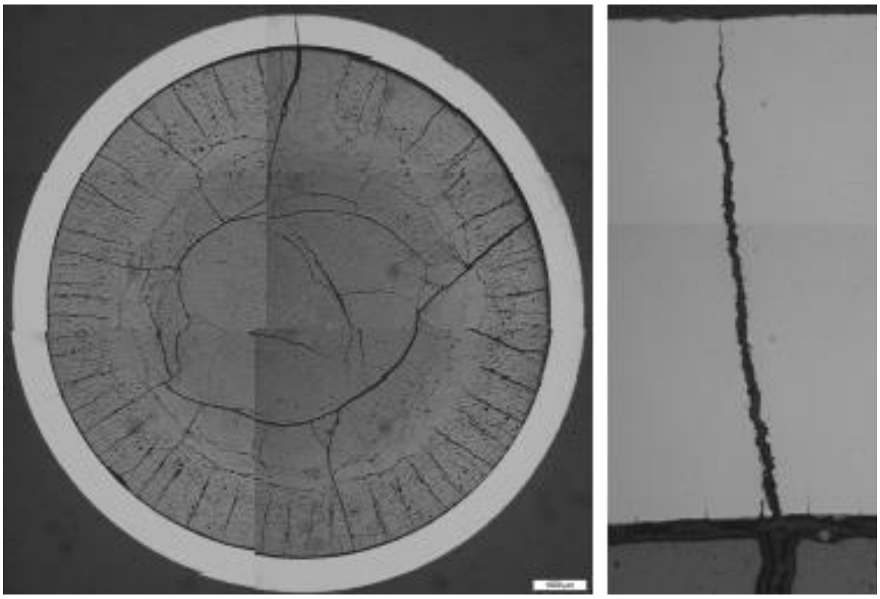

FIG. 9.211. Through-wall crack in fuel cladding aligned with crack in fuel leading to pinhole [9.467].

channel allowed rapid (<0.5 h) removal of a failed bundle, before severe secondary degradation took place; most failed CANDU fuel pins exhibit secondary deuteride blisters [9.482].

Tests conducted in the International TRANS-RAMP I and II programmes appear to have avoided these pitfalls [9.477]. Apparently, specimen preconditioning in these tests achieved sufficiently high power that some fission product release was occurring continually during preconditioning. This situation facilitated the continuous production of ZrI_4 by reaction with the cladding inside surface. When the specimens were ramped, a chemical environment suitable for PCI cracking was already present, and cracks apparently initiated without any incubation time, as shown in Fig. 9.213 [9.477].

The absence of an incubation time in these TRANS-RAMP tests caused some consternation because of the lack of agreement with CANDU refuelling and laboratory split-ring testing. Further simulation experiments [9.462] helped with the interpretation of the TRANS-RAMP results. Short

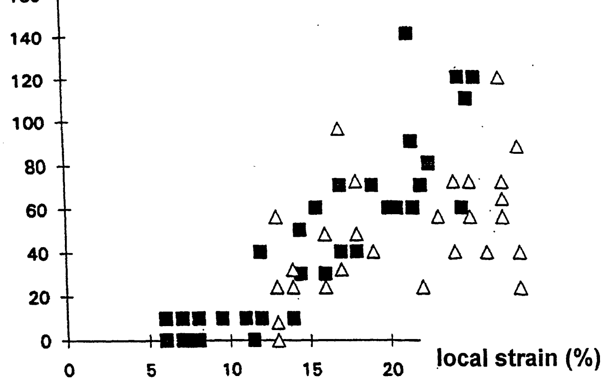

FIG. 9.212. Effect of local strain during uniaxial tensile tests on density of initiation crack during iodine-SCC of Zircaloy-4 plate at 623 K (350°C) in iodine vapour (squares and triangles represent different samples) [9.449].

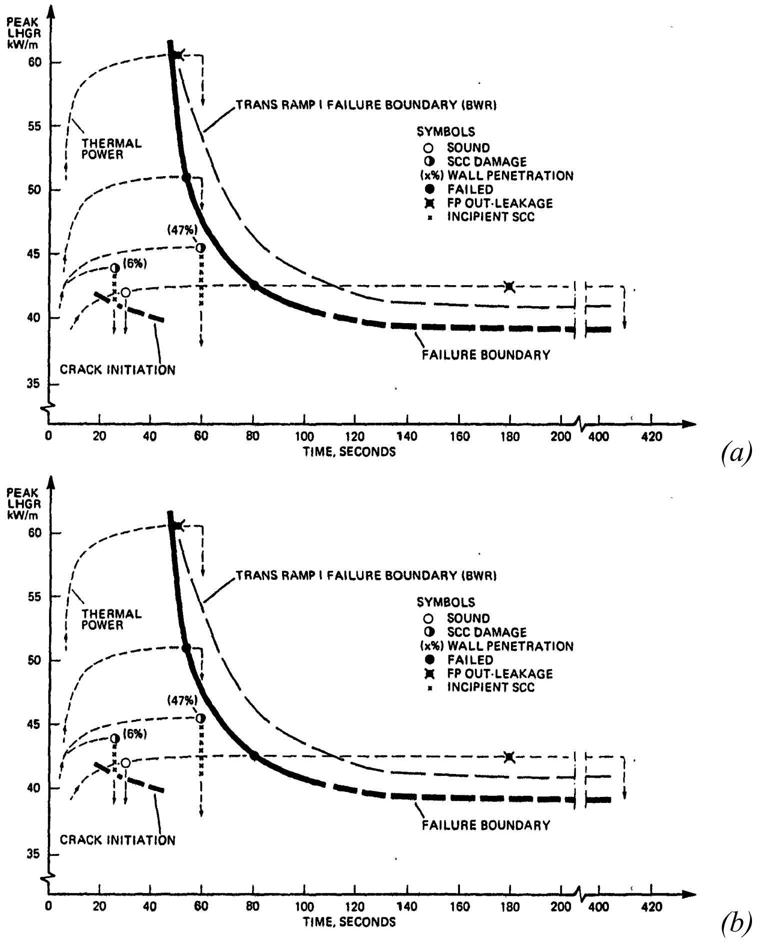

FIG. 9.213. (a) TRANS-RAMP PCI failure progression: BWR fuel [9.477]; (b) TRANS-RAMP PCI failure progression: PWR fuel [9.477].

(75 mm) lengths of CANDU fuel cladding had a small glass break-seal containing ≤1 g I_2 inserted and the tubes were evacuated and sealed by welding. The specimens were mounted on a cam driven compression device, as shown in Fig. 9.214, with a footprint of about 100 cm^2 to compress a small area of the cladding surface giving a maximum local tensile stress of up to 380 MPa. After the specimen had been shaken to break the seal and release the iodine, it was held at 523 to 623 K (250 to 350°C) for a pre-determined time (60 to 1800 s) without stress. After preheating times of about 180 s, partial through-wall cracks could be obtained while applying stress for as little as 5–10 s; through-wall cracks were obtained after being stressed for about 30 s; no cracks could be generated if specimens were allowed to react for more than 1800 s without stress application. Bearing in mind that CANDU fuel cladding has only 0.4 mm in wall thickness, compared with 0.7 mm for the TRANS-RAMP I/II tests, these results were a very good simulation of these ramp tests. In these simulations both crack initiation and propagation were entirely transgranular [9.462]. Intergranular attack is the result of excess I_2 and insufficient ZrI_4 in the specimen environments and is not an essential part of the PCI cracking process.

9.6.8. A mechanistic hypothesis

The importance of achieving the correct chemistry adjacent to the highly stressed region of the specimen (or fuel cladding) cannot be overemphasised. Zirconium iodide (IV) rather than I_2 is regarded as the aggressive cracking species, based on the clear results of Hofmann and Spino [9.468, 9.476].

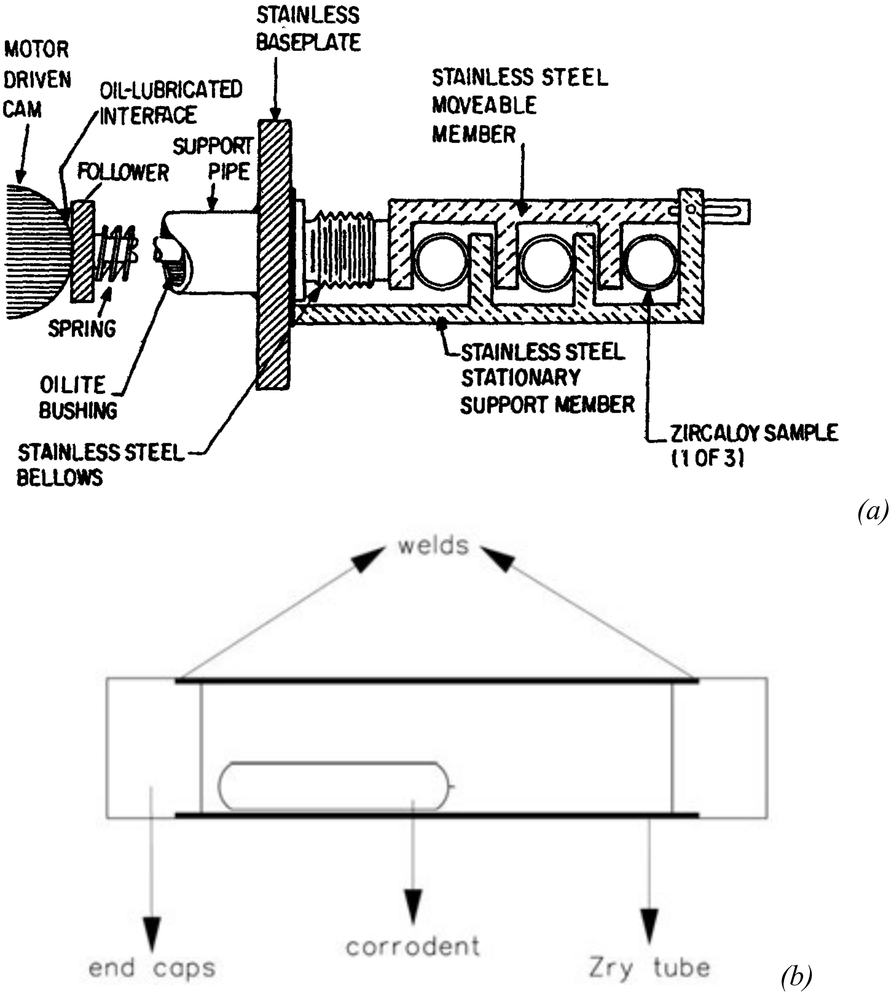

FIG. 9.214. Schematic diagram of (a) specimen compression apparatus and (b) typical specimen [9.462].

In SCC experiments most investigators add I_2 (and not ZrI_4) and do not achieve chemical equilibrium at the test temperature before applying stress to the specimen. Often, high flow rates of inert gas + I_2 sweep away ZrI_4 as it is produced, making it difficult to achieve favourable chemistry adjacent to the highly stressed region of the specimen. Thus, few laboratory tests have the appropriate chemical conditions at the start of the experiment. Dynamic loading will result in large strains to failure before suitable chemistry is achieved.

If there is an excess of I_2 at the start of a test on an already stressed test specimen, then this I_2 will preferentially attack the most highly stressed grain boundaries to produce the required ZrI_4. ZrI_4 is volatile and its evolution will result in initial intergranular corrosion of the specimen. Once sufficient ZrI_4 is present adjacent to the highly stressed region of the specimen, the cracking mode will change to fast transgranular propagation — irrespective of the local stress intensity factor. If ZrI_4 equilibrium is achieved before the stressing of the specimen, then an immediate nucleation of a transgranular crack occurs on application of stress. This result implies that K_{1scc} in ZrI_4 is very low; this value has not been measured.

9.6.9. ZrI_4 and Cs/Cd as potential causes of pellet–clad interaction

The question of whether PCI is caused by ZrI_4 or Cs/Cd has often been asked, but not answered definitively, since the beginning of PCI studies [9.460, 9.483]. Cs/Cd cracking is a metal/vapour induced process analogous to LME. LME in most susceptible metal systems is a purely intergranular cracking process [9.484]. The reverse is true for Zr; in almost all instances, Zr LME is purely transgranular, with ductile tearing of residual webs to produce fluting [9.436, 9.457]. The metals known to cause LME (or a metal/vapour induced process) in Zr alloys are listed in Table 9.32 [9.458]. An exception appears to be cracking in pure Cd, where both intergranular and transgranular failures have been observed.

TABLE 9.32. METALS KNOWN TO CAUSE AT LEAST SOME EMBRITTLEMENT OF ZIRCONIUM [9.458]

Embrittling element	Zr alloy	Type of test	Sources
Li[a]	Zircaloy-2	ZrB alloy irradiation and uniaxial tensile test[a]	[9.25]
Cs	Zircaloy-2	Simulated fuel expansion test[b], bend uniaxial tensile test, DCB	[9.4, 9.7, 9.10, 9.11, 9.26]
Cd	Zircaloy-2	Simulated fuel expansion test, uniaxial tensile test	[9.11, 9.12, 9.26]
Cs/Cd	Zircaloy-2	Simulated fuel expansion test, uniaxial tensile test, compressed tube test	[9.11, 9.26]
Cs/Ca	Zircaloy-2	Uniaxial tensile test	[9.11]
Cs/Sr	Zircaloy-2	Uniaxial tensile test	[9.11]
Cs/Y	Zircaloy-2	Uniaxial tensile test	[9.11]
Cs/Zn	Zircaloy-2	Uniaxial tensile test	[9.11]
Ag	Zircaloy-2	Ag spot welded to Zr, bend	[9.12]
Hg	Zircaloy-2, Zr-2.5Nb	DCB, small compact tension, bend	[9.7–9.10], [9.458]
Ga	Zr-2.5Nb	Small compact tension	[9.458]

[a] This test was designed to show the effect of He bubbles produced under irradiation on tensile properties at 300°C. A Zircaloy-2/boron alloy was prepared and irradiated, annealed at 800°C to grow He bubbles, and tested under uniaxial conditions. The fracture surface was brittle, contained few He bubbles, and was almost 100% TG pseudocleavage. For further details see Ref. [9.458].

[b] Simulated fuel expansion was achieved by inserting either an aluminum or alumina cylinder in the tube and expanding it with ‘rams’ at each end.

The criterion for achieving LME (or a metal/vapour induced process) of Zr alloys is that the aggressive liquid metal or metal vapour must be able to wet a clean Zr surface. Even the presence of a 2 nm air-formed oxide on the Zr surface is sufficient to prevent cracking.

The clean surface usually has to be produced mechanically during crack initiation, under conditions where the liquid metal or metal vapour can wet the freshly produced surface before the air-formed film can reform. LME cracks propagate much faster than iodine SCC cracks, as shown in Fig. 9.215.

Cs/Cd vapour cracking will also arrest immediately when a through-wall crack is achieved in fuel cladding in-reactor, because the ingress of water will immediately oxidize any clean metal surface that is present. In laboratory tests [9.461, 9.483], where the external atmosphere may have been less oxidizing than reactor water, and because of the much higher crack velocity of LME and metal/vapour induced process cracks compared with iodine induced cracks, as shown in Fig. 9.215 [9.445, 9.447], cracks tend to grow to a few mm in length after through-wall penetration before arresting.

Other than the above distinction, it is very difficult to distinguish iodine SCC from a metal/vapour induced process from Cs/Cd based on the fractography of the two processes. At one time [9.461] it was thought that iodine SCC cracks would always show some intergranular cracking features, even if the fracture was almost entirely transgranular; whereas Cs/Cd induced cracks would be entirely transgranular. This distinction is untenable because there is evidence that entirely transgranular cracks could be produced if the iodine chemistry was allowed to equilibrate before stressing, and if the Cs/Cd ratio was varied, then a few intergranular features could be observed fractographically [9.461, 9.483]. Thus, unless evidence to the contrary is obtained, either species could be responsible for PCI failures.

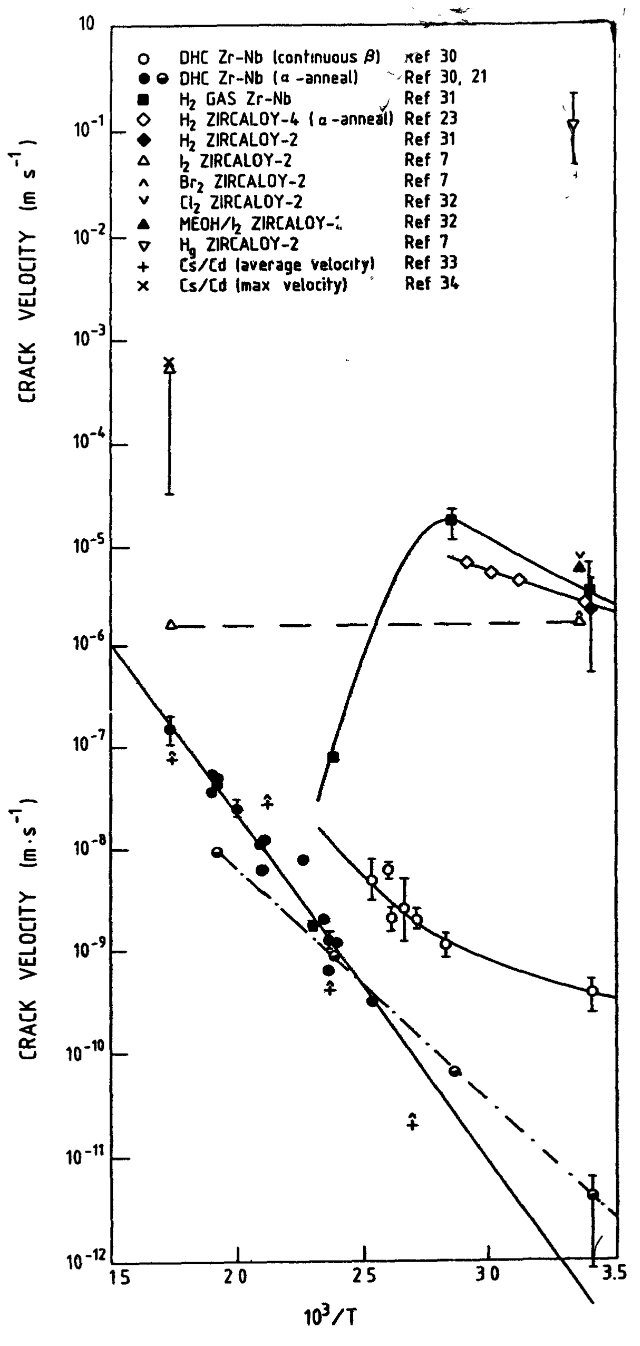

FIG. 9.215. Temperature dependence of crack growth rates for SCC and hydride cracking in zirconium alloys (references provided in [9.447]).

9.6.10. Modelling PCI failures

Attempts to model PCI processes have been notable for their failure to include any components for the iodine/Zr chemical reaction (e.g. Ref. [9.481]), which, as we have seen, is one of the most important components of the mechanism.

Models seem to be based on the following aspects:

- A strain to failure premise that, as we have seen, is not a necessary component of the PCI process; it is usually a result of using a dynamic loading technique and is a consequence of not obtaining a representative iodine chemistry at the beginning of the test.
- There is generally no module covering the $2I_2 + Zr \rightarrow ZrI_4$ reaction, with the intermediate formation of involatile ZrI, ZrI_2 and ZrI_3, as shown in Fig. 9.216 [9.470, 9.484].
- A cumulative damage assumption, for which there is little supporting evidence. It seems to be based on one rod in the TRANS-RAMP-4 tests, for which no good fractography seems to be available.
- Much weight is being placed on the relaxation of the strains from the UO_2 (soft pellets), without any effort to study the cracking patterns of the UO_2 with various additives, or to show that UO_2 relaxation times are fast enough (<60 s) to arrest cracks in the cladding that initiate immediately, without any incubation period.

Widespread use of stress rupture (or other dynamically loaded tests) largely invalidates much of the data used in the models [9.485].

It appears that models that include the chemical kinetics of the process, and the use of statically loaded test methods that do not induce a large, progressively increasing strain into the equation, will be required before any confidence can be placed in the predictive capability of PCI models. Unfortunately, progress in this area is very limited. An attempt to model a series of in-reactor

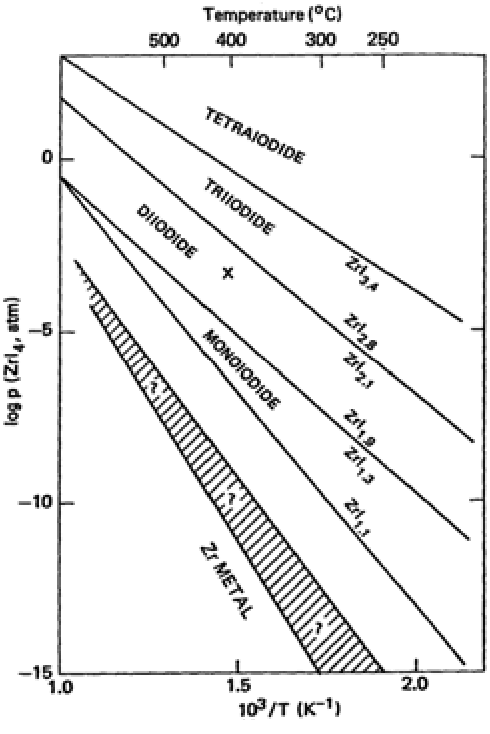

FIG. 9.216. Pressures of ZrI_4 in gas in equilibrium with solid zirconium iodide phases. Lines indicate the regions of stability of any two solid phases. Compositions of the equilibrium solid iodides are indicated in the figure. The areas between the lines represent solid iodides of variable composition. The shaded area with question marks indicates the probable location of chemisorptions curves for iodine on zirconium. The single cross indicates the lowest iodine concentration at which SCC was observed (based on [9.470 and 9.484]).

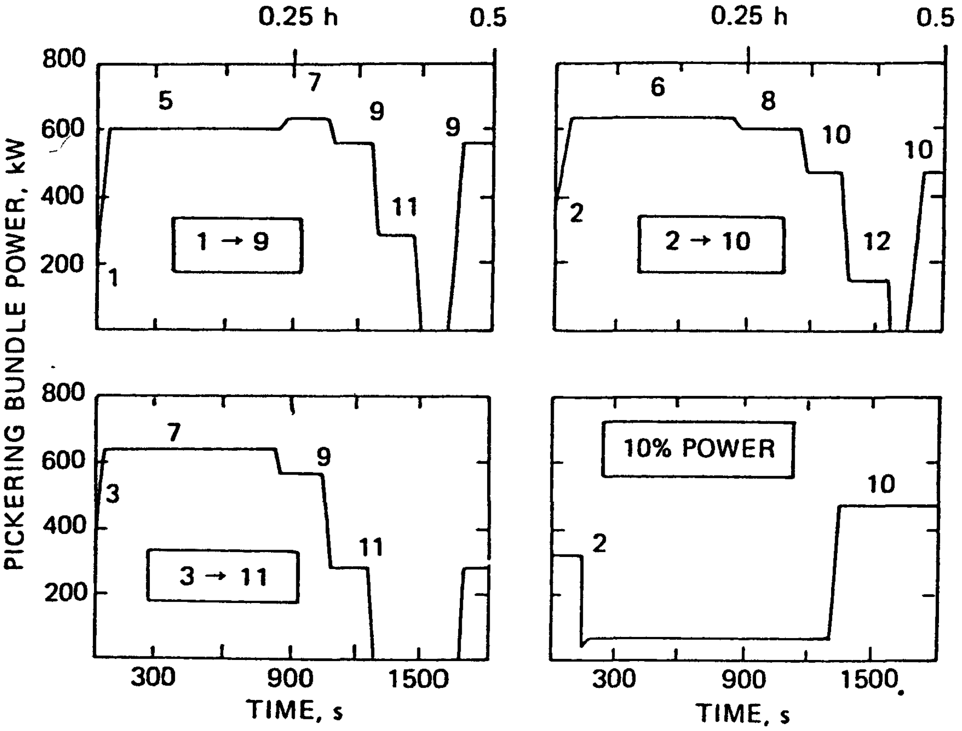

FIG. 9.217. Power variation during 8-bundle shifting in CANDU reactors. The numbers indicate channel positions in which the bundles reside temporarily. Movement of fuel bundles from position 2 to position 10 with the reactor at 10% full power did not cause defects because the fuel did not experience intermediate high powers [9.466].

ramp tests [9.486] still puts much weight on strain to failure criteria and has no involvement with iodine chemical reactions with Zr.

Improved models that include a good physicochemical component and do not prejudge the necessity for strain to failure, coupled with detailed studies of the chemical species present in partial and through-wall cracks, should help to eliminate uncertainties. In LWRs, apart from the necessity for gap closure to occur to develop local stresses, burnup and temperature do not appear to be critical variables, except to the extent that they degrade protective measures. In CANDU reactors, where the cladding collapses onto the fuel early in life, SCC does depend on burnup.

9.6.11. Mitigation

Mitigation of PCI failures can be achieved by operational controls that minimize power ramps, such as those identified in Figs 9.198 and 9.199. Such procedures were implemented in BWRs and CANDU reactors. An example in the latter was changing from 4-bundle shifts to 8-bundle shifts. This procedure reduced the size of the power increase sustained by the most vulnerable fuel bundles, as shown in Fig. 9.217 [9.466]. Such fuel management schemes are costly because of the reduced average fuel burnup and the loss in plant capacity factor. RBMKs minimize such effects by not moving fuel assemblies from a location of low power to one of higher power; also, control rods are in separate channels and movements are limited. RBMK fuel failure rates are low, in the range 0.02–0.05%.

Increasing the tolerance of fuel to power ramps and decreasing susceptibility to PCI has been addressed either by putting a ductile barrier layer on the inside surface of the cladding, or by coating the inside surface of the cladding with a lubricant or a chemical trap; both graphite and siloxane work this way.

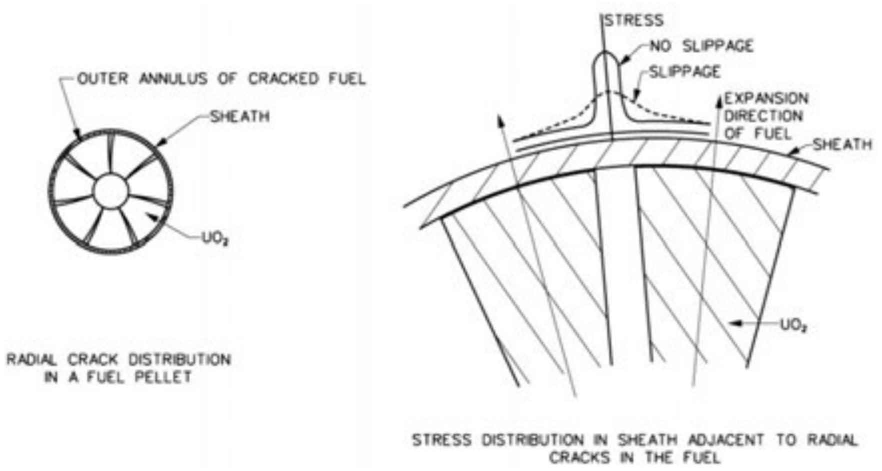

FIG. 9.218. Schematic diagram of the concentration of tensile stress set-up in fuel cladding opposite cracks in the fuel. The stress is reduced if the fuel and cladding can slip.

When the number of fuel failures became significant, programmes were inaugurated to identify the cause. For CANDUs ten potential defect mechanisms were identified [9.487] — including mechanical damage during manufacturing and handling, corrosion, fatigue, hydriding and stress corrosion — and several methods of eliminating them were proposed [9.488]. As indicated earlier, when the power is increased, the fuel cracks and the outer segments expand radially. If there is no slippage between the cladding and the fuel, the stress and strain concentrate in the cladding at the radial cracks in the fuel, as shown in Fig. 9.218. From analysis [9.479], the strain concentration, $\varepsilon_{max}/\varepsilon_{av}$, in the cladding at the point of plastic instability is given by:

$$\varepsilon_{max}/\ \varepsilon_{av} \propto \mu/Nh \tag{9.47}$$

where

ε_{max} is the maximum strain in the cladding;
ε_{av} is the strain if the stress was not concentrated over the cracks;
μ is the coefficient of friction between the fuel and the cladding;
N is the number of cracks in the fuel adjacent to the cladding;

and h is the work hardening coefficient of the cladding material.

To minimize the stress and therefore strain concentration, and subsequent premature fracture, Eq. (9.47) indicates there should be many cracks in the fuel, the work hardening coefficient should be high and the coefficient of friction between the fuel and the cladding should be low. A simulation test was developed, as shown in Fig. 9.219 [9.489], comprising a core of aluminum (to represent the hot centre of the fuel) surrounded by an annulus of UO_2 or Al_2O_3 (to represent the outer part of the fuel) fitted into a short section of cladding. To represent initial irradiation, the soft aluminum was compressed; by expanding radially it cracks the brittle ceramic annulus. A power ramp is simulated by further compression that presses the cracked ceramic against the cladding. The principle of this method has been included in SCC tests [9.490], and in tests on LWR fuel cladding [9.491–9.493]. The expectation from Eq. (9.47) of the effect of the main variables on strain concentration was confirmed [9.489]. The coefficient of friction was lowered by placing a layer of graphite or siloxane on the inside surface of the cladding, resulting in a reduction in strain concentration and increase in ductility, as shown in Fig. 9.220 [9.487]. Full size elements containing graphite or siloxane layers survived large power increases after a period at low power [9.487, 9.489]. The coatings were called CANLUB, a name taken from their role in reducing mechanical interaction. Development of the

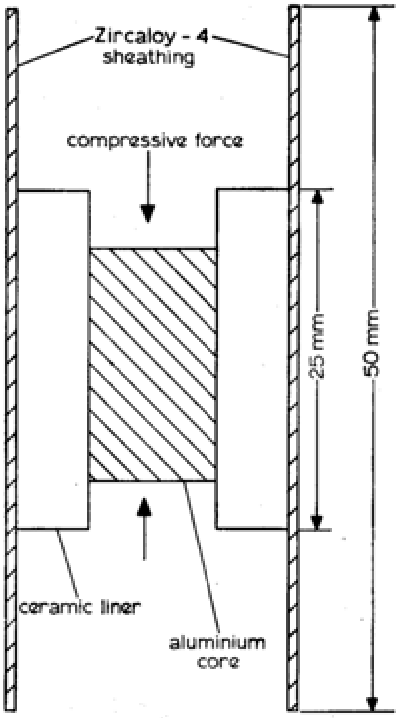

FIG. 9.219. Schematic diagram of the fuel swelling simulation test set-up. The soft aluminium core represents the centre of the fuel and the ceramic liner (or steel segments) represents the peripheral cracks in the fuel. The radial expansion of the aluminium core during compression cracks the ceramic, which in turn interacts with the inside surface of the cladding, stressing it, as shown in Fig. 9.218 [9.489].

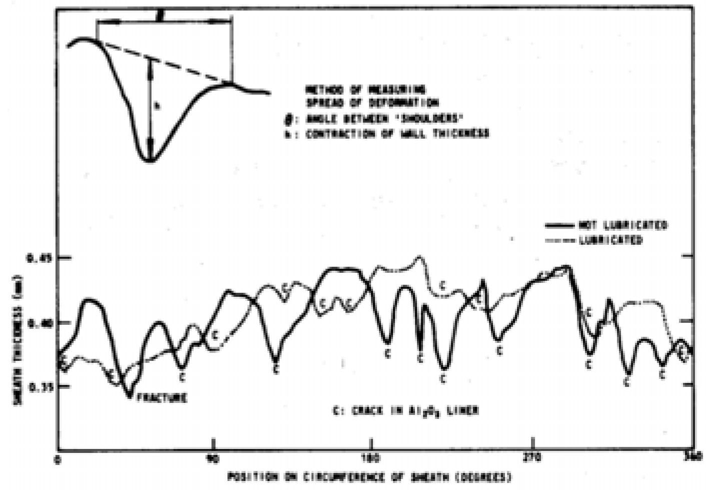

FIG. 9.220. Wall thickness variation in fuel cladding after simulated swelling tests to the same circumferential elongation. When no graphite is present the strains are concentrated over the cracks in the simulated fuel (Al_2O_3) whereas the graphite spreads the deformation more evenly [9.487].

CANLUB graphite coating was sufficiently advanced for it to be introduced in Douglas Point in January 1972 and in Pickering-1 in November 1972; it has been used ever since. The siloxane coating alternative was somewhat more costly than CANLUB graphite and adds hydrogen to the cladding; it has never been adopted. Although separate experiments showed μ was much reduced by the graphite coating, as shown in Fig. 9.221, and reduced the average number of cracks generated in the UO_2, as

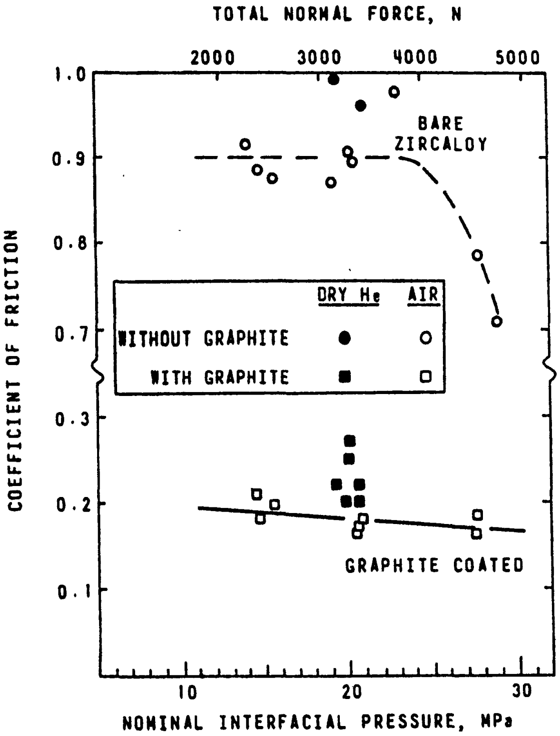

FIG. 9.221. Coefficient of friction between UO₂ and Zircaloy measured at 570 K (300°C) showing the reduction by a graphite layer [9.494].

shown in Fig. 9.222, its role in increasing the tolerance of fuel to power ramps may also include reducing susceptibility to SCC by either trapping the corrodents or acting as a physical barrier [9.494].

A major programme of barrier cladding development was started by General Electric in 1974 [9.464] and the large number of possible barriers was reduced to a choice between zirconium and copper barriers by 1978 [9.491], with zirconium being chosen. The modification to the cladding and its incorporation into fuel elements are described in patents, (e.g. Refs [9.495, 9.496], and the basic fabrication processes are summarized in Chapter 4, in Volume 1 of this publication. In-reactor, the elements were tested in ramps that were increased stepwise at one hour intervals (Fig. 9.223) [9.464]. The zirconium barrier was adopted as the standard by 1987 [9.497, 9.498] and has continued to be effective, although minor compositional adjustments, such as high iron concentrations, have been made to reduce the corrosion rate of the barrier after an initial primary failure, and thus reduce the severity of the secondary hydride induced defects [9.499].

9.6.12. Summary

Cracking of zirconium alloy fuel cladding during a power ramp after operating at lower power has been correlated with stress corrosion by fission products such as iodine and caesium. The source of the stress is differential fuel expansion from the power ramp. Cracking can be minimized by conservative reactor operation or by placing a protective layer between the fuel and the cladding; successful candidates are graphite and zirconium.

9.7. HYDRIDE EMBRITTLEMENT

Hydrides are brittle. They precipitate as platelets, as shown in Fig. 9.224 [9.500, 9.501], or as needles. The format and distribution of hydrides in components and specimens made from zirconium alloys have a wide variation. Their damaging effects may result in a reduction in fracture toughness and tensile ductility or in a form of time dependent cracking. Hydrogen diffuses up stress

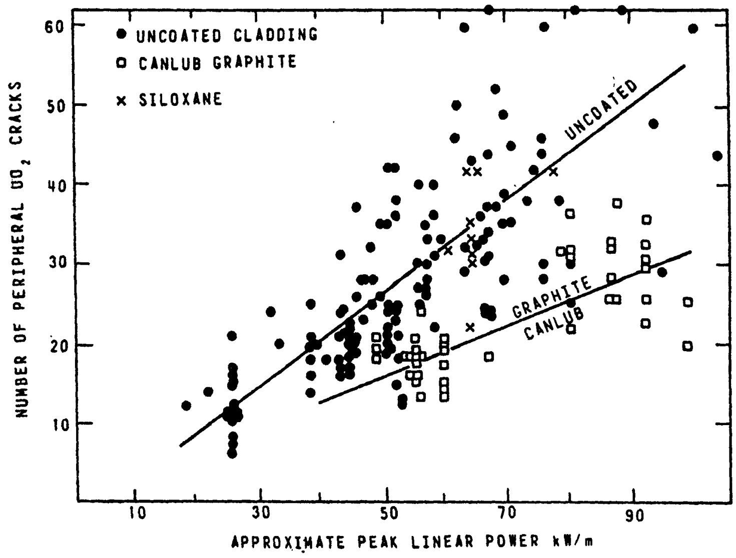

FIG. 9.222. Graphite lubrication decreased the number of peripheral cracks in the cross-sections of irradiated fuel elements whereas siloxane coating had no effect [9.494].

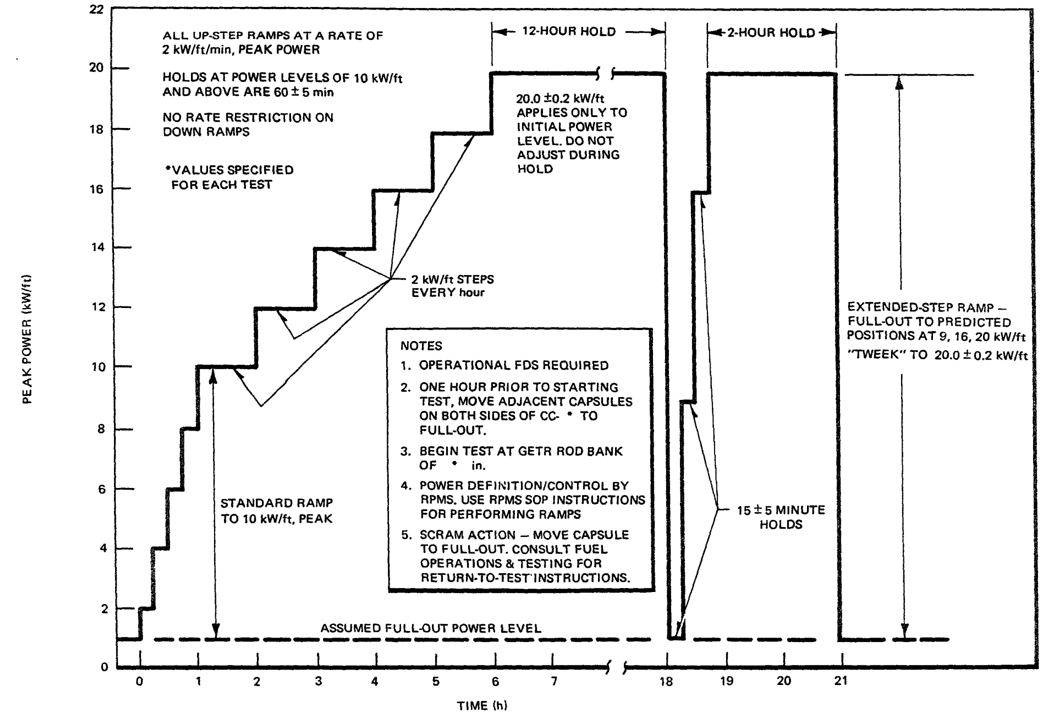

FIG. 9.223. Fuel rod test sequence used to evaluate tolerance of power ramps [9.464].

gradients, down temperature gradients, up or down alloy solute concentration gradients and down hydrogen concentration gradients. This movement may lead to time dependent failure when the solubility limit is exceeded and hydrides form at one end of the gradient. Since hydrogen is sometimes absorbed by a component during service, the hydrogen movement and increase in concentration necessitate continuous vigilance during the life of the component to ensure it performs as designed.

General principles for inspection are described in Chapter 4, in Volume 1 of this publication, while details of hydrogen ingress are described in Chapter 8, in Volume 2 of this publication. Methods for reducing the harmful effects of hydrides can be devised from the knowledge gained from operating experience and laboratory research. Several reviews have been written on hydrides and their consequences [9.502–9.513].

The following sections will first consider the relevant part of the Zr-H phase diagram and the hydrides themselves. Discussion on how the hydrogen moves and how it can be distributed follows. Next the effects of hydrides on fracture properties are described. Failures of components during service caused by hydrides are outlined and finally the information is gathered to discuss how to safeguard structural integrity.

9.7.1. Zr-H phase diagram

Knowledge of the phase diagram of the zirconium-hydrogen system is required to determine when hydrides could be present in a component. The phase diagram is of the eutectoid type, Fig. 2.23 [9.514, 9.515] and Fig. 9.225 [9.516], with the following phases: a random interstitial but terminal solid solution (TSS) in the α phase, with a maximum hydrogen solubility, 5.93 at.% (690 ppm), at the eutectoid temperature, 823 K (550°C); the eutectoid is at a hydrogen concentration of 37.5 at.% (6535 ppm). In the β phase, a random interstitial but TSS extends to a maximum solubility of 51.5 at.% (11 500 ppm) at 1143 K (870°C). Hydrides form when the terminal solid solubility is exceeded.

9.7.1.1. Crystal structure

Four hydrides have been identified called γ, δ, ε and ζ [9.517–9.521]:

The most commonly reported hydride is face centred cubic with a space group of $Fm\bar{3}m$ [9.522]. It has a composition variously reported but usually between $MH_{1.5}$ and $MH_{1.67}$ and a lattice parameter at room temperature of 0.478 nm[4] [9.522]. It is designated the δ phase.

The hydride may take the form of a precipitate with a face centred tetragonal (c/a > 1) structure with a space group of $P4_2/n$ or $I4m_2$ [9.522]. The composition is MH and the lattice parameters at room temperature are $a = 0.460$ nm and $c = 0.497$ nm [9.268]. It is designated the γ phase. Using interference microscopy and transmission electron microscopy (TEM) the precipitation was shown to follow the phenomenological theory of martensitic transformation [9.523].

At high concentrations of hydrogen, $MH_{1.67}$ to MH_2, a face centred tetragonal (c/a < 1) structure appears with a space group of I4/mmm [9.522]. The lattice parameters at room temperature are $a = 0.498$ nm and $c = 0.445$ nm [9.522]. This structure is designated the *ε* phase.

Using X ray diffraction, metallography, interference microscopy and TEM, the transformation of δ-hydride to ε-hydride was shown to follow the phenomenological theory of martensitic transformation [9.524, 9.525].

A transient hydride phase has been reported that is a precursor to γ- or δ-hydrides [9.521, 9.526]. This metastable phase is called ζ-hydride. It has a composition of $ZrH_{0.25-0.5}$ and a hexagonal close packed structure with $a = 0.33$ nm and $c = 1.03$ nm, with a space group of P3m1.

First principle calculations at the atomic level [9.527] have been carried out on several aspects of hydrogen in zirconium using density functional theory with the Vienna Ab initio Simulation Package software and performed with plane-wave expansions for the one-electron wave functions and suitable pseudopotentials [9.527, 9.528]. The complex interactions between electrons in the field of the positive nuclei were described by the generalized gradient approximation. The calculated formation energies of the various hydrides follow their composition [9.527, 9.528], as shown in Fig. 9.226. The hydrides with the lower atomic fraction of hydrogen are metastable with respect to

---

[4] Lattice parameters are often quoted to four significant figures but here they are quoted to three significant figures to cover the reported variation in the last number.

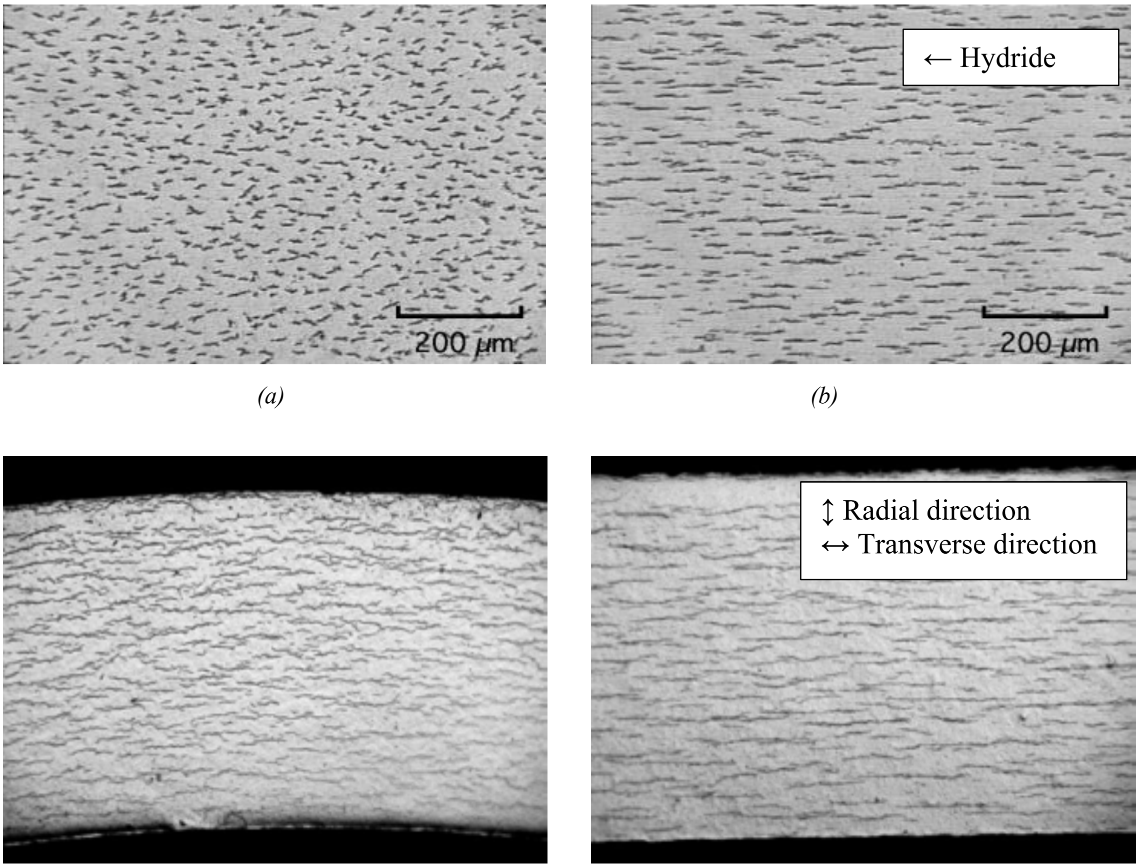

(a) (b) (c) (d)

FIG. 9.224. Distribution of hydrides on (a) transverse-radial plane and (b) longitudinal-radial plane in cold worked Zr-2.5Nb pressure tube material containing 79 ppm (0.72 at.%) hydrogen and (c) transverse-radial plane and (d) longitudinal-radial plane in Zircaloy-4 fuel cladding in the CWSR condition containing 200 ppm (1.79 at.%) hydrogen. [9.500, 9.501].

the remaining three hydrides. Some of the calculations for the δ phase [9.528] predicted lower formation energy for tetragonal hydrides than for the experimentally observed cubic hydride but the differences were very small, less than 2%.

With all the hydrogen in solution at an elevated temperature, rapid cooling to room temperature cannot retain the hydrogen in solution; hydrides precipitate at random and often on dislocations [9.529]. As the cooling rate is reduced in pure Zr and Zircaloy-2 containing 70 to 200 ppm (0.63 to 1.79 at.%) hydrogen, the sequence of precipitation that is observed is as follows: at high rates only γ phase is produced; a mixture of γ and δ hydrides, many of which contain twins, precipitate after intermediate cooling rates; and below 2°C/min only untwinned δ hydrides are observed [9.530–9.534]. The other trend is for more hydrides to precipitate in grain boundaries as the cooling rate is decreased [9.530, 9.531, 9.534]; these hydrides were identified as δ phase after slow cooling [9.533].

When hydrides are precipitated in pure zirconium, the dominant habit plane, as judged from light metallography, is $(10\bar{1}0)$ [9.535, 9.536]. The complex pattern of lattice shears on the prism planes for this habit plane for γ hydride is described by Weatherly [9.531]. With the addition of alloying elements, the habit plane approaches the basal plane, often $(10\bar{1}7)$ [9.537–9.540], which is about 14.7° from the basal plane. For γ-hydride this habit plane is accounted for when the net shape of the transformation is described using lattice shear by the movement of partial dislocations on the basal plane [9.537, 9.541]. Pyramidal planes, including $(10\bar{1}1)$ and $(10\bar{1}3)$, have been reported as habit planes [9.536, 9.538, 9.542, 9.543]; the angles between the basal plane and a $(10\bar{1}1)$ and a $(10\bar{1}3)$ plane are 61.5° and 31.5°, respectively. Similar habit planes are found at grain boundaries in annealed Zircaloy-2, thus explaining the preferred precipitation on grain boundaries that make angles of 35–40° and 60–65° to the basal planes of adjacent grains [9.544, 9.545]. Tilt boundaries were reported to be more favourable sites than twist boundaries [9.546].

Usually the close packed planes and close packed directions of each phase are parallel, providing the relationship between the hydride and the zirconium matrix of $(111)_{\text{hydride}}$ is parallel with $(0001)_{\text{Zr}}$, and $[1\bar{1}0]_{\text{hydride}}$ is parallel with $[11\bar{2}0]_{\text{Zr}}$ [9.530, 9.547]. These crystallographic relationships have been confirmed by subsequent studies, although other crystallographic relationships have been observed for δ-hydrides [9.530, 9.548]:

$$(111)_\delta \parallel (10\bar{1}0)_\alpha;\ [1\bar{1}0]_\delta \parallel [11\bar{2}0]_\alpha,\ \text{and}\ (111)_\delta \parallel (11\bar{2}\,\bar{2})_\alpha;\ [1\bar{1}0]_\delta \parallel [\bar{1}100]_\alpha$$

and γ-hydrides in pure zirconium [9.537] and Zr-1Nb [9.549]:

$$(001)\gamma \parallel (0001)_\alpha;\ [1\bar{1}0]_\gamma \parallel [1\bar{2}10]_\alpha.$$

Carpenter [9.550] used the usual structural relationships to calculate the strains in three directions in Zr from dilatational misfit between the precipitate of zirconium hydride and the metal at room temperature. For δ phase the strain in [0001] was 7.2% and in $[11\bar{2}0]$ and $[1\bar{1}00]$ it was 4.58%, explaining a habit plane of a plate close to the basal plane and providing a volume change of 17.2%. With zirconium deuteride, the same quantities have values of 7.04%, 4.44% and 16.66%, respectively [9.551], based on Ref. [9.552]. As the temperature increases, the calculated strains increase. At 573 K (300°C) the same quantities have values of 7.76%, 5.21% and 19.29%, respectively [9.551], based on Ref. [9.553]. In the γ phase, the strains are similar in [0001] and $[1\bar{1}00]$, being about 5.7%, while in $[11\bar{2}0]$ the strain is only 0.55%, thus explaining easy coherent growth along this direction and the formation of γ-needles. The volume change is 12.3%. Consequently, the elastic strain energy for the formation of γ-hydride is lower than that for δ-hydride [9.554, 9.555]. Based on elastic strain energy, the first phase to nucleate on cooling, possibly from the transient ζ-hydride, is expected to be the γ-hydride.

Much of the large reported variation in the presence of each hydride phase is caused by comparing materials with a range of concentrations of hydrogen, impurity and alloying elements, after various cooling rates and hold times at different temperatures, various grain structures of the zirconium alloy, and different temperatures of examination. The studies of the stability of the γ-phase have yielded conflicting results with different explanations.

In some studies, low hydrogen concentrations, <1.3 at.% (150 ppm), favoured the formation of γ-hydride [9.548, 9.556, 9.557] in pure zirconium and in Zircaloy-4 [9.558]. In Ref. [9.556], above 99 ppm (0.90 at.%) hydrogen, a mixture of δ-hydrides and γ-hydrides was observed, while below 21 ppm (0.19 at.%) hydrogen, only γ-hydride could be detected. To test the stability of the hydride phases, specimens with hydrogen concentrations of 21 and 99 ppm (0.19 and 0.90 at.%) were heated to 473 K (200°C) for two weeks and furnace cooled. Only γ-hydrides were observed, indicating that the γ-phase had not transformed to the δ-phase but vice versa. Most of the hydrides were precipitated within the grains since in this test material the grain size was 500 μm whereas in Ref. [9.533], the grain size was about ten times smaller thus providing a large area of grain boundaries, where δ-hydride was found. In Ref. [9.557], the specimens were re-examined after three years at room temperature and the γ-hydride had not converted to δ-hydride.

The elastic strain energies of the γ- and δ-hydrides were estimated to be 6.9 and 8.4 kJ/mol, respectively, implying that the γ-phase is expected to nucleate first from solid solution [9.555]. If stress relieving accommodation dislocations are formed around the precipitates, the total strain energy declines and depends on the yield strength of the material [9.559]. With low strength material, a ratio of yield strength/shear modulus, σ_y/μ, of 0.001, the strain energies for each hydride phase are small,

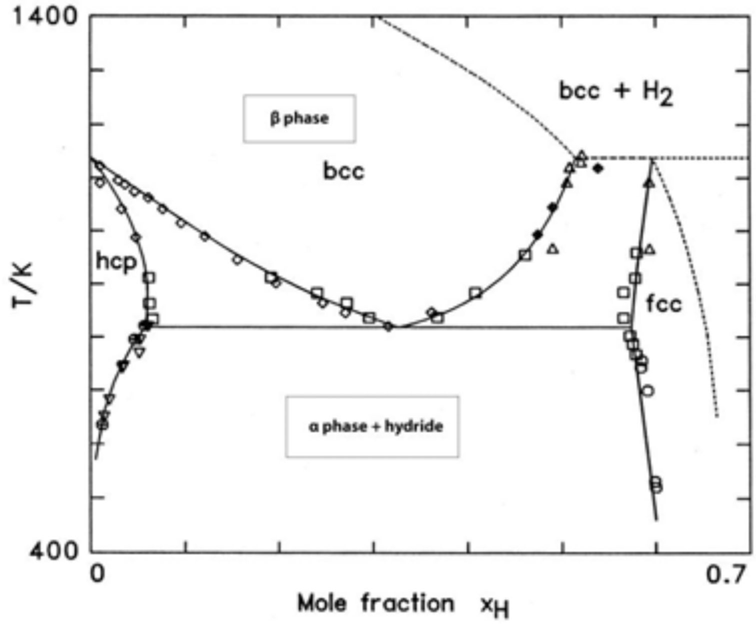

FIG. 9.225. Phase diagram for Zr-H [9.516].

< 0.45 kJ/mol, and about the same size so that once γ-hydride is nucleated it continues to grow [9.555]. In material with high strength, σ_y/μ, of 0.01, the strain energies increase but for δ-hydride the energy required is slightly smaller than for γ-hydride, 2.4 to 2.5 kJ/mol. The analysis assumed an absence of any significant difference in chemical formation energy. Thus, after slow cooling, the δ-hydride was the expected phase in strong materials, except when the hydrogen concentration was less than 100 ppm (0.90 at.%). This analysis was used to explain the presence of γ-phase in zirconium with low oxygen concentration and δ-phase when oxygen was added to the same material [9.555].

In Zircaloy-2 with about 100 ppm (0.9 at.%) hydrogen in solution, the formation of γ-hydride by fast quenching was suppressed by increasing the strength by means of cold work [9.560]. An alternative explanation to the local difference in volume expansion for the effect of strength is that for a given concentration of hydrogen, the lower H/Zr required by γ-hydride compared with δ-hydride provides a higher number density of precipitates, $N_f^\gamma > N_f^\delta$, therefore the total strain required is greater for γ-hydride than δ-hydride. If only γ-hydride formed, the total strain, ε_T^γ, would be ($N_f^\gamma \times 0.123$), whereas if only δ-hydride formed, the total strain, ε_T^δ, would be ($N_f^\delta \times 0.172/1.6$), that is, $N_f^\delta \times 0.108$, so $\varepsilon_T^\gamma > \varepsilon_T^\delta$, thus explaining the effect of strength. If hydride nucleation at dislocations from cold work was the controlling process, precipitation of γ-hydride would be promoted but such an increase was not observed. The following observations were reported:

- When the cooling rate was varied from brine quenching to furnace cooling, the strength effect was not observed in Zr-2.5Nb [9.560, 9.561] when the β-phase was present, which provides hydride nucleation at α/β interfaces [9.562, 9.563]. With low concentrations of hydrogen, 7 ppm (0.06 at.%), only γ-hydride was precipitated, even with furnace cooling; with a moderate concentration, 46 ppm (0.42 at.%), γ-hydride was still observed with oil quenching but δ-hydride was detected after air cooling; a mixture of γ- and δ-hydrides was found after all coolings when the hydrogen concentration was 150 ppm (1.35 at.%); only δ-phase was observed with air cooling and furnace cooling with a hydrogen concentration of 300 ppm (2.66 at.%).

- With hydrogen concentrations of 200 and 500 ppm (1.8 and 4.4 at.%) in pure Zr, γ-hydrides from water quenching transformed almost completely to δ-hydride after ageing at 473 K (200°C) for 3 weeks. Ageing at 423 K (150°C) only partially converted the γ-hydride to δ-hydride after 3 weeks. After furnace cooling from the solution temperature only δ-hydrides were detected; these precipitates did not change with ageing [9.532].
- Lanzani and Ruch [9.564] added between 174 and 1516 ppm (1.56 and 12.2 at.%) hydrogen to Zircaloy-4 by corrosion then subjected specimens to storage at room temperature for various hold times totalling 37 months, with an intermediate heating to 421 K (148°C) for 2212 h. No γ-phase was detected by X ray diffraction.
- Mostly δ-hydrides, with traces of γ-hydride, were observed in Zircaloy containing up to 3000 ppm (21.5 at.%) hydrogen [9.565, 9.566]. ε-hydride was detected in hydride layers containing about 6000 ppm (35.5 at.%) hydrogen on the rim of cladding.
- Specimens of pure Zr containing up to 16 000 ppm (60 at.%) contained a mixture of γ- and δ-hydrides after cooling from the β-phase [9.567]. After furnace cooling the δ-hydride dominated whereas after water quenching γ-hydride was prominent. After ageing for 6.5 months at room temperature, in the water quench materials, the volume of the γ-hydride increased at the expense of the δ-hydride and approached ZrH at 50 at.% hydrogen, as shown in Fig. 9.227. The stability of the γ-phase at room temperature was indicated by the decoration of δ-hydride with γ-hydride in pure Zr containing 13 700 ppm (56 at.%) hydrogen after holding for 174 days following a furnace cool from 773 K (500°C) [9.568]; γ-hydride in the matrix remained unchanged.
- With high concentrations of hydrogen between 10 000 and 16 000 ppm (between 50 and 60 at.%) the material mostly consisted of a mixture of γ-hydride and δ-hydride [9.524, 9.557, 9.567, 9.569]. Heating to over 523 K (250°C) converted all the γ-hydride to δ-hydride.
- In Zircaloy-2 containing 100 ppm (0.90 at.%) hydrogen, electron energy loss spectroscopy showed that the composition of a hydride could vary from ZrH at the tip to $ZrH_{1.7}$ in the core of the hydride [9.570].

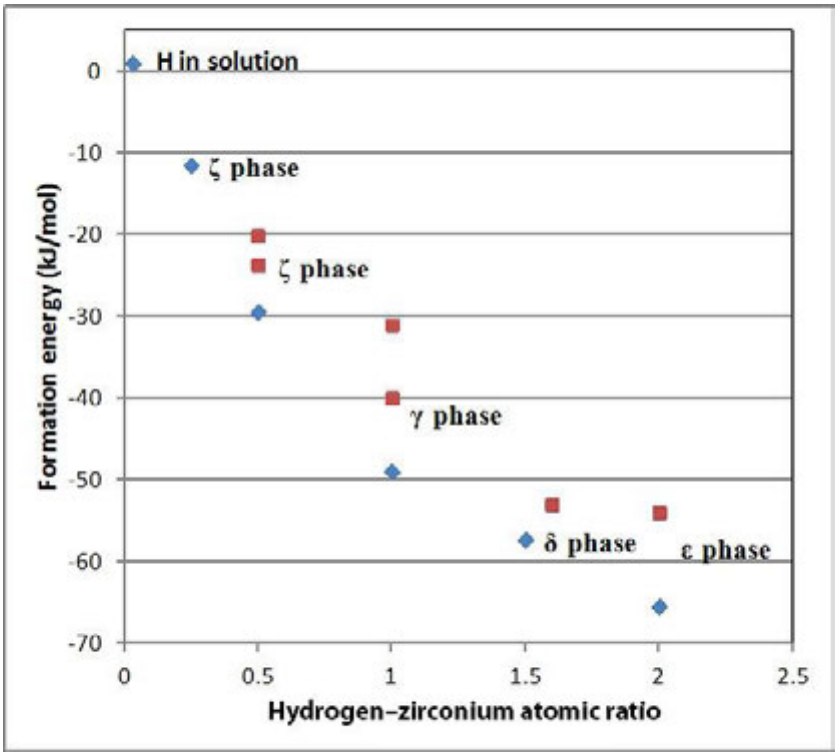

FIG. 9.226. Calculated formation energies of hydrides in zirconium (based on [9.522] (red squares) and [9.528] (blue diamonds)).

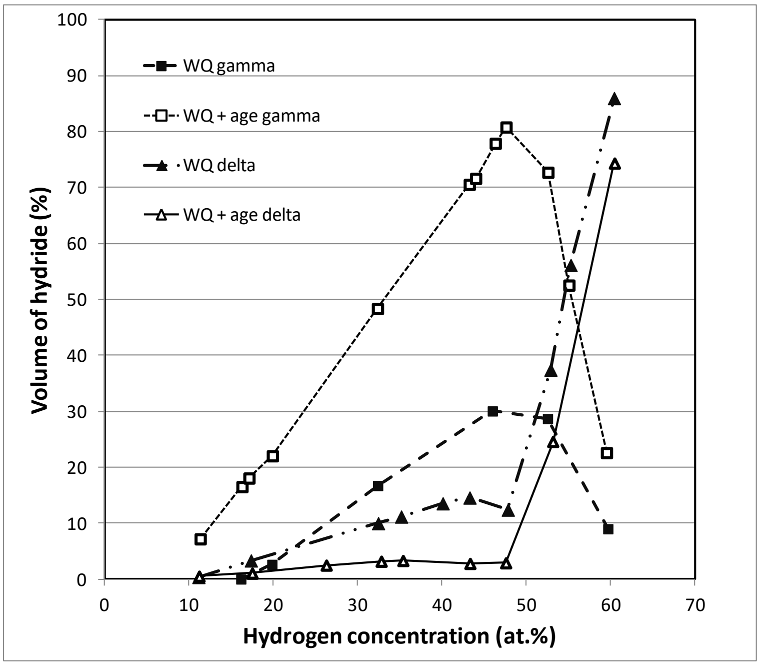

FIG. 9.227. Dependence of volume of γ- and δ-hydrides on hydrogen concentration after water quenching and ageing at room temperature for 6.5 months (based on [9.537]).

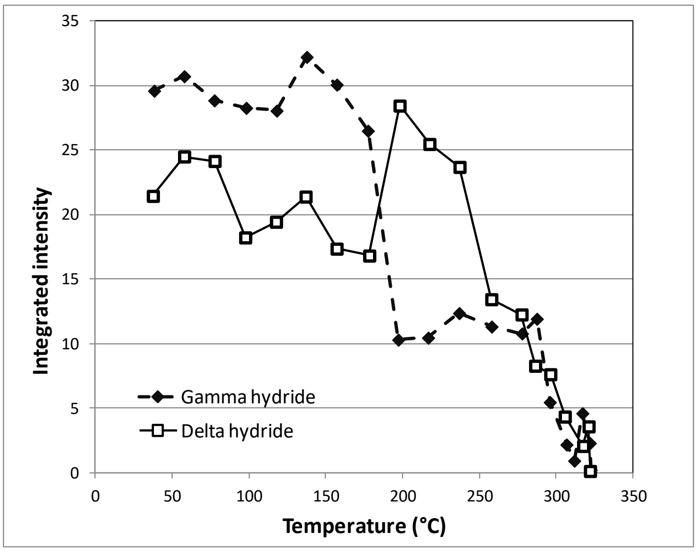

FIG. 9.228. Transformation of γ-hydride to δ-hydride at about 453 K (180°C) during heat up of Zr-2.5Nb containing 0.78 at.% hydrogen isotopes (based on [9.572]).

— No γ-hydride was observed in specimens of Zr-1.15Cr-0.1Fe containing 4200 ppm (27.5 at.%) hydrogen [9.571]; heating for 2200 h at 493 K (220°C) — 20°C below a suspected transformation temperature — yielded no γ-hydride.

Neutron diffraction measurements have shown that the γ-phase is the stable hydride at room temperature in the strong alloy Zr-2.5Nb. During heating of a specimen containing 86.5 ppm (0.78 at.%) hydrogen isotopes, about 60% of the γ-phase transforms to δ-phase at about 450 K (180°C) [9.572], as indicated by the sharp decline in the diffraction intensity for the γ-phase and the corresponding increase in the δ-phase signal, as shown in Fig. 9.228. During cooling from well above

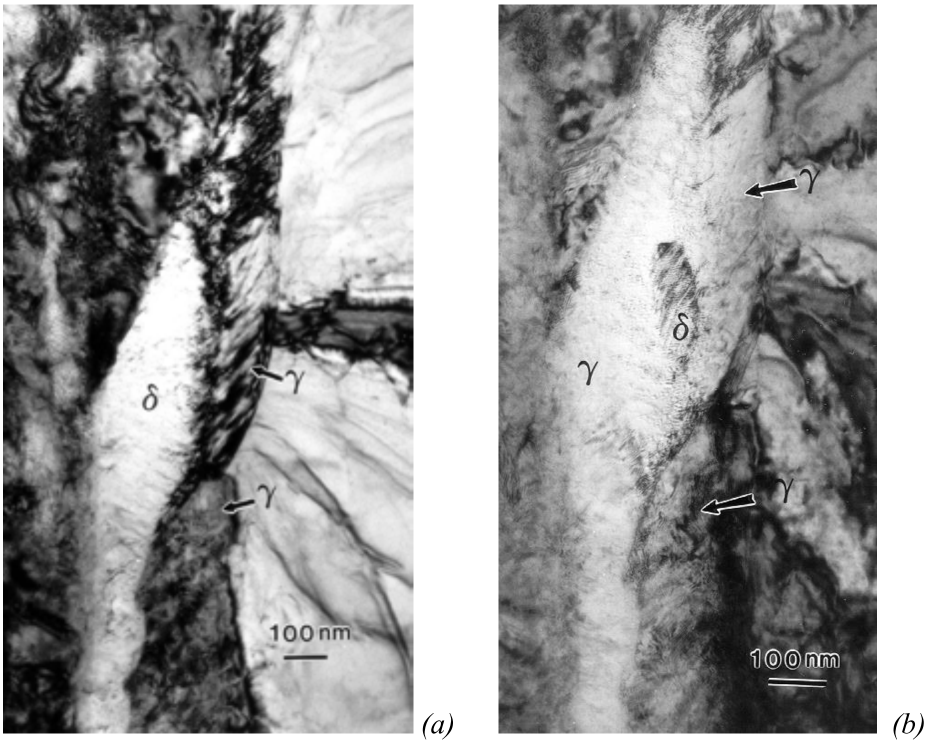

FIG. 9.229. (a) Zr-2.5Nb containing δ-hydride with adjacent γ-hydride in a matrix of α-Zr, examined a few weeks after dissolution and re-precipitate experiments [9.574]; (b) same specimen as for Fig. 9.228 after a further year at room temperature. The δ hydride has transformed to γ-hydride, except for a small core region [9.574].

this transformation temperature the first phase to form is δ-hydride. The transformation to γ-hydride at room temperature is slow, with a characteristic time scale on the order of months [9.573, 9.574]. As shown for hydrides in pure Zr [9.568], the γ-hydride consumes the δ-hydride precipitate from outside-in, as shown in Fig. 9.229(a), and after a further year of storage only a small island of δ-hydride remains, as shown in Fig. 9.229(b) [9.574].

Although most phase diagrams omit the γ-phase, preferring to consider it a metastable phase, some of the above results and observations suggest there is a transformation to γ-hydride at low temperatures within the phase field between the α/(α+δ) and (α+δ)/δ boundaries with a transformation temperature between 453 and 523 K (180 and 250°C). Two studies showed that a difference in strength could affect which hydride formed, either because their plastic strain energies were similar [9.555] or because their composition determined their number density [9.560]. Atomic-scale calculations of the bulk properties of the Zr–H system [9.522, 9.528] indicate that the formation energies of the hydrides are about 5 to 15 times larger than the strain energies and the difference between the formation energies of γ- and δ-hydrides is 15 and 25%, with δ-hydrides being the more stable, as shown in Fig. 9.226. These results suggest that because of the modest differences between each of the contributions to the energies of the precipitation of the two hydrides, when embedded within the zirconium matrix their relative stabilities may depend on mechanical and thermal contributions to their free energies, modified by slight variations in composition and fabrication of the component. Whether γ-hydride or δ-hydride or both are present in a material depends on the hydrogen concentration, zirconium alloy composition and thermomechanical treatments, and time at the low temperature.

When observed by TEM, hydrides are often precipitated in close association with one another to produce stacks of hydrides, forming a composite structure that could appear as a long stringer by light microscopy [9.530, 9.543, 9.565, 9.575–9.577]. The elastic strain associated with the hydride precipitation helps nucleate successive precipitates in an autocatalytic process [9.578]. The alignment

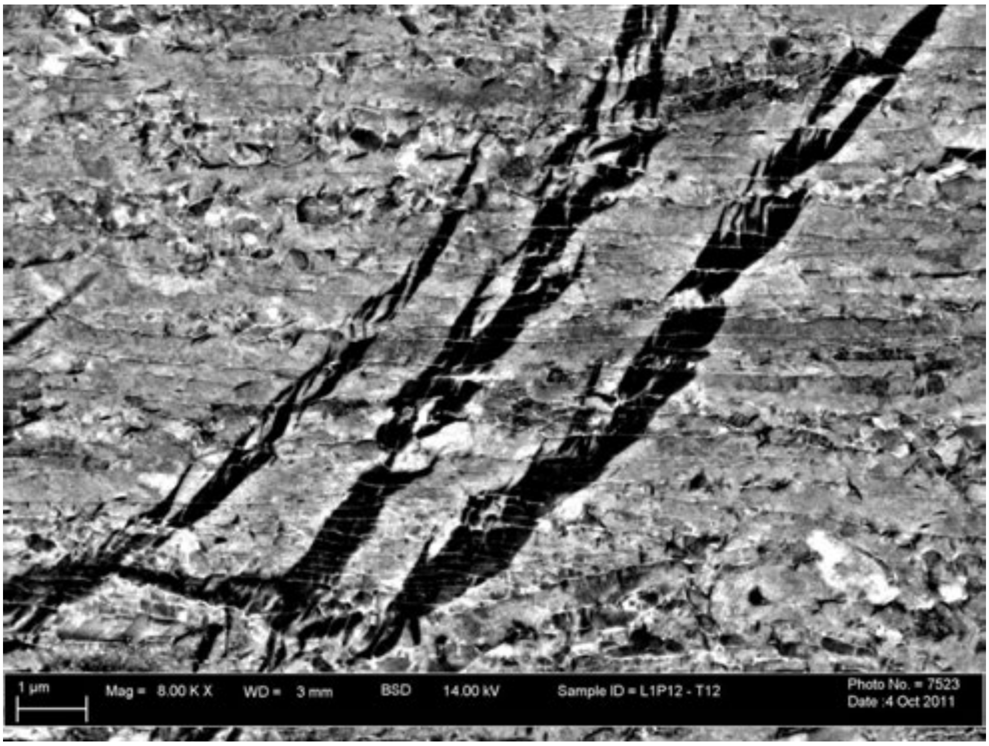

Fig. 9.230. Stacks of hydride crossing narrow α-grains surrounded by β phase in cold worked Zr-2.5Nb (photograph by A. Lockley).

leads to the $(10\bar{1}7)_{Zr}$ habit plane. A martensitic-bainitic mechanism has been invoked for the precipitation, which also accounted for the habit plane. As for a single hydride, movement of partial dislocations on the basal plane leads to the $(10\bar{1}7)_{Zr}$ habit plane while shear on the prism plane produces $\{10\bar{1}0\}_{Zr}$ habit planes.

As indicated above, in α/β alloys hydrides can nucleate at the α/β boundaries. The formation of stacks of hydrides is common. Perovic et al. [9.579] explain the apparent habit plane of the hydrides in Zr-2.5Nb pressure tubes in terms of the geometry of the stacks. The metal consists of flattened α-grains surrounded by a thin layer of β phase, the normal to the α-grains being mostly in the radial direction. The basal poles of α-zirconium are strongly oriented in the transverse direction and therefore one might expect hydrides on the basal planes presenting as radial hydrides in as-fabricated tubes. In light microscopy the hydride platelets appear to be circumferential. When viewed at high magnification, the hydrides have a habit plane close to (0001) but they are stacked along grains where the c-axis is close to the radial direction. When a large hoop stress is applied during a thermal cycle, the hydrides become radial, as observed by light microscopy (see Section 9.7.3). At high magnification, the hydrides form in stacks, with individual hydrides crossing several grains of similar orientation, as shown in Fig. 9.230, and with adjacent plates slightly offset in the stack. Again, the relationship between the hydride and the matrix is $(111)_{hydride}$ parallel with $(0001)_{\alpha\text{-}Zr}$ and $[1\bar{1}0]_{hydride}$ parallel with $[11\bar{2}0]_{\alpha\text{-}Zr}$ and the habit plane is close to $(0001)_{\alpha\text{-}Zr}$. Now the hydrides are in grains where the c-axis is in the transverse direction. After manufacture, in these tubes large residual stresses are present that oppose the tendency to form radial hydrides. These residual stresses contribute to the apparent threshold stress for hydride reorientation.

In an annealed Zircaloy-2 rod, internal stresses from deformation and differential thermal contraction were shown to control the hydride morphology and distribution [9.580]. Transgranular hydrides with a $(10\bar{1}7)$ habit plane grew in grains with their c-direction along the residual tensile stress axis. Hydrides in grain boundaries and twin boundaries had the same habit plane. Large hydrides comprised arrays of small stacked hydrides again with the same habit plane; the angle of the stack of hydrides is determined by the total elastic strain energy developed during thermomechanical treatment. This effect accounts for the large variation between reported apparent habit planes and true habit planes and suggests that residual grain-interaction stresses determine the geometry of the stacks rather than the hydride nucleation and growth processes.

9.7.1.2. Solubility limits for hydrogen in zirconium alloys

As indicated in Fig. 9.225, hydrogen has a stabilizing effect on the β phase with much solubility in this phase but a very low solubility limit in the α phase, the most common phase in commercial alloys. As a result, detailed knowledge of the α/(α + hydride) boundary is required to understand and guard against hydride cracking in the temperature range in which components usually operate in nuclear reactors and with the hydrogen concentrations usually encountered (see Chapter 8, in Volume 2 of this publication). Much effort has been expended to determine this phase boundary. Two temperatures are important:

- On heating it is necessary to know at what temperature all the hydrides have dissolved. This limit is often called the terminal solid solubility for dissolution (TSSD). It can also be used to estimate how much hydride is present at some temperature (e.g. at reactor operating temperature).
- During cooling it is necessary to know at what temperature the hydrogen in solution will precipitate as hydride. This limit is often called the terminal solid solubility for precipitation (TSSP).

The α/(α+hydride) phase boundary has been measured by two different techniques:

- For a given hydrogen concentration the equilibrium vapour pressure, *P*, is measured as a function of temperature, *T*; a change in slope as the hydrogen concentration is increased indicates the solubility limit [9.581].
- The equilibrium vapour pressure is measured isothermally as a function of hydrogen additions and the solubility limit is reached when Sievert's Law [9.582] is no longer obeyed [9.581, 9.583–9.585]. Sievert's law is $C_H = S\sqrt{p_H}$, where C_H is the concentration of hydrogen dissolved in zirconium in equilibrium with gaseous hydrogen at pressure p_H and S is Sievert's constant.

These two techniques are used to add hydrogen to mechanical test specimens from a gaseous environment. To preserve the underlying microstructure, for example, after irradiation damage, hydrogen may be added at moderate temperatures, below 623 K (350°C), using a coulometric titration technique [9.586]. Another technique is isothermal diffusion of hydrogen in a couple of a zirconium alloy: one part contains hydrides and a saturated solid solution of hydrogen while the other part contains a low concentration of hydrogen; after a suitable time to allow the hydrogen to diffuse from one section to the other and to establish equilibrium, the section containing the lower concentration is said to be at the terminal solid solubility [9.587, 9.588]. An alternative is to estimate the concentration of hydrogen in the α phase at the hydride/α phase interface after a concentration gradient is established from a hydride layer [9.589, 9.590] or after sufficient time is allowed for the hydrogen concentration in solution to become uniform [9.591, 9.592].

This latter method has become one of the standard procedures for adding hydrogen in a controlled manner to test specimens, especially those made from irradiated material. The hydride layer is often formed electrolytically. Typically the test material is placed in a bath of 0.2M H_2SO_4 at 335 K (65°C) and electrolysis is performed at a current density of about 1.5 kA/m^2 using a suitable electrode [9.500, 9.501, 9.593]. The procedure is as follows:

- A discontinuity in the hydrogen concentration of hydrogen diffusing along a bar containing a temperature gradient indicates the solubility limit [9.588, 9.594].

- Using a dilatometer, a change in slope of strain with temperature is the solubility limit. TSSD is obtained on heating while TSSP is indicated under cooling [9.584, 9.595–9.598].
- During changes in temperature the internal friction of zirconium progresses through several peaks, usually that at the highest temperature is interpreted as being caused by hydrides, either dissolving on heating or precipitating on cooling [9.599–9.603]. Other applications of internal friction are described in Appendix I.
- The change in the temperature dependence of the dynamic elastic modulus indicates TSSD on heating and TSSP on cooling [9.604].
- Electrical resistivity change with amount of hydrogen in solution can be calibrated by measuring the difference in resistance of specimens containing different amounts of hydrogen as a function of temperature; a change in temperature dependence indicates TSSD [9.605].
- TSSD is indicated by the metallography of specimens quenched from either side of the α/(α + hydride) boundary with those quenched from below the solubility limit containing hydrides [9.566]. Heating zirconium containing hydrides in an electron microscope provides direct observation of dissolution, although care has to be taken because of extra hydrogen from specimen preparation and surface effects, even in high voltage machines [9.606].
- Detecting and measuring the amount of hydride phase and the change in lattice parameter from hydrogen in solution as a function of temperature using neutron [9.572] and synchrotron X ray diffraction [9.607–9.610] provides a direct evaluation of TSSD and TSSP.
- The intensity of small angle neutron scattering from zirconium containing an array of hydride precipitates declines with increase in temperature as the hydrides shrink during dissolution. The temperature at which the intensity of small angle neutron scattering shows no further change is taken as TSSD. The values for two hydrogen concentrations, 9 and 30 ppm (0.08 and 0.27 at.%) hydrogen, were within the scatter of the reported data [9.611].
- Using absolute calorimetry, the relative heat contents of zirconium containing large concentrations of hydrogen can be measured and the boundaries of the phase diagram can be derived [9.612]. The heat capacity increases with increase in hydrogen concentration indicating that heat is required to dissolve hydrides, as shown in Fig. 9.231 [9.19, 9.613]. During differential scanning calorimetry (DSC) [9.614] the thermal response of a sample is compared with a reference when the two are similarly heated or cooled at a constant rate.

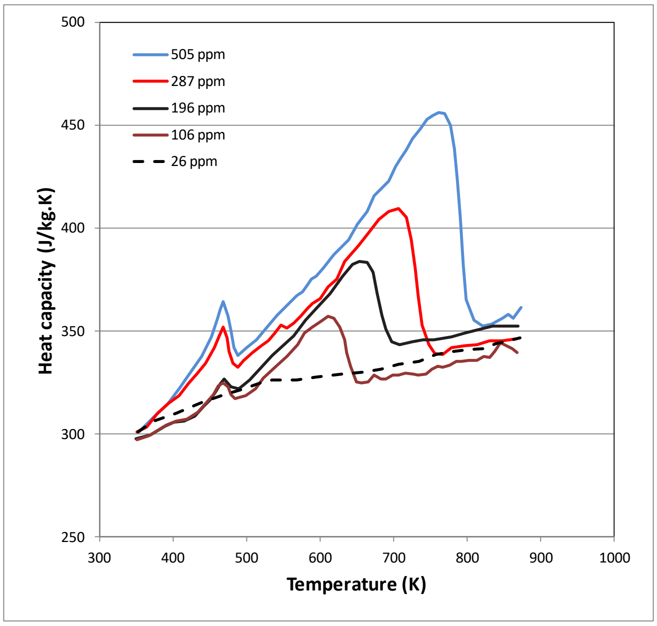

FIG. 9.231. Heat capacity of Zircaloy-2 with various hydrogen concentrations [9.613].

Differential heat flow decreases with increasing temperature as heat is absorbed to dissolve hydrides but reverts to the background baseline once all the hydride has dissolved, as shown in Fig. 9.232. The reverse process takes place during cooling when heat is given out during precipitation, as shown in Fig. 9.233. The discontinuity in heat flow indicates TSSD on heating and TSSP on cooling [9.598, 9.615–9.623].

- After calibrating TSS values with hydrogen concentrations measured by vacuum gas extraction analysis (Section 4.13.8.3, in Volume 1 of this publication), DSC may be used to provide a value of the hydrogen concentration in a specimen or component.
- In a series of DHC experiments on specimens containing a range of hydrogen concentrations, the highest temperature at which cracking is detected is taken as an effective solubility limit [9.624–9.630].

Table 9.33 provides a summary of the methods for determining the solubility limits of hydrogen in the α phase of zirconium alloys, where the usual hydrides are the γ and δ phases. For very high hydrogen concentrations and large agglomerations of hydrides, hydride rims and lens shaped blisters, the presence of the ε phase and the δ/(δ + ε) boundary are important; some of the above studies include this boundary.

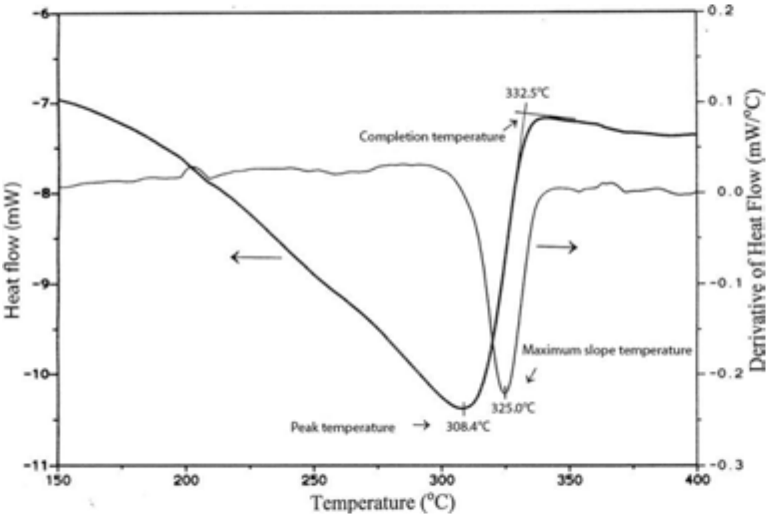

FIG. 9.232. Typical heat flow during differential scanning calorimetry for heating of zirconium containing 63 ppm (0.57 at.%) hydrogen, showing the three temperatures potentially used for TSSD: peak temperature, maximum slope temperature and completion temperature [9.616].

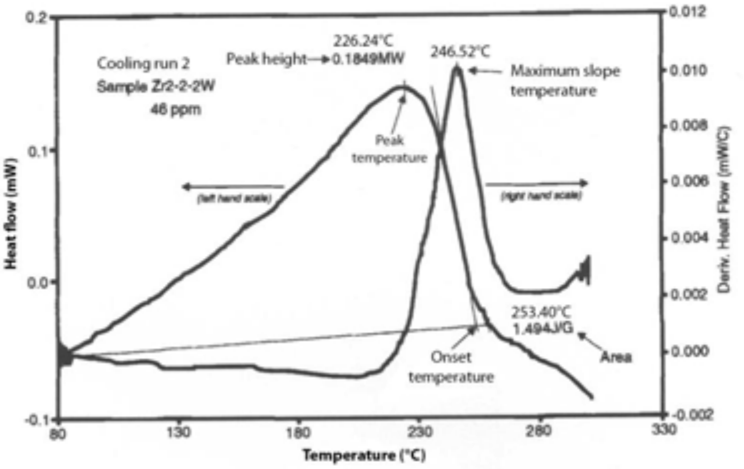

FIG. 9.233. Typical heat flow during differential scanning calorimetry for cooling of Zircaloy-2, showing the three temperatures potentially used for TSSP: peak temperature, maximum slope temperature and onset temperature [9.617].

TABLE 9.33. COMPENDIUM OF METHODS FOR MEASURING SOLUBILITY LIMITS FOR HYDROGEN IN ZIRCONIUM ALLOYS

Material	[H] range (ppm)	T_{MAX} (°C)	Heating — TSSD		C_D at 300°C (ppm)	Cooling — TSSP		C_P at 300°C (ppm)	Method	Source
			A (ppm)	ΔH_D (kJ/mol)		B (ppm)	ΔH_P (kJ/mol)			
Pure zirconium: recrystallized	280–570	500	49 662	28.7	119.5				Diffusion	[9.589]
Pure zirconium: recrystallized	165–713	550	168 721	37.6	62.4				Pressure–composition–temperature	[9.581]
Pure zirconium: recrystallized	86–530	486	151 903	36.1	78.5				Diffusion	[9.590]
Pure zirconium	0–1160	900	64 216	30.9	98.5				Calorimetry	[9.612]
Pure zirconium	55–670	550	197 798	38.9	56.4	104 088	34.2	80.1	Dilatometry	[9.595]
Zircaloy-2 cold worked	50–888	560	86 942	31.9	107.5				Diffusion	[9.591]
Pure zirconium, Zircaloy-2, Zircaloy-4	200–825	520	370 275	41.3	63.4				Pressure–composition–temperature	[9.583]
Sponge zirconium; recrystallized	87–406	486	350 810	42.9	43.1	80 419	31.2	115.6	Dilatometry, pressure–composition–temperature	[9.584]
Zr-2.5Nb cold worked	400–500	500	168 721	37.6	62.4				Pressure–composition–temperature	[9.585]
Zircaloy-4 cold worked and stress relieved	60–437	476	130 352	36.1	67.3				Diffusion data at high temperature	[9.592]
	38–60	300	592	11.0	58.3				Diffusion data at low temperature	
Zircaloy-4 cold worked and tempered	25–275	500	96 086	34.9	63.1	89 322	31.2	127.5	Dilatometry	[9.596]
Pure zirconium, Zircaloy-2, Zircaloy-4	38–550	525	99 000	34.5	70.3				Diffusion	[9.587]
			120 000	35.8	65.5				Summary of 199 data points	
Zircaloy-2, Zr-2.5Nb: α annealed and (α + β) quenched	54–550	520				199 000	38.9	56.2	Temperature gradient	[9.594]

TABLE 9.33. COMPENDIUM OF METHODS FOR MEASURING SOLUBILITY LIMITS FOR HYDROGEN IN ZIRCONIUM ALLOYS (cont.)

Material	[H] range (ppm)	T_{MAX} (°C)	Heating — TSSD		C_D at 300°C (ppm)	Cooling — TSSP		C_P at 300°C (ppm)	Method	Source
			A (ppm)	ΔH_D (kJ/mol)		B (ppm)	ΔH_P (kJ/mol)			
Unalloyed zirconium recrystallized	110–240	360	52 755	42.2	74.6				Resistivity	[9.605]
Pure zirconium	14–32	300				161 000	37.4	62.7	Internal friction data at high temperature	[9.602]
	4–14	250				600	10.0	72.8	Internal friction data at low temperature	
Zr-2.5Nb cold worked	3–100	300				140 000	36.1	71.6	Hydride cracking	[9.624]
Pure zirconium: recrystallized	9–680	650				148 005	36.9	63.6	Pendulum oscillations	[9.603]
Pure zirconium; recrystallized	4–230	480	140 787	37.6	52.5				Metallography: all data	[9.556]
	4–21	250	34 300	32.2	39.8				Metallography data at low temperature	
Zr-2.5Nb cold worked (plus [D])	3–135	350				115 380	35.2	71.2	Hydride cracking	[9.625]
Zr-2.5Nb cold worked	6–30	250	3 262 490	50.5	81.8				Small angle neutron scattering	[9.611]
Zr-2.5Nb cold worked (plus [D])	7–86	304				135 670	35.3	82.5	Hydride cracking	[9.626]
Zr-2.5Nb cold worked and stress relieved	7–99	450	80 794	34.5	57.6	24 731	25.8	109.1	Dynamic elastic modulus	[9.604]
Zircaloy-4 recrystallized	45–520	482	119 372	34.9	78.8	38 600	26.4	152.2	Diffusion anneal (TSSD), temperature gradient (TSSP)	[9.586]
Zr-2.5Nb cold worked and stress relieved	49–87	407	124 119	35.9	65.8	129 962	32.2	150.4	Neutron diffraction	[9.572]
Zircaloy-2 and Zircaloy-4 weld, forged, cold worked	4–78	400	106 447	36.0	55.8	138 746	34.5	100.0	DSC (maximum slope)	[9.617]

TABLE 9.33. COMPENDIUM OF METHODS FOR MEASURING SOLUBILITY LIMITS FOR HYDROGEN IN ZIRCONIUM ALLOYS (cont.)

Material	[H] range (ppm)	T_{MAX} (°C)	Heating — TSSD		C_D at 300°C (ppm)	Cooling — TSSP		C_P at 300°C (ppm)	Method	Source
			A (ppm)	ΔH_D (kJ/mol)		B (ppm)	ΔH_P (kJ/mol)			
Zircaloy-4 recrystallized	40–610	520	263 024	39.3	68.6				DSC (peak)	[9.618]
Zircaloy-2 recrystallized	40–542	600	128 000	36.5	59.7	52 600	28.1	145.3	DSC (maximum slope)	[9.619]
Zircaloy-4 recrystallized	80–640	550	127 470	35.8	70.1				DSC (peak)	[9.620]
Unalloyed zirconium	27–281	500	141 000	38.1	47.4	33 900	27.3	110.0	DSC (maximum slope)	[9.621]
Zircaloy-2 cold worked, stress relieved	43–100	450	81 626	33.8	68	29 250	26	124.7	Dilatometry	[9.597]
Zr-2.5Nb cold worked	24–60	293				7624	22.7	65.6	Hydride cracking	[9.628]
Zircaloy-4 recrystallized	50–650	600	171 687	36.3	84.1	57 228	27.3	186.2	DSC (peak)	[9.622]
Zircaloy-4 recrystallized	20–240	500	52 575	32.1	62.1	40 135	27.3	129.3	DSC (maximum slope)	[9.623]
Zr-2.5Nb cold worked and stress relieved	50–463	400	68 900 61 100	33 32	76.8 72.4	19 900 22 200	23 25	126.5 158.8	DSC (peak) Dilatometry	[9.598]
Zircaloy-4 recrystallized	475-600	570	510 800	45.6	35.5	66 440	29.6	132.2	Synchrotron X ray diffraction	[9.608]
Zircaloy-2 recrystallized	17–204	407	60 200	32.7	62.8	239 187	37.3	94.9	Synchrotron X ray diffraction	[9.609]

Note: DSC — differential scanning calorimetry; TSSD — terminal solid solubility for dissolution; TSSP — terminal solid solubility for precipitation.

(a) TSSD

During the heating of zirconium containing hydrides the concentration of hydrogen in solution gradually increases and the amount of hydride phase decreases until a temperature is reached where no hydrides are present. This temperature, T_D, increases with the concentration of hydrogen, C_D (ppm), and is usually described by the following equation:

$$C_D = A \exp(-\Delta H_D / R T_D) \tag{9.48}$$

where

A is a constant;
ΔH_D is the enthalpy of solution (kJ/mol);

and R is the gas constant, 8.314 J/(K·mol).

Wide variations on the values of the constants in Eq. (9.48) exist, as shown in Table 9.33. The recommended values for pure zirconium are: A = 1.87×10^5 and ΔH = 38.13 kJ/mole [9.514] or $A = 2.56 \times 10^5$ and ΔH = 40.35 kJ/mole [9.515]. With a sufficient number of quality controlled measurements, confidence can be acquired so that values can be included in standards for reactor operation; for example, the recommended values for CWSR Zr-2.5Nb are $A = 8.19 \times 10^4$ and ΔH_D = 34.5 kJ/mol [9.631]. The very low solubility limit is incontrovertible for all alloys, and as a result, with any practical specification and fabrication process, hydrides will always be present at room temperature in fresh components; at the limit allowed by the current technical specification for as-fabricated pressure tubes, 5 ppm (0.045 at.%), hydrides would be present up to 428 K (155°C). For as-fabricated fuel cladding, the maximum concentration allowed is 25 ppm (0.228 at.%) and at the limit, hydrides would be present up to 513 K (240°C). At typical reactor operating temperatures, around 583 K (310°C), TSSD is about 66 ppm (0.60 at.%). For pure zirconium, using [9.514], with 5 ppm (0.045 at.%) hydrogen, hydrides would be present up to 435 K (162°C); at 585 K (312°C), TSSD is about 71 ppm (0.64 at.%). Over the temperature range from 293 to 573 K (20 to 300°C) the differences in TSSD between the three recommendations is well within the scatter of any experiment, as shown in Table 9.34, but at higher temperatures the values deviate considerably, especially between pure zirconium and Zr-2.5Nb. The values of C_D based on the three equations start to deviate above 573 K (300°C). A single value in Zircaloy-2 containing a layer of hydride held at 673 K (400°C) for 3750 h provided a value of 205 ppm (1.83 at.%) [9.632], in close agreement with Ref. [9.514].

TABLE 9.34. COMPARISON OF TSSD EVALUATED FOR ZIRCONIUM [9.514] AND Zr-2.5Nb [9.631]

	Hydrogen concentration (ppm)		
Temperature (°C)	Zirconium	Zr-2.5Nb	Difference
20	0.03	0.06	0.03
150	3.65	4.5	0.85
250	28.77	29.34	0.57
270	39.71	39.3	−0.41
290	53.59	51.56	−2.03
310	70.87	66.39	−4.48
360	131.4	116.5	−14.9
400	202	172	−30

Experimental errors arise during hydrogen analysis and temperature measurement. In most methods the temperature or hydrogen concentration at the deviation of the rate of change in a physical phenomenon is interpreted as the solubility limit. Observation of phase change by metallography or detection of change in crystal structure by diffraction provide direct methods and can help deciding when the solubility limit has been reached. An example of the latter problem is the use of DSC. During heating, three distinct temperatures are indicated on a typical DSC heat flow curve, as shown in Fig. 9.232: a minimum or maximum value of the heat flow, often called peak temperature, T_{pk}, a temperature at maximum slope of the heat flow-temperature curve, T_{ms}, and the temperature of completion, which is often difficult to define. Frequently T_{ms} is used to evaluate T_{D}. One justification is that the diffusion annealing temperature used to add hydrogen to the specimens from a surface hydride layer is close to T_{ms} [9.617]. Complete hydride dissolution indicated by neutron diffraction correlates more closely with T_{pk} in Zr-Nb alloys [9.633]; with a specimen containing 116 ppm (0.53 at.%) hydrogen, T_{ms} was 376°C (649 K), T_{pk} was 630 K (357°C) while neutron diffraction indicated T_{D} was 632 K (359°C), in agreement with T_{pk} [9.631]. For assessments of the health of components the use of T_{ms} to represent T_{D} is conservative.

In temperature ramping experiments, hydrides take a finite time to dissolve on heating beyond T_{D}. Kearns [9.634] showed that dissolution proceeds by diffusion of hydrogen from the hydride and is complete when all the hydrogen initially in the hydride is redistributed into the metal matrix. The dissolution time, t_{s}, was given by:

$$t_{\mathrm{s}} \approx 3.5 \times 10^7\, h^2 /(D \cdot C_{\mathrm{D}}^2) \qquad (9.49)$$

where

h is the hydride thickness in cm (measured as about 2 μm)

and D is the diffusivity of hydrogen in the zirconium matrix.

In Zircaloy-4 dissolution of 60 ppm (0.54 at.%) hydrogen was complete in about 300 s at 573 K (300°C), as shown in Fig. 9.234(a). In Zr-2.5Nb dissolution of hydrides was slower than in Zircaloy and was retarded by tensile stress [9.635], as shown in Fig. 9.234(b). The role of the β phase, the major difference between Zircaloy and Zr-2.5Nb, has not been identified although the difficulty in determining the dissolution temperature was attributed to a strong memory effect in which the hydrides retain previous nucleation sites [9.636].

Hydrogen in solution occupies tetrahedral sites in the zirconium crystal lattice. This conclusion is derived from neutron diffraction at 873 K (600°C) on pure zirconium containing 548 ppm (4.76 at.%) hydrogen [9.637]. An earlier study came to the same conclusion but it was based on neutron diffraction on zirconium powder containing 3.2 at.% (300 ppm) hydrogen at 300 K (27°C), so little hydrogen would be present in the zirconium matrix [9.638]. Calculations have been done to determine which type of interstitial site — tetrahedral or octahedral — was preferred by a single proton [9.639]. The crystal potentials and charge densities of pure zirconium were constructed from the potentials and charge densities of the neutral atoms; the screening of the proton was treated empirically. The energy of the tetrahedral site was about 15% more favourable than the octahedral site for hydrogen occupation in zirconium. This conclusion was confirmed in Refs [9.522, 9.528]. In Ref. [9.528] an energy preference of 5.5 kJ/mol, about 9%, was calculated for tetrahedral over octahedral sites based on total electronic energy. When temperature dependence was included [9.522], the same preference for tetrahedral sites was indicated but the favouring energy difference rose from 0.5 kJ/mol at 0 K (−273°C) to 8.6 kJ/mol at 600 K (327°C). With these small energy differences, some hydrogen atoms may occupy octahedral sites, for example, 6% at 600 K (327°C).

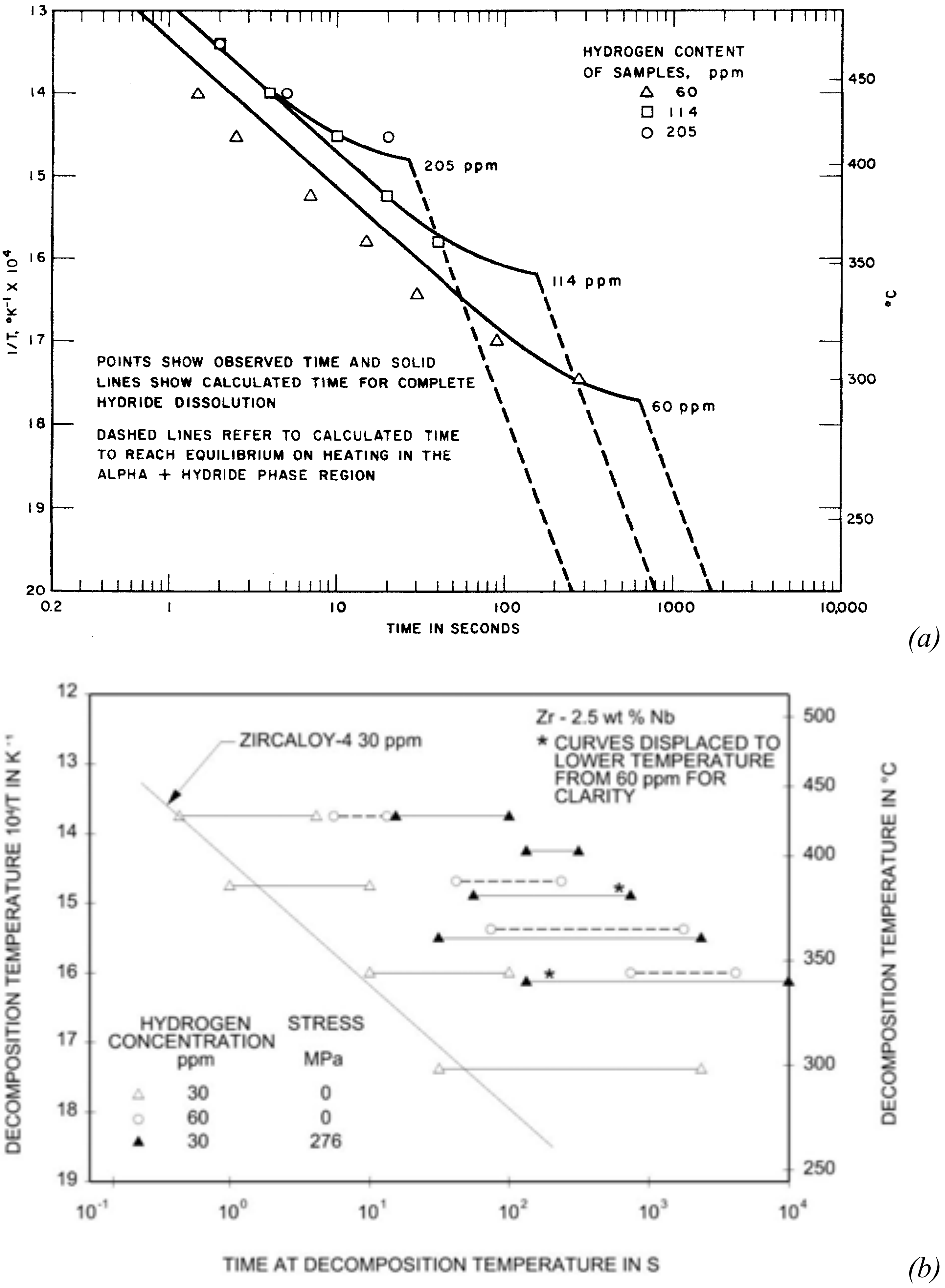

FIG. 9.234. Dissolution kinetics of hydrides in (a) Zircaloy-4 [9.634] and (b) Zr-2.5Nb [9.635].

Detection of changes in lattice parameters from hydrogen in solution is difficult because of the limited solubility at low temperatures so measurements have to be made at elevated temperatures. During heating or cooling the contribution of the hydrogen in solution to lattice expansion has to be separated from thermal expansion. In zirconium an anisotropic expansion caused by hydrogen in solution has been found. When measured by neutron diffraction at 723 and 773 K (450 and 500 °C) with hydrogen and deuterium concentrations between 7 and 597 ppm (0.06 and 2.68 at.%) in pure zirconium the expansion of the a-lattice spacing was 1×10^{-4} nm/at.% and that of the c-lattice spacing was 3×10^{-4} nm/at.% [9.640]. The dilation of the lattice described by Δv, the change in volume per dissolved H atom, was 2.78 Å^3 (2.78×10^{-30} m^3). This value agreed with Peisl's '2.9 Å^3' rule [9.641]. This latter value was based on a plot of Δv against $\Delta v/\Omega$ for several metals, where Ω is the mean atomic volume of a lattice atom. In this plot $\Delta v/\Omega$ was in the range 0.1 to 0.3 whereas Δv was in the range 2.5 to

3.5; for deuterium in zirconium $\Delta v/\Omega$ was 0.118. The value of Δv was overestimated by electronic quantum calculations as 3.9 Å^3 for hydrogen in tetrahedral positions in the zirconium lattice [9.528]. The lattice distortions induced by the presence of interstitial hydrogen is provided by the λ_{ij} tensor [9.640], deduced from the local strain ε_{ij} by the expression $\lambda_{ij} = d\varepsilon_{ij}/dx_H$, where x_H is the hydrogen atomic fraction. For hexagonal crystals, the λ tensor has two principal values: $\lambda_1 = \lambda_2$ and λ_3, related to the variation of the lattice parameters a and c with the hydrogen concentration by: $\frac{1}{2}(\lambda_1 + \lambda_2) = (1/a_0)da/dx_H$ and $\lambda_3 = (1/c_0)dc/dx_H$. For hydrogen in a tetrahedral site, the calculated principal values are $\lambda_1 = 0.033$ and $\lambda_3 = 0.100$ [9.528], the corresponding experimental values being respectively 0.033 and 0.054 for a tetragonality of $\lambda_3/\lambda_1 = 1.64$ [9.640]. Using synchrotron X rays, other experimental values of this anisotropy are 1.47 [9.608] and 1.59 [9.609]. All studies agree qualitatively, as they yield an expansion along the c-axis higher than along the a-axis, although the calculated value along the c-axis is larger than observed in the experiments. These dilations were used to evaluate V_H, the partial molar volume, $V_H = \partial V/\partial n_H$, or the increase in volume in a large quantity of metal when one mole of hydrogen is added without significantly changing the absolute concentration n_H. V_H is usually taken to be constant since the measurements are too inaccurate to detect dependence on temperature or hydrogen concentration. The value of V_H is 1.67×10^{-6} m^3/mol [9.640]. The value of V_H has been confirmed by measurements with a smaller hydrogen concentration range between 17 and 204 ppm (0.15 and 1.83 at.%) using synchrotron X ray diffraction [9.609].

(b) TSSP

The solubility limit is often described with a large apparent thermal hysteresis[5], as shown in Fig. 9.235. During or after cooling from above T_D the metal has an apparent greater capacity to hold hydrogen in solution than after heating to the same temperature from, for example, room temperature; consequently the temperature at which hydrides precipitate is lower than the temperature at which the hydrides dissolve. The temperature dependence is represented similarly to Eq. (9.48):

$$C_P = B \exp(-\Delta H_P/RT_P) \tag{9.50}$$

but now C_P represents the concentration of hydrogen where hydrides start to precipitate at temperature T_P.

The constants determined in various studies reflect this difference between dissolution and precipitation, as shown in Table 9.33. For example, the recommended values for Zr-2.5Nb for B and ΔH_P are 4.11×10^4 and 28 kJ/mol [9.631] with the consequence that up to 673 K (400°C) the temperature for dissolution, T_D, appears to be 50 to 60°C greater than that for precipitation, T_P, as shown in Table 9.35. With Zircaloy a similar temperature difference was noted based on dilatometry [9.584, 9.596] while a difference of between about 44°C and 90°C was found with DSC [9.617, 9.619, 9.622]. This apparent hysteresis is always observed in dynamic experiments; it may be responsible for some of the temperature dependence of cracking and hydride blister formation.

---

[5] For thermodynamic equilibrium, according to the phase rule, composition and temperature cannot be changed independently for two phases to be present in a binary alloy. At the same composition, hydrides should dissolve and precipitate at the same temperature independent of heating or cooling. The presence of two values of the solubility limit indicates that one or both the values do not represent equilibrium and the hysteresis and values are therefore indicated as 'apparent'. In dynamic measurements, values of apparent TSS by heating or cooling are clearly distinguishable and reproducible even if strictly invalid as equilibrium values. They are of practical use for evaluating reactor components and experiments.

TABLE 9.35. DIFFERENCE IN TEMPERATURE TO DISSOLVE HYDRIDES AND PRECIPITATE THEM IN Zr-2.5Nb *(based on Ref. [9.631])*

H concentration ppm	*T* dissolve °C	*T* precipitate °C	*T* difference °C
2	117.7	66.1	51.6
5	154.6	100.6	54.0
10	187.5	131.7	55.8
15	209.2	152.5	56.8
20	225.9	168.5	57.4
30	251.5	193.3	58.2
50	287.7	228.8	58.9
80	325.7	266.6	59.1
100	345.6	286.6	59.0

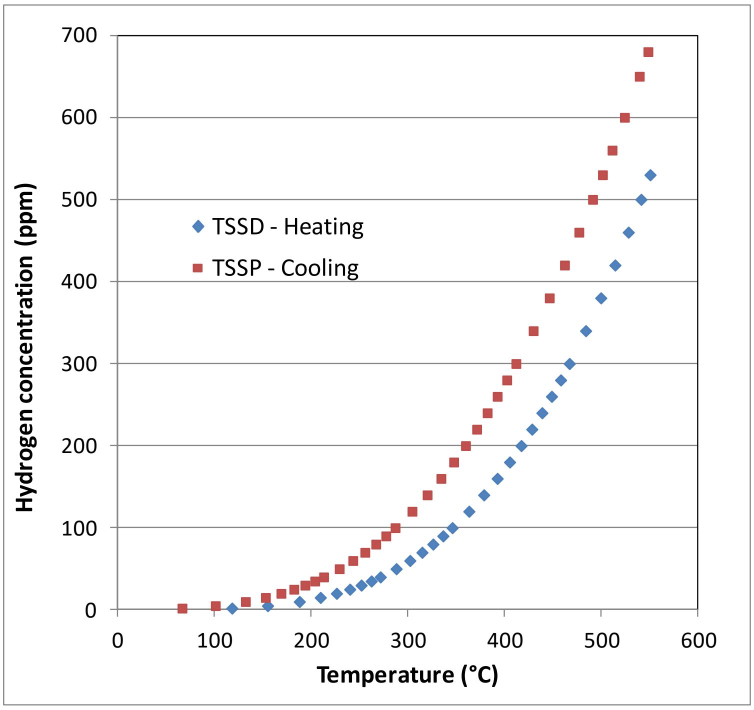

FIG. 9.235. Typical temperature dependence, up to the eutectoid temperature, of values of hydrogen concentration in solution in zirconium when hydrides dissolve on heating and precipitate on cooling; this example is for Zr-2.5Nb (based on [9.631]). Note that the concentration of hydrogen 690 ppm (5.93 at.%), at the eutectoid temperature, 823 K (550 °C), is described by TSSP.

There are indications that below 453 to 523 K (180 to 250°C) there is a phase change in the hydride from δ phase to γ phase (Section 9.7.1.1). The values of TSSD in this regime are small and subject to larger error. Whether the γ phase or δ phase is dissolving seems to have little effect on the enthalpy for dissolution [9.556] although small peaks around 453 K (180°C) in the heat capacity may be a result of this transformation, as shown in Fig. 9.231. Some data suggest that, unlike with dissolution, the phase change alters the temperature dependence of precipitation giving a reduction in ΔH_P [9.602, 9.617]. For example, in unirradiated Zircaloy no effect was discerned but in irradiated Zircaloy, below 443 K (170°C) ΔH_P is equal to 8.3 kJ/mol whereas above 443 K (170°C) ΔH_P is equal to 29.6 kJ/mol [9.617].

As indicated in Section 9.7.1.1, the misfit between the hydride and the zirconium imposes a compressive stress on the hydride and a local tensile stress in the metal. Measurements of the strains from γ- and δ-hydrides in Zircaloy-2 using nanobeam electron diffraction [9.570] show that the strains in [0001] and [$11\bar{2}0$] are similar to the predictions [9.550] but those in [$10\bar{1}0$] were much lower than the predictions. The stress in [$10\bar{1}0$] may be relieved by the formation of dislocations. To accommodate misfit between the zirconium matrix and a hydride, tangles of dislocations, with a Burgers' vector, *b*, of a/3<11$\overline{2}$0>, are associated with hydrides, as shown in Fig. 9.236 [9.548, 9.642]. In this γ-hydride the strain field is small along its length, 0.0055 (Section 9.7.1.1.), leading to easy coherent growth along <11$\overline{2}$0> and no dislocations. The strain in the metal in <10$\overline{1}$0>, 0.057, is sufficient to form a/3<11$\overline{2}$0> dislocations. The strain in [0001] is similar but the energy of a dislocation in this direction is too high for its formation; the dislocation energy is proportional to b^2 and with a high stacking fault energy (Section 5.3.2 in Volume 1 of this publication), the ratio of the dislocation energies in the two directions is 8/3, as shown in Table 5.1. To remove the strain field completely, the number of dislocations that must be generated is approximately 43, given by (misfit strain × precipitate diameter)/b, that is (0.057 × 240 nm)/0.316 nm. Since in this example about eight dislocations are generated on each side of the needle, less than half the elastic misfit stress is relieved plastically. The coherence in <11$\overline{2}$0>, the strain relief in <10$\overline{1}$0> and the suppression of strain in [0001] lead to the precipitates being sword shaped. They do not thicken uniformly, becoming tapered, and complete dislocation loops do not form but end at the precipitates. Accommodation dislocations can remain when hydrides are dissolved by heating, as shown in Fig. 9.237 [9.548, 9.606]. These dislocations are stable up to 674 K (400°C) and may act as nucleation sites for the reprecipitation of the hydrides on cooling. Such biased nucleation is the basis for the ‘memory effect’ [9.636]. If the temperature is raised sufficiently for the dislocations to anneal out, nucleation of hydrides is random or on grain boundaries. The residual dislocations may be one explanation for the observation on cooling of various values of T_P between two limits [9.604, 9.617]; if the maximum temperature is high enough to remove the dislocation debris, T_P is 10 to 20°C lower than if the maximum temperature allows the dislocations to remain. Both these temperatures for precipitation are lower than that for dissolution.

(c) Mechanical interactions

Hydrogen in solution expands the zirconium lattice (Section 9.7.1.2(a)). When hydrides precipitate the metal lattice is expanded locally, leading to another volume increase and its associated molar volume, V^H, with a value of 1.57×10^{-6} m^3/mol for γ-hydride and 1.63×10^{-6} m^3/mol for δ-hydride [9.643], which is similar to V_H. First principle quantum mechanical calculations [9.522] also indicate that the volume change caused by hydrogen in solution is almost the same as that caused by hydride precipitation, particularly in the range of temperatures normally encountered during reactor operation. In the presence of a hydrostatic stress, σ_H, the solubility limit, C^σ, to a first approximation, is given by Eq. (9.51) [9.643]:

$$C^\sigma = C \exp[\sigma_H(V^H - V_H)/RT] \tag{9.51}$$

and the increase in the solvus temperature, ΔT, is:

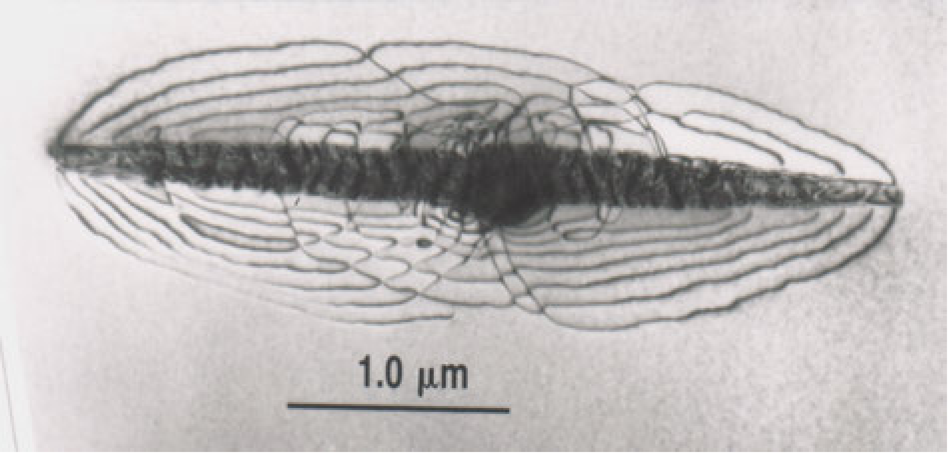

FIG. 9.236. Dislocations around a γ-hydride precipitate in pure zirconium observed by transmission electron microscopy (photograph by S.A. Aldridge).

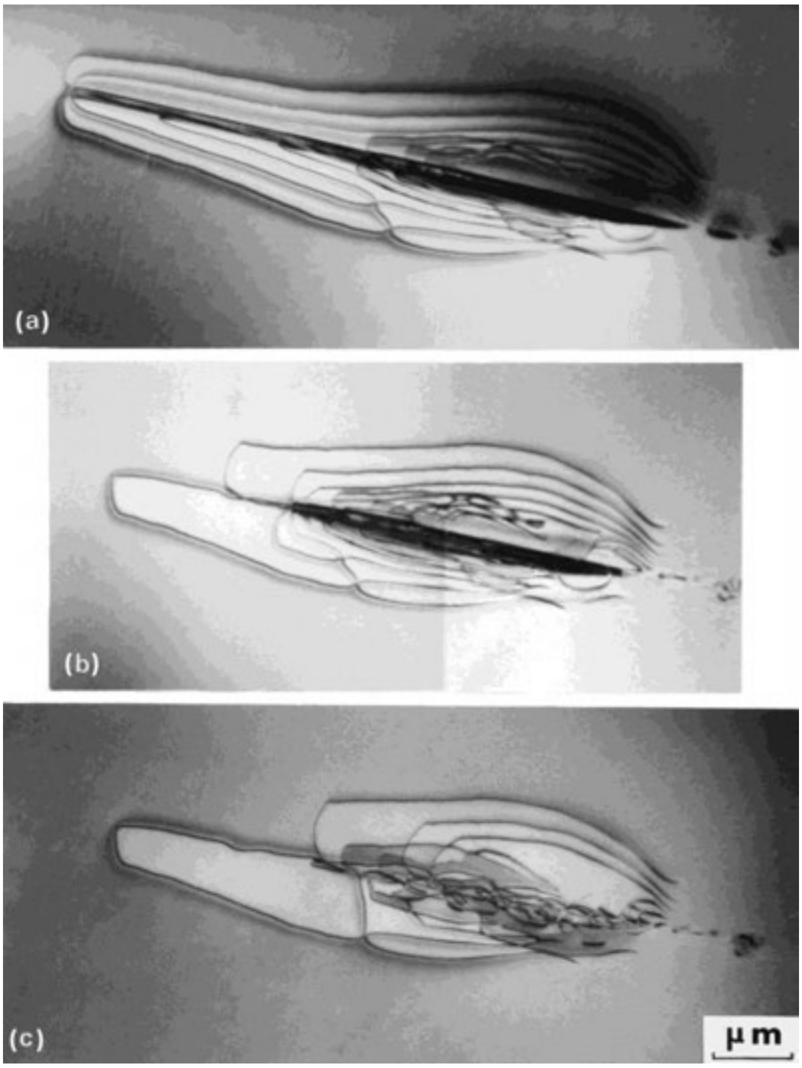

FIG. 9.237. Stages of hydride dissolution in pure Zr during heating in a high voltage electron microscope: (a) room temperature; (b) 350 K (77°C); (c) 390 K (117°C) [9.606].

$$\Delta T = \sigma_{\mathrm{H}}(V^{H} - V_{H})/R\ln(C/A) \tag{9.52}$$

Since $(V^{H} - V_{H})$ is very small, the effect of stress on the solubility limit is small — about 3% at 573 K (300°C) — and within the scatter band of experimental data in materials with yield strengths of interest [9.640, 9.644–9.646]. Consequently, values of the hydrogen concentration and temperature associated with the solubility limit obtained with no stress can be applied when stresses are present.

Calorimetry shows that heat has to be supplied to dissolve the hydrides and that heat is given off when the hydrides precipitate, supplied by the formation energy. Mechanistically several events have to be considered. During heating, the zirconium matrix and the hydride precipitates expand. As the hydrides dissolve, they shrink and the increased hydrogen in solution expands the zirconium lattice further. Once all the hydride is dissolved, the zirconium lattice follows the thermal expansion. During cooling the zirconium lattice decreases from thermal contraction and when hydrides form, the lattice parameters of the zirconium matrix decline at a faster rate because hydrogen is being removed from solution. These processes have been followed in CWSR Zircaloy-4 containing hydrogen concentrations up to 530 ppm (4.61 at.%) using in situ synchrotron X ray diffraction [9.610]. The misfit between the hydride and the zirconium imposes a compressive stress on the hydride as well as a local tensile stress in the metal. At room temperature the compressive strains vary from −0.010 in [110] to −0.013 in [111] in δ-hydrides [9.570]. On heating, the measurements indicate that the d-spacing of the hydride follows the same temperature dependence as the Zircaloy-4 rather than that of thermal expansion of hydride, which is larger than that of zirconium [9.553], and the initial compressive strain declines on heating. Close to T_{D}, the hydride d-spacing increases to the unstressed value. Once hydrides start to precipitate during cooling, they have an initial d-spacing well below the unstressed value, indicating compression of about 660 MPa. With further cooling of about 25°C and more precipitation, the average compressive strain declines and passes through a minimum value, perhaps because of dislocation generation and easier nucleation of new hydrides in the strain field of the first hydrides, as well as differential thermal contraction. With further cooling the hydride strain follows the thermal contraction of the Zircaloy-4, thus renewing the initial compressive stress on the hydride.

The volume expansion when a hydride forms is postulated to be the source of the apparent hysteresis in the solubility limits; a model based on the elastic and plastic accommodation of the precipitate by the metal lattice to account for the phenomenon has been presented [9.512, 9.555, 9.647–9.650]. The approach is that TSSD is a true solvus and one has to rationalize the value of TSSP. The observation of dislocations around hydrides by transmission electron microscope (TEM) is taken as support for this model. At the start of precipitation, the amount of hydride phase will be very small and the particles will not be large enough to generate misfit dislocations [9.548]. The precipitation process itself provides heat from the formation energy [9.522, 9.528], which is sufficient to supply the much smaller strain energy (Section 9.7.1.1). If the strains from precipitation determine that T_P is lower than T_D and provide the apparent hysteresis, they act like an activation energy [9.648].

(d) Nuclear effects

All the isotopes of hydrogen may be found in nuclear reactors but any effect of isotopes on the phase diagram is either negligibly small or nonexistent. The α/(α+hydride) boundary for sponge zirconium containing either deuterium or hydrogen was studied using internal friction [9.651]. The solubility limits were all about 70°C higher than indicated in Fig. 9.235. Although the authors concluded that the values of T_D and T_P for hydrogen were slightly higher than for deuterium, in these experiments the range of deuterium concentrations was small — 0.18 at.% to 0.65 at.% (20 ppm to 71 ppm) — and the scatter on the data was large. In another internal friction study no effect of hydrogen isotopes was detected [9.601]. Measurements of TSSD by dynamic elastic modulus in material containing up to 198 ppm deuterium (0.90 at.%) agreed with data derived from material containing hydrogen. Manifestations of hydride embrittlement below 200 ppm (1.79 at.%) hydrogen and 623 K (350°C) were independent of hydrogen isotope [9.624–9.626, 9.652], also indicating that the α/(α+hydride) boundary is not sensitive to the hydrogen isotope. Although no difference in the fracture behaviour of zirconium alloys due to isotopes of hydrogen could be detected, the lattice parameter of δ-deuteride was slightly smaller (0.2%) [9.653] and the elastic modulus was larger (13%) [9.552] than that of δ-hydride. The β/(β+hydride) and the (β+hydride)/hydride boundaries were similar for both hydrogen and deuterium when measured by pressure-composition isotherms [9.654].

The reports of the effect of neutron irradiation on TSS are conflicting. Irradiation may increase the solubility limit and change the difference between TSSD and TSSP in Zircaloy [9.617, 9.618, 9.622], but two studies reported no effect [9.655, 9.656]. All the evaluations used DSC, and Table 9.36 summarizes details of the test materials, methods and results; Ref. [9.655] is excluded because the experimental details, except for the maximum temperature during DSC, are absent. To attain a value of TSS by DSC one has to heat the material above T_D. If this temperature is greater than the irradiation temperature, irradiation damage will start to anneal out. This process will also contribute heat and complicate the total DSC response and will affect any irradiation induced change to the TSS values.

Three studies evaluated on material containing hydrogen from corrosion during service [9.618, 9.621, 9.622], whereas in Ref. [9.617], with the exception of two specimens, hydrogen was added by diffusing it from a hydride layer after the material was removed from the reactor. In the latter study, care was taken to minimize time above the irradiation temperature, but specimen preparation could have contributed to the results by annealing out small irradiation damage. The first DSC heating run was not included in Ref. [9.617] because of perceived unreliability. In Refs [9.618, 9.622] the criterion for TSS was the peak temperature while in the other two studies the temperature of maximum slope was used. This choice affects the value of T_D and T_P by 15 to 20°C (Figs 9.232 and 9.233) but will have little effect on assessing any changes caused by irradiation.

The value of TSS can be modified with each sampling. For example, in tests on recrystallized Zircaloy-4 irradiated at 553 K (280°C) and containing 156 and 237 ppm (0.71 and 1.07 at.%) hydrogen, the DSC runs to measure TSSD had a maximum temperature of 653 K (380°C) based on an expected T_D for unirradiated material of 636 and 674 K (363 and 401°C), respectively [9.618]. The first runs provided very low values of T_D, 523 and 548 K (250 and 275°C), as shown in Fig. 9.238. The subsequent twelve runs yielded higher values that approached a constant value, presumably as the irradiation damage was annealed out. Annealing at 781 K (508°C) for 2 h provided no further change and the values remained 30°C below those for unirradiated material. In annealed electron beam welds of Zircaloy containing 50 ppm (0.45 at.%) hydrogen added after irradiation, T_D was reduced with irradiation from 565 K to 553 K (292°C to 280°C) while T_P was reduced from 521 K to 498 K (248°C

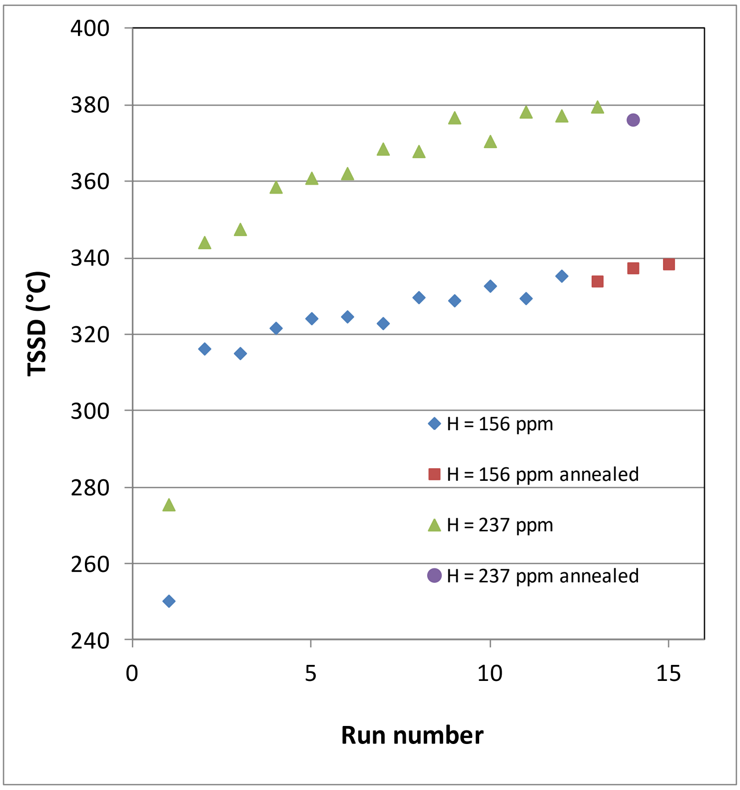

FIG. 9.238. Evolution of TSSD with sequential DSC runs on recrystallized Zircaloy-4 irradiated at 553 K (280°C) to 4.2 × 1025 n/m2, with maximum temperature during a run of 653 K (380°C). Final runs after annealing at 781 K (508°C) for 2 h (based on [9.618]).

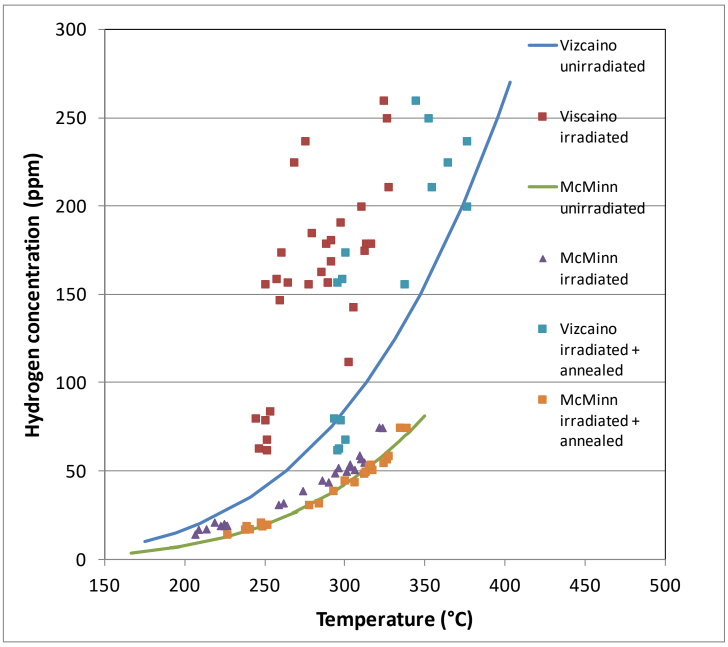

FIG. 9.239. Values of TSSD for hydrogen in Zircaloy, showing experimental variation, effect of irradiation and post-irradiation annealing (based on [9.617, 9.618, 9.622]).

to 225°C); (T_D–T_P) was increased from 317 K (44°C) to 328 K (55°C) by the irradiation [9.617]. The TSSs reverted almost to their unirradiated values after annealing out the irradiation damage at about 473 K (200°C) above the irradiation temperature. (Exceptions were two specimens of Zircaloy-2 pressure tube in which the recovery was incomplete; this material contained a hydrogen concentration of 75 ppm (0.68 at.%) attained during reactor service to a neutron fluence of 10^{26} n/m^2.) In this study [9.617], the effect of irradiation on solubility limits was modest; when values of TSS from the two approaches are compared (Figs 9.239 and 9.240), a large difference is noted. In Fig. 9.239, the values from the first DSC run are used from Refs [9.618, 9.622] while the data from Ref. [9.617] do not include the first DSC run. Although the results for TSSD of unirradiated material appear different on this scale, as shown in Fig. 9.239, when compared with other studies on unirradiated Zircaloy over a wide range of hydrogen concentrations and temperatures, they are within the scatter band, as shown in Fig. 9.241. The first run data from Refs [9.618, 9.622] are well outside the general scatter band for unirradiated material whereas the data for irradiated material from Ref. [9.617] are within the scatter band.

When the hydrogen concentration picked up during irradiation is large, the need to go to high temperatures to estimate TSS complicates DSC measurements because of the exothermic contribution from the recovery of irradiation damage. No effect of irradiation on TSS was observed in sets of measurements on fuel cladding and guide tubes containing up to 415 ppm (3.65 at.%) hydrogen where TSSD was up to 745 K (472°C), 180°C higher than the irradiation temperature [9.655, 9.656]. The recovery of irradiation damage during hydride dissolution was proposed as an explanation for the absence of any effect of irradiation on TSS. One way to avoid this problem may be to use reference blanks made from material that is similarly irradiated, but contains little hydrogen.

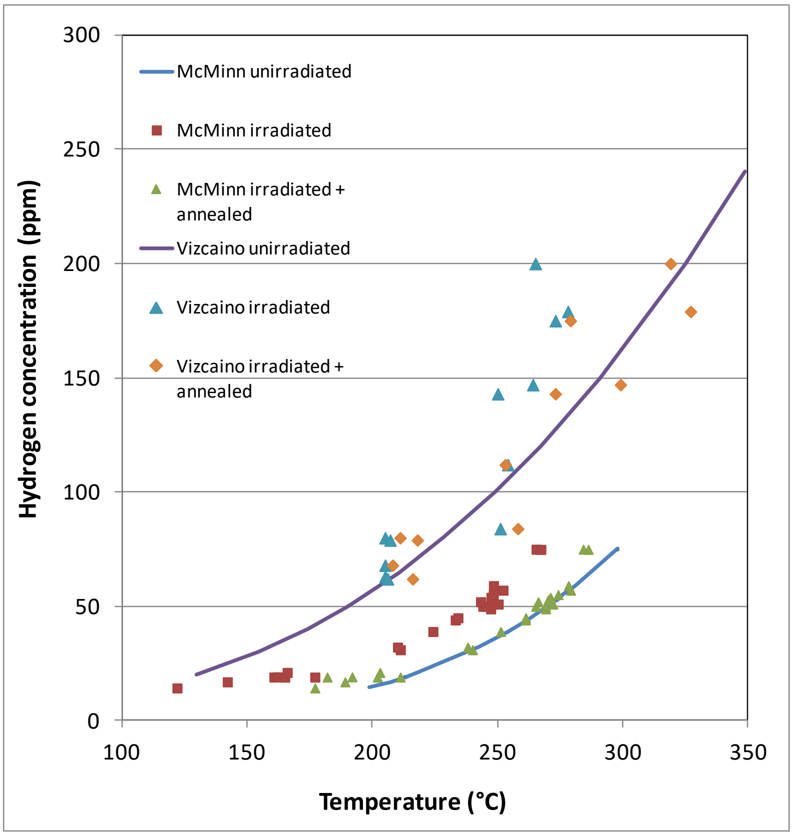

FIG. 9.240. Values of TSSP for hydrogen in Zircaloy, showing experimental variation, effect of irradiation and post-irradiation annealing (based on [9.614, 9.615, 9.619]).

TABLE 9.36. DETAILS OF STUDIES OF EFFECT OF IRRADIATION ON TSS

Author and source	Material	Irradiation temperature (°C)	Neutron fluence 10^{25} n/m^2	Hydrogen			DSC details				Effect of irradiation		
				Source	Concentration (ppm)	Distribution	Heating and cooling rate (°C/min)	Maximum temperature (°C)	Criterion for TSS: peak or maximum slope	First run	TSSD	TSSP	Annealing
McMinn [9.617]	Zircaloy -2, Zircaloy-4 electron beam weld Annealed 760°C for 2 h	250–300	0.55–10	Post-irradiation hydride layer	14–75	Uniform	10	260–320	Maximum slope	Ignored	Modest increase	Medium increase	At or close to unirradiated material
Vizcaino [9.618,9.622]	Zircaloy-4 cooling channel	268–280	4–10	Corrosion in-reactor	62–260	Uniform	20	350–400	Peak	Accepted	Large increase	Medium increase	Approach unirradiated material
Une	Zircaloy-2: BWR cladding and spacer bands	288–340	7.9–12.9	Corrosion in-reactor	21–194	High H in liner	10	310–540	Maximum slope	Accepted	Very small	Very small	None
[9.656]		288	5.4–8.5		166–373	Uniform	10	450–540	Maximum slope		None	None	None

The effect of neutron irradiation on TSS is attributed to trapping the hydrogen at the sites of irradiation damage [9.617, 9.618]. The distribution profile of 100 keV deuterium ions implanted into a surface preirradiated with 4 MeV Zr ions was also attributed to trapping by lattice defects [9.657]. The increase in strength caused by irradiation damage may also play a role in raising TSS, although the effect is thought to provide only a small change of 1 to 2% [9.617]. The DSC signal is linked with the change in hydride concentration. Although the temperature at which hydrides dissolve or precipitate is reduced by irradiation, with solute trapping the amount of mobile hydrogen in solution is not necessarily affected by irradiation. Any decrease in mobility will reduce the availability of the hydrogen to contribute to damaging phenomena such as hydride reorientation and cracking. From quantum calculations, individual vacancies are estimated to attract up to nine hydrogen atoms, six very tightly; hydrogen is attracted to vacancy <a> and <c> loops and retards their collapse [9.522]. Transition element metals that are normally present as precipitates, because of their low solubility limits, may provide extra solubility for hydrogen if they are dispersed into solution by the irradiation [9.658]. Hydrides can be nucleated at dislocations. In Zircaloy material irradiated to 3.3 to 8.6 × 10^{25} n/m^2, hydrides were associated with <c> type dislocations [9.543]. To recover this type of dislocation loop requires a higher temperature (e.g. 873 K (600°C)) than those required to anneal out <a> type loops [9.659]. This difference in annealing temperature may account for some of the incomplete recovery of TSS with specimens that had received large doses of irradiation while early annealing of vacancies and small loops may account for the discrepancy between the various measurements of TSS in irradiated materials because of specimen preparation and the maximum temperature reached during DSC measurements.

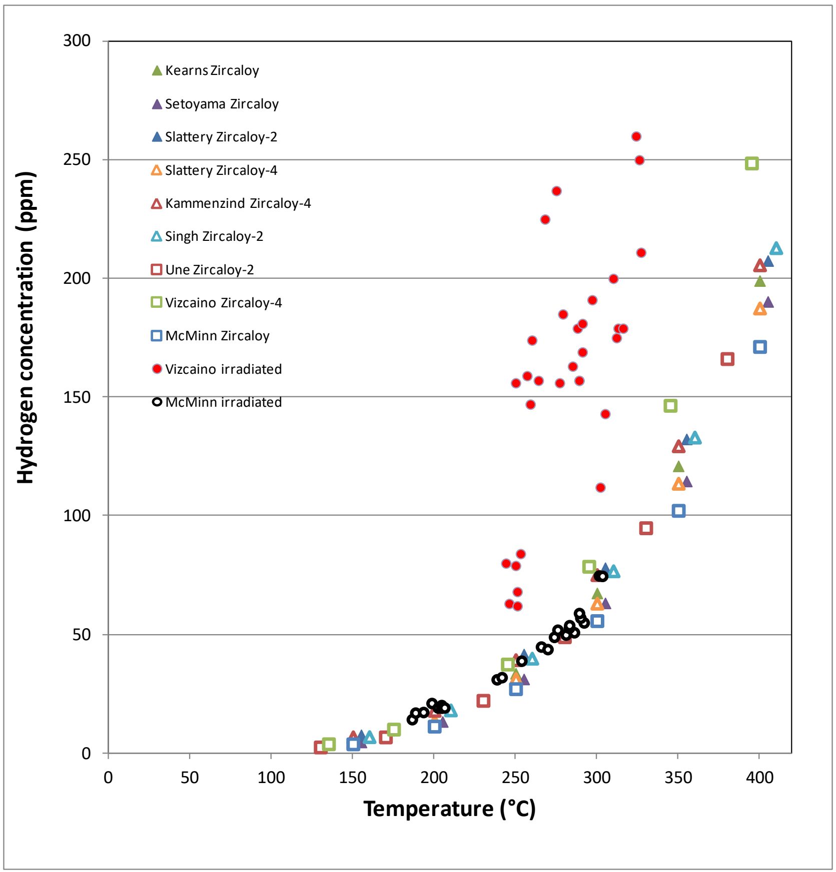

FIG. 9.241. The range of typical measurements of TSSD in Zircaloy illustrating the shift after irradiation (reported data points from [9.617, 9.618, 9.622]). The points for unirradiated material were calculated using Eq. (9.48) from the published values of A and ΔHD using various techniques [9.587, 9.588, 9.596, 9.597, 9.619, 9.661].

e) Effect of alloying

Alloying elements are commonly limited in both choice and amount in zirconium because the capture cross-section for thermal neutrons must be minimized for nuclear applications (Chapter 2, in Volume 1 of this publication). Alloying elements may do the following:

- Change the solubility limit for hydrogen in the α phase;
- Promote the formation of a β phase.

Partitioning hydrogen between the two phases may reduce its concentration in the α-phase.

Although Al, an α stabilizer in Group 4 metals, increases the solubility limit for hydrogen in Ti [9.660], in Zr, within the scatter of the data, α stabilizing elements have little effect on the solubility limit of hydrogen below the eutectoid temperature.

Alloying elements in solution affect the lattice parameter of the zirconium and expansion may lead to increased hydrogen solubility and vice versa. If the alloying element interacts attractively with the hydrogen, the solubility may be increased. These two factors have been evaluated by first principle quantum mechanical calculations [9.658]. The results suggest that despite volume contraction, substitutional Cr and Ni attract hydrogen atoms in solution; for example, each Cr atom can trap two hydrogen atoms. Unless dispersed by irradiation, in practice most of the concentration of these elements will be present as precipitates so their effect from being in solution is expected to be small. DSC measurements indicate some benefit from adding a small amount of chromium [9.661]; the addition of 0.50 wt% (0.87 at.%) Cr to pure Zr appeared to increase TSSD at 573 K (300°C) from 59 ppm (0.54 at.%) to 87 ppm (0.79 at.%). TSSD estimated by dilatometry on Zr-1.15 wt% (2 at.%) Cr could not distinguish TSSD from that of Zircaloy [9.662]. The reason for this discrepancy is not known.

The quantum calculations [9.658] indicate that the volume expansion from Sn is small and that hydrogen is slightly repulsed by Sn so it should have no effect on hydrogen solubility. Zircaloy-2 and Zircaloy-4, essentially Zr-1.5Sn, are α alloys of zirconium and their hydrogen solubility limit is indistinguishable from that of pure Zr [9.584, 9.587, 9.596, 9.661]. The Sn is all in solution and will swamp any effect of the small amount of Cr, Fe and Ni minor alloying elements in solution.

A reduction in hydrogen solvus temperature of about 15°C was measured in Zircaloy-4 with an increase in oxygen concentration from 1100 ppm to 2700 ppm (0.62 to 1.52 at.%) [9.617]. This result is contrary to expectations of no effect based on dilatometry measurements on zirconium containing up to 7700 ppm (4.2 at.%) oxygen [9.584]. Interstitial oxygen atoms occupy octahedral positions in the zirconium lattice and are thought to make three adjacent tetrahedral sites unavailable to hydrogen [9.663]. For this postulate to affect the hydrogen solubility limit, the oxygen concentration would have to be very large. The quantum calculations show that interstitial oxygen causes an expansion of the zirconium lattice but has no effect on the interaction energy with hydrogen in zirconium [9.658]. A CALPHAD assessment of the Zr-O-H system [9.664] indicates a large effect of 3000 ppm (1.69 at.%) oxygen on the α/(α + β) phase boundary but little change on the α/(α + hydride) phase boundary, although the scale of the Figure presenting the results obscures the spread of the results that could accommodate the reported 15°C reduction in TSS. All the information suggests that if there is an effect of moderate concentrations of oxygen (<10 000 ppm (5.44 at.%)) on the solubility limit of hydrogen in zirconium, it is small.

In pure metal, above the eutectoid temperature the solubility limit in the β phase is much higher than in the α phase [9.514, 9.516]. Measurements of TSSD on a β phase alloy, Zr-20Nb, using either diffusion annealing or DSC, follow Eq. (9.48) with A being equal to 5.7×10^4 and 2.88×10^4 and ΔH being equal to 16.5 and 13.2 kJ/mole according to Refs [9.616, 9.665], respectively. The results indicate a solubility limit in the β phase of 73 to 140 ppm (0.66 to 1.26 at.%) hydrogen at 298 K (25°C). Simple extrapolation of one set of measurements [9.665] to the temperature of the maximum value of solubility on the β/(β + hydride) line, 1143 K (870°C), intersects it at 10 042 ppm (48.1 at.%), within 13% of the value indicated in Section 9.7.1, 11 500 ppm (51.5 at.%). This result suggests that the solubility limit is influenced more by crystal structure than chemical composition.

The quantum calculations [9.658] indicate that hydrogen is slightly repulsed by niobium so it should have no effect on hydrogen TSS in the α phase. In (α + β)-Zr-Nb alloys the effective solubility limit in the α phase may be increased by partitioning the hydrogen between the two phases. The quantity of hydride in the α phase depends on the degree of partitioning and the relative amounts of each phase. The partitioning ratio, R_p, is the ratio of the hydrogen in solution in the β and α phases. Khatamian [9.666] found R_p to be between 7 and 9 in Zr-Nb alloys and, as a result, the total hydrogen concentration required to form hydrides increased as the Nb concentration increased; at 503 K (230°C), as the Nb concentration was increased from 0, 1, 2.5 to 5%, C_D increased from 20, 25, 38 to 55 ppm (0.18, 0.23, 0.35 to 0.50 at.%), respectively. Values of R_p between 2 and 4 were derived from diffusion couples between pure Zr and Zr-20Nb [9.665, 9.667]. The β phase decomposes by a series of reactions to α phase and β Nb [9.668, 9.669]. This decomposition affected the distribution of the hydrogen during the preparation of the diffusion couples. With decomposition the partitioning decreases and C_D reverts to the value for the α phase [9.594, 9.596–9.602, 9.616, 9.666, 9.667].

In Zr-3Sn-1Nb-1Mo (an alloy known as Excel), the alloying elements are strongly partitioned with the Sn in the α phase and Nb and Mo in the β phase. The solubility limit for hydrogen is much larger than in the other alloys — at 523 K (250°C) C_D is almost doubled — and the apparent hysteresis is about 80°C [9.615]. The cause of the increase in solubility limit has not been determined, but partitioning of hydrogen to the β phase probably plays an important role.

In summary, the solubility limit for hydrogen in the α phase of zirconium alloys is very low. With dynamic measurements, hydrides precipitate at temperatures about 60°C lower than the temperatures at which they completely dissolve; this behaviour is often interpreted as an apparent large thermal hysteresis. The hydride at the α/(α + hydride) boundary is usually the δ phase, but γ phase may be present at low temperatures, with low hydrogen concentrations and after rapid cooling. The solubility limit can be slightly modified by alloying, especially with the presence of some β phase, and by irradiation, but is not sensitive to stress or to which hydrogen isotopes are present. This information is used to judge when hydrides may be present in reactor components and to evaluate structural integrity.

9.7.2. Hydrogen movement

9.7.2.1. Diffusion of hydrogen in a hydrogen concentration gradient

Knowledge of the diffusion of hydrogen in solution, C, is required to understand its movement in the various gradients that may exist in a component. The hydrogen atoms migrate at least 10^{12} times faster at reactor operating temperatures than the zirconium atoms so the latter can be taken as being stationary. The hydrogen atoms are constantly oscillating and, depending on the temperature, will spontaneously jump with a frequency f from one lattice position to another. The hydrogen atoms jump in all directions an average distance b; the product bf is the average migration velocity of the hydrogen, ν, in m/s. In one dimension, across a plane normal to the hydrogen movement in the x-direction, the flux is $J_x = C\nu$, where J_x is the number of hydrogen atoms/m^{2}s and C is the number of hydrogen atoms/m^3. The number of atoms on each plane is $n = Cb$ and in a short time, Δt, $nf\Delta t$ hydrogen atoms jump from one plane to the next. When a concentration gradient is present in the x-direction, dC/dx, adjacent planes perpendicular to the gradient will have different concentrations, C_1 and C_2, and the number of hydrogen atoms on each plane will be $n_1 = C_1b$ and $n_2 = C_2b$. On average 50% of the jumps in the x-direction will be from plane 1 to plane 2 and 50% will be from plane 2 to plane 1. The number transferring from plane 1 to plane 2 will be $\frac{1}{2}n_1f\Delta t$ and the number transferring from plane 2 to plane 1 will be $\frac{1}{2}n_2f\Delta t$. The flux, J_x, of hydrogen atoms is the net number of hydrogen atoms passing across a plane of unit area in unit time, $J_x = \frac{1}{2}f(n_1 - n_2)$, or in terms of the concentrations, $J_x = \frac{1}{2}fb(C_1 - C_2)$. If $C_1 > C_2$, $C_1 - C_2 = -b(dC/dx)$, and $J_x = -\frac{1}{2}fb^2(dC/dx)$. More hydrogen will cross from the side of the high concentration, C_1, to the one with the low concentration, C_2, than cross in the opposite direction.

This process is also described with a thermodynamic force, F, driving this diffusion, which in turn can be considered as the gradient of chemical potential, μ, of the hydrogen atoms that are diffusing. The hydrogen moves from a position of high chemical potential to one of low chemical potential (compare potentials in gravity, heat or electricity), so $F = -d\mu/dx$. Because the hydrogen is not moving freely, but is constrained to jump between interstitial sites, its velocity is proportional to the force, $v = \Gamma F$, where Γ is the mobility, s/kg. Consequently, $J_x = -C\Gamma d\mu/dx$. The chemical potential is related to the activity, a, of the hydrogen through $\mu = \mu_0 + RTln(a)$, where μ_0 is a reference state of the chemical potential. The activity is linked to the concentration by the activity coefficient, ξ; $a = \xi C \approx C$ as $\xi \sim 1$

for dilute concentrations. In the absence of gradients in other variables such as stress that would modify the chemical potential, $d\mu/dx = RTd(\ln C)/dx = (dC/dx)RT/C$. Thus, $J_x = -\Gamma RTdC/dx = -\frac{1}{2}b^2f\ dC/dx$, where $\Gamma RT = \frac{1}{2}b^2f$ is called the diffusivity or diffusion coefficient, D. This discussion leads to Fick's first empirical law [9.670]:

$$J_x = -D(\partial C/\partial x)_t \tag{9.53}$$

where $(\partial C/\partial x)_t$ is the concentration gradient at time t.

D is often evaluated by observing the one dimensional flux of hydrogen atoms, J_x, moving through the metal in the x-direction from a region of high concentration to one of low concentration. Most of the following examples will be in one dimension.

The temperature dependence of the diffusivity, D, follows an exponential relation:

$$D = D_0 \exp(-Q/RT) \tag{9.54}$$

where

Q is the activation energy for the diffusion process

and D_0 is a constant.

The diffusion of hydrogen through zirconium alloys has not been given the same attention as solubility limits and gaps remain. In some metals D_0 and Q are linearly related — called a compensation effect — but this correlation does not hold for zirconium [9.671].

(a) Diffusion of hydrogen in the α phase

The reported range of D_0 and Q is summarized in Table 9.37 and Fig. 9.242 for the α-phase [9.588–9.591, 9.672–9.676], including values of D and the distance diffused in one hour (based on $\sqrt{(Dt)}$) at 573 K (300°C). The diffusion distances from all the studies agree within a factor of 2, with two exceptions. In Ref. [9.589], only three results are reported so the reliability of D_0 and Q is poor. A technique based on weight gain from hydride formation from hydrogen gas was used in Ref. [9.672] and D could be susceptible to low values if the surface hydride layers impeded the hydrogen migration into the metal. The presence of hydrides in the alloy matrix did not seem to affect D; the specimens used for internal friction [9.675] contained 2.8 at.% (315 ppm) hydrogen and hydrides would be present over most of the temperature range of the experiments. The materials used in the experiments contained concentrations of oxygen ranging from 100 to 1540 ppm (0.057 to 0.87 at.%) as well as a small concentration of alloying elements such as tin and iron; these elements had no discernible effect on Q or the distance diffused by hydrogen; they were within the experimental limit of a factor of two.

TABLE 9.37. DIFFUSIVITY OF HYDROGEN IN ZIRCONIUM ALLOYS IN THE α PHASE

Material	Method	Temperature range °C	D_0 m^2/s $\times 10^{-7}$	Q kJ/mol	D at 300 °C m^2/s $\times 10^{-11}$	Distance moved in 1h at 300 °C mm	Source
Pure zirconium	Weight gain during anneal in H gas from hydride layer	60–250	1.09	47.7	0.48	0.13	[9.672]
Pure zirconium	High H/low H couple	400–600	0.42	23.9	27.8	1.0	[9.589]
Pure zirconium	Anneal in H gas to produce hydride layer	305 –610	0.7	29.6	14.0	0.71	[9.590]
Pure zirconium	High H/low H couple	450–700	4.13	39.6	10.1	0.60	[9.673]
Zircaloy-2	Anneal in H gas to produce hydride layer	260–560	2.17	35.2	13.4	0.69	[9.591]
Pure zirconium, Zircaloy-2, -4	High H/low H welded couple	275–700	7.0	44.7	5.9	0.46	[9.674]
Pure zirconium	Internal friction	210–530	18.3	51.8	3.5	0.35	[9.675]
Pure zirconium	Diffuse from surface layer	400–600	6.91	44.5	6.1	0.47	[9.676]
Zircaloy-4	High H/low H couple	260–482	0.8	33.4	7.2	0.51	[9.588]

Pooling all the data points (except for Ref. [9.672]) yielded a description of the temperature dependence of hydrogen in α-zirconium of:

$$D = 2.32 \times 10^{-6} \exp(-52.04/RT) \text{ m}^2/\text{s} \tag{9.55}$$

The average value of Q for the individual studies listed in Table 9.37 is 38.8±9.1 kJ/mol. The values from quantum calculations agree with this value with a range of values: from either 33.7 to 40.0 kJ/mol [9.528] or 41.9 kJ/mol [9.522]. These calculations confirm that although hydrogen atoms will interact locally with atoms of alloying elements their concentration is usually too low to measurably

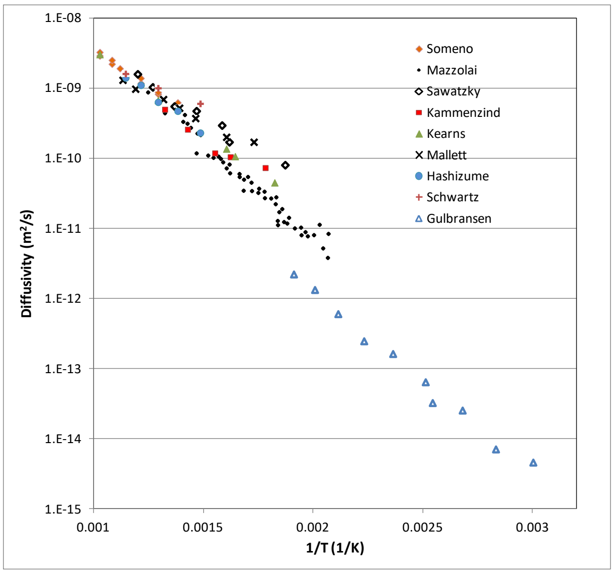

FIG. 9.242. Temperature dependence of diffusivity of hydrogen in zirconium alloys in the α phase [9.588–9.591, 9.672–9.676].

affect the diffusivity of hydrogen. Oxygen is calculated to provide a modest increase in diffusivity; measurements using secondary ion mass spectroscopy on a single crystal confirmed this conclusion with a higher rate of hydrogen segregation in an oxygen enriched layer than towards a clean surface [9.677]. The calculations also suggest that the diffusion of hydrogen should be either isotropic [9.522] or slightly biased in [0001] compared with $\{10\bar{1}0\}$ [9.528]. In polycrystalline Zircaloy-4 texture effects were small, perhaps indicating that diffusion of hydrogen was faster along the c-axis than perpendicular to it [9.674], in agreement with the calculations. Measurements on single crystals [9.677] suggested that diffusivity is about ten times faster in $\{10\bar{1}0\}$ than in [0001]; this contradiction has not been resolved. Any effect of microstructure on diffusivity was not observed; values were within the scatter of the data with materials having grain sizes in the range 10 to 1000 μm after cold working or with a Thomson–Widmanstätten microstructure [9.674].

(b) Diffusion of hydrogen in the β phase and (α + β) phase

Diffusion in the β phase has been measured at high temperatures above the α/β transformation temperature of zirconium by following the flow of hydrogen concentration from a high to a low concentration [9.673], by measuring the rate of sorption of hydrogen [9.678] and by using neutron radiography to follow the distribution of hydrogen during its absorption [9.679]. Diffusion of hydrogen in the β phase at temperatures below the α/β transformation temperature was achieved by using zirconium containing large concentrations of hydrogen and measuring permeation through a thin disc [9.680] or making diffusion couples with Zr-20 Nb in which the beta phase was retained to room temperature by air cooling from 1070 K (800°C) [9.665, 9.681]. The results are summarized in Table 9.38. At high temperature the diffusivities in the three studies are in good agreement, as shown in Fig. 9.243. The values and temperature dependence detailed in Ref. [9.680] are quite different but no adequate explanation for the difference has been given; on the basis of experiments with deliberate surface changes, Gelezunas et al. [9.678] speculated that surface contamination could be the explanation, although Albrecht and Goode [9.680] had paid particular attention to surface treatment. Diffusion of hydrogen is very fast in Zr-20Nb when completely β phase [9.665, 9.681]; at 673 K (400°C) the diffusivity is about ten times that of the extrapolation of the values at high temperature, with the difference becoming greater as the temperature is lowered, as shown in Fig. 9.244. In the investigations reported in Ref. [9.678] the temperature dependence indicated no change with hydrogen concentrations up to 41 at.% (7560 ppm) or in the (α + β) region. The latter result suggests that the temperature dependence of hydrogen diffusion in the three phase-regimes, α, (α + β) and β phase, may be similar; pooling all the data, from measurements at low and high temperature seems to support this suggestion, as shown in Fig. 9.245. Including the pooled results on Zr-20Nb as β phase emphasizes the distinct behaviour in this phase.

TABLE 9.38. DIFFUSIVITY OF HYDROGEN IN ZIRCONIUM ALLOYS IN THE β PHASE AND (α + β) PHASE

Material	Method	Temperature range °C	D_0 m^2/s × 10^{-7}	Q kJ/mol	Source
Pure zirconium	High H/low H couple	870–1100	7.3	35.7	[9.673]
Pure zirconium	Permeation from H gas	650–850	0.61	184	[9.680]
Pure zirconium	Rate of H sorption from H gas	760–1010	5.32	34.8	[9.678]
Zircaloy-4	Neutron radiography following H absorption	550–1200	23	48.3	[9.679]
Zr-20Nb	Welded diffusion couple	200–400	5.38	25.3	[9.665]
Zr-20Nb	Tritium layer by ion bombardment	100–250	0.99	16.7	[9.681]
Zr-2.5Nb	Hydride layer by electrolysis	250–325	4.1	38.4	[9.682]
Zr-2.5Nb	Welded diffusion couple	250–700	1.17	33.6	[9.665]
Zr-2.5Nb	Tritium layer by ion bombardment	267–313	1.1	33.5	[9.681]
Zr-2.5Nb	Deuteride layer by electrolysis	251–301	2.61	39.0	[9.684]
Excel	Hydride or tritium layer	250–308	0.66	26.9	[9.629]

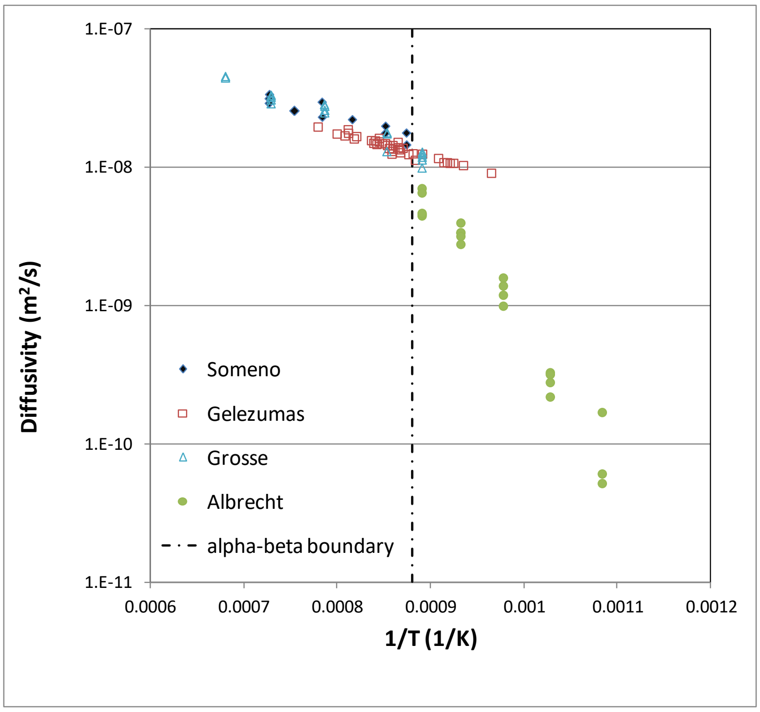

FIG. 9.243. Diffusion of hydrogen in the β phase of zirconium; α/β boundary for pure zirconium [9.673, 9.678–9.680].

In α + β alloys, if the β phase is continuous throughout the α phase, as in extruded Zr-2.5Nb (e.g. as in Fig. 4.86), the β phase can act as a shortcut for hydrogen diffusion. As a result, diffusivity is intermediate between that of the α phase and that of the β phase when the microstructure comprises plates of α phase surrounded by a thin skin of β phase. In Refs [9.665, 9.681] the diffusivity of this mixture of the two phases, D_{Extruded}, is estimated from:

$$D_{\mathrm{Extruded}} = (D_\alpha + \eta\varphi D_\beta)/(1 + \eta\varphi) \quad (9.56)$$

where

η is β grain thickness/α grain thickness, 0.08;

and φ is β phase solubility/α phase solubility, 2.0.

Using the pooled values for D_α and D_β, as shown in Fig. 9.245, provides a close description of the diffusivity of hydrogen[6] in as-extruded Zr-2.5Nb, as shown in Fig. 9.246. If the β phase is decomposed or broken up by heat treatment [9.8, 9.669], the diffusivity is much reduced [9.665, 9.681]. Inserting measured values of D_β in Eq. (9.56) for Zr-20Nb heat treated to reduce the effective β phase to about 30% provides a description of the diffusivity of hydrogen in Zr-2.5Nb with a final heat treatment of 24 h at 400°C (673 K), as shown in Fig. 9.246. Heat treatment at 838 K (565°C) for 24 h reduces the diffusivity even further towards that of the α phase. The hydrogen diffusivity data for Zr-2.5Nb fabricated as plate, cladding or pressure tubes are summarized in Fig. 9.247 [9.665, 9.681, 9.682]. The values converge with those for pure zirconium and Zircaloy at about 723 K (450°C) because of the changes in the β phase during the diffusion anneal. Two values of D, about 10^{-12} m^2/s, were obtained at 318 K (45°C) by measuring the hydrogen distribution from an etched surface [9.683]; they fit with an extrapolation of the values below 723 K (450°C). The few values for Excel are higher than those for Zr-2.5Nb, probably because of the greater amount of β phase [9.629].

The anisotropy of diffusivity has been evaluated in a Zr-2.5Nb pressure tube[6] [9.681] and in a plate with a similar microstructure as a pressure tube [9.684].[7] The microstructure of Zr-2.5Nb pressure tubes is anisotropic both in grain structure and texture; the α phase has dimensions in the ratio 50:5:1 in the axial:transverse:radial directions and the <0001> are concentrated in the transverse direction with few in the axial direction. The diffusivity was 30% greater in the axial direction than in the transverse direction [9.681] suggesting that grain structure rather than crystallography controls hydrogen

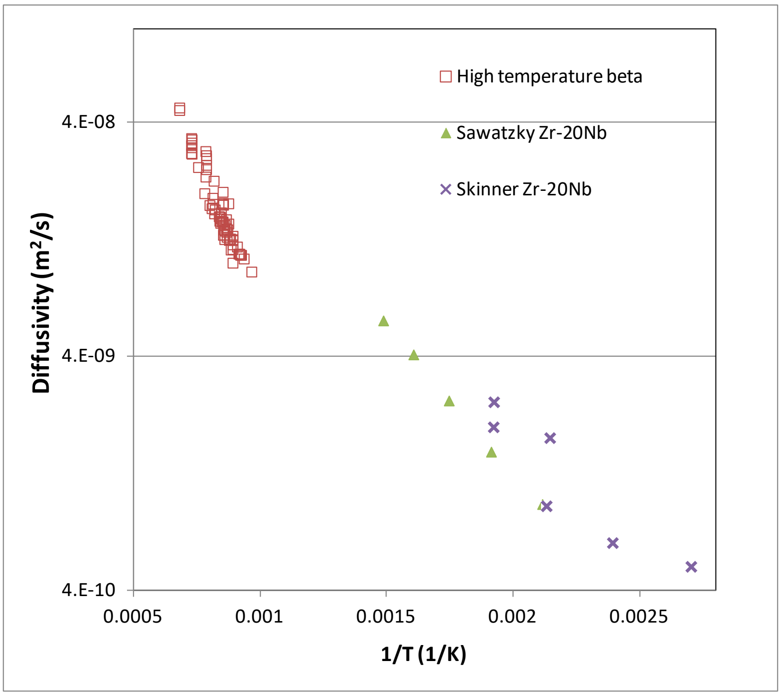

FIG. 9.244. Distinction between diffusivity of hydrogen in β phase at high temperature in zirconium and at modest temperatures in Zr-20Nb β phase [9.665, 9.681].

---

[6] The diffusing species was tritium and measured D values increased by √3. See comments in Section 9.7.2.1(c).

[7] The diffusing species was deuterium and measured D values increased by √2. See comments in Section 9.7.2.1(c).

movement. In the plate material diffusivity was only slightly faster in the axial direction than in the transverse direction but 35% faster than in the radial direction [9.684]. Again, the grain structure in this material could account for this behaviour. The difficulty in determining such effects and distinguishing different temperature dependencies is partly caused by the narrow range of temperature used in some of the experiments. For example, Skinner et al. [9.681] measured D between 540 and 586 K (267 and 313°C), Léger's [9.682] range was 523 to 598 K (250 to 325°C) and Khatamian [9.684] tested between 524 and 574 K (251 and 301°C); for comparison, Sawatzky et al. [9.665] used temperatures between 523 and 973 K (250 and 700°C).

(c) Nuclear effects on the diffusion of hydrogen

In some of the experiments described above, deuterium and tritium were used to distinguish them from hydrogen to study the movement of the hydrogen isotope that is absorbed in practice, to minimize any effects of hydrogen contamination or to improve spatial resolution at low temperatures and short diffusion annealing times. By analogy with Graham's Law [9.685], where the diffusion rate of gases is inversely proportional to the square root of molecular weight, and from rate theory [9.686], the jump rate for diffusion is expected to be inversely proportional to the square root of the isotopic mass, plus a slight slowing effect because the variation in the angle of atomic jumps depends on isotopic mass. Hydrogen represents the largest ratio in isotopic mass of any element and its effects should be the most easily distinguished. An initial expectation is that the diffusivities of hydrogen, D_H, deuterium, D_D, and tritium, D_T, should be in the ratio $1/\sqrt{1}:1/\sqrt{2}:1/\sqrt{3}$ or 1:0.707:0.577.

Although diffusivity experiments using weight gain owing to hydride formation from hydrogen gas did not agree with other measurements, as discussed in Section 9.7.2.1, similar experiments were carried out using deuterium [9.672]. In the original paper the temperature dependence of the diffusivity for each isotope was stated to be the same and D_0 values for deuterium and hydrogen were in the ratio 0.670, close to the expectation. The ratio was found to be smaller, 0.636, when individual values of diffusivity, measured at the same temperature, were compared. Making a similar comparison of individual results between hydrogen and tritium showed that tritium was the slower diffuser but an exact correspondence with the mass effect was also not obtained; the ratio D_T/D_H was 0.507 instead of the expected 0.577 [9.676]. These two results suggest that using only the inverse square root of the isotopic mass to provide an equivalent diffusivity of hydrogen will lead to an underestimation error of between 10 and 12%. These results are summarized in Table 9.39.

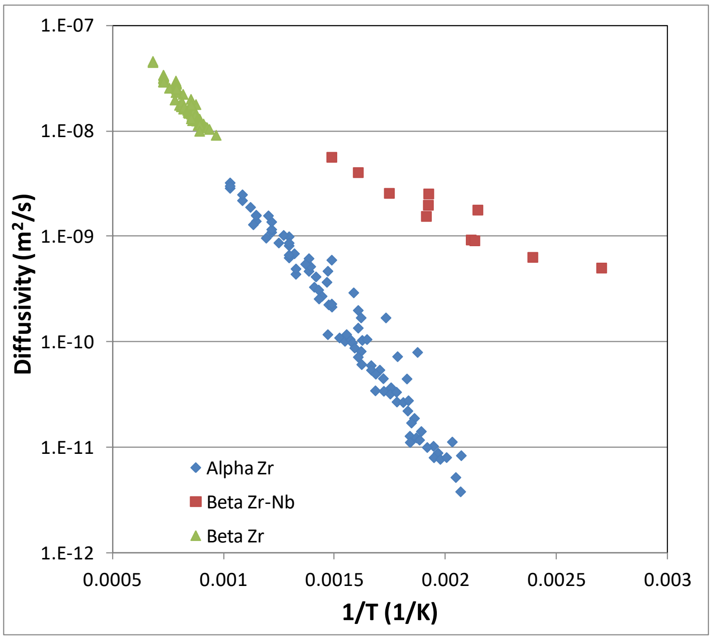

FIG. 9.245. Comparison of temperature dependence of diffusivity of hydrogen in α-zirconium and β-zirconium showing similarity and in β phase in Zr-20Nb showing the difference. Data pooled from Figs 9.242 to 9.244.

TABLE 9.39. COMPARISON OF DIFFUSION OF HYDROGEN ISOTOPES IN ZIRCONIUM

Deuterium and hydrogen [9.672]				
Temperature (°C)	D_H m^2/s	D_D m^2/s	$D_D/\underline{D}_H$	Isotopic mass effect
100	$2.54 \cdot 10^{-14}$	$1.62 \cdot 10^{-14}$	0.638	0.707
150	$1.63 \cdot 10^{-13}$	$7.70 \cdot 10^{-14}$	0.474	
175	$2.47 \cdot 10^{-13}$	$1.64 \cdot 10^{-13}$	0.664	% difference
225	$1.33 \cdot 10^{-12}$	$1.02 \cdot 10^{-12}$	0.769	
		Mean	0.636	10.0

Tritium and hydrogen [9.676]				
Temperature (°C)	D_H m^2/s	D_T m^2/s	D_T/D_H	Isotopic mass effect
400	$2.30 \cdot 10^{-10}$	$1.20 \cdot 10^{-10}$	0.522	0.577
450	$4.70 \cdot 10^{-10}$	$2.40 \cdot 10^{-10}$	0.511	
500	$6.30 \cdot 10^{-10}$	$3.20 \cdot 10^{-10}$	0.508	% difference
550	$1.10 \cdot 10^{-9}$	$5.30 \cdot 10^{-10}$	0.482	
600	$1.40 \cdot 10^{-9}$	$7.20 \cdot 10^{-10}$	0.514	12.1
		Mean	0.507	

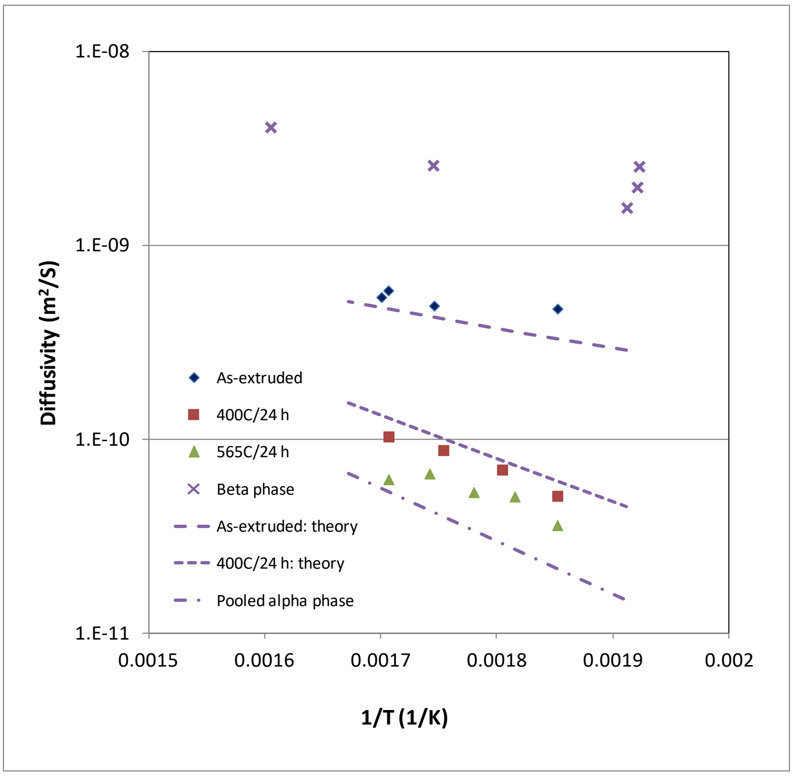

FIG. 9.246. Diffusivity of hydrogen in Zr-2.5Nb after different heat-treatments. Theory based on Eq. (9.56) using pooled values in Fig. 9.245 and observed distributions of β phase (based on [9.665, 9.681]).

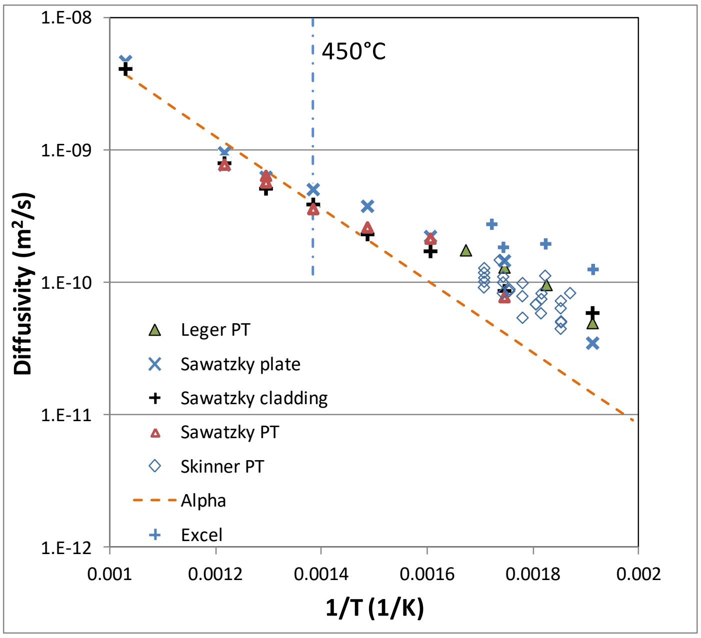

FIG. 9.247. Temperature dependence of diffusivity of hydrogen in Zr-2.5Nb in various forms [9.665, 9.681, 9.683] compared with the mean of the pooled data for α phase alloys and Excel alloy [9.629]. Note the convergence with the α phase alloys above about 723 K (450°C).

The jump frequency of the hydrogen atoms is determined by R_v, the ratio of the vibrational frequency of the interstitial hydrogen in a stable configuration, ν_{isotope}, and its vibrational frequency in an activated state, $\bar{\nu}_{\text{isotope}}$, leading to diffusion; these frequencies will vary with each isotope. The temperature dependence of the ratio D_D/D_H was analysed [9.687] through:

$$D_D/D_H = \left[\frac{\sinh\left(\frac{h\nu_D}{2kT}\right)}{\sinh\left(\frac{h\nu_H}{2kT}\right)}\right]^3 \left[\frac{\sinh\left(\frac{h\bar{\nu}_H}{2kT}\right)}{\sinh\left(\frac{h\bar{\nu}_D}{2kT}\right)}\right]^2 \qquad (9.57)$$

where

h is Planck’s constant;
k is Boltzmann’s constant;
T is temperature;

and $\nu_H = 3.48 \times 10^{13}$/s, based on the energy of hydrogen in the zirconium lattice measured by inelastic neutron scattering [9.637].

The approach was to calculate D_D/D_H assuming the isotopic inverse square root mass relationship for the frequencies of vibration, then choose the best value of R_v that describes values of D_D/D_H from absorption experiments [9.672, 9.687]. The results of the calculations using R_v of 1.25 and 1.10 are depicted in Fig. 9.248. With one exception, the data fit with $R_v = 1.25$. By analogy, the calculations and data for tritium are presented in Fig. 9.249. The best fit seems to be when $R_v = 1.05$. The experimental data need to be expanded to increase confidence to justify the isotopic mass relationships and to use one isotope as a substitute for another.

The results of diffusivities of deuterium and tritium in α zirconium [9.672, 9.676, 9.687, 9.688–9.691] are summarized in Table 9.40. The values for tritium are plotted in Fig. 9.250. The temperature dependence is consistent over a wide range of values of diffusivity. In one study, six measurements were made at room temperature [9.689]; the mean value was 1.08×10^{-14} m²/s and the standard deviation was 5.94×10^{-15} m²/s representing a coefficient of variation, standard deviation/mean, of 55%. When the pooled data for tritium are compared with those for hydrogen over

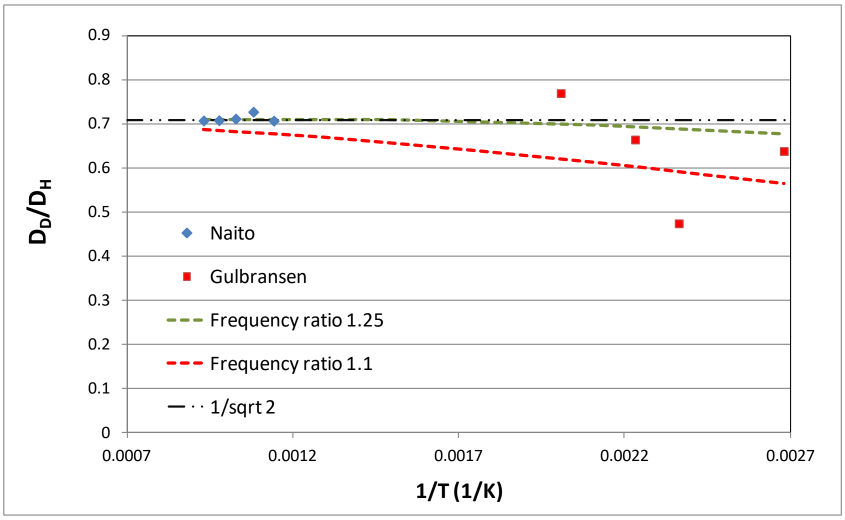

FIG. 9.248. The temperature dependence of the isotopic ratio of the diffusivities of deuterium and hydrogen, DD/DH. The difference in mass dominates as DD/DH is close to 0.707. With one exception, the ratio of the activated to stable state of the hydrogen atoms is 1.25 [9.672, 9.687].

a similar temperature range, as shown in Fig. 9.251, at high temperatures the expected lower diffusivities of tritium compared with hydrogen are observed but the temperature dependencies are slightly different. The variations in measurement methods and the scatter, characterized by standard deviation, suggest that to differentiate diffusion of different isotopes in a material much care must be exercised in comparing large populations of diffusivity measurements; comparing pairs of values for each isotope using the same technique on the same material at the same temperature, as in Table 9.39, is preferable, but with a greater number of values to improve statistical confidence.

TABLE 9.40. DIFFUSIVITY OF DEUTERIUM OR TRITIUM IN ZIRCONIUM ALLOYS IN THE α PHASE

Material	Method	Temperature range °C	D_0 m^2/s × 10^{-7}	Q kJ/mol	Source
Pure zirconium	Weight gain during anneal in D gas; from deuteride layer	100–225	0.73	47.7	[9.672]
Pure zirconium	Tritide layer by electrolysis; autoradiography	149–240	1.53	38.0	[9.688]
Zircaloy-2	Tritium layer from transmutation of ^{6}Li; sectioning	-78–204	0.21	35.6	[9.689]
Zircaloy-2	Tritium implanted by irradiating Cu block with α particles; gas extraction after anneal	200–750	1.04	42.1	[9.690]
Zircaloy-2	Tritium implanted by irradiating Cu block with α particles; gas extraction after anneal	290–720	1.03	42.1	[9.691]
Pure zirconium	Absorption from H and D gas; isotopic diffusivity ratio	500–800	—	—	[9.687]
Pure zirconium	Tritium layer by glow discharge and transmutation of ^{6}Li; vacuum extraction of gas and oxidized to water	400–600	3.11	43.9	[9.676]

As with large concentrations of hydrogen, the presence of large concentrations of oxygen has no effect on tritium diffusion; at 693 K (420°C) the diffusivity in Zircaloy-2 containing 11 320 ppm (at.%) was the same, within experimental error, as with the starting oxygen concentration, 1350 ppm (0.76 at.%) [9.690]. Similarly, at 693 K (420°C) the diffusivity of tritium was independent of whether hydrides were present or not; the values of D_T were the same, within experimental error, for material containing 200 ppm (1.79 at.%) hydrogen, where all the hydrogen would be in solution, and 1000 ppm (8.37 at.%) hydrogen, where about 800 ppm (6.8 at.%) hydrogen would be present as hydrides. Later experiments at lower temperatures [9.691] suggested that hydrides impede diffusivity if they act as sinks for hydrogen and consequently the effective value of D is reduced. The flux of hydrogen will be

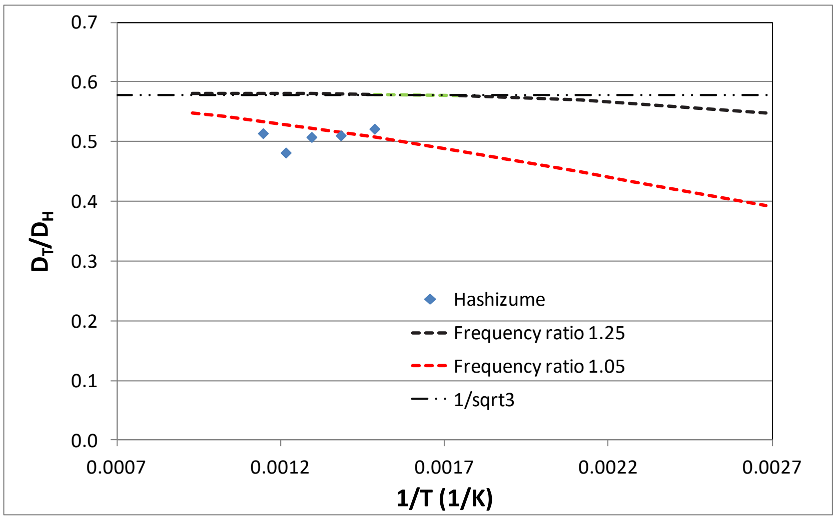

FIG. 9.249. The temperature dependence of the isotopic ratio of the diffusivities of tritium and hydrogen, DT/DH. DT/DH is close to 0.5 rather than 0.577, implying that the ratio of the activated to stable state of the hydrogen atoms is close to 1.05 [9.676].

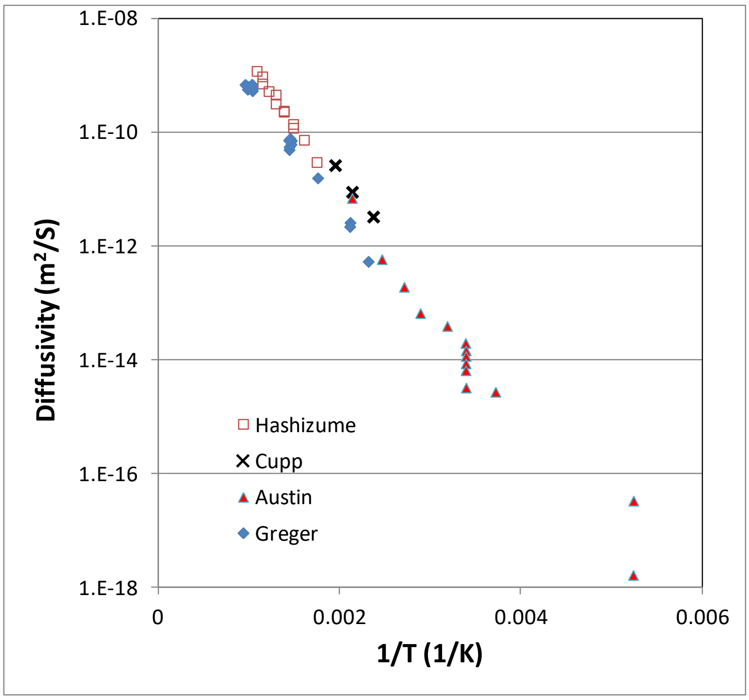

FIG. 9.250. Temperature dependence of diffusivity of tritium in α zirconium [9.676, 9.688–9.690].

dominated by diffusion through the α and β phases as long as the volume fraction of hydride is small (e.g. 1%).

Small amounts of irradiation damage from neutron (10^{18} n/m^2) or proton (1.3×10^{20} p/m^2) irradiation had no discernable effect on D_T [9.691]. In experiments at 673 K (400°C), hydrogen diffusivity was reported to be doubled in Zircaloy-4 with a neutron flux of 1.2×10^{17} n·m^{-2}·s^{-1} ($E > 1$ MeV) to a fluence of 1.4×10^{22} n/m^2 [9.692]. A 30 × 30 mm sheet, 2 mm thick and containing 160 ppm (1.44 at.%) hydrogen was welded to a similar sheet containing 10 ppm (0.09 at.%) hydrogen. The diffusivity was evaluated from the distribution of hydrogen measured by neutron scattering and comparing with separate measurements on similar specimens but with no flux. In another set of experiments, no effect of irradiation flux or fluence was observed on the diffusion coefficient of

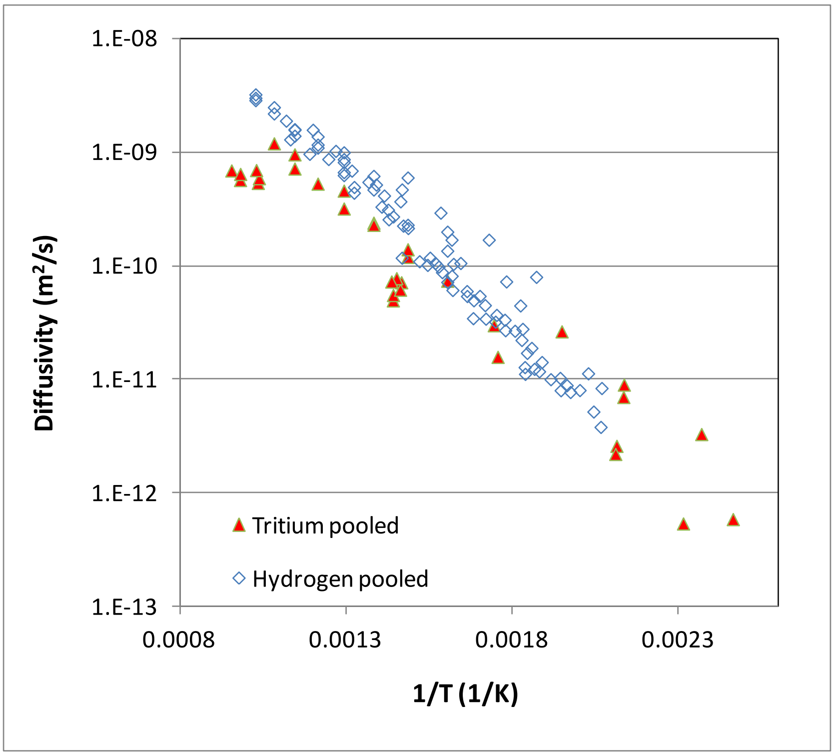

FIG. 9.251. Comparison of diffusivity of hydrogen and tritium in α-zirconium (data from Figs 9.245 and 9.250).

deuterium in Zr-2.5Nb at 536–573 K (263–300°C) [9.693, 9.694]. In these experiments, similar specimens were held in a neutron flux (5×10^{17} $n \cdot m^{-2} \cdot s^{-1}$ ($E > 1$ MeV) and out-of-flux in the same hot water loop for 1146 h. Despite a small temperature difference, 6°C, D_D values were similar and in accord with the values derived from Table 9.38. Further experiments are required to confirm whether an irradiation flux affects hydrogen diffusion.

In summary, the diffusivity of hydrogen follows an exponential behaviour with temperature in both the α and β phases. The average experimental value of Q is described by quantum calculations. Diffusivity is not much affected by the concentration of α stabilizing elements, such as oxygen. The hydride volume fraction is usually too low to affect the flux of hydrogen, even if the effective diffusivity is reduced by their presence. Microstructure is only a consideration when alloy induced β phase is present to increase both solubility and diffusivity. In polycrystals, directional effects on diffusivity from microstructure and texture are small, < 50%. The rate of isotope diffusion is approximately proportional to the inverse square root of the mass. Irradiation may increase diffusivity twofold. The values of diffusivity can be used to evaluate the effects of external gradients and times to distribute hydrogen.

9.7.2.2. Effect of stress gradient on hydrogen diffusion

Components often contain stress gradients, especially at flaws, and the consequences need to be evaluated. The development of a hydrogen concentration gradient by a stress gradient is not the result of producing hydrides because of a change in TSS by stress; such an effect is negligibly small (Section 9.7.1.2(c)). The buildup of a concentration gradient from a stress gradient can be achieved when no hydrides are present. Any change in the distribution of hydrogen is caused by the development of a gradient in chemical potential.

Stress affects the chemical potential, μ_H, of the hydrogen dissolved in metals through Eq. (9.58) [9.695, 9.696]:

$$\mu_H = \mu_H^0 - \sigma_H V_H \tag{9.58}$$

where

$\mu_H{}^0$ is an arbitrarily defined reference state;
σ_H is a hydrostatic stress;

and V_H is the partial molar volume of hydrogen in zirconium.

Tension decreases μ_H while compression increases it. The hydrogen concentration in a highly stressed region, C_σ, in equilibrium with the hydrogen concentration in a region with no stress, C_0, is given by:

$$\ln(C_\sigma/C_0) = \sigma_H V_H/RT \tag{9.59}$$

Thus, if a stress gradient exists, the hydrogen will tend to flow up the stress gradient (e.g. from a region of compression to one of tension [9.697, 9.643] or to a stress raiser like a notch or crack). The flux of hydrogen in a uniaxial stress gradient, J_x, in the x direction is opposed by the consequential hydrogen concentration gradient:

$$J_x = -D\,[dC/dx - CV_H(d\sigma_H/dx)/3RT] \tag{9.60}$$

If the hydrogen concentration does not exceed TSSP, eventually equilibrium is established and J_x is equal to 0.

The reduction in μ_H by tensile stress, its increase by compressive stress and the movement of hydrogen in stress gradients has been demonstrated in several metals, including zirconium [9.698]. In experiments, bars of Zr-2.5Nb containing 55 ppm (0.5 at.%) hydrogen were bent with a stress gradient of 100 MPa/mm from compression to tension at 573 K (300°C); all the hydrogen was in solution and a gradient of about 2 ppm (0.018 at.%) hydrogen/mm was achieved after 6 days when J_x was equal to 0. Using Eq. (9.60), a value of V_H of 1.7×10^{-6} m^3/mol was derived from the measurements, in good agreement with those obtained from measurements of crystal lattice expansion by deuterium or hydrogen in solution [9.609, 9.640]. These results also explain why no effect was detectable in 'dog-bone' specimens of Zircaloy-4 with a stress gradient of only 12.1 MPa/mm [9.645]. In other experiments [9.645], plate specimens containing a flat notch were thermally cycled under load. A single cycle or 10 or 25 cycles consisted of holds of two or four days at 533 to 644 K (260 to 371°C) with applied stresses of −160 to 240 MPa; the latter stress provided a gradient of about 150 MPa/mm at the notch. The Zircaloy-4 material contained up to 350 ppm (3.1 at.%) hydrogen. These test conditions produced a net transfer of hydrogen. The high temperature part of the cycles, T_m, was too low to take all the hydrogen into solution so only part of the inventory was available for diffusion. The results indicated that a small amount of hydrogen transferred with each cycle into the notch region if the stress was tensile or away from the notch if the stress was compressive. In the example shown in Fig. 9.252, at the peak temperature of the cycle, 644 K (371°C), the amount of hydrogen in solution would be 130 ppm (1.17 at.%). The amount of hydrogen transferred per cycle was 7.2 ppm (0.066 at.%), representing 5.5% of that available. At 589 K (316°C) the amount of hydrogen in solution would be 71 ppm (0.64 at.%); about 2 ppm (0.018 at.%) hydrogen was transferred on each cycle representing 3.5% of that available. Any transfer from the 34 ppm (0.31 at.%) available at 533 K (260°C) was too low to detect. The amount of hydrogen transferred depended on the high temperature part of the cycle, the applied stress and the number of cycles, as shown in Fig. 9.253. When Eq. (9.59) was used for these results, the derived value of V_H was 1.8×10^{-6} m^3/mol [9.645]. The evaluations of V_H are gathered in Table 9.41; they show good agreement and suggest that V_H has little dependence on which zirconium alloy is used, on the hydrogen concentration, on temperature in the range 533 to 773 K (260 to 500°C) or on which isotope is present.

TABLE 9.41. EVALUATION OF PARTIAL MOLAR VOLUME, V_H, OF HYDROGEN IN ZIRCONIUM ALLOYS

Material	Method	Isotope	Hydrogen concentration (ppm)	Temperature (°C)	V_H ($\times 10^{-6}$ m^3/mol)	Source
Pure Zr	Lattice parameter; neutron diffraction	D	7.4–597	454–504	1.67	[9.640]
Zr-2.5Nb	Stress gradient; constant temperature	H	13–56	300–308	1.7	[9.698]
Zircaloy-4	Stress gradient; temperature cycling	H	212–349	260–371	1.8	[9.645]
Zircaloy-2	Lattice parameter; X ray diffraction	H	17–200	450	1.68	[9.570]

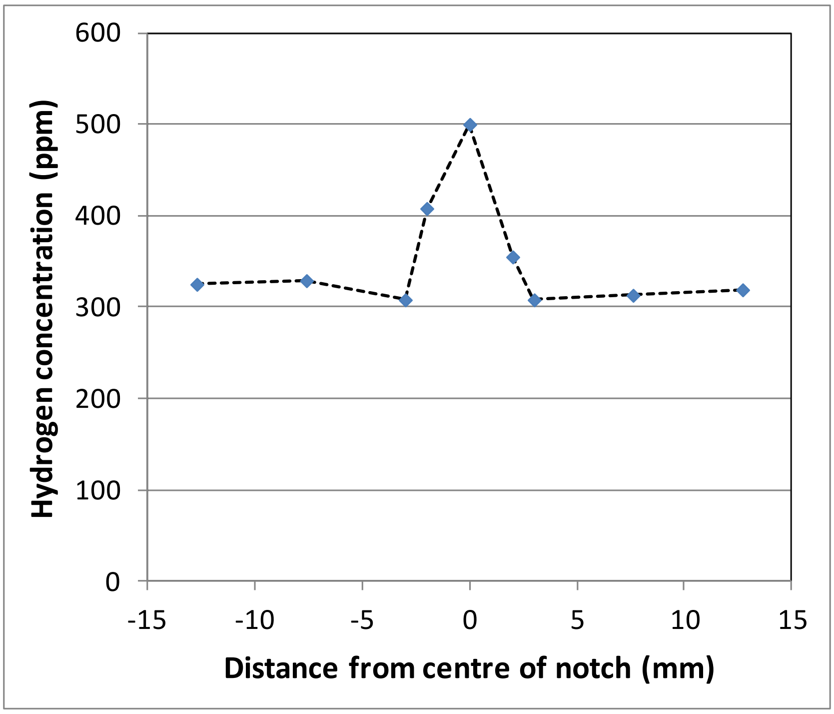

FIG. 9.252. Hydrogen transferred to notched region of Zircaloy-4 tension specimen containing initial concentration of 320 ppm (2.84 at.%) hydrogen. Nominal stress at notch (position 0 mm) was 240 MPa, declining to 48 MPa at ±2.54 mm from the centre of the notch. Temperature cycled 25 times up to 644 K (371°C) and held for 2 days during each cycle [9.645].

The steady increase in hydrogen concentration with number of cycles, as shown in Fig. 9.253, is an example of a ratcheting effect. A similar effect was postulated for a notched specimen by using a temperature cycle with a long hold at temperature, T_H, that was lower than the peak temperature, T_m, imposed for a short time; a load and therefore Eq. (9.59) were applied throughout the cycle [9.699]. If the hydrogen concentration was large enough for hydrides to be present throughout the cycle, the ratcheting effect was caused by C_0, and therefore C_σ, on heating to T_H being smaller than C_0, and therefore C_σ, on cooling to T_H from T_m because of the difference between TSSD and TSSP. On cooling to T_H, and on subsequent cycles, hydrogen was pumped into the high stress region and the hydrogen concentration continued to increase. The size of the effect depended on the hydrogen concentration, time at T_m and T_H, the rate of temperature change and the amplification of the stress at the root of the notch. For example, consider a specimen of zirconium alloy containing a notch that provides an amplification of the hydrostatic stress of 1.7 loaded to a uniaxial stress of 100 MPa. Impose one of two thermal cycles:

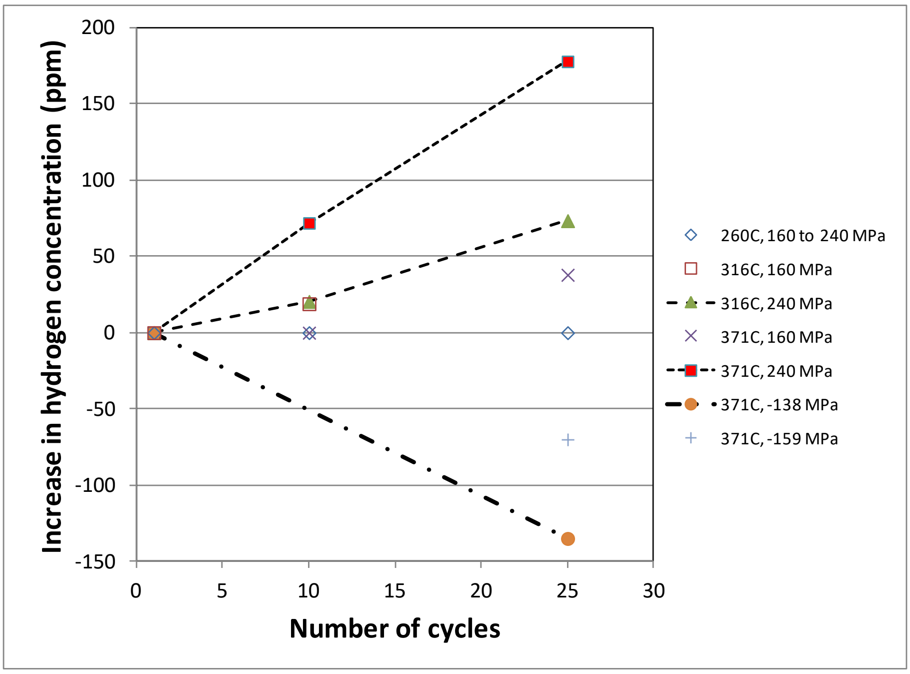

FIG. 9.253. Increase (or decrease) in hydrogen concentration during thermal cycles of notched plate specimens of Zircaloy-4 showing the effect of the number of thermal cycles between about 323 K (50°C) and 533 to 644 K (260 to 371°C) under tensile or compressive stresses. The specimen compressed 159 MPa buckled during the test [9.645].

(a) Room temperature to 513 K (240°C), $T_{m/H}$, hold and return to room temperature;
(b) Room temperature to 573 K (300°C), T_m, hold long enough that diffusion can establish any hydrogen concentration gradients that were developed, cool to 523 K (250°C), T_H, hold and return to room temperature.

Only the hydrogen in solution is available for diffusion and Eqs (9.48) and (9.50) govern how much is in solution at temperature. If the material contains 70 ppm (0.63 at.%) hydrogen, with Cycle (a) hydrides will be present and the maximum concentration of hydrogen in solution is 25.1 ppm (0.23 at.%) at $T_{m/H}$. At the notch the stress amplification raises the concentration in solution to 26.9 ppm (0.24 at.%) and potentially adds 1.8 ppm (0.01at.%) to the concentration of hydrides already present. With Cycle (b), 58.6 ppm (0.53 at.%) hydrogen will be in solution at T_m. At the notch this concentration is augmented to 62.3 ppm (0.57 at.%), which on cooling to T_H potentially adds 37.2 ppm (0.34 at.%) to the concentration of hydrides already present. An example of the collection of hydrogen, and therefore hydrides, is shown in Fig. 9.254 for 1 and 22 thermal cycles [9.700]. (The orientation of the hydrides will be discussed in Section 9.7.3 and the cracking will be described in Section 9.7.4.) The quantification of the effect on irradiated and unirradiated materials, using either local area of hydride, maximum hydride width or hydride length to characterize the microstructure, indicated that most of the accumulation of hydride at a notch tip was achieved in the first few cycles [9.701]. Contributions to this limit are the restricted volume containing amplified stress — as characterized by the nominal stress intensity factor, K_I;–stress relaxation from the formation of the hydrides themselves [9.702]; and creep of the zirconium alloy matrix [9.703]. Hydride length correlates with K_I [9.700, 9.701, 9.703, 9.704] as shown in Fig. 9.255, indicating an important source of the restrictions on hydride growth as well as a threshold K_I for the accumulation and formation of hydrides, and suggests little effect of neutron irradiation on the accumulation of hydrogen at a notch.

9.7.2.3. Effect of temperature gradient on hydrogen diffusion

In a sample of zirconium containing hydrogen in solution at equilibrium with no temperature gradient, the hydrogen atoms jump at close to the same rate in all directions and the concentration of hydrogen remains constant throughout the piece. In a hot sample of zirconium the jump frequency of

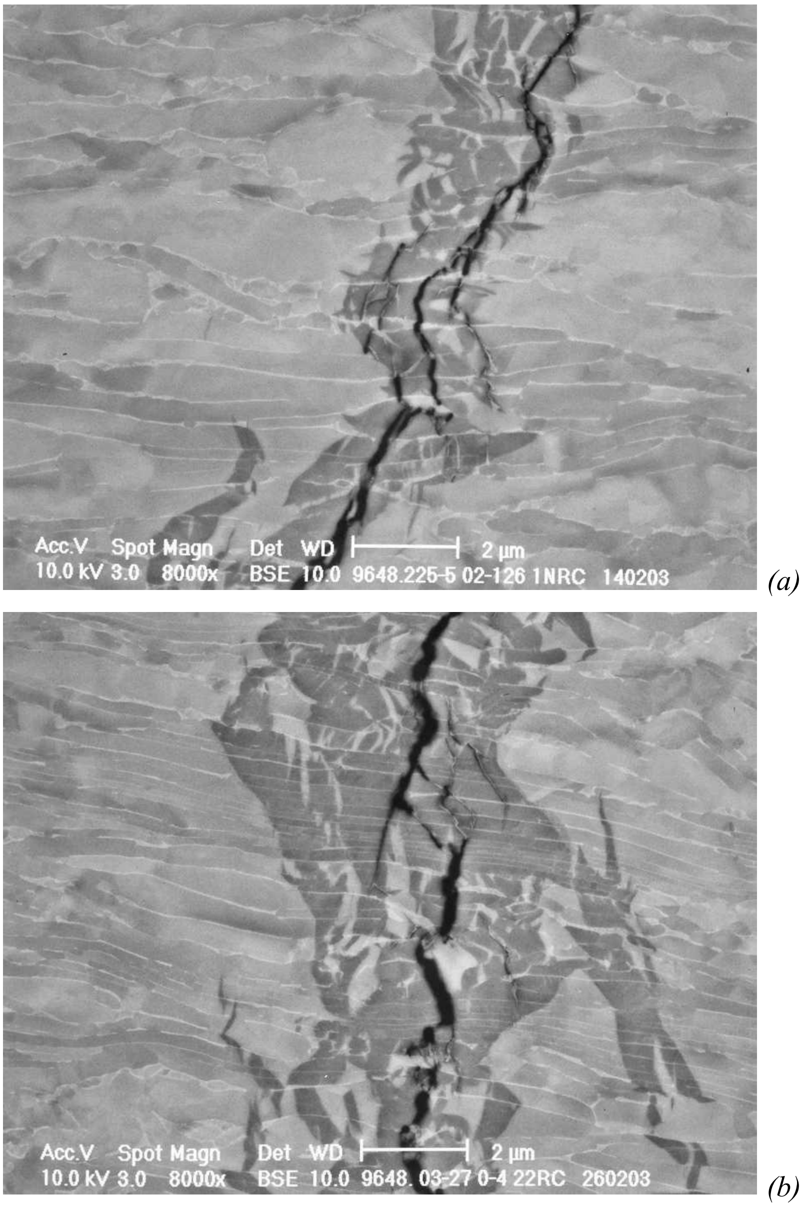

FIG. 9.254. SEM micrographs showing cracked notch tip hydride in samples containing 34 ppm (0.20 at.%) hydrogen formed at a nominal KI of 12 MPa√m after (a) 1 cooldown cycle and (b) an additional 21 ratcheting cycles, showing an increase in hydride thickness as a result of ratcheting thermal cycles; a cycle consisted of heating from 333 K (60°C) to 513 K (240°C), holding for one hour, cooling to 458 K (185°C), holding for three hours, then cooling to 333 K (60°C) [9.700].

hydrogen atoms is greater than in a cold sample. If two such pieces were joined and taken to equilibrium, the number of atoms jumping from the cold region to the hot region per unit time must be equal to the number of atoms jumping from the hot region to the cold region. To satisfy this condition, an amount of energy, Q^*, is transferred between the regions and the concentration of hydrogen atoms must be higher in the cold region than in the hot region; a concentration gradient is set up. In one dimension, the diffusion flux of hydrogen under a temperature gradient in the x direction is described by:

$$J_x = -DC[(d\ln C/dx) + Q^*(dT/dx)/RT^2] \qquad (9.61)$$

where

C is the concentration of hydrogen at the point where the absolute temperature is T;

and Q^* is the heat of transport [9.705].

If all the hydrogen remains in solution, in time J_x is equal to 0, and equilibrium is reached, given by:

$$C = C_0 \exp(Q^*/RT) \tag{9.62}$$

where C_0 is a constant.

Equation (9.62) provides a method of evaluating Q^*.

Below the eutectoid temperature, if the hydrogen concentration can exceed TSSP at the low temperatures in a component subjected to a temperature gradient, the transient distribution of hydrogen has the form shown schematically in Fig. 9.256 [9.706]. A hydride layer forms at the cold end. Next is a metal matrix-plus-hydride region in which the hydrogen concentration increases until there is a discontinuity between the two phase region and a region described by Eq. (9.62). The highest hydrogen concentration in the latter region is the solubility limit for precipitation at the local temperature. Values of the solubility limit from such diagrams are in good agreement with those using other methods [9.588, 9.594]. With time the discontinuity moves towards the cold surface and the two phase region disappears. These hydrogen distributions have been analysed theoretically and verified experimentally [9.706–9.709]. Similar distributions are calculated for temperatures above the eutectoid temperature and these distributions have been evaluated for titanium [9.710]; they should be similar in zirconium.

The redistribution of dissolved hydrogen in a linear temperature gradient is used to evaluate Q^*. For example, with a temperature gradient of about 7°C/mm the difference in hydrogen concentration over the temperature range of 588 to 758 K (315 to 485°C) was 60 ppm (0.54 at.%) [9.706]. Values of Q^* are summarized in Table 9.42. Although there is scatter in the whole population, the most reliable numbers appear to be derived from experiments that approach equilibrium. The value of Q^* in Ref. [9.707] was probably affected by the narrow temperature range. The mean of Q^* for the α phase materials was 26.3±5.8 kJ/mol [9.588, 9.706, 9.707, 9.711]. The effect of the β-phase appears to be to lower Q^*; in Zr-2.5Nb the reduction is modest, down to 20.2±2.3 kJ/mol [9.629, 9.711, 9.712] but Q^* is halved in Excel [9.629]. The reasons for this behaviour are unknown. In Zircaloy and Zr-2.5Nb, no isotopic [9.706], directional [9.712] or stress [9.645, 9.712] effects have been discerned. The reason for the latter is illustrated in Fig. 9.257. The distributions of hydrogen at a notch with and without a stress of 310 MPa were similar, showing a large transfer of hydrogen from the gauge length [9.645]; at the notch the effect of a temperature gradient of 7.8°C/mm dominated a tensile stress gradient of 195 MPa/mm, which, in the absence of a temperature gradient, would have increased the hydrogen concentration into the notch region (Section 9.7.2.2).

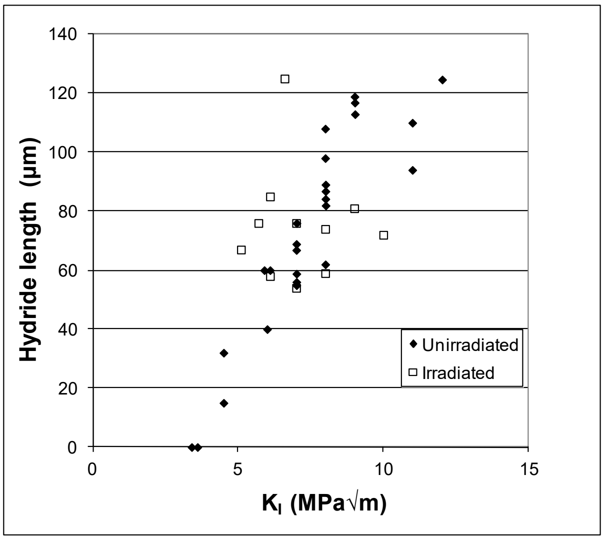

FIG. 9.255. Length of hydrides grown at notches after 10 to 200 temperature cycles in unirradiated and irradiated Zr 2.5Nb containing 40 to 60 ppm (0.36 to 0.54 at.%) hydrogen [9.700, 9.701, 9,703, 9.704].

TABLE 9.42. EVALUATION OF HEAT OF TRANSPORT OF HYDROGEN, Q^*, IN VARIOUS ZIRCONIUM ALLOYS

Material	Hydrogen concentration (ppm)	Temperature range (°C)	Temperature gradient (°C/mm)	Hold time (days)	Q^*	Source
Zircaloy-2 hydrogen	60	300–500	6.8	44	22.7	[9.706]
Zircaloy-2 deuterium	120	300–460	5.4	62	27.3	[9.706]
Zircaloy-2	300	295–450	7.3	30	14.3	[9.707]
Pure zirconium	60	300–500	8	46	24.8	[9.711]
Zr-2.6Nb	68	302–497	7.8	41	23.5	[9.711]
Zr-2.5Nb	28–108	240–500	13–15	10–30	19.3	[9.709]
Zr-2.5Nb	26–29	250–300	1.25	75	21	[9.629]
Excel	29–30	250–300	1.25	75	11	[9.629]
Zircaloy-4	36–332	260–650	6.6–8.7	30–200	28.5	[9.588]

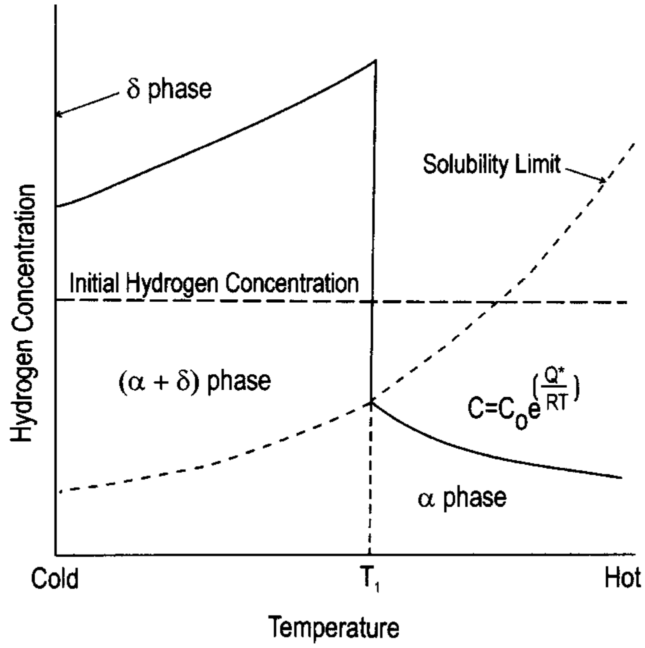

FIG. 9.256. Schematic diagram of transient distribution of hydrogen in zirconium containing a temperature gradient [9.706].

Temperature gradients may be set up in the structural components in nuclear plants, but they are usually small enough that their effects on hydrogen transport, though detectable, are benign. For example, pressure tubes made from Zircaloy-2 in the N-reactor at Hanford and Zr-2.5Nb in the RBMK design, contain through-wall temperature gradients of about 8 to 10°C/mm. The hydrogen tends to collect at the inside surface, which is cooler than the outside surface. In the N-reactor [9.713], where the pressure tubes were horizontal, the top of the tube tended to be about 17°C cooler than the bottom of the tube. A combination of the two temperature gradients led to measurable gradients in hydrogen concentration through the wall of the tube. At the top of one tube, the inner 20% of the tube contained over 500 ppm (4.36 at.%) hydrogen while the outer 60% had a hydrogen concentration of about 50 ppm (0.45 at.%); at the bottom of the tube the gradient was much smaller, with hydrogen concentration being about 80 ppm (0.72 at.%) in the inner 20% and about 30 ppm (0.27 at.%) in the outer 60% of the tube wall.

One harmful situation results when a hot surface makes local contact with a cold surface and a very steep temperature gradient develops at the point of contact; for example, in CANDU when a hot pressure tube, nominally at about 573 K (300°C), touches its calandria tube, at about 343 K (70°C). The temperature distribution in the pressure tube was characterized by Ref. [9.714]:

$$T\,(\mathrm{K}) = \text{constant (1)} + \text{constant (2)}\cdot\ln t \tag{9.63}$$

where t is the distance from the point of contact in mm.

Typical values of constant (1) and constant (2) were 552 and 13.4, leading to a very steep conical temperature gradient near the cold side of the component. With sufficient hydrogen present, the sequence illustrated in Fig. 9.256 followed: hydrogen diffused down the temperature gradient, hydride precipitation was highly localized and approximately circular blisters formed at the cold point, as shown in Figs 9.258(a) and (b) [9.715, 9.716]. The circular blisters consisted of hydride with the cross-section of an ellipsoid at the point of contact. The outer layer gradually gave way to a region of mixed α phase and δ phase and rays of hydride precipitating parallel with the radii of the blister and, if on a tube, in the radial direction of the tube in the metal matrix.

The concentration of deuterium in blisters grown in-reactor and in the laboratory was measured using the D(^{3}He,p)α nuclear reaction [9.717]. The value peaked at a D/Zr of about 1.41 (30 000 ppm (58.5 at.%)), as shown in Fig. 9.259, a little lower than expected for pure δ-hydride. One contribution to the shortfall of this expectation was the residual hydrogen in the zirconium alloy. Another was incomplete conversion of the zirconium to δ-hydride. Blisters grown in the laboratory on Zr-2.5Nb were examined by synchrotron X rays [9.718], and the results suggested that the volume fraction of δ-hydride was about 80%, with the remaining 20% being α-Zr.

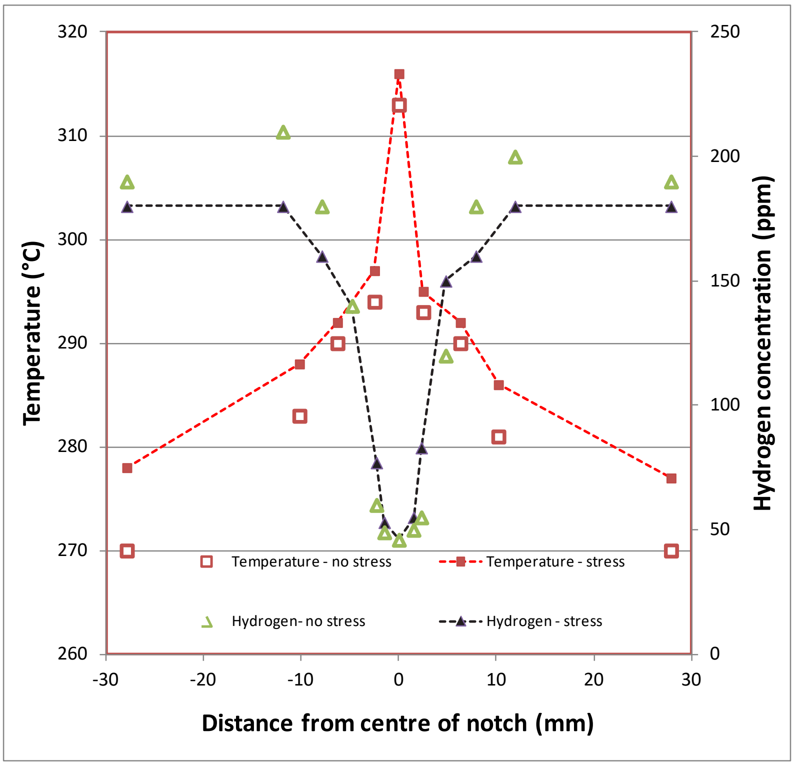

FIG. 9.257. Distribution of hydrogen in temperature gradient in a notched specimen; stress gradient of 195 MPa/mm does not counteract the effect of the temperature gradient (based on [9.645]).

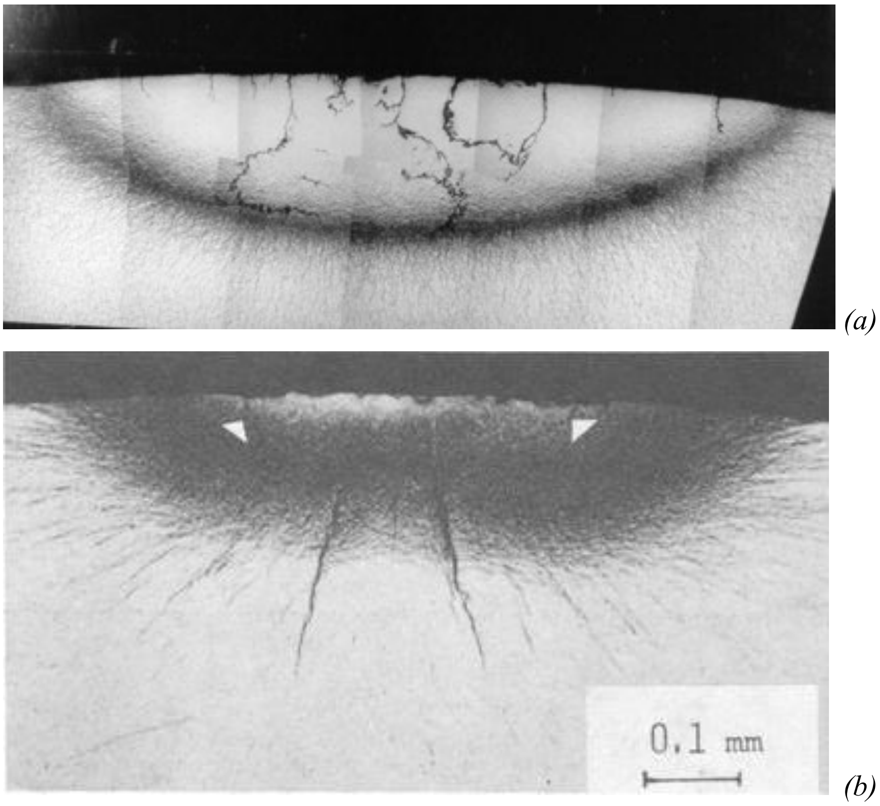

FIG. 9.258. (a) Composite micrograph showing a transverse section through the hydride blister found on the outside surface of the Zircaloy-2 pressure tube removed from fuel channel Pickering Unit 2, lattice position G16. The section was close to the centre of the blister [9.716]; (b) hydride blister grown in the laboratory on the outside of a Zr-2.5Nb pressure tube. Note the surface roughening from contact at the cold spot, between the white arrows [9.715].

Hydride blisters that formed on pressure tubes in-reactor varied in size with depth, b, ranging from 0.5 to 1.3 mm and radius, r_b, ranging from 1 to 4 mm; b/r_b varied around 0.35. In laboratory experiments, blisters were developed by heating a section of zirconium alloy pressure tube containing extra hydrogen and imposing a steep temperature gradient by contact with a cold finger [9.719–9.722], a jet of cold air [9.715] or deliberate hot and cold contact in a pressurized loop [9.712]. The area of contact was smaller than in-reactor and b/r_b was about 0.77.

The critical hydrogen concentration for blister formation, C_B (also called the blister formation threshold), depends on the temperature of the hot region, T_h, the temperature at the point of contact, T_c, and the solubility limit for precipitation, C_P, at T_c [9.714, 9.723]:

$$C_B = C_P \exp[-Q^*/R(1/T_c - 1/T_h)] \tag{9.64}$$

The blister formation threshold (C_B) and maximum blister size for three different hydrogen concentrations are shown schematically in Fig. 9.260 [9.724]. With a T_c of 493 K (220°C) and T_h of 568 K (295°C), C_B is 23 ppm (0.21 at.%) for Zr-2.5Nb. The blister size is limited by the size of the region over which the temperature is reduced and the nominal hydrogen concentration:

- The rate of growth of a blister increases with the steepness of the temperature gradient [9.714]. An example is shown in Fig. 9.261 where the gradient was controlled and increased by increasing the rate of flow in an air jet impinging the zirconium alloy surface [9.717].
- Owing to the volume expansion on converting the Zr to hydride, the blister protrudes from the surface; the profile height, h_b, above the initial surface position was proportional to the blister depth, b, with b/h_b being between 8 and 12. The profile height was described by finite element analysis of blister growth [9.725, 9.726].

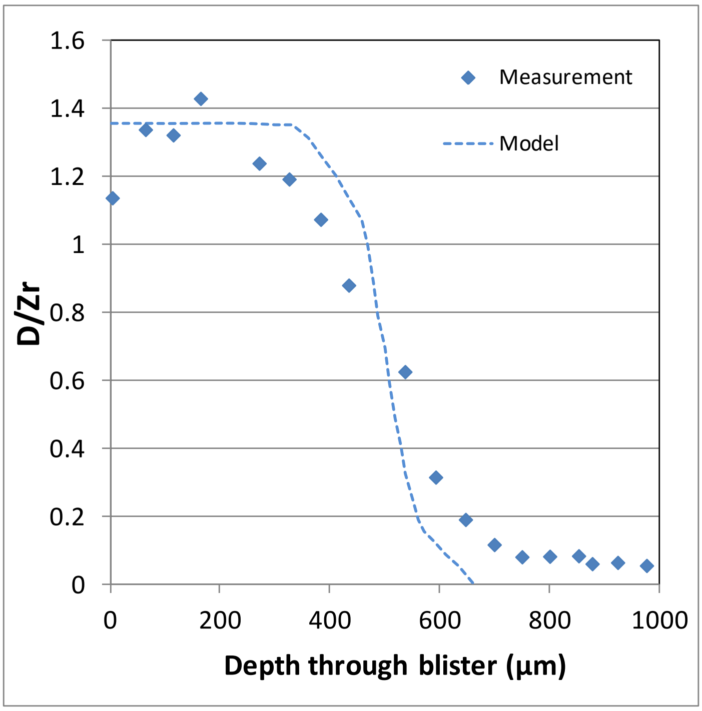

FIG. 9.259. Distribution of deuterium in a blister from the point of contact (based on [9.717]; model calculation from [9.723]).

- A similar approach was used to evaluate stresses built up within and without the blister because of this expansion [9.725, 9.727]. The analyses indicated that much of a blister is in compression, as shown in Fig. 9.262(a), (b) and (c); the examples are for 75% and 100% of the zirconium transformed to hydride. The stresses diminish as the blister matures and a tensile stress may develop close to the tube surface. At the blister–metal matrix interface, depending on the direction and position of examination, the compressive stresses may increase, then gradually diminish, as shown in Fig. 9.262(b), or become tensile in the metal matrix, as shown in Figs 9.262(a) and (c). In blisters formed on Zr-2.5Nb tubing in the laboratory, axial compressive stresses were found in the surface layers by X ray diffraction measurements [9.728]. These stresses reached maximum values of −450 MPa at the blister–matrix interface, as implied by the calculations. The same measurements indicated only tensile stresses in the hoop direction, up to 320 MPa at the interface; tensile hoop stresses of about 130 MPa at the surface, as shown in Fig. 9.262(a), and up to about 150 MPa close to the interface in the metal matrix, as shown in Fig. 9.262(c), were indicated by the calculations but the hoop stress in the main body of the blister was calculated to be compressive.
- The strength of a blister (as measured by hardness) is isotropic and similar to that of Zr-2.5Nb, as shown in Fig. 9.263 [9.715]. Outside the boundaries of the blister, the anisotropy of the Zr-2.5Nb tube dominates with high hardness in the circumferential direction (radial-axial plane), because the <0001> are concentrated in this direction, and corresponding low matrix hardness in the axial direction (radial-circumferential plane), where few <0001> are present.

Calculating and modelling the growth of blisters in finite element or finite difference codes for reactor applications required a three dimensional analysis of heat transfer at the point of contact to determine the temperature distribution and for the application of solubility limit equations, diffusion equations in the form of Eq. (9.48) and thermal diffusivity equations in the form of Eq. (9.61), both in three dimensions. The results of the models described the movement of the blister boundary and provided satisfactory agreement with the results of the laboratory experiments in which the temperature distribution was controlled [9.720, 9.723, 9.729, 9.730]. For example, Fig. 9.259 illustrates the

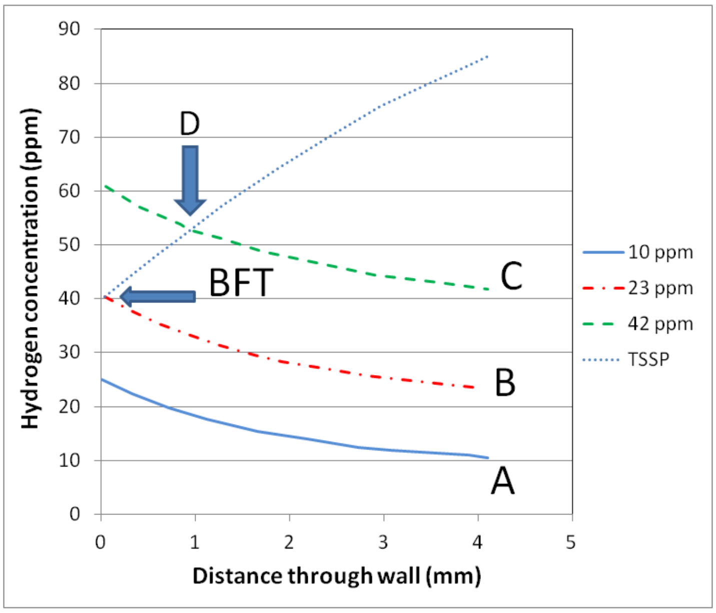

FIG. 9.260. Schematic diagram illustrating the blister formation threshold in a tube with a temperature gradient through the wall and lowest temperature at 0 mm (based on [9.724]). Curves A, B and C show the equilibrium distributions of hydrogen in solution in the temperature field for increasing average concentrations of hydrogen, following Eq. (9.62). Curve A illustrates a case in which no blister will grow because at the coldest location the concentration in solution does not exceed TSSP. Curve B shows a case in which the concentration at the cold spot equals the TSSP. This condition defines the blister formation threshold, which is the concentration in the bulk of the tube (in this case at the 4 mm point) that produces this condition. Curve C shows a case in which the blister formation threshold is exceeded. In this case, the equilibrium can be achieved only when a blister has grown to a depth of point D, which is the intersection of the equilibrium concentration distribution with the TSSP curve. This point defines the maximum blister size.

agreement between calculation and experiment for the distribution of hydrogen isotope concentration in a blister and its surroundings [9.723].

In nuclear fuel with a high heat flux, the temperature gradients through the cladding wall can be large. Consequently, hydrogen will tend to migrate to the outer, cooler surfaces. The concentration difference between the hot inside surface and the cold outside surface, ΔC, is approximated by Eq. (9.65) [9.731]:

$$\Delta C = \bar{C} Q^{*} t (dT/dt)/R\bar{T}^{2} \tag{9.65}$$

where $\bar{C}$ is the mean concentration of hydrogen across the cladding of thickness t and $\bar{T}$ is the mean temperature across the wall.

If the initial hydrogen concentration is at the ASTM limit of the specification, 25 ppm (0.23 at.%), ΔC will be 6.4 ppm (0.06 at.%) and the concentration at the outside surface will be 31.4 ppm (0.29 at.%). As hydrogen is absorbed from corrosion, when the hydrogen concentration exceeds the solubility limit, hydrides will form as a layer or rim on the outside surface of thickness, t_H, approximated by Eq. (9.66) [9.731]:

$$t_H = t(\bar{C} - \bar{C}_s)\rho_{Zr}/\rho_{\delta}\, C_{\delta} \tag{9.66}$$

where

$\bar{C}_s$ is the mean concentration of hydrogen when it is all in solution;
ρ_{Zr} is the density of the zirconium alloy;
ρ_{δ} is the density of the hydride phase;

and C_{δ} is the concentration of hydrogen in the hydride rim, 60 at.% (16 178 ppm) if it is all δ-hydride.

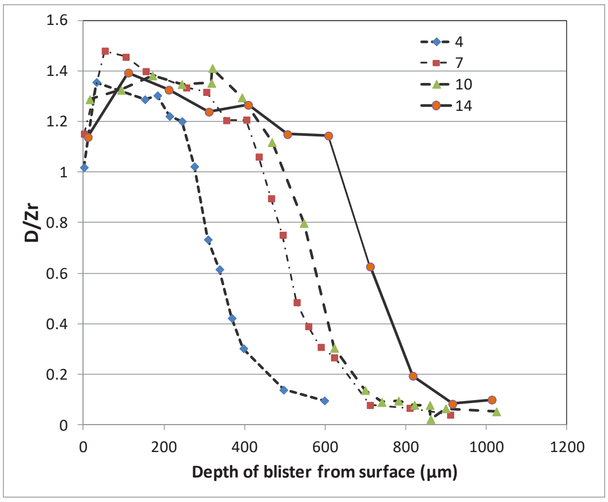

FIG. 9.261. Composition profile in the centre of blisters on Zr-2.5Nb formed in 42 days in the laboratory, using air jets with flow rates of 4, 7, 10, and 14 litres/min, providing different cooling rates (based on [9.717]).

For example, assuming a thermal conductivity of 15.7 W/mK for Zircaloy [9.732] in a PWR, a temperature gradient, dT/dt, of about 40 °C/mm will be established in the cladding of fuel with a power rating of 17.7 kW/m and outside surface temperature of 603 K (330°C), based on a diameter of 9 mm and wall thickness, t, of 0.59 mm [9.733]. From measurements after a burnup of 48 MWd/kg, with an average concentration of hydrogen of 250 ppm (2.23 at.%) the outer surface consisted of a layer of hydride containing 2600 ppm (19.2 at.%) hydrogen. This layer was 20 µm thick, as expected from Eq. (9.66). Note that this layer is not solid δ-phase but a somewhat diffuse mixture of hydride and zirconium alloy. A similar layer was observed on low tin Zircaloy-4 irradiated to a peak pellet burnup of 71 MWd/kg with a final power rating of 30 kW/m [9.734]. The temperature gradient for the period was about 68°C/mm. The average hydrogen concentration was measured to be 700 ppm (6.0 at.%) and the hydride layer was about 100 µm thick, as shown in Fig. 9.264; from Eq. (9.66) the hydride layer would be expected to contain 3500 ppm (24.3 at.%) hydrogen. Similar hydride layers, as shown in Fig. 9.265, have been observed in BWR fuel after a maximum burnup of 55 MWd/kg [9.735]. The local hydrogen concentration was 1600 ppm (12.8 at.%). The hydride layer was 100 µm thick but the calculated thickness was 74 µm, either implying that C_δ was close to being completely δ-phase or that extra hydrogen was being picked up from corrosion of the hydride rather than the metal [9.736, 9.737]. Other factors affecting this model are the change in thermal conductivity as the oxide thickens — the effect may be to increase the temperature gradient — and during service the power rating and therefore temperature gradient will vary. In the remainder of the cladding wall thickness away from the hydride rim, the hydrogen concentration declines and close to the inside surface few hydrides are observed.

9.7.2.4. Effect of concentration gradient in alloying elements on hydrogen diffusion

If the component contains a concentration gradient of immobile alloying element A in the x direction and the chemical potential of hydrogen, μ_H, varies with the concentration C_A of A, then the hydrogen will flow from a region of high chemical potential to one of low chemical potential. As with the other gradients, a hydrogen concentration gradient will arise. The flux of hydrogen is given by:

$$J_x = -D\,[dC/dx + CK_A dC_A/dx] \qquad (9.67)$$

where

K_A is $\partial\mu_H/\partial C_A$.

When dC_A/dx and the difference in μ_H between regions of different A are large, hydrogen will diffuse in the concentration gradient of A and hydrides may accumulate. An early example of this effect

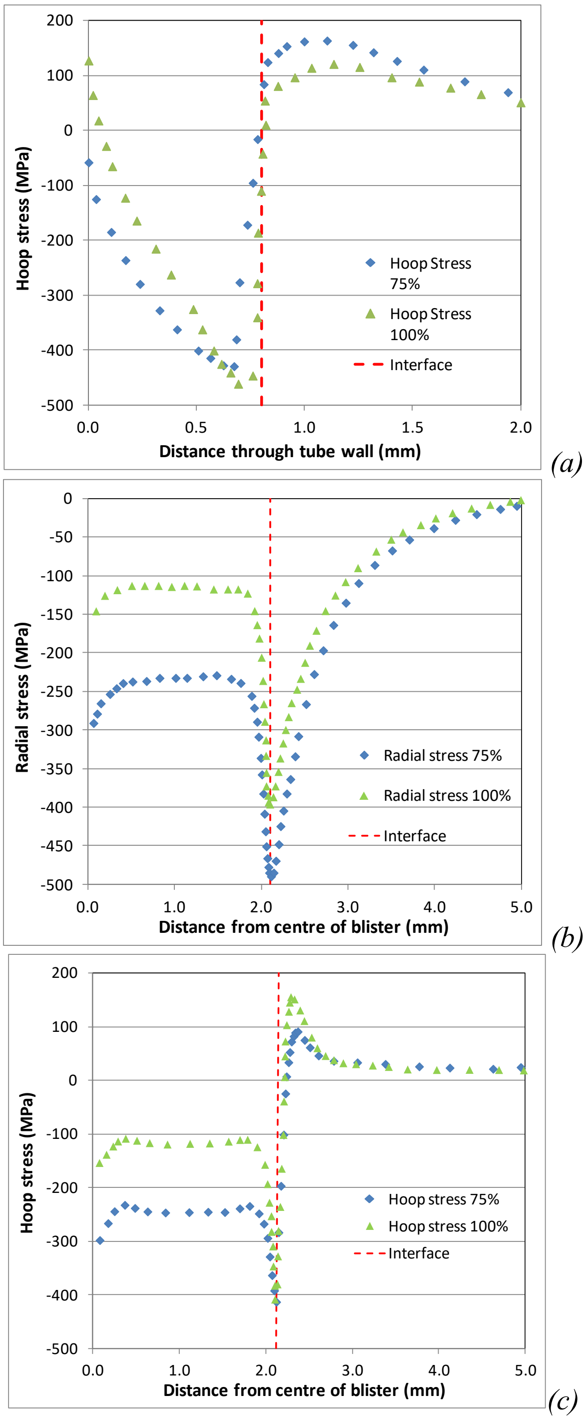

FIG. 9.262. (a) Calculated hoop stress in a hydride blister through the tube wall from the point of contact, 0.0 mm, showing compressive stress in the blister, 0.0 to 0.8 mm, and tensile stress close to the interface between the blister and the Zr-2.5Nb interface, 0.8 mm. The examples are for 75% and 100% of the zirconium transformed to hydride (based on [9.726]); (b) calculated radial stress in a hydride blister close to the outer surface plotted from the point of contact, 0.0 mm, parallel with the surface, showing compressive stress in the blister, 0.0 to 2.1 mm, and steep gradient in compressive stress close to the interface between the blister and the Zr-2.5Nb interface, 2.1 mm. The examples are for 75% and 100% of the zirconium transformed to hydride (based on [9.726]); (c) calculated hoop stress in a hydride blister close to the outer surface plotted from the point of contact, 0.0 mm, parallel with the surface, showing compressive stress in the blister, 0.0 to 2.1 mm, and steep gradient in compressive stress close to the interface between the blister and the Zr-2.5Nb interface, 2.1 mm, leading to a tensile stress in the metal matrix. The examples are for 75% and 100% of the zirconium transformed to hydride (based on [9.726]).

was a weld between two titanium alloys. When pure titanium was joined to an alloy containing aluminium (e.g. T-6Al-4V), hydrides formed on the pure titanium side of the interface because the chemical potential in the alloy was much larger than that in the pure metal [9.738, 9.739].

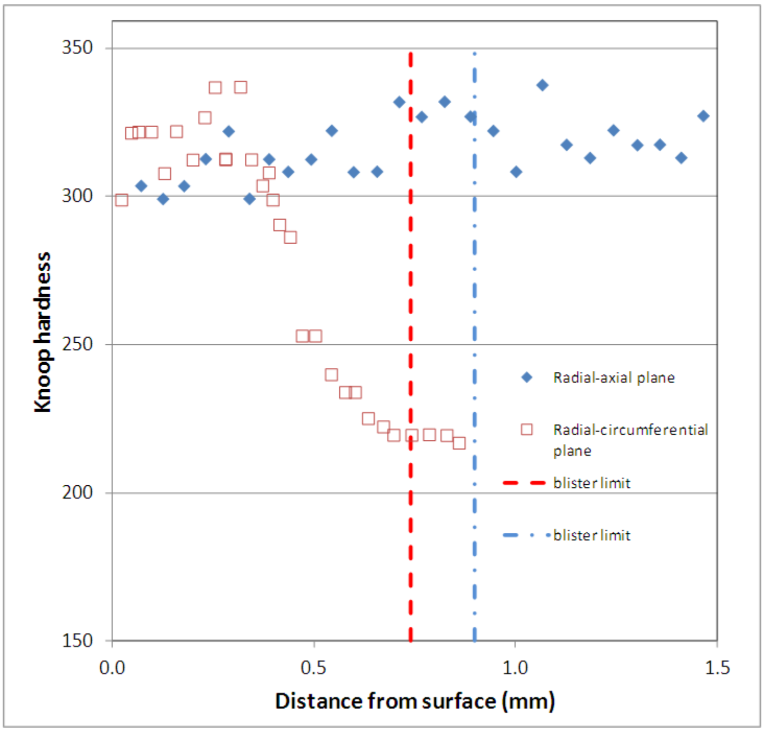

FIG. 9.263. Knoop hardness traces on hydride blister cross-sections in two directions (based on [9.715]).

The partitioning of hydrogen measured in diffusion couples between pure zirconium and the α alloys indicates a small difference in the chemical potential of hydrogen between the materials. The difference appears to reverse around the eutectoid temperature; below 823 K (550°C) the alloys contain a few percent more hydrogen while above 823 K (550°C) they contain a few percent less hydrogen than the pure metal [9.587]. In some designs of nuclear fuel cladding containing duplex and barrier layers, the differences in chemical potential between the two materials will contribute to the accumulation of hydrides at the interfaces. An example for barrier fuel cladding is the accumulation of hydrides in the zirconium on the inside of the cladding, as shown in Fig. 9.265 [9.735]. A similar phenomenon has been found in the outside surface layer of duplex cladding, as shown in Fig. 9.266 [9.740]. A zone denuded of hydrides was observed below the outside regions.

An extension of this phenomenon may be observed when two dissimilar metals are joined. When zirconium and hafnium are joined, the zirconium tends to getter the hydrogen from the hafnium. The chemical potential, μ_H, is related to the activity, a_H, through $\mu_H = \mu_0 + RT\ln a_H$. The activity of hydrogen in hafnium is about five times larger than in zirconium (based on measurements of equilibrium pressure, P [9.741] and taking $a_H = \sqrt{P}$). In a weld between hafnium and Zircaloy-4, with initial hydrogen concentrations of 10 ppm (0.09 at.%), after a period in a nuclear reactor, the hydrogen concentrations had changed to 2 ppm (0.018 at.%) in the hafnium and 42 ppm (0.38 at.%) in the Zircaloy-4 [9.742]. From the differences in activities, the expected values of hydrogen concentration were 3 ppm (0.027 at.%) in the hafnium and 23 ppm (0.21 at.%) in the Zircaloy-4. The extra 19 ppm (0.17 at.%) hydrogen in the Zircaloy-4 came from pick-up during corrosion. The reverse behaviour was observed when yttrium was welded to Zircaloy-2 [9.743, 9.744]; again, the hydrogen was diffusing under the influence of a gradient in chemical potential, but in this couple, it was the zirconium that had the higher potential. In the experiments, a piece of yttrium containing 670 ppm (5.63 at.%) hydrogen was welded to a piece of Zircaloy-2, containing 25 ppm (0.23 at.%) hydrogen that in turn was welded to a piece of Zircaloy-2 containing 320 ppm (2.84 at.%) hydrogen and the assembly was held at 673 K (400°C) for times up to 1566 h. At intervals the hydrogen concentration distribution was evaluated by neutron scattering. The hydrogen diffused from the Zircaloy-2 to the yttrium, despite its initial hydrogen concentration being higher than that of the Zircaloy-2. The results of the experiments are in good agreement with a diffusion model, as shown in Fig. 9.267.

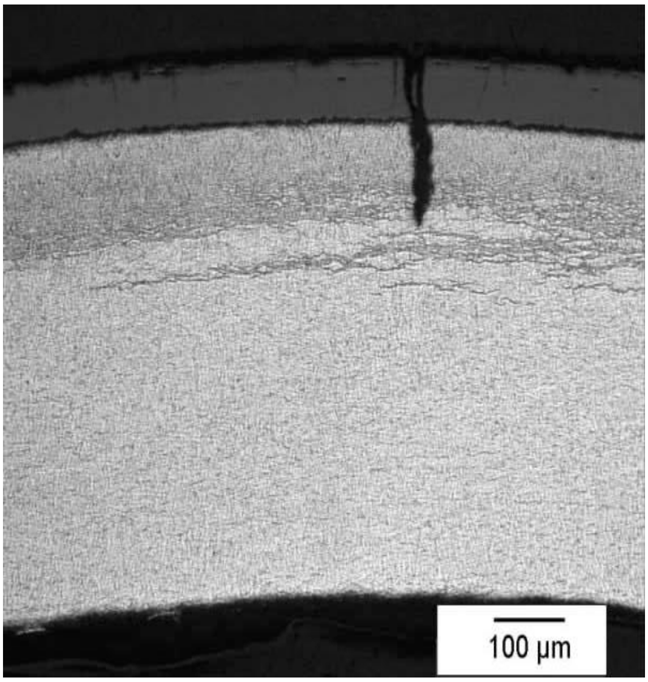

FIG. 9.264. Radial crack through external oxide and outer hydride layer in low-Sn Zircaloy-4 after a power ramp test from an average linear heat rating of 17.9 kW/m up to 30 kW/m following irradiation in a PWR to a burn-up of 52 MWd/kg [9.734].

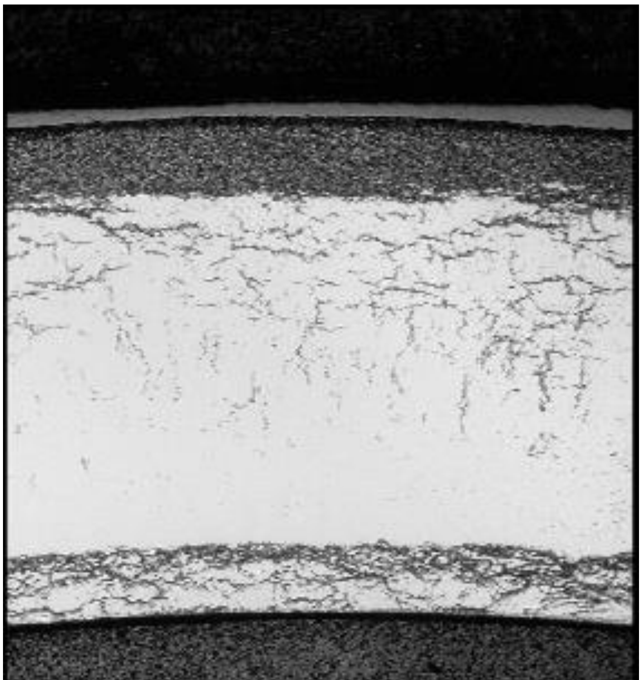

FIG. 9.265. Thick layer of hydride adjacent to the oxide layer on outside surface of Zircaloy-2 fuel cladding irradiated in a BWR up to a burn-up of 55 MWd/kg; the external hydride layer is caused by a large temperature gradient whereas the internal hydride layer is associated with the zirconium barrier layer. Cladding thickness: 0.7 mm [9.735].

9.7.2.5. Effect of combined gradients on hydrogen diffusion

The hydrogen diffusion in each of these gradients is due to a gradient in chemical potential — the hydrogen moves from high to low chemical potential. Each gradient may act independently and, ignoring second order effects, in the general case can be combined. The gradients also act in three

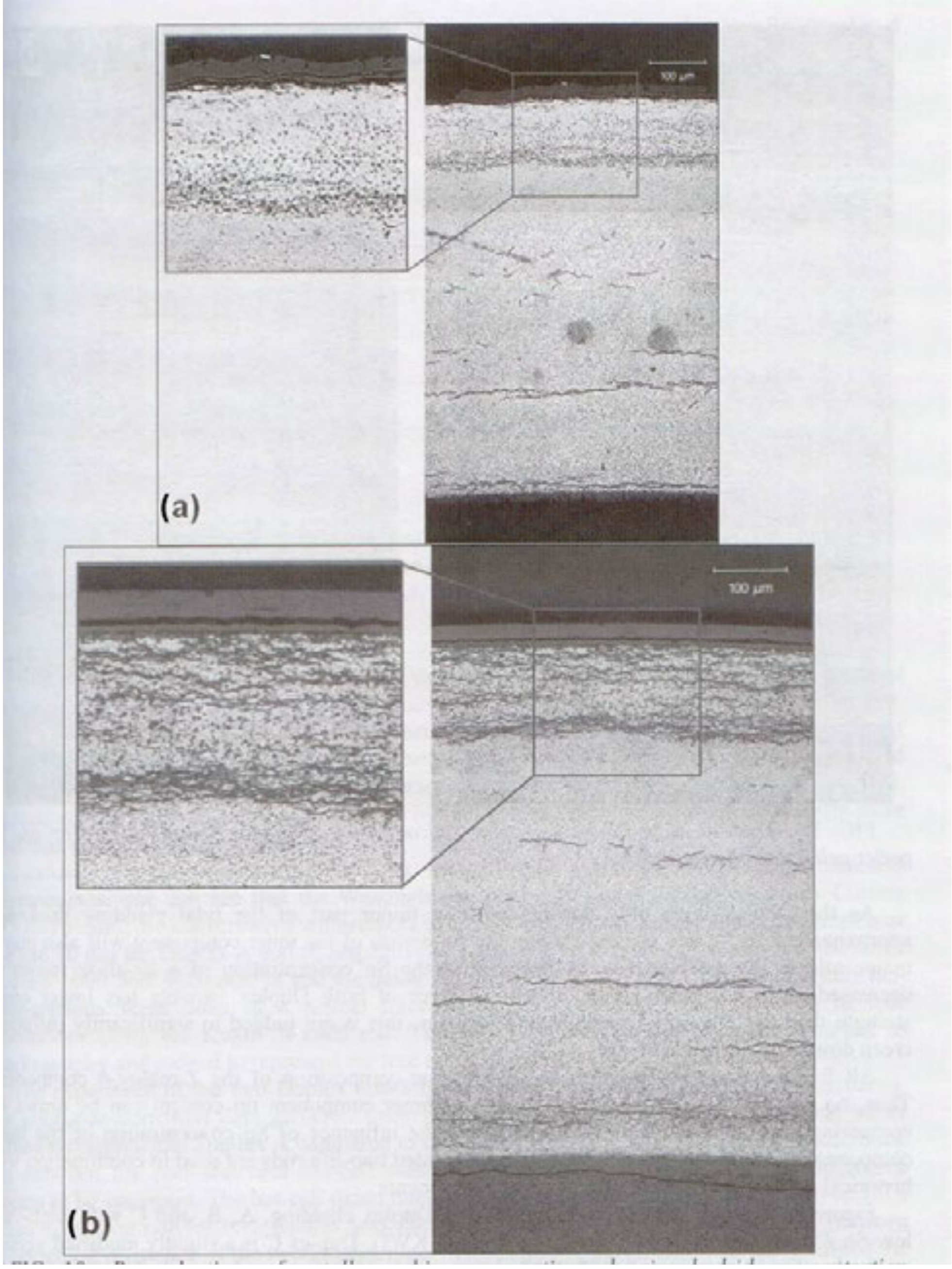

FIG. 9.266. Hydrides accumulated at the interface between Zircaloy-4 and duplex outer layers consisting of Zr-(0.5-0.8) Sn-(0.4 – 0.5)Fe after a fuel burn-up of 67 MWd/kg at different axial locations (a) and (b) of the cladding [9.740].

dimensions but most of the examples have been for one dimension to simplify the discussion and illustrate the principles. The flux of hydrogen in the x-direction is described by combining Eqs (9.60), (9.61) and (9.67):

$$J_x = -D[(dC/dx) + CQ^*(dT/dx)/RT^2 - CV_H(d\sigma_H/dx)/3RT + CK_A dA/dx] \qquad (9.68)$$

In summary, hydrogen can diffuse readily in zirconium alloys. Changes in concentration are driven by gradients in chemical potential; consequently hydrogen moves under gradients of hydrogen concentration, stress, temperature and alloying elements. As a result, hydrides may accumulate at the ends of the gradients when TSSP is exceeded.

9.7.3. Orientation of zirconium hydrides

In light microscopy (Section 4.13.6), hydrides appear as line traces representing clusters of needles or plates, as shown in Fig. 9.224. They are found both within the grains and at grain, twin and phase boundaries. If material is cooled from above the hydrogen solvus temperature, T_D, the size of the hydride precipitates depends on the cooling rate, being smaller as the cooling rate increases [9.503]. With slow cooling the apparent major dimension of the hydride can vary to over 200 µm while the thickness is usually less than 10 µm. Hydrogen cannot be retained in solution by quenching [9.529]. After quenching into water, the subsequent small precipitates can harden the material [9.745] and improve ductility. Any benefits of the quench and refinement of the precipitate size is quickly lost with ageing, even at room temperature. This precipitate refinement can be exploited when interpreting hydride microstructures developed above room temperature; water quenching from the temperature appropriate for the experiment provides confidence that the hydride microstructure observed at room temperature represents that present at the elevated temperature, except for the small background hydride precipitates. This technique is not practised universally; care has to be taken in interpreting at room temperature hydride microstructures formed at elevated temperature.

The orientation of hydrides is important if the hydrides crack and present an easy fracture path. Much variation of the orientation has been observed with some of the variation resulting from different experimental methods, and some resulting from fabrication and operational history, and residual stresses. An early example of the complicated orientations possible is shown in Fig. 9.268. Several quantitative definitions of hydride orientation exist. For tubes, hydride orientation is often quoted as the fraction of the number of hydrides with trace angle to a reference direction in a plane that is in the range x to 90°, where x is usually > 45°; values will range from 0.0 to 1.0. The quantity is called f_x [9.746] or F_n [9.118]. The equivalent quantity may be attained by measuring the area fraction [9.747]. In Zr-2.5Nb pressure tubes, where the hydrides are 5 to 10 times longer in the axial direction than in the radial direction, F_n was estimated from the fraction of the total length in each direction [9.576]. Sometimes hydride orientation is expressed as a hydride continuity coefficient (HCC), which is a measure of the fraction of a cross-section covered by hydride projected on to a plane [9.748]. Usually,

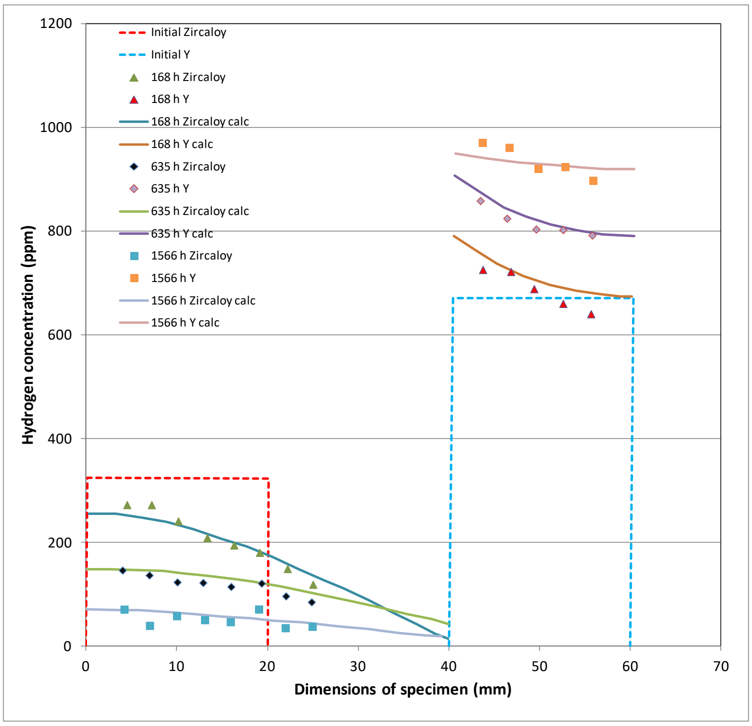

FIG. 9.267. Demonstration of yttrium gettering hydrogen from Zircaloy-2. Compound specimen of Zircaloy-2 sheet (2 mm thick) containing about 320 ppm (2.84 at.%) hydrogen, 0 to 20 mm, welded to Zircaloy-2 containing 25 ppm (0.23 at.%), 20 to 40 mm, welded to yttrium containing 670 ppm (5.63 at.%) hydrogen, 40 to 60 mm, annealed at 673 K (400°C) for various times. Experimental values (points) compared with calculated values (solid lines) (based on [9.744]).

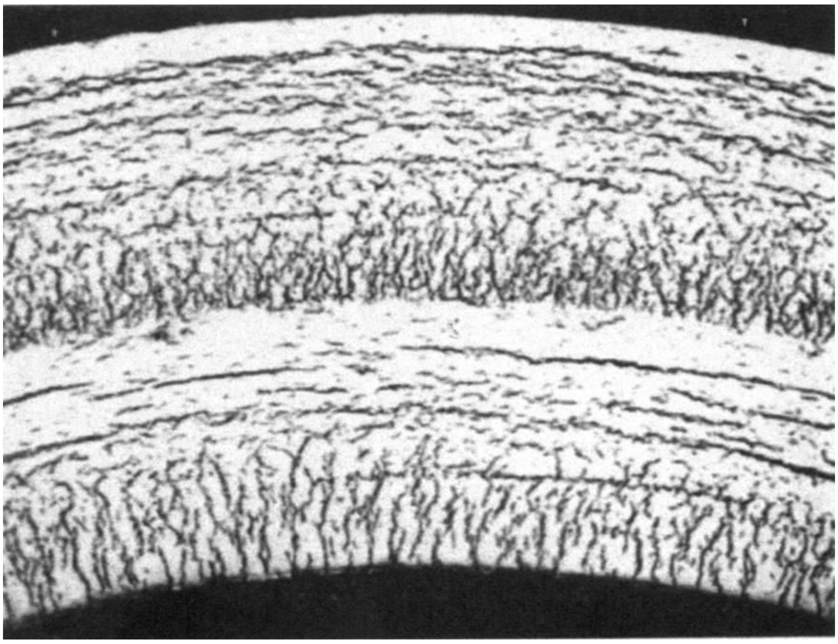

FIG. 9.268. *Distribution of hydrides in Zr-2.5Nb-0.5Cu wire. The material was quenched from 1098 K (825°C), tempered at 808 K (535°C) for 6 h, bent to 10% strain, heated to 673 K (400°C) and slowly cooled. Hydrogen concentration was 150 ppm (1.35 at.%). Wall thickness was 1.5 mm [9.575].*

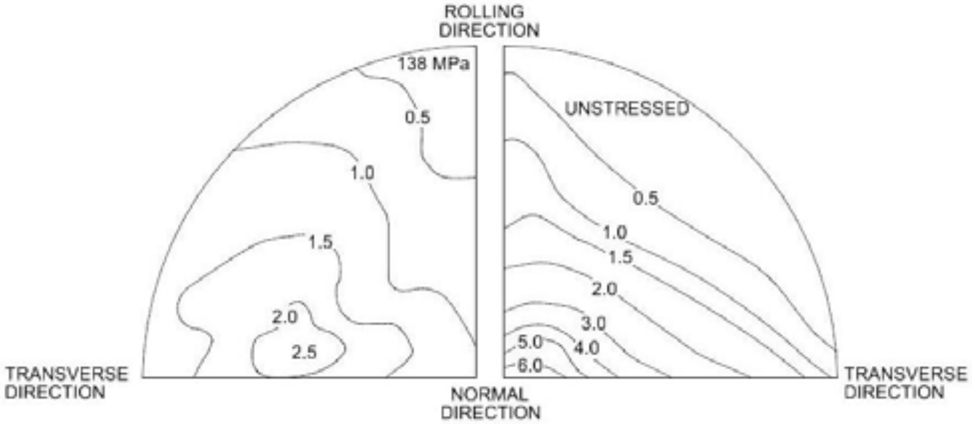

FIG. 2.269. *Pole figures of hydrides in Zircaloy-2 sheet showing shift in orientation with tensile stress in transverse direction. 1.0 represents a random distribution of orientation [9.750].*

HCC is determined over a discrete representative section of the microstructure; if hydride overlap is ignored, values will range from 0.0 to 1.0. If the hydrogen concentration is high and hydrides of different orientation interconnect, the hydride continuity factor (HCF) is the ratio L_R/h_m, where h_m is the wall thickness and L_R is the maximum length of continuous or connecting hydrides projected onto the potential crack path and within a 150 μm sampling width. The appeal of these methods is that the trace of the edge of the hydride is easily observed by light metallography. In tubes, hydride plates with their normal in the circumferential direction are called radial hydrides (their trace is in the radial direction on a transverse section) and F_n and HCC approach 1.0. Hydride plates with their normal in the radial direction are called circumferential hydrides (their trace is in the circumferential direction on a transverse section) and F_n and HCC approach zero. With HCF, if there is a connecting path of radial and circumferential hydrides across the entire wall, the HCF = 100%; since the most deleterious orientation is radial (R), HCF becomes RHCF [9.749].

Another method would be to consider the distribution of the normal to the hydride platelets and then construct pole figures [9.750, 9.751]. An example is shown in Fig. 9.269, for annealed Zircaloy-2 sheet material. In an as-received sheet or tube the concentration of normals to the hydride plates is the highest parallel to the normal to the sheet (or in a tube radial direction), marked ‘unstressed’. After imposing a tensile stress in the transverse (or hoop direction), the orientation of the hydrides shifts so the concentration of normals to the hydride plates approaches the stressing direction, marked ‘138 MPa’.

From the habit planes one might expect an effect of crystallographic texture on the distribution of hydrides in components. In some investigations on Zircaloy-4 nuclear fuel cladding, crystallographic texture seemed to be important [9.752] when the fraction of basal plane normals parallel with a reference direction was high, the fraction of hydrides with their normals parallel with the reference direction was also high, and vice versa. In other studies, especially in components that are cold worked, the hydrides precipitate with the normal to the plates parallel with the compressive direction of working, independent of the texture [9.746, 9.753–9.755]. When the fabrication of tubing involved diameter reduction (sinking), radial hydrides were observed but with mostly wall thinning (for example, in tube reduction) circumferential hydrides were produced. For this reason, all fuel cladding and pressure tubes are fabricated to a schedule based on a large amount of compressive strain in the radial direction in the final stages of processing. This approach is called strain orientation.

Caskey et al. [9.756] were the first to publish a report on a failure caused by radial hydrides in tubes. In their Zircaloy tubing the hydrides were usually circumferential but Louthan and Marshall [9.757] showed that when a tensile stress was applied during hydrogen absorption followed by cooling, the hydrides precipitated with their plate normal parallel with the stressing direction; with a compressive stress the hydride plate normals were perpendicular with the stressing direction. This process is called stress reorientation. In zirconium alloys, much effort has been expended to find the conditions for stress reorientation so they can be avoided [9.576, 9.577, 9.607, 9.746–9.778]. The experimental techniques are summarized for Zircaloy in Table 9.43 and for Zr-2.5Nb in Table 9.44. Several methods of adding hydrogen were used, including gaseous and corrosion methods, with concentrations in a very wide range up to 1000 ppm (8.4 at.%); material removed from power reactors after service has also been studied. Stresses have been applied by the following means:

- Bending a beam, to evaluate simultaneously tensile and compressive stresses [9.757, 9.759, 9.773];
- Applying uniaxial tension, sometimes with tapered specimens [9.576, 9.748, 9.750, 9.761, 9.764, 9.766, 9.768, 9.769];
- Internally pressurizing a tube, to simulate the stress conditions in practice [9.747, 9.751, 9.755, 9.760, 9.762, 9.763, 9.765, 9.767, 9.772, 9.773, 9.775];
- Using ring tensile specimens made from tubes, with supporting finite element analysis of the stress distribution [9.577, 9.768, 9.770, 9.774, 9.778];
- Using ring compression specimens made from tubes [9.776].

TABLE 9.43. HYDRIDE REORIENTATION EXPERIMENTS IN ZIRCALOY

Material	Hydrogen addition method	Hydrogen concentration (ppm)	Cooling temperature (°C)	Cooling rate (°C/min)	Number of cycles	Stressing method	Maximumm applied stress ((MPa)	Count method	F_{n0}	F_{nmax}	σ_{th} MPa	Comment	Source
Annealed Zircaloy-2, wire	Gas	100	325–800	“Slow”	1	Bending	4–19% strain			0.87		Directionality increased by strain and temperature	[9.753]
Zircaloy, strip	Corrosion; gas	20–200	400	1	1	Bending, uniaxial tension	172	Number fraction	0.15–0.4	0.9	38–110	Stressed during H addition	[9.757]
Zircaloy-2 plate, annealed	Gas	120–280	400	2	1	Uniaxial tension	138	Pole Figure	f_{ND} ~ 1	f_{TD} ~ 0.8	≈ 100	Strong texture effect	[9.750]
Zircaloy, various fabrications, plates and tubes	Gas or corrosion	150 (few < 100)	400	1.5	1–90	Uniaxial tension–plate internal pressure tube	138	Angle–reference direction	—	—	—	Hydride orientation and orientation depend on texture, grain size, cold work and temperature cycles	[9.752]
Zircaloy, various fabrications	Gas	50	300–350	0.6–2	1	Uniaxial tension, compression	220	Number fraction	0.02–0.54	0.9	—	Several fabrication routes	[9.758]
Zircaloy-2, cold worked stress relieved cladding	Corrosion	35–1000	300	0.2–1	1–30	Internal pressure	19.6	Qualitative				Radial hydrides increase with stress and number of cycles	[9.760]
Zircaloy-4	—	300	—	—	—	Internal pressure	135	Number fraction	0.09	0.63	90–110	No experimental details	[9.762]

TABLE 9.43. HYDRIDE REORIENTATION EXPERIMENTS IN ZIRCALOY (cont.)

Material	Hydrogen addition method	Hydrogen concentration (ppm)	Cooling temperature (°C)	Cooling rate (°C/min)	Number of cycles	Stressing method	Maximumm applied stress ((MPa)	Count method	F_{n0}	F_{nmax}	σ_{th} MPa	Comment	Source
Zircaloy-2, cladding annealed with liner	Gas	210–510	350	0.3	1	Internal pressure	150	Area fraction	0.12	0.3	<90	Many hydrides in liner-clad interface	[9.767]
Zircaloy-4 cold worked stress relieved, cladding	Gas	200	330–400	1–20	1	Internal pressure	160	Length fraction	0.1	0.45	70	Considers H in solution	[9.765]
Zircaloy-4 cold worked stress relieved, cladding	Gas	130–600	400	1	1–12	Internal pressure	160	Area fraction	≈0	0.95	<160	*F*n increase with number of cycles	[9.772] [9.773]
Zircaloy-4 cold worked stress relieved, cladding	Cathodic charging and annealing	220	200–400	4	1	Ring tensile	68% YS	Qualitative				Largest effect in cooling range 300–200 C, time dependent growth indicated	[9.768]
Zircaloy-4 cold worked stress relieved, cladding irradiated to 10^{26} n/m^2	Gas	900	400	10	1	Ring tensile	190	Location of radial hydrides	—	—	85	Stresses from finite element analysis	[9.770]
	Corrosion	850										Hydride layer on outside surface	[9.770]
Zircaloy-2 annealed; sheet	Cathodic charging and annealing	60–668	290, 355	1	1–10	Tapered tensile, various angles–rolling direction	160	Number fraction	0.02	0.18	80	*F*n increases with number of cycles and increase with number of [0001] in stress direction, *F*n increased by water quench	[9.771]

TABLE 9.43. HYDRIDE REORIENTATION EXPERIMENTS IN ZIRCALOY (cont.)

Material	Hydrogen addition method	Hydrogen concentration (ppm)	Cooling temperature (°C)	Cooling rate (°C/min)	Number of cycles	Stressing method	Maximumm applied stress ((MPa)	Count method	F_{n0}	F_{nmax}	σ_{th} MPa	Comment	Source
Zircaloy-2 annealed, cladding	Gas	250–750	400	0.5		Ring tensile; internal pressure on tapered tube specimen	170	Number fraction Hydride length	0.06	0.35	65 with 250 ppm 120 with 560 ppm	Stresses from finite element analysis	[9.774]
Zircaloy-2; BWR, 55 MWd/kg	Corrosion	>150	250–400	0.5–0.01	1	Internal pressure	100	Number fraction	0.15	0.9	<70	Many hydrides in liner-clad interface	[9.775]
Zircaloy-4; PWR, 48 MWd/kg			250–340				130	Length fraction	0.19	0.4	>100	Hydride layer on outside surface	[9.775]
MDA, PWR, 55 MWd/kg			250–340				130					Reorientation in order: ZIRLO>MDA> Zircaloy	[9.775]
ZIRLO, PWR, 55 MWd/kg			250–340				130						[9.775]
Zircaloy-4 cold worked stress relieved, cladding	Gas	100–500	342	0.4	1	Ring compression	230	Location of radial hydrides	≈0	1	65	Stresses from infinte element analysis	[9.776]
Zircaloy-2, LK3/L, BWR 66 MWD/kg	Corrosion	215–318	334–422	0.5	1–3	Ring tensile	100	Length fraction	0.1	0.3	50	Stresses from finite analysis, many hydrides in liner-clad interface, locally *F*n up to 0.9	[9.778]
Zircaloy-4, recrystallized	Gas	525	550	60	1	Tensile	100	Qualitative	≈0		75–85	Synchrotron X ray diffraction	[9.777]

TABLE 9.44. HYDRIDE REORIENTATION EXPERIMENTS IN Zr-2.5Nb (cont.)

Material	Hydrogen addition method	Hydrogen concentration (ppm)	Cooling temperature (°C)	Cooling rate (°C/min)	No. of cycles	Stressing method	Max. applied stress (MPa)	Count method	F_{n0}/ HCC angle	F_{nmax}/ HCC angle	σ_{th} MPa	Comment	Source
Pressure tube, cold worked flattened sections	Gas	10–200	300–400	2	1	Stepped uniaxial tensile	207	Length fraction	≈0	0.7	70	F_n based on hydride length, not number No reorientation in axial direction	[9.576]
Pressure tube, cold worked flattened sections	Corrosion	140–270	450	Furnace cool	1	Stepped uniaxial tensile	17–200	HCC	0.1	0.9	80–100	σ_{th} declines with temperature	[9.748]
Pressure tube, heat treated	Corrosion	130–300	300–360	?	3–4	Internal pressure	240	Pole Figure	$f_R \sim 1$	$f_T \sim 1$	<70	Banding from fabrication history	[9.751]
Pressure tube, cold worked flattened sections	Gas	50–300	250–400	2–3.3	1	Tapered uniaxial tensile	240	Number fraction	0	1	50	No orientation in axial direction Only H in solution available for reorientation	[9.761]
Pressure tube, cold worked	Gas	50–100	250–320	2	1–30	Tensile, internal pressure	480	HCC	0	0.9	95	No reorientation in axial direction	[9.763]
Pressure tube, cold worked, and Zircaloy, Excel	Gas	100	300	Furnace cool	10	Stepped rings, uniaxial tensile	400	Hydride angle to hoop direction	10°	90°	90	Required 7 h at 400°C to revert radial to circumferential hydrides	[9.577]

TABLE 9.44. HYDRIDE REORIENTATION EXPERIMENTS IN Zr-2.5Nb (cont.)

Material	Hydrogen addition method	Hydrogen concentration (ppm)	Cooling temperature (°C)	Cooling rate (°C/min)	No. of cycles	Stressing method	Max. applied stress (MPa)	Count method	F_{n0}/ HCC angle	F_{nmax}/ HCC angle	σ_{th} MPa	Comment	Source
Pressure tube, cold worked with various heat treatments, Zircaloy flattened sections	Electrolytic hydride layer	500	300	1.5	1	Tapered uniaxial tensile	500 400	Location of radial hydrides	—	—	110–150 Zircaloy 50	Correct for residual stress 190 to 230 MPa Correct for residual stress 70 to 90 MPa	[9.764]
Pressure tube, cold worked flattened sections	Gas	90–148	200–350	1	1	Tapered uniaxial tensile	306	Location of radial hydrides	≈0	1	315 at 200°C135 at 350°C	σ_{th} declines with temperature and yield strength Reported temperatures 50°C too low	[9.766]
Pressure tube, cold worked flattened sections	Gas	41–60	250–400	1	1	Tapered uniaxial tensile	216	Location of radial hydrides	≈0		235 at 250°C145 at 400°C	σ_{th} declines with temperature and yield strength Correct for residual stress 70 to 90 MPa	[9.769]

When evaluating stress reorientation in tubes, if sufficient material is available, testing by internal pressurization provides the clearest result since the stress conditions are immediately applicable to the use of the component, with little adjustment. Using ring tensile methods often requires complicated calculations to find the values of the imposed stresses because of frictional effects and bending. Residual stresses can contribute to the total stress. When tubing has to be flattened to make tensile specimens, care has to be taken to account for the large induced residual stresses from plastic bending. These internal stresses can lead to variation in hydride orientation through the thickness of the material [9.764, 9.769, 9.779].

Usually during tests, specimens were heated to between 523 and 673 K (250 and 400°C) to dissolve some of the hydrogen, held for a short period up to 24 h, then cooled under load at about 1°C/min (usual range 0.28 to 10°C/min). In some studies, the temperature was cycled several times — 10 cycles [9.577, 9.771], 12 cycles [9.772, 9.773], 30 cycles [9.760] and up to 90 cycles [9.752]. To minimize creep deformation, the size of applied stresses depended on the test materials, being higher for strong materials (e.g. 400 MPa in Zr-2.5Nb, or directly relevant to a practical situation, around 100 MPa in fuel cladding for evaluations of storage of spent fuel).

In tubes the important technical parameters are:

- The initial fraction of the number or length of radial hydrides, F_{n0}. In materials cold worked by wall thinning followed by a stress relief, F_{n0} is usually close to zero. In annealed materials, hydrides can precipitate on grain boundaries that have normals in the circumferential direction, providing an F_{n0} larger than zero.
- The maximum fraction of the number or length of radial hydrides, F_{nmax}. This number is the sum of the initial fraction of the number or length of radial hydrides, F_{n0}, plus the fraction reoriented by stress.
- The applied stress where radial hydrides are first observed — this stress is often called a threshold stress, σ_{th}.

Tables 9.45 and 9.46 include values of these parameters.

As a technical guide, the values of F_{nmax} and σ_{th}, and the stress dependence of reorientation can be estimated through a theoretical analysis of hydride reorientation [9.747, 9.780, 9.781]. In Ref. [9.780], using an analysis by Li [9.782], the reorientation, R_σ, was related to tensile stress, σ, through:

$$R_\sigma = R_0 \exp(V_n \varepsilon\omega\sigma/kT) \tag{9.69}$$

where

R_0 is the initial distribution of hydrides;
V_n is the volume of a precipitate nucleus;
ε is the lattice strain in the metal from the precipitate in the direction of the applied stress;
ω is a parameter representing the available sites for precipitation and if ω is associated with hydride habit planes, it can be characterized by crystallographic texture [9.761, 9.780];
k is Boltzmann's constant;

and T is the temperature in K.

For comparison with metallographic measurements, $F_n = R_n/(1 + R_n)$.

In Ref. [9.781], the nucleation rate under external stress was the rate at zero stress modified by an exponential factor. For completeness the effect of the additional strain converting the hydrogen in solution to hydride was included, but as pointed out in Section 9.7.1.2(a), this contribution is very small and is considered to be negligible. The hydride misfit has been approximated as 0.05 based on Ref. [9.550] (see Section 9.7.1.1); in reality the misfit is anisotropic and were it not, stress would not affect the direction of nucleation [9.781]. In the analyses the value of the volume of the precipitate nucleus, V_n, ranged from 2000 to 14 000 Å^3 (2 to 14 × 10^{-27} m^3), depending on the mechanical properties of the zirconium alloy. In Ref. [9.747], F_{n0} was set at 0.02.

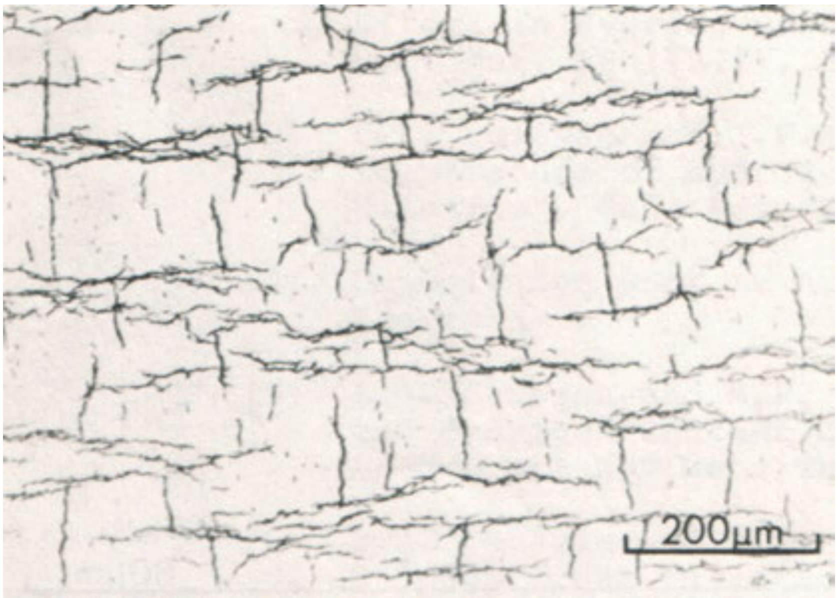

FIG. 9.270. Hydrides in Zr-2.5Nb pressure tube material containing 110 ppm (0.99 at.%) hydrogen showing mixture of 'radial' and 'circumferential' hydrides after slow cooling from 593 K (320°C) under a hoop stress of 420 MPa. F*n = 0.3 (based on length fraction [9.635]).*

The analysis showed the nucleation of precipitates to be the critical stage in the time scale of cooling. The contribution from hydride growth in determining reorientation was very small [9.780, 9.781]. Reorientation through hydride coarsening was considered improbable [9.783], unlike with Au particles in Fe-Mo-Au alloys, where stress reorientation was determined by coarsening [9.783]. The implication of the controlling influence of hydride nucleation is that only the hydrogen that is taken into solution is available for reorientation. Reorientation from the hydrogen in solution was the explanation of the results of early experiments showing that F_n was small in specimens with large hydrogen concentrations when many of the hydrides were not dissolved at the peak temperature [9.576, 9.752]. This effect is illustrated in a cold worked Zr-2.5Nb pressure tube, as shown in Fig. 9.270 [9.635]. In this example, the tube contained 110 ppm (0.99 at.%) hydrogen and was cooled from 593 K (320°C) under a hoop stress of 420 MPa. About 70 ppm (0.63 at.%) of the hydrogen would be in solution at the peak temperature so the microstructure consisted of both circumferential and radial hydrides. Based on the fraction of the length of radial hydrides, F_n was 0.3. In some experiments, not all the available hydrogen in solution precipitates as reoriented hydrides. When interpreting F_n in terms of the hydrogen concentration in solution, C_D, the shortfall in expectation is taken into account by the factor $\psi C_D/C_H$, where C_H is the total hydrogen concentration; in this example the factor ψ is 0.47 and $\psi C_D/C_H$ provides an effective solubility of 33 ppm (0.30 at.%) [9.761].

The effects of peak temperature and hydrogen concentration are explained similarly. Tensile specimens machined from Zr-2.5Nb pressure tube material and containing between 100 and 300 ppm (0.9 and 2.66 at.%) hydrogen were cooled from between 523 and 673 K (250 and 400°C) under tensile stresses up to 400 MPa and F_n was evaluated, as shown in Figs 9.271 and 9.272 [9.761]. The initial hydrides were circumferential, so F_{n0} was very small. As the applied stress was raised, radial hydrides were detected and F_n increased up to a plateau, F_{nmax}. In the fit to Eq. (9.69), R_0 was set to 1×10^{-4}. The original tube had a strong texture with basal plane normals in the transverse direction and as a result ω was set to 0.95. When the temperature was changed, the best fit required V_c to vary but when the hydrogen concentration was changed at a constant temperature, V_c was kept constant at 12×10^{-27} m^3. If the peak temperature < T_D, the maximum amount of radial hydride, F_{nmax}, was controlled by the effective solubility, $\psi C_D/C_H$. When the peak temperature > T_D, all the hydrogen was available to be reoriented and F_{nmax} approached 1.0.

In Figs 9.271 and 9.272, reorientation appears to start at an applied stress of about 60 MPa. Equation (9.69) implies that even a small stress should reorient hydrides but, because the increase in reorientation is gradual and exponential, the effect of the first increment in applied stress may not be

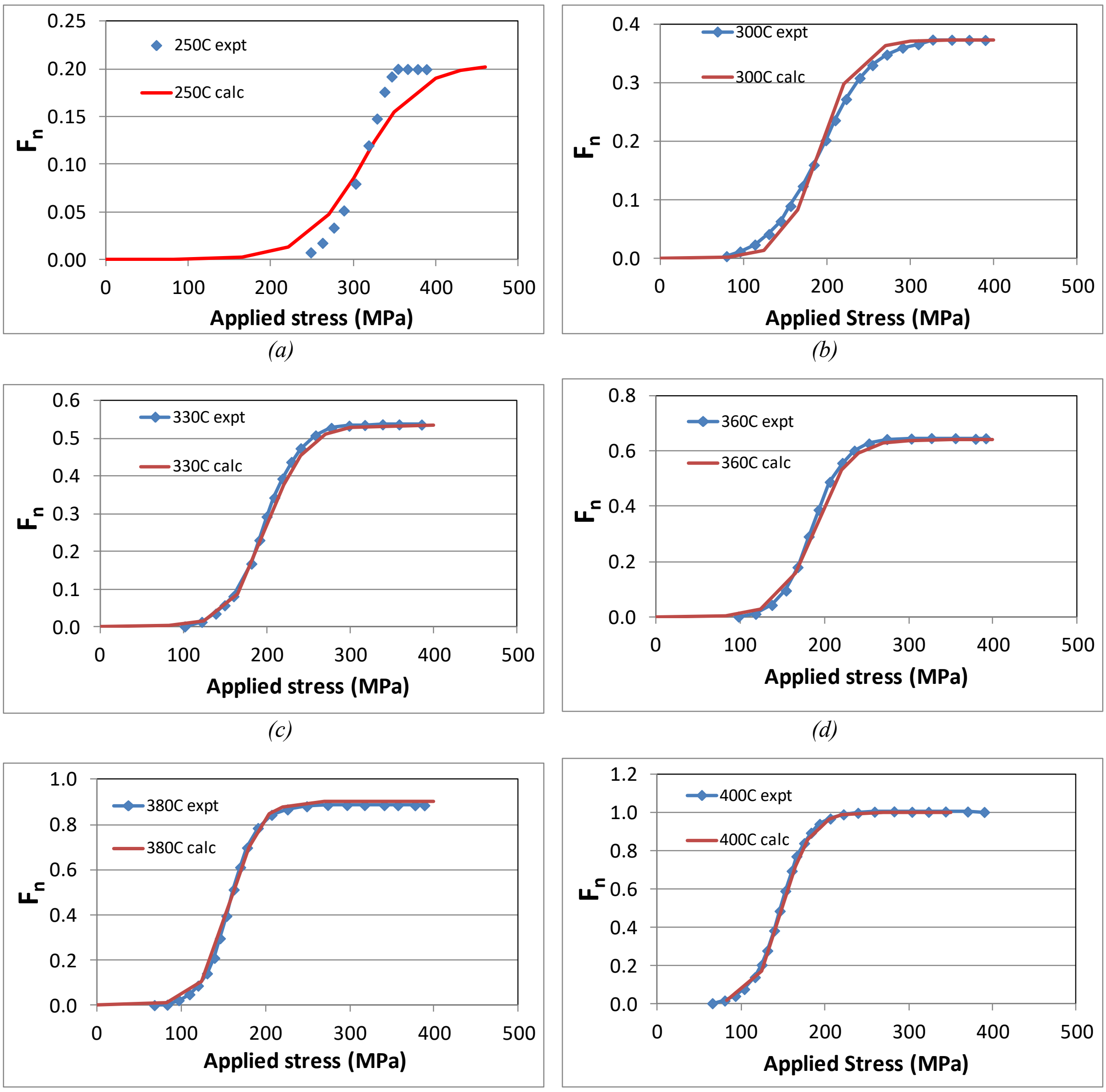

(a) *(b)*

(c) *(d)*

(e) *(f)*

FIG. 9.271. Reorientation of hydrides in Zr-2.5Nb from the indicated peak temperatures. Material contained 100 ppm (0.9 at.%) hydrogen, and specimens were loaded in the transverse direction. In the calculations the parameters ε, ω and R_0 were set at 0.05, 0.95 and 1×10^{-4}, respectively. Vc was (a) 4.5; (b, c) 8.0; (d) 9.0; (e) 11.0; (f) 12 × 10-27 m3 (experimental points from [9.761] and calculations from Eq. (9.69) [9.780].

observed. An early example in Zircaloy is shown in Fig. 9.273 [9.757]. In this example no change in the number of radial hydrides up to a threshold stress of 43 MPa was obtained by extrapolating the data from higher stresses to F_{n0} of 0.41 — labelled ‘original plot’ in Fig. 9.273. The fit to Eq. (9.69) suggests that the threshold stress is an artefact of the method of plotting the results, unless residual stresses oppose the externally applied stress and the threshold stress is a measure of overcoming the internal stresses. The threshold stress for reorientation will appear higher than if the residual stresses were absent, and vice versa. The concept of threshold stress is a useful guide to evaluate practical situations for integrity assessments and it is widely used, although the mechanistic underpinning is lost.

Application of Eq. (9.69) to other data from Zircaloy tubing [9.758] shows the effects of F_{n0} and texture, as seen in Fig. 9.274. For these measurements the hydrogen concentration was 50 ppm (0.45 at.%) and the specimens were cooled under load from 623 K (350°C). For the calculation on each material, V_c was maintained at 8×10^{-27} m^3 but the texture of the matrix was included through ω. For tubes A, B, and C the tubing had a strong radial texture whereas in tube D the basal poles were in the circumferential direction and, although F_{n0} was low, F_n attained a high value once a moderate tensile

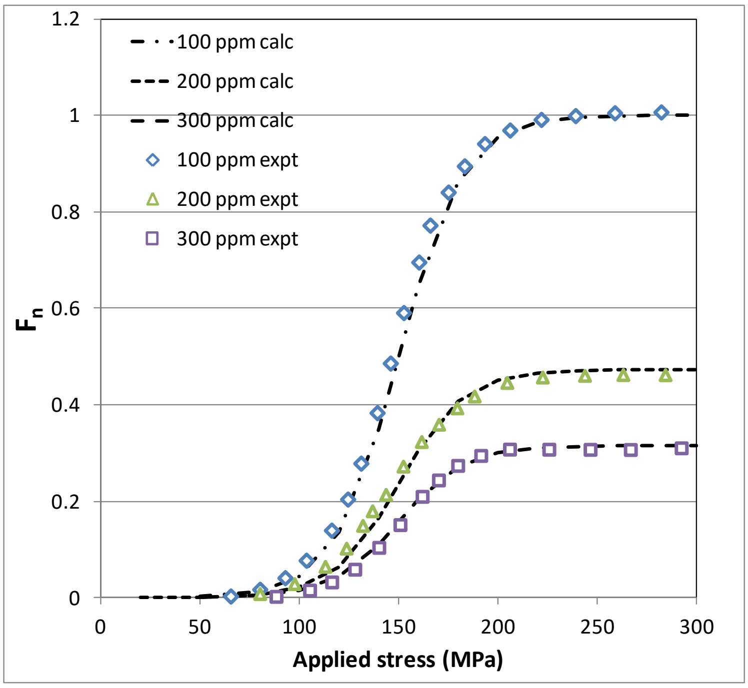

FIG. 9.272. Reorientation of hydrides in Zr-2.5Nb from 673 K (400°C) in material contain the indicated hydrogen concentrations. Specimens were loaded in the transverse direction. In the calculations the parameters ε, ω, R_0, V_c and ψ were set at 0.05, 0.95, 1×10^{-4}, 12×10^{-27} m^3 and 0.55, respectively (experimental points from [9.761] and calculations from Eq. (9.69) [9.780]).

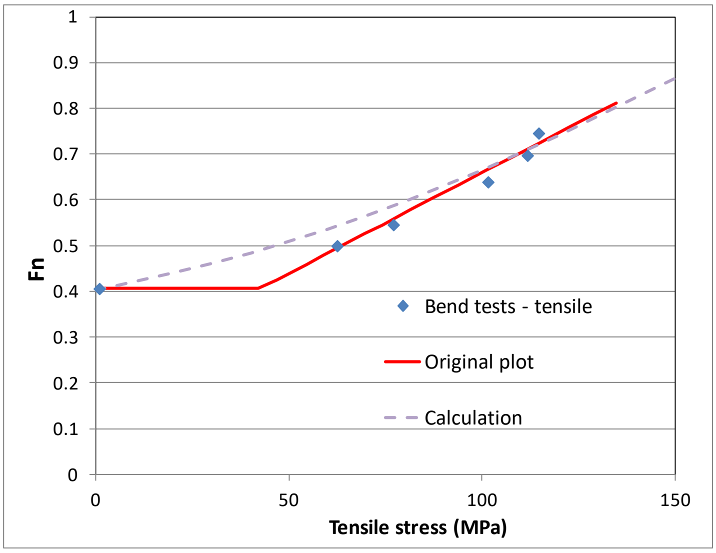

FIG. 9.273. Stress reorientation of hydrides in annealed Zircaloy after cooling from 673 K (400°C) [9.757] (calculation based on contribution from matrix grains and grain boundaries [9.780]).

stress was imposed. In Fig. 9.275, the effect of F_{n0} was suppressed and the tubes with similar texture but different F_{n0} had a similar rate of change of F_n with applied stress.

All experiments show that no hydrides reorient when stressing in a direction where no basal plane normals are present. Equation (9.69) can be used to illustrate the texture effect by keeping all the variables constant except for ω, as shown in Fig. 9.276; when many basal plane normals are parallel with the stressing direction, as represented by $\omega = 0.95$, the hydrides reorient readily whereas when few are available, as represented by $\omega = 0.05$, no radial hydrides are observed. This conclusion is supported

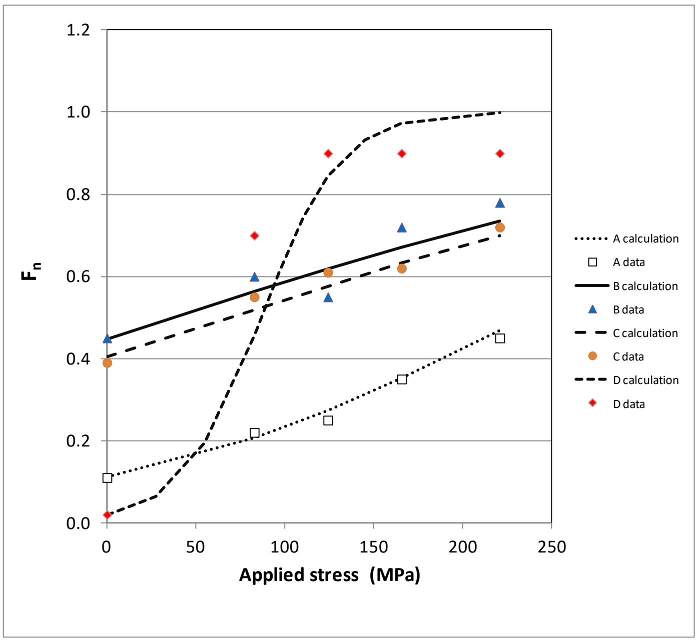

FIG. 9.274. Stress reorientation of hydrides in various cladding made from annealed Zircaloy containing 50 ppm (0.45 at.%) after cooling from 623 K (350°C). Note the variable values of F_{n0}. In the calculations $\varepsilon = 0.05$ and $V_c = 8 \times 10^{-27}$ m^3. To represent texture for A, $\omega = 0.19$, for B and C, $\omega = 0.12$, and for D, $\omega = 0.97$ (data from [9.757] and analysis from [9.761, 9.780]).

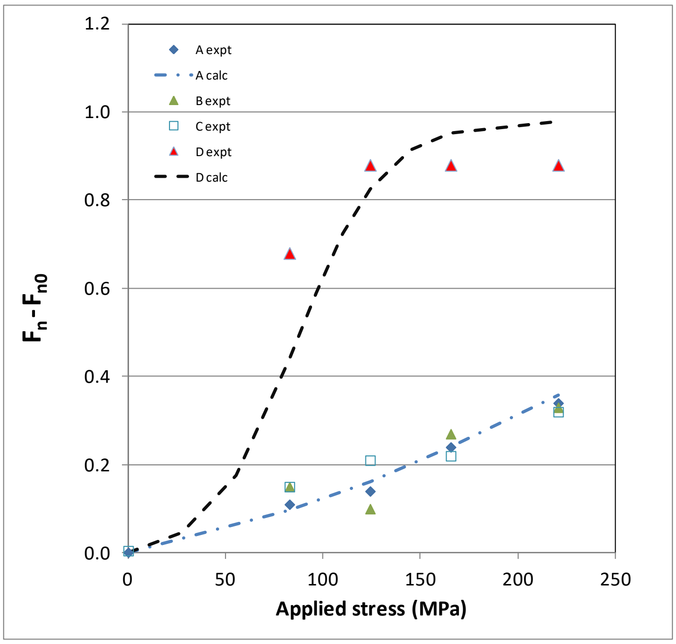

FIG. 9.275. As in Fig. 9.274, with F_{n0} suppressed.

by experiments on sheet materials. With a high concentration of basal poles in the transverse direction, loading up to 138 MPa in this direction produced hydride reorientation during cooling from 673 (400°C) in annealed Zircaloy-2 containing 170 ppm (1.53 at.%) hydrogen, but none in the rolling direction where basal poles were absent [9.750]. In another annealed Zircaloy-2 sheet the basal poles were concentrated in the through-thickness direction, Kearns factor $f_R = 0.72$, moderately concentrated in the transverse direction, $f_T = 0.22$, and contained a very low concentration in the rolling direction, $f_R = 0.06$. Tensile loading to 160 MPa in the transverse direction from 628 K (354°C) produced an F_n of

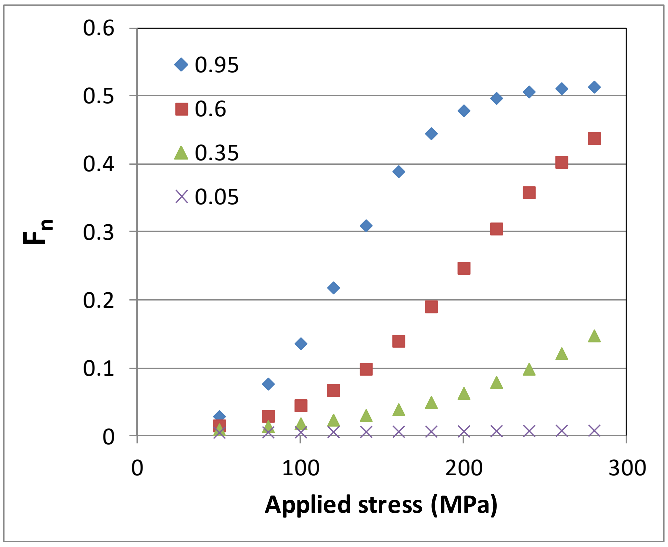

FIG. 9.276. Effect of basal plane texture on reorientation of hydrides. Calculation based on Eq. (9.69) in material containing 400 ppm (1.79 at.%) hydrogen cooled from 673 K (400°C); $\varepsilon = 0.05$, $V_c = 7 \times 10^{-27}$ m³ and $R_0 = 0.01$. A value of $\omega = 0.95$ represents a texture with a high density of basal plane normals parallel with a tensile stress, while $\omega = 0.05$ represents a texture with a low density of basal plane normals parallel with a tensile stress.

0.17 but F_n was 0.02 (unchanged from F_{n0}) when loaded in the rolling direction [9.771]. In most fuel cladding and pressure tubes the basal poles are concentrated in the radial-transverse plane and very few exist along the axial direction; typically, in fuel cladding, $f_R = 0.65$, $f_T = 0.30$ and $f_A = 0.05$, and, in cold worked Zr-2.5Nb pressure tubes, $f_R = 0.34$, $f_T = 0.62$ and $f_A = 0.04$. In experiments under cooling, tensile stresses were imposed in the axial direction of components on specimens containing elevated hydrogen concentration. In neither fuel cladding [9.757, 9.758] nor Zr-2.5Nb pressure tubes [9.576, 9.761, 9.763] was any gross reorientation found leading to radial hydrides with their normal in the axial direction; this result is fortunate because such a configuration would be very dangerous and lead to guillotine failure. In these tubes, if the conditions are appropriate, internal pressurization only produces hydrides with normals parallel with the hoop stress and none from the axial stress, both because of the halved stress and the texture. The common habit plane of the hydride, $(10\bar{1}7)$, is close to the basal plane. With no basal plane normals in the axial direction, the formation of radial hydrides is suppressed. In cladding with the basal poles concentrated 30° from the radial direction, under a hoop stress, circumferential hydrides had a habit plane of $\{10\bar{1}4\}_\alpha$, which is 24.7° from the basal plane, while radial hydrides may precipitate on pyramidal planes, $\{10\bar{1}1\}$, with normals close to the hoop direction [9.543].

The effect of thermal cycling follows from hydride nucleation being the controlling event. Typical metallographic changes are shown in Fig. 9.277 for Zircaloy-4 temperature cycled up to 12 times to 673 K (400°C) under a hoop stress of 160 MPa [9.747, 9.772, 9.773]. At the peak temperature, the hydrogen concentration in solution, C_D, was 172 ppm (1.55 at.%) and the proportion of the hydrogen in solution, C_D/C_H, diminished with increase in hydrogen concentration, C_H: 0.69 with 250 ppm (2.23 at.%) hydrogen, 0.54 with 320 ppm (2.84 at.%) hydrogen and 0.29 with 600 ppm (5.19 at.%). In the experiment a proportion of the hydrogen in solution produced reoriented hydrides on the first cycle but this proportion also diminished with an increase in hydrogen concentration: 0.57 with 250 ppm (2.23 at.%) hydrogen, 0.2 with 320 ppm (2.84 at.%) hydrogen and 0.03 with 600 ppm (5.19 at.%), providing ψ values of 0.83, 0.37 and 0.10, respectively. This result implies that the number of radial hydrides declines with increased hydrogen concentration. With subsequent cycles, part of the dissolved hydrogen precipitated as radial hydrides on cooling and these new radial hydrides added to those formed on the previous cycle. By retaining the proportion of radial hydrides produced on the first cycle for each subsequent cycle, the rate of change in the amount of reorientation diminished with the number of cycles but as the number of cycles increased, the accumulated amount of radial hydride, F_n, increased to a high value, close to 1.0 in two conditions, as depicted in Fig. 9.278.

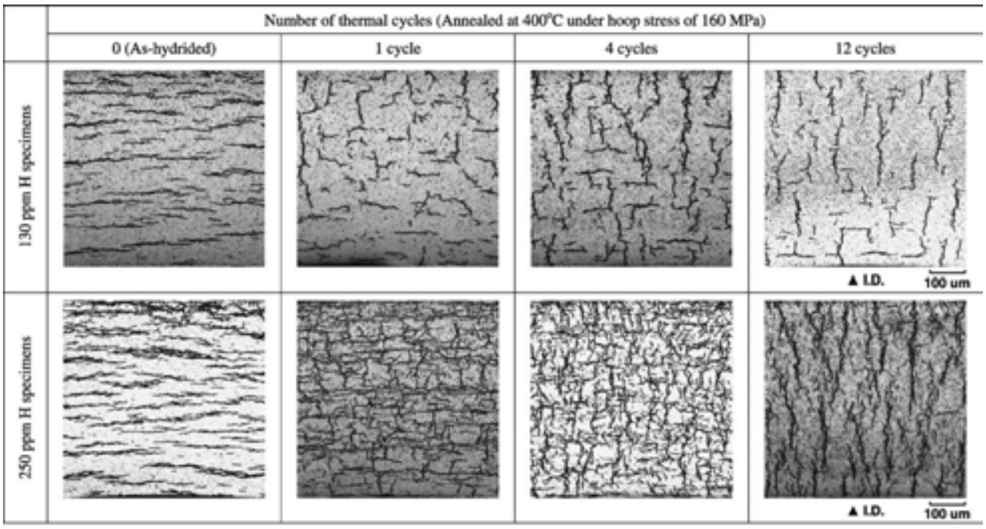

FIG. 9.277. Effect of number of temperature cycles between 443 and 673 K (170 and 400°C) on reorientation of hydrides in CWSR Zircaloy-4 fuel cladding under hoop stress of 160 MPa [9.747].

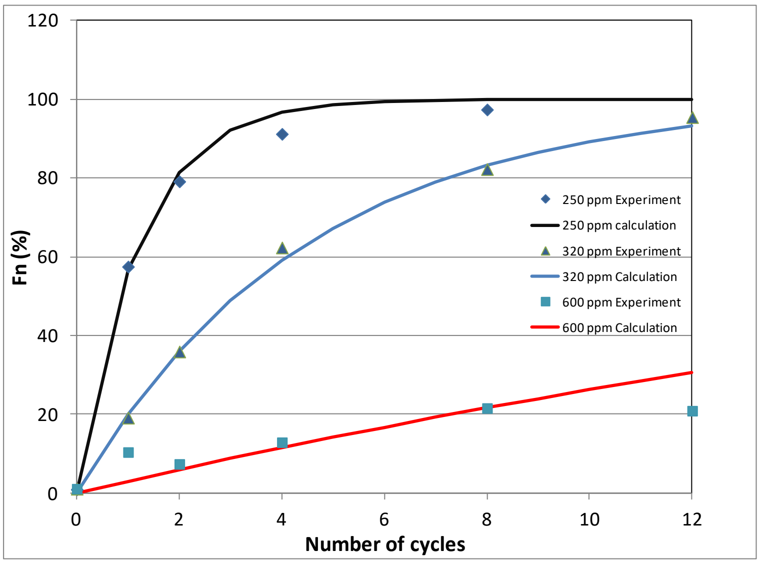

FIG. 9.278. Increase in F_n in CWSR Zircaloy-4 cladding with the number of thermal cycles between 443 and 673 K (170 and 400°C), showing the effect of hydrogen concentration. Calculation based on results from [9.747] assuming the same proportion of hydrides are precipitated with each thermal cycle as in the first cycle: 0.57 with 250 ppm (2.23 at.%) hydrogen, 0.2 with 320 ppm (2.84 at.%) hydrogen, 0.06 with 600 ppm (5.19 at.%) hydrogen.

After the discovery of stress orientation [9.756, 9.757] the modifications to fabrication processes for fuel cladding to prevent the formation of radial hydrides have been largely successful. Post-service examination of fuel cladding from PWRs indicates that most hydrides are circumferential, as shown in Figs 9.264 and 9.266. Examinations of cladding after burnups of 48 MWd/kg [9.775] and 67 MWd/kg [9.770] provide other examples. In BWRs some radial hydrides were found after burnups of 50 MWd/kg [9.775] and 55 MWd/kg, as shown in Fig. 9.265 [9.735]. In one examination, radial hydrides were found in the outer rim of the cladding after a power ramp of 42 kW/m in fuel with a burnup of 61 MWd/kg; the radial hydrides were absent before the ramp [9.784].

A small number of radial hydrides were observed in the Zircaloy-2 pressure tubes irradiated for 4242 d in the N-reactor with a hoop stress of about 60 MPa [9.713]: F_n was 0.15 to 0.20 close to the outer surface but was 0.05 to 0.10 in the bulk of the tube, indicating the effect of increased concentration of hydrogen in solution in the material with the high outer temperature — see Section 9.7.2.3. In CANDU the through-wall temperature gradient is normally very small; <1°C/mm. The hydrides in the Zircaloy-2 pressure tubes of Pickering Units 1 and 2, with an operating hoop stress of 90 to 110 MPa [9.785], and NPD, with an operating hoop stress of 80 MPa [9.155], contained a uniform mixture of radial and circumferential hydrides from hydrogen (deuterium) concentrations in the range 320 to 480 ppm (1.44 to 2.14 at.%). These results indicate that the threshold stress for forming radial hydrides in Zircaloy-2 pressure tubes is <60 MPa. No radial hydrides were observed in cold worked Zr-2.5Nb. After 3000 days of normal operation in KAPS-2, the maximum total hydrogen concentration was 16 ppm (0.15 at.%) and the hydrides were uniformly distributed as fine, randomly oriented precipitates [9.786]. Large circumferential hydrides, 50 μm long, were observed after 4050 days of normal operation with an operating hoop stress of 140 MPa in Pickering Unit 3 [9.787]; in this example, a single pressure tube had picked up 140 ppm (0.63 at.%) deuterium, nearly six times the expected concentration, possibly from the atmosphere between the pressure and calandria tubes. These results indicate that the threshold tensile hoop stress for forming radial hydrides in Zr-2.5Nb pressure tubes is >140 MPa.

Radial hydrides can be produced in pressure tubes under unusual circumstances:

— In CANDUs the pressure tubes are attached mechanically to each side of the reactor by a rolled joint in an end-fitting. Figure 9.279 shows the cross-section of a rolled joint. Three grooves are machined in the end-fitting bore in the rolled joint area. The pressure tube is inserted into the end-fitting covering the grooves. A tube expander is introduced into the pressure tube through the end-fitting and the tube is roll expanded into the end-fitting. The tube wall thickness is reduced by 12% to 15% and the grooves in the end-fitting are partially filled with tube material. Also, tube material is extruded axially in either direction away from the rolled area. The material in the grooves tends to lock the tube to the end-fitting producing satisfactory leak tightness and axial strength. When the rolling was done incorrectly, by inserting the roller too far beyond the taper at the exit of the end-fitting, the pressure tube was no longer supported by the main body of the end-fitting, and large, residual hoop tensile stresses, 500 to 700 MPa, developed over a short length in the pressure tube at this location. A second factor is the clearance between the pressure tube and the end-fitting; the larger the clearance, the higher the residual stress. Temperature cycles during normal reactor operations were sufficient to produce radial hydrides in localized patches, about 20 mm long, from the 15 to 20 ppm (0.14 to 0.18 at.%) hydrogen present, as shown in Fig. 9.280 [9.788].

— In Section 9.7.2.3 tensile hoop stresses were described at the interface between a hydride blister and the zirconium alloy matrix. Radial hydrides at the interface between the blister and the

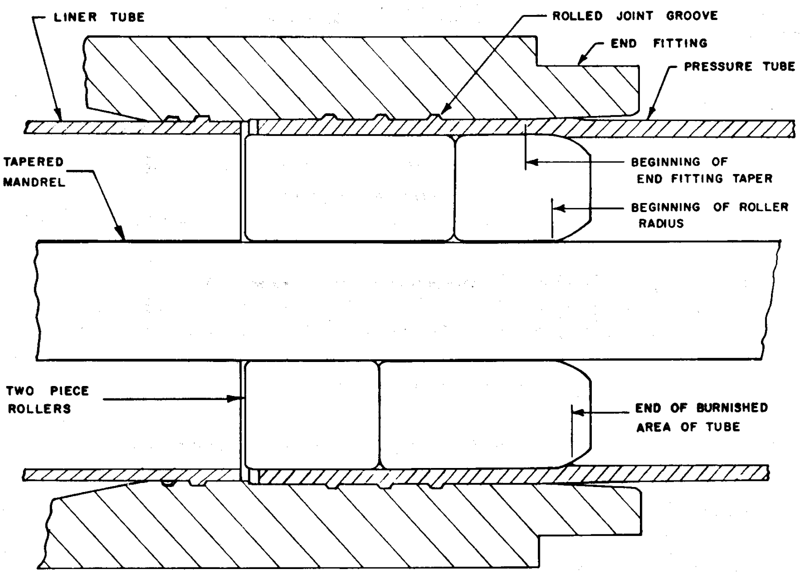

FIG. 9.279. Schematic diagram of a rolled joint for attaching pressure tubes to end-fittings in CANDU fuel channels. A seal is made by rolling the pressure tube into the grooves in the end-fitting. A burnish mark is formed at the limit of rolling. The centre of the reactor is to the right in this diagram.

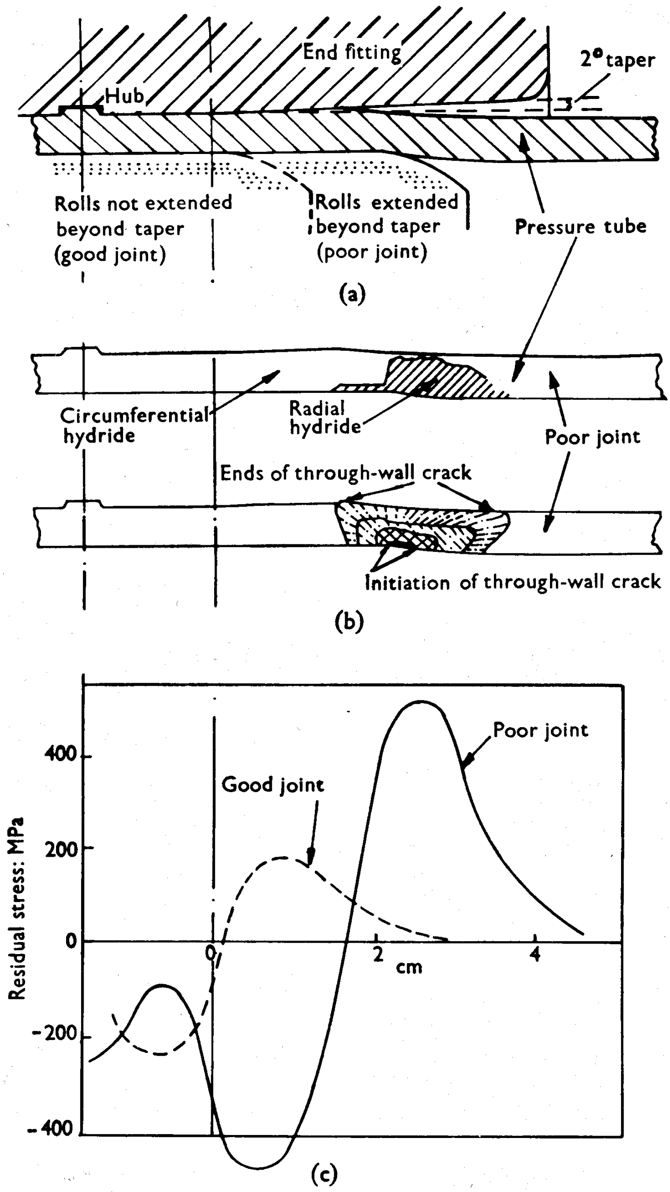

FIG. 9.280. Schematic diagram of rolled joint between a pressure tube and end-fitting in a CANDU reactor indicating the position of the (a) roller; (b) location of radial hydrides and cracking; and (c)residual stresses (based on [9.788]).

matrix were shown in Figs 9.258(a) and (b). Further experiments and analysis based on the misfit between the blister and matrix confirm that the radial hydrides are caused by the induced hoop stress at the interface [9.789], or alternatively, the distribution of the radial hydrides was used to confirm the stress distribution [9.727].

Annealing can eliminate stress induced radial hydrides. In Zr-2.5Nb the temperature for reversion has to be higher than TD and the maximum temperature during stressing. Examples are:

- Material containing 8 ppm (0.07 at.%) hydrogen was stressed at between 550 and 750 MPa at 498 K (225°C), about 50°C above TD, and cooled slowly. The resulting radial hydrides were sites of hydride reprecipitation when unstressed material was held at 523 K (250°C) for over 1000 h, 548 K (275°C) for between 700 and 900 h and 573 K (300°C) for between 25 and 50 h. The new hydrides formed in groups of small, 15 μm long, circumferential precipitates on the sites of the previous large, 50 μm long, radial hydrides [9.636].
- In material containing 100 ppm (0.9 at.%) hydrogen, reoriented hydrides were produced by stressing and cooling from 573 K (300°C). Although TD is about 619 K (346°C), heating for

500 h at 623 K (350°C) or times less than 7 hours at 673 K (400°C) did not eliminate the radial hydrides [9.577].

- Radial hydrides were produced in a tube containing 145 ppm (1.3 at.%) by cooling from 570 K (297°C) under a hoop stress of 555 MPa. No reversion to circumferential hydrides was observed when unstressed samples were held at 570 K (297°C) for 1000 h or for 500 h at 623 K (350°C), about 30°C below TD. After 16 h at 643 K (370°C) reoriented hydrides were still observed but reversion was complete after 16 h at 670 K (397°C), 15°C above TD [9.635].

X ray diffraction experiments have been done with annealed Zircaloy-4 to find the microstructural reason for hydride reorientation [9.610, 9.777]. When precipitated under load with subsequent reorientation, the diffraction signature is an increase in line broadening in the reoriented hydrides, estimated from the full width at half maximum of the (111) diffraction peaks of δ-hydride. No effect was observed on the full width at half maximum of hydrides precipitated with no reorientation (e.g. in hydride planes parallel to the applied stress). The increase in full width at half maximum was attributed to line broadening by strain rather than size.

In summary, nucleation is the critical step determining the orientation of hydride precipitates in zirconium alloys. The controlling factors are tensile stress (including residual stress), crystallographic texture and the amount of hydrogen in solution before nucleation of the precipitates.

Sections 9.7.2 and 9.7.3 describe the wide distribution of hydrides that may be possible in components depending on values of hydrogen concentration and stress, temperature history, alloy composition and various gradients. The next sections describe the important properties for structural integrity.

9.7.4. Fracture properties of hydrides

Pure zirconium hydride is brittle in tension. Measuring mechanical properties on macrospecimens of pure hydride is fraught with difficulties because of the cracking during preparation that illustrates both the property and the problems with testing. Testing yields the following typical results:

- In uniaxial tensile tests between room temperature and 773 K (500°C) the ductility of δ-hydride was less than 1% and the fracture stress was 48 to 69 MPa [9.790, 9.791]. A very low value, 18 MPa, with zero ductility was reported for $ZrH_{1.73}$ [9.792].

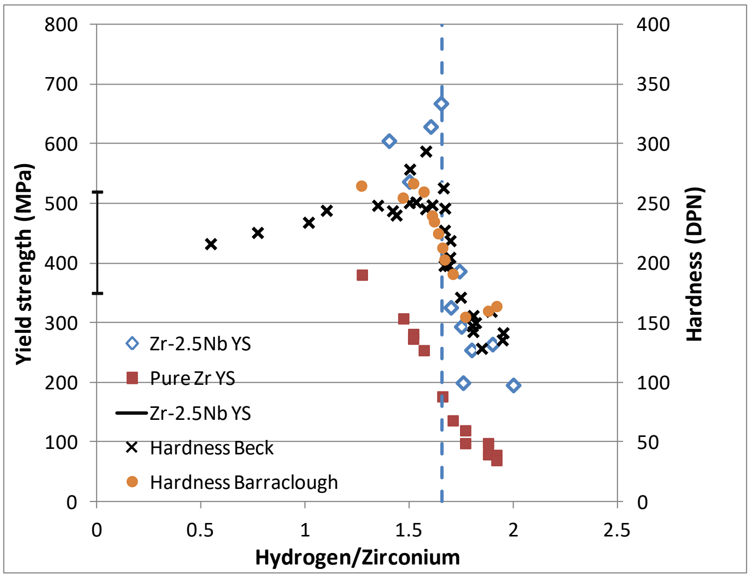

FIG. 9.281. Yield strength and hardness of zirconium hydride as a function of H/Zr at room temperature [9.520, 9.524, 9.791, 9.793, 9.794].

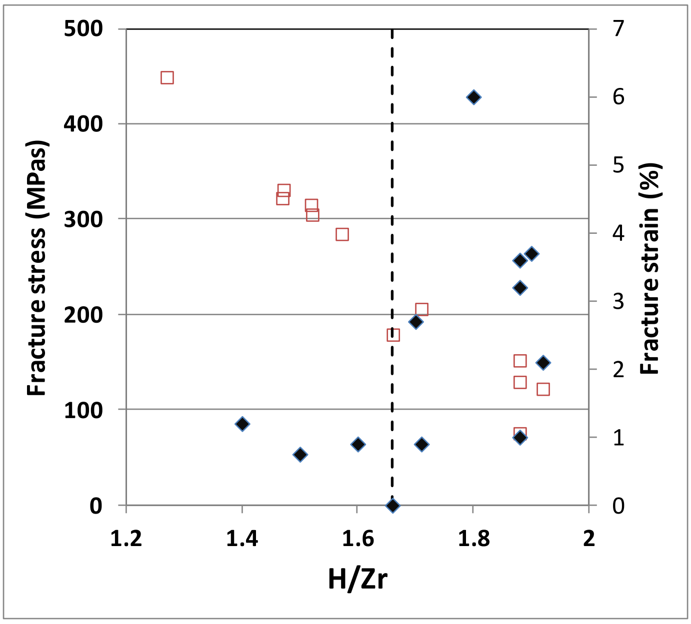

FIG. 9.282. Dependence of fracture stress (open squares) and strain (closed diamonds) of zirconium hydride on H/Zr [9.791, 9.793, 9.794].

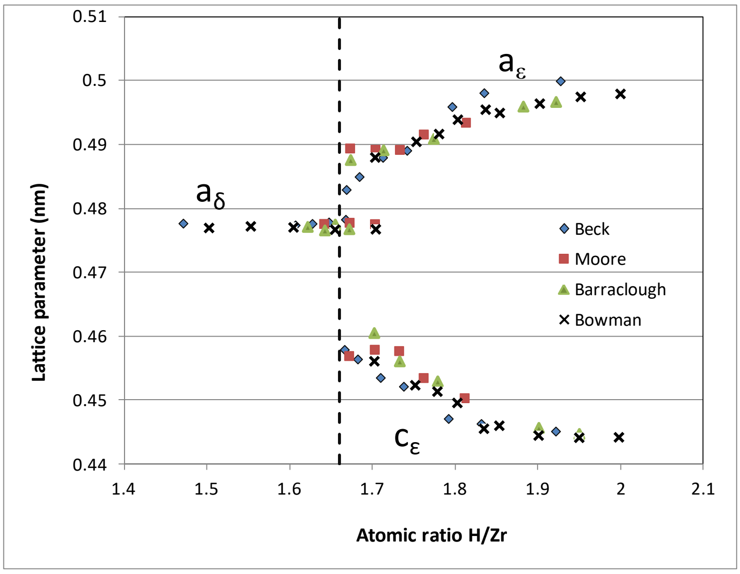

FIG. 9.283. Phase transformation from δ-hydride to ε-hydride [9.520, 9.524, 9.796, 9.797].

— Compression tests were done in attempts to study the deformation of hydrides. Specimens of δ-hydride (H/Zr = 1.66) were brittle up to 373 K (100°C). At room temperature when the hydride was made with pure zirconium the proportional limit was about 170 MPa [9.791] while with annealed Zr-2.5Nb the strength was between 600 and 700 MPa [9.793]. The strength, as shown in Fig. 9.281, declined as the hydrogen concentration increased towards ZrH_2 [9.791, 9.793, 9.794]. Hardness measurements suggested a maximum value in the range $ZrH_{1.5}$ to $ZrH_{1.6}$ [9.520, 9.524] whereas measurements of microhardness indicated a gradual decline in the H/Zr range of 1.47 to 1.69 [9.553].

— The fracture stress followed the same trend with composition as the strength, as shown in Fig. 9.282, while ductility was lowest around $ZrH_{1.66}$. Although slip on {111} was observed in $ZrH_{1.66}$, probably with $b = a/2[110]$, little ductility was attained up to 633 K (360°C).

- Based on compression tests at room temperature, Young's modulus, E_H, of hydride was similar to that of Zr up about $ZrH_{1.6}$ but thereafter declined rapidly by 60% when the composition was $ZrH_{1.8}$ [9.793]. Nanohardness tests supported the elastic modulus of the $ZrH_{1.83}$ being lower than that of Zr, but only by 25% [9.795]; this technique avoids the defects in macrospecimens. When E_H was obtained by ultrasonic pulse echo measurements, the values in the H/Zr range of 1.47 to 1.69 were 30 to 40% higher than the value for pure zirconium [9.553]. These differences have not been resolved.
- Any sudden drop in modulus, strength and ductility corresponded with the phase change from δ- to ε-hydride, as shown in Fig. 9.283 [9.520, 9.524, 9.796, 9.797]. The microstructure of ε-hydride consists of lamellae, as shown in Fig. 9.284 [9.520, 9.794], and deformation was by movement of lamellar boundaries and creation of new lamellae as well as slip. When H/Zr was around 1.9, sudden yield drops were sometimes observed.
- Up to $ZrH_{1.77}$ the strength of the hydrides declined with temperature but appeared independent of temperature when H/Zr > 1.88, as shown in Fig. 9.285.

The fracture toughness of δ-hydride, K_{IC}^{H}, is very low, ranging from <1 to 2 MPa√m [9.795, 9.798, 9.799]. Figure 9.286 depicts measurements of toughness [9.1] using compact tension specimens of pure Zr and Zr-2.5Nb containing a wide range of hydrogen concentrations [9.798]. The phase in material with H/Zr ≥ 1.5 and ≤ 1.65 was identified by electron diffraction as δ-hydride. It failed with no deviation in the load-deflection test plots, no shear lips were present on the cracks and the fracture surface consisted of 100% transgranular cleavage. At elevated temperatures the results were scattered; two specimens of pure Zr with H/Zr of 1.6 had a K_{IC}^{H} of about 4 MPa√m at 573 K (300°C) while other values were around 1 MPa√m. Similar scatter was observed at 673 K (400°C) with values at 2 and 5 MPa√m. As H/Zr decreased below 1.4 the fracture toughness increased because of the presence of γ phase — cracks may be arrested by this phase when mixed with δ-phase [9.791] — and when H/Zr ≤ 1.0, α phase was present, too.

In Fig. 9.286 a single point of 0.74 MPa√m for ε-hydride is included, based on microhardness, H_H, with an H/Zr of 1.83 [9.795]. K_{IC}^{H} was estimated from Eq. (9.70) [9.800]:

$$K_{IC}^{H} = \varphi[E_H/H_H]^{1/2}[P/c^{3/2}] \tag{9.70}$$

where

E_H is Young's modulus of hydride;
H_H is the hardness of hydride;
P is the applied load;
c is the crack length at the vertex of the hardness impression;

and φ is an empirical constant equal to 0.016 for Vickers indenter.

When Vickers hardness was measured on a 100 μm thick hydride layer formed gaseously on the surfaces of a Zircaloy-2 tube, cracks formed at the vertices of the diamond indentations [9.801]. Using Eq. (9.70), at room temperature a value of 2.3 MPa√m was derived for K_{IC}^{H} of this layer. The hydride phase was not identified but the hardness impressions were isotropic suggesting δ-phase. The incidence of cracking declined as the test temperature was raised; no cracks were detected at 423 K (150°C).

A theoretical estimate of the minimum value of K_{IC}^{H} was made based on the cleavage strength of the hydride, σ_f^*, and a characteristic distance from a crack tip [9.802]:

$$K_{IC}^{H} = \sigma_f^*\sqrt{[(E_H t\varepsilon_\perp)/(4\sigma_y(1-\nu^2)(1/(1-2\nu)-\sigma_f^*/\sigma_y)]} \tag{9.71}$$

where

$\varepsilon_\perp$ is the transformation strain of hydride;

t is the thickness of hydride;
v is Poisson's ratio of hydride;

and σ_y is the yield strength of Zr alloy.

The calculated temperature dependence of K_{IC}^{H} is displayed in Fig. 9.287. In the original paper σ_f^* was taken as a fraction of Young's modulus — representing the ideal strength; in the example E_H was that of Zr. The calculation was modified using a measured estimate of the modulus for hydride [9.793, 9.795] but retaining the same Poisson's ratio and temperature dependence. The second modification used actual values of σ_f^* [9.791]. Some of the experimental data were described by the original calculation while the remainder followed the estimates with the modified values of the mechanical properties. Despite these uncertainties, up to 673 K (400°C) zirconium hydride is demonstrated to have the toughness, K_{IC}, of a ceramic; examples are: soda glass: 1.2 MPa√m; SiC: 2.5 MPa√m; Al_2O_3: 3.5 MPa√m; and Si_3N_4: 5.5 MPa√m [9.803].

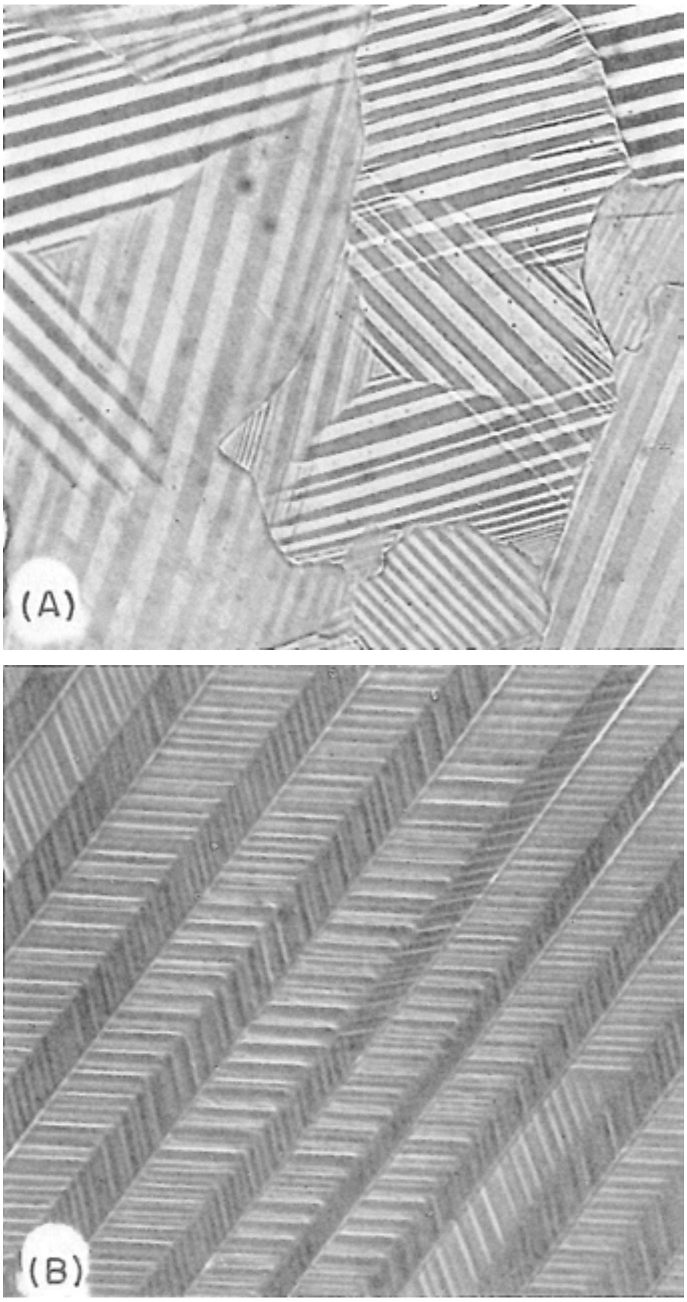

FIG. 9.284. Lamellar structure in two ε-hydride particles (A) and (B) [9.520].

When a zirconium alloy matrix containing hydrides is deformed, the hydrides may crack, either across their thickness [9.804–9.808] or along their length [9.749, 9.809–9.818]. Through-thickness cracking is usually associated with small hydrides having their traces parallel with the stress (plate normal perpendicular to the stress) and with the matrix material having low strength. Less deformation is required to crack a hydride if the matrix is deformed by twinning rather than slip. Figure 9.288

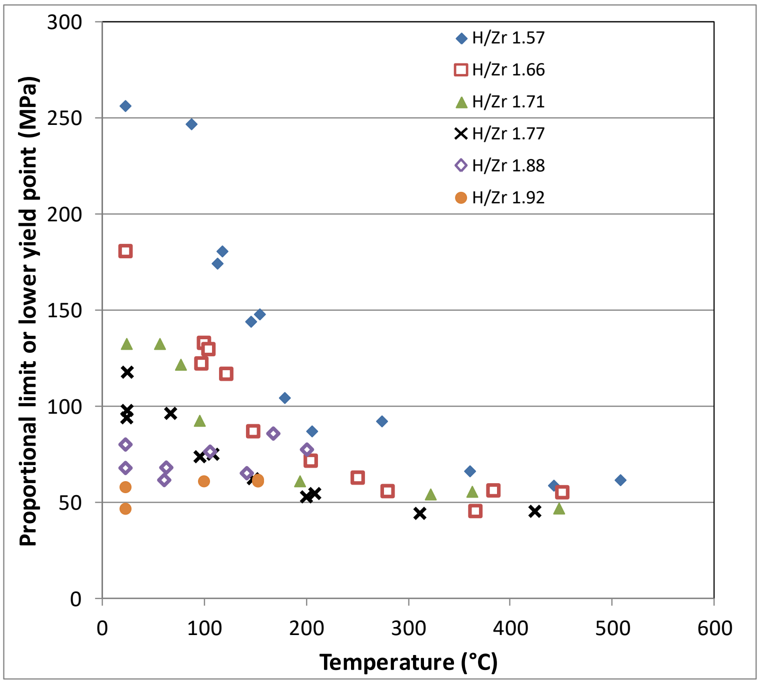

FIG. 9.285. Temperature dependence of initial deformation of zirconium hydride with H/Zr between 1.57 and 1.92 [9.791, 9.794].

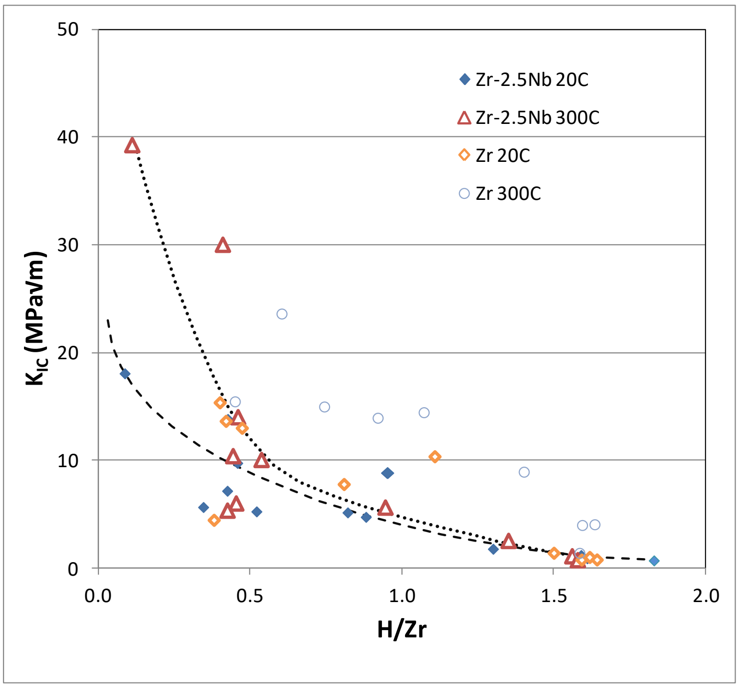

FIG. 9.286. Fracture toughness of zirconium hydride made from pure Zr and Zr-2.5Nb. All data from compact tension specimens [9.798] except for microhardness value at H/Zr of 1.83 [9.795].

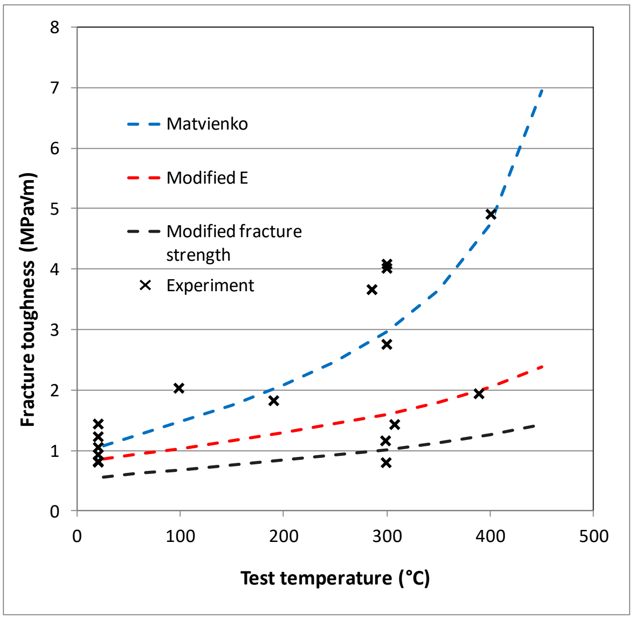

FIG. 9.287. Calculated temperature dependence of K_{IC}^{H}; blue line is original values of variables [9.802]; red line is model, including representative values of Young's modulus for hydride [9.793, 9.795]; green line is model, including representative values of fracture strength of hydride [9.791]. 'Experiment' is measured values of toughness [9.798].

illustrates cracking of a hydride by twinning in pure Zr while cracking by slip in the Zr matrix is shown in Figs 9.289(a) and (b). The extension of the crack into the Zr in Fig. 9.289(a) has stopped; with increased deformation, more through-thickness cracks may form and such cracks widen and blunt without propagating further into the metal. In light metallography these cracks appear as voids [9.65, 9.804, 9.806, 9.808]. When hydrides are oriented so the main tensile stress is perpendicular to their trace (parallel with the plate normal[8]), cracking often follows the length of a collection of hydrides, as shown in Fig. 9.290. Figure 9.254 shows cracks through hydrides that are crossing α grains surrounded by β phase in Zr-2.5Nb. With contiguous hydrides, cracks can propagate along grain boundaries [9.812], and through both radial and circumferential hydrides, as shown in Fig. 9.291(a) or through radial hydrides, Fig. 9.291(b); the latter two examples are in ZIRLO [9.749].

Cracking is observed in both γ- and δ-hydrides [9.807, 9.812, 9.814]:

- Particles extracted from fracture surfaces by plastic replica were analysed by select area diffraction to be consistent with δ-hydride [9.807];
- Tensile specimens containing the same number of large δ-hydrides, produced by slow cooling, or fine γ-precipitates, produced by quenching, had similar ductilities [9.812];
- Hydrides grown and cracked close to room temperature in an electron microscope were identified as γ phase [9.814].

Depending on the configuration and size of the hydrides, and the yield stress of the zirconium alloy matrix, cracking of hydrides requires some strain and achievement of a critical stress, σ_f. To build up this stress requires more plastic strain in softer materials than in strong materials. The estimates of the stress to crack hydrides are summarized in Table 9.45 for a wide range of materials, including values based on interpretation of acoustic emission [9.808, 9.815–9.817, 9.819], fracture stress of specimens with very low strains to failure [9.809, 9.810, 9.818], limiting stress to initiate cracking under constant load [9.813], metallography [9.806] or a relative change in lattice parameters of the hydride and the zirconium [9.820].

---

[8] Although it is recognized that hydrides that appear large by light metallography are made up of several small precipitates (Section 9.1.1.1), their fracture behaviour often appears to be that of a monolithic hydride.

TABLE 9.45. HYDRIDE FRACTURE STRENGTH

Material	Hydrogen concentration (ppm)	Reoriented	Method	Temperature (°C)	Yield strength (MPa)	Hydride fracture strength (MPa)	Criterion for value of σ_f	Hydride fracture	Source
Zircaloy-2	80	Yes	Tensile test	25	420	338	Zero ductility, $F_n = 0.96$	Along length	[9.809]
Pure Zr	100	No	Tensile test	-196	214	179	Metallography, tapered specimen	Through-thickness	[9.806]
Zircaloy-2	200	Yes	Tensile test	25	690	414	Fracture stress and ductility	Along length	[9.810]
Zr-2.5Nb	100	Yes	Bend test	80–250	720–560	550–585	Probability of rupture in constant load test, 1 out of 21 failed at 413 MPa at 150°C	Along length	[9.813]
Zr-2.5Nb	180	Yes	Notched tensile test	25	841–993	818–981	Increase in acoustic emission	Along length	[9.815]
Zircaloy-2	100	Yes	Notched tensile test	25	814	872	Increase in acoustic emission	Along length	[9.816]
Zr-2.5Nb	100	Yes	Notched tensile test	25	930	915	Increase in acoustic emission	Along length	[9.816]
Excel	100	Yes	Notched tensile test	25	1104	1094	Increase in acoustic emission	Along length	[9.816]
Zr	100	No	Tensile test: smooth, Tensile Test: notched	25 25	177–191 327–358	174–210 269–333	Increase in acoustic emission	Through-thickness	[9.808]
Zr-2.5Nb	100	Yes	Tensile	25	810	575	Increase in acoustic emission	Along length	[9.817]
Zr-2.5Nb	100	Yes	Tensile	25	760	644	Increase in acoustic emission	Along length*	[9.819]

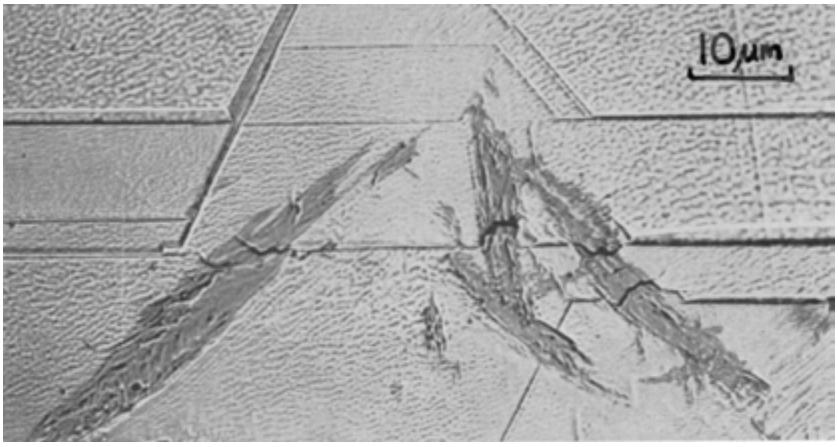

FIG. 9.288. Hydrides cracked by twinning in pure Zr deformed at 77 K (-196°C) [9.805].

Two contributions to σ_f are the applied stress needed to crack the hydride, σ_m, and σ_t. To a first approximation:

$$\sigma_f = \sigma_m + \sigma_t \tag{9.72}$$

The value of σ_t may have two parts:

(1) An elastic interaction between the hydride and the zirconium matrix because the elastic properties of the two phases may be different;
(2) Before the hydride is placed in tension, a compressive transformation stress must be overcome [9.821] because of the extra volume required to form a hydride (Section 9.7.1.1).

Consequently, the applied stress to nucleate a crack in an embedded hydride, σ_m, may be higher than the actual stress required to fracture the hydride because of σ_t:

For (1), the differential strain between a hydride and its surrounding zirconium matrix was evaluated by measuring the change in lattice parameters during stressing of Zircaloy-2 using X rays [9.820]. At room temperature the lattice strains of the two phases were similar up to a stress of 270 MPa beyond which the Zircaloy-2 deformed plastically and the load was transferred to the hydride phase. Similar elastic tracking of the lattice parameters was observed during the early parts of hydride dissolution during heating experiments, despite the thermal expansion of the two phases being different [9.610].

For (2) the value of σ_t decreases as the hydride grows and the thickness to length ratio, t_l/l_l, decreases. With t_l/l_l in the range of 0.04−0.02, in Zr-2.5Nb σ_t was calculated with a finite element model to be in the range –350 to –175 MPa [9.817]. Similar calculations for Zircaloy-2 predicted a similar effect but with smaller values — with t_l/l_l values of 0.1, 0.05 and 0.025, σ_t was estimated to be –180, –60 and –40 MPa, respectively, with a very small effect once a 1 µm thick hydride grew to 100 µm for a t_l/l_l of 0.01 [9.818].

The tensile stress at crack initiation was measured using the onset of rapid accumulation of acoustic emission during tensile tests on Zr-2.5Nb containing radial hydrides [9.817]. With average hydride lengths shorter than 25 µm or a maximum length less than about 70 µm, estimates of σ_m depended on hydride size while with longer hydrides, this stress was between 650 and 750 MPa independent of hydride size [9.816, 9.817, 9.819]. Figure 9.292 illustrates the dependence on maximum hydride length of the tensile stress at crack initiation for Zr-2.5Nb containing radial hydrides; the insensitivity to l_l once it exceeds 25 to 70 µm suggests that σ_t is small and within the experimental scatter. The first hydride to fracture will be that with the lowest t_l/l_l. The stress on the hydride is generated by slip or twinning. Hydrides below the threshold t_l/l_l, mostly governed by l_l, will require the metal matrix to attain the stress by a moderate amount of plastic deformation, whereas those hydrides above the threshold dimensions require deformations less than the amount used to define the yield

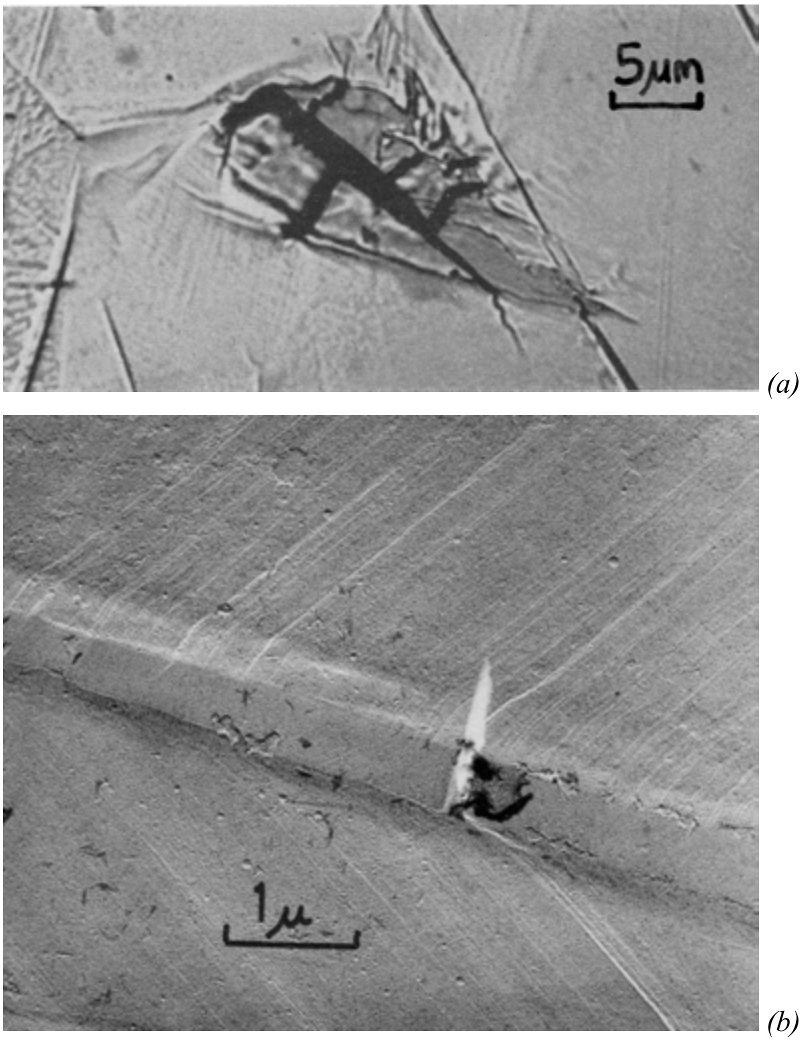

FIG. 9.289. Hydrides cracked by slip in pure Zr deformed at (a) 77 K (-196°C) [9.805] and (b) 273 K (20°C) [9.807]. Note the arrested crack in the Zr matrix in (a). In (b), the hydride is in a grain boundary and slip from adjacent grains was observed.

strength. Values of the stress to crack hydrides in notched specimens of Zircaloy-2, Zr-2.5Nb and Excel were determined using the acoustic emission technique; the length of hydride was about 50 μm, at which the stress to crack it was lower than, but independent of, the flow stress, as shown in Fig. 9.293 [9.816]. If the cracking of a hydride only requires the build up of stress from the small amount of strain associated with the usual measurement of the yield strength, for example, 0.2%, σ_f will depend on the yield strength, σ_y, of the zirconium matrix. The values from Table 9.45 from several different materials over a wide range of yield strength are highly correlated exponentially with a threshold stress for hydride cracking of 135 MPa, as shown in Fig. 9.294.

Hydride cracking is promoted by triaxiality, which concentrates the deformation and raises the local stress [9.502, 9.812, 9.815, 9.816, 9.818]. In pure zirconium containing 600 ppm (5.19 at.%) hydrogen, a single edge notch reduced the elongation to failure from 10% down to 1% [9.812]. A semicircular notch focused the deformation in specimens of Zircaloy-2, Zr-2.5Nb and Excel containing 100 ppm (0.9 at.%) radial hydrides [9.816]. The values of σ_m fitted with other data used in the correlation with yield strength when using the net section value of the yield strength, as shown in Fig. 9.294.

As the temperature is raised from room temperature, the yield strength of the zirconium alloy matrix declines rapidly — about 1 MPa/°C for Zr-2.5Nb — but the fracture strength of the hydride has only small temperature dependence, as shown in Figs 9.285 and 9.287. At a critical temperature, sufficient stress to crack the hydride cannot be generated by plastic deformation and a transition from early cracking to ductile behaviour is observed. As an example, hydride cracking was detected by

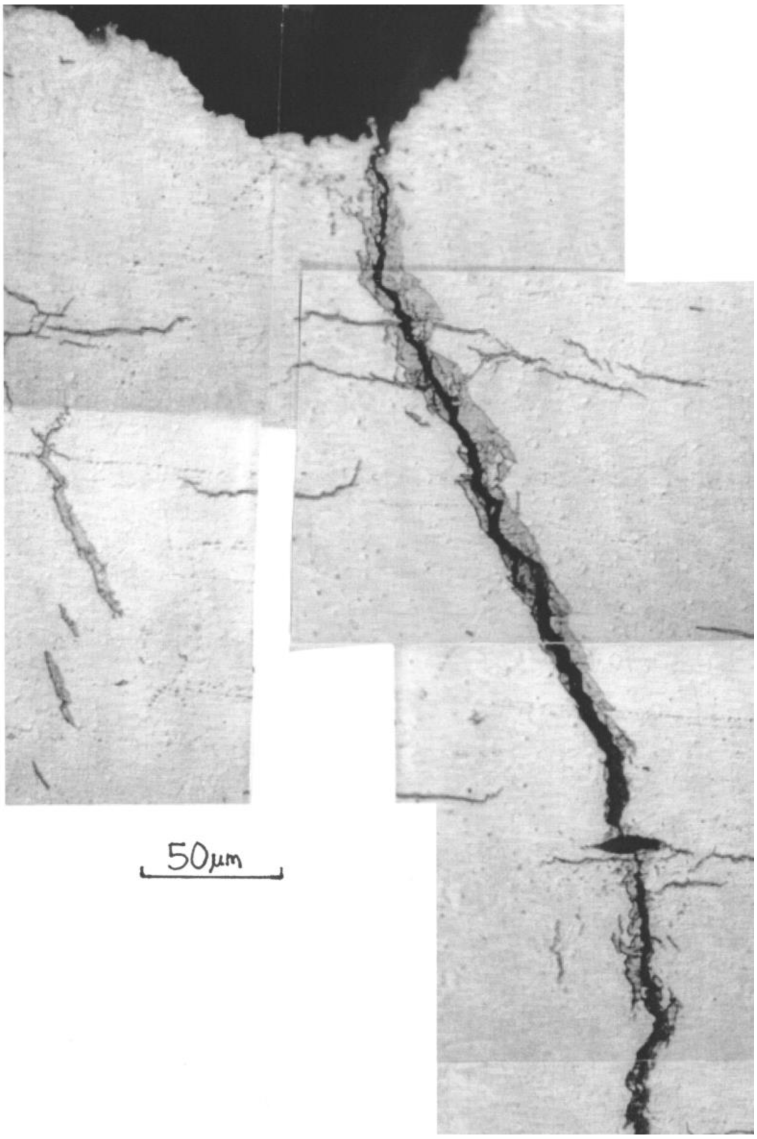

FIG. 9.290. Crack propagating through hydride in Zr-2.5Nb (photomicrograph by S. Sagat).

acoustic emission in tensile specimens of Zr-2.5Nb containing 100 ppm (0.09 at.%) radial hydrides but only up to about 413 K (140°C), as shown in Fig. 9.295. At higher temperatures no hydride cracking was detected and the strength followed plastic yield rather than fracture. In ring tensile tests on Zircaloy-2 containing 90 to 130 ppm (0.81 to 1.17 at.%) radial hydrides, the failure strain increased from close to zero at 373 K (100°C) to that of as-received material, 60%, at about 473 K (200°C) in plane stress. When a notch was present the rise in ductility was postponed to 548 K (275°C) with moderate ductility, 20%, at about 573 K (300°C) [9.818].

In summary, hydrides have been shown to have the toughness of ceramics. When within the matrix of a zirconium alloy, both γ- and δ-hydrides contribute to embrittlement. Hydrides having their trace parallel with the stress tend to crack across their thickness whereas hydrides with their trace perpendicular to the stress crack along their length. Hydride cracking requires deformation of the matrix; long, hydride platelets perpendicular to a tensile stress may crack before the 0.2% yield strength is attained. The stress to crack hydrides is strongly correlated with the matrix strength. Triaxiality augments the imposed stress and increases the stress to crack the hydride. A temperature can be reached where the stress imposed by deformation of the matrix is insufficient to crack the hydride. This temperature is raised by orienting the hydrides to have their trace perpendicular to the stress and by increasing triaxiality. It is these cracked hydrides that are the source of concern for reduced ductility.

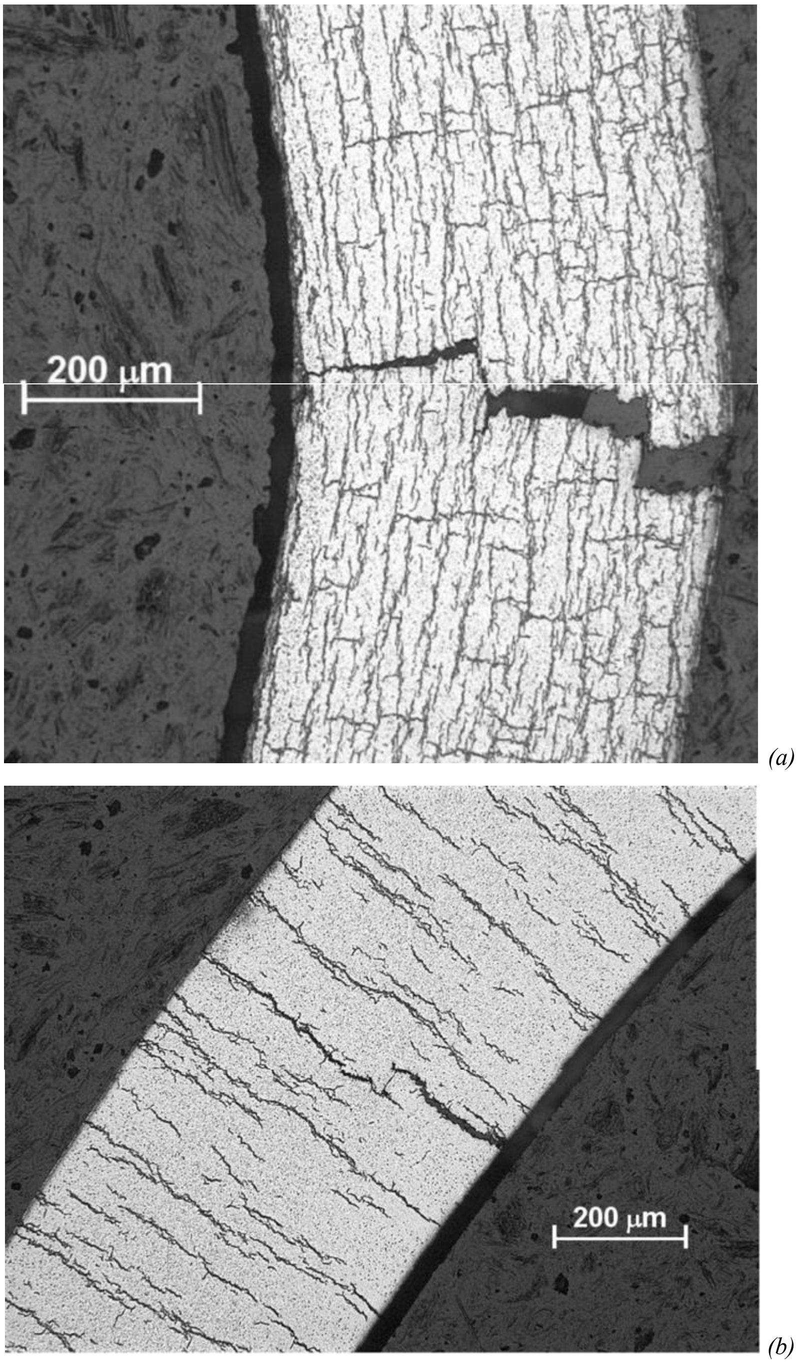

FIG. 9.291. Through-wall crack propagating through radial and circumferential hydrides in Zirlo: (a) 630 ppm (5.4 at.%) hydrogen; (b) 180 ppm (1.6 at.%) hydrogen [9.749].

9.7.5. The effect of hydrides on short term mechanical properties

In the early 1950s, low notch-impact values were observed in specimens machined from some ingots [9.822, 9.823]. This poor performance was related to the hydrogen concentration, which in turn was associated with the presence of a second phase identified as a hydride. A transition temperature was observed [9.824], as shown in Fig. 9.296; it was not only a transition from brittle, low energy to ductile, high energy fracture but represented a change from unstable to stable fracture, as demonstrated in slow bend tests [9.825, 9.826]. The transition temperature increased, and the range of transition temperature decreased with increases in hydrogen concentration, as shown in Fig. 9.296, which is based on impact tests, and in Fig. 9.297, which is based on the transition from unstable to stable cracking in

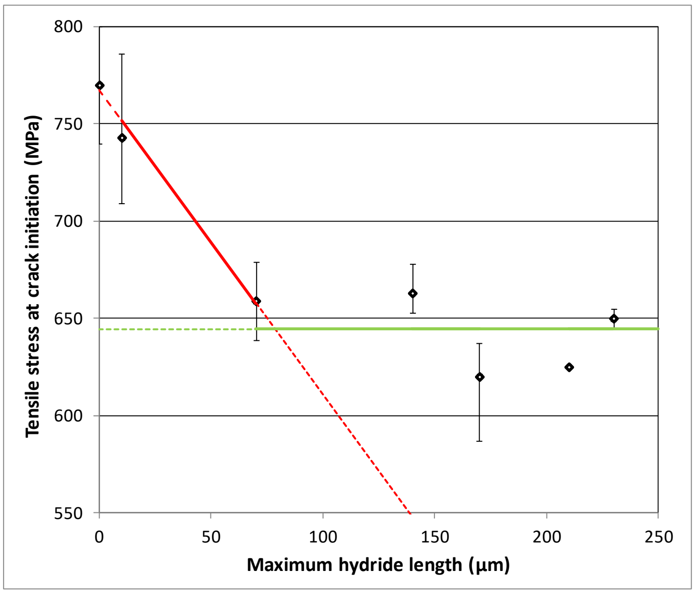

FIG. 9.292. Dependence on maximum hydride length of tensile stress required to initiate cracking in hydrides in Zr-2.5Nb at room temperature [9.819].

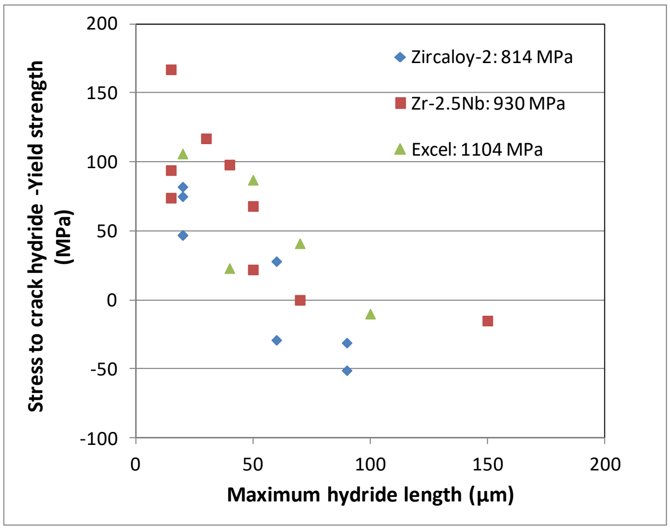

FIG. 9.293. Illustration of the effect of hydride length on the stress to crack the hydride in notched tensile specimens at room temperature: below a hydride length of about 50 µm macro-plastic flow is required (based on [9.816]).

slow bend tests on annealed zirconium. The transition temperature was sensitive to material composition, through its effect on the mechanical properties of the zirconium matrix. For example, the transition temperature was very low when the oxygen concentration was low; with 100 ppm (0.9 at.%) hydrogen, a crack was stable under 273 K (0°C) with 380 ppm (0.22 at.%) oxygen but the transition increased to between 323 and 343 K (50 and 70°C) when the oxygen concentration was 1300 to 1600 ppm (0.74 to 0.91 at.%). In annealed zirconium containing 100 ppm (0.9 at.%) hydrogen, the transition temperature based on crack stability increased by about 250°C with a strain rate increase of 10^7, as shown in Fig. 9.298 [9.825]; similarly in 26% cold worked Zircaloy-2 containing 180 ppm (1.61 at.%) and 700 ppm (6.0 at.%) hydrogen, the transition temperature based on fracture energy increased by about 120°C when the strain rate was increased by a factor of about 2 × 10^4 [9.827], as shown in Fig. 9.299.

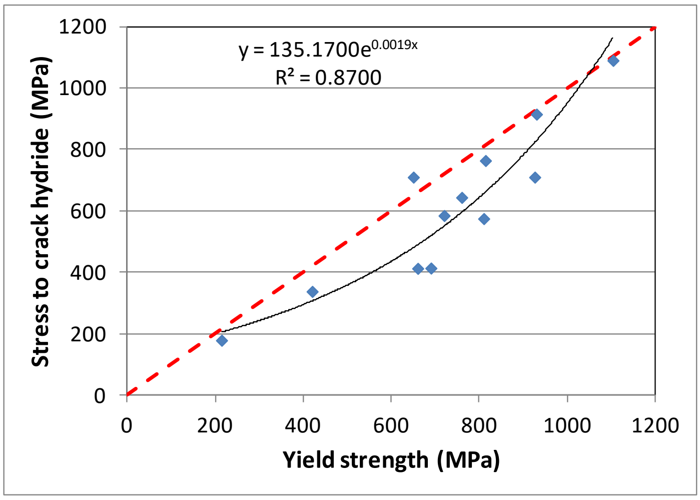

FIG. 9.294. Relationship between yield strength and stress to crack embedded hydrides in zirconium, Zircaloy, Zr-2.5Nb and Excel. Dotted red line is perfect linear correlation whereas the best correlation for values is exponential (black solid line) as compared with experimental points (blue diamonds), with a threshold stress of 135 MPa to crack a hydride [9.806, 9.808–9.810, 9.813, 9.815–9.819].

The microstructure of both the hydride and the metal matrix affects ductility. The size, spacing and orientation of the hydrides control the volume of cracks while the metal controls the condition to crack the hydrides and the resistance to crack extension between hydrides. Some examples follow:

- In a tensile test, when the normal to the hydride plates was perpendicular to the axis of tensile stress, very large concentrations of hydrogen, over 500 ppm (4.4 at.%), were necessary to produce a loss of ductility in Zircaloy-2 at room temperature [9.828].
- In recrystallized Zircaloy-4 containing up to 950 ppm (8.0 at.%) hydrogen and tested at room temperature, intergranular hydrides started to crack at a plastic strain of about 0.2 while transgranular hydrides cracked just before final rupture [9.829].

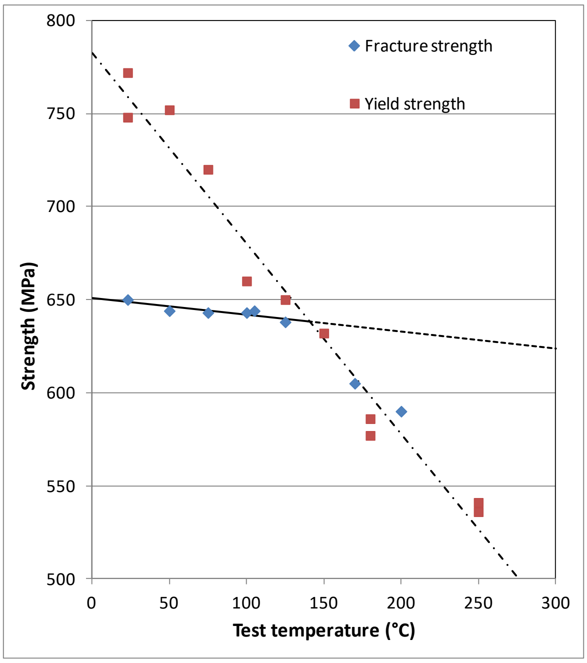

FIG. 9.295. Temperature dependence of fracture strength of hydride and yield strength of Zr-2.5Nb; average hydride length of 85 µm and t_l/l_l of 0.022 [9.819].

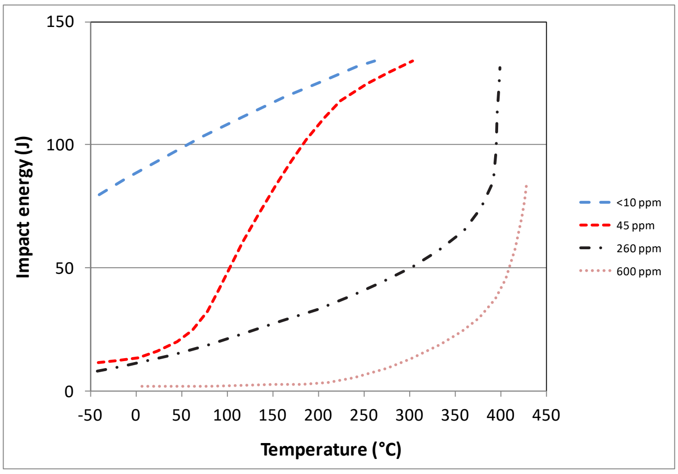

FIG. 9.296. Effect of temperature and hydrogen concentration on impact energy of zirconium [9.824].

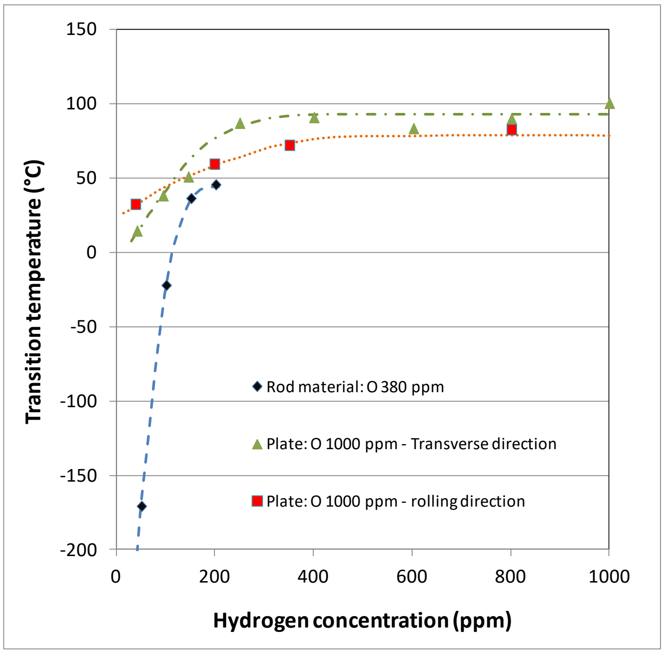

FIG. 9.297. Effect of hydrogen concentration on transition temperature based on transition from unstable to stable cracking in slow bend tests on pure zirconium [9.825, 9.826].

- A transition between ductile and brittle behaviour with hydrogen concentration was observed in ring tensile tests at 293 K (20°C) on Zircaloy materials containing large amounts of hydrogen. In stress relieved material the reduction in area declined gradually from 50% to 0% over the range of hydrogen concentration of 1500 to 2400 ppm (12 to 18 at.%) while in recrystallized material the drop in ductility was sudden at about 800 ppm (6.8 at.%) hydrogen, as shown in Fig. 9.300 [9.830].
- A hydrogen concentration of 100 ppm (0.9 at.%) reduced tensile ductility in pure and commercially pure zirconium when the grain size was large; no effect was observed when the grain size was 10 μm but when the grains were grown to 100 to 200 μm the reduction in area was approximately halved [9.806, 9.831].
- Very low failure strains at room temperature were attributed to a continuous grain boundary network of hydride formed when 600 to 800 ppm (5.2 to 6.8 at.%) hydrogen were added to annealed zirconium [9.812, 9.830]. Such a continuous network depends on the Zr alloy

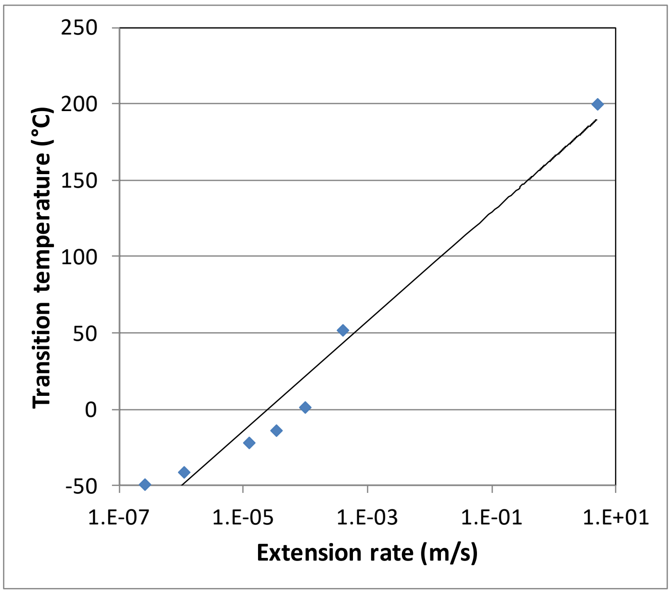

FIG. 9.298. Dependence on strain rate of transition temperature based on crack stability in annealed zirconium containing 100 ppm (0.9 at.%) hydrogen [9.825].

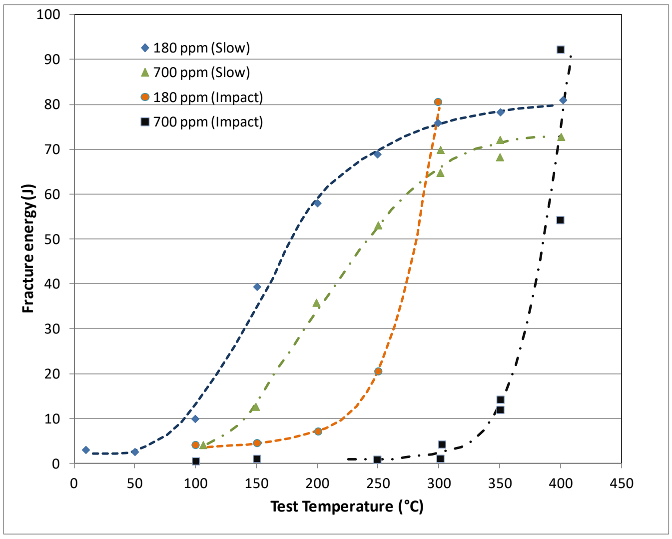

FIG. 9.299. Change in transition temperature, based on fracture energy, by increase in deflection rate in Zircaloy-2 containing two hydrogen concentrations. 'Slow' corresponds to a deflection rate of 2.3 × 10^{-4} m/s and 'Impact' corresponds to a deflection rate of 5 m/s [9.827].

microstructure. Full coverage was achieved more easily with a Thomson–Widmanstätten structure than with a recrystallized structure. At room temperature the reduction in area was zero with the former structure containing about 200 ppm (1.8 at.%) hydrogen whereas about 750 ppm (6.4 at.%) hydrogen were required with the latter structure for complete embrittlement [9.832, 9.833].

- In zirconium containing 250 ppm (2.2 at.%) hydrogen and with a grain size of about 70 µm, the elongation was found to decrease from about 14% down to 3% as the thickness of the sheet specimen was decreased from 0.53 mm to 0.13 mm [9.834]; this behaviour was ascribed to a continuous network of hydride across the thickness in some parts of the specimen when it was very thin.

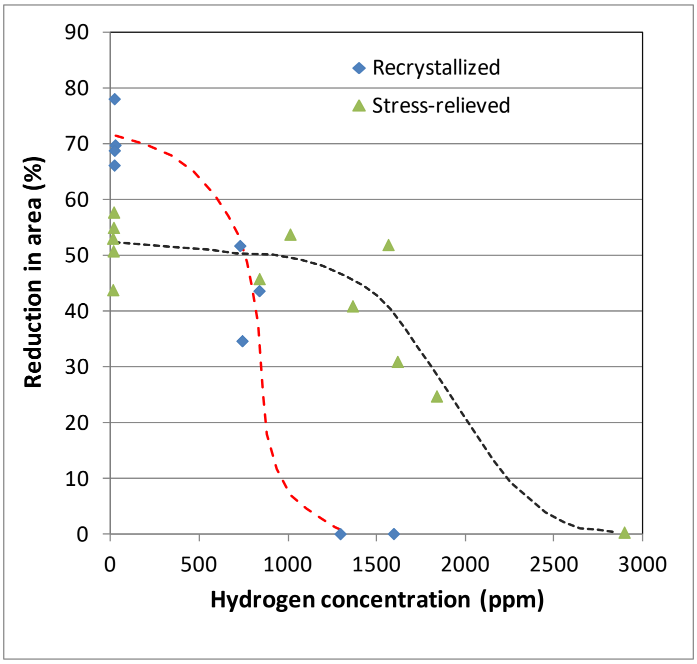

FIG. 9.300. Effect of hydrogen concentration on ductility in ring-tensile tests on recrystallized and stress relieved Zircaloy [9.830].

In pure zirconium, when hydrides were finely divided after quenching into water from above the solvus temperature, the fracture strain was high and the strength was increased by (hydrogen concentration)$^{0.5}$ whereas material quenched from well below the solvus temperature or slowly cooled from above the solvus temperature contained large hydride precipitates and were weaker and had much lower fracture strains [9.745, 9.835]. For instance, material with a grain size of 60 µm containing 410 ppm (3.6 at.%) had a strength of 417 MPa and fracture strain of 42% when quenched from 873 K (600°C) but these quantities decreased to about 275 MPa and 15% when the material was quenched from 573 K (300°C) or slowly cooled from 873 K (600°C). Similar effects were observed in impact tests on Zr-2.5 wt% Sn. Specimens containing 147 ppm (1.32 at.%) hydrogen quenched from 1273 K (1000°C) had similar behaviour as the <10 ppm material depicted in Fig. 9.296, but after ageing for 3 h at 588 K (315°C) the behaviour was qualitatively the same as the 260 ppm material [9.836].

The ductility of zirconium depends on the stress state as well as crystallographic texture [9.837–9.839]. Figure 9.301 depicts the effect on ductility of the ratio of hoop stress to axial stress, σ_H/σ_A, in Zircaloy-4 fuel cladding along with the effect of texture. With a strong radial texture, the minimum ductility was found when $\sigma_H/\sigma_A = 1$. These effects are exacerbated by cracking of hydrides. When the hydrides in a 0.8 mm thick sheet of Zircaloy-2 were cracked across their thickness, the minimum ductility was obtained with equibiaxial tension [9.840]. The sensitivity of embrittlement to the presence of notches is demonstrated from tensile specimens machined from impact specimens of commercially pure zirconium [9.502]; at 293 K (20°C) a hydrogen concentration of 100 ppm (0.9 at.%) reduced the impact energy by 70% while the reduction in area in a tensile test was unaffected. In tensile tests at room temperature, the presence of a notch promoted hydride embrittlement [9.812, 9.841–9.843]. Usually, zero ductility was observed with between 400 and 600 ppm (3.5 to 5.2 at.%) hydrogen. With hydrogen concentrations up to 340 ppm (3.0 at.%), heating to 373 K (100°C) was sufficient to restore ductility [9.841].

Neutron irradiation, because it both strengthens metals and promotes plastic instability, exacerbates hydride embrittlement. In impact tests the fracture energy was reduced and the transition temperature was increased [9.652, 9.844, 9.845]. With a neutron fluence over 10^{24} n/m^2 the transition temperature was shifted between 383 and 443 K (110 and 170°C) when the hydrogen concentration was 100 ppm (0.9 at.%) but the shift was lowered to between 323 and 393 K (50 and 120°C) when the hydrogen concentration was increased to 400 ppm (3.5 at.%). In irradiated fuel cladding, notched to produce a strain concentration of about 2.8, material containing between 600 and 810 ppm (5.2 and

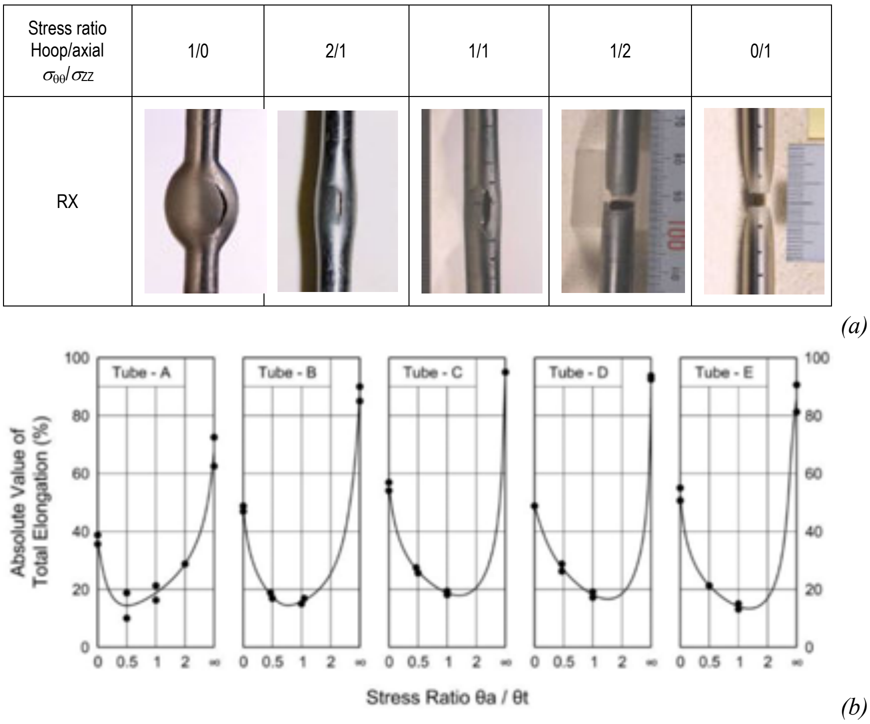

FIG. 9.301. (a) Appearance of Zircaloy-4 cladding after fracture in biaxial tensile tests with various stress ratios; (b) dependence of fracture ductility on biaxial stress ratio and texture. Angle between [0001] and radial direction: Tube A — 45°; Tube B — 20°; Tube C — 15°; Tube D — 10°; Tube E — 5°. Note that the stress ratio is σ_A/σ_H in (b); [(a) [9.839], (b) [9.837].

6.9 at.%) hydrogen had no ductility at 295 K (22°C) but the ductility was moderate and insensitive to hydrogen concentration in tests at 605 K (332°C) [9.843].

Very harmful effects were observed in tensile tests on Zircaloy-2 when the normal of the hydride plates was parallel with the tensile stress [9.809]. Very small concentrations of these hydrides could produce a large reduction in tensile ductility. The ductility depended on an effective hydrogen concentration, H_{eff}:

$$H_{\mathrm{eff}} = H_{\mathrm{T}}\,F_{\mathrm{n}} \tag{9.73}$$

where H_{T} is the total hydrogen concentration and F_{n} is a measure of the orientation of the hydrides (Section 9.7.3).

At room temperature the reduction in area was reduced to zero when H_{eff} was about 30 ppm (0.27 at.%) in Zircaloy-2, as shown in Fig. 9.302. For these tests F_{n} was controlled by stress reorientation. When tensile specimens were machined in the thickness direction of a thick plate of cold worked Zircaloy-2, the natural orientation of the hydrides was with their traces perpendicular to the tensile stress. Similar to the results with bend and ring tensile tests, the low ductility of material containing these hydrides was restored at high test temperature [9.810]; a similar saturation effect on the transition temperature with increased hydrogen concentration was observed, as shown in Fig. 9.303. Other examples are:

— Many radial hydrides were produced when a section of Zircaloy-4 fuel cladding containing 220 ppm (1.97 at.%) hydrogen was cooled from 572 to 473 K (300 to 200°C) while stressed in a ring tensile mode to 70% of the yield stress. At room temperature the ductility was zero at a fracture stress of 380 MPa [9.768].

— The stress relieved Zircaloy-4 fuel cladding containing various amounts of radial hydrides, described in Figs 9.277 and 9.278, was tested in tension [9.773]. No effect of radial hydrides on strength or ductility was discerned with stressing in the axial direction of the tubes. The properties in the hoop direction were evaluated at room temperature with a tensile stress in an arc of tubing containing a slot on the outside surface; the slot was 50% through the tube wall and 1 mm long in the circumferential direction. Both the elongation and strength were diminished by radial hydrides, as shown in Fig. 9.304. The values depended on both the total amount of hydrogen, H_T, and its distribution through F_n. The acceptance criterion for ductility was taken as 1% elongation and that for strength was 600 MPa. The dependence of the acceptance criteria on H_T and H_{eff} are summarized in Table 9.46.

TABLE 9.46. REFERENCE CONCENTRATIONS OF RADIAL HYDRIDES FOR BRITTLE FRACTURE OF STRESS RELIEVED ZIRCALOY-4 CLADDING AT ROOM TEMPERATURE [9.773]

	1% strain criterion		600 MPa criterion	
H_T (ppm)	H_{eff}	%	H_{eff}	%
130	74	56.9	60	46.2
250	157	62.8	100	40
320	106	33.1	75	23.4
600	37	6.2	33	5.5

— Cladding made from Zr-1Nb-1Sn-0.1Fe and containing 250 and 500 ppm (2.23 and 4.36 at.%) hydrogen was held in a ring tensile configuration, heated to 673 K (400°C), stressed to 150 MPa after 2 hours and cooled under load at 0.3, 2.0, 4.0 or 15.0°C/min [9.846]. With the lower hydrogen concentration, F_n declined from 0.75 to 0.42 as the cooling rate increased while with the upper concentration the decline was from 0.45 to 0.15. The radial hydrides tended to be shorter as the cooling rate and hydrogen concentration increased; the latter effect was caused by the circumferential hydrides limiting the growth of radial hydrides. At room temperature the elongation was zero for all the material containing 250 ppm (2.23 at.%) hydrogen, except after a cooling rate of 15.0°C/min whereas with 500 ppm (4.36 at.%) hydrogen, only the material with the slowest cooling rate was completely brittle. This behaviour was attributed to the circumferential hydrides diverting the crack and involving the zirconium alloy matrix in the

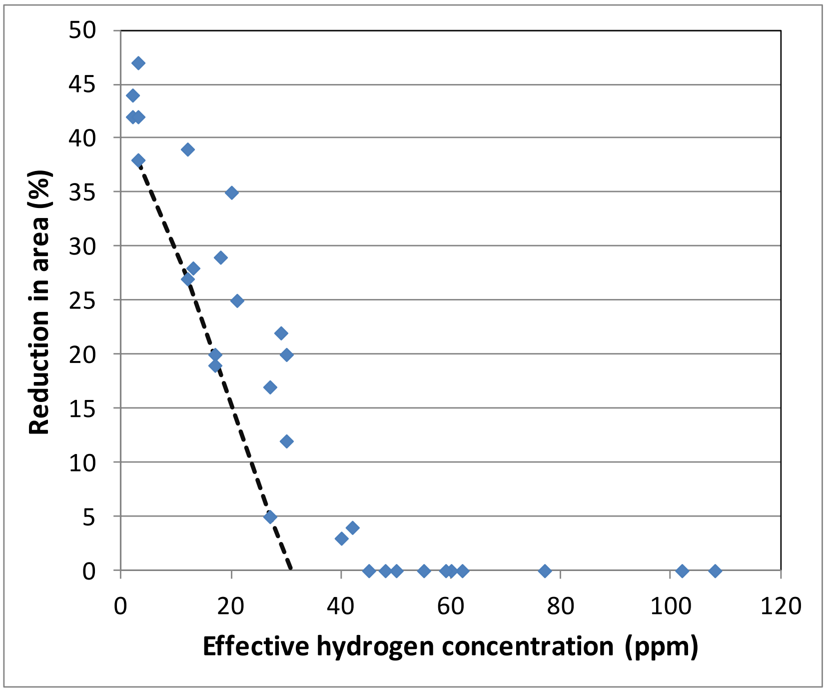

FIG. 9.302. Large reduction in tensile ductility at room temperature of Zircaloy-2 by hydrides with traces perpendicular to the stress axis. Zero ductility with $H_{eff} \geq 30$ ppm [9.809].

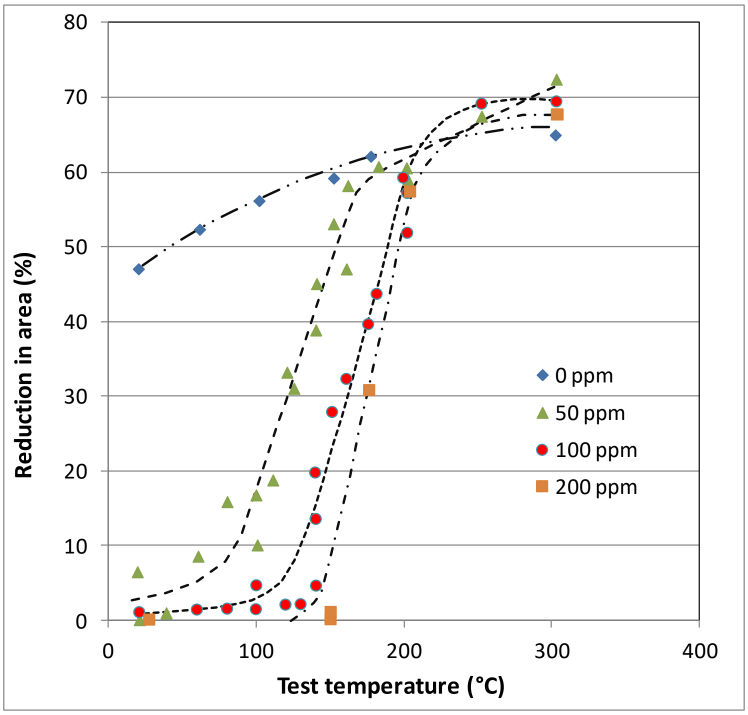

FIG. 9.303. Temperature dependence of tensile ductility of cold worked Zircaloy-2 containing hydrides with traces perpendicular to the stress axis [9.810].

fracture process. The limit of H_{eff} for completely brittle behaviour was between 75 and 100 ppm (0.68 and 0.90 at.%).

— The behaviour of unirradiated Zircaloy-4 cladding and cladding after a burnup of 67 MWd/kg (1.4×10^{26} n/m^2, $E > 1$ MeV) was compared [9.770]. Hydrogen concentrations ranged from 250 to 900 ppm (2.23 to 7.59 at.%). In both materials the initial hydride orientation was circumferential. In the irradiated cladding, the concentration of hydrogen was larger towards the outside surface because of the temperature gradient during service in the power reactor (see Section 9.7.2.3), but again confirmed the lack of hydride reorientation during normal reactor operation. Reorientation was achieved with a ring tensile configuration using a temperature of 673 K (400°C) for 2 h followed by cooling at 10°C/min under tensile stresses between 0 and 190 MPa. During the treatment about 5% of the irradiation hardening was recovered; also, hydrogen diffused towards the centre of the cladding to flatten the hydrogen gradient. Although a gradient in hydride orientation was observed that was caused by the stress gradient in the ring specimens, the threshold stress for reorientation was determined to be about 80 MPa for both materials. The ductility was evaluated by ring compression testing at room temperature and 423 K (150°C). Using finite element analysis, the maximum tensile stresses were calculated to be at 12 and 6 o'clock on the inside surface and 3 and 9 o'clock on the outside surface, while the maximum tensile hoop strain was at 12 and 6 o'clock. Both these results indicate 12 and 6 o'clock on the inside surface as the most likely position for crack initiation during this kind of test. The cracks followed the hydrides as shown in Fig. 9.291. In unirradiated material, unstable cracking was accompanied by a single load drop in the load displacement curves when propagating through radial hydrides, similar to that shown in Fig. 9.291(b). When circumferential hydrides were present, they diverted the crack, encouraging stable cracking and requiring a continuous strain to propagate the crack in a zig-zag path, Fig. 9.291(a). The load displacement curves for the irradiated material were characterized by sudden load drops that corresponded with crack propagation through regions with radial hydrides partway through the cladding wall and stopping at circumferential hydrides. The hoop stress and hoop strain required to initiate cracking were calculated as a function of the hoop stress used to reorient the hydrides and compared with experimental data.

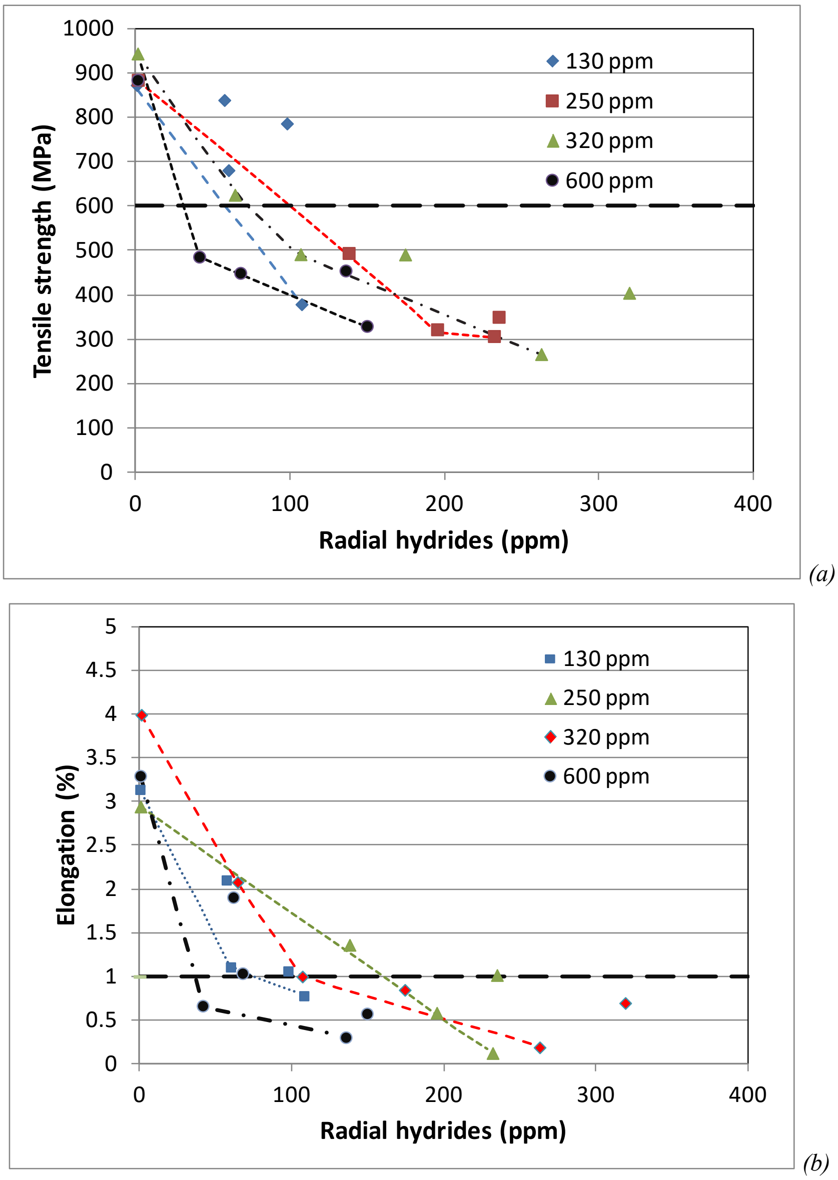

FIG. 9.304. Tensile strength (a) and elongation (b) of Zircaloy-4 as a function of H_{eff} at room temperature [9.773].

A large reorienting hoop stress provided radial hydrides. The results indicate another type of ductile–brittle transition: as the number of radial hydrides increased with an increase in reorientation hoop stress above 90 MPa, embrittlement followed, as shown in Fig. 9.305. Little effect of irradiation on hydride reorientation was detected. Cracking was controlled by radial hydrides rather than by irradiation.

— Similar experiments on Zircaloy-4 and ZIRLO fuel cladding after burnups up to 70 MWd/kgU [9.749] have supported the above behaviour. Post-irradiation metallography confirmed that radial hydrides were not formed during normal reactor operation, but a hydride rim was observed on the outside layer of the cladding (see Section 9.7.2.3). Hydride reorientation was induced by pressurizing a section of tube at room temperature, sealing it and allowing the heating to 673 K (400°C) to supply hoop stresses of 110 and 140 MPa through the ideal gas law. The cooling rate was 5°C/h. F_n was characterized by a radial HCF. The criterion to distinguish brittle from ductile behaviour in a ring compression test was 2% offset strain before

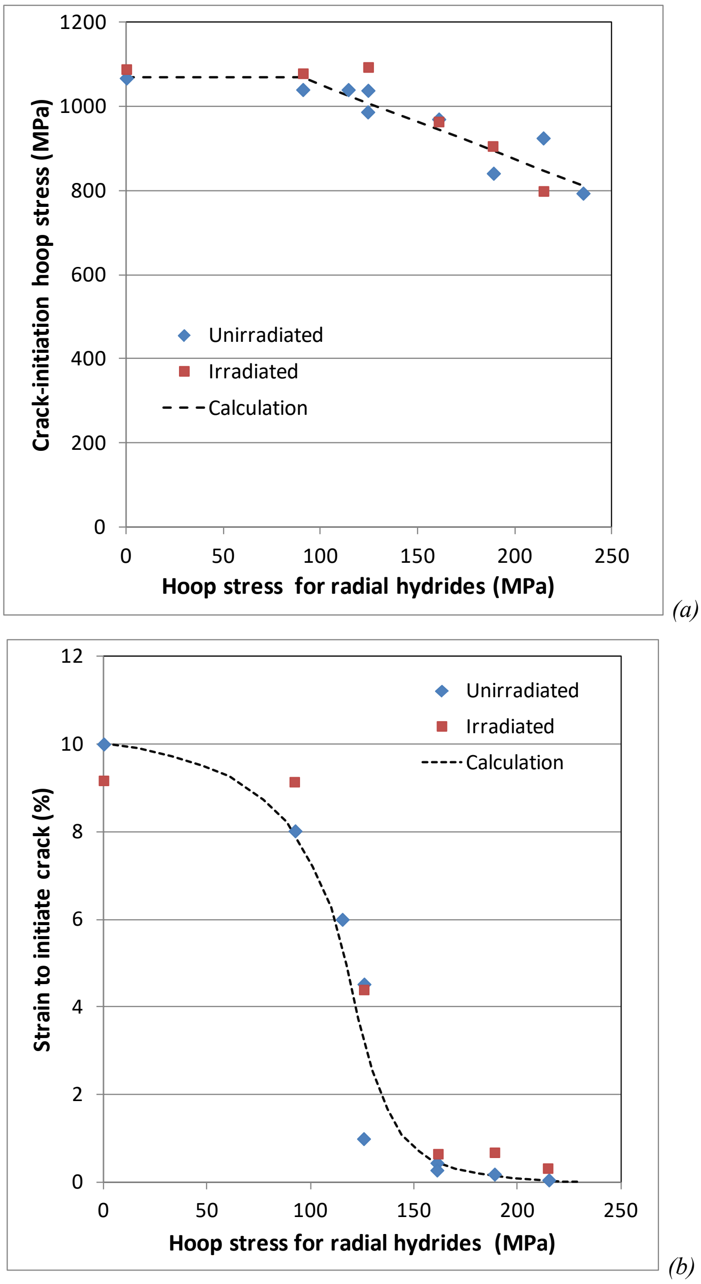

FIG. 9.305. The hoop stress (a) and hoop strain (b) for crack initiation after a heat treatment with a hoop stress to form radial hydrides. Zircaloy-4 material irradiated to 1.4 × 10^{26} n/m^2 (E > 1 MeV). Calculation by finite element analysis (based on [9.770]).

the first crack extended > 50% through the clad wall. The results are summarized in Fig. 9.306. A transition temperature is apparent, similar to that shown in Figs 9.296, 9.299 and 9.303. The fitted lines cross the 2% ductility criterion as follows: ZIRLO with F_n 65±17%: 458 K (185°C); ZIRLO with F_n 30±12%: 398 K (125°C); Zircaloy-4 with F_n 16±4%: 328 K (55°C); Zircaloy-4 with F_n 9±5%: <293 K (<20°C).

— Some Zircaloy-2 claddings for BWRs contain a soft inner liner of zirconium that tends to getter the hydrogen (see Section 9.7.2.4) resulting in only the outer 50% to 60% of wall thickness containing hydrides. When irradiated material was subjected to the reorientation process, it was mainly these hydrides that became radial [9.775]. In the experiments, the cladding was stressed by internal pressure and the cooling rates from the reorientation temperature varied from 0.5 to 0.01°C/min. With a reorientation temperature of 573 K (300°C), a maximum of about 60 ppm (0.54 at.%) hydrogen would be available for reorientation that resulted in a moderate hoop stress dependence of F_n, based on hydride lengths rather than number. With a reorientation temperature of 673 K (400°C), a maximum of about 170 ppm (1.53 at.%) hydrogen would be available and much reorientation was produced with moderate hoop stresses, as shown in Fig. 9.307. When no liner was present, all 40 ppm (0.36 at.%) hydrogen formed as radial hydrides across the full thickness of the cladding with a reorientation temperature of 573 K (300°C) and hoop stress of 70 MPa. In ring compression tests at room temperature, when the liner was absent, cracking started on the inside surface at 12 or 6 o'clock, as shown in Fig. 9.308, as expected from the previous paragraphs. When present, the liner's ductility

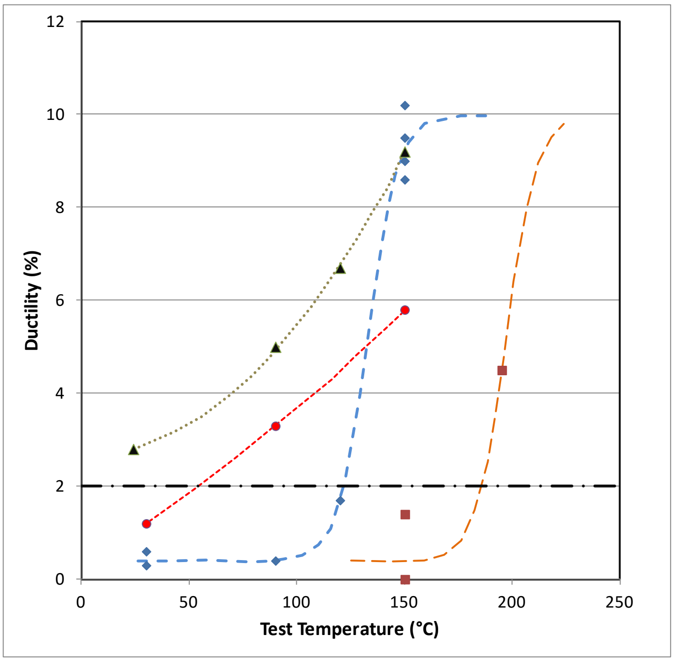

FIG. 9.306. Temperature dependence of ductility in ring compression tests on irradiated fuel cladding after hydride reorientation by cooling at 5°C/h °C/min from 673 K (400°C). Zircaloy-4: black triangles: reorientation stress 110 MPa, F_n of 9 ± 5%; red circles: reorientation stress 140 MPa, F_n of 16 ± 4%; Zirlo: blue diamonds: reorientation stress 110 MPa, F_n of 30 ± 12%; maroon squares: reorientation stress 140 MPa, F_n of 65 ± 17%. Based on [9.749].

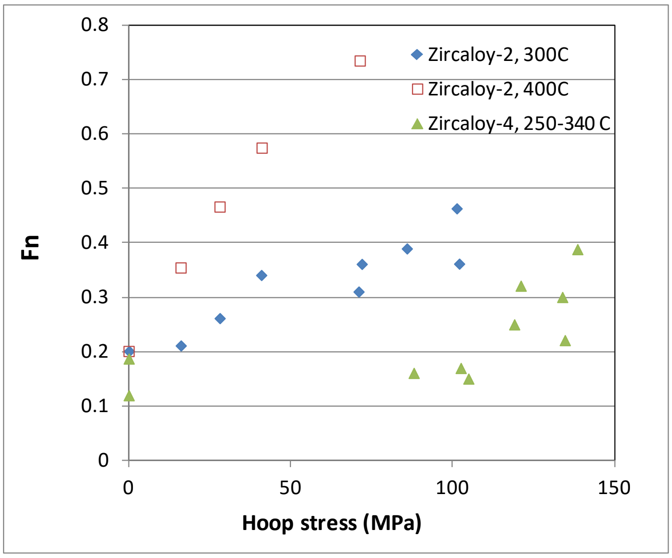

FIG. 9.307. Development of reorientation of hydrides with two maximum temperatures and a cooling rate of 0.5 °C/min in recrystallized Zircaloy-2 cladding with a liner, irradiated in BWRs. Similar measurements on stress relieved Zircaloy-4 from PWRs. F_n was evaluated by hydride length (based on [9.775]).

suppressed cracking at the 12 and 6 o'clock positions. Cracking started from the outside surface at the 3 and 6 o'clock positions and sometimes the liner–matrix interface delaminated, as shown in Fig. 9.309. Samples of Zircaloy-4 from PWRs were tested by the same methods. The results of reorientation measurements indicated less susceptibility to form radial hydrides as the threshold stress appeared higher and the amount of hydride reoriented was lower than in Zircaloy-2, as shown in Fig. 9.307.

— When cold worked Zr-2.5Nb pressure tube material containing 100 ppm (0.9 at.%) hydrogen was cooled from 623 K (350°C) under a stress of around 170 MPa, the full cross-section

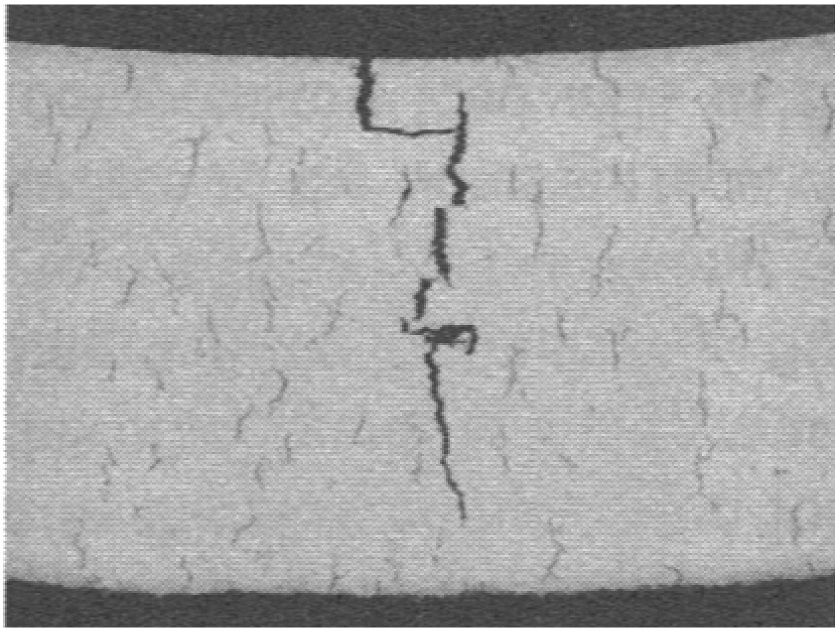

FIG. 9.308. Cracking initiated on the inside surface of irradiated Zircaloy-2 with no liner during a ring compression test at room temperature. Hydride orientation conditions were maximum temperature 573 K (300°C), cooling rate of 3°C/h and hoop stress 70 MPa. [9.775].

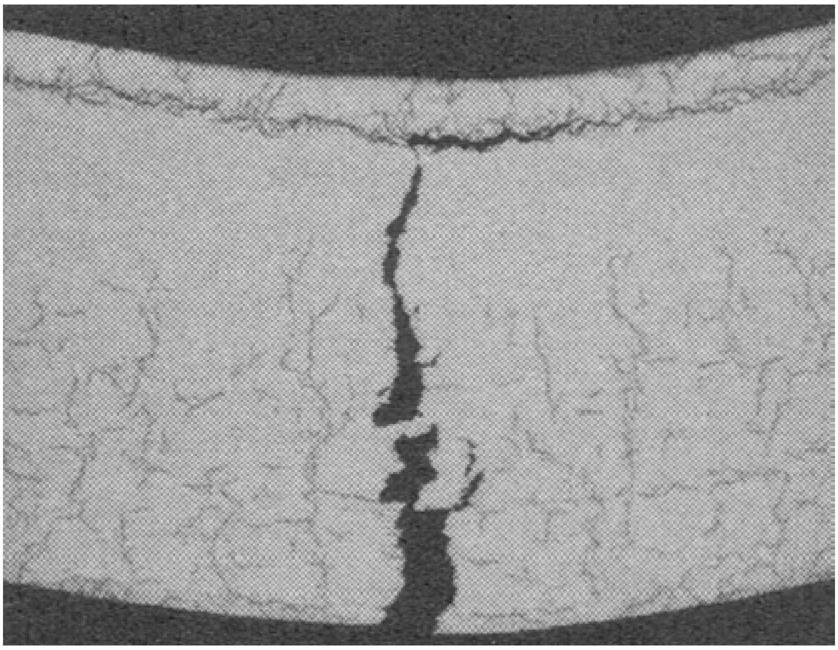

FIG. 9.309. Cracking initiated on the outside surface of irradiated Zircaloy-2 with a liner during a ring compression test at room temperature. Hydride orientation conditions were maximum temperature 673 K (400°C), cooling rate of 0.5°C/min and hoop stress 28 MPa. Note the delamination at the liner-matrix interface [9.775].

contained reoriented hydrides [9.763]. The tensile ductility was much affected at low test temperatures. At room temperature the reduction in area was zero but recovered to about 50%, similar to that of unhydrided material, around 423 K (150°C). The total elongation behaved similarly.

In fracture mechanics tests, hydrides were found to reduce fracture toughness. Often in the tests the strict validity criteria were not met, but the effects of the hydrides were clear. As with the other mechanical tests, toughness can be reduced as the hydrogen concentration is increased but is restored as the test temperature is raised. Tests at room temperature on sheets of Zircaloy-2 and Zr-2.5Nb showed that the effect of hydrides on toughness depended on the distribution of the hydrides [9.847]. Both materials were cold rolled either 20% or 40%; the Zircaloy-2 was also tested in the annealed condition while the Zr-2.5Nb was also tested in the quenched and aged condition. Single edge notch specimens were used. When the hydrogen concentration was very low, toughness values were in the range 60 to 110 MPa√m and were insensitive to microstructure and direction, indicating that crystallographic texture and grain shape had little effect on toughness. The hydrides were well aligned in the highly cold worked materials. The toughness of these materials was not affected by hydrogen concentrations up to 500 ppm (4.4 at.%) when the normal to the crack plane was in the transverse direction of the sheet (i.e. perpendicular to the normal of the hydrides). When tested with the crack plane normal to the thickness direction (i.e. parallel to the normal of the hydrides), 100 ppm (0.9 at.%) hydrogen was sufficient to reduce the toughness to about 20 MPa√m. In all the other material conditions, some hydrogen embrittlement was discerned in the transverse direction because the hydrides were less well aligned.

Davies and Stearns [9.848] tested cold worked Zircaloy-2 pressure tube material containing radial hydrides using compact tension specimens. As the HCC increased the room temperature toughness at maximum load decreased modestly; with an HCC of about 0.3, the toughness was 40 MPa√m, which reduced to 23 MPa√m as HCC was increased to 0.85. The transition temperature behaviour was greatly affected by HCC. At a low value of HCC, toughness increased linearly with temperature reaching upper shelf behaviour, over 150 MPa√m, at 250 K (175°C). With an HCC of 0.85, the toughness did not start to increase until the test temperature reached 500 K (230°C), then the transition was very steep as the upper shelf was attained at 540 K (270°C). Cold worked Zr-2.5Nb pressure tube material [9.849, 9.850] and irradiated and cold worked Zircaloy-2 and Zr-2.5Nb [9.851–9.853] behaved in a similar manner. In irradiated Zircaloy-2 fuel cladding, the toughness at 573 K (300°C) with 400 ppm (3.5 at.%) hydrogen is similar to that of material containing little hydrogen, between 70 and 120 MPa√m, but at higher hydrogen concentrations the toughness declines rapidly reaching 20 MPa√m at 1000 ppm (8.4 at.%) hydrogen [9.854].

The fracture process consists of crack initiation leading to voids and crack propagation by linking the voids to final rupture. The number of cracks increases continuously with strain and leads to continous void formation. The voids have a range of sizes and shapes depending on when they form and which hydride cracks. The final rupture is by ductile fracture through the zirconium matrix. A transition from unstable, low energy, low strain fracture to stable, high energy, high strain fracture is observed either as a function of hydrogen concentration, hydride distribution or temperature. The latter could have several explanations:

- Dissolution of hydride. The quantity of hydride decreases as the temperature is increased and leads to a smaller amount of embrittling agent. The extra hydrogen in solution may affect the strength and ductility of the zirconium matrix. These two effects are too small to explain the transition because the solubility limit dictates that the changes in concentration are low over the relevant temperature range (Section 9.7.1.2). For example, the impact curves for specimens containing 100 ppm (0.9 at.%) hydrogen were similar to calculated curves for material containing 100 ppm (0.9 at.%) hydrogen precipitated as hydride [9.855], as shown in Fig. 9.310. Having transition temperatures <273 K (0°C), as shown in Fig. 9.298, where changes with temperature in hydride and hydrogen concentration in solution are tiny, also confirmed that lack of hydrides and increase in hydrogen in solution are not the explanation.
- Ductility of hydride. Some evidence has been presented that hydrides can deform plastically during tensile tests of Zircaloy fuel cladding [9.856, 9.857]. The individual hydrides that make

up the stacks forming the hydride stringers can follow the deformation of the zirconium alloy matrix (e.g. in the neck formed during a tensile test), and give the appearance of ductility [9.810, 9.817, 9.841]; detailed examination often reveals cracks and incipient voids in these hydrides. As described in Section 9.7.4, hydrides have very low toughness up to at least 673 K (400°C) so an increase in hydride ductility does not explain the transition.

- Reduction in local stress to crack hydride. As indicated in Section 9.7.4, a critical temperature may be reached where insufficient stress is available to crack the hydride by plastic deformation of the zirconium matrix, indicating a change in behaviour. This process will contribute to the transition. For example, Fig. 9.298 shows that the transition temperature increased by about 250°C over a change in extension rate of about 10^7; in α zirconium the strength change with such a strain rate change [9.52] was similar to that for the range of transition temperature [9.36], about 250 MPa.
- Change in fracture mode. Although the transition is often called a brittle to ductile transition, unlike in carbon steels, no change in fracture mode has been discerned through the temperature range of the transition. The fracture surfaces consisted of a mixture of cleavage of hydride and ductile fracture of the metal matrix. Figure 9.289 shows the crack in a massive hydride progressing only a further short distance when it encounters the ductile zirconium matrix. For brittle behaviour, the cracks in the hydrides — whether along their length or across their thickness — must link up in an unstable manner through the metal matrix. Decreasing the spacing between hydrides, by increasing the hydrogen concentration, by heat treatment or by reorientation, reduces the amount of zirconium that is available to withstand cracking. The interhydride spacing and transition temperatures saturate with hydrogen concentration in a similar fashion emphasizing their direct association [9.826]. A critical condition must be exceeded for unstable rupture of the remaining matrix ligaments. The temperature dependence leading to the transition arises from the strength or ductility of the metal matrix suppressing the attainment of the critical condition at low strains.

The change in behaviour at a single temperature with either hydrogen concentration or distribution of hydrides supports the notion of the transition being controlled by the zirconium matrix ligaments between cracked hydrides. This picture has been modelled by associating the interhydride spacing, and therefore intercrack spacing, with various criteria for unstable fracture:

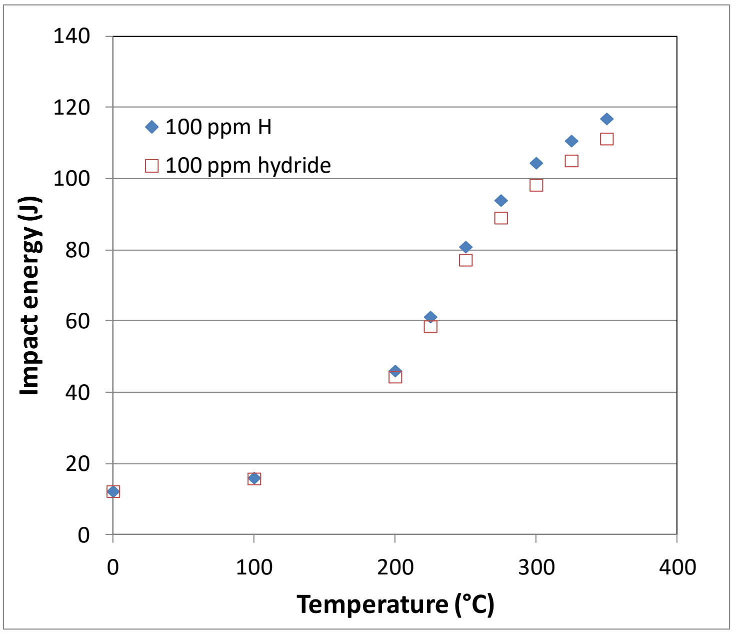

FIG. 9.310. Temperature dependence of Charpy impact energies in Zr-2.5Nb demonstrating the small effect of hydride solubility on the transition behaviour (based on [9.855]).

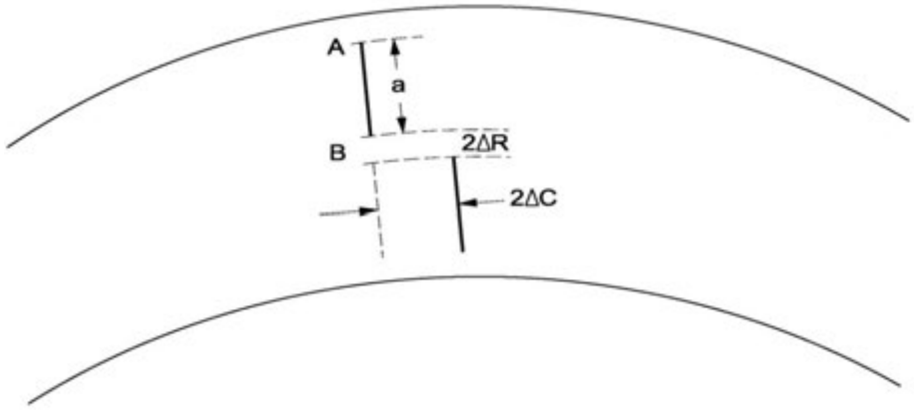

FIG. 9.311. Geometry of hydrides of length a *in a tube with outboard end at A and inboard end at B. 2ΔR is spacing between hydride tips and 2ΔC is circumferential spacing of hydrides (based on model in [9.862]).*

- Achieving a critical local displacement at a stress concentration with highly confined plastic strain before general yield [9.858–9.860] was exacerbated by two coplanar cracks, representing cracked hydrides [9.502]. This geometry led to a critical interhydride spacing for unstable cracking. For example, zirconium containing 100 ppm (0.9 at.%) hydrogen was heat treated to vary the hydride distribution; during slow bending tests at 293 K (20°C), brittle behaviour was observed when the interhydride spacing was <160 μm. This type of approach highlighted the importance of the size and mechanical properties of the remaining ligament of metal in controlling fracture resistance.
- A similar model consisted of idealizing the matrix ligament between cracked hydrides and calculating the strain concentration and failure of the ligament connecting two interacting microcracks [9.861]. The array of hydrides (cracks) consisted of length $2a$, centre-to-centre spacing L and stacking spacing s. Calculations showed that of the variables, L had the greatest influence on ductility; the limiting volume fraction was greater when s was small and L large than when the reverse was the case. Calculated ductilities based on properties of the microstructure describe experimental results on Zircaloy-4. When L was small after a β heat treatment, a volume fraction of about 1% was sufficient for zero ductility but the critical volume fraction was increased to about 6% when L was increased by stress relief or recrystallization [9.833].
- Finite element analysis was used to calculate the J integral imposed at room temperature by various internal pressures and arrays of hydrides, modelled as cracks, in a Zircaloy-4 tube with an outer diameter of 10.1 and wall thickness of 0.614 mm [9.862]. The crack variables were number density, length, relative location, orientation and shape. A sharply rising J could be taken as the point of failure. The computer code allowed the numerical convergence of the mesh. Two radial cracks with the configuration shown in Fig. 9.311 were modelled, with typical results depicted in Fig. 9.312 for crack lengths of 150 μm and a pressure of 5 MPa. The two cracks strongly interacted when they were close. For a positive value of ΔR, J for the outboard end of a crack, A, increased and passed through a maximum value when ΔR was slightly negative, as shown in Fig. 9.312(a). When the overlap became large, a shielding effect was observed because of local unloading. The value of J of the inboard end of the crack, B, had a sharp maximum value when ΔR was zero, as shown in Fig. 9.312 (b). This value was much larger than for the outboard end suggesting link-up between cracks when the configuration was appropriate before the cracks extended at their outboard ends. Extending the analysis to arrays of several hydrides (cracks) showed that failure pressure was more affected by the crack/ligament ratio than the crack length, as shown in Fig. 9.313. The effect of the circumferential spacing was more pronounced with short cracks than long cracks. To assist in evaluating crack growth resistance, these results confirmed the importance of the ligaments of zirconium, which in turn are controlled by hydride continuity and concentration.

When stable cracking was modelled by finite element analysis [9.863], by applying theories of ductile rupture [9.864–9.866], the picture was linkage of voids formed at hydrides after the start of necking in ductile Zircaloy-4. Similar to the situation of cavity nucleation, growth and coalescence discussed in Section 9.2.1, a decrease in the strain to nucleate voids was followed by a corresponding strain induced rise in their volume fraction when the concentration of sites was enlarged by an increase in hydrogen concentration, as shown in Fig. 9.314. The decrease in reduction in area with increase in hydrogen concentration was accurately described. A representative simulation of ductile crack propagation in a centre crack panel depended on mesh size in the finite element analysis. The mesh size that corresponded with a good description of crack advance in Zircaloy-4 containing 1310 ppm (10.7 at.%) hydrogen was used to represent accurately crack propagation at lower hydrogen concentrations. Unfortunately, the best mesh size could not be related to any metallurgical parameter.

In summary, cracking of hydrides in zirconium alloy components can lead to unstable crack propagation at low enough strains that the behaviour can be called brittle. The ductile zirconium matrix controls whether the crack becomes unstable but the amount of zirconium available to exercise this control is influenced by the geometry of the hydrides.

9.7.6. Time dependent failure

Time dependent cracking associated with hydrogen and hydrides was recognized as an important failure mechanism in titanium alloys in the 1950s [9.867]. This failure mechanism was characterized by a crack growth rate, V_c, that was highly dependent on temperature but had low

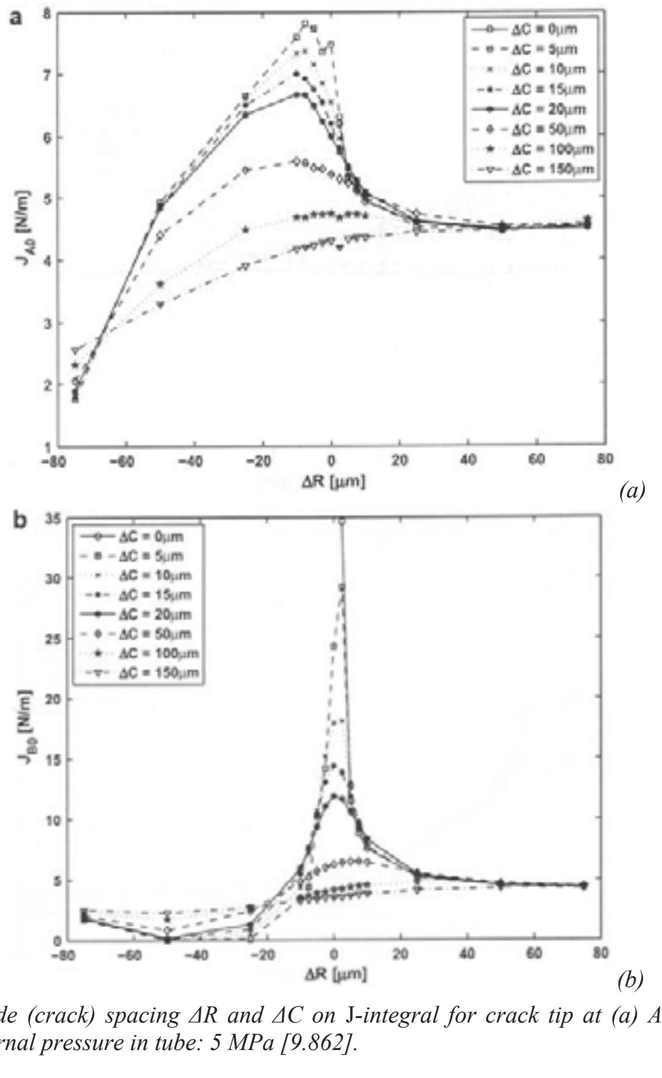

(a)

(b)

FIG. 9.312. Effect of hydride (crack) spacing ΔR and ΔC on J*-integral for crack tip at (a) A, and (b) B, in Fig. 9.311. Crack lengths: 150 µm; internal pressure in tube: 5 MPa [9.862].*

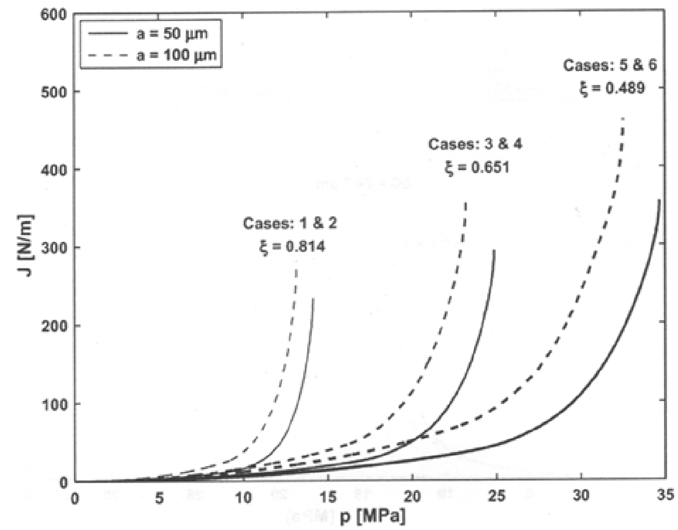

FIG. 9.313. Effect on J*-integral of internal pressure in fuel cladding for various arrays of cracks (hydrides) [9.862]. ΔC, the circumferential spacing of cracks, is zero. N is number of cracks. Case 1: N = 10; Case 2: N = 5; Case 3: N = 8; Case 4: N = 4; Case 5: N = 6; Case 6: N = 3. ξ represents the portion of tube wall thickness,* t*, containing cracks; Cases 1 and 2: 500/614; Cases 3 and 4: 400/614; Cases 5 and 6: 300/614.*

dependence on load once a threshold value was exceeded. Zirconium alloys are much more sensitive to time dependent hydride cracking than Ti alloys, yet surprisingly the phenomenon became more than a laboratory curiosity in Zr alloys only in the mid-1970s. Early indications were that Zr alloys had high tolerance to such time dependent fracture. Notched tensile specimens of Zr-1.25Al-1Sn-1Mo in the annealed condition and containing 500 ppm (4.36 at.%) hydrogen showed the characteristic behaviour of increase in time to failure as the applied stress was reduced in tests at room temperature; specimens failed in 3 hours at about half the notched UTS, in 200 hours at 0.3 notched UTS, and did not fail in over 1100 hours at 0.2 notched UTS [9.868], as shown in Fig. 9.315. Quenched and aged Zr-2.5Nb gave a slight indication of delayed failure within the limits of the test time (1000 hours), while annealed or cold worked Zircaloy was completely resistant. Östberg [9.869] found some suggestion of delayed failure in Zircaloy containing 0.09 at.% (10 ppm) hydrogen in tests at 373 K (100°C). The cracking of Zr-2.5Nb pressure tubes in CANDU and RBMK reactors in the 1970s generated much research into the phenomenon. In the literature on zirconium alloys, time dependent cracking has been known by several names[9] but the most accepted is DHC. The majority of the experiments have been done on Zr-2.5Nb pressure tubes. In most tests, the value of K_I is low enough for valid LEFM in specimens from tubes 4 to 5 mm thick. The phenomenology is similar to that in titanium alloys.

9.7.6.1. Component failure by DHC

(a) Pickering Units 3 and 4, 1974 and 1975

High residual stresses, over 500 MPa, at the rolled joints (described in Section 9.7.3) were responsible for crack initiation in Zr-2.5Nb pressure tubes after two to three years of operation, as shown in Fig. 9.280. The hoop stress from the operating pressure was at least three times lower than the residual stresses. When the cracks penetrated the pressure tube wall in 1974 (Pickering-3) and 1975 (Pickering-4), heat transport heavy water leaked and was detected in the gas annulus between the pressure and calandria tubes, and the reactor was shut down. This behaviour is an example of an

---

[9] The other names that have been used in the technical literature are: delayed failure hydrogen embrittlement, delayed hydrogen embrittlement, delayed hydrogen cracking, hydrogen assisted subcritical crack growth, hydrogen induced delayed cracking and hydride induced crack growth. Similar cracking in fuel cladding has been called corrosion hydride cracking.

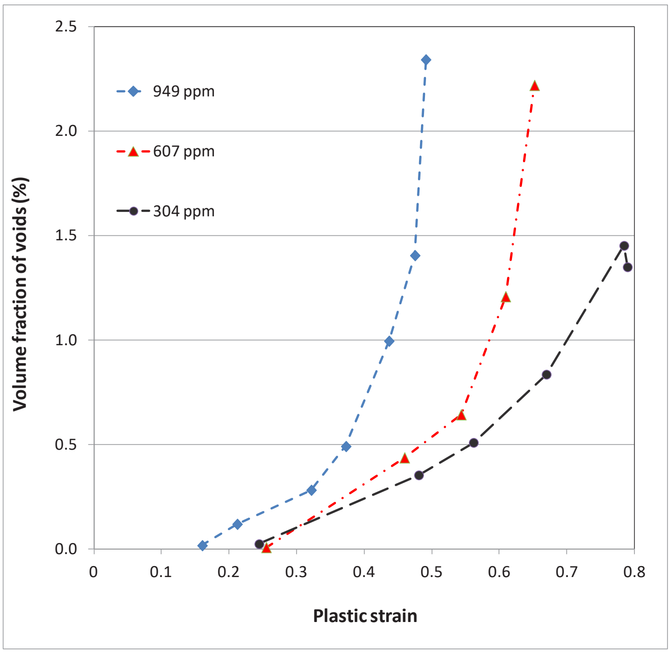

FIG. 9.314. Kinetics of nucleation of voids with plastic strain for three hydrogen concentrations (based on [9.863]).

approach to leak-before-break (LBB): detect and identify a growing and leaking but stable crack before it reaches its critical crack length (CCL) and becomes unstable. Once the leaking tubes had been identified, they were removed and replaced. Out of 780 tubes, 18 in Pickering-3 and 2 in Pickering-4 leaked [9.788, 9.870]. Only one more leaking crack was detected after the initial set of failures.

The cracks initiated on the inside surface because the residual stresses were higher at the inside than at the outside of the pressure tube. The cracks grew radially and axially in a series of bands on a plane normal to the hoop direction with a depth to length ratio of about 3, as shown in Fig. 9.316. The fracture surfaces had the characteristics of broken hydride and hydrides were observed at the tips of surface cracks, as shown in Fig. 9.317. The interpretation was that the cracks grew at low temperatures by DHC, but once the reactor was at power and the pressure tubes were at a high temperature, >523 K (250°C), cracking stopped because the low hydrogen concentration, <15 ppm (0.14 at.%), was all in solution, and the crack surfaces oxidized. Cracking continued during subsequent reactor shutdowns, and the stopped crack continued to oxidize during power production. Each band on the fracture surface corresponded with a reactor shutdown and period of operation [9.871]. The crack growth rates in these failures ranged from 9×10^{-11} to 5.5×10^{-10} m/s at 308 K (35°C) (about 3 to 17 mm in one year) to 7×10^{-9} m/s at 138°C (411 K) (about 4.2 mm in one week).

Most of the cracking was at a specific side of the reactors (the west end) and at the inlet ends of the fuel channels. The reasons for these observations were:

- The back ends (the end of the tube that exits the extrusion press last) were placed at the west end. The grain size is smaller at the back ends so they tend to be stronger than the front ends; residual stresses would be higher with the stronger material.
- The rolled joints for the west face were installed after those for the east face. The procedures at the time allowed for more over-rolling — about 13 mm — and greater clearance between the outside of the pressure tube and inside of the end-fitting at the west face than at the east face. If the pressure tube to end-fitting clearance was greater than 0.3 mm, the residual stresses tended to be large and the probability of cracking was high.
- Across the reactor face, the inlet and outlet to the fuel channel alternate. The temperature of the heat transport water is lower at the inlet end and the rate and amount of stress relaxation at the rolled joint from reactor operation would be smaller than at the outlet end.

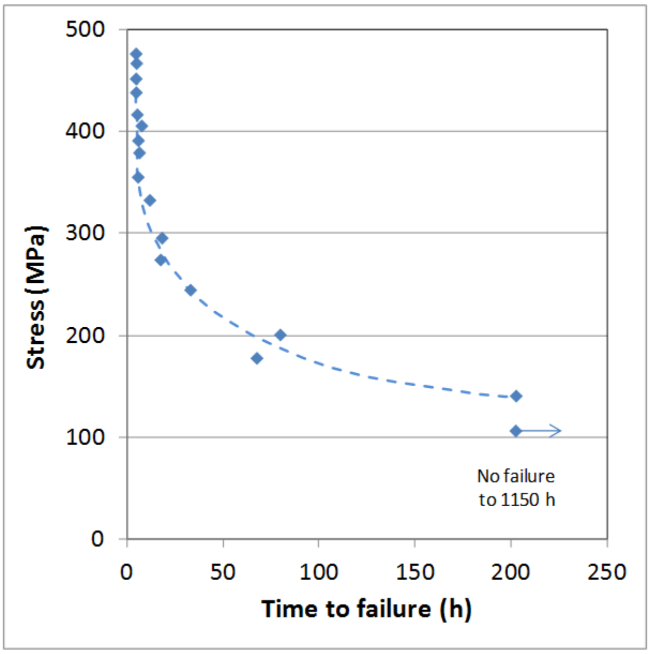

FIG. 9.315. Delayed failure curve at room temperature for notched specimens of Zr-1.25Al-1Sn-Mo containing 500 ppm (4.36 at.%) hydrogen [9.868].

Large crack initiators were absent. Small surface flaws, for example, from sand blasting, or small radial hydrides perpendicular to the tube surface were sufficient to start cracking [9.872]. The tubes that cracked tended to come from ingots that had high oxygen concentrations. The mean value of oxygen concentration of the tubes that cracked was 260 ppm higher than the mean concentration of the non-cracking tubes. Consequently, the tensile strength at room temperature was about 30 MPa higher [9.873] than in the non-cracking tubes, leading to larger residual stresses in these rolled joints. Since each of the above factors was distributed, pressure tubes tended to crack in rolled joints that contained all the factors at the damaging end of their distribution, that is, west inlets with tubes containing high oxygen concentrations. Rolled joints that contained none or only one or two damaging features tended not to crack, thus explaining why only a few tubes cracked and why this type of cracking was not a continuous problem.

(b) Bruce 2, 1982

At the time of the discovery of the cracks in the Pickering reactors, the rolled joints in the first two Bruce reactors had already been made. Before these reactors went into service, the large residual stresses were removed by heat treatment — 773 K (500°C) for 30 min. The efficacy of this heat treatment to reduce residual hoop tensile stresses was demonstrated in a pressure tube removed from Bruce-2 before it started operating: after installation the maximum tensile stress was about 550 MPa and after heat treatment it had been reduced to about 100 MPa [9.874]. In the two years between rolling and heat treatment, cracks had already initiated in four tubes. In Bruce 2, three tubes leaked in 1982 [9.875, 9.876] and one other leaked in 1986 [9.877]. The initial maximum residual tensile hoop stresses in these rolled joints were in the range 525 to 620 MPa; on removal these stresses were in the range 67 to 90 MPa, confirming that the joints had been stress relieved. No cracking was detected in Bruce-1 because the rolled joints were made after those in Bruce-2 and the time interval between installation and stress relief was shorter in Bruce-1, providing less time for cracks to initiate.

In later reactors, the rolled joints were made with low residual stresses by minimizing the gap between the pressure tube and the end-fitting — called a zero-clearance rolled joint — and ensuring that the rolled part of the pressure tube was firmly supported by not over-rolling. Typically, the maximum residual hoop tensile stresses at the inside surface were now less than 100 MPa.

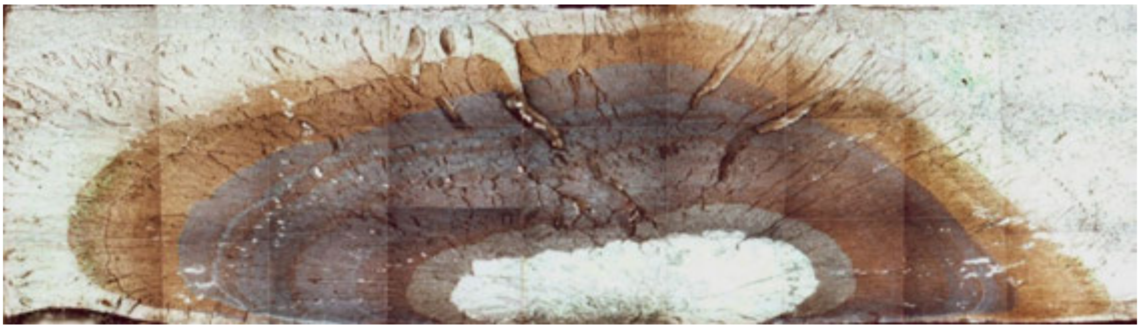

FIG. 9.316. A through-wall crack at a rolled joint in a Zr-2.5Nb pressure tube in Pickering Unit 3. The crack started on the inside surface and leaked at the outside surface. The coloured bands represent periods of cracking and subsequent oxidation after 8 major thermal cycles. The tube wall thickness was 4 mm [9.871].

A characteristic of the cracks in Bruce-2 was that the cracks had extended axially inboard from the initial elliptical area of fracture, as shown in Fig. 9.318 — the compressive stresses at the outboard end extending into the rolled joint prevented crack growth in that direction. With increased time of operation, extra hydrogen (as deuterium) was picked up in the rolled joint area [9.878] forming a concentration gradient into the main body of the tube. Hydrides were available at higher temperatures over a greater distance than with the cracks in Pickering-3 and -4, thus cracking could progress at these higher temperatures away from the initiation site [9.874]. In Bruce-2 the cracks grew with a heat transport water temperature between 503 and 523 K (230 and 250°C) at 3.3 to 4.6 × 10^{-8} m/s, about 3.5 mm/day. Another factor contributing to the shape of the crack was thought to be the cooling effect from the heat transport water flashing to steam across the crack surface; the crack's outer regions were cooler than the inner regions, so hydrides were available for cracking close to the outside surface. Hydrogen migrated to the cooled region and extra hydrides agglomerated towards the outside surface (see Section 9.7.2.3.)

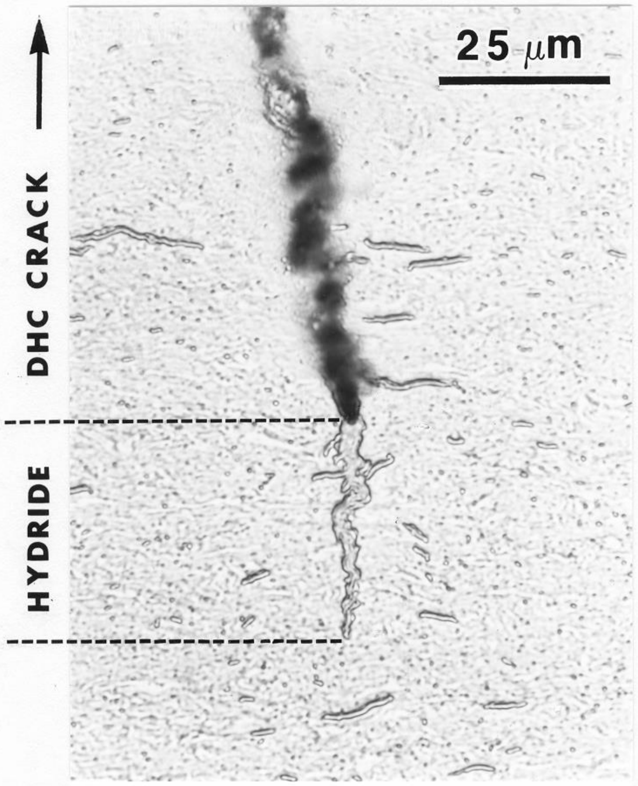

FIG. 9.317. Hydride grown at end of crack grown by DHC (photograph by D.K. Rodgers).

FIG. 9.318. Fracture surface of crack in a Zr-2.5Nb pressure tube in Bruce Unit 2. Note the suppression of cracking in the compression zone at the rolled joint end of the crack and the crack extension towards the centre of the reactor. The tube wall thickness was 4 mm [9.874].

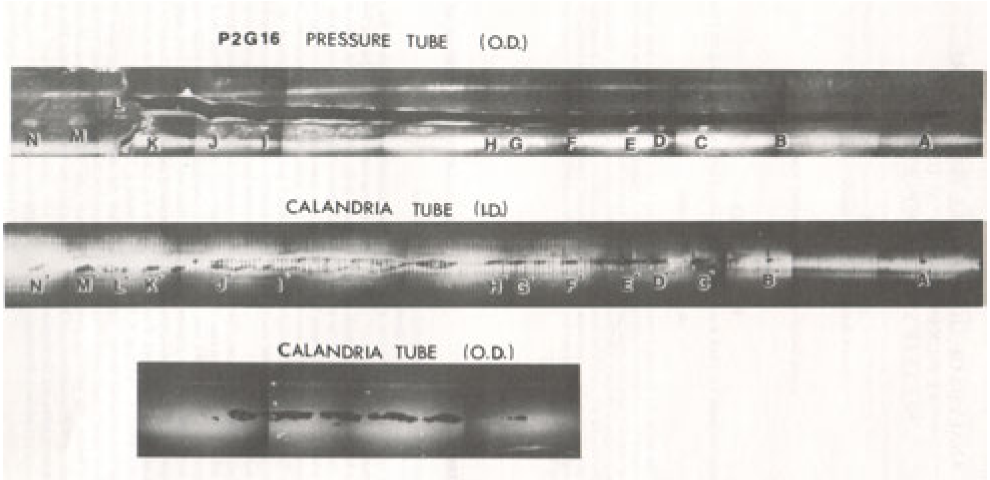

FIG. 9.319. Large crack in the cold worked Zircaloy-2 pressure tube of fuel channel G16 of Pickering Unit 2. Hydride blisters on the outside surface of the pressure tube are labelled A to N. Corresponding points of contact were observed on the inside surface of the surrounding calandria tube and areas attributed to local boiling of the moderator were found on the outside surface of the calandria tube [9.880].

(c) RBMK

Cracking in the Zr-2.5Nb pressure tubes in RBMK reactors had a similar cause. The final stage of fabrication involved straightening that induced residual tensile stresses on the outside surface. The stresses were reported to be about 350 MPa, although this value appears too low to cause cracking. After about two years of reactor operation 20 tubes out of a population of 20 000 leaked because of cracking by DHC initiated on the outside surface. These cracks initiated and grew while the reactors were cold; the cracks would stop during operation because the temperature was high enough to dissolve all the hydrides and the outside surface of the pressure tubes was about 30°C hotter than the inside surface. The crack surface was oxidized very little because the cover gas was a mixture of 90% helium and 10% nitrogen. The failures took place in the first two years of operation of the reactors in Kursk and Chernobyl and there were no subsequent failures because the residual stresses had relaxed; after 1000 h of operation the residual stresses were calculated to have been reduced to between 160 and 240 MPa while after 1.2 years these stresses had fallen to between 70 and 150 MPa [9.879]. Again, the solution was to reduce the residual stresses by modifying the straightening process.

(d) Zircaloy-2 pressure tubes

No cracking at rolled joints was detected in the Zircaloy-2 pressure tubes originally installed in NPD, Douglas Point, Pickering Units 1 and 2, and in Indian CANDU reactors, nor in the Zircaloy-2 pressure tubes in SGHWR or the N-Reactor. The tubes in Pickering Unit 1 and Pickering Unit 2 were over-rolled because this procedure was thought to increase the strength of the joint; the practice was continued for the Zr-2.5Nb pressure tubes in Pickering Units 3 and 4, and Bruce Units 1 and 2.

In 1983 a pressure tube made from Zircaloy-2 ruptured in lattice position G16 in Pickering Unit 2 while the reactor was at full power [9.880]. The crack was about 2 m long and, unlike the cracks described in Sections 9.7.6.1(a) to (c), no warning leakage was detected. The crack initiated at a series of hydride blisters formed on the outside surface of the tube, as shown in Fig. 9.319. The formation of hydride blisters is discussed in Section 9.7.2.3. The following sequence of events led to the forming of the blisters:

- The garter spring spacers separating the pressure tube from the surrounding calandria tube were inadvertently moved out of their design location by vibration induced in making the second rolled joint of the fuel channel, and during service.
- Because the tubes are horizontal, the increased span between supports allowed the hot pressure tube, nominally about 573 K (300°C), to sag into point contact with the cool calandria tube, about 70°C (343 K), setting up a steep temperature gradient on the outside of the pressure tube.
- Hydrogen diffused down the temperature gradient and since the hydrogen concentration was large, about 150 ppm (1.35 at.%), and exceeded a threshold value, as shown in Fig. 9.260, hydride blisters formed at the cold spots on the outside of the pressure tube.
- With time, the blisters grew large enough that they cracked and when the sum of some of the cracks exceeded a critical value, they were able to grow.
- The cracks from three or four adjacent blisters linked to form a partial through-wall crack that became unstable.

Other Zircaloy-2 pressure tubes contained similar blisters and high concentrations of hydrogen and more failures were predicted, based on the statistics of spacer location and time in contact. Since Zr-2.5Nb picks up less deuterium during operation than Zircaloy-2 (see Chapter 8, in Volume 2 of this publication, Appendix IV), it was decided to replace all the Zircaloy-2 pressure tubes in Pickering-1 and -2 with tubes made from Zr-2.5Nb. Also, the spacers were redesigned to minimize movement from their design location and their number was increased from two to four to reduce the span and risk of contact.

(e) Fuel cladding

In some Zircaloy-2 nuclear fuel cladding used in BWRs, hydride cracking was strongly implicated in long splits that allowed substantial leakage of fission products [9.854, 9.881–9.884]. Such failures have been observed after modest fuel burnups, as low as 17 MWd/kg. If the cladding wall is penetrated during operation (e.g. by fretting), cracks may propagate from such primary defects. Alternatively, cracks may be initiated from hydride sunbursts or blisters formed as follows. Water from the heat transport system can enter the fuel cavity, through the primary defect, where, because of the low pressure, steam is produced. Much hydrogen is generated because the steam oxidizes the fuel and the inside surface of the cladding, reducing the partial pressure of oxygen and leaving a gas rich in hydrogen. This process is called oxygen starvation. At some distance from the primary defect the gas stream becomes almost pure hydrogen, and with breakdown of the protective oxide layer, copious quantities of hydrogen may be absorbed by the cladding [9.885] producing sunbursts of hydride on the inside surface. Although the pure Zr liner was often found to be completely corroded, and therefore contributed hydrogen to the inventory and stress through expansion via the oxide, it was not a necessary requirement for the secondary damage because unlined fuel cladding behaved in a similar manner. With fuel expansion during fuel rearrangement, the hydrided cladding was stressed, which led to crack initiation. The cracks grew through-wall, propagated axially, and could be over 1 m long. Brittle regions in chevrons characterized the fractures, as shown in Fig. 9.320, with the crack being longer on the outside surface than the inside surface of the cladding [9.884, 9.886]. The lower bounds of the crack growth rates were in the range 4×10^{-8} to 8×10^{-7} m/s (3.5 to 69 mm/day) based on assuming constant growth rates in the time between first detection of the defect and removal of the fuel. The mechanism of cracking appeared to be a form of DHC [9.882, 9.884, 9.887], perhaps exacerbated by a continuous additional supply of hydrogen from the steam inside the fuel element [9.884, 9.888]. This type of

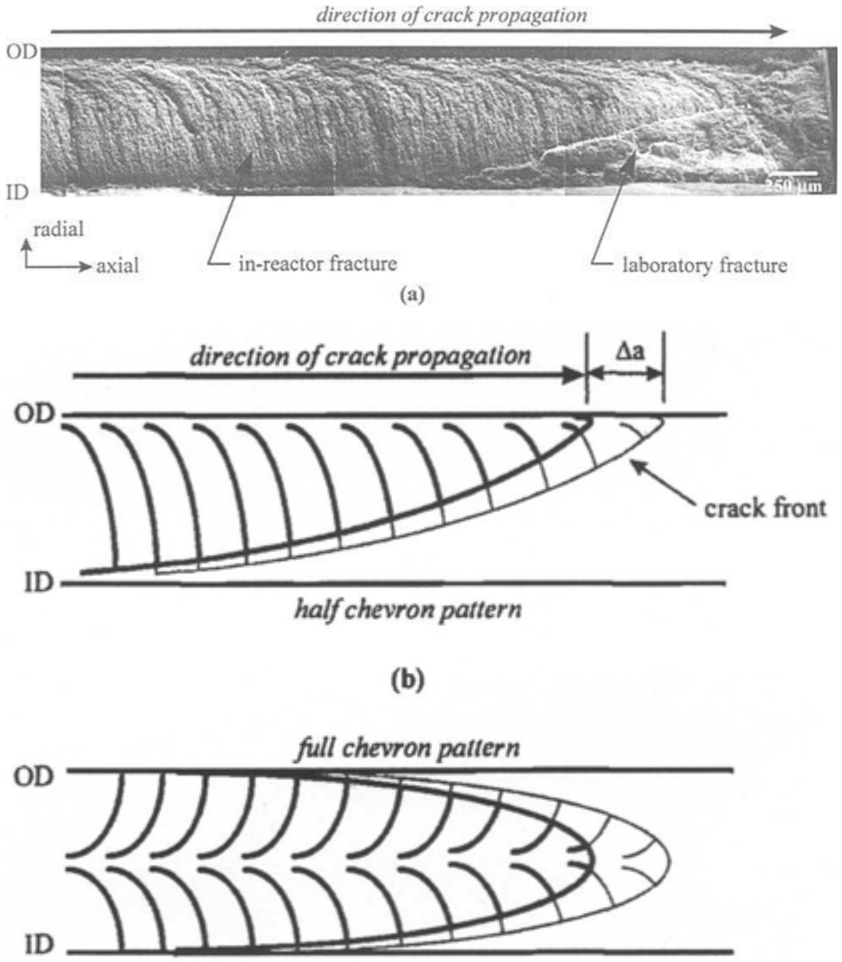

FIG. 9.320. (a) SEM micrograph of cracked Zircaloy-2 fuel cladding after a burnup of 17 MWd/kg. The crack initiated at a fretting flaw; (b) a schematic representation of half and full chevron fracture pattern [9.884].

cracking in fuel cladding has been called corrosion hydride cracking, with the fracture surface being distinguished from that of DHC in Zr-2.5Nb — see Section 9.7.6.3.

Radial cracking from the outside surface, again with fracture features similar to DHC, has been observed in tests with power ramps to 42 to 62 kW/m after burnups of 43 to 61 MWd/kg in a commercial BWR [9.889]. The time to failure after the power ramp was between 9 and 149 min. The cracks initiated at radial hydrides and were propagated by a form of DHC. Subsequent laboratory tests on unirradiated cladding simulating the loading conditions showed that the cracking had the properties of DHC and that the growth rate of DHC in the radial direction of the tube had the temperature dependence expected for DHC and V was about 10^{-7} m/s (8.6 mm/day) at 548 K (275°C) [9.890, 9.891]. Further studies of this phenomenon were summarized in Ref. [9.892] as follows:

- With a large linear heat rate, the resulting temperature gradient drove the hydrogen accumulated in the inside liner towards the outside surface, which was kept at 561 K (288°C) (see Section 9.7.2.3). The value of 58 kJ/mol for Q^* estimated from the experiments appears about two times too big (see Table 9.42).
- A hoop stress of 200 MPa was sufficient for radial hydrides to form at the outside surface in unirradiated cladding and irradiated cladding after hydrogen charging at 563 K (290°C).
- A threshold outer fibre stress of 650 MPa for failure under 2 h was measured independently of a linear heat rate >35 kW/m.

These conditions of a relatively cold crack tip, a large temperature gradient (80°C/mm [9.893]) and a large force from the power ramp were ideal for the DHC process. Such radial cracking has been reproduced in similar power ramp tests of 42 kW/m after a burnup of 62 MWd/kg in BWR conditions [9.894]. Care has to be taken with the results of these types of power ramp experiments because the in-reactor test conditions were outside the usual operating range of BWRs.

Similar cracks have been observed in low tin Zircaloy-4 after a burnup of 52 MWd/kg in a PWR, followed by a deliberate power ramp in a research reactor. The outer rim of hydride (see Section 9.7.2.3) contained several cracks that stopped in the metal matrix, possibly because the metal retains good ductility at the high operating temperature, see Fig. 9.264 [9.734].

Cracks in the axial direction, about 20 mm long and close to the end-plugs of CANDU fuel, have been detected [9.895]. The burnup was very low, 0.4 MWd/kg, so the inventory of fission products would be too small to cause SCC. Several partial radial cracks had also started from the inside surface. The hydrogen concentration was 42 ppm (0.38 at.%), which may have been picked up from residual moisture in the fuel. The source of the large hoop stress driving the crack was attributed to fuel expansion from the fuel operating well outside its design power, although the cause of this anomaly was not identified.

(e) Cracking in welds

Welding induces residual stresses. If the yield stress of the parent material is high, the tensile stresses set up in the HAZ of the weld may be high enough to initiate cracking. Zr-2.5Nb is susceptible to DHC driven by such residual tensile stresses. In experimental CANDU fuel, magnetic force resistance welds between the end caps and fuel cladding made from Zr-2.5Nb cracked in the HAZ during storage at room temperature [9.896]. Cracking attributed to DHC has been observed in gas tungsten arc welds in Zr-2.5Nb components used for chemical processing [9.897]. Cracking in both types of weld was eliminated by heat treatment; an ameliorating heat treatment for Zr-2.5Nb is prescribed in the ASME Boiler and Pressure Vessel Code [9.3]. Over 50 000 electron beam welds in the Zr-2.5Nb pressure tubes of RBMK nuclear reactors have performed without problem for up to 15 years [9.898]. Electron beam welding appears to be less harmful than gas tungsten arc welding, presumably because the volume of material affected by the weld is small and the surrounding material provides much support. These explanations do not seem to apply to spot welds used to attach instrument leads to Zr-2.5Nb tubes before pressure testing. For example, during laboratory experiments on pressurized tubes, cracks started from spot welds on the outside surface even though the section of pressure tube contained large machined flaws, typically 10 mm long by 1.2 mm deep, on the inside surface.

No similar cracking has been reported in over 10^7 welds in fuel clad in the softer Zircaloys or in the various versions of Zr-1Nb. No DHC has been reported in over 70 km of tungsten inert gas welds in calandria tubes made from Zircaloy-2. These welds are annealed at 1023 K (750°C) for 0.5 h within days of welding.

In summary, all these failures showed that:

- Components made from α alloys, such as Zircaloy, and (α + β) alloys, such as Zr-2.5Nb, are susceptible to a form of time dependent cracking associated with hydrides that is an important factor in their structural integrity. Most of the failures have been linked to DHC.
- In the absence of flaws that would make the component rejectable, high tensile stresses are required to initiate cracking; increasing tensile stresses during service may induce cracking. Reducing residual stress, either by continued reactor operation or local heat treatment, reduces the incidence of cracking; as a corollary, increasing alloy strength allows high residual stress to be sustained, apparently reducing the tolerance to the cracking mechanism.
- Hydrides are required as the cracking agent; initial concentrations of hydrogen, which meet the requirements of the specification, are only sufficient for crack initiation at low temperatures. As hydrogen is picked up during reactor operation, cracking eventually becomes possible close to operating temperatures.
- Temperature gradients can induce hydride layers or blisters that may become the site for crack initiation. Temperature gradients exacerbate the cracking when the crack is cooler than the remainder of the component.

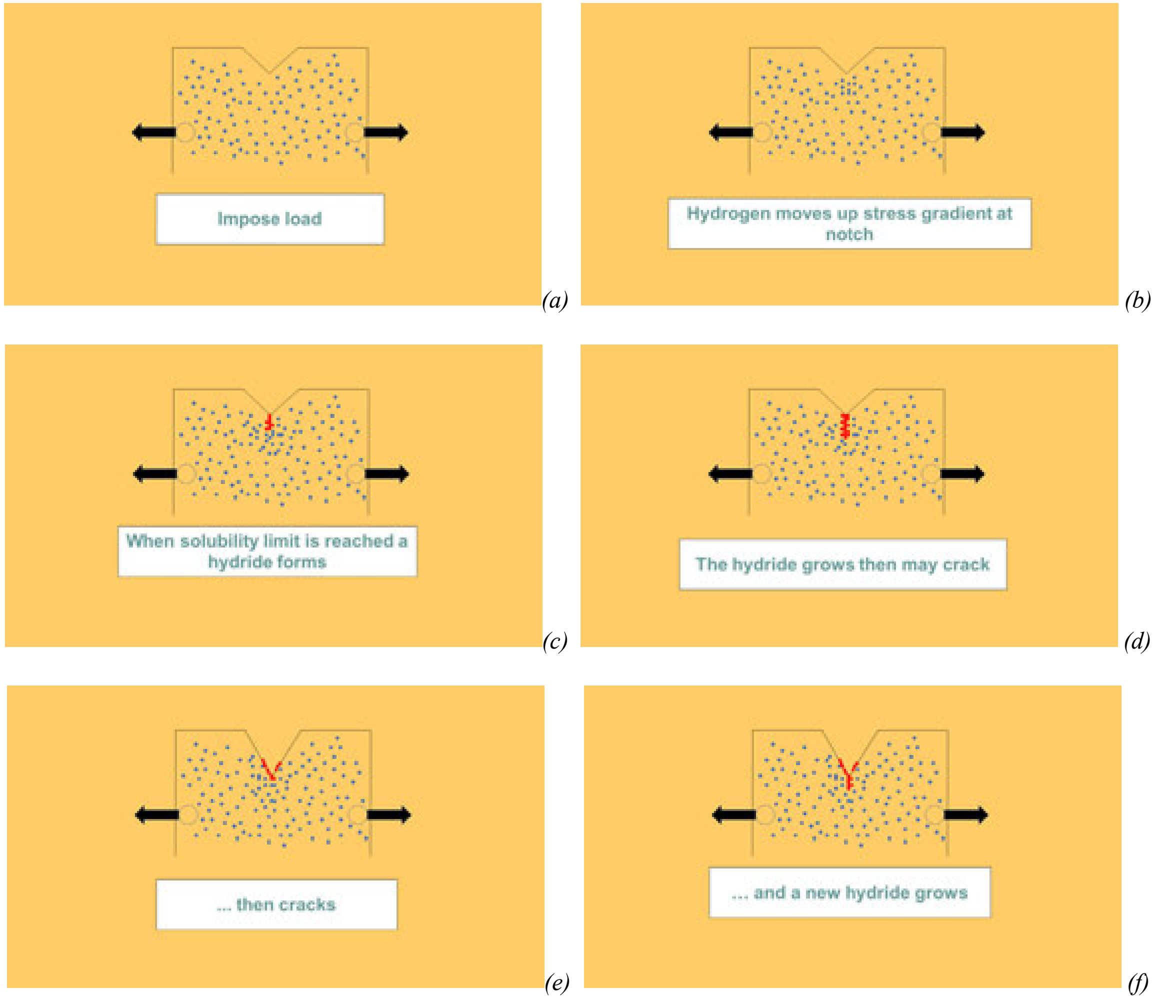

FIG. 9.321. Schematic diagram of the mechanism of DHC. In (a), a tensile load is imposed on a component of zirconium alloy containing hydrogen in solution (blue dots) and a surface flaw, (a). Hydrogen in solution diffuses up the stress gradient at the flaw tip, (b), and, if TSSP is exceeded, forms a hydride (red dots), whose trace is perpendicular to the stress, (c). With time the hydride grows, (d). It cracks, (e), if the stress is large enough. The process then repeats at the new crack tip, (f).

9.7.6.2. Mechanism[10] of DHC growth rate

A consequence of hydrogen movement in gradients of chemical potential (see Section 9.7.2) is that the accumulated hydrogen may exceed the solubility limit (see Section 9.7.1.2) and hydrides may form at the end of the gradient where the chemical potential is lowest. Under tensile stresses, the hydrides may precipitate with a harmful orientation (see Section 9.7.3). Since the hydrides have low toughness and cause embrittlement (see Section 9.7.4), in time, cracking in components may be possible (see Section 9.7.6.1). The outcome is either DHC or cracking of hydride blisters or layers. Figure 9.321 is a schematic illustration of the sequence leading to DHC. A surface flaw may exist in a zirconium alloy component containing hydrogen in solution, as shown in Fig. 9.321(a). Under a tensile load, hydrogen diffuses up the stress gradient close to the flaw tip and increases the local hydrogen concentration, as shown in Fig. 9.321(b). A hydride precipitates at the flaw if sufficient hydrogen accumulates for C_P to be exceeded, as shown in Fig. 9.321(c). If the crystal orientation is appropriate, the hydride forms with its plate normal parallel with the stress. With time the flaw tip hydride grows larger and more hydride accumulates, as shown in Fig. 9.321(d). If the critical conditions of hydride size, maximum stress and strain are reached, the flaw tip hydride cracks and extends by the length of the hydride, as shown in Fig. 9.321(e). The process of hydride nucleation, growth and fracture is then

---

[10] The mechanism of crack growth by DHC has been controversial and the subject of much debate. Appendix 9.II summarizes the issues and provides justification for the approach used here.

repeated, as shown in Fig. 9.321(f), and the crack extends in a stable manner. The micrograph in Fig. 9.317 illustrates a stage in this sequence. In-situ observations in electron microscopes have also confirmed this process [9.814, 9.899], as shown in Fig. 9.322.

To quantify this picture of the hydrogen diffusing from the unstressed region to the flaw tip, the flux of hydrogen, *J*, is described by the Nernst-Einstein equation (see Section 9.7.2.2), which can be written for this application as Eq. (9.74) [9.900]:

$$J = -D(\nabla C + \frac{CV_H}{\mathrm{R}T}\nabla\sigma_h) \tag{9.74}$$

where

D is the hydrogen diffusivity;
C is the hydrogen concentration in solution, which is assumed to be dilute;
R is the gas constant (8.314 kJ/mol.K);
T is the temperature in K;
V_H is the partial molal volume of hydrogen in zirconium;

and σ_h is the hydrostatic stress.

Initially, if the hydrogen concentration in solution is the same everywhere (i.e. the gradient $\nabla C = 0$) then hydrogen will tend to flow because of the stress gradient towards a flaw under tension (i.e. $J < 0$), and the hydrogen concentration at the flaw will increase until equilibrium is reached and the flux of hydrogen goes to zero. Under these conditions the movement of hydrogen is opposed by the hydrogen concentration gradient, which grows more and more negative with time, and becomes equal to the stress gradient term in Eq. (9.74) at equilibrium where J is equal to 0.

Cracking is not an equilibrium process. If sufficient hydrogen accumulates at the flaw tip to exceed the TSSP concentration, C_P, hydrides form. Equilibrium cannot be attained and steady state ensues. At the flaw tip, the hydrogen concentration in solution is fixed at C_P and the steady state hydrogen flux continually provides hydrogen that allows the hydride precipitate to grow. The rate of growth of the hydride is controlled by the diffusion of hydrogen into the flaw tip region. Its subsequent cracking is controlled by the stress state and the fracture toughness of the hydride. The diffusion takes time and thus the cracking is delayed.

An equation for the crack growth rate, V_c, can be derived from Eq. (9.74) with the assumption that the steady state flux of hydrogen to the flaw is controlling the process [9.900]:

$$V_\mathrm{c} = W[C_\mathrm{b} - C_\mathrm{P}\, exp(\sigma_\mathrm{h} V_\mathrm{H}/RT)] \tag{9.75}$$

where

W is approximately equal to constant × D;
C_b is a concentration of hydrogen in solution in the bulk material;
σ_h is $-\zeta$ × yield strength;

and ζ is a stress amplification factor at the flaw and is assigned values between 1.9 and 2.4.

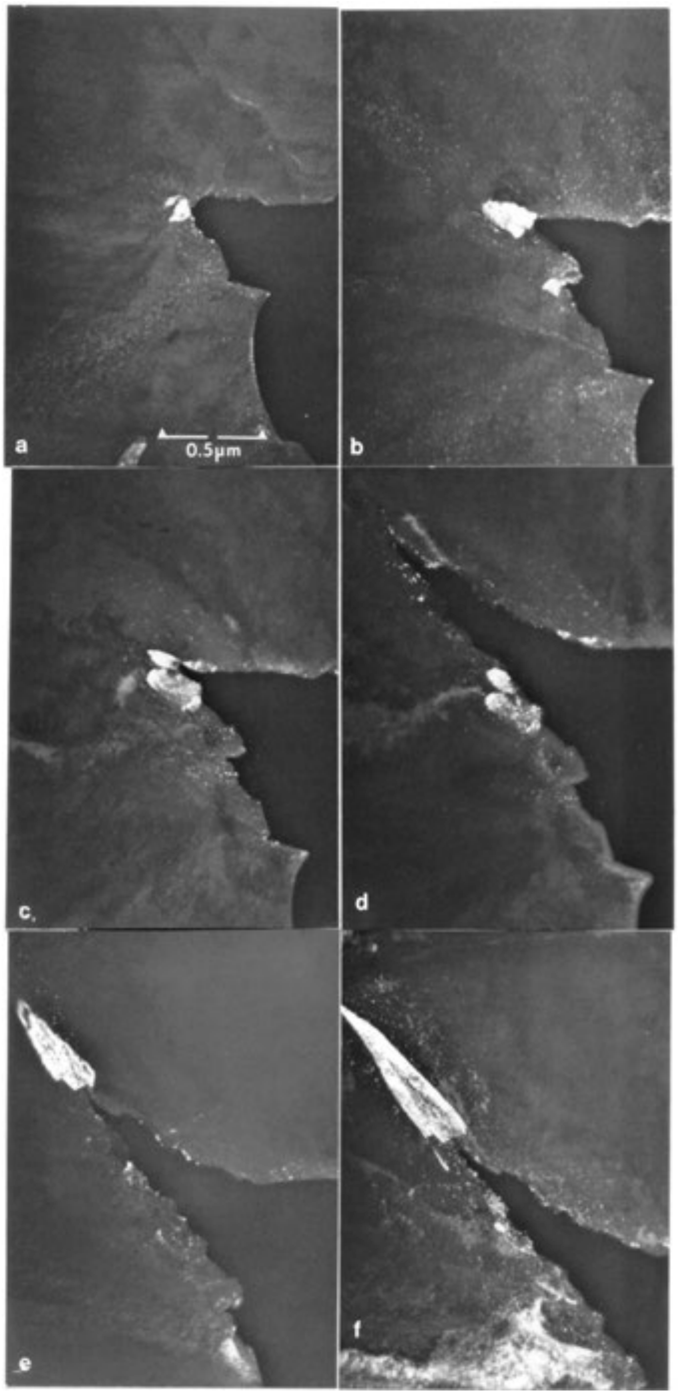

FIG. 9.322. Dark-field images of crack-tip hydrides in zirconium with 100 ppm (0.9 at.%) hydrogen: (a) 3h after initial strain imposed; (b) hydride precipitation at new crack tip 1 h after more strain; (c) fracture of this hydride and new hydride 3.5 h later; (d) crack growth 2 days later with imaging conditions to show hydrides in (c); (e) as (d) but imaging conditions to show new crack-tip hydride; (f) coarsening of this hydride in 1 day [9.814].

The constant is based on experimental values of DHC during temperature cycling [9.901, 9.902]. This approach has been called the diffusion first model.

Inferences from this basic picture are as follows [9.901]:

(1) Although hydrides are the microstructural feature that cracks, hydrides are not required in the zirconium matrix for them to be formed at the stress concentration.
(2) A temperature will be reached where no cracking is possible because the hydrogen concentration cannot reach C_P at the flaw tip and all the hydrogen remains in solution. This situation sets the first

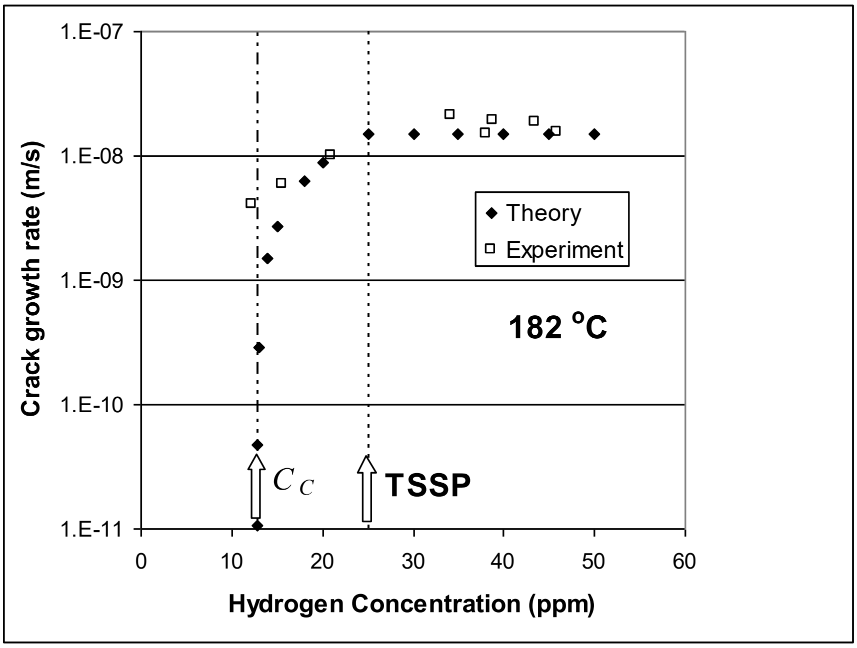

FIG. 9.323. Crack growth rate in Zr-2.5Nb at 455 K (182°C), showing a limit of DHC based on hydrogen concentration, Cc. The experimental results are from [9.901] and the theory is determined using experimentally measured properties of Zr-2.5Nb in Eq. (9.75) [9.900].

limit on DHC. Lack of DHC when all the hydrogen is in solution was surmised during the interpretation of the coloured bands on the cracks in Pickering Units 3 and 4.

(3) Time is required before the critical conditions for the initiation of cracking are attained. The long periods before leakage was detected in power reactors included the time it took to set up the conditions for cracking. The difference between the behaviours of rolled joints in Bruce Unit 1 and Unit 2 provided an example of forestalling the attainment of the critical condition.

(4) Cracking is intermittent. After the first hydride is cracked, the condition for crack extension has to be repeated, as shown in Fig. 9.321(e) and (f). Cracking the whole notch tip front simultaneously seems unlikely, because local microstructural variations will affect the critical conditions for cracking. Consequently, the time interval for subsequent cracking steps will probably appear shorter than the initial step once cracking is established along the whole crack front and the time interval between steps will continue to be short.

(5) The critical condition for cracking will depend on the local stress state, suggesting a threshold condition has to be attained; as a minimum, the fracture toughness of hydride has to be exceeded. Few tubes cracked in early reactors showing that Inference (1) is not a sufficient condition for cracking. The lack of further cracking in early CANDU and RBMK reactors suggests that stress relieving from reactor operation prevented the critical conditions for cracking from being attained in the remaining fuel channels. This threshold condition sets a second limit on DHC.

(6) The fracture surface should contain mostly fractured hydrides.

(7) The crack growth rate through the hydride is very rapid (see Section 9.7.4) so the rate controlling process of cracking will depend on the rate of the precipitation, which in turn will depend on the rate of accumulation of hydrogen at the crack tip. This rate depends on:
    (a) The diffusion of hydrogen to the crack tip, so the temperature dependence of crack growth rate, V_c, will include the temperature dependence of the diffusivity of hydrogen in the zirconium alloy, D;
    (b) The amount of hydrogen available to diffuse to the crack tip, so the temperature dependence of V_c will include the hydrogen concentration and the temperature dependence of the solubility limit of hydrogen, C_p, in the zirconium alloy;

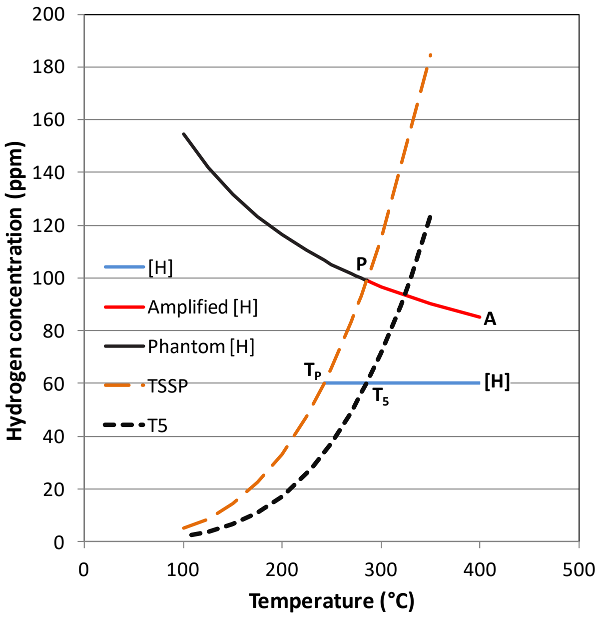

FIG. 9.324. Formulation of critical concentration and temperature for DHC on cooling (based on [9.900]).

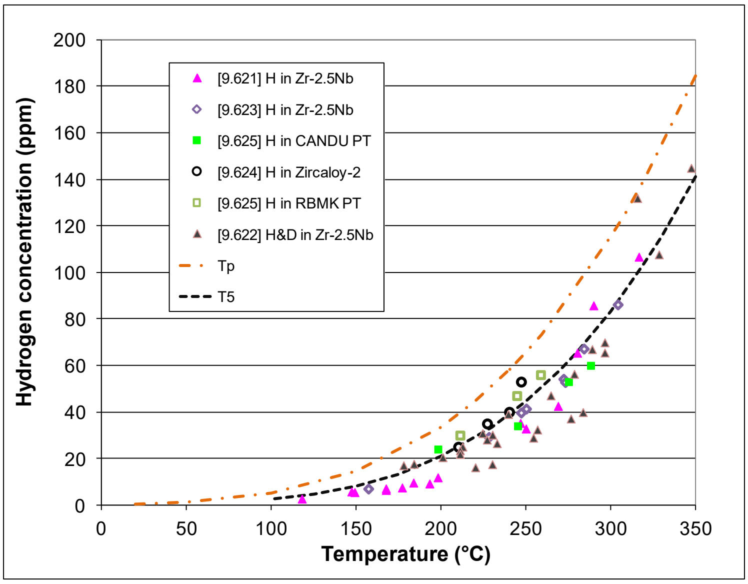

FIG. 9.325. Verification of model of critical hydrogen concentration and temperature for DHC described by Fig. 9.324.

(c) The amount of hydrogen available to diffuse to the crack tip, so the temperature dependence of V_c will include the hydrogen concentration and the temperature dependence of the solubility limit of hydrogen, C_P, in the zirconium alloy;

(d) The yield stress since it drives the hydrogen to the crack tip, so the temperature dependence of V_c will include the temperature dependence of the yield stress of the zirconium alloy, σ_y.

(8) Since the hydrogen in solution controls V_c, it will have little dependence on hydrogen concentration once Inference (1) has been satisfied.

(9) Once cracking has been initiated, its rate of growth will have little dependence on crack length, and therefore stress intensity factor, K_I, because the stress distribution, and therefore stress gradient, at the crack tip stays approximately constant as the crack grows. Also, D and C_P do not change with K_I.

(10) Hydrides will grow faster in stronger materials because the stress gradient and the maximum sustainable stress at the crack tip will be higher than in weaker materials. A corollary is that eventually a temperature will be reached where DHC will be absent because the material becomes too weak to support a large stress gradient and sufficient stress to crack hydrides. This upper temperature represents a third limit on DHC.

(11) The critical condition for cracking will depend on the local microstructure of the metal matrix since the distribution of the hydrides, especially their orientation, is determined by the metal matrix. V_c will also be affected by the way microstructure controls D (see Section 9.7.2.1(b)), and the solubility limit (see Section 9.7.1.2(e)). An early indication of the importance of microstructure was the elliptical shape of the leaking cracks in Zr-2.5Nb pressure tubes, as shown in Fig. 9.316.

9.7.6.3. Phenomenology of DHC

The properties of most interest to the users of zirconium alloys are the limiting conditions for cracking and the rate of cracking, V_c. These properties have been evaluated in pressure tube materials and plates using cantilever beams, notched tensile and compact toughness specimens and full scale tubes and in fuel cladding using half-sections, pin-loading tension, central mandrels and internal pressurization. The onset and progress of cracking have been detected by acoustic emission, potential drop and crack opening displacement. The main variables are load and loading history (interpreted as K_I), temperature and temperature history, and microstructure.

DHC has characteristics that have been observed in several studies, confirming the inferences listed in Section 9.7.6.2. The characteristics are as described in the remainder of this section.

At a particular temperature, a critical hydrogen concentration, C_C, is required in solution in the metal matrix so that the flow of hydrogen to the flaw tip is sufficient to form a hydride. Hydrides are not required to be present in the metal matrix for DHC, but once they are present in the metal matrix, the crack growth rate is independent of hydrogen concentration. Figure 9.323 provides an example [9.902]. Crack growth rate was measured in Zr-2.5Nb at a test temperature of 455 K (182°C) as a function of hydrogen concentration. Cracking was observed below TSSP but the rate declined towards C_C, as calculated by Eq. (9.75); see Inferences (1), (2) and (8) above.

C_C provides an effective solubility limit [9.624–9.628]. An alternative for a given hydrogen concentration is to invoke a critical temperature, T_C, below which DHC is possible. T_C increases with an increase in hydrogen concentration. This behaviour is expected from Inferences (1) and (2) above; again, T_C, may be attained with no hydrides present in the zirconium matrix. The principle is illustrated in Fig. 9.324. A compact toughness specimen containing a sharp crack and 60 ppm (0.54 at.%) hydrogen was heated to 673 K (400°C), where all the hydrogen was in solution. When loaded in tension, the hydrogen concentration at the crack tip was raised to 84.9 ppm (0.77 at.%), indicated in Fig. 9.324 by ‘A’, by applying Eq. (9.59). On cooling, the concentration of hydrogen in the bulk does not change appreciably remaining at 60 ppm (0.54 at.%) (indicated by the blue solid line in Fig. 9.324) because the affected volume at the crack tip is very small compared with the remainder of the specimen. The concentration at the crack tip rises (indicated by the red solid line in Fig. 9.324) through the direct temperature dependence in Eq. (9.59) and because the yield strength increases. When the temperature reaches 558.5 K (285.5°C) the concentration of hydrogen at the crack tip reaches 98.9 ppm (0.89 at.%), and T_P is exceeded locally, P. This temperature is T_C; it will later be renamed T_5 to align with other significant temperatures. As the temperature is lowered further, the hydrogen concentration in solution at the crack tip follows TSSP (orange dotted line); the hydrogen in solution at the crack tip cannot follow the equilibrium line to higher values (indicated by the green solid line labelled ‘phantom’ beyond ‘P’ in the Figure). At 515.8 K (242.8°C) hydride starts to precipitate in the bulk as TSSP is exceeded in the whole specimen; in this example, cracking can start 42.7°C above TSSP. The locus of T_C (T_5) for other bulk concentrations is the effective solubility limit — marked as the black dotted line. Similar explanations are given in Refs [9.626, 9.627, 9.900]. Experimental verification from several sources on both Zircaloy and Zr-2.5Nb is provided in Fig. 9.325. Components always contain residual hydrogen concentrations after fabrication. These small concentrations are sufficient for DHC at low temperatures. For example, DHC has been observed at 393 K (120°C) with Zr-2.5Nb material containing 2 to 3 ppm (0.018 to 0.027 at.%) hydrogen [9.624]. During reactor operation, components pick up hydrogen as a result of corrosion and DHC becomes possible at high temperatures. For example, the cracks in Bruce

Unit 2 propagated at much higher temperatures than those in Pickering Units 3 and 4. Note that at 572 K (300°C), where C_P is 115 ppm (1.04 at.%), a hydrogen concentration of about 75 ppm (0.68 at.%) is sufficient to initiate DHC.

Hydrides have been observed with several different configurations at stressed crack tips. Hydrides both single and in groups have been observed at crack tips in Zircaloy fuel cladding, after both failure [9.889, 9.903] and cracking experiments [9.887]. In Zr-2.5Nb sometimes the hydrides appear along shear bands, indicating dislocation assisted nucleation; these hydrides may be manifest as large clumps, as shown in Fig. 9.326 [9.904]. When the formation of reoriented hydrides is difficult, usually because of the crystallographic texture, hydrogen is still attracted to the crack tip but the hydrides are diffuse and precipitate in the shear bands, as shown in Fig. 9.327 [9.763]. Frequently, single traces of hydride are found at a notch root, as shown in Figs 9.317 and 9.322, and they are often tapered, being thicker close to the crack tip. The maximum tensile stress developed in the plastic zone may be displaced a short distance from the crack tip and hydrides are sometimes observed with a similar small gap to the crack tip. Often an incubation time, t_I, is required before cracking starts. This time is interpreted as the time it takes to grow a hydride at a crack tip to a critical size, usually taken as length,

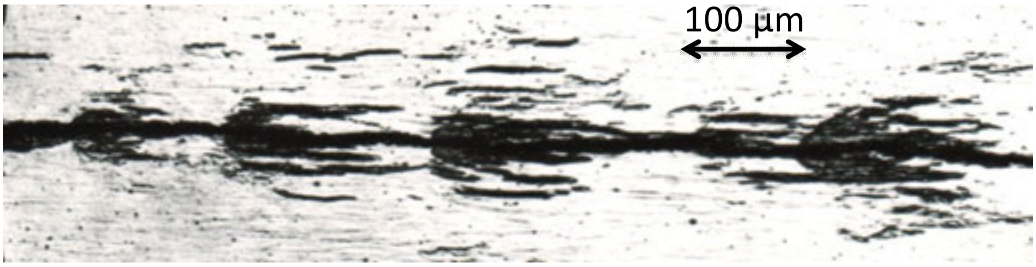

FIG. 9.326. Hydrides within shear bands at flaw tips arranged as clumps along a propagating crack [9.904].

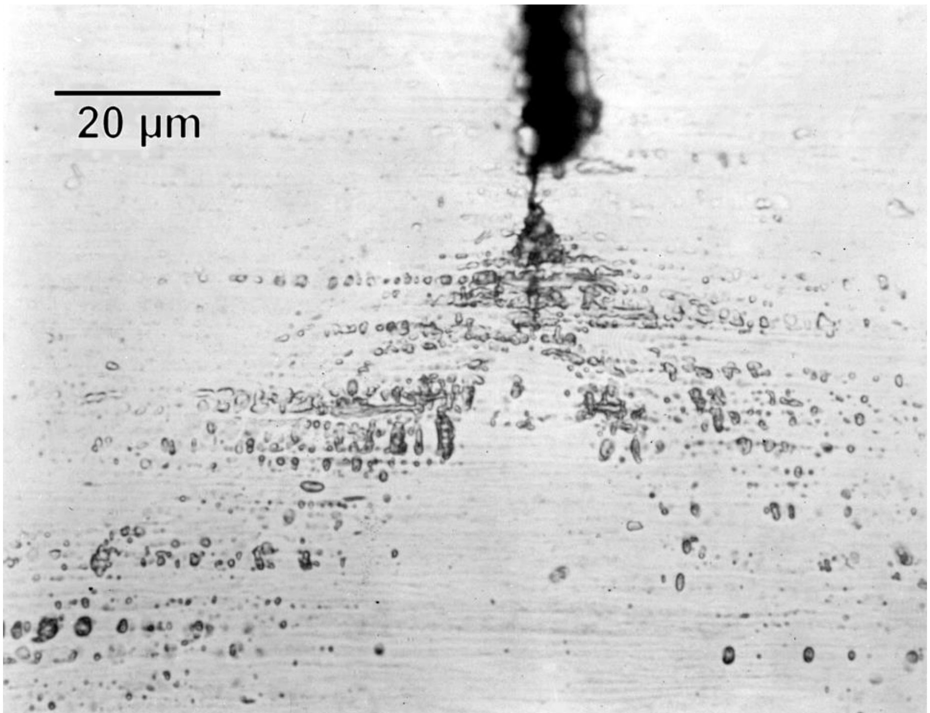

FIG. 9.327. Hydrogen attracted to stress raiser but precipitated along shear zones because of difficulty in forming radial hydrides with a stress perpendicular to basal plane normals in the longitudinal direction of Zr-2.5Nb pressure tube [9.763].

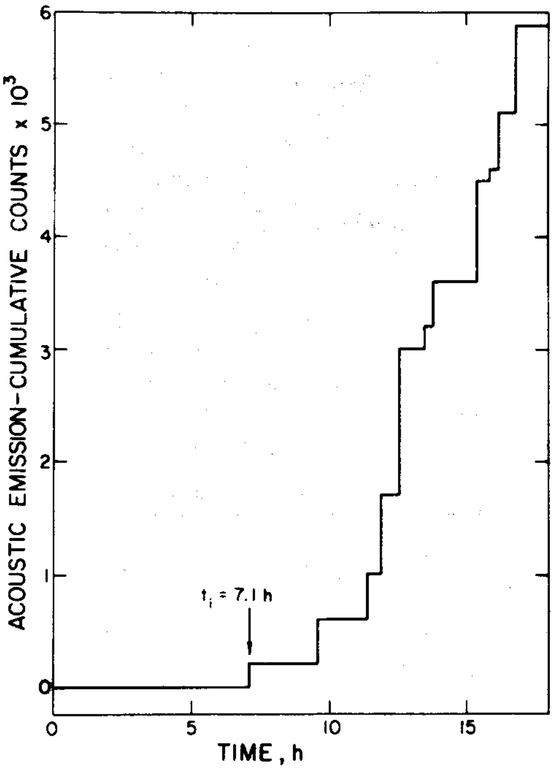

FIG. 9.328. Generation of acoustic emission during DHC in Zr-2.5Nb containing 26 ppm (0.24 at.%) hydrogen at 423 K (150°C) and 15 MPa√m. Cracking, as indicated by the first acoustic event, started after an incubation time of 7.1 h, but the interval between subsequent cracking was much shorter [9.624].

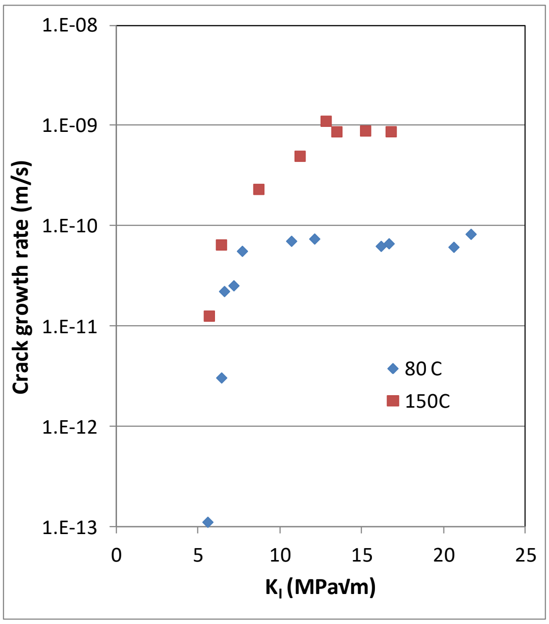

FIG. 9.329. Dependence of crack growth rate on K_I and test temperature in Zr-2.5Nb pressure tube material. The cracks grew in the radial direction in cantilever beam specimens [9.905].

ℓ_c, before it fractures. Figure 9.328 indicates the start of acoustic emission a short period after the imposition of a load [9.624]. (Acoustic emission was associated with the elastic waves from cracking hydrides in Zr-2.5Nb and was strongly correlated with other measures of crack propagation such as direct current potential drop and crack opening [9.905–9.908]). The intervals between subsequent indications of cracking are usually shorter than the initial time. This behaviour is expected from Inferences (3) and (4), above. This inferred discontinuous hydride cracking has been observed directly with in-situ experiments in a Scanning Electron Miscroscopy (SEM) on Zircaloy-2 fuel cladding; at 523 K (250°C) cracking was intermittent as hydrides grew about 6 μm at a crack tip before fracture [9.897]. This experiment provided an estimate of ℓ_c at a surface.

Uncracked hydrides up to 28 μm long were observed at the crack tip after quenching a cantilever beam specimen of Zr-2.5Nb from 458 K (185°C) after 0.8 t_I [9.625]. Based on this experiment, hydrides were grown in the radial direction for times less than t_I and their average length at the time of first cracking was derived from extrapolation of crack lengths at short times [9.909]. This length was taken as the critical length for DHC, ℓ_c. The hydride lengths had a large variation, especially at short times, with a range of about a factor of 5; they were not always coplanar with the crack, and were often a small, but highly variable, distance from the crack tip. The mean hydride length had a dependence close to $(\text{time})^{1/3}$ in Zr-2.5Nb pressure tube material, similar to particle coarsening. The large scatter in the data supported multiple hydride nucleation, variable growth, and cracking at different times at different positions along the crack front (see Inferences (3) and (4), above). Similar experiments were performed at 423 K (150°C) on cracks in the axial direction of a Zr-2.5Nb tube [9.910]. Up to a K_I of about 4 MPa√m, no hydrides were detected at the crack tip after 80 h; this result was unexpected because the hydrostatic stress should have been sufficient to attract extra hydrogen to the crack tip. (A similar result is illustrated in Fig. 9.255 where the limit for growing hydrides at a crack tip is about 4 MPa√m.) Around 6 MPa√m unbroken hydrides up to 22 μm were observed after a hold of 60 h. Modelling the growth of hydrides at a crack tip [9.911] using numerical calculations based on diffusion in a hydrostatic stress field showed that it took time to exceed TSSP; rapid precipitate growth followed. At long times, when the hydride had grown well outside the plastic zone, the diffusion and the stress driving terms were equal, $J = 0$, and the hydride stopped growing. This model has been extended to temperature transients, taking into account the apparent hysteresis in the solubility limits [9.912, 9.913]. Similar calculations have been performed for materials in which the hydrides were accommodated elastically [9.914] using the properties of niobium as an example; again, the rate of accumulation of hydride volume fraction at the crack tip slowed with time. An alternative approach, using finite element analysis, was to follow the redistribution of stress because of the transformation strain from a hydride growing at a crack tip [9.702]. As the hydride grew, the hydrostatic and normal stresses decreased to a constant value that extended in length away from the crack tip. Large hydrides were predicted to form tapers, as indicated in Figs 9.317 and 9.322.

If a sharp flaw is present in a component, the stress distribution around its tip can be described by the formalism of LEFM. The stress intensity factor, K_I, is related to the tensile stress, σ, and crack

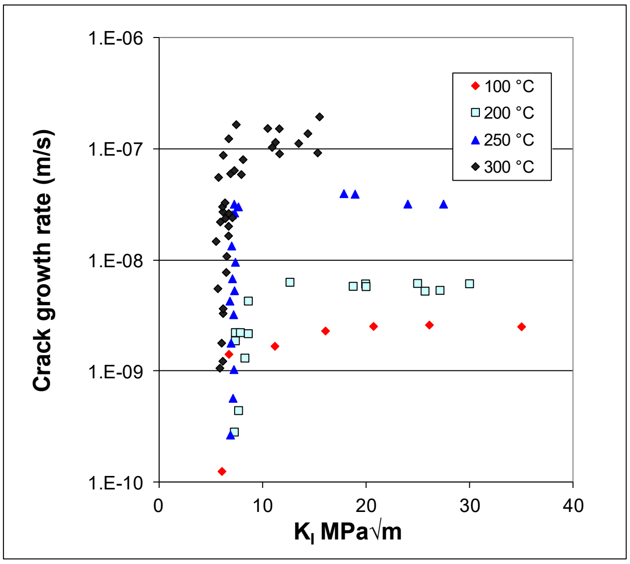

FIG. 9.330. Dependence of crack growth rate on K_I and test temperature in Zr-2.5Nb pressure tube material. The cracks grew in the axial direction in compact toughness specimens (based on [9.915]).

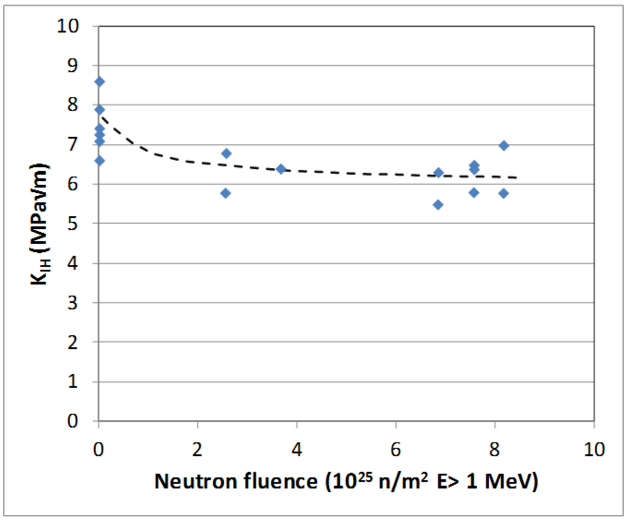

FIG. 9.331. Dependence of K_{IH} on fluence of fast neutrons; Zr-2.5Nb pressure tube material removed from power reactor. Tests in the range 413 to 523 K (140 to 250°C) where the temperature dependence of K_{IH} is small [9.921].

size, $2a$, through (constant x ($\sigma\sqrt{a}$)). Values of V_c at various temperatures are shown as a function of K_I in Figs 9.329 and 9.330 [9.905, 9.915]. These data show that DHC requires a threshold mechanical load to be exceeded, as expected from Inference (5), above. Combining these results with the behaviour described in Section 9.7.5 shows that hydride cracking follows a similar load dependence to SCC — see Fig. 9.191. Once the threshold is exceeded, the crack growth rate is very sensitive to K_I over a very narrow range — this part of the V_c vs K_I curve is sometimes called Stage 1. After Stage 1, the crack growth rate has little dependence on K_I, and is called Stage 2. Rupture follows once the crack is long enough, or the load is large enough, or both. In DHC the threshold is called K_{IH}. In Zr-2.5Nb and Zircaloy the value of K_{IH} is variable, with reported values ranging from close to 4 MPa√m up to 12 MPa√m [9.627, 9.905, 9.915, 9.916–9.920]. At moderate temperatures K_{IH} is not very sensitive to material strength, which typically declines about 200 MPa between room temperature and 523 K (250°C). While neutron irradiation increases the yield strength of the zirconium alloy by 200 to 300 MPa, irradiation causes only a small reduction in K_{IH} [9.887, 9.917, 9.919, 9.921, 9.922]. In Fig. 9.331 the maximum reduction of K_{IH} in Zr-2.5Nb was about 35% with a neutron fluence attained in power reactors of 2×10^{25} n/m^2 ($E >$ 1MeV) with little subsequent change up to 8×10^{25} n/m^2 [9.921]. A similar small decrease was observed with Zircaloy-2 pressure tubes removed from the N-Reactor after 7.7×10^{25} n/m^2 [9.917].

To exceed K_{IH}:

- The material must contain sufficient hydrogen in solution and have had a temperature history suitable for C_C to be reached at the crack tip (i.e. hydrides must form, as described in Inference (1) and (2), above).
- These hydrides must be able to grow to ℓ_c, as described in Inference (3), above, and crack if a critical tensile stress, σf, is present, as described in Inference (5), above.

The first two requirements are discussed above while the third item is covered in Section 9.7.5. The value of ℓ_c at a notch has been analysed using Eq. (9.76) as [9.923, 9.924]:

$$\ell_c = \alpha E\, \varepsilon\perp t/(1 - \nu^2)(\sigma_{max} - \sigma_f) \tag{9.76}$$

where

α is the hydride shape factor;
E is the Young's modulus;

$\varepsilon\perp$ is the transformation strain normal to hydride platelet;
t is the thickness of hydride;
v is the Poisson's ratio of hydride;

and $\sigma_{\max}$ is a maximum tensile stress at hydride.

For a sharp crack, $\sigma_{\max} = \sigma_y/(1 - 2v)$, where σ_y = yield strength of the Zr alloy.

Values of ℓ_c in Stage 1 have been estimated numerically from Eq. (9.76) as a function of K_I and verified by metallographic experiments [9.910, 9.925], as shown in Fig. 9.332. The value of ℓ_c becomes very large as K_I is reduced, suggesting a contribution to the threshold for cracking: difficulty in nucleating and growing hydrides with low K_I [9.910] and a critical condition for cracking leading to a limit for DHC. In several analyses of K_{IH} a hydride fracture stress is invoked [9.923, 9.924, 9.926–9.930] while others use a critical energy release rate [9.928, 9.929]. If cracking is confined to breaking hydride, a lower bound, K_{IH}^{∞}, is estimated from Refs [9.923, 9.927, 9.928]:

$$(K_{IH}^{\infty})^2 = E^2\varepsilon\perp t/8\pi(1 - v^2)^2((1/1 - 2v) - \sigma_f/\sigma_y) \qquad (9.77)$$

K_{IH}^{∞} increases as $t^{1/2}$; some of the variation in measured values may be the result of different hydride configurations at the crack tip. K_{IH}^{∞} decreases with increase in strength, as observed with the effect of irradiation. The temperature dependence of K_{IH}^{∞} is mainly controlled by the temperature dependence of the elastic properties and the strength of the zirconium alloy, and the fracture strength of the hydride precipitate. The crack tip described by Eq. (9.77) is assumed to be completely covered by hydride and low values of the threshold are predicted. As discussed, much variation of hydride configuration is observed at the crack tip and some of the cracking resistance will be because of the presence of some zirconium alloy. This material has higher toughness, K_{IC}, than the hydride so it will contribute to raising the threshold for cracking. If f represents the fraction of the crack front covered by hydride, using a rule of mixtures, a practical evaluation of the threshold would be:

$$K_{IH} = f\,K_{IH}^{\infty} + (1 - f)K_{IC}. \qquad (9.78)$$

An evaluation of Eqs (9.77) and (9.78) is provided as a function of temperature, T (°C), in Fig. 9.333 for both unirradiated and irradiated materials as well as a crack front with 1% zirconium alloy present. The values of the variables were t of 2 μm, $\sigma_f = 650 - 0.091$ T [9.819], $\Delta\sigma_y$ from irradiation

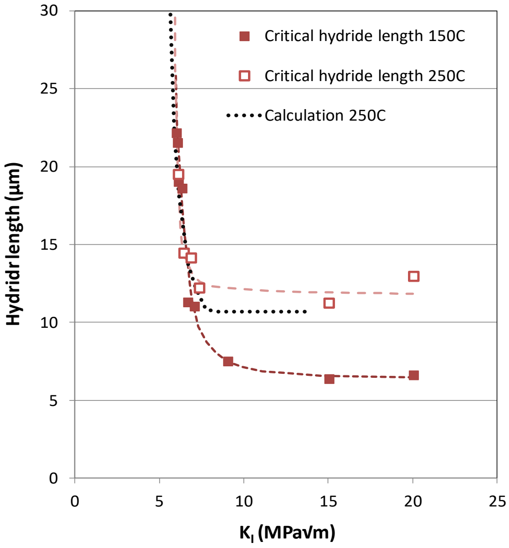

FIG. 9.332. Dependence of ℓ_c on K_I. Experiments on Zr-2.5Nb at 423 and 523 K (150 and 250°C) (K) [9.910, 9.925] and calculation represents behaviour at 523 K (250°C) (K) [9.923, 9.924].

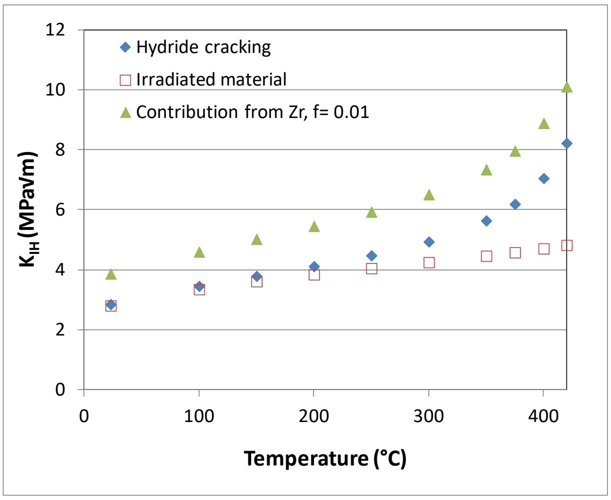

FIG. 9.333. Calculations of the temperature dependence of K_{IH} in both unirradiated and irradiated materials as well as a crack front with 1% zirconium alloy present. The values at low temperature are small and have weak temperature dependence. The decrement with neutron irradiation is only discerned at temperatures above 523 K (250°C). The presence of a small amount of metal is powerful at increasing K_{IH} (based on [9.923, 9.819, 9.849]).

of 300 MPa and $K_{IC} = 76.8 - 0.035T + 0.0002T^2$ [9.849]. The values of K_{IH} at low temperature are small and have weak temperature dependence. The decrement with neutron irradiation is only discerned at temperatures above 523 K (250°C). The temperature dependence of t [9.907] and variability of the distribution of the hydride at the crack tip, leading to the presence of a small amount of metal, are potentially powerful ways to increase K_{IH}.

Once K_{IH} has been exceeded, the subsequent crack propagation rate, V_C, is almost independent of the applied stress intensity factor, K_I, as expected from Inference (9), above, illustrated in Fig. 9.191 and demonstrated with Figs 9.329 and 9.330. V_c is studied in this region of K_I independence, which extends to high values of K_I, at least up to 40 MPa√m, as shown in Fig. 9.330. As indicated in Fig. 9.191, once K_{IC}, or its equivalent for rupture, is exceeded, the crack growth rate will increase and the crack will become unstable.

V_c is very sensitive to temperature, as demonstrated by Figs 9.329 and 9.330 and as expected for a process that depends on diffusion, solubility limit and strength (see Inference (7), above). Often V_c is described by an exponential equation:

$$V_c = \mathrm{C}\exp(-E/RT) \tag{9.79}$$

where

C is a constant;
E is the apparent activation energy for cracking;
R is the gas constant;

and T is the temperature in K.

The value of E is reported to range from about 40 to 70 kJ/mol. This wide range is caused by the effects of temperature history providing variation and the low number of tests contributing to the scatter. Often E is interpreted as the sum of the temperature dependencies of the hydrogen solvus and hydrogen diffusivity. Based on two IAEA programmes, as part of which many specimens were tested at up to 10 laboratories using consistent temperature histories in the temperature range 144 to 283°C (417–556 K) for axial cracking in Zircaloy-4 fuel cladding, E was about 55 kJ/mol [9.931] and in cold worked Zr-2.5Nb pressure tube material, E was about 45 kJ/mol [9.901], as shown in Fig. 9.334. The calculated points were derived from Eq. (9.74) using the tensile properties of the tubes, TSSP values from the Canadian Standards Association standard [9.631] and a value for V_H from Ref. [9.640]. For the CANDU material, Q for diffusivity was assigned a value of 35.2 kJ/mol, as shown in Table 9.38. The

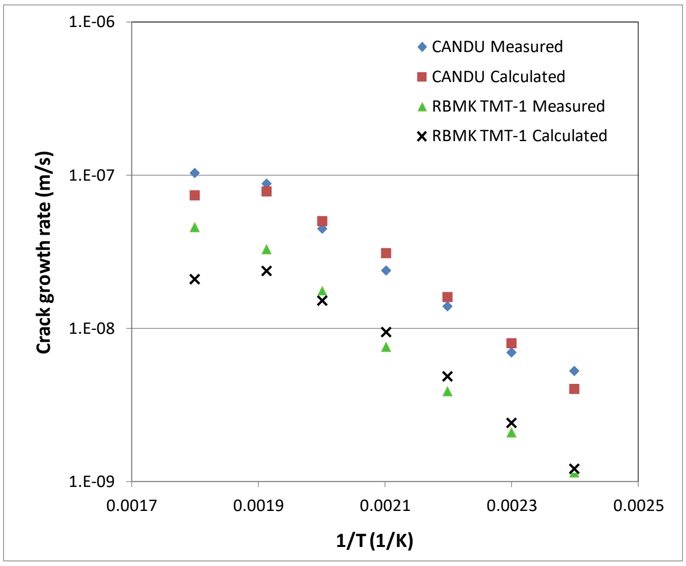

FIG. 9.334. Temperature dependence of crack growth rate by DHC in CANDU and RBMK versions of Zr-2.5Nb pressure tube material. Experimental values from [9.901] and calculated values from Eq. (9.75).

diffusivity of the RBMK material was reduced by 40% to account for its microstructure. The importance of temperature history is shown schematically in Fig. 9.335 [9.876].

Regarding heating, as the temperature is raised from T_1, the crack growth rate follows Eq. (9.78) until a temperature is reached where the cracking rate starts to decline, T_2, and eventually stops (i.e. $V_{min} = 0$) at a slightly higher temperature, T_3, even if hydrides are present in the component. This temperature represents a fourth limit of DHC. Experimental data are depicted in Fig. 9.336 [9.849, 9.932, 9.933] where similar specimens were loaded, either after cooling or heating to the test temperature. A marked difference in behaviour is observed starting at about 450 K (180°C). (Note that in Ref. [9.933] T_3 was termed T_{DAT}.) In dynamic experiments the crack growth can be switched on by cooling and switched off by heating [9.627, 9.849, 9.932, 9.934–9.936]. The value of (T_3-T_1) falls as T_1 is increased [9.627, 9.900, 9.933]. The behaviour on cooling is described above. The behaviour with heating cannot be inferred directly from the mechanism described in Section 9.7.6.2. The principle is illustrated in Figs 9.337 and 9.338 for two starting temperatures, 503 K (230°C) and 296 K (23°C).

A compact toughness specimen containing a sharp crack and 100 ppm (0.90 at.%) hydrogen was held at 503 K (230°C) after cooling from 653 K (380°C) where all the hydrogen was in solution. Hydrides were present in addition to 50.8 ppm (0.46 at.%) hydrogen in solution. When loaded in tension, if TSSP had not been exceeded, the equilibrium hydrogen concentration at the crack tip would have been raised to 79.4 ppm (0.72 at.%) by applying Eq. (9.59). The flux of hydrogen was negative and hydrogen flowed from the bulk to the crack tip. Cracking was at the rate given by Eq. (9.74). On heating, the concentration of hydrogen in the bulk started to increase as the bulk hydrides started to dissolve (indicated by the blue solid line in the Figures); such dissolution has not been formally demonstrated but seems likely. The virtual equilibrium concentration of hydrogen at the crack tip declined (indicated by the red solid line in the Figures) because the decrease from the direct temperature dependence in Eq. (9.59) and reducing yield strength exceeded the increase in hydrogen concentration from the dissolving hydride. Consequently, the crack growth (black dotted line) slowed down. When the temperature reached 537 K (264°C) the flux of hydrogen was zero as the concentration of hydrogen at the crack tip equaled TSSP at P. This temperature was T_3. As the temperature was raised further, the hydrogen flux became positive, and hydrogen flowed from the hydrides at the crack tip to the bulk and the crack stopped growing. The subsequent concentration of hydrogen in solution at the crack tip was lower than TSSP (indicated by the orange dotted line in Figs 9.337, 9.338). The hydrogen in solution at the crack tip followed the line labelled ‘phantom’ in Figs 9.337, 9.338 at higher temperatures (indicated by the green solid line in the Figures beyond P). The crack growth rate did not pass through a maximum value, as indicated in Fig. 9.336, but followed the behaviour shown schematically in Fig. 9.335. This heating effect has been described in Refs [9.627, 9.900].

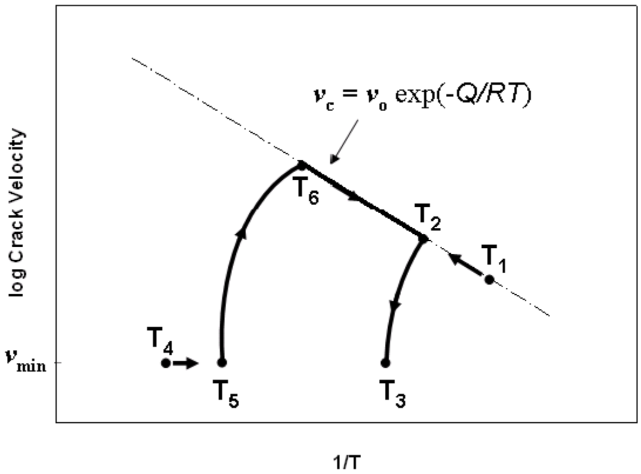

FIG. 9.335. Schematic diagram of the temperature dependence of the DHC growth rate, showing the effect of temperature history. On heating from T_1, the crack starts to slow at T_2 and stops at T_3, even if hydrides are present. (Both T_2 and T_3 have been called T_{DAT}, with T_3 being preferred since that is the temperature at which the crack arrests.) On cooling from T_4, where T_4 is often above TSSD, cracking starts at T_5; with further cooling, V_c rises to a maximum value at T_6, corresponding with TSSP, then decreases following an exponential relationship with temperature. (T_5 is sometimes called T_{RIT} or T_C.) T_5 is greater than T_P when $T_4 >$ TSSD [9.876].

Similar behaviour is expected starting at lower temperatures. The chief problem with simulating the behaviour starting at low temperatures is how to choose the solubility limit. There are indications [9.602, 9.617] that rather than being almost insoluble at low temperature, as predicted by extrapolation from dynamic measurements at high temperature, the temperature dependence is low, and at room temperature TSSP is a few ppm of hydrogen. To describe the behaviour depicted in Fig. 9.336, one can invoke a TSSP equation such as $C_P = 76 \exp(-4988/RT)$. Following the same procedure as for Fig. 9.337, with everything else the same except for the starting temperature of 296 K (23°C) and the altered solvus, the cracking behaviour was approximately described, as shown in Fig. 9.338. The rate had a maximum value at 413 K (140°C), T_2, and cracking stopped at 448 K (175°C), T_3 when the flux of hydrogen was zero, at P. One possibility for this behaviour is that it represents the solvus for γ-hydride, but the values of TSSP for this phase have yet to be measured with any confidence. From these two estimates, ($T_3 - T_1$) was 34°C when T_1 was 503 K (230°C) but increased to 152°C when T_1 was 296 K (23°C), as expected from experimental data [9.627, 9.933].

Regarding cooling, in Fig. 9.335, on cooling from some high temperature, T_4, a temperature is reached where cracking starts, T_5 (termed T_C above and T_{RIT} in Ref. [9.933]), and with additional cooling, the crack growth rate reaches a maximum value at T_6, which corresponds with TSSP. Cracking at subsequent lower temperatures again follows Eq. (9.78). Examples of this cool down process are shown in Fig. 9.339, where experimental results [9.937] are described by the application of Eq. (9.74).

An extension of these behaviours is the dependence of V_c on the peak temperature, T_4. If the test temperature is attained by heating followed by cooling, the maximum value of V_c is only attained when all the hydrogen is taken into solution at T_4. This behaviour is illustrated in Fig. 9.340 [9.934], with the data being described by Eq. (9.74). The amount of hydrogen in solution is also important for K_{IH}. Measurements after cooling to 523 K (250°C) showed that K_{IH} declined with increase in peak temperature; for example, in Zr-2.5Nb containing 100 ppm (0.90 at.%) hydrogen, K_{IH} was reduced from 13.1 MPa√m to 9 MPa√m when the peak temperature was increased from 543 K (270°C) up to 583 K (310°C) [9.938]. This behaviour has been explained by limiting ℓ_c [9.924, 9.938].

If these heating–cooling effects are not taken into account during testing, they contribute to the scatter in the values of crack growth rate and K_{IH}. They also provide the rationale for preheating often prescribed for DHC testing so that the maximum value of V_C and the minimum value of K_{IH} are obtained. The effects can be exploited to minimize cracking during reactor operation by manoeuvrering the temperature to be attained by heating [9.849, 9.934–9.936].

Although Figs 9.329 and 9.330 and measurements on irradiated material between 413 and 523 K (140 and 250°C) [9.921] indicate that K_{IH} was not very sensitive to temperature, above a certain

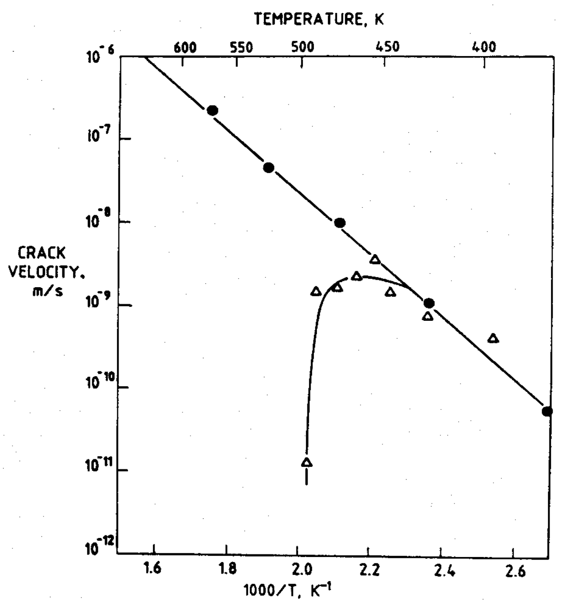

FIG. 9.336. Temperature dependence of crack growth rates resulting from heating to the test temperature (Δ) and cooling to the test temperature (●). Tests on cantilever beams of Zr-2.5Nb containing 110 ppm hydrogen [9.932, 9.933, 9.849].

temperature — at around 582 K (310°C) for Zr-2.5Nb — K_{IH} increased markedly towards 20 MPa√m, as shown in Fig. 9.341 [9.939], and V_c declined, as expected from the corollary of Inference (10), above. At a high enough temperature, T_{MAX}, V_c passes through a maximum value before declining to zero at the upper temperature limit, T_{UTL}. This effect results when the tensile stress normal to the hydride plate is insufficient to fracture a hydride formed at the crack tip, even when the temperature is reached by cooling from above T_D. This effect results from a combination of the following:

- The temperature dependence of the yield strength being much lower than that of the fracture strength of the hydride.
- At temperatures above 573 K (300°C), the high stresses at the crack tip can relax by high stress creep, leading to the stress concentrating effect of the crack being much diminished and the crack being blunted.

In the first experiments to demonstrate T_{UTL}, specimens were required to contain high concentrations of hydrogen, otherwise the cessation of DHC would have been caused by lack of hydrides at the high test temperatures (i.e. $T_{test} > T_P$). In specimens containing 195 ppm (1.75 at.%) hydrogen in which T_P was 673 K (400°C), cracking slowed after about 573 K (300°C) and T_{UTL} was 632 K (313°C) [9.940]. This result was confirmed with material containing 170 ppm (1.53 at.%); with T_P at about 657 K (384°C), T_{UTL} was 623 K (350°C) [9.941]. In these specimens the lack of hydrides was not the reason for the result. Finding T_{UTL} with irradiated material is difficult when the hydrogen concentration is low, as in Zr-2.5Nb pressure tubes after service, because the techniques used to add large amounts of hydrogen also require temperatures higher than the temperature of irradiation; thus, avoiding recovery of irradiation damage is a problem. The T_{max} and T_{UTL} effects were not observed in experiments with irradiated material containing up to 105 ppm (0.95 at.%) hydrogen. Even when 153 ppm (1.38 at.%) hydrogen were added to irradiated material, V_c started to slow at about 598 K (325°C) and completely stopped at 638 K (365°C); theoretical analysis suggested that T_{UTL} for this material, strengthened by irradiation, should be higher than 638 K (365°C) and that the cessation of cracking in this experiment was caused by insufficient hydrogen to form hydrides at the crack tip. Any increase in the solubility limits by irradiation would raise the amount of hydrogen required to show T_{UTL}. This suppression of DHC can be thought of as an elevation of K_{IH} to very high values.

Similar behaviour was observed in Zircaloy-4 fuel cladding, as shown in Fig. 9.342 [9.931, 9.942, 9.943]. Tests on fuel cladding made from Zr-1Nb, Zr-2.5Nb and Zr-0.8Nb-0.8Sn-0.3Fe, as well

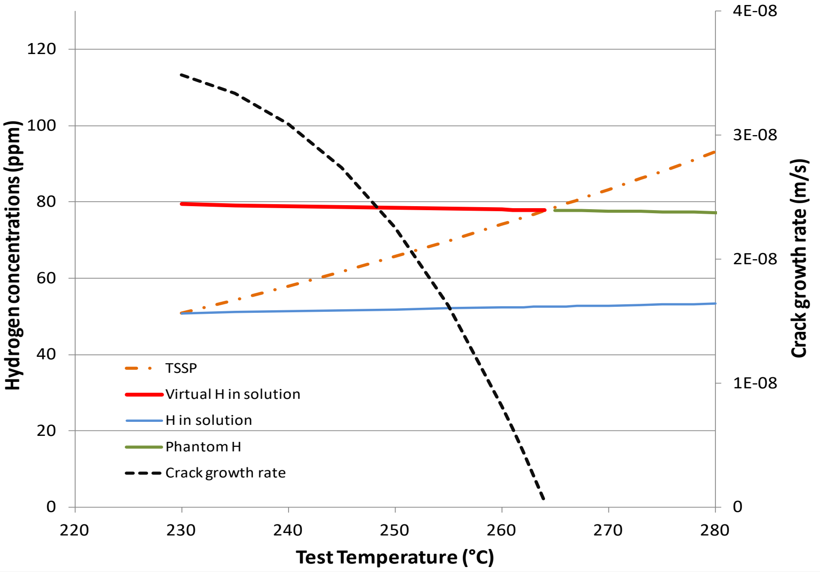

FIG. 9.337. DHC slowing as the specimen is heated from 503 K (230°C). Hydrogen concentration was 100 ppm (0.90 at.%). Virtual equilibrium hydrogen concentration (solid red line) that would have been present at crack tip if TSSP (orange dotted line) had not been exceeded. Once the temperature is sufficient for TSSP to be exceeded in the bulk, at P, the hydrogen concentration at the crack tip is lower than TSSP (solid green line) and the crack stops growing (dotted black line). The hydrogen in solution in the bulk gradually increases with temperature (solid blue line).

as Zircaloy-4, exhibited similar behaviour with the drop-off in V_c starting as low as 505 K (232°C) in Zr-1Nb [9.944]. T_{max} declined with a drop in matrix strength. ZIRLO cladding contained 375 ppm (3.3 at.%) after a burnup of 70 MWd/kgU was tested by the pin-loaded tension method [9.945]. T_{max} was similar for both unirradiated and irradiated material at 583 to 588 K (310 to 315°C) but T_{UTL} was 608 K (335°C) for unirradiated material and increased to 648 K (375°C) with irradiation. This drop-off in V_c was not caused by lack of hydrogen since T_P was well over 673 K (400°C). The difference produced by irradiation is an effect of increase in matrix strength.

V_c also depends on other metallurgical conditions. If the β phase in Zr-2.5Nb is continuous it can provide an easy pathway for hydrogen diffusion whereas if the β phase is discontinuous, hydrogen diffusion is determined by the lower diffusivity of the α phase, as discussed in Section 9.7.2.1(b). Consequently, V_c is expected to be higher when the former microstructure is present. This proposition was expected from Inference (11), above, and confirmed by keeping the strength constant during low temperature anneals that were sufficient to disintegrate the β phase [9.946, 9.947], as shown in Fig. 9.343, or by observing the reduction in V_c by annealing that reduced the strength and broke up the β phase [9.948]. In general, V_c is lower in Zircaloy than in Zr-2.5Nb because it is weaker and contains no β phase.

As expected from Inference (10), above, and Eq. (9.74), strong versions of Zr-2.5Nb [9.159, 9.934, 9.949] and Zircaloy-4 [9.931] cracked faster than weak ones. Neutron irradiation to over 6×10^{25} n/m^2 ($E > 1$MeV) in a power reactor resulted in V_c being increased, after a transient of about 2×10^{25} n/m^2, by up to a factor of 10 in Zr-2.5Nb, depending on the temperature of irradiation [9.921, 9.950]. The two sets of results shown in Fig. 9.344 were from the centre (3.55 m from the inlet) and outlet end (5.65 m from the inlet) of a CANDU fuel channel. The flux was higher, 3.5×10^{17} n·m^{-2}·s^{-1} vs. 0.65×10^{17} n·m^{-2}·s^{-1}, but the temperature was lower, 551 vs. 568 K (278 vs. 295°C), at 3.55 m compared with 5.65 m. After 14 years of service, the fluence in each location was beyond the expected transient for DHC, so the effect of irradiation temperature was responsible for the difference in V_c. When Eq. (9.74) was applied to these results, initially the increase in strength from irradiation was sufficient to describe the values at 5.65 m but not at 3.55 m. In the centre of the reactor the β phase starts to be reconstituted. If this process is sufficient to increase D by about a factor of 2.3, a good description of V_c is obtained. A very large increase in V_c, about 40 times, was reported for two specimens of Zircaloy-2 pressure tube removed from the N-Reactor [9.917]. In both these pressure tube materials,

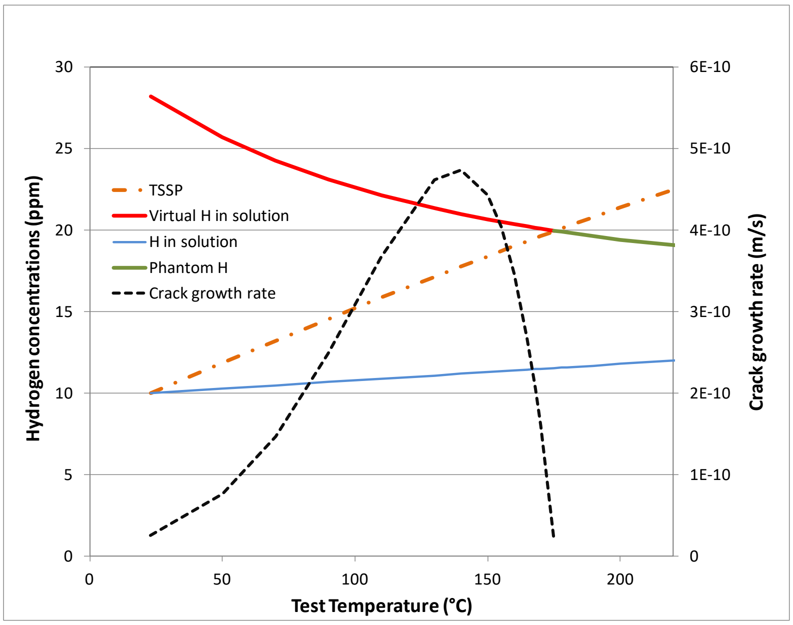

FIG. 9.338. DHC slowing as the specimen is heated from 296 K (23°C). Hydrogen concentration was 100 ppm (0.90 at.%). Virtual equilibrium hydrogen concentration (solid red line) that would have been present at crack tip if TSSP (orange dotted line) had not been exceeded. Once the temperature is sufficient for TSSP to be exceeded in the bulk, at P, the hydrogen concentration at the crack tip is lower than TSSP (solid green line) and the crack stops growing (dotted black line). The hydrogen in solution in the bulk gradually increases with temperature (solid blue line).

irradiation increased the strength by 300 to 380 MPa. In the highly irradiated ZIRLO described above, the increase in strength was 182 MPa and the increase in V_c was 2.8 times [9.945], illustrating the contribution of matrix strength to DHC. In Zircaloy-2 fuel cladding in the LK-2 condition, the increase in V_c at 573 K (300°C) after a burnup of 35.9 MWd/kgU was a modest factor of 1.7, but again fitted to a correlation with strength [9.887].

High flux irradiations have been performed in the research reactor Osiris to obtain fluences up to the expected life of a Zr-2.5Nb pressure tube. The irradiation temperature was between 523 and 533 K (250 and 260°C) for most of the ten year experiment [9.951]. The value of V_c up to a fluence of nearly 3×10^{26} n/m^2 is depicted in Fig. 9.345 along with an estimate based on Eq. (9.74), again taking into account the reconstitution of the β phase. The crack growth rate was increased by about ten times. The strength transient was over by 1×10^{25} n/m^2 but the V_c transient followed the β phase transient taking up to about 5×10^{25} n/m^2. Thereafter there was little change in V_c.

If the tensile stress is parallel with the basal plane normal DHC is easy. In tubes of cold worked Zr-2.5Nb hydride cracking is easy on the plane normal to the transverse direction, where the texture parameter for [0001], F_T, is about 0.63, and very difficult on planes normal to the longitudinal direction, where the texture parameter for [0001], F_L, is about 0.06 [9.763]. The formation of hydride plates perpendicular to a tensile stress in the longitudinal direction at a crack is replaced by a diffuse collection of small hydrides, as shown in Fig. 9.327. The value of V_c is between 25 and 100 times lower under a longitudinal stress than a transverse stress. Similar behaviour is observed in tubes made from Zircaloy-2 [9.917]. Experiments on plates with various textures confirmed that DHC was fastest when stressing parallel to [0001] [9.947, 9.952–9.954]. In cold worked materials, the hydrides can be aligned by the working conditions. When stresses are applied perpendicular to such hydrides, no reorientation is required. Even if the crystallographic texture is unfavourable for DHC, it progresses at the same rate as if the texture were favourable for hydride reorientation [9.954]. Although this discussion implies that a strong radial may offer a degree of protection, Zircaloy-4 fuel cladding with an F_R of 0.6 cracked by DHC readily on the plane with normal in the hoop direction [9.884, 9.887, 9.918, 9.919, 9.931]. Crystallographic texture is the microstructural feature that seems to have the most influence on K_{IH}. This large effect on K_{IH} is because of the sensitivity of hydride reorientation to texture [9.763], as

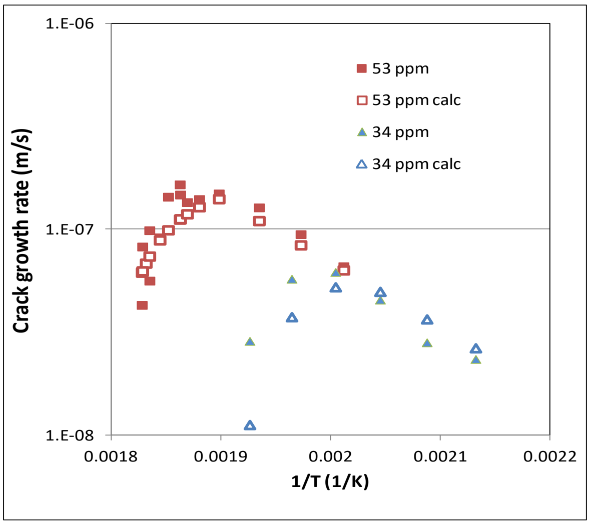

FIG. 9.339. Verification of the cooling part of the schematic temperature history diagram, Fig. 9.335; comparison of experiment (full symbols) [9.937] and model (open symbols) [9.900] for T_5 and T_6 during cooling from T_4 in Zr-2.5Nb containing two concentrations of hydrogen. Note that cooling is from left to right.

discussed in Inference (11), above. When tensile stresses are parallel with [0001], K_{IH} is low and when tensile stresses are perpendicular to [0001], K_{IH} is high. The value of K_{IH} appears to vary linearly with the texture factor for [0001] in the direction of the tensile stress, F_σ [9.955, 9.956], ranging from 4.5 to 10 MPa√m with an F_σ of about 0.6 to 15 to 30 MPa√*m* when F_σ is around 0.1.

A positive temperature gradient (i.e. when the crack tip is cooler than the metal matrix) increases V_c and shifts T_2 and T_3 to higher values [9.957]. These effects are caused by combining the diffusion of hydrogen up the stress gradient (see Section 9.7.2.2) and down the temperature gradient (Section 9.7.2.3). For example, in Zr-2.5Nb, with a temperature gradient of 20°C/mm, V_c is increased by a factor of 2.6 and T_3 is raised by 423 K (150°C). A rise of 90°C was demonstrated by experiment with a gradient of 10°C/mm, as shown in Fig. 9.346. In Zircaloy-2 fuel cladding, cracking was absent in isothermal conditions at 561 K (288°C) but with a temperature gradient of about 70°C/mm, the cladding cracked readily from the outside surface [9.958].

After DHC, the fracture surfaces contain much hydride, in agreement with Inference (6). With α/β alloys (e.g. Zr-2.5Nb), remarkable concentric bands, called striations, shown in Fig. 9.347(a), are formed perpendicular to the cracking direction [9.959, 9.960]. This behaviour is in sharp contrast to the fissures formed at circumferential hydrides during final rupture after DHC, shown in Fig. 9.347(b). Striations were interpreted as forming with each crack step. Crack jumps, indicated by large amounts of acoustic emission and changes in potential drop, exactly corresponded with interstriation spacing and the number of hydride clusters along the crack path, supporting the interpretation that the interstriation spacing represented the critical length of hydride for fracture during DHC [9.907]. Striations consisted of regions of ductile fracture bounding cleavage of hydride, possibly caused by back-linkage to the crack tip, or brittle crack overshoot or both. The interstriation spacing increased with an increase in test temperature, as shown in Fig. 9.348 [9.901, 9.915, 9.961–9.963], and with either little dependence on K_I above about 12 MPa√m or an increase with decrease in K_I, especially as K_{IH} is approached. Interstriation spacing also increased as the strength decreased, either as a consequence of increase in test temperature or because of microstructural change. Microstructure must play a role in striation formation since none has been observed on DHC fracture surfaces in Zircaloy [9.884, 9.887, 9.917, 9.918, 9.931]. Typically, regions of flat fracture are found, often arranged in arcs, as shown in Fig. 9.349, which strongly resemble those observed on failed Zircaloy fuel cladding, as shown in Fig. 9.320. Often areas of cleavage corresponding with cracked hydrides are observed, but no striations, as shown in Fig. 9.350. These observations suggest that striations are not a fundamental characteristic of DHC and that their absence cannot be used to eliminate DHC as a crack propagation mechanism.

In summary, zirconium alloys can fracture by a stable cracking process called DHC. The temperature and loading dependence of properties of DHC have been firmly established by experiment

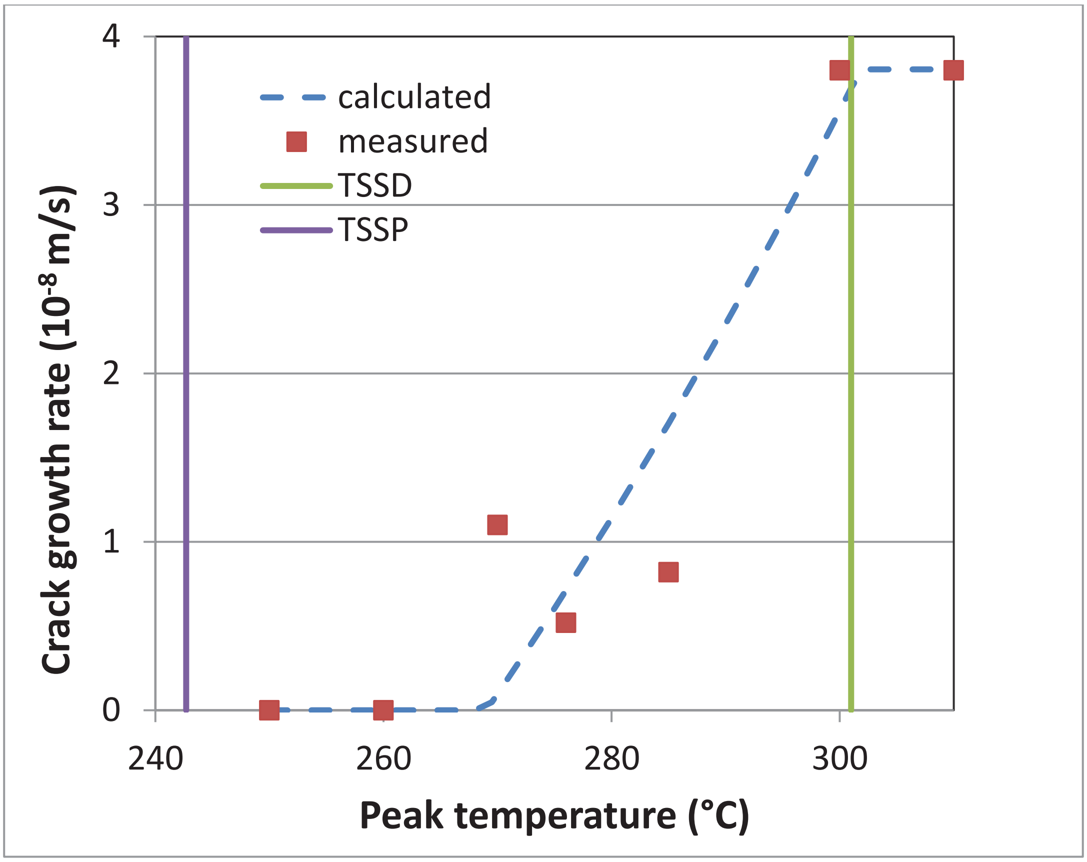

FIG. 9.340. Demonstration of requirement that to attain the maximum value of crack growth rate at 523 K (250°C), the peak temperature should exceed T_D [9.934]. Specimens of cold worked Zr-2.5Nb contained 60 ppm (0.54 at.%) hydrogen, have T_D of about 575 K (302°C) and T_P of about 516 K (243°C); cracking took place with temperature >T_P. Calculated values based on Eq. (9.75) [9.900].

and the basic mechanism has been confirmed. Although high stresses can initiate cracking, the discussion has focused on starting the process from sharp flaws. Four limits for cracking exist:

- Sufficient hydrogen should be present so that hydrides can nucleate, grow and crack at the stress concentration at the flaw tip.
- The combination of flaw size and tensile load, forming a stress intensity factor, K_I, should exceed a critical value, K_{IH}.
- Above about 453 K (180°C), cracking can be halted by heating a few °C.
- Above some high temperature, zirconium alloys are immune from DHC, even if the previous limits have been satisfied.

9.8. STRUCTURAL INTEGRITY

Methods have been developed to prevent failure by the cracking processes discussed in previous sections. The basic methods are to prevent crack initiation by controlling tensile stresses, the chemical and thermal environment, and the presence of crack initiation sites. Hydrogen has caused several problems and is used as an example. The kind of information needed to evaluate components is discussed first, then the development of initial cracks from nominally smooth surfaces and rounded defects is outlined. Despite these precautions, a flaw may become an active crack. As a defence-in-depth, methods have been developed to prevent an active crack becoming a safety issue as well as an economic one.

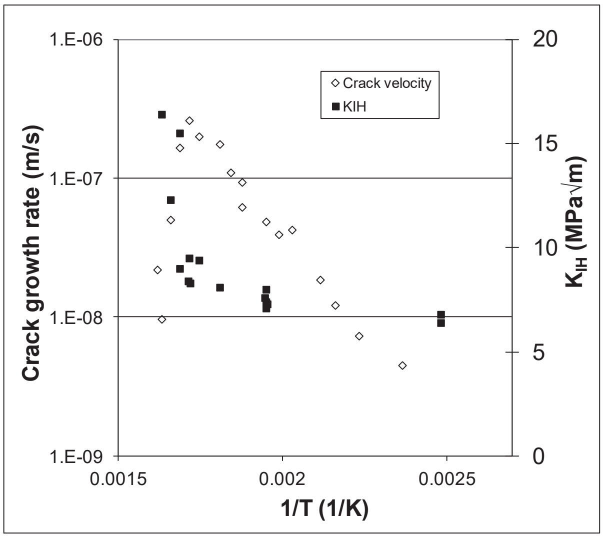

FIG. 9.341. Temperature dependence of DHC in Zr-2.5Nb showing sharp increase in K_{IH} and concomitant decline in crack growth rate [9.912].

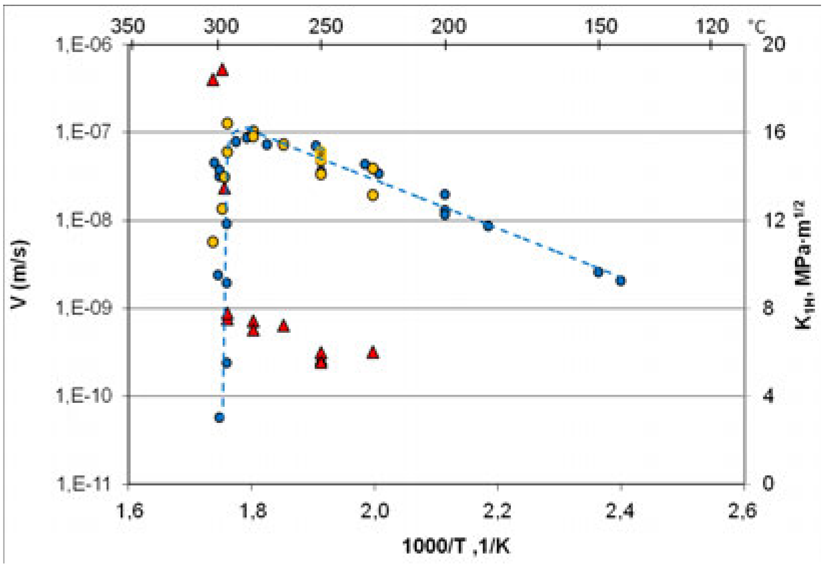

FIG. 9.342. Temperature dependence of DHC in Zircaloy-4 showing sharp increase in K_{IH} and concomitant decline in crack growth rate. Blue circles are V_c from [9.931] and yellow circles are V_c and red triangles are K_{IH} from [9.943].

9.8.1. Rules of engagement

Operating a component outside the limits of DHC can prevent crack propagation. The issue becomes how close to the limits for DHC a component is during its lifetime. To discover the potential for failure in a component, or understand a failure so it can be avoided in the future, one needs to evaluate the margins on the limits for DHC and answer the seven questions listed in Table 9.47. Two examples will be discussed to illustrate the principles.

9.8.1.1. Welding Zr-2.5Nb

Cracks at welds were discussed in Section 9.7.6.1(a). In each case, cracking was not discovered until several months after welding. Cracks were initiated at small surface flaws such as a notch at the weld, porosity, a brittle oxygen-rich layer or a bolt thread. The cracking was found either at room temperature before the components went into service or after a series of thermal cycles during operation. Although the hydrogen concentration was within the specification, hydrides could still form at room temperature at a stress raiser. Large residual crystal lattice strains, indicating large residual stresses, were measured by neutron diffraction. The maximum depth of a sharp surface flaw, a_c, that can be tolerated without crack growth by DHC, is estimated with Eq. (9.80) [9.962]:

$$a_c = (S/1.21\pi)\,(K_{IH}/\sigma_D)^2 \tag{9.80}$$

The shape factor, S, is about 1.5 when the flaw length is 3 times the flaw depth. With a K_{IH} of 4.5 MPa√m, and a residual stress, σ_D, of 230 MPa, the value of a_c is about 0.15 mm. Such a flaw could be missed by inspection. Thus all the questions except for (4) can be answered affirmatively. The main solution to this problem was to reduce the residual stresses by heat treatment; a treatment of 803 K (530°C) for 1 hour soon after welding is sufficient to reduce the residual stresses by 60% and increase the critical flaw depth to 1.3 mm. This size of flaw should be found during inspection. The combination of stress relieving within a certain time and careful inspection should eliminate crack initiation by DHC in welds.

9.8.1.2. Storing nuclear fuel without DHC

The conditions during the dry storage of spent nuclear fuel were outlined in Section 9.3.3 where the discussion focused on the possibility of stress rupture. The temperature is highest at the start of storage, being no higher than 673 K (400°C) (the maximum value recommended by the NRC); consequently, the pressure and the hoop stresses are also highest at the beginning of dry storage. Since with time the temperature declines, the temperature history during dry storage is perfect for DHC. As the temperature is reduced, the pressure also decreases. If the cladding creeps, the pressure also decreases even further because of the extra volume. DHC becomes less likely during storage because the hoop stress steadily decreases with time. In Section 9.7.6.1(e) Zircaloy fuel cladding was shown to be susceptible to DHC, which may occur if the correct conditions exist. Although the loading is mostly in plane stress, a stress gradient is set up at any flaw, which is sufficient to induce hydrogen migration to the flaw tip. A typical flaw may be caused by fretting.

About 275 ppm (2.45 at.%) hydrogen are required to exceed TSSP at 673 K (400°C) and such high hydrogen concentrations have been observed in LWR cladding (e.g. after a fuel burnup of about 57 MWd/kgU, low tin Zircaloy-4 contained between 600 and 820 ppm (5.19 and 6.96 at.%) hydrogen [9.734]). Thus, DHC would not be limited by lack of hydrogen during dry fuel storage.

Even with favourable stressing conditions, a maximum temperature, T_{UTL}, exists above which DHC cannot start. In Section 9.7.6.3 this temperature is given as around 573 K (300°C) in unirradiated cladding material but may be as high as 633 K (360°C) in irradiated material. This phenomenon suggests that spent fuel that started storage at the NRC stipulated maximum temperature of 673 K (400°C) would be immune from DHC until the temperature reached the critical temperature. This period of immunity is about three years, using the expected cooling curve, as shown in Fig. 9.51. If T_{UTL} depends on irradiation damage, its value may be reduced if the damage is annealed out during early storage. Thus, the period of immunity may be much longer than estimated; if T_{UTL} returns to 573 K 300°C (300°C), the period of immunity increases to about 12 years, as shown in Fig. 9.51. The hoop stress will be simultaneously lowered, providing further protection. Once the period of absolute immunity is over, the stress conditions have to be examined.

The hoop stress during storage was discussed in Section 9.3.3. The maximum hoop stress recommended by the NRC is 90 MPa. The application of Eq. (9.80) with a value of 4.5 MPa√m for K_{IH} and the recommended maximum hoop stress from the internal gas pressure suggests that for cracks to propagate by DHC they would have to be through-wall and therefore detectable before storage started [9.963]. Experience of dry storage of nuclear fuel indicates no cracking for times ranging from 15 to 20 years [9.197, 9.199], supporting the idea that DHC is unlikely during dry storage of LWR fuel after service.

The answers to the seven questions are summarized in Table 9.47 for these two examples. Despite the failures in welds and the spectre of cracking during fuel storage, zirconium alloys can be used free from DHC if some of the questions can be answered in the negative. Tensile stress must be carefully controlled if components contain hydrides or have the prospect of precipitating hydrides at a flaw. The conditions for the generation of flaws are considered next.

TABLE 9.47. SEVEN QUESTIONS ON POSSIBILITY OF DHC IN WELDS AND STORAGE OF SPENT FUEL

	Questions	Welds in Zr-2.5Nb	Spent nuclear fuel dry storage
1	Is the material susceptible to DHC?	Yes	Yes, No, because of the value of T_{UTL} at the start
2	Is sufficient hydrogen present to form hydrides at a crack tip?	Yes, but only at low temperatures	Yes, from reactor operation
3	Was the temperature history conducive to DHC?	Yes, cooling after welding and plant operation	Yes, No, because of the value of T_{UTL} at the start
4	Were any temperature gradients present?	No	No
5	Are any sharp flaws present and if so, how large are they?	Yes, notch in weld, porosity, brittle oxygen-rich layer	Maybe, possibly from fretting, SCC, radial hydrides and cracked hydride rim
6	Are large tensile stresses present?	Yes, residual stresses, No, if removed by heat treatment	Yes, from internal gas pressure
7	Is the combination of (5) and (6) sufficient to exceed K_{IH}?	Yes, No, when stress relieved	No, unless flaw through-wall, then pressure and stress zero

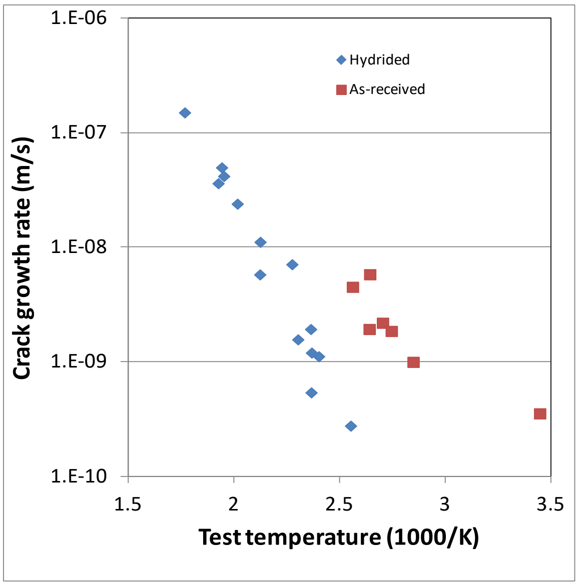

FIG. 9.343. Change in V_c by heat treatment that breaks up the β-phase (hydrided) compared with material in the as-fabricated condition (as-received) where the β-phase was continuous (based on [9.946]).

9.8.1.3. Crack initiation on a plane surface

Pressure tubes do not have mirror smooth surfaces. In early production, small nicks and embedded sand particles were observed about 40 μm deep. After a few fuel loadings the lower part of a pressure tube contained longitudinal rounded scratches, usually about 15 μm deep, from the sliding

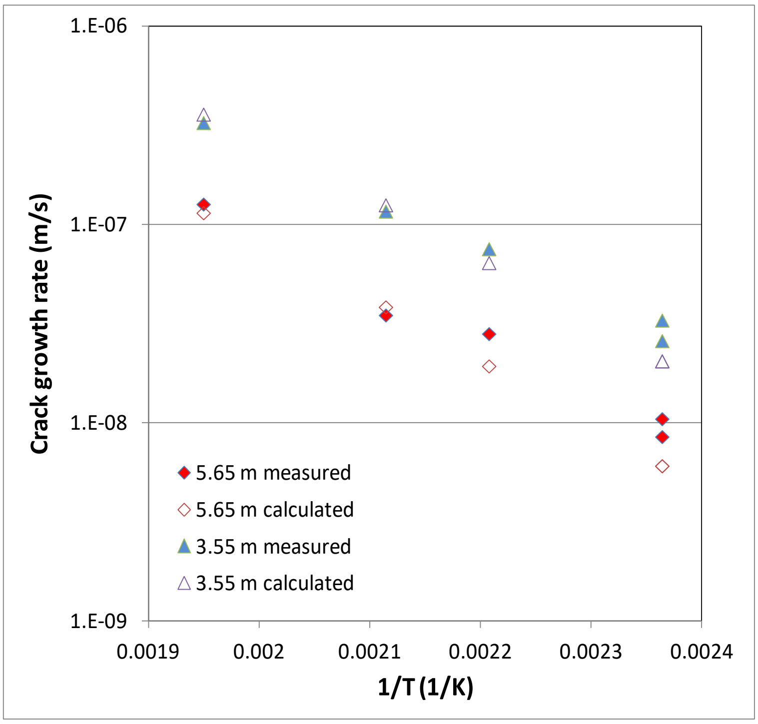

FIG. 9.344. Crack growth rate in samples of Zr-2.5Nb removed from two axial positions in a CANDU pressure tube [9.950]. Only irradiation induced strength is used for the calculations of V_c at 5.65 m but account is taken of reconstituted β-phase as well as irradiation induced strength for values at 3.55 m.

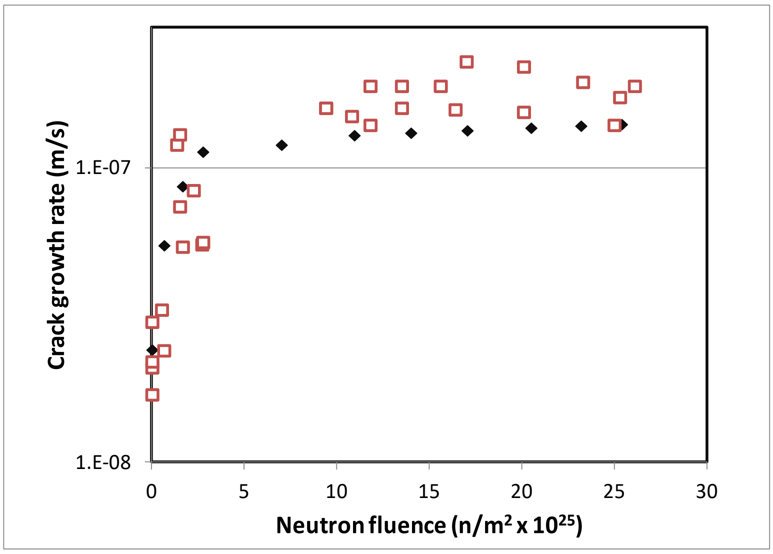

FIG. 9.345. Increase in DHC rate at 523 K (250°C) after irradiation in Osiris [9.951]. Red squares are measurements and black diamonds are estimates using Eq. (9.75), taking account of increase in strength and reconstitution of β phase by irradiation.

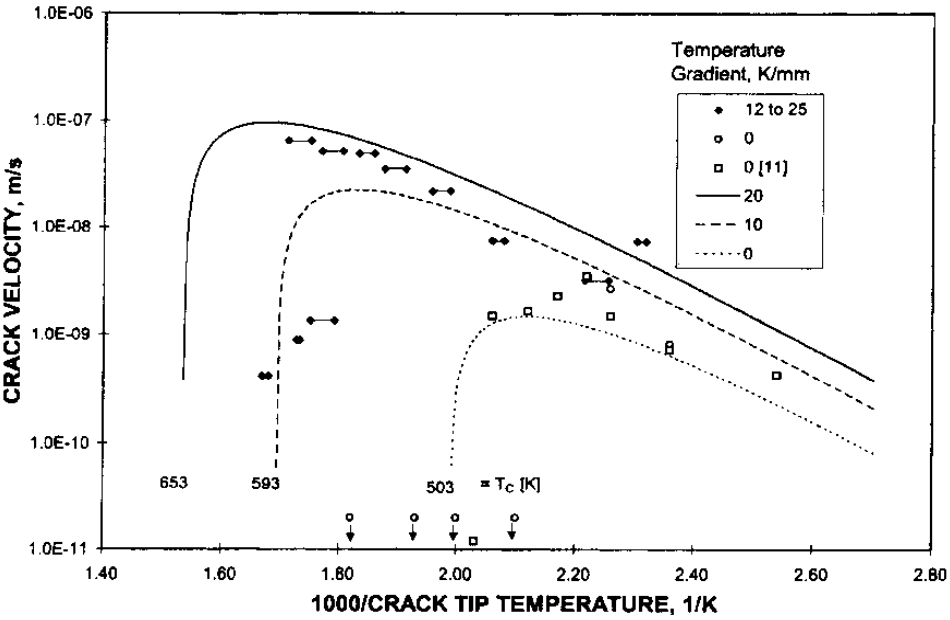

FIG. 9.346. Delayed hydride cracking after heating to test temperature, showing 90°C rise in T_3 with increase in temperature gradient of 10 °C/mm (crack tip cooler than surroundings) [9.957].

of the fuel on the pressure tube during refuelling. These surfaces were defined as smooth. Fuel cladding may be subject to fretting from either interaction with spacer grids or random debris. To evaluate conditions for crack initiation, many specimens have to be tested because specimens fail over a wide range of times. At nominally the same test conditions not all specimens fail; the probability of failure was taken as the number of specimens failed divided by the number of specimens tested. Thermal cycles may promote cracking by assisting the stress orientation of hydrides into a harmful configuration and increasing the local hydrogen concentration by ratcheting. For flaw analysis and design, the aim of tests using specimens with such surfaces is to find the threshold stress for crack initiation, called p_c. Groups of cantilever beams, with nominally smooth surfaces, from both unirradiated and irradiated Zr-2.5Nb pressure tube material containing up to 100 ppm hydrogen, were loaded to various outer fibre stresses and subjected to thermal cycles and long hold times. Specimens failed over a very wide range of times [9.813, 9.876]. The probability of failure in unirradiated material decreased as the stress was reduced. For example, at 425 K (152°C), with a stress of 620 MPa the probability of failure was 0.75 (6 out of 8 specimens); at 585 MPa it was 0.69 (11 out of 16 specimens); at 550 MPa it was 0.17 (4 out of 23 specimens); at 413 MPa it was 0.05 (1 out of 21 specimens) and there were no failures at outer fibre stresses below 413 MPa with test times up to 6400 h. Tests on cantilever beam specimens machined from pressure tubes removed from power reactors were loaded to various outer fibre stresses and thermally cycled. Of 20 specimens, 6 failed when loaded with an outer fibre stress of 550 MPa while 9 specimens loaded between 410 and 450 MPa survived up to 35 thermal cycles with test times up to 5880 h. The value of p_c for reactor application based on these tests is 450 MPa [9.631]. The values of p_c were at least double the threshold stress for hydride reorientation, suggesting that radial hydrides are a necessary condition but are not a sufficient condition for crack initiation. The time scales, probability of cracking and values of p_c help explain the distribution of cracking observed at rolled

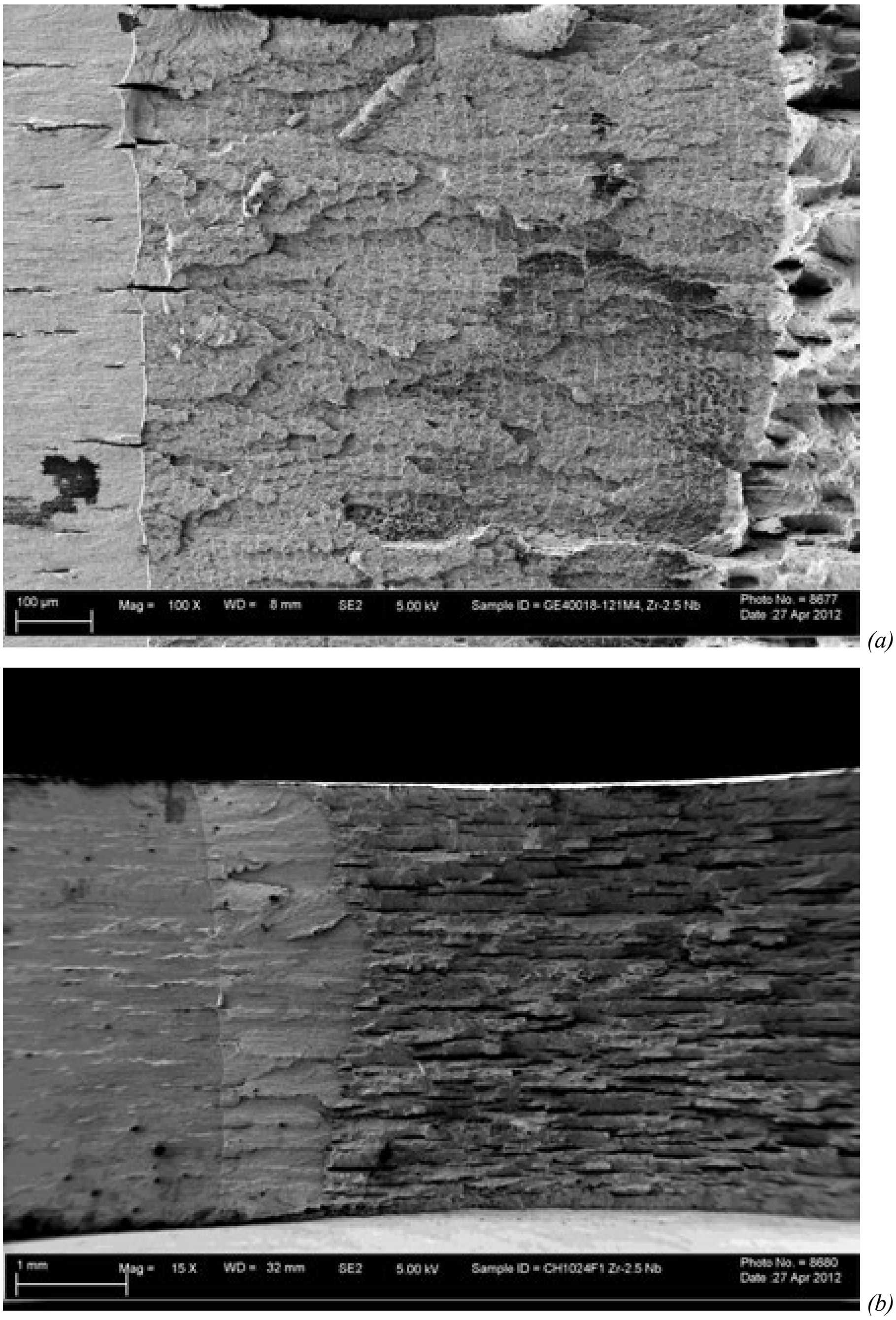

FIG. 9.347. (a) Fracture surface of Zr-2.5Nb pressure tube material tested at 523 K (250°C) for DHC. Cracking on the radial-axial plane travelling from left to right. On left side is fatigue cracking with occasional fissures from residual cracked circumferential hydrides. Central region shows striations formed during DHC. On right side is start of ductile fracture and large hydride fissures in post-DHC-test rupture (fractograph by C. Mayhew, AECL); (b) lower magnification fractograph of surface of Zr-2.5Nb pressure tube material tested at 523 K (250°C) for DHC. Cracking on the radial-axial plane travelled from left to right. On left side is fatigue cracking with occasional fissures from residual cracked circumferential hydrides. Central region shows surface formed during DHC and on the right side is fracture surface containing large hydride fissures in post-DHC test rupture (fractograph by C. Mayhew, AECL).

joints in Pickering-3 and -4, as indicated in Section 9.7.6.1(a). Care has to be taken in directly applying the results from cantilever beams to pressure tubes since the stress distribution is different with each geometry — in cantilever beams the stress varies from tensile to compressive across the specimen while in a pressurized tube the gradient in tensile stress is small across the wall of the tube.

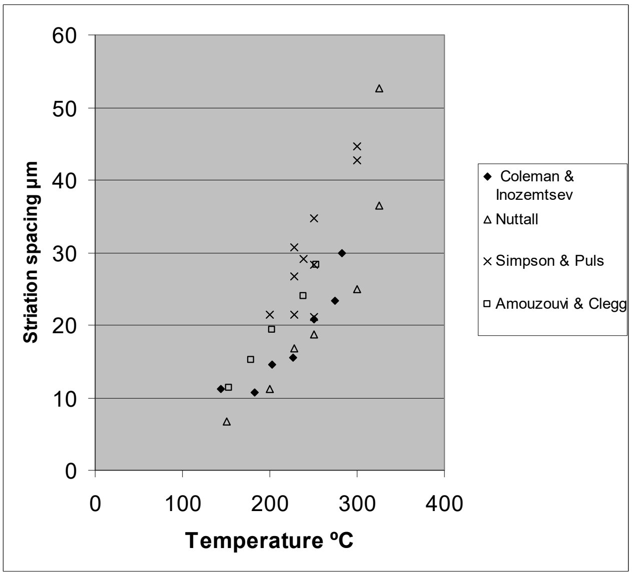

FIG. 9.348. Temperature dependence of interstriation spacing in cold worked Zr-2.5Nb after DHC [9.901, 9.915, 9.960, 9.961].

9.8.1.4. Crack initiation from notches

Specimens of pressure tube material containing machined notches were tested to gain insight into the behaviour of flaws encountered by components during operation. The stress conditions were between the severe localization at a sharp crack, which can be analysed by K_I, and the wide distribution of stress over a large region with a smooth surface. As with specimens with smooth surfaces, in the large test matrices to measure the effects of notch shape and applied stress, much of the time to failure was taken up with setting up the conditions for crack initiation since the time of crack propagation and final rupture was short compared with the time to initiate the crack.

For test matrices on notched specimens, the effect of loading would be overestimated by using an apparent K_I and underestimated by the general stress, thus the maximum local stress at the notch tip was used to evaluate data. In one test matrix [9.964], 240 cantilever beam specimens were machined from a single Zr-2.5Nb pressure tube containing 1.2 at.% (130 ppm) deuterium and hydrogen. The specimens were arranged in groups of 10 that had the same stress condition, using different notch depths and bend loads, then held for 130 h at 523 K (250°C), attained by cooling after weekly thermal cycles between 333 and 573 K (60 and 300°C) on a schedule designed to promote DHC. Over more than 3 years and 165 thermal cycles, 123 specimens failed. The probability of failure increased, as shown in Fig. 9.351, and the time to failure declined, as shown in Fig. 9.352, with increase in peak stress, σ_{yy}^{max}, at the crack tip. A threshold value was in the range 675 to 750 MPa, which is similar to the estimates of hydride fracture stresses derived from tensile tests and evaluation of the compressive stress inside the hydride; see Section 9.7.4. The results were interpreted in terms of the stress required to fracture the hydride once it reached a critical length [9.964, 9.965]. Below the threshold, no failures were recorded up to 150 thermal cycles and 28 000 hours. The majority of the failures were within 30 hours of cooldown to the hot hold temperature part of the cycle, emphasizing the importance of the direction of temperature change. The susceptibility to failure was very sensitive to the sharpness of the notch, further emphasizing that the general stress and K_I approach are inappropriate for rounded flaws and supporting the notion of a critical stress to initiate cracking.

The approach for notches has been extended by postulating that two conditions must be met for flaw extension by DHC [9.966]: both the stress, p_c, and displacement across the flaw, v_c, must exceed critical values in a process zone:

$$v_c p_c = (K_{IH})^2(1 - \nu^2)/E \qquad (9.81)$$

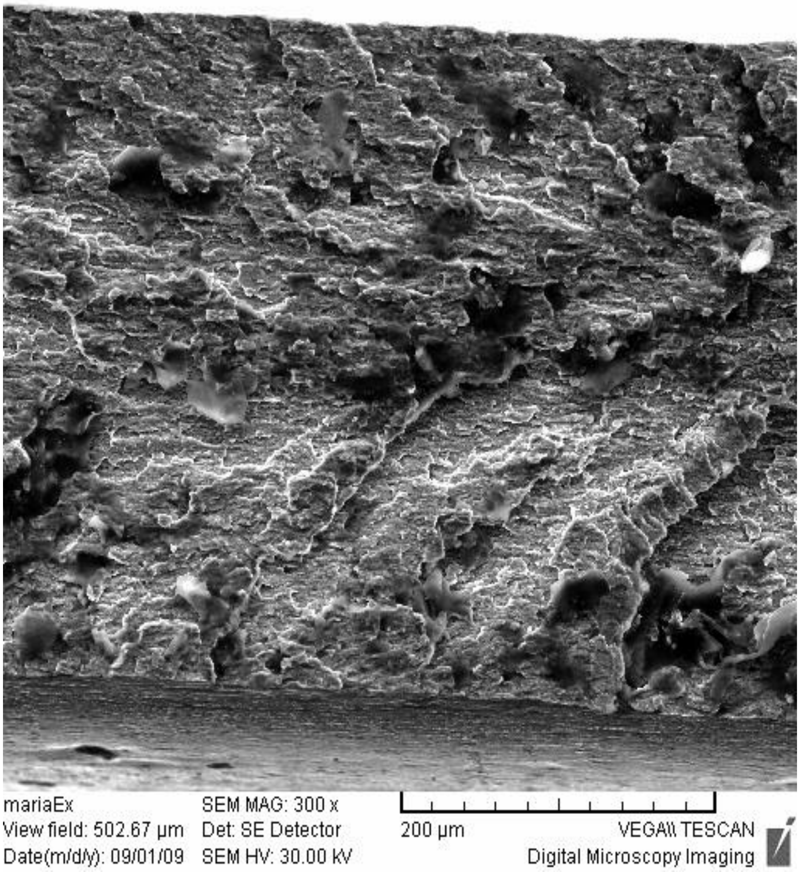

FIG. 9.349. Delayed hydride cracking on CANDU Sandvik Zircaloy tested at 523 K (250°C) showing areas of flat fracture interspersed by curved features that correspond to changes in crack plane or direction [9.931].

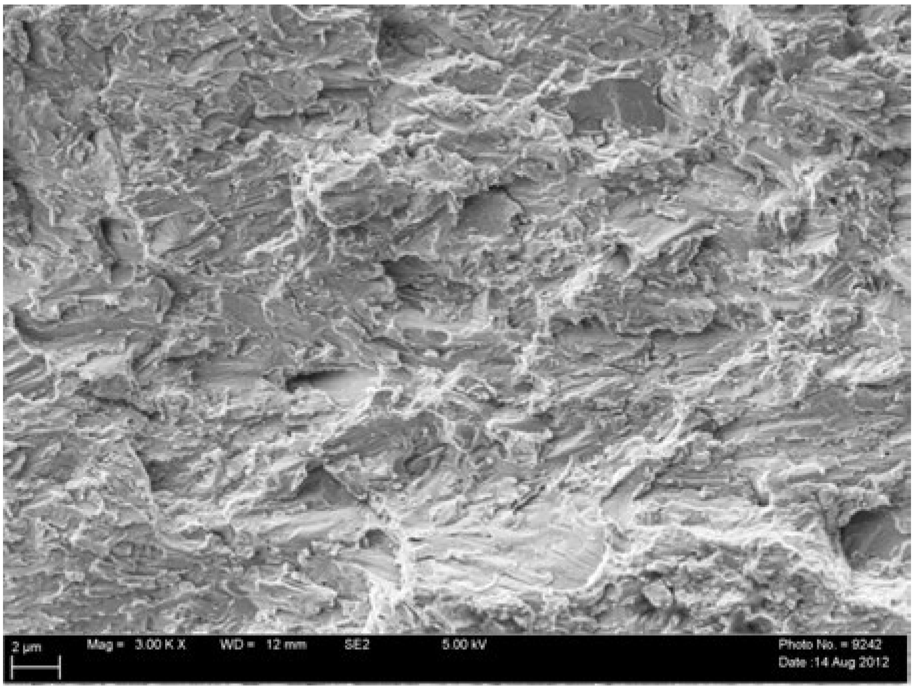

FIG. 9.350. Areas of cleavage on fracture surface of Zircaloy-4 fuel cladding subject to DHC at 523 K (250°C) (fractograph by C. Mayhew, AECL).

This model, which takes into account the flaw depth accurately as well as the strain due to hydride precipitation and creep, is used for engineering assessments [9.630].

If a flaw escapes detection and propagates, the issue becomes whether the crack will become unstable before it is detected. Non-destructive inspection is not usually practised during reactor operation so any active crack must be detected and located by other means. If a crack penetrates the wall of a pressurized tube, the pressurizing medium can be detected either from leakage of radioactivity or water before the crack has grown too big. This situation is called LBB.

9.8.2. Leak-before-break

During operation, fuel cladding may be under tensile stress from fuel expansion and a flaw may continue to grow. For example, through-wall cracks over 1 m long have been detected in BWRs [9.884], although they appear to have been stable. During spent fuel storage, if a crack develops and propagates through the tube wall, the gas will escape, the pressure driving the crack will disappear and the crack will stop growing. Its presence should be detectable from escaping fission products. As an example, the cover gas of containers can be sampled for the fission product Kr^{85} to indicate leakage through wall-penetrating cracks in the fuel cladding. Krypton-85 is a radioactive isotope with a half-life of 10.74 years. Surveillance of several thousand LWR fuel rods after a burnup of up to 35 MWd/kgU and pool storage of between 2.2 and 10.1 years indicated no release of Kr^{85} for 12 years of dry storage [9.967]. The initial temperature of the Zircaloy clad was between 383 and 678 K (110 and 405°C). Krypton-85 was detected when the cask was rotated or the fuel was consolidated, which involves pulling and twisting the rods. Rotation induced two indications out of 16 700 fuel rods, a failure rate of 0.012%, whereas consolidation was more damaging with about 12 failures out of 9800 rods, or about a tenfold increase in failure rate. The loading during handling was thought to enlarge incipient cracks rather than trigger them although the source of the cracks was not identified. These failures are examples of both LBB and failing safely, in the sense that the crack is stable; clearly the wide distribution of fission products and fuel is undesirable.

This form of LBB is useful for components made from materials that can degrade during service by the mechanisms of time dependent crack propagation discussed in Sections 9.5, 9.6 and 9.7. In pressure tubes, with the exception of the cracks in Zircaloy-2 containing hydride blisters [9.880], all the

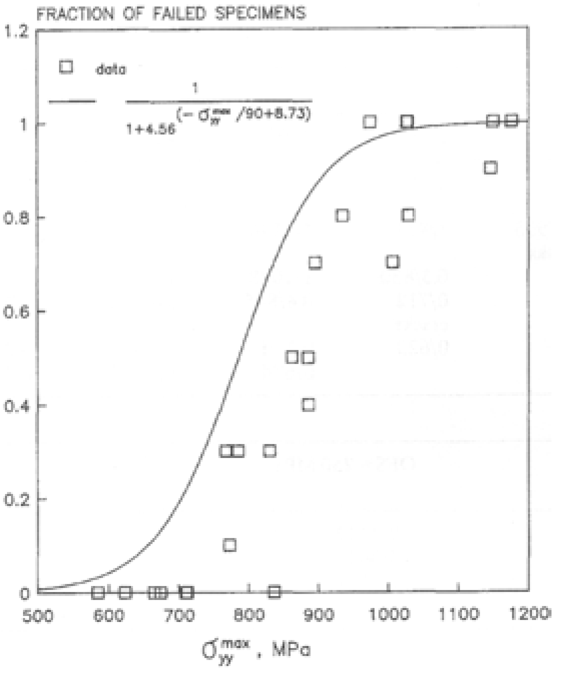

FIG. 9.351. The dependence on σ_{yy}^{max} of probability of failure of Zr-2.5Nb at 523 K (250°C) with thermal cycling. The probability density function, derived from the best fit to the data, represents the upper bound of the data [9.964].

cracks in Zr-2.5Nb pressure tubes that have grown by DHC alone, in both CANDUs and RBMKs, have demonstrated LBB, as discussed in Sections 9.7.6.1(a), 9.7.6.1(b) and 9.7.6.1(c). The pressure, and therefore hoop stress, are retained when a crack penetrates the tube wall and leaks. The principle of LBB relies on knowing the timescales of the cracking process and the response time of the reactor system. To be sure that LBB is guaranteed, one must show that the crack length at wall penetration is less than the critical crack length (CCL) for unstable propagation, and that the leakage from the through-wall crack can be detected in time to put the reactor in a safe condition before the CCL is exceeded [9.968, 9.969]. For assessments one needs to know how much time, t_R, is required to detect the leak, and how much time, t_A, is available between the crack penetrating the tube wall and becoming unstable, and then show that $t_A >> t_R$. In CANDU reactors, alarms based on dew point and rate of rise in dew point in the dry gas annulus between the calandria and pressure tubes are triggered by a few g/h of moisture and the value of t_R is less than 10 hours [9.969] but could be less than 1 hour [9.970]. To evaluate t_A one needs to know the crack length at first leakage, C_L, the rate of crack growth by DHC, V_c, and the value of CCL (discussed in Section 9.8.3). In the simple illustrative case of Eq. (9.82) [9.968]:

$$t_A = (CCL - C_L)/2V_c \tag{9.82}$$

As a conservative example, with values of CCL (50 mm), C_L (4 × wall thickness = 16 mm) and V_c (2.6×10^{-7} m/s), $t_A > 18$ hours, providing a margin of at least 1.8. In assessments, the calculations are more involved than is suggested by Eq. (9.82); they include the effect on the DHC growth rate and the CCL of reducing the pressure and temperature of the heat transport system as the reactor cools. One has to show that during cooling the CCL value remains higher than the current crack length. The analysis is amenable to a probabilistic approach using the distributions of the material properties and changes during shutdown [9.971, 9.972]. The analyses ignore the effect of leakage on crack growth. This approach is conservative because leaking cracks tended to grow more slowly than dry cracks because they were cooled as escaping pressurized water flashed to steam [9.968]. Another conservatism is the leakage rate increased from a few g/h to a few kg/h with small crack growth increments thus aiding in crack detection and identification; for example, the leak rate was about 10 kg/h with an increment in crack length of 5 mm from the initial leak length and increased to 100 kg/h with an increment of crack length of about 16 mm. A similar approach to LBB was used for the Fugen reactor [9.973] since it had a similar dry gas annulus between the calandria and pressure tubes as in CANDU.

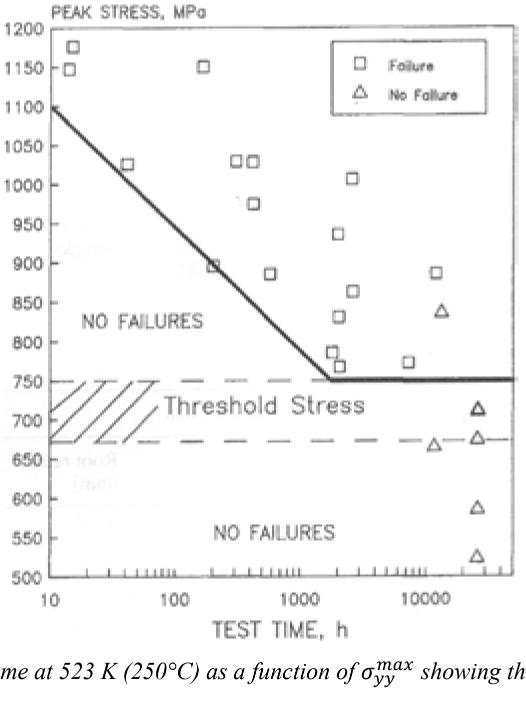

FIG. 9.352. Minimum total time at 523 K (250°C) as a function of σ_{yy}^{max} showing threshold for fracture [9.964].

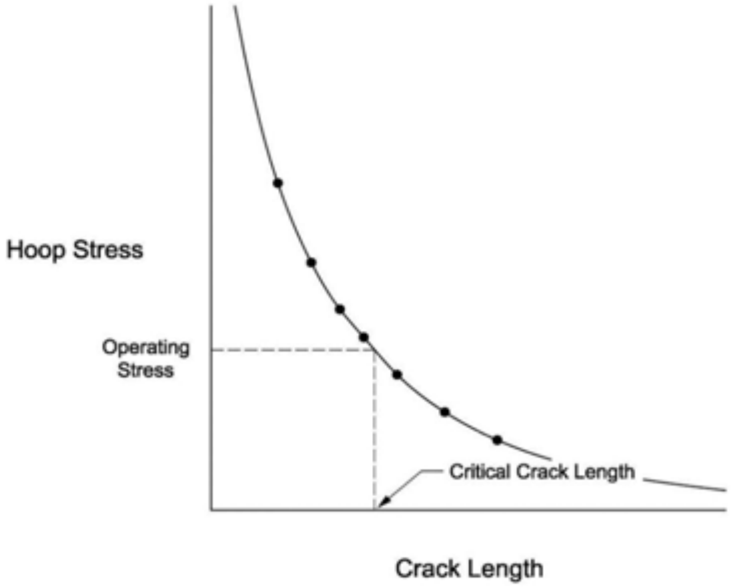

FIG. 9.353. Schematic diagram for determining the critical crack length at operating conditions by bursting tube sections containing axial slits of various lengths.

An RBMK-1500 does not have a container around its pressure tubes and the leak rate required for assured detection is at least 100 kg/h [9.974]. To produce this minimum leak rate, an axial through-wall crack has to be 28 mm long. This crack length is much smaller than the estimated CCL, 70 mm, for an operating hoop stress of about 100 MPa. If the crack grew by DHC at 2.5×10^{-7} m/s, then the time available to place the reactor in a safe mode is about 23 h.

Methods have been developed for the evaluation of the CCL and the metallurgical factors affecting the controlling properties, fracture toughness and crack growth resistance. Most of the examples are for testing well above room temperatures so the effects of neutron irradiation can be discerned without interference from the effects of large concentrations of hydrides, as discussed in Section 9.7.5. In zirconium alloys, irradiation strengthens and reduces ductility as measured in tensile tests (see Section 6.4.3, in Volume 2 of this publication and Section 9.2.2) so effects on cracking would be expected.

9.8.3. Limit of stable crack growth and exceeding the CCL

9.8.3.1. Direct measurement

As indicated in Fig. 9.191, if a crack grows very long, the load is very high or both, the crack may become unstable and the specimen or component may rupture — the CCL has been exceeded. With a tube containing an inside pressure, an axial crack has to withstand the hoop stress. In pressure tubes the direct method to find CCL is to place an axial, through-wall flaw, 20 to 100 mm long, in the centre of a section of tube, usually about 500 mm long, and measure the pressure required to extend the crack to failure. The location of the flaw is covered with a shim to prevent loss of pressure from leakage. Usually, each flaw tip is sharpened by fatigue cycles. The crack growth is followed by direct current, potential drop. From a series of such tests with various lengths, one interpolates the length of the crack that would be unstable at the operating pressure, as shown in Fig. 9.353. In tests between 513 and 573 K (240 and 300°C) on unirradiated material much ductility was evident, the slit gaped open and the liner deformed allowing the pressure to dissipate. The crack was stable throughout the test and grew only a short distance. With irradiated material, initially the crack grew a short distance in a stable manner but then became unstable and often grew the length of the specimen. This qualitative difference demonstrated the reduction in crack growth resistance by irradiation without any contribution of embrittlement by hydrides. Typical results for irradiated cold worked Zircaloy-2 [9.109, 9.975, 9.976] cold worked Zr-2.5Nb [9.976–9.981] and heat treated Zr-2.5Nb [9.39, 9.156] are provided in Fig. 9.354.

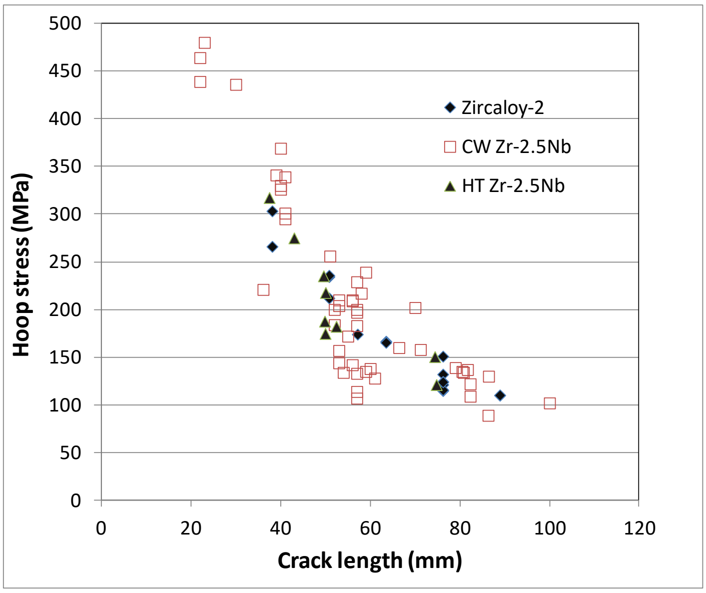

FIG. 9.354. Results of slit-burst tests on irradiated pressure tubes. Zircaloy-2 tested at 573 K (300°C) [9109, 9.975, 9.976]; cold worked Zr-2.5Nb tested between 513 and 573 K (240 and 300°C) [9.976–9.981]; heat treated Zr-2.5Nb tested at 573 K (300°C) [9.39, 9.156].

All three materials respond in a similar manner. If the design stress were 150 MPa, the lower bound CCL would be about 50 mm. When the fracture property is normalized as the product hoop stress × √(crack length), no effect of neutron fluence can be discerned for Zircaloy-2 or heat treated Zr-2.5Nb because of the scatter and low fluences; a decline in fracture property was observed with cold worked Zr-2.5Nb, but again the scatter was very large, as shown in Fig. 9.355.

9.8.3.2. Indirect measurement of CCL through fracture toughness

Since pressure tubes can be tested on full sections of the actual component, no extrapolation of behaviour from small specimens to the full size is needed. A similar argument may be made for fuel cladding although interpretation is not straightforward because of interactions with the fuel and the very thin wall. A fracture mechanics interpretation of a single test may be made, although one has to be aware of the restrictions on validity imposed by the thin wall and low strength of most components using zirconium alloys (Section 9.1). Small specimens machined from the components save on material and allow the effects of variables such as test temperature and microstructure to be examined. The material property controlling CCL is fracture toughness or crack growth resistance. In a burst test the crack length is derived from potential drop methods and the hoop stress is calculated from the tube dimensions and internal pressure that are then used to calculate the J integral. The equivalent stress intensity factor may be estimated from $\sqrt{JE/(1-\nu^2)}$. The CCL is determined using either the critical stress intensity factor, K_C, or by matching the crack driving force and the measured crack growth resistance curve. The critical stress intensity, K_C, is determined using:

$$K_C = [8a_i\,(\sigma_f)^2/\pi\,\ln(\sec\,(\pi M_b\sigma_{h\ max})/2\sigma_f))]^{½} \tag{9.83}$$

where

σ_f is the flow stress (average of 0.2% offset yield stress and ultimate tensile stress);
a_i is the initial half crack length;
$\sigma_{h\ max}$ is the maximum hoop stress, $p_{max}r_i/w$;
p_{max} is the maximum internal pressure;
r_i is the internal radius of the pressure tube;
w is the wall thickness;

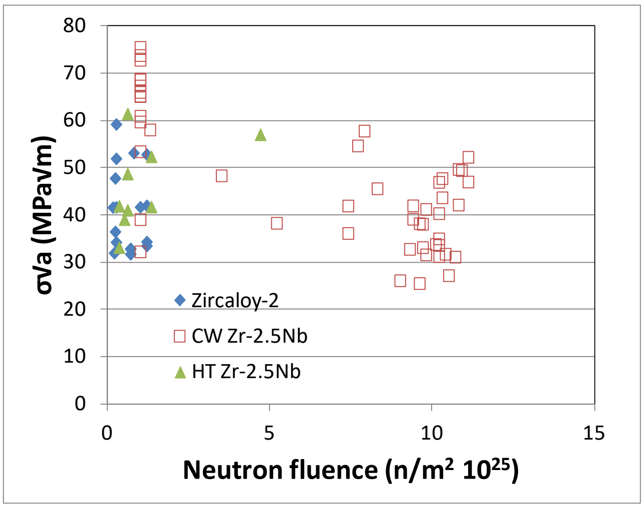

FIG. 9.355. Effect of neutron fluence on fracture of zirconium alloy pressure tubes in slit burst tests. Interpreted as the product hoop stress × √(crack length). Zircaloy-2 tested at 573 K (300°C) [9.109, 9.975, 9.976]; cold worked Zr-2.5Nb tested between 513 and 573 K (240 and 300°C) [9.976–9.981]; heat treated Zr-2.5Nb tested at 573 K (300°C) [9.39, 9.156].

M_b is the bulging correction factor $(1 + 2.55(a^2/(r_m w)) - 0.0135(a^4/(r_m w)^2))^{1/2}$;
a is the half the instantaneous crack length;

and r_m is the mean radius of the pressure tube.

Equation (9.83) can be used to determine the CCL from K_c:

$$\mathrm{CCL} = \frac{K_c^2 \pi}{4\sigma_f^2 \ln\left(\sec\left(\frac{\pi M_b \sigma_{h\,max}}{2\sigma_f}\right)\right)} \tag{9.84}$$

Since the bulging correction factor also depends on the crack length, Eq. (9.84) cannot be solved by direct substitution. Instead, CCL is determined by iteration.

Alternatively, the CCL can be determined by matching the crack driving force and the measured crack growth resistance curve or *J-R* curve. The *J* integral is determined using Eq. (9.85):

$$J = \frac{8\sigma_f^2}{\pi E} \ln\left(\sec\left(\frac{\pi M_b \sigma_h}{2\sigma_f}\right)\right) \tag{9.85}$$

where E is Young’s modulus and σ_h is hoop stress.

The CCL is then determined by matching the crack driving force for an axial through-wall crack in a pressure tube and the measured crack growth resistance curve as shown in Fig. 9.356 [9.851]. The instability point is taken as the point of tangency between these two curves. The CCL is defined at either the point of instability, CCL_t, or at the initial crack length, CCL_0. The second definition is inherently more conservative since it does not include any stable crack growth.

Fracture toughness and crack growth resistance can also be measured with small specimens, often made from components, especially after irradiation. One of the most widely used small specimen geometries for testing fracture properties is the compact tension specimen [9.1, 9.2]. If the ASTM criterion for validity, thickness/$(2.5(K_I/\sigma_y)^2) > 1$, is met, K_I represents K_{IC}. If the validity criterion is not met, then the *J* formalism may be used. The crack growth resistance, *J-R*, curve can be characterized by several parameters:

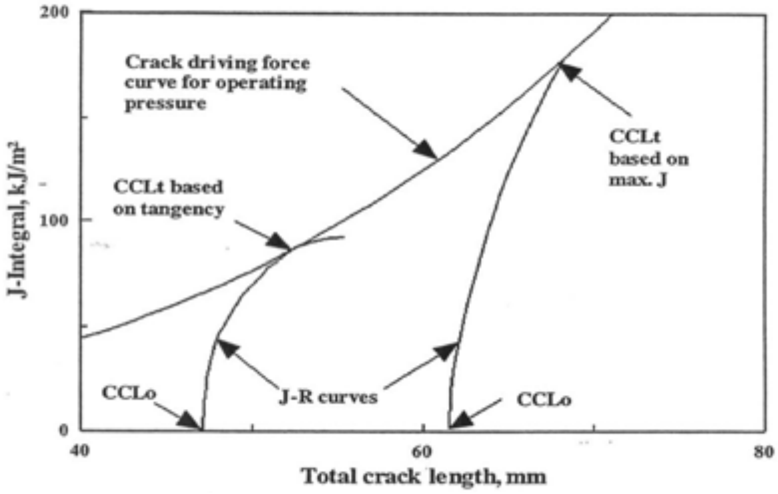

FIG. 9.356. Geometric technique for evaluating CCL, using the crack driving force curve (J) and the measured crack growth resistance curve (J-R) [9.851].

- The crack initiation toughness, $J_{0.2}$, representing the J integral value at the intersection of the *J-R* curve and the offset line at 0.2 mm of crack growth, Δa; the offset line is usually taken as $J = 2\sigma_f\Delta a$, where σ_f = (yield strength + UTS)/2.
- The toughness at maximum load, J_{ml}.
- $J_{1.5}$ is the J integral value at the intersection of the offset line for 1.5 mm of crack growth and the *J-R* curve; with very tough and ductile materials other crack lengths may be used.
- Crack growth resistance, *dJ*/*da*, is usually a linear regression of the *J-R* curve between 0.15 and 1.5 mm offset lines. Except when many radial hydrides are present and testing is below the transition temperature, zirconium alloys have a high capacity for stable crack growth. This stable cracking can be taken into account when evaluating CCL. Values of *dJ*/*da* are used to characterize this toughness; this parameter is sensitive to several test and metallurgical variables and is therefore useful for comparisons.

The *J-R* curve from a small specimen may be used to evaluate CCL as shown in Fig. 9.356 [9.982]. Small specimens may be made from burst test specimens, as shown in Fig. 9.357,

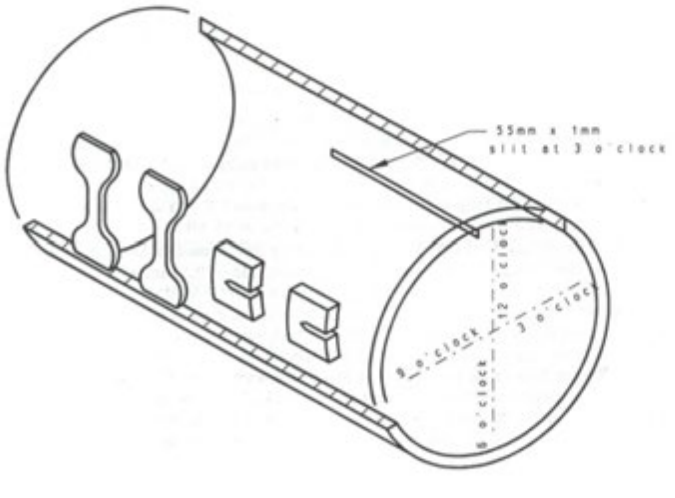

FIG. 9.357. Schematic diagram indicating small specimen sampling from burst test section of a CANDU pressure tube [9.983].

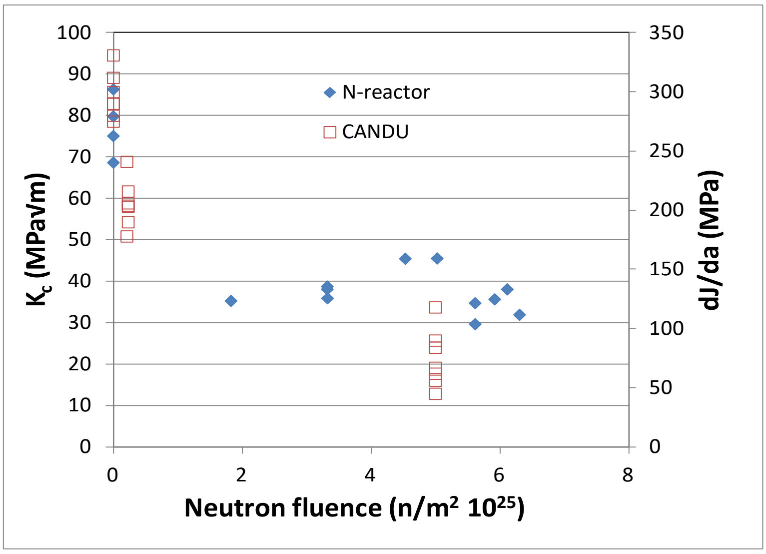

FIG. 9.358. Reduction in fracture toughness and crack growth resistance of cold worked Zircaloy-2 by neutron irradiation. Tests between 523 and 573 K (250 and 300°C) [9.98, 9.852].

although direct correlation between full size specimens and small specimens is not always achieved because of differences in crack length, crack tunnelling, toughness and stressing mode — tensile vs. bending [9.983–9.986].

9.8.3.3. Measurements of fracture toughness in material thicker than 1mm

Studies on annealed Zircaloy-2 plate material, not related to any particular reactor component, unexpectedly indicated an increase in fracture toughness with irradiation up to 2 × 10^{25} n/m^2 [9.987]. The specimens were 10 mm thick but the ASTM criterion for validity, thickness/$(2.5(K_I/\sigma_y)^2) > 1$, was not met, being only about 0.6 for tests at room temperature. The reported values of K_{IC} near room temperature were around 40 MPa√m. This value and the cracking behaviour indicated that Zircaloy-2 was a tough material, even after irradiation. Kreyns et al. [9.742] tested Zircaloy-2 and -4 using a modified compact tension specimen about 10 mm thick. They found that irradiation decreased the room temperature K_{IC} from 40 MPa√m (unirradiated) to about 30 MPa√m (2 to 8 × 10^{25} n/m^2); the irradiated material provided valid values of K_{IC}. At 533 K (260°C) K_{IC} was measured as about 60 MPa√m after 15 × 10^{25} n/m^2; the validity criterion was about 0.3, indicating a tough material. After a very high neutron fluence, 3 × 10^{26} n/m^2 (E > 1 MeV), at 563 K (290°C) a 6.4 mm thick annealed Zircaloy-2 plate was still tough [9.988]. The value of K_{IC} at 573 K (300°C), calculated from a measured J_{max}, was about 70 MPa√m.

The combined effect of cold work and irradiation reduced toughness. Tests performed mostly below room temperature on DCBs machined parallel and perpendicular to the rolling direction of a 9.5 mm thick plate of Zircaloy-2 showed the following [9.989]:

- Anisotropy from microstructure and texture with the transverse specimens being 12 to 15% tougher than those in the rolling direction of the plate;
- Cold working annealed material by 40% reduced toughness by 32 to 37%;
- Irradiation up to 10^{25} n/m^2 at 553 K (280°C) reduced the toughness of annealed material by 30 to 45% and in 40% cold worked material by 16 to 30%.

These examples are for tests at 213 K (−60°C) where hydrogen pick-up during the irradiation may be contributing to the reductions in toughness from initial values in the range 73 to 80 MPa√m.

Tests between 523 and 573 K (250 and 300°C) on cold worked Zircaloy-2 pressure tubes removed from power reactors confirmed the reduction in toughness by irradiation. Material from the

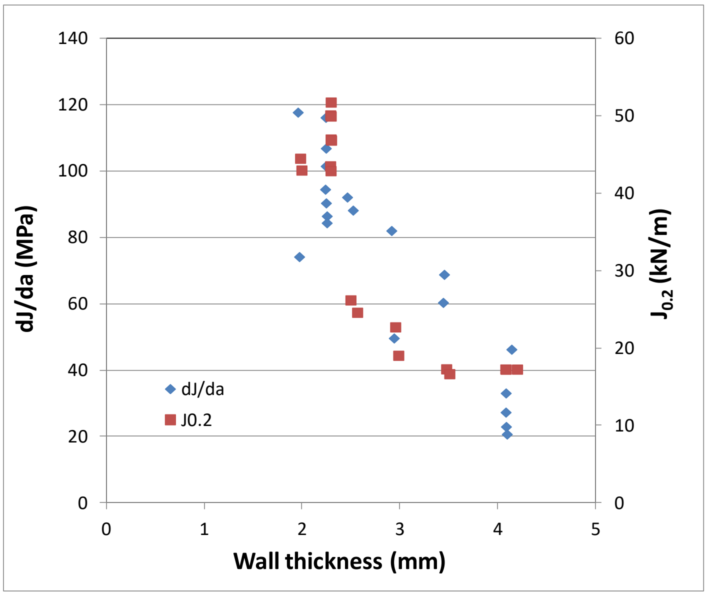

FIG. 9.359. Dependence of $J_{0.2}$ and dJ/da on specimen thickness in irradiated Zr-2.5Nb [9.992].

N-Reactor was tested with 5 mm thick compact tension specimens after irradiations up to 6.3×10^{25} n/m^2 [9.98, 9.990]. The nominal values of K_{IC} were reduced with fluence from 77 to 36 MPa√m with the latter having thickness/$(2.5(K_I/\sigma_y)^2)$ of about 0.7. Similar tests on CANDU material were evaluated with *dJ*/*da* [9.852]. Again, irradiation reduced the crack growth resistance. These results are combined in Fig. 9.358 suggesting the rate of decline in toughness decreased as the neutron fluence increased.

A similar decline in measured K_c was found with heat treated Zr-2.5Nb. Surveillance specimens irradiated in Fugen [9.991] and a single pressure tube irradiated in NPD [9.156] indicated a drop of up to 30% with a neutron fluence of 5.7×10^{25} n/m^2 in measurements between 503 and 573 K (230 and 300°C). In these tests the validity criterion for K_c based on thickness was < 0.3. The tube in NPD had a thickness of 2.3 mm. The importance of wall thickness was evaluated with J using these tubes as well as an example of irradiated, cold worked Zr-2.5Nb [9.992]. Both the crack initiation toughness, $J_{0.2}$, and crack growth resistance, *dJ*/*da*, declined with an increase in wall thickness, as shown in Fig. 9.359. The values of $J_{0.2}$ levelled off around 3 mm whereas *dJ*/*da* seemed to be still dropping as the thickness increased to 4.2 mm. This difference in the effect of thickness on the two parameters is caused by the relative sizes of the plastic zones as the crack grows.

Crack growth resistance of several pressure tubes made from cold worked Zr-2.5Nb has been measured at 3 main positions along a fuel channel using small specimens: the inlet, where the temperature is lowest, 523 to 538 K (250 to 265°C); the centre, where the neutron flux is largest, 3.7×10^{17} n·m^{-2}·s^{-1} ($E > 1$ MeV); and the outlet, where the temperature is the highest, 563 to 588 K (290 to 315°C). The test temperatures were between 513 and 573 K (240 and 300°C), where hydride effects were absent and little temperature dependence was observed [9.993]. The pooled data are depicted in Fig. 9.360 as a function of neutron fluence. Despite the large variation in values, a general trend is for *dJ*/*da* to decline with irradiation fluence. No effect of irradiation temperature or initial strength was found, although the range of these variables was small.

In the late 1980s a programme called Erable was started to irradiate fracture toughness specimens from a single source to the design end-of-life fluence, φt, for a CANDU reactor — about 30×10^{25} n/m^2 ($E > 1$ MeV) — in the high flux Osiris reactor at Saclay, France. This work was initiated because scatter in the data from surveillance pressure tubes masked any long term effect of irradiation on mechanical properties [9.993]. A complementary irradiation programme was also undertaken in NRU to investigate the possible influence of difference in flux between the Osiris reactor and CANDU. The maximum flux of Osiris was approximately ten times larger than in NRU, which is similar to a CANDU reactor. In the Osiris and NRU reactors the irradiation temperatures were 523±5 K and 538 K

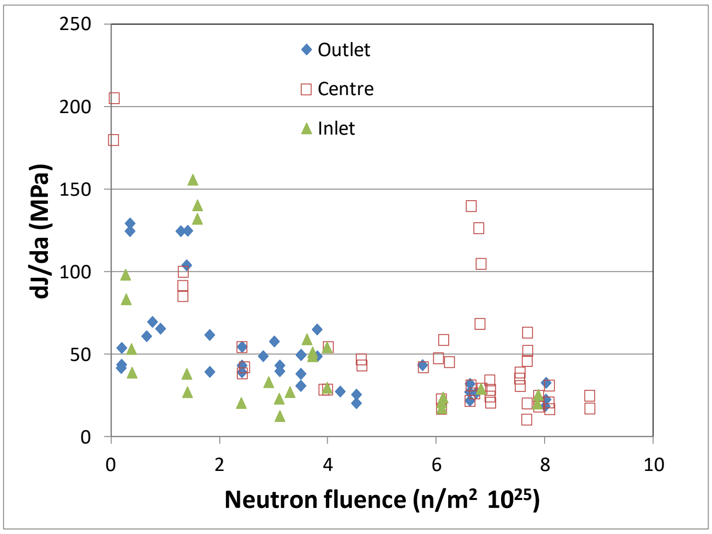

FIG. 9.360. Effect of neutron irradiation on crack growth resistance of cold worked Zr-2.5Nb pressure tubes between 513 and 573 K (240 and 300°C) sampled at the inlet, centre and outlet of several fuel channels in CANDU reactors [9.993].

(250±5°C and 265°C), respectively. For this investigation all mechanical test specimens were machined from a single low toughness tube, H737. Transverse tensile (gauge length 16 mm) and curved compact toughness specimens (thickness 4 mm) were tested at 513 K (240°C) and the results are summarized in Figs 9.361 and 9.362 [9.951, 9.994, 9.995]. Strength (represented by UTS), ductility (represented by total elongation), and fracture property (represented by *dJ*/*da*), all exhibited a transient change in the first 4×10^{24} n/m^2. An initial increase in UTS of about 200 MPa was followed by a small but steady linear rise with higher fluence at a rate of 3.2 MPa/10^{25} n/m^2; the correlation coefficient, R^2, was moderate, 0.79. The elongation also had a low fluence transient, dropping from about 11% to 5% followed by a small but steady linear decrease with higher fluence at a rate of 0.06%/10^{25}n/m^2; R^2 was low, 0.25, because of the large scatter. The initial crack growth resistance decreased from around 185 MPa to approximately 20 MPa with little further change after the transient. A linear regression of the data in the fluence range 0.4×10^{25} to 26.1×10^{25} n/m^2 resulted in $dJ/da = 20.4 + 0.21\varphi t$, $R^2 = 0.08$. Following the initial transient at low fluence there was no statistically significant change in toughness with irradiation. The low correlation coefficient, compared with the linear fit to UTS, may be due to γ-heating in the larger specimen in the high flux test facility and material variability. At low fluence ($\varphi t \leq 1 \times 10^{25}$ n/m^2) there was also good agreement between data from specimens irradiated in NRU and Osiris test reactors, suggesting that the difference in neutron flux does not affect these mechanical properties.

In the Erable specimens, microstructural characterization using TEM and X ray diffraction indicated a rapid increase in prism plane line broadening in the early stages of irradiation that was attributed to a-type dislocation loop formation. The a-type dislocation density increased rapidly at low fluence ($<1 \times 10^{25}$ n/m^2) and then achieved a steady state. In comparison, the c-component dislocation structure evolved gradually, and the density saturated at a fluence greater than 16×10^{25} n/m^2. The evolution of the a-type dislocation structure related directly to the change in UTS; at low fluence both the strength and the dislocation loop density increased rapidly. After this initial transient the gradual increase in prism plane line broadening can be attributed to an increase in the a-type dislocation density and an increase in the a-component of a changing c+a–type dislocation structure. TEM evidence showed that the c-component dislocation structure evolved over a long time. At high fluence, $>16 \times 10^{25}$ n/m^2, the c-component dislocation density and the tensile properties saturated with fluence.

9.8.3.4. Fractography and variability of fracture properties

For all Zircaloy materials, after high temperature tests where no hydrides were present, the fracture surface mainly consisted of ductile dimples [9.98, 9.987, 9.988, 9.990], showing that the

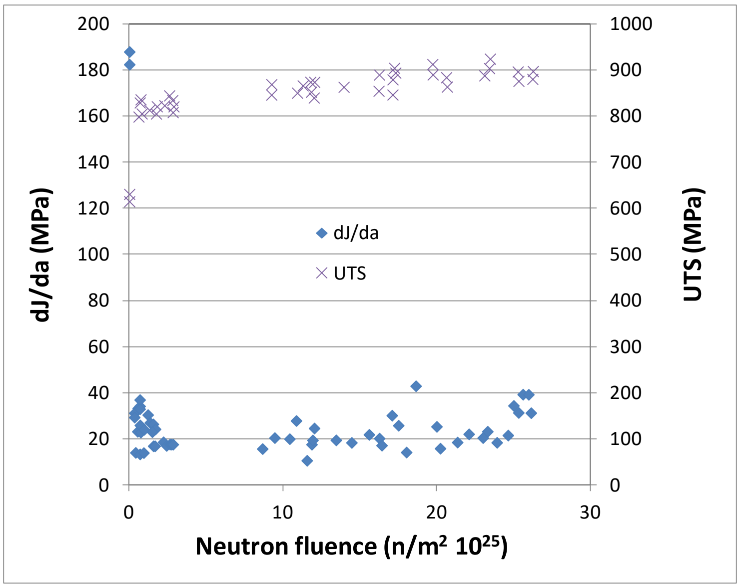

FIG. 9.361. Change in strength and dJ/da with fluence of fast neutrons of Zr-2.5Nb from a single tube. Testing at 513 K (240°C) [9.951, 9.994, 9.995].

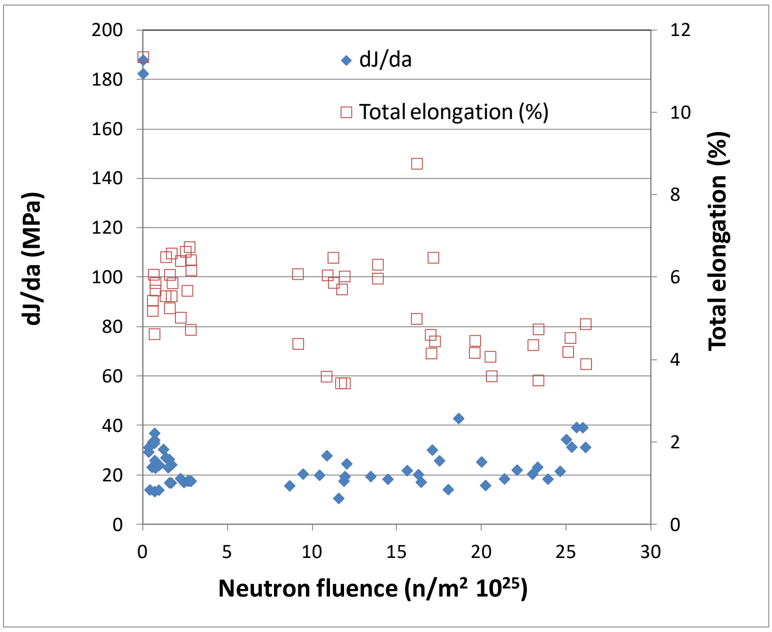

FIG. 9.362. Change with fluence of fast neutrons of elongation and dJ/da in single tube of Zr-2.5Nb. Testing at 518 K (240°C) [9.951, 9.994, 9.995].

fracture process consisted of linking up of voids. These observations are consistent with the behaviour in tensile tests described in Sections 9.2.1 and 9.2.2, confirming that irradiation does not introduce any new embrittlement process but reduces fracture parameters through its effect on plastic deformation.

Fracture toughness of cold worked Zr-2.5Nb can be very variable. Once the deleterious effects of hydrides were removed, residual variability still existed, as shown in Figs 9.354 and 9.360. Examples of *J-R* curves illustrate the range of variation on nominally identical material, as shown in Fig. 9.363 [9.994]. This variability was observed in both unirradiated and irradiated materials. In unirradiated materials, the crack growth resistance, *dJ*/*da*, at about 523 K (250°C) can vary between 60 and about 400 MPa [9.994, 9.996, 9.997] while after a neutron fluence of 6.5 × 10^{25} n/m^2, *dJ*/*da* was in the range 10 and 290 MPa [9.993, 9.995, 9.998]. Since the toughness before and after irradiation was correlated, the variability arose mainly from variations in the toughness of as-fabricated components. The response

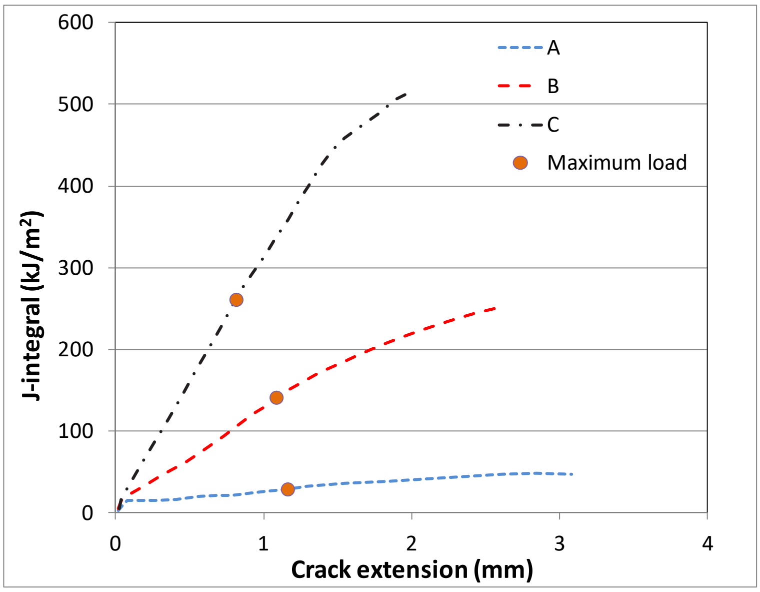

FIG. 9.363. Variation in J-R curves for irradiated Zr-2.5Nb tested at 523 K (250°C) [9.995].

to irradiation depended on the initial value of the crack growth resistance, with low initial values losing relatively more toughness than high values, as shown in Fig. 9.364 [9.951, 9.994, 9.998, 9.999].

Understanding this high variability allows fabrication routes to be chosen that consistently deliver components with high toughness and avoids routes that produce components with low toughness. When high toughness is maintained, analysis of the fitness of the components for service is simplified and unnecessary maintenance on healthy components is avoided. First the chemical aspects are discussed, and then some effects of microstructural variation are described.

The fracture surfaces of the broken specimen consisted of:

(a) Dimples, indicating void growth and coalescence, which is a ductile and high energy process.
(b) Occasional particles, 1 to 3 µm in diameter and identified as carbides, associated with void formation, and cracked particles, 25 by 50 µm in cross-section and identified as phosphides, shown in Fig. 9.365 [9.994, 9.997].
(c) Fissures along the axial direction of the tube with sides having planes normal to the radial direction, as shown in Fig. 9.366(a), (b) and (c) [9.993, 9.997]; these fissures were absent in very tough materials. Often cracks, perpendicular to the fracture surface, were detected, as shown in Figs 9.366(b) and (c). The ridges between the fissures contained ductile dimples. Care has to be taken with interpretation because fissures with a similar appearance were formed with highly aligned hydrides, as shown in Fig. 9.347(b). In fractures formed above 520 K (250°C) with hydrogen concentrations < 30 ppm (0.27 at.%), all the hydrogen was in solution and no hydride effects were observed, so the fissures of the type shown in Fig. 9.366 have a different source. Matching both fracture surfaces from the same specimen confirmed these features were fissures rather than matching ridges and valleys. The density and length of the fissures increased with decreasing toughness, indicating their formation is a low energy process, as shown in Fig. 9.367 [9.996]. The density of fissures was increased by irradiation. The nature of the microstructural features responsible for fissures was found by breaking small specimens inside a scanning Auger electron microscope and chemically analysing the plane normal to the radial direction of the pressure tube. Bands of low energy fracture, 10 to 15 µm wide, 10 nm thick and several hundred micrometres long, corresponding to the fissures, contained chlorine and carbon [9.996]. The size of a thin process zone at the crack tip was modelled by separating the fracture into flat strips of low energy fracture, with its normal in the radial direction, bounded by ligaments of ductile fracture. The material adjacent to crack tunnelling exerted little constraint on crack propagation at short crack lengths [9.1000, 9.1001].

Crack growth resistance correlated well with the concentration of chlorine, as shown in Fig. 9.368 [9.996–9.998]. Similar correlations were found with phosphorus and carbon when the effect of the other two elements was minimized. Comparison of the efficacy of each element in reducing *dJ*/*da*, as shown in Fig. 9.369 [9.994, 9.996, 9.998, 9.1002] shows the order of damaging ability: to reduce *dJ*/*da* from about 400 to 200 MPa requires approximately 0.001 at.% chlorine, 0.01 at.% phosphorus and 0.1 at.% carbon.

The sources and removal of these impurities are as follows:

- Chlorine is present as a remnant of the Kroll reduction process used to make zirconium sponge. The chlorine concentration is reduced during each subsequent vacuum arc melt, as shown in Fig. 9.370 [9.997]. Until the early 1990s, pressure tubes were made from materials that were melted twice. During pressure tube manufacture, an extrusion hollow is made by trepanning the central core of a forged billet. When ingots are made up of 100% trepanned cores and then melted, the resulting material has been melted four times. This material has a very low concentration of chlorine and a very high toughness, if the phosphorus and carbon concentrations are also low.
- The main source of phosphorus is the original ore: zircon sand. Phosphorus is removed during the chlorination process, but its concentration can be variable. Control of phosphorus concentration is by judicious selection of zirconium sponge.
- Carbon is mainly introduced during carbochlorination of ZrO_2 as feed stock for the Kroll process. Again, the control of this impurity is by careful selection of zirconium sponge.

These observations and controls led to the practice of quadruple melting Zr-2.5Nb using zirconium sponge chosen for its low concentration of carbon and phosphorus impurities. Implementation of the above controls are reflected in the specification for the maximum allowed concentration of these impurities:

- Chlorine, with a maximum impurity concentration of 0.5 ppm (wt), 0.00013 at.%;
- Phosphorus, with a maximum impurity concentration of 10 ppm (wt), 0.0029 at.%;
- Carbon, with a maximum impurity concentration of 125 ppm (wt), 0.095 at.%.

Pressure tubes made from this material have high values of fracture toughness with low variability, as shown in Fig. 9.371 [9.998]; the range in values of *dJ*/*da* at 523 K (250°C) was 330 to 410 MPa. To confirm that these materials would maintain their high crack growth resistance during service, specimens from 4 representative tubes were irradiated to 2.2×10^{25} n/m^2 at about 533 K (260°C) and tested at 523 K (250°C) [9.998]. Specimens from the same tube used in the Erable irradiation were used as controls. The values of *dJ*/*da* for both sets of material dropped within the first 4×10^{24} n/m^2 but thereafter showed little change. The values for the quadruple melted material after irradiation were greater than 150 MPa, indicating that much toughness remained whereas that of the double melted material was less than 50 MPa.

When pressure tubes are fabricated from new materials or different routes, the process must be qualified by showing that the properties remain satisfactory. Properties not covered by the technical specification can be addressed with a set of guidelines. For fracture properties, *dJ*/*da* of archive, unirradiated material was compared with the CCL measured from burst tests on the same tubes, after their removal from power reactors after several years of operation, as shown in Fig. 9.372. The initial benefit for CCL of irradiated material with an increase in *dJ*/*da* of unirradiated material was not maintained beyond about 200 MPa; the guideline value for *dJ*/*da* for qualification was set at 250 MPa to provide an acceptable CCL during service of over 60 mm, and some margin for unknown factors

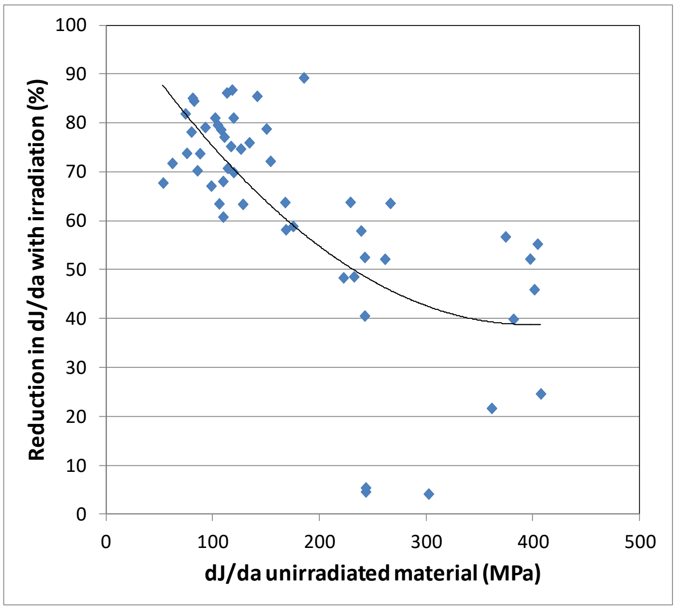

FIG. 9.364. Dependence on initial crack growth resistance of the reduction of dJ/da *by irradiation [9.951, 9.994, 9.998, 9.999].*

[9.998]. Many tubes for early reactors would not have met the guideline value whereas tubes made to the new specification easily exceed the minimum guideline value.

Two reactor sets of CANDU pressure tubes have been made from electrolytic powder, formed into electrodes and arc-melted twice. This material contained no chlorine but showed traces of fluorine. The range of *dJ/da* was from just below the guideline limit up to 320 MPa, as shown in Fig. 9.371. Examination of fracture surfaces revealed fluorine-rich particles associated with cavities, but their damaging ability and any correlation with fluorine concentration seemed to be less than those with chlorine. The intermediate crack growth resistance was maintained after irradiation [9.998, 9.999].

Currently, pressure tubes are made by extruding hollows at 1088 K (815°C) after a 15 minute preheat. Extruding at a lower temperature may be less costly and produce a refined microstructure that is very strong and tough. Half-length prototype tubes were made using an extrusion temperature of 1053 K (780°C) [9.1003]. These tubes were very strong and tough; with a soak time of 15 minutes the UTS in the longitudinal direction at 573 K (300°C) was 572 MPa and *dJ/da* at 523 K (250°C) was 374 MPa. Stress relief at 773 K (500°C) for 6 hours reduced the UTS to 510 MPa but increased *dJ/da* to 445 MPa. After irradiation the drop in crack growth resistance was much larger than for materials extruded at 1088 K (815°C) even though the final values may be acceptable, greater than 90 MPa. Since the grains were well aligned in this material, they may be highly susceptible to strain localization by clearing out irradiation damage and this deformation could lead to premature shear or slant failure.

One idea to improve resistance to in-reactor creep is to increase the tube wall thickness from 4 to 5 mm and reduce the cold work from the current 27% down to either 22 or 12%. Although such materials were expected to have a UTS at 573 K (300°C) in the longitudinal direction of 435 MPa, compared with 480 MPa specified for current tubes, prototype tubes either met or almost met the specified requirement for current tubes. After irradiation [9.998], tubes made with either version of lesser cold work showed low degradation in crack growth resistance, <25%, suggesting a fruitful direction for improving the performance of pressure tubes.

Low toughness is often associated with high strength. The number of void nucleation sites is increased when the local stress state is raised at the crack tip, thus the increase in strength by irradiation would be expected to reduce toughness. This general trend has been observed in zirconium alloys when hydrogen and chlorine were present [9.852]. The same trend is apparent after irradiation in power reactors [9.983, 9.985] or for tubes made from the same ingot but with different amounts of cold work [9.998] or from similar source material, electrolytic powder, but with a range of fabrication routes that varied from annealed to cold worked to quenched and aged conditions [9.999, 9.1004], as shown in Fig. 9.373. The data are for tests at 523 K (250°C) on material with little interference from hydrogen and chlorine; concentrations were <15 ppm (0.137 at.%) and <1 ppm (0.00026 at.%), respectively. These plots have moderate correlations, possibly indicating that the forced linear fit may not be the correct relation between toughness and strength and that other microstructural features, such as crystallographic texture, are important. Tubes made from quadruple melted Kroll material appear to have superior toughness to that of tubes made from double melted electrolytic powder; triple or

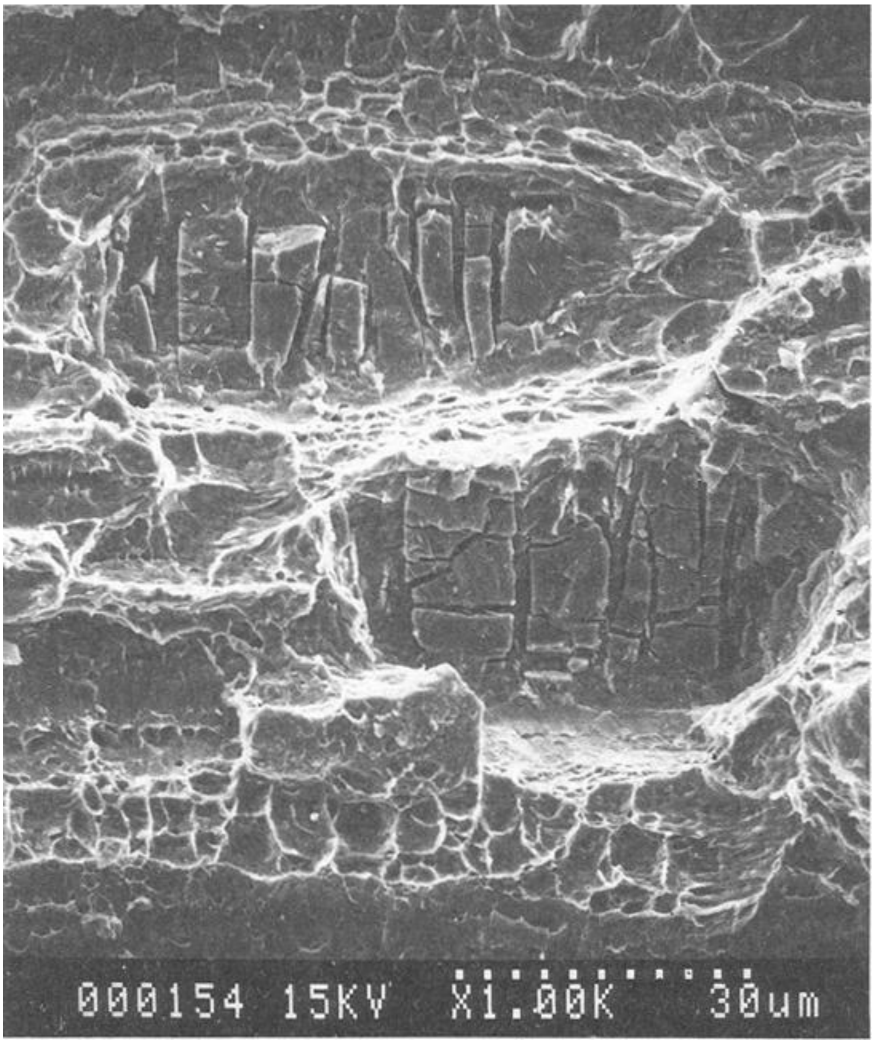

FIG. 9.365. Scanning electron fractograph containing cracked phosphide particles and regions of ductile fracture [9.994, 9.997].

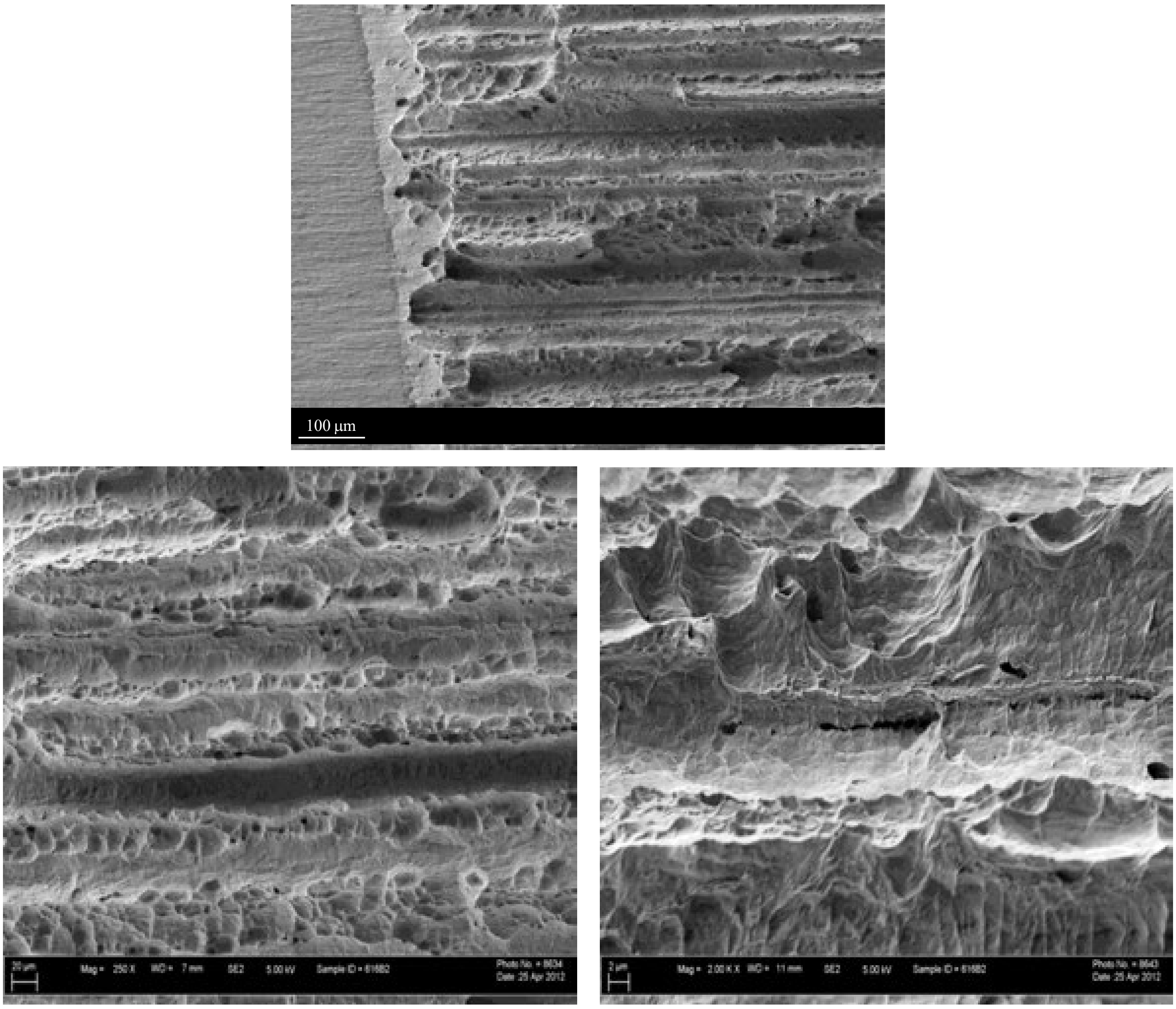

FIG. 9.366. (a) Fissures formed at the plane of initial crack stretch zone adjacent to fatigue pre-crack (left side) in Zr-2.5Nb pressure tube material. Note the ductile dimples between the fissures. The crack propagated from left to right on the axial-radial plane (fractograph from S. St. Lawrence, AECL); (b) fissures and crack (A-A) formed in the centre of the fracture surface of Zr-2.5Nb pressure tube material. Note the ductile dimples between the fissures. The crack propagated from left to right on the axial-radial plane (fractograph from S. St. Lawrence, AECL); (c) cracks in fissure (A) formed in the centre of the fracture surface of Zr-2.5Nb pressure tube material. The fracture propagated from left to right on the axial-radial plane (fractograph from S. St. Lawrence, AECL).

quadruple melting of the latter material needs to be explored to determine whether trace elements responsible for the lower toughness can be eliminated.

9.8.3.5. Some applications of the results to pressure tubes

The principle of LBB was amply demonstrated in practice in the pressure tubes of early CANDU and RBMK reactors that used Zr-2.5Nb — the through-wall cracks allowing detectible leakage were much shorter than the CCL (Sections 9.7.6.1(a)–(c)). The potential for failure to meet the conditions for LBB led to the recommendation to discontinue using the Zircaloy-2 tubes in NPD [9.853]. A warning was given from the examination of Zircaloy-2 pressure tubes removed from the reactor after 22 years of service. The maximum deuterium concentration was 300 ppm (1.35 at.%) and the material had a brittle–ductile transition of about 493 K (220°C). Fractography confirmed that low toughness was caused by cleavage of hydrides while the principal feature with high toughness was ductile dimples. With another three years of service, the maximum hydrogen concentration had risen to 470 ppm (2.1 at.%) and the brittle–ductile transition was now 553 K (280°C). This temperature was above the operating temperature of the reactor. The CCL at the operating conditions had declined from over 70 mm down to 50 mm. In NPD the annulus between the pressure and calandria tubes was not

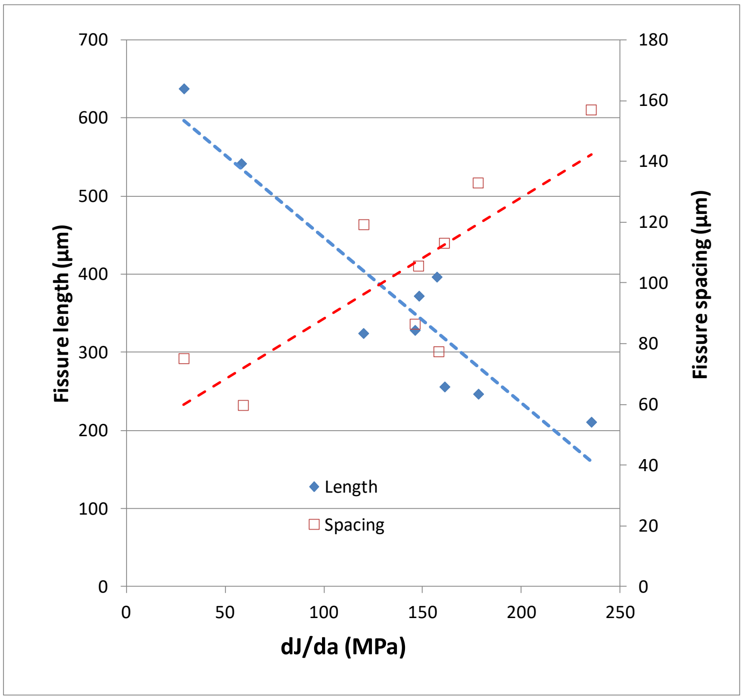

FIG. 9.367. Change in fissure geometry with crack growth resistance [9.996].

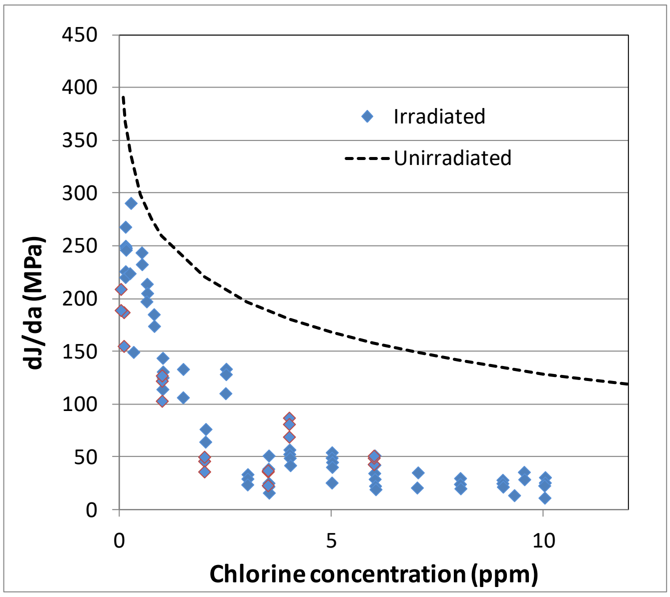

FIG. 9.368. The decline in crack growth resistance with increase in chlorine concentration. Irradiation exacerbates the decrease in toughness by chlorine [9.996–9.998].

closed and the leak detection time was much longer than in other CANDU reactors (Section 9.8.2). When CCL was 70 mm the detection time was about 40 h. Since only about 24 h were available to grow a leaking crack to the short CCL, the time was considered to be insufficient for leak detection and confirmation that it was from a pressure tube. Consequently, LBB could not be guaranteed. Continuing use of this set of pressure tubes could not be justified and the reactor was closed down.

If blister formation is suspected in a pressure tube, LBB should not be used because wall penetration by the crack cannot be guaranteed before the CCL is exceeded. Although the measurements

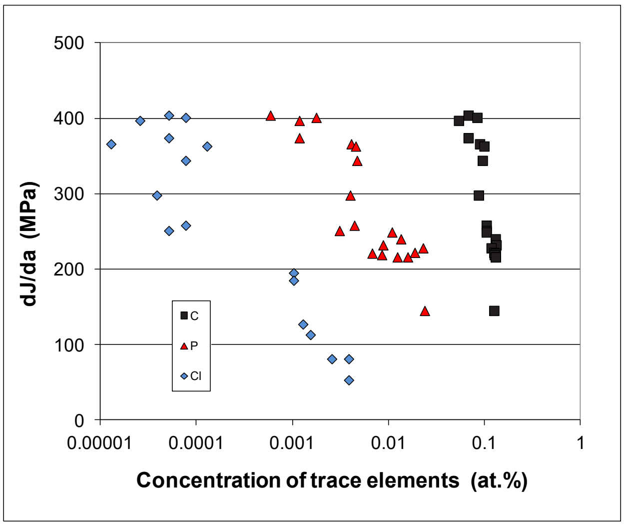

FIG. 9.369. Comparison of embrittling effect of Cl, P and C on cold worked Zr-2.5Nb when the other two elements are minimized and hydrides are absent (data from [9.994, 9.996, 9.998, 9.1002]).

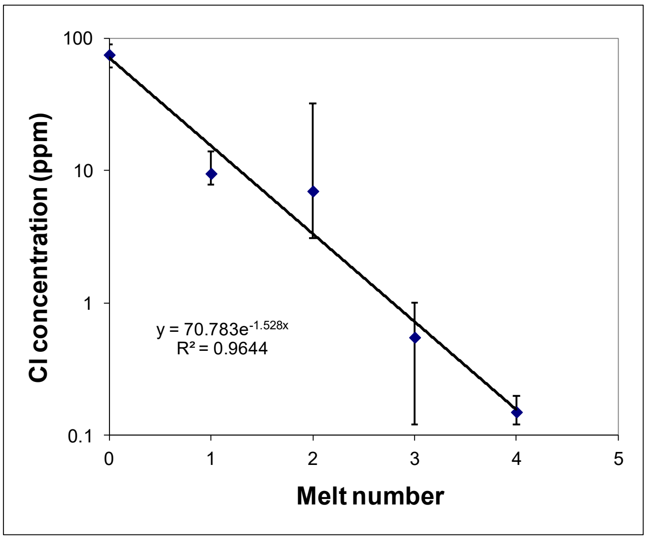

FIG. 9.370. Reduction in chlorine concentration in Zr-2.5Nb with number of melts (based on [9.997]).

had a large scatter, the stress to initiate cracks in blisters decreased as the blister size increased; a tensile stress of about 800 MPa was required to crack a blister 0.15 mm deep whereas a blister 0.96 mm deep could be cracked by 200 MPa [9.715]. No temperature dependence was detected between room temperature and 473 K (200°C), as expected from the tensile and fracture behaviour of bulk hydride. The value of K_I to propagate the blister cracks was higher than expected, 10 to 16 MPa√m [9.719], perhaps because of the internal compressive stresses, heating to the test temperature in many tests or insufficient time being allowed for the tests. When the tests were carried out with the temperature gradient applied throughout, the cracks propagated by DHC despite the temperature being attained by heating. This result corroborated the effect of temperature gradient on DHC [9.957]. Curved compact tension specimens [9.1005] were machined from the ruptured tube described in Section 9.7.6.1(d) and crack growth resistance was measured [9.851] close to and away from the region of crack initiation. The test temperature was 503 K (230°C), the average temperature at crack initiation in the tube. The combination of irradiation and hydrogen concentration of up to 80 ppm (0.72 at.%) led to brittle fracture and values of fracture toughness between 40 and 50 MPa√m. The calculated value of the stress intensity factor of the actual crack boundary was also 40 and 50 MPa√m (calculation by Davies, reported in Ref. [9.851]). Converting these values at the operating stress of 90 MPa to CCL provided lengths of about 50 mm, which are shorter than the partial through-wall crack in the failed tube, about 100 mm [9.880]. The differences between the values of CCL are because the crack in the component had a thin, tough ligament separating it from the surface and it was made up of three or four separate initiating sites that had to link up; the small toughness specimens underestimated CCL because the wall thickness and crack length were too small for valid plane-strain fracture toughness or J resistance measurements. Away from the points of contact the operating temperature was 553 K (280°C). Specimens containing over 100 ppm (0.9 at.%) hydrogen, much as radial hydrides (Section 9.7.3), were brittle, indicating a ductile–brittle transition with hydrogen concentration, as described in Section 9.7.5.

Some tubes made from the top of some ingots of Zr-2.5Nb contained the residue of the solidification pipe. These defects were planes of impurity particles subtending a shallow angle with the inside surface of the pressure tube, forming a lamination. In fuel channel N06 of Bruce Unit 2, B2N06, this plane preferentially corroded and formed a crack that grew sufficiently to leak [9.877]. Very localized stresses can arise from oxidation because of the 56% expansion during its formation. In a demonstration experiment, rapidly oxidizing inserts placed in the notch of a compact tension specimen of Zr-2.5Nb imposed a K_I of 35 MPa√m after 106 days oxidation in air at 573 K (300°C) [9.1005]. A similar oxide wedging process exacerbated the crack growth in B2N06 [9.1006]. In searching for the leakage the tube was pressurized to 8.4 MPa at 318 K (45°C), which led to an unstable crack that grew to 3.7 m in length, less than the full length of the tube, which was 6 m. The CCL at the rupture temperature was estimated to be between 43 and 57 mm from small specimen and burst tests; the CCL of the failure was evaluated from the area of fracture to be 48 mm, within the range of the test results. The fracture toughness values were similar at the end of the unstable crack, therefore a region of tougher material did not cause the crack arrest. The likely reason for crack arrest was the driving force disappearing because the decompression wave within the pressure tube was faster, about 940 m/s, than the crack velocity, estimated to be between 550 and 890 m/s. The lamination problem was eliminated by modifying the melting process to minimize pipes, instituting an inspection of the top of the ingot to locate the pipe and rejecting this top section so only solid metal was processed further, and adding to the final inspection a normal beam ultrasonic examination capable of detecting shallow angle defects.

9.8.3.6. Measurements of fracture toughness in material less than 1 mm thick

The wall thickness of cladding tubing is much too small for LEFM and even severely tests the limits of the J integral approaches. Originally driven by a need to understand long-axial-split phenomena in failed BWR fuel rods [9.888] several laboratories have developed techniques to generate relevant fracture toughness information for irradiated fuel tubing. Often the term ‘relevant’ is used in a relative sense because the data depend on the geometry and the loading in the specific test method. A round robin programme was directed towards comparing various specimen types and testing techniques on the same materials [9.1007]. The test materials consisted of Zircaloy-4 tubing heat treated to two conditions: fully recrystallized (final anneal at 855 K (582°C) for 2 h) and stress relieved annealed (SRA) (final anneal at 764 K (491°C) for 4 h). The tube dimensions were outside diameter 9.5 mm and wall thickness 0.57 mm. As a control, tube specimens with the same dimensions were machined out of an aluminium alloy plate that was 12.5 mm thick; the material was Alloy 7050:

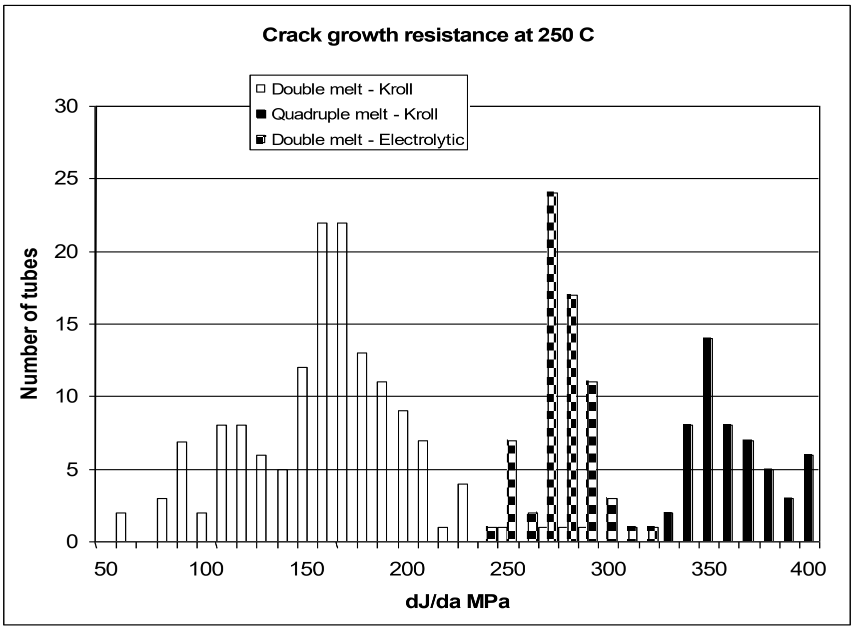

FIG. 9.371. Frequency distribution of crack growth resistance, dJ/da*, at 523 K (250°C) for Zr-2.5Nb pressure tubes made from Kroll sponge, double and quadruple melted, and electrolytic powder, double melted [9.998].*

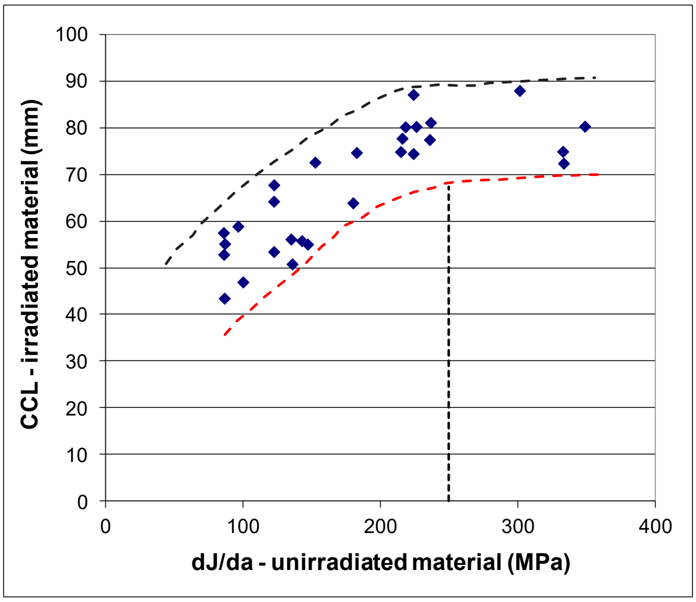

FIG. 9.372. Basis for value of initial crack growth resistance, dJ/da, to be used in guideline of properties not covered by specification [9.998]. Blue diamonds — experimental points; dotted lines determine the variation range.

Al-6.2Zn-2.3Cu-2.3Mg-0.1Zr. In all specimens the starting flaw was sharpened by fatigue and propagated in the axial direction (except in a burst test in which the crack grew in both the radial and axial directions). Five specimen configurations were used that could be described as compact tension or three-point bending and were amenable to the format of the ASTM standards [9.2] while two others fell outside the descriptions in the ASTM standards:

- Equivalent to compact tension:
  - Pin-loaded tension [9.919, 9.1008];
  - New compact tension (modified pin-loading tension) [9.1009];

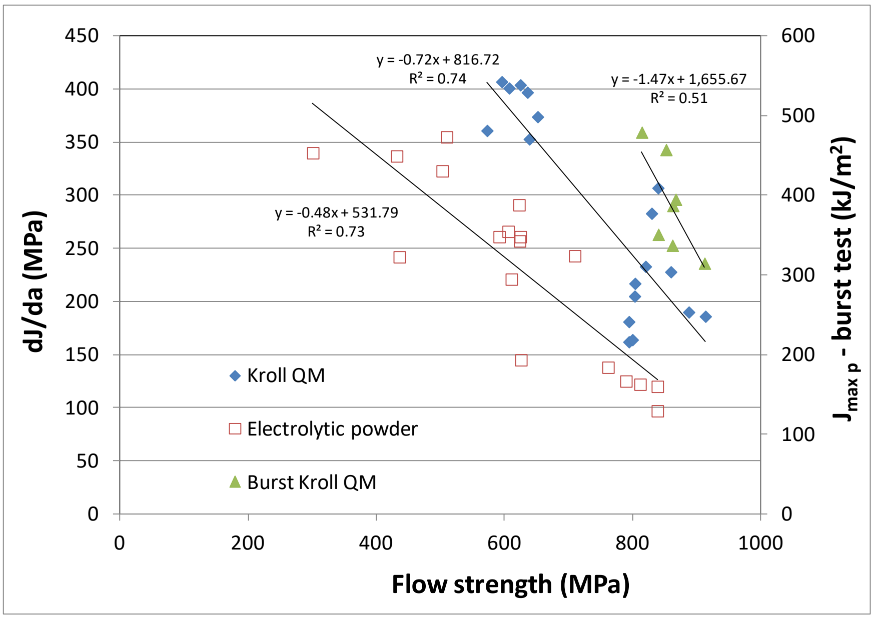

FIG. 9.373. Effect of strength on crack growth resistance (small specimens [9.998, 9.999, 9.1004]) and $J_{max\ p}$ (burst tests [9.983, 9.986]) for Zr-2.5Nb from two different sources.

  - X-specimen [9.1010];
  - Double-edge notched tension [9.1011];
- Equivalent to three-point bend:
  - Vallecitos embedded charpy [9.854];
- Other geometry:
  - Internal conical mandrel [9.1012];
  - Burst test [9.1013].

Some of the toughness parameters, $J_{0.2}$, J_{max} and dJ/da (Section 9.8.3.2), were evaluated at 293 K (20°C) for all materials and at 573 K (300°C) for SRA Zircaloy-4. The number of specimens tested for any one condition was small (e.g. 1 to 7 for the tests on SRA material at room temperature (except for 13 for the X-specimen)). The mean values of $J_{0.2}$, J_{max} and dJ/da for SRA Zircaloy-4 at room temperature were 86.0±33.7 kN/m, 92.4±10.2 kN/m and 109.4±23.2 MPa, respectively. The values for fully recrystallized material at 293 K (20°C) and SRA at 573 K (300°C) were sparse and highly scattered. A complete suite of J values was obtained for the pin-loading tension specimens; fully recrystallized material was 2 to 3 times tougher than the SRA material and the SRA material was 15% tougher at (300°C) than at 293 K (20°C). All methods showed that the SRA Zircaloy-4 was over twice as tough as the aluminium alloy.

Sources of variability are experimental because the same material was being tested by each laboratory so the material variability was small. Often the crack changed from propagating on the axial-radial plane to one about 45° from this plane. The amount of friction between the specimen and the loading member varied between each test set-up. The analysis of the load and crack growth information to calculate J varied between experimenters and would contribute to the variation. The values were partly controlled by the geometry of the cladding and the very thin wall and were not considered material properties because they did not meet the requirements of the ASTM standards. Since differences in properties can be distinguished and the effects of hydrides [9.1009] and irradiation [9.919] can be discerned, these methods have been developed for cladding-specific tests.

In summary, methods for evaluating flaws that may develop into cracks are discussed and examples based mostly on pressure tubes indicate how to avoid cracks. Should a crack escape early detection, LBB can mitigate the prospect of exceeding the CCL leading to unstable cracking. Methods for evaluating the CCL are available but they are not yet reliable for thin wall components such as fuel cladding. Chemical composition contributes to values of fracture toughness; trace elements such as chlorine, phosphorus, carbon and hydrogen should be minimized.

9.9. SUMMARY

The effects of composition; microstructure, including irradiation damage; and test conditions on the tensile properties of zirconium alloys are well established. Under most circumstances the materials have adequate ductility to meet operational requirements. Long term operation in a neutron flux does not present a creep ductility problem during operation, while creep ductility will not be a problem during the storage of spent fuel. Load cycling leading to fatigue crack propagation has also not led to long term difficulties. Although components made from zirconium alloys are susceptible to stress corrosion and hydride cracking, they can be used safely and economically if the conditions for these failure mechanisms are minimized. Good performance can be achieved through assuring that imperfections cannot propagate by paying special attention to curtailing flaws — produced during fabrication or operation; to control tensile loads — from interaction with fuel, from internal pressure or from construction; and to control the operating environment. Surveillance and in-service inspection can provide confidence that the component is behaving as designed and required or warn of an unexpected poor response to operating conditions. Accidents from reduction in heat transfer by loss of heat transport fluid by a pipe break are characterized through knowledge of the behaviour of the zirconium alloys at either high temperatures, strain rates or both.

REFERENCES

[9.1] ASTM INTERNATIONAL, Standard Test Method for Linear-Elastic Plane-Strain Fracture Toughness K_{Ic} of Metallic Materials, E399-09, ASTM International, West Conshohocken, PA (2009).

[9.2] ASTM INTERNATIONAL, Standard Test Method for Measurement of Fracture Toughness, E1820-11, ASTM International, West Conshohocken, PA (2011).

[9.3] AMERICAN SOCIETY OF MECHANICAL ENGINEERS, The Boiler and Pressure Vessel Code, Section VIII — Rules for Construction of Pressure Vessels, American Society of Mechanical Engineers, New York (1992) 183.

[9.4] ASTM INTERNATIONAL, Standard Test Methods for Tension Testing of Metallic Materials, E8/E8M-09, ASTM International, West Conshohocken, PA (2009).

[9.5] ASTM INTERNATIONAL, Standard Test Methods for Elevated Temperature Tension Tests of Metallic Materials, E21-09, ASTM International, West Conshohocken, PA (2009).

[9.6] KEELER, J.H., Tensile characteristics of unalloyed zirconium at low and moderate temperatures, Trans. ASM **47** (1955) 157–192.

[9.7] COLEMAN, C.E., HARDIE, D., Grain-size dependence in the flow and fracture of alpha-zirconium, J. Inst. Met. **94** (1966) 387–391.

[9.8] WEINSTEIN, D., Yield point occurrence in polycrystalline alpha-zirconium, Electrochem. Technol. **4** (1966) 307–312.

[9.9] RAMANI, S.V., RODRIGUEZ, P., Grain size dependence of the deformation behaviour of alpha zirconium, Can. Metall. Q. **11** (1972) 61–67.

[9.10] LEE, D., The strain rate dependent plastic flow behaviour of zirconium and its alloys, Metall. Trans. **1** (1970) 1607–1616.

[9.11] THORPE, W.R., SMITH, I.O., Tensile properties of Zr-1 wt.% Nb alloy, J. Nucl. Mater. **78** (1978) 49–57.

[9.12] HOLLOMON, J.H., Tensile deformation, Trans. Metall. Soc. AIME **162** (1945) 268–290.

[9.13] RAMBERG, W., OSGOOD, W.R., Description of Stress–Strain Curves by Three Parameters, Technical Note No. 902, National Advisory Committee for Aeronautics, Washington, DC (1943).

[9.14] SWIFT, H.W., Plastic instability under plane stress, J. Mech. Phys. Solids **1** (1952) 1–18.

[9.15] VOCE, E., The relationship between stress and strain for homogeneous deformation, J. Inst. Met. **74** (1948) 537–562.

[9.16] HOLLOMON, J.H., The mechanical equation of state, Trans. AIME **13** (1947) 171.

[9.17] BALAKRISHNAN, K.S., CHATTERJEE, S., "Strain hardening parameter evaluation of irradiated Zircaloy-2", Effects of Radiation on Materials: Sixteenth International Symposium, Proc. ASTM STP 1175, Aurora, 1992 (KUMAR, A.S., GELLES, D.S., NANSTAD, R.K., LITTLE, E.A., Eds), ASTM International, West Conshohocken, PA (1994) 1129–1139.

[9.18] KOCKS, U.F., "Strain hardening and 'strain-rate hardening'", Mechanical Testing for Deformation Model Development, ASTM STP 765 (ROHDE, R.W., SWEARENGEN, J.C., Eds), ASTM International, West Conshohocken, PA (1982) 121–138.

[9.19] SIEFKEN, L.J., CORYELL, E.W., HARVEGO, E.A., HOHORST, J.K., "MATPRO — A library of materials properties for light-water-reactor accident analysis", Idaho National Engineering and Environmental Laboratory Idaho Falls, 2001, NUREG/CR-6150, Vol. 4, Rev. 2, SCDAP/RELAP 5/MOD 3.3 Code Manual, Nuclear Regulatory Commission, Washington, DC (2001).

[9.20] KOCKS, F., MECKING, H., Physics and phenomenology of strain hardening: the FCC case, Prog. Mater. Sci. 48 (2003) 171–273.

[9.21] CONRAD, H., "High strength Materials", Proc. 2nd Berkeley International Materials Conference: High-strength Materials — Present Status and Anticipated Developments, Berkeley, CA, 1964 (ZACKAY, V.F., Ed.), Wiley, New York (1965) 436.

[9.22] WEI, Q., CHENG, S., RAMESH, K.T., MA, E., Effect of nanocrystalline and ultrafine grain sizes on the strain rate sensitivity and activation volume: Fcc versus bcc metals, Mater. Sci. Eng. A **381** (2004) 71–79.

[9.23] HART, E.W., Theory of the tensile test, Acta Metall. **15** (1967) 351–355.

[9.24] CAMPBELL, J.D., Plastic instability in rate-dependent materials, J. Mech. Phys. Solids **15** (1967) 359–370.

[9.25] COLEMAN, C.E., HOLT, R.A., HOSBONS, R.R., Numerical calculation of plastic instability during tensile deformation, Nucl. Metall. **20** (1976) 807–815.

[9.26] JONAS, J.J., HOLT, R.A., COLEMAN, C.E., Plastic stability in tension and compression, Acta Metall. **24** (1976) 911–918.

[9.27] GHOSH, A.K., Tensile instability and necking in materials with strain hardening and strain-rate hardening, Acta Metall. **25** (1977) 1413–1424.

[9.28] KOCKS, U.F., JONAS, J.J., MECKING, H., The development of strain-rate gradients, Acta Metall. **27** (1979) 419– 432.

[9.29] NICHOLS, F.A., Plastic instabilities and uniaxial tensile ductilities, Acta Metall. **28** (1980) 663–673.

[9.30] BEMENT, A.L., Jr., Effects of Cold Work and Neutron Irradiation on the Tensile Properties of Zircaloy-2, Hanford Labs, Report No. HW-74955, Hanford Labs, Richland, WA (1963).

[9.31] ELLS, C.E., CHEADLE, B.A., "The anisotropy of fracture ductility in flat tension-test bars of alpha zirconium alloy", Applications-Related Phenomena in Zirconium and Its Alloys, ASTM STP 458 (BAROCH, E.F., Ed.), ASTM International, West Conshohocken, PA (1969) 68–91.

[9.32] ADAMSON, R.B., WISNER, S.B., TUCKER, R.P., RAND, R.A., “Failure strain for irradiated Zircaloy based on subsized specimen testing and analysis”, The Use of Small-Scale Specimens for Testing Irradiated Material, ASTM STP 888 (CORWIN, W.R., LUCAS, G.E., Eds), ASTM International, West Conshohocken, PA (1986) 171–185.

[9.33] WOODFORD, D.A., Strain-rate sensitivity as a measure of ductility, ASM Trans. Q. **62** (1969) 291–293.

[9.34] YOO, J.S., KIM, I.S., Effect of (α+β) heat treatment on the mechanical properties of Zircaloy-4, J. Nucl. Mater. **185** (1991) 87–95.

[9.35] WOO, O.T., TSENG, D., TANGRI, K., MacEWEN, S.R., Flow stress and dynamic strain-ageing of β-transformed Zircaloy-4, J. Nucl. Mater. **87** (1979) 135–143.

[9.36] HARDY, D.G., “The effect of neutron irradiation on the mechanical properties of zirconium alloy fuel cladding in uniaxial and biaxial tests”, Irradiation Effects on Structural Alloys for Nuclear Reactor Applications, ASTM STP 484 (BEMENT, A.L., Ed.), ASTM International, West Conshohocken, PA (1970) 215–258.

[9.37] ELLS, C.E., FIDLERIS, V., Effect of neutron irradiation on tensile properties of the zirconium-2.5 wt% niobium alloy, J. Electrochem. Technol. **4** (1966) 268–274.

[9.38] PICKLES, B.W., Embrittlement of heat-treated Zr-2.5wt% Nb pressure tubes, Can. Metall. Q. **11** (1972) 139–146.

[9.39] LANGFORD, W.J., MOODER, L.E.J., BRYSON, J.G., Metallurgical properties of heat-treated Zr-2.5 wt% Nb pressure tubes irradiated under power reactor conditions, Can. Metall. Q. **11** (1972) 147–156.

[9.40] GRIGORIEV, V., et al., “Evaluation of an irradiated Zr-2.5Nb pressure tube removed from the Ignalina RBMK reactor”, Proc. 16th Int Conf. on Structural Mechanics in Reactor Technology, SMiRT 16, Washington, 2001, International Association for Structural Mechanics in Reactor Technology, Raleigh, NC (2001) Paper 1924.

[9.41] PARRY, G.W., The Effect of Fast Neutron Irradiation on the Tensile Properties of Specimens from Cold-worked Zirconium-2.5 wt% Niobium Pressure Tubes, Report No. AECL-2625, Atomic Energy of Canada Limited, Chalk River, ON (1966).

[9.42] PICKLESIMER, M.L., Deformation, creep and fracture in alpha-zirconium alloys, J. Electrochem. Technol. **4** (1966) 289–300.

[9.43] CHEADLE, B.A., ELLS, C.E., VAN DER KUUR, J., “Plastic instability in irradiated Zr-Sn and Zr-Nb alloys”, Zirconium in Nuclear Applications: Second International Symposium, Proc. ASTM STP 551, Portland, OR, 1973 (SCHEMEL, J.H., ROSENBAUM, H.S., Eds), ASTM International, West Conshohocken, PA (1974) 370–384.

[9.44] KELLY, P.M., SMITH, P.D., Strain-ageing in zirconium-oxygen alloys, J. Nucl. Mater. **46** (1973) 23–34.

[9.45] HOLT, R.A., Work hardening and ductility of Zr-1.14% Cr-0.1% Fe, J. Nucl. Mater. **51** (1974) 309–320.

[9.46] ELLS, C.E., QUENNEVILLE, A.F., KIDD, K.V., MOAN, G.D., The Tensile Properties of Sixteen Calandria Tubes, Report No. RC-287, Atomic Energy of Canada, Chalk River, ON (1990).

[9.47] KIM, Y.S., Role of twinning and slip in deformation of a Zr-2.5Nb tube, J. ASTM International **5** (2008) Paper JAI101120.

[9.48] STEWARD, K.P., The Properties of Cold-worked Zirconium-2.5 wt% Niobium Fuel Sheathing, Report No. AECL-2250, Atomic Energy of Canada Limited, Chalk River, ON (1965).

[9.49] AZZARTO, F.J., BALDWIN, E.E., WIESINGER, F.W., LEWIS, D.M., Unirradiated, in-pile and post-irradiation low strain rate tensile properties of Zircaloy-4, J. Nucl. Mater. **30** (1969) 208–218.

[9.50] DAUM, R.S., MAJUMDAR, S., BILLONE, M.C., Experimental and analytical investigation of the mechanical behaviour of high-burnup Zircaloy-4 fuel cladding, J. ASTM International **5** (2008) Paper JAI101209.

[9.51] LEE, D., HART, E.W., Stress relaxation and mechanical behavior of metals, Metall. Trans. **2** (1971) 1245–1248.

[9.52] FONG, R.W.L., et al., “Tensile properties of irradiated calandria tubes at low to high rates of strain”, Proc. 18th Annu. Conf. Can. Nucl. Soc., Toronto, 1997, Atomic Energy of Canada Limited, Chalk River, ON (1997).

[9.53] LEE, D., Strain rate dependent hardening in zirconium and zirconium-niobium alloy, Can. Metall. Q. **11** (1972) 113–117.

[9.54] ELBACHIRI, K., et al., Characterization of local strain distribution in Zircaloy-4 and M5® alloys, J. ASTM International **5** (2008) Paper JAI101125.

[9.55] TYSON, W., Deformation of Zircaloy-2, J. Nucl. Mater. **24** (1967) 101–103.

[9.56] MILLS, D., CRAIG, G.B., The plastic deformation of zirconium-oxygen alloy single crystals in the range 77 to 950 K, Trans. AIME **242** (1968) 1881–1890.

[9.57] HONG, S.I., RYU, W.S., RIM, C.S., Elongation minimum and strain rate sensitivity minimum of Zircaloy-4, J. Nucl. Mater. **116** (1983) 314–316.

[9.58] LEE, K.W., KIM, S.K., KIM, K.T., HONG, S.I., Ductility and strain rate sensitivity of Zircaloy-4 nuclear fuel claddings, J. Nucl. Mater. **295** (2001) 21–26.

[9.59] VEEVERS, K., Strain ageing in zirconium alloys, J. Nucl. Mater. **55** (1975) 109–110.

[9.60] RITCHIE, I.G., ROSINGER, H.E., ATRENS, A., Anelastic relaxation and the diffusion of oxygen in alpha-zirconium, J. Nucl. Mater. **62** (1976) 1–8.

[9.61] GARDE, A.M., Strain aging in α-zirconium and α-Zircaloy at 1000 K, J. Nucl. Mater. **80** (1979) 195–206.

[9.62] NIKULIN, S.A., SHTREMEL, M.A., MARKELOV, V.A., Influence of secondary phase particles on Zr-alloy plastic flow stability and fracture, J. de Phys. IV **6** C6 (1996) C6-133–C6-143.

[9.63] BROEK, D., Elementary Engineering Fracture Mechanics, Springer, Heidelberg, Germany (1982) 24–66.

[9.64] CARE, S., ZAOUI, A., Cavitation at triple nodes in α-zirconium polycrystals, Acta Mater. **44** (1996) 1323–1336.

[9.65] FORSCHER, F., Strain-induced porosity and hydrogen embrittlement in zirconium, J. Met. **8** (1956) 536–543.

[9.66] GAILLAC, A., LEMAIGNAN, C., BARBÉRIS, P., Damage build-up in zirconium alloys during mechanical processing: Application to cold pilgering, J. ASTM International **8** (2011) Paper JAI103026.

[9.67] CRÉPIN, J., BRETHEAU, T., CALDEMAISON, D., Cavity growth and rupture of β-treated zirconium: A crystallographic model, Acta Mater. **44** (1996) 4927–4935.

[9.68] BELL, L.G., DICKS, T.S., The effect of prior beta grain size on the ductility of zirconium-2.5 weight per cent niobium alloy, Can. Metall. Q. **4** (1965) 259–268.

[9.69] ELLS, C.E., WILLIAMS, C.D., Beta embrittlement of the Zr-2.5 wt percent Nb(Cb) alloy, Trans. Metall. Soc. AIME **245** (1969) 1321–1328.

[9.70] HOWE, L.M., THOMAS, W.R., The effect of neutron irradiation on the tensile properties of Zircaloy-2, J. Nucl. Mater. **2** (1960) 248–260.

[9.71] BEMENT, A.L., JR., "Radiation damage in hexagonal close-packed metals and alloys", Proc. AIME Metall. Soc. Conf. on Radiation Effects, New York (1967) 671–725.

[9.72] COLEMAN, C.E., MILLS, D., VAN DER KUUR, J., Deformation parameters of neutron irradiated Zircaloy-4 at 300°C, Can. Metall. Q. **11** (1972) 91–100.

[9.73] ROSENBAUM, H.S., RIEGER, G.F., LEE, D., Localized deformation and fracture in neutron irradiated Zircaloy-2, Metall. Trans. **5** (1974) 1867–1874.

[9.74] HOLT, R.A., The effect of metallurgical condition and irradiation on strength and ductility of Zr-1.14% Cr-0.1% Fe, J. Nucl. Mater. **50** (1974) 207–214.

[9.75] ELLS, C.E., WILLIAMS, C.D., COLEMAN, C.E., "Temperature dependence of irradiation damage in zirconium alloys", Mechanical Behavior of Materials, Proc. Symp. on Mechanical Behavior of Materials, Kyoto, 1974 (GAKKAI, N.Z., Ed.), Society of Materials Science, Kyoto (1974) 77–89.

[9.76] BAROCH, C.J., "Effect of irradiation at 130, 650, and 775°F on tensile properties of Zircaloy-4 at 70, 650 and 775°F", Properties of Reactor Structural Alloys after Neutron or Particle Irradiation, ASTM STP 570, Proc. 7th ASTM Int. Symp. on Effects of Radiation on Structural Materials, Gatlinburg, 1974 (BAROCH, C.J., Ed.), ASTM International, West Conshohocken, PA (1975) 129–142.

[9.77] ONCHI, T., KAYANO, H., HIGASHIGUCHI, Y., Effect of neutron irradiation on deformation behaviour of zirconium, J. Nucl. Sci. Technol. **14** (1977) 359–369.

[9.78] ELLS, C.E., COLEMAN, C.E., CHOW, C.K., Properties of a CANDU calandria tube, Can. Metall. Q. **24** (1985) 215–223.

[9.79] ADAMSON, R.B., BELL, W.L., "Effects of neutron irradiation and oxygen content on the microstructure and mechanical properties of Zircaloy", Proc. Int. Symp. on Microstructure and Mechanical Behaviour of Materials, Xian, China, 1985, EMAS, Warley, UK (1986) 237–246.

[9.80] MORIZE, P., BAICRY, J., MARDON, J.P., "Effect of irradiation at 588 K on mechanical properties and deformation behaviour of zirconium alloy strip", Zirconium in the Nuclear Industry: Seventh International Symposium, Proc. ASTM STP 939, Strasbourg, 1985 (ADAMSON, R.B., VAN SWAM, L.F.P., Eds), ASTM International, West Conshohocken, PA (1987) 101–119.

[9.81] YASUDA, T., NAKATSUKA, M., YAMASHITA, K., "Deformation and fracture properties of neutron-irradiated recrystallized Zircaloy-2 cladding under uniaxial tension", Zirconium in the Nuclear Industry: Seventh International Symposium, Proc. ASTM STP 939, Strasbourg, 1985 (ADAMSON, R.B., VAN SWAM, L.F.P., Eds), ASTM International, West Conshohocken, PA (1987) 734–747.

[9.82] WEI, X., THEAKER, J.R., GRIFFITHS, M., Deformation anisotropy of annealed Zircaloy-2 as a function of fast neutron fluence, J. ASTM Int. **5** (2008) Paper JAI101135.

[9.83] COCKERAM, B.V., SMITH, R.W., LEONARD, K.J., BYUN, T.S., SNEAD, L.L., Development of microstructure and irradiation hardening of Zircaloy during low dose neutron irradiation at nominally 358°C, J. Nucl. Mater. **418** (2011) 46–61.

[9.84] LUFT, A., Microstructural processes of plastic instabilities in strengthened metals, Prog. Mater. Sci. **35** (1991) 97–204.

[9.85] HIMBEAULT, D.D., CHOW, C.K., PULS, M.P., Deformation behaviour of irradiated Zr-2.5Nb pressure tube material, Metall. Mater. Trans. **25** (1994) 135–145.

[9.86] ONCHI, T., KAYANO, H., HIGASHIGUCHI, Y., Inhomogeneous plastic deformation and its relevance to iodine stress corrosion cracking susceptibility in irradiated Zircaloy-2 tubing, J. Nucl. Mater. **116** (1983) 211–218.

[9.87] FARRELL, K., BYUN, T.S., HASHIMOTO, N., Deformation mode maps for tensile deformation of neutron-irradiated structural alloys, J. Nucl. Mater. **335** (2004) 471–486.

[9.88] ONCHI, T., KAYANO, H., HIGASHIGUCHI, Y., The inhomogeneous deformation behaviour of neutron irradiated Zircaloy-2, J. Nucl. Mater. **88** (1980) 226–235.

[9.89] FREGONESE, M., et al., "Failure mechanisms of irradiated Zr alloys related to PCI: Activated slip systems, localized strains, and iodine-induced stress corrosion cracking", Zirconium in the Nuclear Industry: Twelfth International Symposium, Proc. ASTM STP 1354, Toronto, 1998 (SABOL, G.P., MOAN, G.D., Eds), ASTM International, West Conshohocken, PA (2000) 377–398.

[9.90] ONIMUS, F., MONNET, I., BÉCHADE, J.L., PRIOUL, C., PILVIN, P., A statistical TEM investigation of dislocation channeling mechanism in neutron irradiated zirconium alloys, J. Nucl. Mater. **328** (2004) 165–179.

[9.91] WILLIAMS, C.D., ADAMSON, R.B., OLSHAUSEN, K.D., "Effects of boiling water reactor irradiation on tensile properties of Zircaloy", Proc. European Conf. on Irradiation Behavior of Fuel Cladding and Core Component Materials, Karlsruhe, 1974, Kerntechnische Gesellschaft im Deutschen Atomforum, Bonn (1974) 189–192.

[9.92] LEE, D., ADAMSON, R.B., “Modelling of localized deformation in neutron irradiated Zircaloy-2”, Zirconium in the Nuclear Industry: Third International Symposium, Proc. ASTM STP 633, Quebec City, 1976 (LOWE, A.L., Jr., PARRY, G.W., Eds), ASTM International, West Conshohocken, PA (1977) 385–401.

[9.93] REGNARD, C., VERHAEGHE, B., LEFEBVRE-JOUD, F., LEMAIGNAN, C., “Activated slip systems and localized straining of irradiated Zr alloys in circumferential loadings”, Zirconium in the Nuclear Industry: Thirteeth International Symposium, Proc. ASTM STP 1423, Annecy, 2001 (MOAN, G.D., RUDLING, P., Eds), ASTM International, West Conshohocken, PA (2002) 384–399.

[9.94] AKHTAR, A., Basal slip in zirconium, Acta Metall. **21** (1973) 1–11.

[9.95] BOURDILIAU, B., et al., Impact of irradiation damage recovery during transportation on the subsequent room temperature tensile behaviour of irradiated zirconium alloys, J. ASTM International **7** (2010) Paper JAI103006.

[9.96] HIGASHIGUCHI, Y., KAYANO, H., Effect of fast-neutron irradiation on twinning deformation of zirconium, J. Nucl. Sci. Technol. **15** (1978) 263–271.

[9.97] BELL, W.L., “Operable Deformation Systems and Mechanical Behavior of Textured Zircaloy Tubing: Discussion”, Zirconium in Nuclear Applications: Second International Symposium, Proc. ASTM STP 551, Portland, OR, 1973 (SCHEMEL, J.H., ROSENBAUM, H.S., Eds), ASTM International, West Conshohocken, PA (1974) 199–200.

[9.98] HUANG, F.H., Fracture Properties of Irradiated Alloys, Avante Publishing, Richland, WA (1995).

[9.99] HUANG, P.Y., MAHMOOD, S.T., ADAMSON, R.B., “Effects of thermomechanical processing on in-reactor corrosion and post-irradiation mechanical properties of Zircaloy-2”, Zirconium in the Nuclear Industry: Eleveneth International Symposium, Proc. ASTM STP 1295, Garmisch-Partenkirchen, 1995 (BRADLEY, E.R., SABOL, G.P., Eds), ASTM International, West Conshohocken, PA (1996) 726–757.

[9.100] GARDE, A.M., SMITH, G.P., PIREK, R.C., “Effects of hydride precipitate localization and neutron fluence on the ductility of irradiated Zircaloy-4”, Zirconium in the Nuclear Industry: Eleventh International Symposium, Proc. ASTM STP 1295, Garmisch-Partenkirchen, 1995 (BRADLEY, E.R., SABOL, G.P., Eds), ASTM International, West Conshohocken, PA (1996) 407–430.

[9.101] HOLT, R.A., GILBERT, R.W., (c) component dislocations in annealed Zircaloy irradiated at about 570K, J. Nucl. Mater. **137** (1986) 185–189.

[9.102] CHRISTODOULOU, N., MacEWEN, S.R., MECKE, J.F., WOO, O.T., “Effect of irradiation on the work hardening and rate sensitivity of Zircaloy-2 and Ti”, Proc. 2nd Int. Symp. on Environmental Degradation of Materials in Nuclear Power Systems — Water Reactors, Monterey, 1985, American Nuclear Society, La Grange Park, IL (1985) 515–522.

[9.103] PETTERSSON, K., VESTERLUND, G., ANDERSSON, T., “Effect of irradiation on the strength, ductility, and defect sensitivity of fully recrystallized Zircaloy tube”, Zirconium in Nuclear Applications: Fourth International Symposium, Proc. ASTM STP 681, Stratford-upon-Avon, 1978 (SCHEMEL, J.H., PAPAZOGLOU, T.P., Eds), ASTM International, West Conshohocken, PA (1979) 155–173.

[9.104] ONIMUS, F., BÉCHADE, J.L., DUGUAY, C., GILBON, D., PILVIN, P., Investigation of neutron radiation effects on the mechanical behaviour of recrystallized zirconium alloys, J. Nucl. Mater. **358** (2006) 176–189.

[9.105] TOMALIN, D.S., “Localized ductility of irradiated Zircaloy-2 cladding in air and iodine environments”, Zirconium in the Nuclear Industry: Third International Symposium, Proc. ASTM STP 633, Quebec City, 1976 (LOWE, A.L., Jr., PARRY, G.W., Eds), ASTM International, West Conshohocken, PA (1977) 557–572.

[9.106] GARDE, A.M., “Effects of irradiation and hydriding on the mechanical properties of Zircaloy-4 at high fluence”, Zirconium in the Nuclear Industry: Eighth International Symposium, Proc. ASTM STP 1023, San Diego, 1988 (VAN SWAMM, L.F.P., EUCKEN, C.M., Eds), ASTM International, West Conshohocken, PA (1989) 548–569.

[9.107] WISNER, S.B., ADAMSON, R.B., Combined effects of radiation damage and hydrides on the ductility of Zircaloy-2, Nucl. Eng. Des. **185** (1998) 33–49.

[9.108] IRVIN, J.E., Effects of irradiation and environment on the mechanical properties and hydrogen pickup of Zircaloy, J. Electrochem. Technol. **4** (1966) 240–249.

[9.109] COWAN, A., LANGFORD, W.J., Effect of hydrogen and neutron irradiation on the failure of flawed Zircaloy-2 pressure tubes, J. Nucl. Mater. **30** (1969) 271–281.

[9.110] HILL, R., A new method for determining the yield criterion and plastic potential of ductile metals, J. Mech. Phys. Solids **1** (1953) 271–276.

[9.111] HOSBONS, R.R., COLEMAN, C.E., HOLT, R.A., “Numerical simulation of tensile behaviour of nuclear fuel cladding materials”, 3rd Int. Conf. on Structural Mechanics in Reactor Technology, IASMiRT, London, 1975, Atomic Energy of Canada, Chalk River, ON (1975) Paper C 2/7.

[9.112] HOLT, R.A., HOSBONS, R.R., COLEMAN, C.E., Simulation of nuclear fuel sheath deformation following fuel power transients, Nucl. Metall. **20** (1976) 991–1000.

[9.113] ODETTE, G.R., HE, M.Y., DONAHUE, E.G., LUCAS, G.E., “On the relation between engineering load-displacement curves and true stress strain behaviour in tests of flat tensile specimens”, Small Specimen Test Techniques, Vol. 4, ASTM STP 1418 (SOKOLOV, M., LANDES, J., LUCAS, G., Eds), ASTM International, West Conshohocken, PA (2002) 221–233.

[9.114] ONIMUS, F., et al., Plastic deformation of irradiated zirconium alloys: TEM investigations and micro-mechanical modeling, J. ASTM International **2** (2005) Paper JAI12424.

[9.115] ONIMUS, F., BÉCHADE, J.-L., A polycrystalline modeling of the mechanical behaviour of neutron irradiated zirconium alloys, J. Nucl. Mater. **384** (2009) 163–174.

[9.116] GEYER, P., FEAUGAS, X., PILVIN, P., “Modelling of the anisotropic viscoplastic behavior of fully annealed Zircaloy-4 tubes by a polycrystalline approach”, Constitutive and Damage Modeling of Inelastic Deformation and Phase Transformation, Proc. Plasticity ‘99: 7th Int. Symp. on Plasticity and Its Current Applications, Cancun, 1999 (KHAN, A.S., Ed.), Neat Press, Fulton, MD (1999) 133–136.

[9.117] ASTM INTERNATIONAL, Standard Specification for Wrought Zirconium and Zirconium Alloy Seamless and Welded Tubes for Nuclear Service (Except Nuclear Fuel Cladding), ASTM B353-07, ASTM International, West Conshohocken, PA (2017).

[9.118] ASTM INTERNATIONAL, Standard Specification for Wrought Zirconium Alloy Seamless Tubes for Nuclear Reactor Fuel Cladding, ASTM B811-02, ASTM International, West Conshohocken, PA (2007).

[9.119] BURTON, B., The upper limit to the creep life of solids under a tensile force, J. Mater. Sci. **17** (1982) 2441–2448.

[9.120] GRANT, N.J., MONKMAN, E.C., “An empirical relationship between rupture life and minimum creep rate in creep-rupture tests”, Proc. ASTM **56** (1956) 91–103.

[9.121] COLEMAN, C.E., Tertiary creep in cold-worked Zircaloy-2, J. Nucl. Mater. **42** (1972) 180–190.

[9.122] IBRAHIM, E.F., COLEMAN, C.E., Effect of stress sensitivity on stress-rupture ductility of Zircaloy-2 and Zr-2.5 wt% Nb, Can. Metall. Q. **12** (1973) 285–287.

[9.123] CLAY, B.D., REDDING, G.B., Creep rupture properties of alpha-phase zircaloy cladding relevant to the loss-of-coolant accident, J. Br. Nucl. Ener. Soc. **15** (1976) 253–256.

[9.124] BURTON, B., Creep fracture processes in zircaloy, J. Nucl. Mater. **113** (1983) 172–178.

[9.125] LIMON, R., LEHMANN, S., A creep rupture criterion for Zircaloy-4 fuel cladding under internal pressure, J. Nucl. Mater. **335** (2004) 322–334.

[9.126] EVANS, H.E., Mechanisms of Creep Fracture, Elsevier, New York–London (1984).

[9.127] ANDERSSON-ÖSTLING, H.C.M., SANDSTRÖM, R., Survey of Creep Properties of Copper Intended for Nuclear Waste Disposal, Technical Report TR-09-32, Swedish Nuclear Fuel and Waste Management Co., Stockholm (2009).

[9.128] WATKINS, B., WOOD, D.S., “The significance of irradiation-induced creep on reactor performance of a Zircaloy-2 pressure tube”, Applications-Related Phenomena in Zirconium and Its Alloys, ASTM STP 458 (BAROCH, E.F., Ed.), ASTM International, West Conshohocken, PA (1969) 226–240.

[9.129] BURTON, B., A criterion for predicting creep fracture mechanisms, Res. Mech. **8** (1983) 235–259.

[9.130] YOO, M.H., “Suppression of void formation in zirconium”, Zirconium in Nuclear Applications: Second International Symposium, Proc. ASTM STP 551, Portland, 1973 (SCHEMEL, J.H., ROSENBAUM, H.S., Eds), ASTM International, West Conshohocken, PA (1974) 292–307.

[9.131] KEUSSEYAN, R.L., HU, C.P., LI, C.Y., Creep damage in Zircaloy-4 at LWR temperatures, J. Nucl. Mater. **80** (1979) 390–392.

[9.132] HAYES, T.A., ROSEN, R.S., KASSNER, M.E., Creep fracture of zirconium alloys, J. Nucl. Mater. **353** (2006) 109–118.

[9.133] WOOD, D.S., WATKINS, B., A creep limit approach to the design of Zircaloy-2 reactor pressure tubes at 275 ºC, J. Nucl. Mater. **41** (1971) 327–340.

[9.134] LARSON, F.R., MILLER, J., Time-temperature relationship for rupture and creep stresses, Trans. ASME **74** (1952) 765–775.

[9.135] FIDLERIS, V., Uniaxial in-reactor creep of Zirconium alloys, J. Nucl. Mater. **26** (1968) 51–76.

[9.136] COLEMAN, C.E., et al., “Rejuvenation of fracture properties of irradiated Zr-2.5 Nb by heat-treatment”, Effects of Irradiation on Materials: Fifteenth International Symposium, Proc. ASTM STP 1125 (STOLLER, R.E., KUMAR, A.S., GELLES, D.S., Eds), ASTM International, West Conshohocken, PA (1992) 318–336.

[9.137] HOFF, N.J., The necking and the rupture of rods subjected to constant tensile loads, J. Appl. Mech. **20** (1953) 105–108.

[9.138] CLAY, B.D., EVANS, H.E., The computation of constant-load creep curves, Nucl. Eng. Des. **39** (1976) 289–292.

[9.139] WOODFORD, D.A., Measurement and interpretation of the stress dependence of creep at low stresses, Mater. Sci. Eng. **4** (1969) 146–154.

[9.140] ROSS-ROSS, P.A., HUNT, C.E.L., The in-reactor creep of cold-worked Zircaloy-2 and Zirconium-2.5 wt% niobium pressure tubes, J. Nucl. Mater. **26** (1968) 2–17.

[9.141] IBRAHIM, E.F., In-reactor tubular creep of Zircaloy-2 at 260 to 300 ºC, J. Nucl. Mater. **46** (1973) 169–182.

[9.142] COLEMAN, C.E., CAUSEY, A.R., FIDLERIS, V., In-reactor creep of zirconium-2.5 wt% niobium at 570 K, J. Nucl. Mater. **60** (1976) 185–194.

[9.143] NICHOLS, F.A., Evidence for ductility during irradiation creep, Mater. Sci. Eng. **6** (1970) 167–175.

[9.144] GITTUS, J.H., Creep, Viscoelasticity and Creep Fracture in Solids, Wiley, New York (1975).

[9.145] ELLS, C.E., IBRAHIM, E.F., CAUSEY, A.R., “Predicted creep ductility of zirconium alloy pressure tubes in power reactors”, Proc. Int. Conf. on Creep, Tokyo, 1986, Japan Society of Mechanical Engineers, Tokyo (1986) 59–64.

[9.146] WOOD, D.S., “High deformation creep behavior of 0.6-in.-diameter zirconium alloy tubes under irradiation”, Zirconium in Nuclear Applications: Second International Symposium, Proc. ASTM STP 551, Portland, 1973 (SCHEMEL, J.H., ROSENBAUM, H.S., Eds), ASTM International, West Conshohocken, PA (1974) 274–291.

[9.147] IBRAHIM, E.F., Creep ductility of cold-worked Zr-2.5 wt% Nb and Zircaloy-2 tubes in-reactor, J. Nucl. Mater. **96** (1981) 297–304.

[9.148] KOIKE, M., ASADA, T., Irradiation creep and growth of pressure tubes in HWR Fugen, J. Nucl. Mater. **159** (1988) 62–74.

[9.149] KOIKE, M., AKIYAMA, T., NAGAMATSU, K., SHIBAHARA, I., "Change of mechanical properties by irradiation and evaluation of the heat-treated Zr-2.5 Nb pressure tube", Zirconium in the Nuclear Industry: Tenth International Symposium, Proc. ASTM STP 1245, Baltimore, 1993 (GARDE, A.M., BRADLEY E.R., Eds), ASTM International, West Conshohocken, PA (1994) 183–201.

[9.150] IBRAHIM, E.F., Deformation of cold-drawn tubes of Zr-2.5 wt% Nb after 7 years in-reactor, J. Nucl. Mater. **118** (1983) 260–268.

[9.151] GONCHAROV, V.V., PLATONOV, P.A., IVANOV, A.N., FROLOV, I.A., Investigation of in-reactor creep and irradiation growth of zirconium-2.5 wt% niobium channel tubes, J. Nucl. Mater. **90** (1980) 224–231.

[9.152] WOOD, D.S., "Dose dependence of irradiation creep of Zircaloy-2", Properties of Reactor Structural Alloys after Neutron or Particle Irradiation, ASTM STP 570 (BAROCH, C.J., Ed.), ASTM International, West Conshohocken, PA (1975) 207–217.

[9.153] ROGERSON, A., Serco Assurance, personal communication, 1980.

[9.154] CHRISTODOULOU, N., et al., "Modeling in-reactor deformation of Zr-2.5Nb pressure tubes in CANDU power reactors", Zirconium in the Nuclear Industry: Eleveth International Symposium, Proc. ASTM STP 1295, Garmisch-Partenkirchen, 1995 (BRADLEY, E.R., SABOL, G.P., Eds), ASTM International, West Conshohocken, PA (1996) 518–537.

[9.155] COLEMAN, C.E., et al., "Evaluation of Zircaloy-2 pressure tubes from NPD", Zirconium in the Nuclear Industry: Eighth International Symposium, Proc. ASTM STP 1023, San Diego, 1988 (VAN SWAM, L.F.P., EUCKEN, C.M., Eds), ASTM International, West Conshohocken, PA (1989) 35–49.

[9.156] CHOW, C.K., et al., "Properties of an irradiated heat-treated Zr-2.5Nb pressure tube removed from the NPD reactor", Zirconium in the Nuclear Industry: Eleventh International Symposium, Proc. ASTM STP 1295, Garmisch-Partenkirchen, 1995 (BRADLEY, E.R., SABOL, G.P., Eds), ASTM International, West Conshohocken, PA (1996) 469–491.

[9.157] MAYO, W., Atomic Energy of Canada Limited, personal communication, 1999.

[9.158] PLATONOV, P.A., et al., Creep of the RBMK pressure tubes from Zr.2.5Nb alloy, Mater. Sci. & Novel Mater. **36** (1990) 22–33.

[9.159] COLEMAN, C., et al., Mechanical properties of Zr-2.5Nb pressure tubes made from electrolytic powder, J. ASTM Int. **4** (2008) Paper JAI101111.

[9.160] GLASSTONE, S., SESONSKE, A., Nuclear Reactor Engineering, Wiley, Hoboken, NJ (1967).

[9.161] INTERNATIONAL ATOMIC ENERGY AGENCY, Spent Fuel Reprocessing Options, IAEA-TECDOC-1587, IAEA, Vienna (2009).

[9.162] JOHNSON, A.B., Jr., Behavior of Spent Nuclear Fuel in Water Pool Storage, Battelle Pacific Northwest Labs Report No. BNWL-2256, Battelle Pacific Northwest Labs, Richland, WA (1977).

[9.163] INTERNATIONAL ATOMIC ENERGY AGENCY, Survey of Wet and Dry Spent Fuel Storage, IAEA-TECDOC-1100, IAEA, Vienna (1999).

[9.164] KANG, K.H., RYU, H.J., SONG, K.C., YANG, M.S., Thermal expansion of UO_2 and simulated DUPIC fuel, J. Nucl. Mater. **301** (2002) 242–244.

[9.165] BUNNELL, L.R., BATES, J.L., MELLINGER, G.B., Some high-temperature properties of Zircaloy-oxygen alloys, J. Nucl. Mater. **116** (1983) 219–232.

[9.166] SNOW, R.K., SNOW, M.M., Annual temperature range time-series trends and long-range forecasting, Natl. Weather Dig. **29** (2005) 3–12.

[9.167] LEATHERS, D.J., PALECKI, M.A., ROBINSON, D.A., DEWEY, K.F., Climatology of the daily temperature range annual cycle in the United States, Clim. Res. **9** (1998) 197–211.

[9.168] WASYWICH, K.M., Temperature Measurements of Irradiated Fuel Bundles Stored in a Concrete Canister, Report No. WNRE-262, Atomic Energy of Canada Limited, Chalk River, ON (1981).

[9.169] SUFFIELD, S.R., et al., Thermal Modeling of NUHOMS HSM-15 and HSM-1 Storage Modules at Calvert Cliffs Nuclear Power Station ISFSI, Pacific Northwest National Lab. Report No. PNNL-21788, Pacific Northwest National Lab., Richland, WA (2012).

[9.170] PIRON, J., PELLETIER, M., "Spent nuclear fuel evolution in a closed system", Proc. 8th Int. Conf. on Radioactive Waste Management and Environmental Remediation, ASME, Bruges, 2001, ASME International, New York (2001).

[9.171] NUCLEAR REGULATORY COMMISSION, Standard Review Plan for Spent Fuel Dry Storage Systems at a General License Facility, NUREG-1536, Rev. 1A, Nuclear Regulatory Commission, Washington, DC (2009).

[9.172] BRACH, E.W., "Cladding considerations for the transportation and storage of spent fuel", USNRC Interim Staff Guidance – 11, Rev. 3, NRC, Washington, DC (2003).

[9.173] GOLL, W., LEGER, A.C., McCOY, K., "Spent fuel behavior under dry cask storage conditions", Proc. Int. Topical Mtg on LWR Fuel Performance, TopFuel 2003, Würzburg, 2003, American Nuclear Society, La Grange Park, IL (2003).

[9.174] EINZIGER, R.E., BROWN, C.L., HORNSETH, G.P., INTERRANTE, C.G., Data needs for storage and transportation of high-burnup fuel, Radwaste Solut. **12** (2005) 44–57.

[9.175] WASYWICH, K.M, FREIRE-CANOSA, J., NAQVI, S.J., "Canadian spent fuel storage experience", Proc. Int. Symp. on Safety and Engineering Aspects of Spent Fuel Storage, Vienna, 1994, IAEA, Vienna (1995) 41–55.

[9.176] SPILKER, H., PEEHS, M., DYCK, H.-P., KASPAR, G., NISSAN, K., Spent LWR fuel dry storage in large transport and storage casks after extended burn-up, J. Nucl. Mater. **250** (1997) 63–74.

[9.177] RASHID, J., MACHIELS, A., “Threat of hydride re-orientation to spent fuel integrity during transportation accidents: myth or reality?”, Proc. Int. Topical Mtg on LWR Fuel Performance, TopFuel 2007, ANS/ENS, San Francisco, 2007, American Nuclear Society, La Grange Park, IL (2007) paper 1039.

[9.178] EINZIGER, R.E., McKINNON, M.A., MACHIELS, A.J., “Extending dry storage of spent LWR fuel for up to 100 years”, Proc. Int. Symp on Storage of Spent Fuel from Power Reactors, Vienna, 1998, IAEA, Vienna (1999) 339–349.

[9.179] RASHID, Y.R., SUNDERLAND, D.J., MONTGOMERY, R.O., Creep as the Limiting Mechanism for Spent Fuel Dry Storage, Electric Power Research Institute Report No. 1001207, Electric Power Research Institute, Palo Alto, CA (2000).

[9.180] PEEHS, M., GARZAROLLI, F., GOLL, W., “Assessment of dry storage performance of spent LWR fuel assemblies with increasing burnup”, Proc. Symp. on Storage of Spent Fuel from Power Reactors, IAEA-TECDOC-1089, IAEA, Vienna (1999) 313–324.

[9.181] BOUFFIOUX, P., RUPA, N., “Impact of hydrogen on plasticity and creep of unirradiated Zircaloy-4 cladding tubes”, Zirconium in the Nuclear Industry: Twelfth International Symposium, Proc. ASTM STP 1354, Toronto, 1998 (SABOL, G.P., MOAN, G.D., Eds), ASTM International, West Conshohocken, PA (2000) 399–422.

[9.182] BOUFFIOUX, P., LEGRAS, L., “Effect of hydriding on the residual cold work recovery and creep of Zircaloy-4 cladding tubes”, Int. Topical Mtg on LWR Fuel Performance, Park City, UT, 2000, American Nuclear Society, La Grange Park, IL (2000).

[9.183] RUPA, N., CLAVEL, M., BOUFFIOUX, P., DOMAIN, C., LEGRIS, A., “About the mechanisms governing the hydrogen effect on viscoplasticity of unirradiated fully annealed Zircaloy-4 sheet”, Zirconium in the Nuclear Industry: Thirteenth International Symposium, Proc. ASTM STP 1423, Annecy, 2001 (MOAN, G.D., RUDLING, P., Eds), ASTM International, West Conshohocken, PA (2002) 811–836.

[9.184] SONIAK, A., et al., “Irradiation creep behavior of Zr-base alloys”, Zirconium in the Nuclear Industry: Thirteenth International Symposium, Proc. ASTM STP 1423, Annecy, 2001 (MOAN, G.D., RUDLING, P., Eds), ASTM International, West Conshohocken, PA (2002) 837–862.

[9.185] ITO, K., KAMIMURA, K., TSUKUDA, Y., “Evaluation of irradiation effect on spent fuel cladding creep properties”, Proc. Int. Topical Mtg on LWR Fuel Performance, Orlando, FL, 2004, American Nuclear Society, La Grange Park, IL (2004) 440–451.

[9.186] KASPAR, G., PEEHS, M., STEINBERG, E., SCHÖNFELD, H., “Experimental investigation of post-pile creep of Zircaloy cladding tubes”, Proc. 8th Int. Conf. on Structural Mechanics in Reactor Technology, IASMiRT, Brussels, 1985, International Association for Structural Mechanics in Reactor Technology, Raleigh, NC (1985) Paper C1/8.

[9.187] CAPPELAERE, C., et al., “Impact of irradiation defects annealing on long-term thermal creep of irradiated Zircaloy-4 cladding tube”, Zirconium in the Nuclear Industry: Thirteenth International Symposium, Proc. ASTM STP 1423, Annecy, 2001 (MOAN, G.D., RUDLING, P., Eds), ASTM International, West Conshohocken, PA (2002) 720–739.

[9.188] CHIN, B.A., KHAN, M.A., TARN, J.C.L., Deformation and Fracture Map Methodology for Predicting Cladding Behaviour During Dry Storage, Pacific Northwest Lab. Report No. PNL 5998, Pacific Northwest Lab., Richland, WA (1986).

[9.189] LUCAS, G.E., PELLOUX, R.M.N., Some observations on time-hardening and strain-hardening rules for creep in Zircaloy-2, Nucl. Technol. **53** (1981) 46–57.

[9.190] MATSUO, Y., “Creep behavior of Zircaloy cladding under variable conditions”, Zirconium in the Nuclear Industry: Eighth International Symposium, Proc. ASTM STP 1023, San Diego, 1988 (VAN SWAM, L.F.P., EUCKEN, C.M., Eds), ASTM International, West Conshohocken, PA (1989) 678–691.

[9.191] LIMON, R., CAPPELAERE, C., BREDEL, T., BOUFFIOUX, P., “A formulation of the spent fuel cladding creep behaviour for long term storage”, Proc. Int. Topical Mtg on LWR Fuel Performance, Park City, 2000, American Nuclear Society, La Grange Park, IL (2000).

[9.192] BOUFFIOUX, P., LECLERCQ, S., CAPPELAERE, C., BREDEL, T., “Interim dry storage of PWR spent fuel assemblies — development of a long term creep law to assess the fuel cladding integrity”, Proc. 8th Int. Conf. on Radioactive Waste Management and Environmental Remediation, Bruges, 2001 (TABOAS, A., VANBRABANT, R., BENDA, G., Eds), American Society of Mechanical Engineers, New York (2002).

[9.193] GOLL, W., SPILKER, H., TOSCANO, E.H., Short-term creep and rupture tests on high burnup fuel rod cladding, J. Nucl. Mater. **289** (2001) 247–253.

[9.194] KAMIMURA, K., et al., “Thermal creep tests of BWR and PWR spent fuel cladding”, Storage of Spent Fuel from Power Reactors, Proc. Int. Conf., Vienna, 2003, IAEA-CSP-20, IAEA, Vienna (2003).

[9.195] TSAI, H., BILLONE, M.C., Thermal creep of irradiated Zircaloy cladding, J. ASTM International **3** (2006) Paper JAI12425.

[9.196] QUECEDO, M., et al., Results of thermal creep test on highly irradiated Zirlo, Nucl. Eng. Technol. **41** (2009) 179–186.

[9.197] EINZIGER, R.E., TSAI, H., BILLONE, M.C., HILTON, B.A., Examination of spent pressurized water reactor fuel rods after 15 years in dry storage, Nucl. Technol. **144** (2003) 186–200.

[9.198] GRIGORIEV, V., JAKOBSSON, R., “Delayed hydrogen cracking velocity and J-integral measurements on irradiated BWR cladding”, Zirconium in the Nuclear Industry: Fourteenth International Symposium, Proc. ASTM STP 1467, Stockholm, 2004 (RUDLING, P., KAMMENZIND, B., Eds), ASTM International, West Conshohocken, PA (2005) 711–728.

[9.199] SASAHARA, A., MATSUMURA, T., Post-irradiation examination focused on fuel integrity of spent BWR-MOX and PWR-UO2 fuels stored for 20 years, Nucl. Eng. Des. **238** (2008) 1250–1259.

[9.200] NUCLEAR ENERGY AGENCY, ORGANISATION FOR ECONOMIC CO-OPERATION AND DEVELOPMENT, Nuclear Fuel Behaviour in Loss-of-Coolant Accident (LOCA) Conditions, NEA No. 6846, OECD, Paris (2009).

[9.201] WEIDINGER, H.G., CHELIOTIS, G., WATZINGER, H., STEHLE, H., "LOCA-fuel rod behaviour of KWU pressurised water reactors", Proc. CSNI Specialists Mtg on the Behaviour of Water Reactor Fuel Elements under Accident Conditions, Spåtind, Norway (1976) Paper 26.

[9.202] CHUNG, H.M., KASSNER, T.F., Embrittlement Criteria for Zircaloy Cladding Applicable to Accident Situations in Light-water Reactors: Summary Report, Argonne National Lab., NUREG/CR-1344, NRC, Washington, DC (1980).

[9.203] RUDLING, P., ADAMSON, R.B., GARZAROLLI, F., Loss of Coolant Accidents, LOCA, and Reactivity Initiated Accidents, RIA, in BWRs and PWRs", ZIRAT-9 Special Topics Report, ANT International, Tollered, Sweden (2004).

[9.204] KOHN, E., FEHRENBACH, P.J., LAU, J.H.K., CANDU Fuel Behaviour under LOCA Conditions", Report No. AECL-9788, Atomic Energy of Canada Limited, Chalk River, ON (1989).

[9.205] AMERICAN NUCLEAR SOCIETY, Nuclear Technology, Vol. 87, Taylor and Francis, Oxford (1989).

[9.206] WORLD NUCLEAR ASSOCIATION, Fukushima Daiichi Accident (2013), https://world-nuclear.org/information-library/safety-and-security/safety-of-plants/fukushima-daiichi-accident.aspx

[9.207] STRICKLAND, E., What Went Wrong in Japan's Nuclear Reactors (2011), https://spectrum.ieee.org/tech-talk/energy/nuclear/explainer-what-went-wrong-in-japans-nuclear-reactors

[9.208] INTERNATIONAL ATOMIC ENERGY AGENCY, The Chernobyl Accident: Updating of INSAG-1, INSAG-7, IAEA, Vienna (1992).

[9.209] NUCLEAR REGULATORY COMMISSION, Acceptance Criteria for Emergency Core Cooling Systems for Light-Water Nuclear Power Reactors, 10 CFR 50.46, US Govt Printing Office, Washington, DC (1973).

[9.210] NUCLEAR REGULATORY COMMISSION, Acceptance Criteria for Emergency Core Cooling Systems for Light-Water Nuclear Power Reactors, 10 CFR 50.46, US Govt Printing Office, Washington, DC (2007).

[9.211] NUCLEAR REGULATORY COMMISSION, ECCS Evaluation Models, 10 CFR 50, Appendix K, Rev. US Govt Printing Office, Washington (2021).

[9.212] NUCLEAR REGULATORY COMMISSION, Best-estimate Calculations for Emergency Core Cooling System Performance, Regulatory Guide 1.157, US Govt Printing Office, Washington, DC (1989).

[9.213] ERBACHER, F.J., LEISTIKOW, S., "Zircaloy fuel cladding behavior in a loss-of-coolant accident: A review", Zirconium in the Nuclear Industry: Seventh International Symposium, Proc. ASTM STP 939, Strasbourg, 1985 (ADAMSON, R.B., VAN SWAM, L.F.P., Eds) ASTM International, West Conshohocken, PA (1987) 451–488.

[9.214] WENSAUER, A., "LOCA: An operator's view on German licensing practice", Fuel Behaviour and Modelling under Severe Transient and Loss of Coolant Accident (LOCA) Conditions, IAEA-TECDOC-CD-1709, IAEA, Vienna (2013).

[9.215] CANADIAN NUCLEAR SAFETY COMMISSION, Design of New Nuclear Power Plants, Regulatory Document RD-337, Canadian Nuclear Safety Commission, Ottawa (2008).

[9.216] CANADIAN NUCLEAR SAFETY COMMISSION, Safety Analysis for Nuclear Power Plants, Regulatory Document RD-310, Canadian Nuclear Safety Commission, Ottawa (2008).

[9.217] JOHNSTON, W.V., "Zircaloy — three years after the hearings", Zirconium in the Nuclear Industry: Third International Symposium, Proc. ASTM STP 633, Quebec City, 1976 (LOWE, A.L., PARRY, G.W., Eds), ASTM International, West Conshohocken, PA (1977) 5–23.

[9.218] GRANDJEAN, C., A State-of-the-art Review of Past Programs Devoted to Fuel Behaviour under LOCA Conditions, Part 1: Clad Swelling and Rupture Assembly Flow Blockage, Institut de Radioprotection et de Sûreté Nucléaire Technical Report No. SEMCA-2005-313, IRSN, Fontenay-aux-Roses (2005).

[9.219] GRANDJEAN, C., A State-of-the-art Review of Past Programs Devoted to Fuel Behaviour under LOCA Conditions, Part 2: Impact of Clad Swelling upon Assembly Cooling, Institut de Radioprotection et de Sûreté Nucléaire Technical Report No. SEMCA-2006-183, IRSN, Fontenay-aux-Roses (2006).

[9.220] LEWIS, B.J., IGLESIAS, F.C., DICKSON, R.S., WILLIAMS, A., Overview of high-temperature fuel behaviour with relevance to CANDU fuel, J. Nucl. Mater. **394** (2009) 67–86.

[9.221] GARDE, A.M., CHUNG, H.M., KASSNER, T.F., Micrograin superplasticity in Zircaloy at 850ºC, Acta Metall. **26** (1978) 153–166.

[9.222] ROSE, K.M., HINDLE, E.D., "Diameter increases in steam generating heavy water reactor Zircaloy cans under loss-of-coolant accident conditions", Zirconium in the Nuclear Industry: Third International Symposium, Proc. ASTM STP 633, Quebec City, 1976 (LOWE, A.L., PARRY, G.W., Eds), ASTM International, West Conshohocken, PA (1977) 24–35.

[9.223] LEE, D., BACKOFEN, W.A., Superplasticity in some titanium and zirconium alloys, Trans. Metall. Soc. AIME **239** (1967) 1034–1040.

[9.224] BOČEK, M., HOFMANN, P., PETERSEN, C., "Superplasticity of Zircaloy-4", Zirconium in the Nuclear Industry: Third International Symposium, Proc. ASTM STP 633, Quebec City, 1976 (LOWE, A.L., PARRY, G.W., Eds), ASTM International, West Conshohocken, PA (1977) 66–81.

[9.225] GARDE, A.M., CHUNG, H.M., KASSNER, T.F., Uniaxial Tensile Properties of Zircaloy Containing Oxygen: Summary Report, Argonne National Lab. Report No. ANL-77-30, NRC, Washington, DC (1977).

[9.226] KEARNS, J.J., McCAULEY, J.E., NICHOLS, F.A., Effect of alpha/beta phase constitution on superplasticity and strength of Zircaloy-4, J. Nucl. Mater. **61** (1976) 169–184.

[9.227] NUTTALL, K., Superplasticity in the Zr-2.5% Nb alloy, Scripta Metall. **10** (1976) 835–840.

[9.228] EMMERICH, K.M., JUENKE, E.F., WHITE, J.F., "Failure of pressurized zircaloy tubes during thermal excursions in steam and in inert atmospheres", Applications-Related Phenomena in Zirconium and Its Alloys, ASTM STP 458 (BAROCH, E.F., Ed.), ASTM International, West Conshohocken, PA (1969) 252–268.

[9.229] WILLIAMS, A.F., Atomic Energy of Canada Limited, personal communication, 1998.

[9.230] HARDY, D.G., High Temperature Expansion and Rupture Behaviour of Zircaloy Tubing, Specialist Mtg on the Safety of Water Reactors Fuel Elements, Saclay, 1973, NEA-CSNI-R-1973-1, OECD/NEA, Paris (1973) 687–706.

[9.231] HUNT, C.E.L., FOOTE, D.E., High Temperature Strain Behaviour of Zircaloy-4 and Zr-2.5Nb Fuel Sheaths, Zirconium in the Nuclear Industry: Third International Symposium, Proc. ASTM STP 633, Quebec City, 1976 (LOWE, A.L., PARRY, G.W., Eds), ASTM International, West Conshohocken, PA (1977) 50–65.

[9.232] EMERY, A.D., SCOTT, D.B., STEWART, J.R., Effects of heating rate and pressure on expansion of Zircaloy tubing during sudden heating conditions, Nucl. Technol. **11** (1971) 474–478.

[9.233] HOBSON, D.O., OSBORNE, M.F., PARKER, G.W., Comparison of rupture data from irradiated fuel rods and unirradiated cladding, Nucl. Technol. **11** (1971) 479–490.

[9.234] FIVELAND, W.A., BARBER, A.R., LOWE, A.L., Jr., "Rupture characteristics of Zircaloy-4 cladding with internal and external simulation of reactor heating", Zirconium in the Nuclear Industry: Third International Symposium, Proc. ASTM STP 633, Quebec City,1976 (LOWE, A.L., PARRY, G.W., Eds), ASTM International, West Conshohocken, PA (1977) 36–49.

[9.235] CHUNG, H.M., GARDE, A.M., KASSNER, T.F., "Deformation and rupture behavior of zircaloy cladding under simulated loss-of-coolant accident conditions", Zirconium in the Nuclear Industry: Third International Symposium, Proc. ASTM STP 633, Quebec City, 1976 (LOWE, A.L., PARRY, G.W., Eds), ASTM International, West Conshohocken, PA (1977) 82–97.

[9.236] CHAPMAN, R.H., CROWLEY, J.L., LONGEST, A.W., HOFMANN, G., "Zirconium cladding deformation in a steam environment with transient heating", Zirconium in the Nuclear Industry: Fourth International Symposium, Proc. ASTM STP 681, Stratford-upon-Avon, 1978 (SCHEMEL, J.H., PAPAZOGLOU, T.P., Eds), ASTM International, West Conshohocken, PA (1979) 393–408.

[9.237] ERBACHER, F.J., NEITZEL, H.J., ROSINGER, H., SCHMIDT, H., WIEHR, K., "Burst criterion of Zircaloy fuel claddings in a loss-of-coolant accident", Zirconium in the Nuclear Industry: Fifth International Symposium, Proc. ASTM STP 754, Boston, 1980 (FRANKLIN, D.G., Ed.), ASTM International, West Conshohocken, PA (1982) 271–283.

[9.238] FORGERON, T., et al., "Experimental and modeling of advanced fuel rod cladding behavior under LOCA conditions: Alpha-beta phase transformation kinetics and EDGAR methodology", Zirconium in the Nuclear Industry: Twelfth International Symposium, Proc. ASTM STP 1354, Toronto, 1998 (SABOL, G.P., MOAN, G.D., Eds), ASTM International, West Conshohocken, PA (2000) 256–278.

[9.239] CHAPMAN, R.H., Multirod Burst Test Program Progress Report for January–June 1982, Oak Ridge National Lab. Report No. NUREG/CR-2911, NRC, Washington, DC (1982).

[9.240] RIZKALLA, A.S., HOLT, R.A., JONAS, J.J., "Effect of oxygen on the deformation of Zircaloy-2 at elevated temperatures", Zirconium in the Nuclear Industry: Fourth International Symposium, Proc. ASTM STP 681, Stratford-upon-Avon, 1978 (SCHEMEL, J.H., PAPAZOGLOU, T.P., Eds), ASTM International, West Conshohocken, PA (1979) 497–513.

[9.241] CHOUBEY, R., JONAS, J.J., HOLT, R.A., ELLS, C.E., "Flow stress of oxygen-enriched Zircaloy-2 between 1023 and 1873 K", Zirconium in the Nuclear Industry: Fifth International Symposium, Proc. ASTM STP 754, Boston, 1980 (FRANKLIN, D.G., Ed.), ASTM International, West Conshohocken, PA (1982) 350–369.

[9.242] HUNT, C.E.L., FOOTE, D.E., GRANT, D., The Effect of Steam Oxidation on the Strain of Fuel Sheathing at High Temperature, CSNI Specialists Mtg on the Behaviour of Water Reactor Fuel Elements under Accident Conditions, Spåtind, 1976, AECL-5559, Atomic Energy of Canada Limited, Chalk River, ON (1976).

[9.243] DONALDSON, A.T., EVANS, H.E., Oxidation-induced creep in Zircaloy-2: I. Basic observations; J. Nucl. Mater. **99** (1981) 38–46.

[9.244] SAGAT, S., SILLS, H.E., WALSWORTH, J.A., "Deformation and failure of zircaloy fuel sheaths under LOCA conditions", Zirconium in the Nuclear Industry: Sixth International Symposium, Proc. ASTM STP 824, Vancouver, 1982 (FRANKLIN, D.G., ADAMSON, R.B., Eds), ASTM International, West Conshohocken, PA (1984) 709–733.

[9.245] BRADHURST, D.H., HEUER, P.M., The effects of deformation on the high-temperature steam oxidation of Zircaloy-2, J. Nucl. Mater. **55** (1975) 311–326.

[9.246] HINDLE, E.D., MOWAT, J.A.S., Swelling Behaviour of SGHWR Fuel Cladding in Steam in Laboratory Tests Simulating LOCA Involving Temperatures Above 900°C, Proc. Specialists Mtg on the Behaviour of Water Reactor Fuel Elements under Accident Conditions, CSNI Report No. 13, Spåtind, Norway, Nuclear Energy Agency, NEA/OECD, Paris (1976) 19–20.

[9.247] BRACHET, J.C., et al., “Influence of hydrogen content on the α/β phase transformation temperatures and on the thermal-mechanical behaviour of Zy-4, M4 (ZrSnFeV) and M5™ (ZrNbO) alloys during the first phase of LOCA transient”, Zirconium in the Nuclear Industry: Thirteenth International Symposium, proc. ASTM STP 1423, Annecy, 2001 (MOAN, G.D., RUDLING, P., Eds), ASTM International, West Conshohocken, PA (2002) 673–701.

[9.248] BAUER, A.A, LOWRY, L.M., GALLAGHER, W.J., “Tube-burst response of irradiated zircaloy spent-fuel cladding”, Zirconium in the Nuclear Industry: Fourth International Symposium, Proc. ASTM STP 681, Stratford-upon-Avon, 1978 (SCHEMEL, J.H., PAPAZOGLOU, T.P., Eds), ASTM International, West Conshohocken, PA (1979) 465–476.

[9.249] McGRATH, M.A., et al., “The effect of short-term dry-out transients on the cladding properties of fresh and pre-irradiated fuel rods”, Zirconium in the Nuclear Industry: Thirteenth International Symposium, Proc. ASTM STP 1423, Annecy, 2001 (MOAN, G.D., RUDLING, P., Eds), ASTM International, West Conshohocken, PA (2002) 637–657.

[9.250] TORIMARU, T., YASUDA, T., NAKATSUKA, M., Changes in mechanical properties of irradiated Zircaloy-2 fuel cladding due to short term annealing, J. Nucl. Mater. **238** (1996) 169–174.

[9.251] BILLONE, M., YAN, Y., BURTSEVA, T., DAUM, R., Cladding Embrittlement During Postulated Loss-of-coolant Accidents, Argonne National Lab. Report No. NUREG/CR-6967, NRC, Washington, DC (2008).

[9.252] FLANAGAN, M., ASKELJUNG, P., Observations of Fuel Fragmentation, Mobility and Release in Integral, High-burnup, Fueled LOCA Tests, Studsvik Nuclear Lab. Report No. ML 12257A284, NRC, Washington, DC (2012).

[9.253] SAGAT, S., SILLS, H.E., WALSWORTH, J.A., FOOTE, D.E., SHIELDS, D.F., Deformation and Failure of Zircaloy Fuel Sheaths under LOCA Conditions, Report No. AECL-7754, Atomic Energy of Canada Limited, Chalk River, ON (1982).

[9.254] HUNT, C.E.L., NEWELL, W.G., “Effect of β-phase heat treatment on the subsequent α-phase ballooning behavior of Zircaloy-4 fuel sheaths”, Zirconium in the Nuclear Industry: Fourth International Symposium Proc. ASTM STP 681, Stratford-upon-Avon, 1978 (SCHEMEL, J.H., PAPAZOGLOU, T.P., Eds), ASTM International, West Conshohocken, PA (1979) 447–463.

[9.255] SELL, H.J., ORTLIEB, E., “Effects of alpha-beta transformation on high temperature (LOCA) creep behavior of Zr-alloys”, Zirconium in the Nuclear Industry: Thirteenth International Symposium, Proc. ASTM STP 1423, Annecy, 2001 (MOAN, G.D., RUDLING, P., Eds), ASTM International, West Conshohocken, PA (2002) 658–672.

[9.256] CHAPMAN, R.H., Multirod Burst Test Program Progress Report for April–June 1979, Oak Ridge National Lab. Report No. NUREG/CR-1023, NRC, Washington, DC (1979).

[9.257] POWERS, D.A., MEYER, R.O., Cladding Swelling and Rupture Models for LOCA Analysis, Nuclear Regulatory Commission Report No. NUREG-0630, NRC, Washington, DC (1980).

[9.258] BOČEK, M., Lifetime and Failure Strain Prediction for Material Subjected to Non-stationary Tensile Loading Conditions: Applications to Zircaloy-4”, Zirconium in the Nuclear Industry: Fifth International Symposium, Proc. ASTM STP 754, Boston, 1980 (FRANKLIN, D.G., Ed.), ASTM International, West Conshohocken, PA (1982) 329–349.

[9.259] SILLS, H.E., HOLT, R.A., “Predicting high-temperature transient deformation from microstructural models”, Zirconium in the Nuclear Industry: Fourth International Symposium, Proc. ASTM STP 681, Stratford-upon-Avon, 1978 (SCHEMEL, J.H., PAPAZOGLOU, T.P., Eds), ASTM International, West Conshohocken, PA (1979) 325–341.

[9.260] SILLS, H.E., HOLT, R.A., NIRVANA, A High-temperature Creep Model for Zircaloy Fuel Sheathing, Report No. AECL–6412, Atomic Energy of Canada Limited, Chalk River, ON (1979).

[9.261] JONES, P.M., GITTUS, J.H., HINDLE, E.D., “CANSWEL: A computer model of clad behaviour during a loss-of-coolant accident”, Proc. CSNI Conference, Spåtind, Norway, 1976, The Reactor Group Report No. 2901(S), Abingdon, UK (1976).

[9.262] HILL, R., A theory of the yielding and plastic flow of anisotropic metals, Proc. R. Soc. A **193** (1948) 281–297.

[9.263] BRZOSKA, B., CHELIOTIS, G., KUNICK, A., SENSKI, G., “A new high temperature model for Zircaloy clad ballooning under hypothetical LOCA conditions”, 4th Int. Conf. on Structural Mechanics in Reactor Technology, SMiRT 4, San Francisco, 1977, North Holland, Amsterdam (1977) Paper C1/8.

[9.264] ROSINGER, H.E., NEITZEL, H.J., ERBACHER, F.J., The development of a burst criterion for Zircaloy fuel cladding under LOCA conditions, Res Mech. **2** (1981) 91–107.

[9.265] ROSINGER, H.E., A model to predict the failure of Zircaloy-4 fuel sheathing during postulated LOCA conditions, J. Nucl. Mater. **120** (1984) 41–54.

[9.266] SHEWFELT, R.S.W., The ballooning of fuel cladding tubes: Theory and experiment, Res Mech. **25** (1988) 261–294.

[9.267] MATTHEWS, J.R., The effect of anisotropy on the ballooning of Zircaloy cladding, Nucl. Eng. Des. **77** (1984) 87–95.

[9.268] EBERLE, R., WUNDERLICH, M., DISTLER, I., “Deterministic modelling of the LOCA creep and rupture behavior of Zircaloy cladding tubes”, Proc. ANS/ENS Topical Mtg on Reactor Safety Aspects of Fuel Behavior, Sun Valley, ID, 1981, American Nuclear Society, La Grange Park, IL (1981) 310–320.

[9.269] SHEWFELT, R.S.W., GODIN, D.P., Ballooning of thin-walled tubes with circumferential temperature variations, Res. Mech. **18** (1986) 21–33.

[9.270] SHEWFELT, R.S.W., Ballooning of Thin-walled Tubes with an Azimuthal Temperature Gradient, Report No. AECL-7799, Atomic Energy of Canada Limited, Chalk River, ON (1982).

[9.271] SHEWFELT, R.S.W., GODIN, D.P., The effect of axial scratches on the ductile creep rupture of internally pressurized thin-walled tubes, Res. Mech. **13** (1985) 1–13.

[9.272] SAGAT, S., SILLS, H.E., WALSWORTH, J.A., "Deformation and failure of Zircaloy fuel sheaths under LOCA conditions", Zirconium in the Nuclear Industry: Sixth International Symposium, Proc. ASTM STP 824, Vancouver, 1982 (FRANKLIN, D.G., ADAMSON, R.B., Eds), ASTM International, West Conshohocken, PA (1984) 709–733.

[9.273] BURTON, B., et al., The Interaction of Oxidation and Creep in Zircaloy-2, CEGB Report No. RD/B/N4280, Central Electricity Generating Board, Solihull, UK (1978).

[9.274] SILLS, H.E., SAGAT, S., TOSS: A Model for the High-temperature Deformation and Rupture of Zircaloy in a Steam Environment, Report No. AECL-6880, Atomic Energy of Canada Limited, Chalk River, ON (1982).

[9.275] KARB, E.H., In-pile tests at Karlsruhe of LWR fuel-rod behaviour during the heatup phase of a LOCA, Nucl. Saf. **21** (1980) 26–37.

[9.276] KARB, E.H., PRÜSSMANN, M., SEPOLD, L., HOFMANN, P., SCHANZ, G., LWR Fuel Rod Behavior in the FR2 In-pile Tests Simulating the Heatup Phase of a LOCA, Report No. KfK 3346, Kernforschungszentrum Karlsruhe, Karlsruhe, Germany (1983).

[9.277] BROUGHTON, J.M., MASON, R.E., McCARDELL, R.K., MacDONALD, P.E., PBF LOCA Test Series, Test LOC-3 and LOC-5 Fuel Behavior Report, Report No. NUREG/CR-2073, NRC, Washington, DC (1981).

[9.278] BROUGHTON, J.M., VINJAMURI, K., HAGRMAN, D.L., GOLDEN, D.W., MacDONALD, P.E., PBF LOCA Test LOC-6 Fuel Behavior Report, Report No. NUREG/CR-3184, NRC, Washington, DC (1983).

[9.279] JONES, P.M., et al., "EOLO-JR: A single rod burst test programme in the Essor reactor", ANS/ENS Topical Mtg on Reactor Safety Aspects of Fuel Behaviour, Sun Valley, 1981, American Nuclear Society, La Grange Park, IL (1981).

[9.280] JONES, P.M., MARKOVINA, A., RANDLES, J., SIMONI, O., ZEYEN, R., "EOLO-JR: A single rod burst test programme in the Essor reactor", ANS/ENS Topical Mtg on Reactor Safety Aspects of Fuel Behavior, Sun Valley, 1981, Vol. 1, American Nuclear Society, La Grange Park, IL (1981) 2-328–2-341.

[9.281] BRUET, M., JANVIER, J.C., "FLASH experiments in Siloe reactor: Fuel rod behaviour during LOCA tests", Proc. OECD-NEA-CSNI/IAEA Specialists' Mtg on Water Reactor Fuel Safety and Fission Product Release in Off-normal and Accident Conditions, Risø, Denmark, 1983, IWGFPT-16, IAEA, Vienna (1983).

[9.282] BRUET, M., LEMAIGNAN, C., HARBOTTLE, J., MONTAGNON, F., LHIAUBET, G., "High burnup fuel behaviour during a LOCA type accident: The FLASH 5 experiment", Proc. Tech. Mtg on Behaviour of Core Materials and Fission Product Release in Accident Conditions in LWRs, Aix-en-Provence, 1992, IAEA-TECDOC-706, IAEA, Vienna (1993) 59–67.

[9.283] KOLSTAD, E., WIESENACK, W., OBERLÄNDER, B., TVERBERG, T., "High burn-up fuel behaviour under LOCA conditions as observed in Halden reactor experiments", Fuel Behaviour and Modelling under Severe Transient and Loss of Coolant Accident Conditions, IAEA-TECDOC-CD-1709, IAEA, Vienna (2013), CD-ROM, 195–206.

[9.284] KOLSTAD, E., WIESENACK, W., OBERLÄNDER, B., "A comparison of fuel fragmentation and relocation behaviour in Halden reactor LOCA experiments", paper presented at Fuel Safety Research Mtg, Tokai, Japan, 2009.

[9.285] RAYNAUD, P.A.C., Fuel Fragmentation, Relocation, and Dispersal During the Loss-of-Coolant Accident, Report No. NUREG-2121, NRC, Washington, DC (2012).

[9.286] CHAPMAN, R.H., CROWLEY, J.L., LONGEST, A.W., "Effect of bundle size on cladding deformation in LOCA simulation tests", Zirconium in the Nuclear Industry: Sixth International Symposium, Proc. ASTM STP 824, Vancouver, 1982 (FRANKLIN, D.G., ADAMSON, R.B., Eds), ASTM International, West Conshohocken, PA (1984) 693–705.

[9.287] WIEHR, K., ERBACHER, F.J., NEITZEL, H.J., "Influence of a cold control rod guide thimble on the ballooning behaviour of Zircaloy cladding in a LOCA", Proc. CSNI Specialist Mtg on Safety Aspects of Fuel Behaviour in Off-normal and Accident Conditions, Espoo, 1980, OECD, Paris (1981) 141–154.

[9.288] KAWASAKI, S., HASHIMOTO, M., OTOMO, T., FURUTA, T., UETSUKA, H., Effect of burst temperature on coolant channel restriction in multirods burst tests, J. Nucl. Sci. Technol. **20** (1983) 246–253.

[9.289] KAWASAKI, S., et al., "Effect of non-heated rods on the ballooning behavior in a fuel assembly under loss-of-coolant condition", ANS/ENS Topical Mtg on Reactor Safety Aspects of Fuel Behavior, Sun Valley, 1981, Vol. 1, American Nuclear Society, La Grange Park, IL (1981) 2-114–2-125. {J. Nucl. Sci. Technol. **20** (1983) 246–253}

[9.290] KAWASAKI, S., UETSUKA, H., FURUTA, T., "Multirods burst tests under loss-of-coolant conditions", Proc. OECD-NEA-CSNI/IAEA Specialists' Mtg on Water Reactor Fuel Safety and Fission Product Release in Off-Normal and Accident Conditions, Risǿ, Denmark, 1983, IWGFPT-16, IAEA, Vienna (1983) 17–28.

[9.291] GRANDJEAN, C., Coolability of blocked regions in a rod bundle after ballooning under LOCA conditions: Main findings from a review of past experimental programmes, Nucl. Eng. Des. **237** (2007) 1872–1886.

[9.292] HOCHREITER, L.E., FLECHT SEASET Program. Final report, Report No. NUREG/CR-4167, NRC, Washington, DC (1985).

[9.293] LEE, N., et al., PWR FLECHT SEASET Unblocked Bundle, Forced and Gravity Reflood Task, Data Evaluation and Analysis Report, Report No. NUREG/CR-2256, NRC, Washington, DC (1982).

[9.294] PEARSON, K.G., COOPER, C.A., JOWITT, D., KINNEIR, J.H., Reflooding Experiments on a 49-Rod Cluster Containing a Long 90% Blockage, Report No. AEEW-R 1591, UK Atomic Energy Authority, Abingdon, UK (1983).

[9.295] COOPER, C.A., PEARSON, K.G., JOWITT, D., The THETIS 80% Blocked Cluster Experiment, Part 3: Forced Reflood Experiments, Report No. AEEW-R 1765, UK Atomic Energy Authority, Abingdon, UK (1984).

[9.296] IHLE, P., RUST, K., PWR reflood experiments using full length bundles of rods with Zircaloy claddings and alumina pellets, Nucl. Eng. Des. **99** (1987) 223–237.

[9.297] HAARMAN, J.W., "Thermal conductivity measurements of He, Ne, Ar, Kr, N_2 and CO_2 with a transient hot wire method", AIP Conf. Proc. **11** (1973) 193–198.

[9.298] IHLE, P., RUST, K., FEBA — Flooding Experiments with Blocked Arrays, Report No. KfK 3657, Kernforschungszentrum Karlsruhe, Karlsruhe, Germany (1984).

[9.299] RUSSCHER, G.E., et al., LOCA Simulation in the NRU Reactor: Materials Test-1, Report No. NUREG/CR-2152, Vol.1, NRC, Washington, DC (1981).

[9.300] BARNER, J.O., et al., Materials Test-2: LOCA Simulation in the NRU Reactor, Report No. NUREG/CR-2509, NRC, Washington, DC (1982).

[9.301] MOHR, C.L., et al., LOCA Simulation in the National Research Universal Reactor Program: Data Report for the 3rd Materials Experiment (MT-3), Report No. NUREG/CR-2528, NRC, Washington, DC (1983).

[9.302] WILSON, C.L., et al., LOCA Simulation in the NRU Program: Data Report for the Fourth Materials Experiment (MT-4), Report No. NUREG/CR-3272, NRC, Washington, DC (1983).

[9.303] FRESHLEY, M.D., HESSON, G.M., "Summary results of the LOCA simulation program conducted in NRU", Proc. 11th Water Reactor Safety Research Information Mtg, Gaithersburg, MD, 1983, NRC, Washington, DC (1983).

[9.304] DUCO, J., RÉOCREUX, M., TATTEGRAIN, A., "PHEBUS program main results and status for severe fuel damage studies", Proc. 4th European Nuclear Conf., Geneva, 1986, Commissariat à L'Énergie Atomique Report No. CEA-CONF-8659, CEA Centre d'Etudes Nucleaires, Fontenay-aux-Roses, France (1986).

[9.305] RÉOCREUX, M., SCOTT de MARTINVILLE, E.F., A study of fuel behaviour in PWR design basis accident: an analysis of results from the PHEBUS and EDGAR experiments, Nucl. Eng. Des. **124** (1990) 363–378.

[9.306] FEHRENBACH, P.J., WALSWORTH, J.A., SPENCER, R.C., CHASE, W.R., DELANEY, R.D., "In-reactor LOCA tests of Zircaloy-sheathed UO_2 fuel at Chalk River", Proc. 6th Conf. Canadian Nuclear Society, Ottawa, 1985, Atomic Energy of Canada Limited, Chalk River, ON (1985).

[9.307] KOHN, E., FEHRENBACH, P.J., LAU, J.H.K., ARCHINOFF, G.H., HARDY, D.G., "A LOCA blowdown test of CANDU fuel elements", Proc. 6th Conf. Canadian Nuclear Society, Ottawa, 1985, Atomic Energy of Canada, Chalk River, ON (1985).

[9.308] SILLS, H.E., ELOCA: Fuel Element Behaviour During High-temperature Transients, Report No. AECL-6357, Atomic Energy of Canada Limited, Chalk River, ON (1979).

[9.309] WILLIAMS, A.F., "The ELOCA fuel modelling code: Past, present and future", Proc. 9th Int. Conf. on CANDU fuel, 'Fuelling a Clean Future', Belleville, ON, 2005, Canadian Nuclear Society, Toronto, ON (2005) Paper B4007.

[9.310] KOHN, E., SAGAT, S., "Beryllium assisted cracking in Zircaloy", 6th Canadian Fracture Conference, Harrison Hot Springs, 1982, Canadian Nuclear Society, Toronto, ON (1982).

[9.311] SHEWFELT, R.S.W., LYALL, L.W., GODIN, D.P., A high-temperature creep model for Zr-2.5 wt% Nb pressure tubes, J. Nucl. Mater. **125** (1984) 228–235.

[9.312] SHEWFELT, R.S.W., GODIN, D.P., LYALL, L.W., Verification Tests of a High-temperature Transverse Creep Model for Zr-2.5 wt% Nb Pressure Tube, Report No. AECL-7813, Atomic Energy of Canada Limited, Chalk River, ON (1984).

[9.313] SHEWFELT, R.S.W., GODIN, D.P., Verification Tests for GRAD, a Computer Program to Predict the Non-uniform Deformation and Failure of Zr-2.5 wt% Nb Pressure Tubes during a Postulated Loss-of-Coolant Accident", Report No. AECL-8384, Atomic Energy of Canada Limited, Chalk River, ON (1985).

[9.314] GILLESPIE, G.E., MOYER, R.G., THOMPSON, P.D., "Moderator boiling on the external surface of a calandria tube in a CANDU reactor during a loss-of-coolant accident", Proc. Int. Mtg on Thermal Reactor Safety, Chicago,1982, Report No. NUREG/CP-0027, Vol. 3, NRC, Washington, DC (1983).

[9.315] TAMM, H., et al., Overview of the Technical Basis for the Safety of CANDU Reactors, Atomic Energy of Canada Limited Report No. AECL-9559, Atomic Energy of Canada Limited, Chalk River, ON (1988).

[9.316] COLEMAN, C.E., FONG, R.W.L., DOUBT, G.L., NITHEANANDAN, T., SANDERSON, D.B., Improving the Calandria Tubes for CANDU Reactors, Report No. AECL-11815, Atomic Energy of Canada Limited, Chalk River, ON (1997).

[9.317] NITHEANANDAN, T., TIEDE, R.W., SANDERSON, D.B., FONG, R.W.L., COLEMAN, C.E., "Enhancing the moderator effectiveness as a heat sink during loss-of-coolant accidents in CANDU-PHW reactors using glass-peened surfaces", Experimental Tests and Qualification of Analytical Methods to Address Thermohydraulic Phenomena in Advanced Water Cooled Reactors, IAEA-TECDOC-1149, IAEA, Vienna (2000) 121–138.

[9.318] FONG, R.W.L., McRAE, G.A., COLEMAN, C.E., NITHEANANDAN, T., SANDERSON, D.B., Correlation between the critical heat flux and the fractal surface roughness of zirconium alloy tubes, J. Enhanc. Heat Transf. **8** (2001) 137–146.

[9.319] SANDERSON, D.B., MOYER, R.G., LITKE, D.G., ROSINGER, H.E., GIRGIS, S., Reduction of Pressure-tube to Calandria-tube Contact Conductance to Enhance the Passive Safety of a CANDU-PHW Reactor, Report No. AECL-10892, Atomic Energy of Canada Limited, Chalk River, ON (1993).

[9.320] COLEMAN, C.E., "Simulating the behaviour of zirconium-alloy components in nuclear reactors", Zirconium in the Nuclear Industry: Thirteenth International Symposium, Proc. ASTM STP 1423, Annecy, 2001 (MOAN, G.D., RUDLING, P., Eds), ASTM International, West Conshohocken, PA (2002) 3–19.

[9.321] MURPHY, E.V., HAVELOCK, F., Emissivity of zirconium alloys in air in the temperature range 100–400°C, J. Nucl. Mater. **60** (1976) 167–176.

[9.322] POWERS, D.A., MEYER, R.O., Cladding Swelling and Rupture Models for LOCA Analysis, Report No. NUREG-0630, NRC, Washington, DC (1980).

[9.323] GEELHOOD, K.J., LUSCHER, W.G., BEYER, C.E., FRAPTRAN 1.4: Integral Assessment, Report No. NUREG/CR-7023, Vol. 2, NRC, Washington, DC (2011).

[9.324] CHUNG, H.M., KASSNER, T.F., Pseudobinary Zircaloy-oxygen phase diagram, J. Nucl. Mater. **84** (1979) 327–339.

[9.325] RUDLING, P., STRASSER, A., "Cladding performance under accident conditions", Fuel Design Review Handbook, ANT International, Tollered, Sweden (2010) 11-1–11-20.

[9.326] SAWATZKY, A., LEDOUX, G.A., JONES, S., "Oxidation of zirconium during a high-temperature transient", Zirconium in the Nuclear Industry: Third International Symposium, Proc. ASTM STP 633, Quebec City, 1976 (LOWE, A.L., Jr., PARRY, G.W., Eds), ASTM International, West Conshohocken, PA (1977) 134–149.

[9.327] TRECO, R.M., Some properties of high purity zirconium and dilute alloys with oxygen, Trans. ASM **45** (1953) 872–892.

[9.328] SAWATZKY, A., "A proposed criterion for the oxygen embrittlement of Zircaloy-4 fuel cladding", Zirconium in the Nuclear Industry: Fourth International Symposium, Proc. ASTM STP 681, Stratford-upon-Avon, 1978 (SCHEMEL, J.H., PAPAZOGLOU, T.P., Eds), ASTM International, West Conshohocken, PA (1979) 479–496.

[9.329] CHUNG, H.M., GARDE, A.M., KASSNER, T.F., "Development of an oxygen embrittlement criterion for zircaloy cladding applicable to loss-of-coolant accident conditions in light-water reactors", Zirconium in the Nuclear Industry: Fourth International Symposium, Proc. ASTM STP 681, Stratford-upon-Avon, 1978 (SCHEMEL, J.H., PAPAZOGLOU, T.P., Eds), ASTM International, West Conshohocken, PA (1979) 600–627.

[9.330] KADEN, W., DEBRAY, W., "Oxygen embrittlement of zirconium-copper alloys at high temperatures", Applications-Related Phenomena in Zirconium and Its Alloys, ASTM STP 458 (BAROCH, E.F., Ed.), ASTM International, West Conshohocken, PA (1969) 179–193.

[9.331] LEHR, P., DEBUIGNE, J., "Fragilisation du zirconium par l'oxygène interstitial", 6^{e} Colloque de Métallurgie, Relations Entre Défauts a l'Échelle Atomique et Propriétés Macroscopiques, Gilf-sur-Yvette, France (1962) 139–150.

[9.332] STERN, A., et al., Investigations of the microstructure and mechanical properties of prior-β structure as a function of the oxygen content in two zirconium alloys, J. ASTM Int. **5** (2008) Paper JAI101119.

[9.333] BRACHET, J.-C., et al., Hydrogen content, preoxidation, and cooling scenario effects on post-quench microstructure and mechanical properties of Zircaloy-4 and M5® alloys in LOCA conditions, J. ASTM Int. 5 (2008) Paper JAI101116.

[9.334] COLEMAN, C.E., Acoustic Emission from Zirconium Alloys During Mechanical and Fracture Testing, Atomic Energy of Canada Limited Report No. AECL-9111, Atomic Energy of Canada Limited, Chalk River, ON (1986).

[9.335] HOBSON, D.O., RITTENHOUSE, P.L., Embrittlement of Zircaloy-clad Fuel Rods by Steam During LOCA Transients, Report No. ORNL 4758, Oak Ridge National Lab., Oak Ridge, TN (1972).

[9.336] HOBSON, D.O., "Ductile-brittle behavior of Zircaloy fuel cladding", Proc. ANS Topical Mtg on Water-Reactor Safety, Salt Lake City, 1973, Oak Ridge National Lab., Oak Ridge, TN (1973).

[9.337] SCATENA, G.J., Fuel Cladding Embrittlement During a Loss of Coolant Accident, Report No. NEDO-10674, General Electric Company, Boston, MA (1972).

[9.338] NAGASE, F., HÓZER, Z., VOGLEWEDE, J., LOCA Criteria Basis and Test Methodology, CSNI Technical Opinion Papers No. 13, OECD/NEA Report No. 6986, OECD Publishing, Paris (2011).

[9.339] BILLONE, M., YAN, Y., BURTSEVA, T., DAUM, R., Cladding Embrittlement During Postulated Loss-of-coolant Accidents, Report No. NUREG/CR-6967, NRC, Washington, DC (2008).

[9.340] HACHE, G., CHUNG, H.M., The History of LOCA Embrittlement Criteria, Proc. 28th Water Reactor Safety Information Mtg, Bethesda, 2000, Report No. NUREG/CP-0172, NRC, Washington, DC (2000).

[9.341] CHUNG, H.M., Fuel behaviour under loss-of-coolant accident situations, Nucl. Eng. Technol. **37** (2005) 327–362.

[9.342] BAKER, L., JUST, L.C., Studies of Metal-Water Reactions at High Temperatures. III Experimental and Theoretical Studies of the Zirconium-Water Reaction, Report No. ANL-6548, Argonne National Laboratory, Lemont, IL (1962).

[9.343] PAWEL, R.E., Oxygen diffusion in beta Zircaloy during steam oxidation, J. Nucl. Mater. **50** (1974) 247–258.

[9.344] HESSON, J.C., IVINS, R.O., WILSON, R.E., NISHIO, K., BARNES, C., Jr., Laboratory Simulations of Cladding-Steam Reactions Following Loss-of-coolant Accidents in Water-cooled Power Reactors, Report No. ANL-7609, Argonne National Laboratory, Lemont, IL (1970).

[9.345] MASSIH, A.R., Review of Experimental Data for Modelling LWR Fuel Cladding Behaviour under Loss of Coolant Accident Conditions, SKI Report No. 2007:14, Swedish Nuclear Power Inspectorate, Stockholm (2007).

[9.346] BALLINGER, R.G., DOBSON, W.G., BIEDERMAN, R.R., Oxidation reaction kinetics of Zircaloy-4 in an unlimited steam environment, J. Nucl. Mater. **62** (1976) 213–220.

[9.347] CATHCART, J.V., et al., Zirconium Metal-water Oxidation Kinetics, IV Reaction Rate Studies, Report No. ORNL/NUREG-17, Oak Ridge National Lab., Oak Ridge, TN (1977).

[9.348] PAWEL, R.E., CATHCART, J.V., McKEE, R.A., The kinetics of oxidation of Zircaloy-4 in steam at high temperatures, J. Electrochem. Soc. **126** (1979) 1105–1111.

[9.349] KAWASAKI, S., FURUTA, T., SUZUKI, M., Oxidation of Zircaloy-4 under high temperature steam atmosphere and its effect on ductility of cladding, J. Nucl. Sci. Technol. **15** (1978) 589–596.

[9.350] URBANIC, V.F., "Oxidation of zirconium alloys in steam at 1000 to 1850°C", Zirconium in the Nuclear Industry: Third International Symposium, Proc. ASTM STP 633, Quebec City, 1976 (LOWE, A.L., Jr., PARRY, G.W., Eds), ASTM International, West Conshohocken, PA (1977) 168–181.

[9.351] URBANIC, V.F., HEIDRICK, T.R., High-temperature oxidation of Zircaloy-2 and Zircaloy-4 in steam, J. Nucl. Mater. **75** (1978) 251–261.

[9.352] BROWN, A.F., HEALEY, T., The kinetics of total oxygen uptake in steam-oxidised Zircaloy-2 in the range 1273–1673 K. J. Nucl. Mater. **88** (1980) 1–6.

[9.353] YAN, Y., BRAY, T.S., TSAI, H.C., BILLONE, M.C., "High temperature steam oxidation of Zircaloy cladding from high burnup fuel rods", Proc. 28th Water Reactor Safety Information Mtg, Bethesda, 2000, NRC, Washington, DC (2001).

[9.354] LE BOURHIS, A., "Justification of the M5 behavior in LOCA", Proc. Topical Mtg on LOCA Fuel Safety Criteria, Aix-en-Provence, France, 2001, OECD Publishing, Paris (2001) 105–133.

[9.355] LEECH, W.J., "Ductility testing of Zircaloy-4 and Zirlo cladding after high temperature oxidation in steam", Proc. Topical Mtg on LOCA Fuel Safety Criteria, Aix-en-Provence, 2001, OECD Publishing, Paris (2001) 135–143.

[9.356] YAN, Y., STRAIN, R.V., BRAY, T.S., BILLONE, M.C., High Temperature Oxidation of Irradiated Limerick BWR Cladding, Argonne National Lab. Report No. ANL/ET/CP-107073, Argonne National Laboratory, Argonne, IL (2002).

[9.357] NAGASE, F., OTOMO, T., UETSUKA, H., Oxidation kinetics of low-Sn Zircaloy-4 at the temperature range from 773 to 1573 K, J. Nucl. Sci. Technol. **40** (2003) 213–219.

[9.358] SCHANZ, G., ADROGUER, B., VOLCHEK, A., Advanced treatment of Zircaloy cladding high-temperature oxidation in severe accident code calculations, Part 1: Experimental database and basic modeling, Nucl. Eng. Des. **232** (2004) 75–84.

[9.359] VOLCHEK, A., ZVONAREV, Y., SCHANZ, G., Advanced treatment of Zircaloy cladding high-temperature oxidation in severe accident code Calculations, Part 2: Best-fitted parabolic correlations, Nucl. Eng. Des. **232** (2004) 85–96.

[9.360] GRANDJEAN, C., CAUVIN, R., JACQUES, P., "Oxidation and quenching experiments with high burnup cladding under LOCA conditions: Revision of previous data and main trends of recent tests", Proc. 26th Water Reactor Safety Information Mtg, Bethesda, 1998, Vol. 3, NRC, Washington, DC (1998) 191–200.

[9.361] GRANDJEAN, C., CAUVIN, R., LEBUFFE, C., WAECKEL, N., "French investigations of high burnup effect on LOCA thermomechanical behavior, Part 2: Oxidation and quenching experiments under simulated LOCA conditions with high burnup clad material", Proc. 24th Water Reactor Safety Information Mtg, Bethesda, 1996, Vol. 1, NRC, Washington, DC (1997) 161–172.

[9.362] UETSUKA, H., FURUTA, T., KAWASAKI, S., Failure-bearing capability of oxidized Zircaloy-4 cladding under simulated loss-of-coolant conditions, J. Nucl. Sci. Technol. **20** (1983) 941–950.

[9.363] NAGASE, F., UETSUKA, H., Study of High Burnup Fuel Behaviour Under LOCA Conditions at JAERI: Hydrogen effects on the Failure-bearing Capability of Cladding Tubes, NUREG/CR-0176, NRC, Washington, DC (2001) 335–342.

[9.364] NAGASE, F., FUKETA, T., Effect of pre-hydriding on thermal shock resistance of Zircaloy-4 cladding under simulated loss-of-coolant accident conditions, J. Nucl. Sci. Technol. **41** (2004) 723–730.

[9.365] NAGASE, F., FUKETA, T., Behavior of pre-hydrided Zircaloy-4 cladding under simulated LOCA conditions, J. Nucl. Sci. Technol. **42** (2005) 209–218.

[9.366] NAGASE, F., FUKETA, T., Fracture behaviour of irradiated Zircaloy-4 cladding under simulated LOCA conditions, J. Nucl. Sci. Technol. **43** (2006) 1114–1119.

[9.367] WHITE, A.J., SAWATZKY, A., JONES, S., LEDOUX, G.A., "A failure criterion for CANDU fuel cladding subjected to thermal-quench loads", Proc. Int. Topical Mtg on Safety of Thermal Reactors, Portland, OR, 1991, American Nuclear Society, La Grange Park, IL (1991) 555–562.

[9.368] UETSUKA, H., FURUTA, T., KAWASAKI, S., Embrittlement of Zircaloy-4 due to oxidation in environment of stagnant steam, J. Nucl. Sci. Technol. **19** (1982) 158–165.

[9.369] UETSUKA, H., FURUTA, T., KAWASAKI, S., Zircaloy-4 cladding embrittlement due to inner surface oxidation under simulated loss-of-coolant conditions, J. Nucl. Sci. Technol. **18** (1981) 705–717.

[9.370] SETOYAMA, D., YAMANAKA, S., Phase diagram of Zr-O-H ternary system, J. Alloys Compd. **370** (2004) 144–148.

[9.371] DURIEZ, C., et al., Characterization of oxygen distribution in LOCA situations, J. ASTM Int. **8** (2011) Paper JAI103156.

[9.372] ROWLAND, T.C., et al., "Power cycling operation tests of Zr-barrier fuel", Proc. Int. Topical Mtg on LWR Fuel Performance: Fuel for the 90's, Avignon, 1991, American Nuclear Society, La Grange Park, IL (1991) 808–817.

[9.373] NUCLEAR REGULATORY COMMISSION, Standard Review Plan, Report No. NUREG-0800, NRC, Washington, DC (1981).

[9.374] O'DONNELL, W.J., LANGER, B.F., Fatigue design basis for Zircaloy components, Nucl. Sci. Eng. **20** (1964) 1–12.

[9.375] COFFIN, L.F., "Low cycle fatigue — a thirty year perspective", Proc. 2nd Int. Conf. on Fatigue and Fatigue Thresholds, Birmingham, 1984 (BEEVERS, C.J., Ed.), Engineering Materials Advisory Services, Warley, UK (1984) 1213–1234.

[9.376] A.N.T. International, http://www.antinternational.com/index.php?id=zirat_full_information

[9.377] GOODMAN, J., Mechanics Applied to Engineering, Longmans, Green and Co., London (1899).

[9.378] HAIGH, B.P., Experiments on the fatigue of brasses, J. Inst. Met. **18** (1917) 55–86.

[9.379] GERBER, W., Bestimmung der zulässigen Spannungen in Eisen-Constructionen, Z. Bayer. Archit. Ing. Ver. 18746 (1874) 101–110.

[9.380] SODERBERG, C.R., Factor of safety and working stress, Trans. Am. Soc. Mech. Eng. **52** (1939) 13–28.

[9.381] SENDECKYJ, G.P., "History of constant life diagrams", High Cycle Fatigue of Structural Materials (SOBOYEJO, W.O., SRIVATSAN, T.S., Eds), TMS, Warrendale, PA (1998), 95–107.

[9.382] DOWLING N.E., Mechanical Behaviour of Materials, 2nd edn, Prentice Hall, Upper Saddle River, NJ (1999).

[9.383] DIETER G.E., Mechanical Metallurgy, McGraw-Hill, New York (1961).

[9.384] RANSOM, J.T., "General discussion", Symp. on Statistical Apects of Fatigue", ASTM STP 121, ASTM International, West Conshohocken, PA (1952) 59–64.

[9.385] GROVER, H.J., Fatigue of Aircraft Structures, NAVAIR 01-1A-13, US Govt Printing Office, Washington, DC (1966).

[9.386] SINCLAIR, G.M., DOLAN, T.J., Effects of stress amplitude on statistical variability in fatigue life of 75S-T6 aluminium alloy, Trans. ASME **75** (1953) 867–872.

[9.387] RICHARDS, C.W., Engineering Materials Science, Wadsworth, Belmont, CA (1961).

[9.388] HARTMANN, E.C., HOWELL, F.M., "Laboratory fatigue testing of materials", Metal Fatigue (SINES, G., WAISMAN, J.L., Eds), McGraw-Hill, New York (1959) 89–111.

[9.389] NAKATSUKA, M., KUBO, T., HAYASHI, Y., "Fatigue behavior of neutron iradiated Zircaloy-2 fuel cladding tubes", Zirconium in the Nuclear Industry: Ninth International Symposium, Proc. ASTM STP 1132, Kobe, 1990 (EUCKEN, C.M., GARDE, A.M., Eds), ASTM International, West Conshohocken, PA (1991) 230–245.

[9.390] WISNER, S.B., REYNOLDS, M.B., ADAMSON R.B., "Fatigue behavior of irradiated and unirradiated zircaloy and zirconium", Zirconium in the Nuclear Industry: Tenth International Symposium, Proc. ASTM STP 1245, Baltimore, 1993 (GARDE, A.M., BRADLEY, E.R., Eds), ASTM International, West Conshohocken, PA (1994) 499–520.

[9.391] ARMAS, A.F., ALVAREZ-ARMAS, I., "Cyclic behavior of Zircaloy-4 at elevated temperatures", Zirconium in the Nuclear Industry: Seventh International Symposium, Proc. ASTM STP 939, Strasbourg, 1985 (ADAMSON, R.B., VAN SWAM, L.F.P., Eds), ASTM International, West Conshohocken, PA (1987) 617–630.

[9.392] KUBO, T., MOTOMIYA, T., WAKASHIMA Y., Low-cycle corrosion fatigue of Zircaloy-2 in iodine atmospheres, J. Nucl. Mater. **140** (1986) 185–196.

[9.393] AMZALLAG, C., "Environmentally assisted fatigue of stainless steels in PWR environment", paper presented at ANT Int. LCC6 Seminar, Clearwater Beach, FL, Dubrovnik (2011).

[9.394] MADEYSKI, A., ALBERTIN, L., "Fractographic method of evaluation of the cyclic stress amplitude in fatigue failure analysis", Fractography in Failure Analysis, ASTM STP 645 (STRAUSS, B.M., CULLEN, W.H., Jr., Eds), ASTM International, West Conshohocken, PA (1978) 73–83.

[9.395] ADAMSON, R.B., "Effects of neutron irradiation on microstructure and properties of zircaloy", Zirconium in the Nuclear Industry: Twelfth International Symposium, Proc. ASTM STP 1354, Toronto, 1998 (SABOL, G.P., MOAN, G.D., Eds), ASTM International, West Conshohocken, PA (2000) 15–31.

[9.396] JAMES, L.A., Crack propagation behavior of Zircaloy-2, Nucl. Appl. **6** (1969) 307–312.

[9.397] LEE, D., The role of plastic anisotropy in the fatigue behavior of Zircaloy, Met. Trans. B **3** (1972) 315–322.

[9.398] WALKER, T.J., KASS, J.N., "Variation of Zircaloy fracture toughness with irradiation", Zirconium in Nuclear Applications: Second International Symposium, Proc. ASTM STP 551, Portland, 1973, (SCHEMEL, J.H., ROSENBAUM, H.S., Eds), ASTM International, West Conshohocken, PA (1974) 328–354.

[9.399] LEE, D., HILL, P.T., Effect of oxygen on the fatigue behaviour of Zircaloy, J. Nucl. Mater. **60** (1976) 227–230.

[9.400] SNOWDEN, K.U., STATHERS, P.A., The fatigue behaviour of α-zirconium and Zircaloy-2 in the temperature range 20 to 700°C, J. Nucl. Mater. **67** (1977) 215–228.

[9.401] PICKLES, B.W., PICKER, C., "The effects of environment and neutron irradiation on the fatigue crack growth behaviour of Zircaloy-2", Proc. of 6th Int. Conf. on Structural Mechanics in Reactor Technology, SMiRT 6, Paris, 1981, North Holland, Amsterdam (1981) C, Paper F6/4.

[9.402] BRUN, G., et al., "Cumulative fatigue and creep-fatigue damage at 350°C on recrystallised Zircaloy-4," Zirconium in the Nuclear Industry: Seventh International Symposium, Proc. ASTM STP 939, Strasbourg, France, 1985 (ADAMSON, R.B., VAN SWAM, L.F.P., Eds), ASTM International, West Conshohocken, PA (1987) 597–616.

[9.403] ISHIMOTO, S., KUBO, T., KUBOTA, O., "Development of new zirconium alloys for higher burnup fuel", paper presented at Int. Topical Mtg on LWR Fuel Performance, TopFuel 2003, Würzburg, Germany (2003).

[9.404] CHOW C.K., et. al., "Properties of an irradiated heat-treated Zr-2.5Nb pressure tube removed from the NPD reactor", Zirconium in the Nuclear Industry: Eleventh International Symposium, Proc., ASTM STP 1295, Garmisch-Partenkirchen, 1995 (BRADLEY, E.R., SABOL, G.P, Eds), ASTM International, West Conshohocken, PA (1996) 469–491.

[9.405] SONIAK, A., LANSIART, S., ROYER, J., MARDON, J.P., WAECKEL, N., "Irradiation effect on fatigue behavior of Zircaloy-4 cladding tubes", Zirconium in the Nuclear Industry: Tenth International Symposium, Proc. ASTM STP 1245, Baltimore, 1993 (GARDE, A.M., BRADLEY, E.R., Eds), ASTM International, West Conshohocken, PA (1994) 549–558.

[9.406] KIM, J.H., LEE, M.H., CHOI, B.K., JEONG, Y.H., Deformation behavior of Zircaloy-4 cladding under cyclic pressure, J. Nucl. Sci. Technol. **44** (2007) 1275–1280.

[9.407] PETTERSSON, K., Low-cycle fatigue properties of Zircaloy-2 cladding, J. Nucl. Mater. **56** (1975) 91–102.

[9.408] LIN, X., HAICHENG, G., Low cycle fatigue properties and microscopic deformation structure of Zircaloy-4 in recrystallized and stress-relieved conditions, J. Nucl. Mater. **265** (1999) 213–217.

[9.409] PANDARINATHAN, P.R., VASUDEVAN, P., Low-cycle fatigue studies on nuclear reactor Zircaloy-2 fuel tubes at room temperature, 300 and 350°C, J. Nucl. Mater. **91** (1980) 47–58.

[9.410] NAKATSUKA, M., HAYASHI, Y., Effect of iodine on fatigue properties of Zircaloy-2 fuel cladding under cyclic tensile stress, J. Nucl. Sci. Technol. **18** (1981) 785–792.

[9.411] HOSBONS, R.R., "Low-cycle fatigue behavior of Zircaloy at 573 K", Fatigue at Elevated Temperatures, ASTM STP 520 (CARDEN, A.E., McEVILY, A.J., WELLS, C.H., Eds), ASTM International, West Conshohocken, PA (1973) 482–490.

[9.412] STAAL, H.U., Results from a Literature Review of Fatigue and Fracture Toughness Properties of Zircaloy, Report No. HWR-189, Institutt for Energieteknikk (IFE), OECD Halden Reactor Project, Halden, Norway (1987).

[9.413] SCHUSTER, I., LEMAIGNAN, C., "Link between stress corrosion and corrosion-fatigue behavior of zircaloy in an iodine environment", Zirconium in the Nuclear Industry: Eighth International Symposium, Proc. ASTM STP 1023, San Diego, 1988 (VAN SWAM, L.F.P., EUCKEN, C.M., Eds), ASTM International, West Conshohocken, PA (1989) 535–547.

[9.414] WANHILL, R.J.H., RYDER, D.A., DAVIES, T.J., Metallographic studies of fatigue in 20% cold-worked Zircaloy-2 containing zirconium hydride, J. Nucl. Mater. **43** (1972) 75–85.

[9.415] TAN, J., YING, S., LI, C., SUN, C., Effect of zirconium hydrides on cyclic deformation behavior of Zr-Sn-Nb alloy, Scr. Mater. **55** (2006) 513–516.

[9.416] PRAT, F., BESSON, J., GRANGE, M., ANDRIEU, E., Behavior and rupture of hydrided ZIRCALOY-4 tubes and sheets, Metall. Mater. Trans. A **29** (1998).

[9.417] MacEWEN, S.R., ELLS, C.E., WOO, O.T., The Bauschinger effect in Zircaloy-2, J. Nucl. Mater. **101** (1981) 336–349.

[9.418] CHRISTODOULOU, N., Evolution of the Bauschinger effect in tension and compression in Zircaloy-2, Acta Metall. **37** (1989) 529–539.

[9.419] LI, C., et al., Cyclic stress–strain response of textured Zircaloy-4, J. Nucl. Mater. **321** (2003) 60–69.

[9.420] KUHLMANN-WILSDORF, D., LAIRD, C., Dislocation behavior in fatigue, II. Friction stress and back stress as inferred from an analysis of hysteresis loops, Mater. Sci. Eng. **37** (1979) 111–120.

[9.421] XIAO, L., GU, H., Dislocation structures in zirconium and Zircaloy-4 fatigued at different temperatures, Metall. Mater. Trans. A **28** (1997) 1021–1033.

[9.422] ARMAS, A.F., HEREÑÚ, S., BOLMARO, R., ALVAREZ-ARMAS, I., Cyclic softening mechanisms of Zircaloy-4, J. Nucl. Mater. **326** (2004) 195–200.

[9.423] BOLMARO, R.E., et al., Cyclic softening mechanisms of Zry-4 at room temperature: The unlikely influence of texture variations, Scr. Mater. **51** (2004) 617–621.

[9.424] ALVAREZ-ARMAS, I., HEREÑÚ, S., Influence of dynamic strain aging on the dislocation structure developed in Zircaloy-4 during low-cycle fatigue, J. Nucl. Mater. **334** (2004) 180–188.

[9.425] JAMES, L.A., Environmental-aggravated fatigue cracking of Zircaloy-2, Nucl. Appl. Technol. **9** (1970) 260–267.

[9.426] MOWBRAY, D.F., Effects of 1.0% superimposed mean strain on the bending fatigue strength of Zircaloy-4, J. Nucl. Appl. **1** (1965) 39–48.

[9.427] GEE, C.F., SCOTT, P.M., TRUSWELL, A.E., "Factors affecting fatigue crack growth rates in Zircaloy components", 4th International Symposium, Proc. on Environmental Degradation of Materials in Nuclear Power Systems, Water Reactors, Jekyll Island, 1989, National Association of Corrosion Engineers, Houston, TX (1989) 10.47–10.58.

[9.428] PICKLES, B.W., PICKER, C., "The enhancement of fatigue crack growth rates in zirconium alloys in a reactor environment", Proc. Int. Conf. on Dimensional Stability and Mechanical Behaviour of Irradiated Metals and Alloys, Brighton, 1983, Thomas Telford, London (1983) 179–182.

[9.429] GEE, C.F., "Fatigue properties of Zircaloy-2 in a PWR water environment", First Int. Symp. on Environmental Degradation of Materials in Nuclear Power Systems — Water Reactors, Myrtle Beach, SC, 1983, National Association of Corrosion Engineers, Houston, TX (1984) 687–700.

[9.430] GARLEA, E., et al., Hydride-phase formation and its influence on fatigue crack propagation behavior in a Zircaloy-4 alloy, Metall. Mater. Trans. A **41** (2010) 2816–2828.

[9.431] PRICE, E.G., et al., "Investigation into the failure of fuel bundle end plates in a Darlington reactor", Int. Symp. on Contributions of Materials Investigation to the Resolution of Problems encountered in Pressurized Water Reactors, Société Français d'Energie, Fontevraud, France (1994) 635–642.

[9.432] HO, E.T.C., et al., "Development of fatigue failure criteria for Darlington fuel bundle end-plates", paper presented at 13th Annual CNS Conference, Saint John, Canada, 1992.

[9.433] URBANIC, V.F., MAGUIRE, M.A., RAMASUBRAMANIAN, N., "Dating the fractures in Darlington end plates from oxide thickness measurements", paper presented at 13th Annual CNS Conference, Saint John, Canada, 1992.

[9.434] ANDERSON, H.L., FERMI, E., GROSSE, A.V., Branching ratios in the fission of uranium (235), Phys. Rev. **59** (1941) 52–56.

[9.435] GRUMMITT, W.E., WILKINSON, G., Fission products of U^{235}, Nature **158** (1946) 158–163.

[9.436] AITCHISON, I., COX, B., Interpretation of fractographs of SCC in hexagonal metals, Corrosion **28** (1972) 83–87.

[9.437] GARZAROLLI, F., MANZEL, R., PEEHS, M., STEHLE, H., "Observations and hypotheses on pellet-clad interaction failures", Kerntechnik **20** (1978) 27–31.

[9.438] LYONS, M.F, COPLIN, D.H., JONES, G.G., High Performance UO_2 Fuel Program, Quarterly Progress Reports No. GEAP-3771-10–12, General Electric Company, Boston, MA (1963–64).

[9.439] DUNHAM, J.T., KATO, H., Stress-corrosion Cracking Susceptibility of Zirconium in Ferric Chloride Solutions, Report No. BM-RI-5784, US Bureau of Mines, Washington, DC (1961).

[9.440] PAYNE, B.S., PRIEST, D.K., Intergranular corrosion of commercially pure zirconium, Corrosion **17** (1961) 196t–200t.

[9.441] HARDY, D.G., WOOD, J.C., BAIN, A.S., CANDU Fuel Performance and Development, Report No. AECL-6213, Atomic Energy of Canada Limited, Chalk River, ON (1978).

[9.442] GARLICK, A., A Critical Review of Available Information on Fuel Failures in Douglas Point and Some AECL Loop Experiments, Report No. TRG Memo 5002 (W), UK Atomic Energy Authority, Abingdon, UK (1969).

[9.443] COX, B., Pellet-cladding interaction (PCI) failures of zirconium alloy fuel cladding — A review, J. Nucl. Mater. **172** (1990) 249–292.

[9.444] BLACKBURN, N.J., FEENEY, J.A., BECK, T.R., "Stress-corrosion cracking of titanium alloys", Advances in Corrosion Science and Technology, vol. 3 (FONTANA, M.G., STAEHLE, R.W., Eds), Springer, Boston, MA (1973) 67–292.

[9.445] COX, B., Environmentally induced cracking of zirconium alloys, Corrosion **1** (1972) 367–422.

[9.446] COX, B., Stress corrosion cracking of zirconium alloys, Langmuir **3** (1987) 867–873.

[9.447] COX, B., Environmentally-induced cracking of zirconium alloys — A review, J. Nucl. Mater. **170** (1990) 1–23.

[9.448] SPEIDEL, M.O., HYATT, M.V., "Stress-corrosion cracking of high-strength aluminium alloys", Advances in Corrosion Science and Technology (FONTANA, M.G., STAEHLE, R.W., Eds), Springer, Boston, MA (1973) 115–335.

[9.449] JACQUES, P., LEFEBVRE, F., LEMAIGNAN, C., Deformation-corrosion interactions for Zr alloys during I-SCC crack initiation, Part 2: Localised stress and strain contributions, J. Nucl. Mater. **264** (1999) 249–256.

[9.450] SCHUSTER, I., LEMAIGNAN, C., JOSEPH, J., Testing and modelling the influence of irradiation on iodine-induced stress corrosion cracking of Zircaloy-4, Nucl. Eng. Des. **156** (1995) 343–349.

[9.451] BANKER, J.G., et al., Explosion cladding: An enabling technology for zirconium in the chemical process industry, J. ASTM International **7** (2010) Paper JAI103050.

[9.452] COX, B., "Zirconium alloy corrosion", Uhlig's Corrosion Handbook, 2nd edn (REVIE, W.R., Ed.), Wiley, New York (2000) Ch. 29, 905–914.

[9.453] COX, B., Evaluation of Further Cracks in the Zircaloy-lining of a Chemical Plant Absorber Tower, Report No. CNEUT-90-17, Univ. of Toronto, Toronto, Canada (1990).

[9.454] COX, B., "Stress corrosion cracking of zircaloy in iodine containing environments", Zirconium in Nuclear Applications: Second International Symposium, Proc. ASTM STP 551, Portland, 1973 (SCHEMEL, J.H., ROSENBAUM, H.S., Eds), ASTM International, West Conshohocken, PA (1974) 419–434.

[9.455] COX, B., Environmentally induced cracking of zirconium alloys, Corrosion **28** (1972) 207–217.

[9.456] FARINA, S.B., DUFFO, G.S., GALVELE, J.R., Stress corrosion cracking of zirconium and Zircaloy-4 in aqueous halide solutions, Corros. Sci. **45** (2003) 2497–2512.

[9.457] COX, B., Environmentally-induced Cracking of Zr Alloys. II Liquid Metal Embrittlement, Report No. AECL-3612, Atomic Energy of Canada Limited, Chalk River, ON (1970).

[9.458] COX, B., WONG, Y.-M., Liquid metal embrittlement of Zr-2.5% Nb alloy, J. Nucl. Mater. **245** (1997) 34–43.

[9.459] ROSENBAUM, H.S., The interaction of iodine with Zircaloy-2, J. Electrochem. Technol. **4** (1966) 153–156.

[9.460] GRUBB, W.T., MORGAN, M.H., "A survey of chemical environments for activity in the embrittlement of Zircaloy-2", Zirconium in the Nuclear Industry: Fourth International Symposium, Proc. ASTM STP 681, Stratford-upon-Avon, 1978 (SCHEMEL, J.H., PAPAZOGLOU, T.P., Eds), ASTM International, West Conshohocken, PA (1979) 145–154.

[9.461] COX, B., SURETTE, B.A., WOOD, J.C., "Pellet-clad interaction on failures: Stress corrosion cracking by iodine or metal vapour embrittlement by cesium/cadmium vapours?" Proc. 2nd Int. Conf. on Environmental Degradation of Engineering Materials in Aggressive Environments, Blacksburg, 1981, Virginia Polytechnic Institute and State University, Blacksburg, VA (1981) 293–304.

[9.462] HADDAD, R., COX, B., On the initiation of cracks in Zircaloy tubes by I_2 and Cs/Cd vapours, J. Nucl. Mater. **138** (1986) 81–88.

[9.463] COX, B., SURETTE, B.A., WOOD, J.C., Stress corrosion cracking of Zircaloys in unirradiated and irradiated CsI, J. Nucl. Mater. **138** (1986) 89–98.

[9.464] DAVIES, J.H., ARMIJO, J.S., ROSENBAUM, H.S., Accelerated Pellet-cladding Interaction Tests of Barrier Fuel, Report No. GEAP-25356, General Electric Company, Boston, MA (1981).

[9.465] GARLICK, A., WOLFENDEN, P.D., HINDMARCH, P., Stress Corrosion Cracking of Zircaloy in Iodine Vapour: A Probable Failure Mechanism in Water Reactor Fuel Pins, TRG Report No. 1905 (W), UK Atomic Energy Authority Reactor Development Laboratories, Windscale, UK (1969).

[9.466] PENN, W.J., LO, R.K., WOOD, J.C., CANDU fuel-power ramp performance criteria, Nucl. Technol. **34** (1977) 249–268.

[9.467] HOFFMANN, P.B., DEWES, P., "Post-irradiation examination and ramp testing of fuel rods with Fe-enhanced liner cladding at high burnup", Proc. Int. Topical Mtg on LWR Fuel Performance, Orlando, 2004, American Nuclear Society, La Grange Park, IL (2004) 238–243.

[9.468] HOFMANN, P., SPINO, J., "Can one expect low ductility failure of Zircaloy-4 tubing due to iodine-induced SCC in a LOCA transient?", Proc. Topical Mtg on Reactor Safety Aspects of Fuel Behaviour, Sun Valley, 1981, Vol. 2, American Nuclear Society, La Grange Park, IL (1981) 410–421.

[9.469] SHIMADA, S., MATSUURA, T., NAGAI, M., Stress corrosion cracking of Zircaloy-2 by metal iodides, J. Nucl. Sci. & Technol. **20** (1983) 593–602.

[9.470] PEEHS, M., JUNG, W., STEHLE, H., STEINBERG, E., "Experiments to settle an ISCC hypothesis for Zry tubing", Specialists' Mtg on Pellet–Cladding Interaction in Water Reactors, Denmark, 1980, IAEA, Vienna (1980) 170.

[9.471] WOOD, J.C., Factors affecting stress corrosion cracking of Zircaloy in iodine vapour, J. Nucl. Mater. **45** (1972) 105–122 .

[9.472] INTERNATIONAL ATOMIC ENERGY AGENCY, Iodine Induced Stress Corrosion Cracking of Zircaloy Fuel Cladding Materials, IAEA-TECDOC-1185, IAEA, Vienna (2000).

[9.473] WOOD, J.C., Interactions between stressed zirconium alloys and iodine at 300°C, Nucl. Technol. **23** (1974) 63–79.

[9.474] HOFMANN, P., "Corrosion induced failure of internally pressurized Zircaloy tubes at high temperatures", Proc. Conf. on Interaction Between Corrosion and Mechanical Stress at High Temperatures (GUTTMAN. V., MERZ, M., Eds), Petten, 1980, Applied Science Publishers, London (1980) 135–149.

[9.475] HOFMANN, P., SPINO, J., Determination of the critical iodine concentration for stress corrosion cracking failure of Zircaloy-4 tubing between 500 and 900°C, J. Nucl. Mater. **107** (1982) 297–310.

[9.476] HOFMANN, P., SPINO, J., Chemical aspects of iodine-induced stress corrosion cracking failure of Zircaloy-4 tubing above 50°C, J. Nucl. Mater. **114** (1983) 50–65.

[9.477] MOGARD, H., HOWE, D., GROUNES, M., "The international TRANS-RAMP project — A study of the effects of rapid power ramping on PCI resistance of PWR fuel", Proc. Topical Mtg on LWR Fuel Performance, Williamsburg, 1988, American Nuclear Society, La Grange Park, IL (1988) 232–244.

[9.478] HOPPE, N., "PCMI modelling in COMETHE", paper presented at IAEA Specialists Mtg on Pellet–Cladding Interaction in Water Reactors, Risø, Denmark, 1980.

[9.479] GITTUS, J.H., Theoretical analysis of the strains produced in nuclear fuel cladding tubes by the expansion of cracked cylindrical fuel pellets, Nucl. Eng. Des. **18** (1972) 69–82.

[9.480] CARTER, T.J., Experimental investigation of various pellet geometries to reduces strains in zirconium alloy cladding, Nucl. Technol. **45** (1979) 166–176.

[9.481] YAGNIK, S.K., SUNDERLAND, D.J., CHENG, B.C., "Effects of PWR re-start ramp rate on pellet-cladding interactions", Proc. Sem. on Pellet-Clad Interaction in Water Reactor Fuels, Aix-en-Provence, 2004, NEA/OECD, Paris (2005) 9–11.

[9.482] KEE, F.J., LIPSETT, J.J., CANDU Operating Experience with a Delayed Neutron Failed Fuel Location System, Report No. AECL-3682, Atomic Energy of Canada Limited, Chalk River, ON (1970).

[9.483] COX, B., "Re-evaluation of the fractography of I_2, Cs and Cs/Cd cracks in CANDU fuel clad tubing", paper presented at Studsvik PCI Seminar, 2005.

[9.484] CUBICCIOTTI, D., HOWARD, S.M., JONES, R.L., The formation of iodine-induced stress corrosion cracks in zircaloys, J. Nucl. Mater. **78** (1978) 2–16.

[9.485] LeBOULCH, D., FOURNIER, L., SAINTE-CATHERINE, C., "Testing and modelling iodine induced stress corrosion cracking in stress relieved Zircaloy-4", Proc. Sem. on Pellet-Clad Interaction in Water Reactor Fuels, Aix-en-Provence, 2004, NEA/OECD, Paris (2005) Paper 17.

[9.486] MASSIH, A.R., JERNKVIST, L.O., LINDBÄCK, J.E., ZHOU, G., "Analysis of pellet-clad interaction of LWR fuel rods during power ramps", Proc. 18th Int. Conf. Structural Mechanics in Reactor Technology, SMiRT 18, Beijing, 2005, International Association for Structural Mechanics in Reactor Technology, Raleigh, NC (2005).

[9.487] BAIN, A.S., WOOD, J.C., COLEMAN, C.E., Fuel Designs to Eliminate Defects on Power Increases, Proc. British Nuclear Energy Society, Atomic Energy of Canada Report No. AECL-4518, Atomic Energy of Canada, Chalk River, ON (1973) Paper 56.

[9.488] ROBERTSON, J.A.L., "Learning from history: A case study in nuclear fuel", Zirconium in the Nuclear Industry: Eleventh International Symposium, Proc. ASTM STP 1295, Garmisch-Partenkirchen, 1995 (BRADLEY, E.R., SABOL, G.P., Eds), ASTM International, West Conshohocken, PA (1996) 3–11.

[9.489] COLEMAN, C.E., "Simulation of interaction between cracked UO_2 fuel and Zircaloy cladding", Proc. Int. Conf. on Physical Metallurgy of Reactor Fuel Elements, Berkeley, 1973, The Metals Society, London (1974) 302–307.

[9.490] WOOD, J.C., SURETTE, B.A., LONDON, I.M., BAIRD, J., Environmental induced fracture of Zircaloy by iodine and caesium: the effects of strain-rate, localized stress and temperature, J. Nucl. Mater. **57** (1975) 155–179.

[9.491] TOMALIN, D.S., ADAMSON, R.B., GANGLOFF, R.P., "Performance of irradiated copper and zirconium barrier-modified zircaloy cladding under simulated pellet-cladding interaction conditions", Zirconium in the Nuclear Industry: Fourth International Symposium, Proc. ASTM STP 681, Stratford-upon-Avon, 1978 (SCHEMEL, J.H., PAPAZOGLOU, T.P., Eds), ASTM International, West Conshohocken, PA (1979) 122–144.

[9.492] NOBREGA, B.N., KING, J.S., WAS, G.S., WISNER, S.B., Improvements in the design and analysis of the segmented expanding mandrel test, J. Nucl. Mater. **131** (1985) 99–104.

[9.493] FOSTER, J.P., LEASURE, R.A., “Simulated fuel expansion testing of Zircaloy tubing”, Zirconium in the Nuclear Industry: Eighth International Symposium, Proc. ASTM STP 1023, San Diego, 1988 (VAN SWAMM, L.F.P., EUCKEN, C.M., Eds), ASTM International, West Conshohocken, PA (1989) 517–534.

[9.494] WOOD, J.C., SURETTE, B.A., AITCHISON, I., CLENDENING, W.R., Pellet-cladding interaction — evaluation of lubrication by graphite, J. Nucl. Mater. **88** (1980) 81–94.

[9.495] ARMIJO, J.S., JOSEPH, S., COFFIN, Jr., LOUIS, F., Nuclear Fuel Element, US Patent 4200492, issued Apr. 1980.

[9.496] ARMIJO, J.S., COFFIN, Jr., LOUIS, F., Nuclear Fuel Element, US Patent 4372817, issued Jan. 1983.

[9.497] ROSENBAUM, H.S., et al., “Large scale demonstration of barrier fuel”, Proc. Tech. Mtg on Improvements in Water Reactor Fuel Technology, Stockholm, 1986, IAEA, Vienna (1987) 117–134.

[9.498] ARMIJO, J.S., COFFIN, L.F., ROSENBAUM, H.S., “Development of zirconium-barrier fuel cladding”, Zirconium in the Nuclear Industry: Tenth International Symposium, Proc. ASTM STP 1245, Baltimore, 1993 (GARDE, A.M., BRADLEY, E.R., Eds), ASTM International, West Conshohocken, PA (1994) 3–18.

[9.499] CHENG, B., OBERLÄNDER, B.C., WIESENACK, W., YAGNIK, S., TURNBULL, J., “An in-reactor simulation test to evaluate root cause of secondary degradation of defective BWR fuel rod”, Zirconium in the Nuclear Industry: Thirteenth International Symposium, Proc. ASTM STP 1423, Annecy, 2001 (MOAN, G.D., RUDLING, P., Eds), ASTM International, West Conshohocken, PA (2002) 616–633.

[9.500] INTERNATIONAL ATOMIC ENERGY AGENCY, Delayed Hydride Cracking in Zirconium Alloys in Pressure Tube Nuclear Reactors, IAEA-TECDOC-1410, IAEA, Vienna (2004).

[9.501] INTERNATIONAL ATOMIC ENERGY AGENCY, Delayed Hydride Cracking of Zirconium Alloy Fuel Cladding, IAEA-TECDOC-1649, IAEA, Vienna (2010).

[9.502] COLEMAN, C.E., HARDIE, D., The hydrogen embrittlement of α-zirconium — A review, J. Less Common Met. **11** (1966) 168–185.

[9.503] ELLS, C.E., Hydride precipitates in zirconium alloys (A review), J. Nucl. Mater. **28** (1968) 129–151.

[9.504] COLEMAN, C.E., AMBLER, J.F.R., Delayed hydrogen cracking in Zr-2.5 wt% Nb alloy, Rev. Coat. Corr. **3** (1979) 105–157.

[9.505] NORTHWOOD, D.O., KOSASIH, U., Hydrides and delayed hydrogen cracking in zirconium and its alloys, Int. Met. Rev. **28** (1983) 92–121.

[9.506] EADIE, R.L., SMITH, R.R., Modelling delayed hydride cracking in zirconium alloys, Can. Metall. Q. **27** (1988) 213–223.

[9.507] PRICE, E.G., Highlights of the Metallurgical Behaviour of CANDU Pressure Tubes, Report No. AECL-8338, Atomic Energy of Canada Limited, Chalk River, ON (1984).

[9.508] ALADJEM, A., “Zirconium-Hydrogen in Hydrogen Metal Systems 1”, Solid State Phenomena, Vols 49–50 (LEWIS, F.A., ALADJEM, A., Eds), SCITEC Publications, Zurich (1996) 281–329.

[9.509] SAWATZKY, A., ELLS, C.E., “Understanding hydrogen in zirconium”, Zirconium in the Nuclear Industry: Twelfth International Symposium, Proc. ASTM STP 1354, Toronto, 1998 (SABOL, G.P., MOAN, G.D., Eds), ASTM International, West Conshohocken, PA (2000) 32–48.

[9.510] COLEMAN, C.E., “Cracking of hydride-forming metals and alloys”, Comprehensive Structural Integrity: Fracture of Materials from Nano to Macro, Vol. 6 (PETIT, J., SCOTT, P.M., Eds), Elsevier, Oxford (2003) Ch. 6.03, 103–161.

[9.511] PULS, M.P., Review of the thermodynamic basis for models of delayed hydride cracking rate in zirconium alloys, J. Nucl. Mater. **393** (2009) 350–367.

[9.512] PULS, M.P., The Effect of Hydrogen and Hydrides on the Integrity of Zirconium Alloy Components: Delayed Hydride Cracking, Springer, London (2012).

[9.513] CHAN, K.S., An assessment of delayed hydride cracking in zirconium alloy cladding tubes under stress transients, Int. Mater. Rev. **58** (2013) 349–373.

[9.514] ZUZEK, E., ABRIATA, J.P., SAN-MARTIN, A., MANCHESTER, F.D., The H-Zr (hydrogen-zirconium) system, Bull. Alloy Phase Diagr. **11** (1990) 385–395.

[9.515] DUPIN, N., et al., A thermodynamic database for zirconium alloys, J. Nucl. Mater. **275** (1999) 287–295.

[9.516] KÖNIGSBERGER, E., ERIKSSON, G., OATES, W.A., Optimisation of the thermodynamic properties of the Ti–H and Zr–H systems, J. Alloys Compd. **288** (2000) 148–152.

[9.517] HÄGG, G., Röntgenuntersuchungen über die hydride von Titan, Zirkonium, Vanadin und Tantal, Z. Phys. Chem. B **11** (1931) 433–454.

[9.518] GULBRANSEN, E.A., ANDREW, K.F., Crystal structure and thermodynamic studies on the zirconium-hydrogen alloys, J. Electrochem. Soc. **101** (1954) 474–480.

[9.519] VAUGHAN, D.A., BRIDGE, J.R., High temperature X-ray diffraction investigation of the Zr-H system, Trans. Metall. Soc. AIME **8** (1956) 528–531.

[9.520] BECK, R.L., Zirconium-hydrogen phase system, Trans. ASM **55** (1962) 542–555.

[9.521] ZHAO, Z., et al., Characterization of zirconium hydrides and phase field approach to a mesoscopic-scale modeling of their precipitation, J. ASTM International **5** (2008) Paper JAI101161.

[9.522] CHRISTENSEN, M., et al., “Effect of hydrogen on dimensional changes of zirconium and the influence of alloying elements: First-principles and classical simulations of point defects, dislocation loops, and hydrides”, Zirconium in the Nuclear Industry: Seventeenth International Symposium, Proc. ASTM STP 1543, Hyderabad, 2013 (COMSTOCK, R., BARBÉRIS, P., Eds), ASTM International, West Conshohocken, PA (2015) 55–92.

[9.523] CASSIDY, M.P., WAYMAN, C.M., The crystallography of hydride formation in zirconium: I. The δ → γ transformation, Metall. Mater. Trans. A **11** (1980) 47–56.

[9.524] BARRACLOUGH, K.G., BEEVERS, C.J., Some observations on the phase transformations in zirconium hydrides, J. Nucl. Mater. **34** (1970) 125–134.

[9.525] CASSIDY, M.P., WAYMAN, C.M., The crystallography of hydride formation in zirconium: II. The δ → ε transformation, Metall. Mater. Trans. A **11** (1980) 57–67.

[9.526] ZHAO, Z., et al., Identification and characterization of a new zirconium hydride, J. Microsc. **232** (2008) 410–421.

[9.527] HAFNER, J., Atomic-scale computational materials science, Acta Mater. **48** (2000) 71–92.

[9.528] DOMAIN, C., BESSON, R., LEGRIS, A., Atomic-scale Ab-initio study of the Zr-H system: I. Bulk properties, Acta Mater. **50** (2002) 3513–3526.

[9.529] WESTLAKE, D.G., Disposition of hydrogen in quenched zirconium–hydrogen alloys, J. Nucl. Mater. **16** (1965) 215–219.

[9.530] BRADBROOK, J.S., LORIMER, G.W., RIDLEY, N., The precipitation of zirconium hydride in zirconium and Zircaloy-2, J. Nucl. Mater. **42** (1972) 142–160.

[9.531] RIDLEY, N., CAULKIN, K.G., LORIMER, G.W., "Zirconium hydride precipitation in Zircaloy-2", Proc. Int. Congr. on Hydrogen in Metals, Jülich, 1972 (BASTIEN, P., Ed.), Éditions de Science et de L'Industrie, Paris (1972) 484–488.

[9.532] NATH, B., LORIMER, G.W., RIDLEY, N., The relationship between gamma and delta hydrides in zirconium-hydrogen alloys of low hydrogen concentration, J. Nucl. Mater. **49** (1974) 262–280.

[9.533] NATH, B., LORIMER, G.W., RIDLEY, N., Effect of hydrogen concentration and cooling rate on hydride precipitation in α-zirconium, J. Nucl. Mater. **58** (1975) 153–162.

[9.534] GILL, B.J., COTTERILL, P., BAILEY, J.E., Aspects of the constitution of zirconium-hydrogen alloys, J. Less-Common Met. **39** (1975) 189–193.

[9.535] LANGERON, J.P., LEHR, P., Préparation de gros cristaux de zirconium et détermination de l'orientation des précipités d'hydrure de zirconium, Metall. Res Technol. **55** (1958) 901–906.

[9.536] WESTLAKE, D.G., FISHER, E.S., Precipitation of zirconium hydride in alpha zirconium crystals, Trans. Metall. Soc. AIME **224** (1962) 254–258.

[9.537] WEATHERLY, G.C., The precipitation of γ-hydride plates in zirconium, Acta Metall. **29** (1981) 501–512.

[9.538] BABYAK, W.J., Hydride habit in zirconium and in unstressed and stressed Zircaloy-4, Trans. AIME **239** (1967) 252–257.

[9.539] WESTLAKE, D.G., The habit planes of zirconium hydride in zirconium and Zircaloy, J. Nucl. Mater. **26** (1968) 208–216.

[9.540] PEGOUD, J., GUILLAUMIN, J., Orientations cristallographiques de l'hydrure dans le Zircaloy-2 polycristallin, J. Nucl. Mater. **45** (1972–73) 69–72.

[9.541] CARPENTER, G.J.C., The precipitation of γ-zirconium hydride in zirconium, Acta Metall. **26** (1978) 1225–1235.

[9.542] LOUTHAN, M.R., ANGERMAN, C.L., The influence of stress on the hydride habit plane in Zircaloy-2, Trans. Metall. Soc. AIME **236** (1966) 221–222.

[9.543] CHUNG, H.M., DAUM, R.S., HILLER, J.M., BILLONE, M.C., "Characteristics of hydride precipitation and reorientation in spent-fuel cladding", Zirconium in the Nuclear Industry: Thirteenth International Symposium, Proc. ASTM STP 1423, Annecy, 2001 (MOAN, G.D., RUDLING, P., Eds), ASTM International, West Conshohocken, PA (2002) 561–582.

[9.544] ARUNACHALAM, V.S., LEHTINEN, B., ÖSTBERG, G., The orientation of zirconium hydride on grain boundaries in Zircaloy-2, J. Nucl. Mater. **21** (1967) 241–248.

[9.545] AMBLER, J.F.R., Grain boundary hydride habit in Zircaloy-2, J. Nucl. Mater. **28** (1968) 237–245.

[9.546] MISHIMA, Y., ISHINO, S., KAWANISHI, H., "Grain boundary hydride precipitates in Zircaloy-2", Proc. Int. Congr. on Hydrogen in Metals, Jülich, 1972 (BASTIEN, P., Ed.), Éditions de Science et de L'Industrie, Paris (1972) 469–473.

[9.547] PEGOUD, J., GUILLAUMIN, J., Orientations cristallographiques de l'hydrure dans le Zircaloy-2 polycristallin, J. Nucl. Mater. **45** (1972) 69–72.

[9.548] BAILEY, J.E., Electron microscope observations on the precipitation of zirconium hydride in zirconium, Acta Metall. **11** (1963) 267–280.

[9.549] NEOGY, S., et al., Microstructural study of hydride formation in Zr-1Nb alloy, J. Nucl. Mater. **322** (2003) 195–203.

[9.550] CARPENTER, G.J.C., The dilatational misfit of zirconium hydrides precipitated in zirconium, J. Nucl. Mater. **48** (1973) 264–266.

[9.551] SINGH, R.N., STÅHLE, P., MASSIH, A.R., SHMAKOV, A.A., Temperature dependence of misfit strains of β-hydrides of zirconium, J. Alloys Compd. **436** (2007) 150–154.

[9.552] YAMANAKA, S., et al., Isotope effects on the physicochemical properties of zirconium hydride, J. Alloys Compd. **293–295** (1999) 908–914.

[9.553] YAMANAKA, S., et al., Thermal and mechanical properties of zirconium hydride, J. Alloys Compd. **293–295** (1999) 23–29.

[9.554] PULS, M.P., "Hydrogen-induced delayed cracking: 1. Strain energy effects on hydrogen solubility", Report No. AECL-6302, Atomic Energy of Canada Limited, Chalk River, ON (1978).

[9.555] CANN, C.D., PULS, M.P., SEXTON, E.E., HUTCHINGS, W.G., The effect of metallurgical factors on hydride phases in zirconium, J. Nucl. Mater. **126** (1984) 197–205.

[9.556] CANN, C.D., ATRENS, A., A metallographic study of the terminal solubility of hydrogen in zirconium at low hydrogen concentrations, J. Nucl. Mater. **88** (1980) 42–50.

[9.557] SIDHU, S.S., SATYA MURTHY, N.S., CAMPOS, F.P., ZAUBERIS, D.D., "Neutron and x-ray diffraction studies of nonstoichiometric metal hydrides", Argonne National Lab., ANL-FGF-332, Atomic Energy Commission, Washington, DC (1963).

[9.558] KATZ, O.M., Tetragonal hydride in low hydrogen content Zircaloy, J. Nucl. Mater. **36** (1970) 335–339.

[9.559] LEE, J.K., EARMME, Y.Y., AARONSON, H.I., RUSSELL, K.C., Plastic relaxation on the transformation strain energy of a misfitting spherical precipitate: Ideal plastic behavior, Metall. Trans. A **11** (1980) 1837–1847.

[9.560] TULK, E., KERR, M., DAYMOND, M.R., Study on the effects of matrix yield strength on hydride phase stability in Zircaloy-2 and Zr2.5 wt% Nb, J. Nucl. Mater. **425** (2012) 93–104.

[9.561] NORTHWOOD, D.O., LIM, D.T.H., TEM metallographic study of hydrides in a Zr-2.5wt%Nb alloy, Metallography **14** (1981) 21–35.

[9.562] PEROVIC, V., WEATHERLY, G.C., The nucleation of hydrides in Zr-2.5 wt% Nb alloy, J. Nucl. Mater. **126** (1984) 160–169.

[9.563] MANI KRISHNA, K.V., et al., Role of grain/phase boundary nature on the formation of hydrides in Zr–2.5%Nb alloy, J. Nucl. Mater. **414** (2011) 270–275.

[9.564] LANZANI, L., RUCH, M., Comments on the stability of zirconium hydride phases in Zircaloy, J. Nucl. Mater. **324** (2004) 165–176.

[9.565] VELEVA, M., ARSENE, S., RECORD, M.-C., BECHADE, J.L., BAI, J., Hydride embrittlement effects on the hoop mechanical properties of pressurized water reactor (PWR) and boiling-water reactor (BWR) Zircaloy cladding tubes, Part 2: Morphology of hydrides investigated at different magnifications and their interaction with the processes of plastic deformation, Metall. Mater. Trans. A **34** (2003) 567–578.

[9.566] DAUM, R.S., CHU, Y.S., MOTTA, A.T., Identification and quantification of hydride phases in Zircaloy-4 cladding using synchrotron X-ray diffraction, J. Nucl. Mater. **392** (2009) 453–463.

[9.567] MISHRA, S., SIVARAMAKRISHNAN, K.S., ASUNDI, M.K., Formation of the gamma phase by a peritectoid reaction in the zirconium-hydrogen system, J. Nucl. Mater. **45** (1972) 235–244.

[9.568] BARACLOUGH, K.G., BEEVERS, C.J., The nature of the γ-phase in zirconium-hydrogen alloys, J. Less-Common Met. **35** (1974) 177–179.

[9.569] MOORE, K.E., Phase relationships in the α + δ region of the Zr-H system, J. Nucl. Mater. **32** (1969) 46–56.

[9.570] BARROW, A.T.W., KORINEK, A., DAYMOND, M.R., Evaluating zirconium–zirconium hydride interfacial strains by nano-beam electron diffraction, J. Nucl. Mater. **432** (2013) 366–370.

[9.571] NORTHWOOD, D.O., Gamma and delta hydrides in zirconium alloys, J. Less-Common Met. **48** (1976) 173–175.

[9.572] ROOT, J.H., FONG, R.W.L., Neutron diffraction study of the precipitation and dissolution of hydrides in Zr-2.5Nb pressure tube material, J. Nucl. Mater. **232** (1996) 75–85.

[9.573] SMALL, W.M., ROOT, J.H., KHATAMIAN, D., Observation of kinetics of γ zirconium hydride formation in Zr-2.5Nb by neutron diffraction, J. Nucl. Mater. **256** (1998) 102–107.

[9.574] ROOT, J.H., SMALL, W.M., KHATAMIAN, D., WOO, O.T., Kinetics of the δ to γ zirconium hydride transformation in Zr-2.5 Nb, Acta Mater. **51** (2003) 2041–2053.

[9.575] PARRY, G.W., Strain Induced Directionality of Zirconium Hydride Precipitates in Zirconium-2.5 wt.% Niobium 0.5 wt.% Copper Alloy, Report No. AECL-1888, Atomic Energy of Canada Limited, Chalk River, ON (1963).

[9.576] PARRY, G.W., Stress-reorientation of Hydrides in Cold-worked Zr-2.5% Nb Pressure Tubes, Atomic Energy of Canada Report No. AECL-2624, Atomic Energy of Canada, Chalk River, ON (1966).

[9.577] CHEADLE, B.A., COLEMAN, C.E., IPOHORSKI, M., "Orientation of hydrides in zirconium alloy tubes", Zirconium in the Nuclear Industry: Sixth International Symposium, Proc. ASTM STP 824, Vancouver, 1982 (FRANKLIN, D.G., ADAMSON, R.B., Eds), ASTM International, West Conshohocken, PA (1984) 210–221.

[9.578] PEROVIC, V., PURDY, G.R., BROWN, L.M., Autocatalytic nucleation and elastic stabilization of linear arrays of plate-shaped precipitates, Acta Metall. **29** (1981) 889–902.

[9.579] PEROVIC, V., WEATHERLY, G.C., SIMPSON, C.J., Hydride precipitation in α/β zirconium alloys, Perspectives in Hydrogen in Metals (ASHBY, M.F., HIRTH J.P. Eds), Pergamon, Oxford (1986) 469–479.

[9.580] PEROVIC, V., WEATHERLY, G.C., MacEWEN, S.R., LÉGER, M., The influence of prior deformation on hydride precipitation in Zircaloy, Acta Metall. Mater. **40** (1992) 363–372.

[9.581] GULBRANSEN, E.A., ANDREWS, K.F., Solubility and decomposition pressures of hydrogen in alpha-zirconium, JOM. J. Miner. Met. Mater. Soc. **7** (1955) 136–144.

[9.582] SIEVERTS, A., Absorption of gases by metals, Z. Metall. **21** (1929) 37–46.

[9.583] ÖSTBERG, G., Determination of hydride solubility in alpha phase zirconium, Zircaloy-2 and Zircaloy-4, J. Nucl. Mater. **5** (1962) 208–215.

[9.584] ERICKSON, W.H., HARDIE, D., The influence of alloying elements on the terminal solubility of hydrogen in α-zirconium, J. Nucl. Mater. **13** (1964) 254–262.

[9.585] ERICKSON, W.H., Hydrogen solubility in zirconium alloys, J. Electrochem. Technol. **4** (1966) 205–211.

[9.586] SAOUDI, M., MOURIS, J., HE, Z., "Development of gaseous hydrogen charging of Zr alloys using a coulometric titration technique", Proc. 31st Conf. Canadian Nuclear Society, Montreal, 2010, Canadian Nuclear Society, Toronto (2010).

[9.587] KEARNS, J.J., Terminal solubility and partitioning of hydrogen in the alpha phase of zirconium, Zircaloy-2 and Zircaloy-4, J. Nucl. Mater. **22** (1967) 292–303.

[9.588] KAMMENZIND, B.F., FRANKLIN, D.G., PETERS, H.R., DUFFIN, W.J., "Hydrogen pickup and redistribution in alpha-annealed Zircaloy-4", Zirconium in the Nuclear Industry: Eleventh International Symposium, Proc. ASTM

STP 1295, Garmisch-Partenkirchen, 1995 (BRADLEY, E.R., SABOL, G.P., Eds), ASTM International, West Conshohocken, PA (1996) 338–370.

[9.589] SCHWARTZ, C.M., MALLETT, M.W., Observations on the behaviour of hydrogen in zirconium, Trans. AIME **46** (1954) 640–654.

[9.590] MALLETT, M.W., ALBRECHT, W.M., Low-pressure solubility and diffusion of hydrogen in zirconium, J. Electrochem. Soc. **104** (1957) 142–146.

[9.591] SAWATZKY, A., The diffusion and solubility of hydrogen in the alpha phase of Zircaloy-2, J. Nucl. Mater. **2** (1960) 62–68.

[9.592] DANIEL, A.R., Terminal Solid Solubility of Hydrogen in Zircaloy-2, Report No. AECL-2453, Atomic Energy of Canada Limited, Chalk River, ON (1965).

[9.593] SAWATZKY, A., Hydriding Zircaloy-2 by Electrolysis, Report No. AECL-1046, Atomic Energy of Canada Limited, Chalk River, ON (1960).

[9.594] SAWATZKY, A., WILKINS, B.J.S., Hydrogen solubility in zirconium alloys determined by thermal diffusion, J. Nucl. Mater. **22** (1967) 304–310.

[9.595] ESPAGNO, L., AZOU, P., BASTIEN, P., Étude dilatométrique entre l’ambiante et 550°C du système zirconium-hydrogène, C. R. Acad. Sci. **248** (1959) 2003–2005.

[9.596] SLATTERY, G.F., The terminal solubility of hydrogen in zirconium alloys between 30 and 400°C, J. Inst. Met. **95** (1967) 43–47.

[9.597] SINGH, R.N., MUKHERJEE, S., GUPTA, A., BANERJEE, S., Terminal solid solubility of hydrogen in Zr-alloy pressure tube materials, J. Alloys. Compd. **389** (2005) 102–112.

[9.598] GIROLDI, J.P., VIZCAÍNO, P., FLORES, A.V., Hydrogen terminal solid solubility determinations in Zr-2.5Nb pressure tube microstructure in an extended concentration range, J. Alloys Compd. **474** (2009) 140–146.

[9.599] BUNGARDT, K., PREISENDANZ, H., Dämpfung und Schubmodul von Zirconium und Zirconium-Wasserstoff-Legierungen, Z. Metall. **51** (1960) 280–289.

[9.600] POVOLO, F., BISOGNI, E.A., Internal friction in zirconium-hydrogen alloys at low temperatures, J. Nucl. Mater. **29** (1969) 82–102.

[9.601] PROVENZANO, V., SCHILLER, P., SCHNEIDERS, A., Internal friction study of zirconium alloyed with hydrogen and deuterium, J. Nucl. Mater. **52** (1974) 75–84.

[9.602] MISHRA, S., ASUNDI, M.K., “Determination of solid solubility limit of hydrogen in alpha zirconium by internal friction measurements”, Zirconium in Nuclear Applications: Second International Symposium, Proc. ASTM STP 551, Portland, 1973 (SCHEMEL, J.H., ROSENBAUM, H.S., Eds), ASTM International, West Conshohocken, PA (1974) 63–71.

[9.603] RITCHIE, I.G., SPRUNGMANN, K.W., Hydride Precipitation in Zirconium Studied by Pendulum Techniques, Report No. AECL-7806, Atomic Energy of Canada Limited, Chalk River, ON (1983).

[9.604] PAN, Z.L., RITCHIE, I.G., PULS, M.P., The terminal solid solubility of hydrogen and deuterium in Zr-2.5Nb alloys, J. Nucl. Mater. **228** (1996) 227–237.

[9.605] MISHIMA, Y., ISHINO, S., NAKAJIMA, S., A resistometric study of the solution and precipitation of hydrides in unalloyed zirconium, J. Nucl. Mater. **27** (1968) 335–344.

[9.606] CARPENTER, G.J.C., WATTERS, J.F., An in-situ study of the dissolution of γ-zirconium hydride in zirconium, J. Nucl. Mater. **73** (1978) 190–197.

[9.607] COLAS, K.B., et al., In situ study of hydride precipitation kinetics and re-orientation in Zircaloy using synchrotron radiation, Acta Mater. **58** (2010) 6575–6583.

[9.608] ZANELLATO, O., et al., Synchrotron diffraction study of dissolution and precipitation kinetics of hydrides in Zircaloy-4, J. Nucl. Mater. **420** (2012) 537–547.

[9.609] BARROW, A.T.W., TOFFOLON-MASCLET, C., ALMER, J., DAYMOND, M.R., The role of chemical free energy and elastic strain in the nucleation of zirconium hydride, J. Nucl. Mater. **441** (2013) 395–401.

[9.610] COLAS, K., MOTTA, A., DAYMOND, M., ALMER, J., “Mechanisms of hydride reorientation in Zircaloy-4 studied in-situ”, Zirconium in the Nuclear Industry: Seventeenth International Symposium, Proc. ASTM STP 1543, Hyderabad, 2013 (COMSTOCK, R.J., BARBÉRIS, P., Eds), ASTM International, West Conshohocken, PA (2015) 1–31.

[9.611] FONG, R.W.L., SPOONER, S., Investigation of zirconium hydrides and hydrogen solubility limit in Zr-2.5 Nb alloy by small angle neutron scattering, Scr. Metall. Mater. **30** (1994) 649–654.

[9.612] DOUGLAS, T.B., The zirconium-hydrogen system: Some thermodynamic properties from a heat content study, J. Am. Chem. Soc. **80** (1958) 5040–5046.

[9.613] UNE, K., ISHIMOTO, S., Heat capacity of hydrogenated Zircaloy-2 and high Fe Zircaloy, J. Nucl. Mater. **323** (2003) 101–107.

[9.614] TASHIRO, K.M., Hydrogen measurement by differential scanning calorimetry, Ont. Hydro Res. Rev. **8** (1993) 29–30.

[9.615] KHATAMIAN, D., PAN, Z.L., PULS, M.P., CANN, C.D., Hydrogen solubility limits in Excel, an experimental zirconium-based alloy, J. Alloys Compd. **231** (1995) 488–493.

[9.616] KHATAMIAN, D., LING, V.C., Hydrogen solubility limits in α- and β-zirconium, J. Alloys Compd. **253–254** (1997) 162–166.

[9.617] McMINN, A., DARBY, E.C., SCHOFIELD, J.S., “The terminal solid solubility of hydrogen in zirconium alloys”, Zirconium in the Nuclear Industry: Twelfth International Symposium, Proc. ASTM STP 1354, Toronto, 1998 (SABOL, G.P., MOAN, G.D., Eds), ASTM International, West Conshohocken, PA (2000) 173–195.

[9.618] VIZCAÍNO, P., BANCHIK, A.D., ABRIATA, J.P., Solubility of hydrogen in Zircaloy-4: Irradiation induced increase and thermal recovery, J. Nucl. Mater. **304** (2002) 96–106.

[9.619] UNE, K., ISHIMOTO, S., Dissolution and precipitation behavior of hydrides in Zircaloy-2 and high Fe Zircaloy, J. Nucl. Mater. **322** (2003) 66–72.

[9.620] VIZCAÍNO, P., BANCHIK, A.D., ABRIATA, J.P., Calorimetric determination of the δ hydride dissolution enthalpy in Zircaloy-4, Metall. Mater. Trans. A **35** (2004) 2343–2349.

[9.621] UNE, K., ISHIMOTO, S., Terminal solid solubility of hydrogen in unalloyed zirconium by differential scanning calorimetry, J. Nucl. Sci. Technol. **41** (2004) 949–952.

[9.622] VIZCAÍNO, P., et al., Hydrogen solubility and microstructural changes in Zircaloy-4 due to neutron irradiation, J. ASTM Int. **8** (2011) Paper JAI102949.

[9.623] TANG, R., YANG, X., Dissolution and precipitation behaviours of hydrides in N18, Zry-4 and M5 alloys, Int. J. Hydrogen Energy **34** (2009) 7269–7274.

[9.624] COLEMAN, C.E., AMBLER, J.F.R., Measurement of effective solvus temperature of hydrogen in Zr-2.5 wt% Nb using acoustic emission, Can. Metall. Q. **17** (1978) 81–84.

[9.625] COLEMAN, C.E., AMBLER, J.F.R., Solubility of hydrogen isotopes in stressed hydride-forming metals, Scr. Metall. **17** (1983) 77–82.

[9.626] SHI, S.-Q., SHEK, G.K., PULS, M.P., Hydrogen concentration limit and critical temperatures for delayed hydride cracking in zirconium alloys, J. Nucl. Mater. **218** (1995) 189–201.

[9.627] SCHOFIELD, J.S., DARBY, E.C., GEE, C.F., “Temperature and hydrogen concentration limits for delayed hydride cracking in irradiated Zircaloy”, Zirconium in the Nuclear Industry: Thirteenth International Symposium, Proc. ASTM STP 1423, Annecy, 2001 (MOAN, G.D., RUDLING, P., Eds), ASTM International, West Conshohocken, PA (2002) 339–357.

[9.628] CIRIMELLO, P., DOMIZZI, G., HADDAD, R., Influence of metallurgical variables on delayed hydride cracking in Zr–Nb pressure tubes, J. Nucl. Mater. **350** (2006) 135–146.

[9.629] ELLS, C.E., COLEMAN, C.E., CHEADLE, B.A., SAGAT, S., RODGERS, D.K., The behaviour of hydrogen in Excel alloy, J. Alloys Compd. **231** (1995) 785–791.

[9.630] PONZONI, L.M.E., MIEZA, J.I., DE LAS HERAS, E., DOMIZZI, G., Comparison of delayed hydride cracking behavior of two zirconium alloys, J. Nucl. Mater. **439** (2013) 238–242.

[9.631] CANADIAN STANDARDS ASSOCIATION, Technical Requirements for In-service Evaluation of Zirconium Alloy Pressure Tubes in CANDU Reactors, Update 2, No. N285.8-10, Canadian Standards Association, Toronto, ON (2013).

[9.632] WESTERMAN, R., Charging Zircaloy-2 with hydrogen beyond the solubility limit, J. Nucl. Mater. **18** (1966) 31–38.

[9.633] KHATAMIAN, D., ROOT, J.H., Comparison of TSSD results obtained by differential scanning calorimetry and neutron diffraction, J. Nucl. Mater. **372** (2008) 106–113.

[9.634] KEARNS, J.J., Dissolution kinetics of hydride platelets in Zircaloy-4, J. Nucl. Mater. **27** (1968) 64–72.

[9.635] ELLS, C.E., CHEADLE, B.A., COLEMAN, C.E., VAN DER KUUR, J.H., “The decomposition of hydrides in zirconium alloys”, Proc. 3rd Int. Cong. on Hydrogen in Metals, Paris, 1982, Pergamon Press, Oxford (1982) 137–142.

[9.636] CAMERON, D.J., DUNCAN, R.G., On the existence of a memory effect on hydride precipitation in cold-worked Zr-2.5% Nb, J. Nucl. Mater. **68** (1977) 340–344.

[9.637] KHODA-BAKHSH, R., ROSS, D.K., Determination of the hydrogen site occupation in the α phase of zirconium hydride and in the α and β phases of titanium hydride by inelastic neutron scattering, J. Phys, F Met. Phys. **12** (1982) 15–24.

[9.638] NARANG, P.P., PAUL, G.L., TAYLOR, K.N.R., Location of hydrogen in α-zirconium, J. Less-Common Met. **56** (1977) 125–128.

[9.639] DARBY, M.I., READ, M.N., TAYLOR, K.N.R., The energy of interstitial hydrogen in α-zirconium, Phys. Status Solidi A **50** (1978) 203–211.

[9.640] MacEWEN, S.R., COLEMAN, C.E., ELLS, C.E. FABER, J., Jr., Dilation of h.c.p. zirconium by interstitial deuterium, Acta Metall. **33** (1985) 753–757.

[9.641] PEISL, H., “Lattice strains due to hydrogen in metals”, Hydrogen in Metals 1: Basic Properties (ALEFELD, G., VÖLKL, J., Eds), Topics in Applied Physics, Vol. 28, Springer, Berlin (1978) 53–74.

[9.642] CARPENTER, G.J.C., WATTERS, J.F., GILBERT, R.W., Dislocations generated by zirconium hydride precipitates in zirconium and some of its alloys, J. Nucl. Mater. **48** (1973) 267–276.

[9.643] ELLS, C.E., SIMPSON, C.J., “Stress induced movement of hydrogen in zirconium alloys”, Proc. Int. Conf. on Effects of Hydrogen on Materials Properties and Selection and Structural Design, Champion, 1973 (BERNSTEIN, I.M., THOMPSON, A.W., Eds), American Society for Metals, Metals Park, OH (1974) 345–360.

[9.644] EADIE, R.L., COLEMAN, C.E., Effect of stress on hydride precipitation in zirconium-2.5% niobium and on delayed hydride cracking, Scr. Metall. **23** (1989) 1865–1870.

[9.645] KAMMENZIND, B.F., BERQUIST, B.M., BAJAJ, R., KREYNS, P.H., FRANKLIN, D.G., “The long-range migration of hydrogen through Zircaloy in response to tensile and compressive stress gradients”, Zirconium in the

Nuclear Industry: Twelfth International Symposium, Proc. ASTM STP 1354, Toronto, 1998 (SABOL, G.P., MOAN, G.D., Eds), ASTM International, West Conshohocken, PA (2000) 196–233.

[9.646] PULS, M.P., LEITCH, B.W., SHI, S.-Q., "The effect of applied stress on the accommodation energy and the solvi for the formation and dissolution of zirconium hydride", Hydrogen Effects on Material Behavior and Corrosion Deformation Interaction (MOODY, N.R., THOMPSON, A.W., RIKER, R.E., WAS, G.W., JONES, R.H., Eds), The Minerals, Metals and Materials Society, Warrendale, PA (2003) 233–248.

[9.647] PULS, M.P., The effects of misfit and external stresses on terminal solid solubility in hydride-forming metals, Acta Met. **29** (1981) 1961–1968.

[9.648] PULS, M.P., Elastic and plastic accommodation effects on metal-hydride solubility, Acta Metall. **32** (1984) 1259–1269.

[9.649] LEITCH, B.W., PULS, M.P., Finite element calculations of the accommodation energy of a misfitting precipitate in an elastic-plastic matrix, Metall. Trans. A **23** (1992) 797–806.

[9.650] LEITCH, B.W., SHI, S.-Q., Accommodation energy of formation and dissolution for a misfitting precipitate in an elastic-plastic matrix, Model. Simul. Mater. Sci. Eng. **4** (1996) 281–292.

[9.651] NUMAKURA, H., ITO, T., KOIWA, M., Low-frequency internal friction study of Zr-H and Zr-D alloys, J. Less-Common Met. **141** (1988) 285–294.

[9.652] SAWATZKY, A., The Effect of Neutron Irradiation on the Mechanical Properties of Hydrided Zirconium Alloys, Report No. AECL-1986, Atomic Energy of Canada Limited, Chalk River, ON (1964).

[9.653] YAMANAKA, S., et al., Characteristics of zirconium hydride and deuteride, J. Alloys Compd. **330–332** (2002) 99–104.

[9.654] SINGH, K.P., GORDON PARR, J., Solubility of deuterium in the zirconium-deuterium system, Trans. Faraday Soc. **59** (1963) 2256–2259.

[9.655] OGATA, K., et al., "Progress in the research programs to elucidate axial cracking fuel failure at high burnup", Proc. Int. LWR Fuel Performance Mtg/TopFuel 2007 'Zero by 2010', San Francisco, 2007, American Nuclear Society, La Grange Park, IL (2007) Paper 1024.

[9.656] UNE, K., et al., The terminal solid solubility of hydrogen in irradiated Zircaloy-2 and microscopic modelling of hydride behaviour, J. Nucl. Mater. **389** (2009) 127–136.

[9.657] LEWIS, M.B., Deuterium-defect trapping in ion-irradiated zirconium, J. Nucl. Mater. **125** (1984) 152–159.

[9.658] CHRISTENSEN, M., et al., Effect of alloying elements on the properties of Zr and Zr-H system, J. Nucl. Mater. **445** (2014) 241–250.

[9.659] ADAMSON, R.B., Recovery of Irradiation Damage by Post-irradiation Thermal Annealing-relevance to Hydrogen Solubility and Dry Storage Issues, Report No. EPRI-1013446, Electric Power Research Institute, Palo Alto, CA (2006).

[9.660] PATON, N.E., HICKMAN, B.S., LESLIE, D.H., Behavior of hydrogen in α-phase Ti-Al alloys, Metall. Trans. **2** (1971) 2791–2796.

[9.661] SETOYAMA, D., et al., Influence of additive elements on the terminal solid solubility of hydrogen for zirconium alloy, J. Nucl. Mater. **344** (2005) 291–294.

[9.662] SLATTERY, G.F., The terminal solubility of hydrogen in the zirconium/2 at % chromium/0.16 at % iron alloy, J. Nucl. Mater. **32** (1969) 30–38.

[9.663] MARTIN, S.L.H., REES, A.L.G., Interpretation of the solubility of hydrogen in zirconium, Trans. Faraday Soc. **50** (1954) 343–352.

[9.664] SETOYAMA, D., YAMANAKA, S., Phase diagram of Zr–O–H ternary system, J. Alloys Compd. **370** (2004) 144–148.

[9.665] SAWATZKY, A., LEDOUX, G.A., TOUGH, R.L., CANN, C.D., "Hydrogen diffusion in zirconium-niobium alloys", Proc. Int. Symp. on Metal-Hydrogen Systems, Miami Beach, 1981 (VEZIROĞLU, T.N., Ed.), Pergamon Press, Oxford (1981) 109–120.

[9.666] KHATAMIAN, D., Solubility and Partitioning of Hydrogen in Meta-stable Zr-based Alloys Used in the Nuclear Industry Report No. AECL-11950, Atomic Energy of Canada Limited, Chalk River, ON (1998).

[9.667] CANN, C.D., SEXTON, E.E., DUCLOS, A.M., SMITH, G.G., The effect of decomposition of beta-phase Zr-20 at% Nb on hydrogen partitioning with alpha-zirconium, J. Nucl. Mater. **210** (1994) 6–10.

[9.668] CHEADLE, B.A., ALDRIDGE, S.A., The transformation and age hardening behaviour of Zr-19 wt% Nb, J. Nucl. Mater. **47** (1973) 255–258.

[9.669] GRIFFITHS, M., WINEGAR, J.E., BUYERS, A., The transformation behaviour of the β-phase in Zr-2.5Nb pressure tubes, J. Nucl. Mater. **383** (2008) 28–33.

[9.670] FICK, A., On liquid diffusion, Philosoph. Mag. **10** (1855) 30–39.

[9.671] WATANABE, K., ASHIDA, K., SONOBE, M., The compensation effect on diffusion constants of hydrogen in metals, J. Nucl. Mater. **173** (1990) 294–306.

[9.672] GULBRANSEN, E.A., ANDREW, K.F., Diffusion of hydrogen and deuterium in high purity zirconium, J. Electrochem. Soc. **101** (1954) 560–566.

[9.673] SOMENO, M., Solubility and diffusion of hydrogen in zirconium, Nippon Kinzoku Gakkai-shi **24** (1960) 249–253 (in Japanese).

[9.674] KEARNS, J.J., Diffusion coefficient of hydrogen in alpha zirconium, Zircaloy-2 and Zircaloy-4, J. Nucl. Mater. **43** (1972) 330–338.

[9.675] MAZZOLAI, F.M., RYLL-NARDZEWSKI, J., An anelastic study of the diffusion coefficient of hydrogen in α-zirconium, J. Less-Common Met. **49** (1976) 323–327.

[9.676] HASHIZUME, K., SUGISAKI, M., HATANO, K., OHMORI, T., ŌGI, K., Application of discharge implantation method to measurement of diffusion coefficient of hydrogen isotopes in zirconium, J. Nucl. Sci. Technol. **31** (1994) 1294–1300.

[9.677] ZHANG, C.-S., LI, B., NORTON, P.R., The study of hydrogen segregation on Zr(0001) and $Zr(10\bar{1}0)$ surfaces by static secondary ion mass spectroscopy, work function, Auger electron spectroscopy and nuclear reaction analysis, J. Alloys Compd. **231** (1995) 354–363.

[9.678] GELEZUNAS, V.L., CONN, P.K., PRICE, R.H., The diffusion coefficients for hydrogen in β-zirconium, J. Electrochem. Soc. **110** (1963) 799–805.

[9.679] GROSSE, M., VAN DEN BERG, M., GOULET, C., KAESTNER, A., In-situ investigation of hydrogen diffusion in Zircaloy-4 by means of neutron radiography, J. Phys: Conf. Ser. **340** (2012).

[9.680] ALBRECHT, W.M., GOODE, W.D., The Diffusion of Hydrogen in Beta Zirconium, Report No. BMI-1373, Battelle Memorial Institute, Columbus, OH (1959).

[9.681] SKINNER, B.C., DUTTON, R., “Hydrogen diffusivity in alpha-beta zirconium alloys and its role in delayed hydride cracking”, Hydrogen Effects on Material Behavior (MOODY, N.R., THOMPSON, A.W., Eds), The Minerals, Metals and Material Society, Warrendale, PA (1990) 73–83.

[9.682] LÉGER, M., Hydrogen Diffusion in the Axial Direction of Zr-2.5% Nb Pressure Tubes, Report No. 80-223-K, Ontario Hydro, Toronto, ON (1980).

[9.683] BARASHEVA, T.V., ANISIMOVA, I.A., GUS’KOVA, E.I., ERMOLOVA, M.I., Hydrogen diffusion in titanium and zirconium alloys, Met. Sci. Heat Treat. **20** (1978) 341–343.

[9.684] KHATAMIAN, D., Deuterium diffusion along the three principal directions in anisotropic Zr-2.5Nb, J. Alloys Compd. **580** (2013) S58–S62.

[9.685] GRAHAM, T., On the law of the diffusion of gases, Philosoph. Mag. **2** (1833) 351–358.

[9.686] VINEYARD, G.H., Frequency factors and isotope effects in solid state rate processes, J. Phys. Chem. Solids **3** (1957) 121–127.

[9.687] NAITO, S., HASHINO, T., KAWAI, T., Kinetic isotope effects in hydrogen absorption by α-zirconium, J. Chem. Phys. **81** (1984) 3489–3494.

[9.688] CUPP, C.R., FLUBACHER, P., An autoradiographic technique for the study of tritium in metals and its application to diffusion in zirconium at 149° to 240°C, J. Nucl. Mater. **6** (1962) 213–228.

[9.689] AUSTIN, J.H., ELLEMAN, T.S., VERGHESE, K., Tritium diffusion in Zircaloy-2 in the temperature range –78 to 204°C, J. Nucl. Mater. **51** (1974) 321–329.

[9.690] GREGER, G.U., MÜNZEL, H., KUNZ, W., SCHWIERCZINSKI, A., Diffusion of tritium in Zircaloy-2, J. Nucl. Mater. **88** (1980) 15–22.

[9.691] KUNZ, W., MÜNZEL, H., HELFRICH, U., Diffusion of tritium in Zircaloy: Influence of low irradiation damage, oxygen concentration and formation of δ-hydrides, J. Nucl. Mater. **105** (1982) 178–183.

[9.692] FRISIUS, F., HACKBARTH, H., WILLE, P., Experiments concerning the influence of reactor irradiation on hydrogen diffusion in Zircaloy, Atomkernenergie **28** (1976).

[9.693] KHATAMIAN, D., SHADDICK, A., URBANIC, V.F., Influence of neutron irradiation on H diffusion in Zr-2.5 Nb alloy, J. Alloys Compd. **293–295** (1999) 324–328.

[9.694] KHATAMIAN, D., Diffusion of deuterium in Zr-2.5Nb alloy under neutron irradiation, J. Alloys Compd. **509** (2011) S797–S800.

[9.695] YANG, L., HORNE, G.T., POUND, G.M., “Effect of electric strain on the electrode potential of metals”, Physical Metallurgy of Stress Corrosion Fracture (RHODIN, T.N., Ed.), American Institute of Mining, Interscience, New York (1959) 29–39.

[9.696] LI, J.C.M., ORIANI, R.A., DARKEN, L.S., The thermodynamics of stressed solids, Z. Phys. Chem. Neue Folge **49** (1966) 271–279.

[9.697] STEVENS, R.N., DUTTON, R., The Effect of Temperature, Pressure and Concentration Gradients on Diffusion Report No. AECL-3793, Atomic Energy of Canada Limited, Chalk River, ON (1971).

[9.698] EADIE, R.L., TASHIRO, K., HARRINGTON, D., LÉGER, M., The determination of the partial molar volume of hydrogen in zirconium in a simple stress gradient using comparative microcalorimetry, Scr. Metall. Mater. **26** (1992) 231–236.

[9.699] EADIE, R.L., METZGER, D.R., LÉGER, M., The thermal ratchetting of hydrogen in zirconium-niobium — An illustration using finite element modelling, Scr. Metall. Mater. **29** (1993) 335–340.

[9.700] SHEK, G.K., CUI, J., PEROVIC, V., Overload fracture of flaw tip hydrides in Zr-2.5Nb pressure tubes, J. ASTM International **2** (2005) Paper JAI12435.

[9.701] SAGAT, S., NEWMAN, G.W., SCARTH, D.A., “Crack initiation by delayed hydride cracking at sharp notches in Zr-2.5Nb alloys”, Proc. Int. Conf. on Hydrogen Effects on Material Behaviour and Corrosion Deformation Interaction, Moran, 2002 (MOODY, N.R., Ed.), The Minerals, Metals and Materials Society, Warrendale, PA (2003).

[9.702] METZGER, D.R., SAUVÉ, R.G., “A self-induced stress model for simulating hydride formation at flaws”, Proc. ASME Pressure Vessels and Piping Conference, PVP 326, Montreal, 1996, American Society of Mechanical Engineers, New York (1996) 137–142.

[9.703] CHAPUT, H., LEITCH, B., METZGER, D.R., "Effect of creep relaxation on the delayed hydride cracking behaviour of irradiated zirconium 2.5%wt niobium pressure tube material", Proc. ASME Pressure Vessels and Piping Conference, Vancouver, 2006, American Society of Mechanical Engineers, New York (2006) Paper PVP2006-933921.

[9.704] CUI, J., SHEK, G.K., SCARTH, D.A., WANG, Z., Delayed hydride cracking initiation at notches in Zr-2.5Nb alloys, J. Pressure Vessel Technol. **131** (2009).

[9.705] DENBIGH, K.G., The Thermodynamics of the Steady State, Methuen, London (1951).

[9.706] SAWATZKY, A., Hydrogen in Zircaloy-2: Its distribution and heat of transport, J. Nucl. Mater. **2** (1960) 321–328.

[9.707] MARKOWITZ, J.M., The thermal diffusion of hydrogen in alpha-delta Zircaloy-2, Trans. Met. Soc. AIME **221** (1961) 819–824.

[9.708] VARIAS, A.G., MASSIH, A.R., Simulation of hydrogen embrittlement in zirconium alloys under stress and temperature gradients, J. Nucl. Mater. **279** (2000) 273–285.

[9.709] BRUNI, G., LEWIS, B.J., THOMPSON, W.T., Framework model for hydrogen redistribution in Zircaloy sheathing, J. Nucl. Mater. **409** (2011) 33–39.

[9.710] SAWATZKY, A., DUCLOS, M., Thermal diffusion above the eutectoid temperature in titanium-hydrogen type systems, Trans. Met. Soc. AIME **245** (1969) 831–839.

[9.711] SAWATZKY, A., The heat of transport of hydrogen in zirconium alloys, J. Nucl. Mater. **9** (1963) 364.

[9.712] JOVANOVIC, M., et al., Thermal diffusion of hydrogen and hydride precipitation in Zr–Nb pressure tube alloys, Can. Metall. Q. **27** (1988) 323–330.

[9.713] LANNING, D.D., JOHNSON, A.B., Jr., TRIMBLE, D.J., BOYD, S.M., "Corrosion and hydriding of N reactor pressure tubes", Zirconium in the Nuclear Industry: Eigth International Symposium, Proc. ASTM STP 1023, San Diego, 1988 (VAN SWAMM, L.F.P., EUCKEN, C.M., Eds), ASTM International, West Conshohocken, PA (1989) 3–19.

[9.714] SAWATZKY, A., Formation of hydride blisters in zirconium alloy pressure tubes, Can. Metall. Q. **24** (1985) 227–234.

[9.715] LÉGER, M., MOAN, G.D., WALLACE, A.C., WATSON, N.J., "Growth, fracture and non-destructive evaluation of hydride blisters in Zr-2.5 Nb pressure tubes", Zirconium in the Nuclear Industry: Eighth International Symposium, Proc. ASTM STP 1023, San Diego, 1988 (VAN SWAMM, L.F.P., EUCKEN, C.M., Eds), ASTM International, West Conshohocken, PA (1989) 50–65.

[9.716] MOAN, G.D., RODGERS, D.K., Hydride blister features in Zircaloy-2 pressure tubes removed from Pickering Units 1 and 2: A selction of micrographs", The Formation and Characteristics of Hydride Blisters in c.w. Zircaloy-2 Pressure Tubes (PRICE, E.G., Ed.), Report No. AECL-11106, Atomic Energy of Canada Limited, Chalk River, ON (1994) 88–128.

[9.717] LAURSEN, T., et al., The measurement of the deuterium concentration distributions in deuteride blisters on zirconium-alloy pressure tube material, J. Nucl. Mater. **165** (1989) 156–163.

[9.718] VICENTE ALVAREZ, M.A., SANTISTEBAN, J.R., DOMIZZI, G., ALMER, J., Phase and texture analysis of a hydride blister in a Zr-2.5%Nb tube by synchrotron X-ray diffraction, Acta Mater. **59** (2011) 2210–2220.

[9.719] PULS, M.P., Determination of fracture initiation in hydride blisters using acoustic emission, Metall. Mater. Trans. A **19** (1988) 2247–2257.

[9.720] DOMIZZI, G., ENRIQUE, R.A., OVEJERO-GARCÍA, J., BUSCAGLIA, G.C., Blister growth in zirconium alloys: Experimentation and modeling, J. Nucl. Mater. **229** (1996) 36–47.

[9.721] CHEONG, Y.-M., GONG, U.-S., CHOO, K.-N., KIM, S.-S., KIM, Y.-S., Formation and growth of hydride blisters in Zr-2.5Nb pressure tubes, Nucl. Eng. Technol. **33** (2001) 192–200.

[9.722] SINGH, R.N., KISHORE, R., SINHA, T.K., KASHYAP, B.P., Hydride blister formation in Zr-2.5wt%Nb pressure tube alloy, J. Nucl. Mater. **301** (2002) 153–164.

[9.723] BYRNE, T.P., LÉGER, M., MOAN, G.D., "Blister growth in Zircaloy-2 pressure tubes", The Formation and Characteristics of Hydride Blisters in c.w. Zircaloy-2 Pressure Tubes (PRICE, E.G., Ed.), Report AECL-11106, Atomic Energy of Canada Limited, Chalk River, ON (1994) 73–87.

[9.724] BYRNE, T.P., WONG, H., "Worked examples and discussion (on blister formation)", The Formation and Characteristics of Hydride Blisters in c.w. Zircaloy-2 Pressure Tubes (PRICE, E.G., Ed.), Report No. AECL-11106, Atomic Energy of Canada Limited, Chalk River, ON (1994) 176–191.

[9.725] VANDERGLAS, M.L., KIM, Y.J., Stresses due to volumetric expansion of zirconium hydride inclusions, Int. J. Press. Vessels Piping **22** (1986) 177–196.

[9.726] WALLACE, A.C., "Numerical analysis of zirconium hydride blisters in CANDU reactor pressure tubes", Structural mechanics in reactor technology, Vol. C: Fuel Elements and Assemblies, Trans. 9th Int. Conf. on Structural Mechanics in Reactor Technology, Lausanne, 1987, CRC Press, Boca Raton, FL (1987) 87–92.

[9.727] SINGH, R.N., KISHORE, R., SINHA, T.K., BANERJEE, S., KASHYAP, B.P., Stress field estimation around a semi-constrained inclusion and its validation by interpreting hydride platelet orientation around a blister in a Zr-2.5Nb alloy, Mater. Sci. Eng. A **339** (2003) 17–28.

[9.728] SANTISTEBAN, J.R., STEUWER, A., DOMIZZI, G., PEEL, M.J., Determination of residual stresses around blisters in Zr-2.5%Nb pressure tubes, Powder Diffr. **24** Suppl. 1 (2009) S72–S76.

[9.729] BYRNE, T.P., METZGER, D.R., LÉGER, M., "Zirconium hydride blister modelling and the application to the P2-G16 failure", Trans. 11th Int. Conf. on Structural Mechanics in Reactor Technology (SMiRT 11), Tokyo, 1991, Tokyo Society, Tokyo (1991) Paper B13/1.

[9.730] WHITE, A.J., SAWATZKY, A., WOO, C.H., A Computer Model for Hydride-blister Growth in Zirconium Alloys, Report No. AECL-8386, Atomic Energy of Canada Limited, Chalk River, ON (1985).

[9.731] ASHER, R.C., TROWSE, F.W., The distribution of hydrogen in zirconium alloy fuel cladding: The effects of heat flux, J. Nucl. Mater. **35** (1970) 115–121.

[9.732] INTERNATIONAL ATOMIC ENERGY AGENCY, Thermophysical Properties Database of Materials for Light Water Reactors and Heavy Water Reactors, IAEA-TECDOC-1496, IAEA, Vienna (2006).

[9.733] NAGASE, F., UETSUKA, H., "Hydrogen morphology and hydrogen embrittlement of Zircaloy fuel cladding used in NSRR/HBO experiment", Proc. Int. Topical Mtg on LWR Fuel Performance, Portland, 1997, American Nuclear Society, La Grange Park, IL (1997) 677–684.

[9.734] TSUKUDA, Y., et al., "Performance of advanced fuel materials for high burnup", Nuclear Fuel for Today and Tomorrow: Experience and Outlook, TopFuel 2003, Würzburg, Germany, 2003, Inforum, Berlin (2003).

[9.735] MIYASHITA, T., et al., "Corrosion and hydrogen pick-up behaviors of cladding and structural components in BWR high burnup 9×9 lead use assemblies", Int. Topical Mtg on LWR Fuel Performance, San Francisco, 2007, American Nuclear Society, La Grange Park, IL (2007) 401–408.

[9.736] GARDE, A.M., "Enhancement of aqueous corrosion of Zircaloy-4 due to hydride precipitation at the metal-oxide interface", Zirconium in the Nuclear Industry: Ninth International Symposium, Proc. ASTM STP 1132, Kobe, 1990 (EUCKEN, C.M., GARDE, A.M., Eds), ASTM International, West Conshohocken, PA (1991) 566–594.

[9.737] BLAT, M., LEGRAS, L., NOEL, D., AMANRICH, H., "Contribution to a better understanding of the detrimental role of hydrogen on the corrosion rate of Zircaloy-4 cladding materials", Zirconium in the Nuclear Industry: Twelfth International Symposium, Proc. ASTM STP 1354, Toronto, 1998 (SABOL, G.P., MOAN, G.D., Eds), ASTM International, West Conshohocken, PA (2000) 563–591.

[9.738] WAISMAN, J.L., SINES, G., ROBINSON, L.B., Diffusion of hydrogen in titanium alloys due to composition, temperature, and stress gradients, Metall. Trans. **4** (1973) 291–302.

[9.739] WAISMAN, J.L., TOOSKY, R., SINES, G., Uphill diffusion and progressive embrittlement: Hydrogen in titanium, Metall. Trans. A **8** (1977) 1249–1256.

[9.740] ARBORELIUS, J., et al., The effect of duplex cladding outer component tin content on corrosion, hydrogen pick-up, and hydride distribution at very high burnup, J. ASTM International **2** (2005) Paper JAI12411.

[9.741] WATANABE, K., Equilibrium pressures of hydrogen and deuterium dissolved in titanium, zirconium and hafnium at low concentrations, J. Nucl. Mater. **136** (1985) 1–5.

[9.742] KREYNS, P.H., et al., "Embrittlement of reactor core materials", Zirconium in the Nuclear Industry: Eleventh International Symposium, Proc. ASTM STP 1295, Garmisch-Partenkirchen, 1995 (BRADLEY, E.R., SABOL, G.P., Eds), ASTM International, West Conshohocken, PA (1996) 758–782.

[9.743] SPALTHOFF, W., WILHELM, H., "Use of hydrogen getters for prevention of hydrogen embrittlement in zirconium-alloy fuel cans", Applications-Related Phenomena in Zirconium and Its Alloys, ASTM STP 458 (BAROCH, E.F., Ed.), ASTM International, West Conshohocken, PA (1969) 338–344.

[9.744] FRISIUS, F., LAHANN, H.J., MERTINS, H., SPALTHOFF, W., WILLE, P., On the isothermal hydrogen diffusion in Zircaloy–Yttrium combinations, Ber. Bungsenges Phys. Chem. **76** (1972) 1216–1220.

[9.745] WESTLAKE, D.G., Precipitation strengthening in crystals of zirconium-hydrogen alloys containing oxygen as an impurity, Acta Metall. **12** (1964) 1373–1380.

[9.746] MARSHALL, R.P., Influence of fabrication history on stress-oriented hydrides in Zircaloy tubing, J. Nucl. Mater. **24** (1967) 34–48.

[9.747] CHU, H.C., WU, S.K., KUO, R.C., Hydride reorientation in Zircaloy-4 cladding, J. Nucl. Mater. **373** (2008) 319–327.

[9.748] BELL, L.G., DUNCAN, R.G., Hydride Orientation in Zr-2.5%Nb; How it is Affected by Stress, Temperature and Heat-treatment, Report No. AECL-5110, Atomic Energy of Canada Limited, Chalk River, ON (1975).

[9.749] BILLONE, M.C., BURTSEVA, T.A., EINZIGER, R.E., Ductile-to-brittle transition temperature for high-burnup cladding alloys exposed to simulated drying-storage conditions, J. Nucl. Mater. **433** (2013) 431–448.

[9.750] RITTENHOUSE, P.L., PICKLESIMER, M.L., Precipitation of Hydrides in Zircaloy-2 as Affected by Preferred Orientation, Elastic Stress and Hydrogen Content, Report No. ORNL-TM-1239, Oak Ridge National Laboratory, Oak Ridge, TN (1965).

[9.751] PRICE, E.G., Hydride orientation and tensile properties of Zr-2.5 wt.% Nb pressure tubing hydrided while internally pressurized, Can. Metall. Q. **11** (1972) 129–138.

[9.752] KEARNS, J.J., WOODS, C.R., Effect of texture, grain size, and cold work on the precipitation of oriented hydrides in Zircaloy tubing and plate, J. Nucl. Mater. **20** (1966) 241–261.

[9.753] PARRY, G.W., EVANS, W., The effect of strain on the directional precipitation of zirconium hydride in Zircaloy-2, Report No. AECL-1707, Atomic Energy of Canada Limited, Chalk River, ON (1962).

[9.754] HINDLE, E.D., SLATTERY, G.F., The influence of processing variables on the grain structure and hydride orientation in Zircaloy-2 tubing, J. Inst. Metals **94** (1966) 245–249.

[9.755] CHEADLE, B.A., COLEMAN, C.E., LICHT, H., CANDU-PHW pressure tubes: Their manufacture, inspection, and properties, Nucl. Technol. **57** (1982) 413–425.

[9.756] CASKEY, G.R., COLE, G.R., HOLMES, W.G., "Failure of UO_2 fuel tubes by internal hydriding of Zircaloy-2 sheaths", Proc. Symp. on Powder Packed Uranium Dioxide Fuel Elements, CEND-153 II, USA–Euratom, Combustion Engineering, Windsor, CT (1961) Paper IV-E-1.

[9.757] LOUTHAN, M.R., Jr., MARSHALL, R.P., Control of hydride orientation in Zircaloy, J. Nucl. Mater. **9** (1963) 170–184.

[9.758] MARSHALL, R.P., Control of hydride orientation in Zircaloy by fabrication practice, J. Nucl. Mater. **24** (1967) 49–59.

[9.759] SCHELZKE, E., Hydridorientierung in Zircaloy-rohren in Abhängigkeit von Verformung, Textur und Spannungen, J. Nucl. Mater. **30** (1969) 324–336.

[9.760] MISHIMA, Y., OKUBO, T., Effect of thermal cycling on the stress orientation and circumferential ductility in Zircaloy-2, Can. Metall. Q. **11** (1972) 157–164.

[9.761] HARDIE, D., SHANAHAN, M.W., Stress reorientation of hydrides in zirconium-2.5% niobium, J. Nucl. Mater. **55** (1975) 1–13.

[9.762] STEHLE, H., KADEN, W., MANZEL, R., External corrosion of cladding in PWRs, Nucl. Eng. Des. **33** (1975) 155–169.

[9.763] COLEMAN, C.E., “Effect of texture on hydride reorientation and delayed hydrogen cracking in cold-worked Zr-2.5Nb”, Zirconium in the Nuclear Industry: Fifth International Symposium, Proc. ASTM STP 754, Boston, 1980, (FRANKLIN, D.G., Ed.), ASTM International, West Conshohocken, PA (1982) 393–411.

[9.764] LÉGER, M., DONNER, A., The effect of stress on orientation of hydrides in zirconium alloy pressure tube materials, Can. Metall. Q. **24** (1985) 235–243.

[9.765] OOHAMA, T., OKUNISHI, M., SENDA, Y., MURAKAMI, K., SUGANO, M., “Study on hydride re-orientation properties in Zircaloy-4 cladding tube”, NUTHOS-6: Proc. 6th Int. Conf. on Nuclear Thermal Hydraulics, Operation and Safety, Nara, 2004, Atomic Energy Society of Japan, Tokyo (2004) Paper N6P117.

[9.766] SINGH, R.N., KISHORE, R., SINGH, S.S., SINHA, T.K., KASHYAP, B.P., Stress-reorientation of hydrides and hydride embrittlement of Zr-2.5 wt% Nb pressure tube alloy, J. Nucl. Mater. **325** (2004) 26–33.

[9.767] NAGASE, F., FUKETA, T., Influence of hydride re-orientation on BWR cladding rupture under accidental conditions, J. Nucl. Sci. Technol. **41** (2004) 1211–1217.

[9.768] HONG, S.I., LEE, K.W., Stress-induced reorientation of hydrides and mechanical properties of Zircaloy-4 cladding tubes, J. Nucl. Mater. **340** (2005) 203–208.

[9.769] SINGH, R.N., et al., Influence of temperature on threshold stress for reorientation of hydrides and residual stress variation across thickness of Zr-2.5Nb alloy pressure tube, J. Nucl. Mater. **359** (2006) 208–219.

[9.770] DAUM, R.S., MAJUMDAR, S., LIU, Y., BILLONE, M.C., Radial-hydride embrittlement of high-burnup Zircaloy-4 fuel cladding, J. Nucl. Sci. Technol. **43** (2006) 1054–1067.

[9.771] SAKAMOTO, K., NAKATSUKA, M., Stress reorientation of hydrides in recrystallized Zircaloy-2 sheet, J. Nucl. Sci. Technol. **43** (2006) 1136–1141.

[9.772] CHU, H.C., WU, S.K., CHIEN, K.F., KUO, R.C., CHENG, S.C., “Effect of radial hydrides on mechanical properties of Zircaloy-4 cladding”, Proc. Water Reactor Fuel Performance Mtg, Kyoto, 2005, Atomic Energy Society of Japan, Tokyo (2005) 481–497.

[9.773] CHU, H.C., WU, S.K., CHIEN, K.F., KUO, R.C., Effect of radial hydrides on the axial and hoop mechanical properties of Zircaloy-4 cladding, J. Nucl. Mater. **362** (2007) 93–103.

[9.774] ALAM, A.M., HELLWIG, C., Cladding tube deformation test for stress reorientation of hydrides, J. ASTM Int. **5** (2008) Paper JAI101110.

[9.775] AOMI, M., et al., Evaluation of hydride reorientation behavior and mechanical properties for high-burnup and fuel-cladding tubes in interim dry storage, J. ASTM Int. **5** (2008) Paper JAI101262.

[9.776] BUSSER, V., DESQUINES, J., DURIEX, C., BAIETTO-DUBOURG, M.-C., MARDON, J.-P., “Zircaloy-4 cladding hydride reorientation under ring compression test conditions”, Proc. Int. Topical Mtg on LWR Fuel Performance, TopFuel 2009, Paris, 2009, Curran, Red Hook, NY (2009) Paper 2104.

[9.777] COLAS, K.B., MOTTA, A.T., DAYMOND, M.K., KERR, M., ALMER, J.D., Hydride platelet reorientation in zircaloy studied with synchrotron radiation diffraction, Zirconium in the Nuclear Industry: Sixteenth International Symposium, Proc. ASTM STP 1529, Chengdu, 2010 (LIMBÄCK, M., BARBÉRIS, P., Eds), ASTM International, West Conshohocken, PA (2012) 496–522.

[9.778] VALANCE, S., BERTSCH, J., ALAM, A.M., Statistical analysis of hydride reorientation properties in irradiated Zircaloy-2, J. ASTM Int. **8** (2011) Paper JAI102957.

[9.779] HARDIE, D., SHANAHAN, M.W., The effect of residual stresses on hydride orientation in a zirconium-2.5% niobium alloy, J. Nucl. Mater. **50** (1974) 40–46.

[9.780] ELLS, C.E., The stress orientation of hydrides in zirconium alloys, J. Nucl. Mater. **35** (1970) 306–315.

[9.781] PULS, M.P., Effect of Stress on Hydride Reorientation in Zirconium Alloys, Report No. AECL-CONF-657, Atomic Energy of Canada Limited, Chalk River, ON (1985).

[9.782] LI, J.C.M., Appendix to NAKADA, Y., LESLIE, W.C., CHURAY, T.P., Stress-orienting of $Fe_{16}N_2$ precipitates in an Fe-N alloy, Trans. ASM **60** (1967) 223–227.

[9.783] SAUTHOFF, G., Orienting of precipitating Au particles in a FeMoAu alloy by external elastic stress, Z. Metallkd. **66** (1975) 106–109.

[9.784] HAYASHI, H., ETOH, Y., TSUKUDA, Y., SHIMADA, S., SAKURAI, H., “Outside-in failure of BWR segment rods during power ramp tests”, Fuel Failure in Water Reactors: Causes and Mitigation, IAEA-TECDOC-1345, IAEA, Vienna (2003) 148–163.

[9.785] URBANIC, V.F., COX, B., Long-term corrosion and deuteriding behaviour of Zircaloy-2 under irradiation, Can. Metall. Q. **24** (1985) 189–196.

[9.786] SAH, D.N., et al., Post irradiation examination of reactor operated pressure tube S-07 of KAPS-2, J. Nucl. Mater. **383** (2008) 128–131.

[9.787] URBANIC, V.F., WARR, B.D., MANOLESCU, A., CHOW, C.K., SHANAHAN, M.W., Oxidation and deuterium uptake of Zr-2.5Nb pressure tubes in CANDU-PHW reactors, Zirconium in the Nuclear Industry: Eighth International Symposium, Proc. ASTM STP 1023, San Diego, 1988 (VAN SWAM, L.F.P., EUCKEN, C.M., Eds), ASTM International, West Conshohocken, PA (1989) 20–34.

[9.788] ROSS-ROSS, P.A., DUNN, J.T., MITCHELL, A.B., TOWGOOD, G.R., HUNTER, T.A., Some Engineering Aspects of the Investigation into the Cracking of Pressure Tubes in the Pickering Reactors, Report No. AECL-5261, Atomic Energy of Canada Limited, Chalk River, ON (1976).

[9.789] DOMIZZI, G., VIGNA, G., BERMÚDEZ, S., OVEJERO-GARCÍA, J., Hydride distribution around a blister in Zr-2.5Nb pressure tubes, J. Nucl. Mater. **275** (1999) 255–267.

[9.790] BECK, R.L., MUELLER, W.M., "Nuclear metallurgy", Proc. Symp. on Metallic Moderators and Cladding Materials, Vol. VII, AIME, New York (1960) 63–66.

[9.791] BEEVERS, C.J., BARRACLOUGH, K.G., Some observations on the deformation characteristics of bulk polycrystalline zirconium hydrides, Part 1: The deformation and fracture of hydrides based on the δ-phase, J. Mater. Sci. **4** (1969) 518–525.

[9.792] KURODA, M., et al., Influence of precipitated hydride on the fracture behaviour of zircaloy fuel cladding tube, J. Nucl. Sci. Technol. **37** (2000) 670–675.

[9.793] PULS, M.P., SHI, S.-Q., RABIER, J., Experimental studies of mechanical properties of solid zirconium hydrides, J. Nucl. Mater. **336** (2005) 73–80.

[9.794] BEEVERS, C.J., BARRACLOUGH, K.G., Some observations on the deformation characteristics of bulk polycrystalline zirconium hydrides, Part 2: The deformation of ε-hydrides, J. Mater. Sci. **4** (1969) 802–808.

[9.795] XU, J., SHI, S.-Q., Investigation of mechanical properties of ε-zirconium hydride using micro-and nano-indentation techniques, J. Nucl. Mater. **327** (2004) 165–170.

[9.796] MOORE, K.E., YOUNG, W.A., Phase studies of the Zr-H system at high hydrogen concentrations, J. Nucl. Mater. **27** (1968) 316–324.

[9.797] BOWMAN, R.C., Jr., CRAFT, B.D., CANTRELL, J.S., VENTURINI, E.L., Effects of thermal treatments on the lattice properties and electronic structure of ZrH_x, Phys. Rev. B **31** (1985) 5604–5615.

[9.798] SIMPSON, L.A., CANN, C.D., Fracture toughness of zirconium hydride and its influence on the crack resistance of zirconium alloys, J. Nucl. Mater. **87** (1979) 303–316.

[9.799] LANIN, A.G., ZALIVIN, I.M., TURCHIN, V.N., BOJKO, E.B., Mechanical properties of zirconium, titanium and yttrium hydride alloys, Strength Mater. **16** (1984) 869–876.

[9.800] RIESTER, L., BRIDGE, R.J., BREDER, K., Characterization of Vickers, Berkovich, spherical and cube cornered diamond indenters by nanoindentation and SFM, MRS Online Proceedings Library **522** (1998) 45–52.

[9.801] AMBLER, J.F.R., The Effect of Temperature on the Micro-indentation Properties of Zirconium Hydride, Report No. AECL-2538, Atomic Energy of Canada Limited, Chalk River, ON (1966).

[9.802] MATVIENKO, Y.G., A theoretical estimation of fracture toughness of zirconium hydride, J. Mater. Sci. Lett. **19** (2000) 1697–1699.

[9.803] GOGOTSI, G.A., Fracture toughness of ceramics and ceramic composites, Ceram. Int. **29** (2003) 777–784.

[9.804] YOUNG, A.P., SCHWARTZ, C.M., Observations on microcrack formation in hydrogen-embrittled zirconium, Trans. Met. Soc. AIME **212** (1958) 309–10.

[9.805] WESTLAKE, D.G., Initiation and propagation of microcracks in crystals of zirconium-hydrogen alloys, ASM Trans. Q. 5**6** (1963) 1–10.

[9.806] BEEVERS, C.J., Fracture of zirconium and zirconium-hydrogen alloys, Trans. Met. Soc. AIME **233** (1965) 780–786.

[9.807] COLEMAN, C.E., HARDIE, D., Some observations on the fracture characteristics of hydrided α-zirconium, J. Less-Common Met. **10** (1966) 12–21.

[9.808] PULS, M.P., Fracture initiation at hydrides in zirconium, Metall. Trans. A **22** (1991) 2327–2337.

[9.809] MARSHALL, R.P., LOUTHAN, M.R., Jr., Tensile properties of Zircaloy with oriented hydrides, Trans. ASM **56** (1963) 693–700.

[9.810] EVANS, W., PARRY, G.W., The deformation behaviour of Zircaloy-2 containing directionally oriented zirconium hydride precipitates, J. Electrochem. Technol. **4** (1966) 225–231.

[9.811] ÖSTBERG, G., Crack propagation in hydrided Zircaloy-2, Int. J. Fract. Mech. **4** (1968) 95–98.

[9.812] GILL, B.J., BAILEY, J.E., COTTERILL, P., The effects of hydride precipitates on the mechanical properties of zirconium-hydrogen alloys, J. Less-Common Met. **40** (1975) 129–138.

[9.813] CHEADLE, B.A., ELLS, C.E., "Crack initiation in cold-worked Zr-2.5 wt%Nb by delayed hydrogen cracking", Hydrogen in Metals: Proceedings of the 2nd International Congress, Paris, 1977, Pergamon Press, Oxford (1977) Paper 3C8.

[9.814] CANN, C.D., SEXTON, E.E., An electron optical study of hydride precipitation and growth at crack tips in zirconium, Acta Metall. **28** (1980) 1215–1221.

[9.815] SIMPSON, L.A., Criteria for fracture initiation at hydrides in zirconium-2.5 pct niobium alloy, Metall. Trans. A **12** (1981) 2113–2124.

[9.816] PULS, M.P., The influence of hydride size and matrix strength on fracture initiation at hydrides in zirconium alloys, Metall. Trans. A **19** (1988) 1507–1522.

[9.817] CHOUBEY, R., PULS, M.P., Crack initiation at long radial hydrides in Zr-2.5Nb pressure tube material at elevated temperatures, Metall. Mater. Trans. A **25** (1994) 993–1004.

[9.818] KUBO, T., KOBAYASHI, Y., UCHIKOSHI, H., Determination of fracture strength of δ-zirconium hydrides embedded in zirconium matrix at high temperatures, J. Nucl. Mater. **435** (2013) 222–230.

[9.819] SHI, S.-Q., PULS, M.P., Fracture strength of hydride precipitates in Zr-2.5Nb alloys, J. Nucl. Mater. **275** (1999) 312–317.

[9.820] KERR, M., DAYMOND, M.R., HOLT, R.A., ALMER, J.D., Strain evolution of zirconium hydride embedded in a Zircaloy-2 matrix, J. Nucl. Mater. **380** (2008) 70–75.

[9.821] LEITCH, B.W., PULS, M.P., Finite element calculations of the accommodation energy of a misfitting precipitate in an elastic-plastic matrix, Metall. Trans. A **23** (1992) 797–806.

[9.822] DAYTON, R.W., et al., Hydrogen Embrittlement of Zirconium, Report No. BMI-767, US Atomic Energy Commission, Washington, DC (1952).

[9.823] MUDGE, W.L., Effect of Hydrogen on the Embrittlement of Zirconium and Zirconium-tin Alloys, Report No. WAPD-T-20, US Atomic Energy Commission, Washington, DC (1952).

[9.824] MUEHLENKAMP, G.T., SCHWOPE, A.D., Effect of Hydrogen on the Mechanical Properties of Zirconium and Its Tin Alloys, Report No. BMI-845, US Atomic Energy Commission, Washington, DC (1953).

[9.825] COLEMAN, C.E., HARDIE, D., The hydrogen embrittlement of zirconium in slow-bend tests, J. Nucl. Mater. **19** (1966) 1–8.

[9.826] HARDIE, D., The influence of the matrix on the hydrogen embrittlement of zirconium in bend tests, J. Nucl. Mater. **42** (1972) 317–324.

[9.827] FEARNEHOUGH, G.D., COWAN, A., The effect of hydrogen and strain rate on the "ductile-brittle" behaviour of Zircaloy, J. Nucl. Mater. **22** (1967) 137–147.

[9.828] BURTON, H.H., Hydrogen Effects on Zircaloy-2 Tensile Properties, Report No. HW-61077, US Atomic Energy Commission, Germantown, MD (1959).

[9.829] GRANGE, M., BESSON, J., ANDRIEU, E., Anisotropic behavior and rupture of hydrided ZIRCALOY-4 sheets, Metall. Mater. Trans. A **31** (2000) 679–690.

[9.830] ARSENE, S., BAI, J.B., BOMPARD, P., Hydride embrittlement and irradiation effects on the hoop mechanical properties of pressurized water reactor (PWR) and boiling water reactor (BWR) zircaloy cladding tubes, Part 1: Hydride embrittlement in stress-relieved, annealed, and recrystallized zircaloys at 20°C and 300°C, Metall. Mater. Trans. A **34** (2003) 553–566.

[9.831] COLEMAN, C.E., HARDIE, D., The influence of grain size on the tensile properties of hydrided α-zirconium, J. Nucl. Mater. **19** (1966) 201–203.

[9.832] BAI, J.B., FRANÇOIS, D., Some evidence of a brittle-ductile transition of zirconium hydride between 20 and 350°C, J. Nucl. Mater. **187** (1992) 186–189.

[9.833] BAI, J.B., PRIOUL, C., FRANÇOIS, D., Hydride embrittlement in Zircaloy-4 plate, Part 1: Influence of microstructure on the hydride embrittlement in Zircaloy-4 at 200°C and 350°C, Metall. Mater. Trans. A **25** (1994) 1185–1197.

[9.834] WALTERS, G.P., Hydride morphology in stressed zirconium and the influence of specimen size on ductility, J. Electrochem. Technol. **4** (1966) 216–221.

[9.835] WESTLAKE, G.G., The combined effects of oxygen and hydrogen on the mechanical properties of zirconium, Trans. Metall. Soc. AIME **233** (1965) 368–372.

[9.836] MUDGE, W.L., Jr., "Effect of hydrogen on the embrittlement of zirconium and zirconium-tin alloys", Proc. Symp. on Zirconium and Zirconium Alloys, Los Angeles, 1953, American Society for Metals, Metals Park, OH (1953) 146–167.

[9.837] MAKI, H., OOYAMA, M., Plastic deformation and fracture behavior of Zircaloy-2 fuel cladding tubes under biaxial stress, J. Nucl. Sci. Technol. **12** (1975) 423–435.

[9.838] ANDERSSON, T., WILSON, A., "Ductility of zircaloy canning tubes in relation to stress ratio in biaxial testing", Zirconium in the Nuclear Industry: Fourth International Symposium, Proc. ASTM STP 681 Stratford-upon-Avon, 1978 (SCHEMEL, J.H., PAPAZOGLOU, T.P., Eds), ASTM International, West Conshohocken, PA (1979) 60–71.

[9.839] FUKUDA, T., MIHARA, T., AMAYA, M., SUGIYAMA, T., NAGASE, F., "The cladding fracture behaviour under biaxial stress conditions", Fuel Behaviour and Modelling Under Severe Transient and Loss of Coolant Accident (LOCA) Conditions, IAEA-TECDOC-CD-1709, IAEA, Vienna (2013) 77–84.

[9.840] YUNCHANG, F., KOSS, D.A., The influence of multiaxial states of stress on the hydrogen embrittlement of zirconium alloy sheet, Metall. Trans. A **16** (1985) 675–681.

[9.841] HUANG, J.-H., HUANG, S.-P., Effect of hydrogen contents on the mechanical properties of Zircaloy-4, J. Nucl. Mater. **208** (1994) 166–179.

[9.842] PRAT, F., BESSON, J., GRANGE, M., ANDRIEU, E., Behavior and rupture of hydrided ZIRCALOY-4 tubes and sheets, Metall. Trans. A **29** (1998) 1643–1651.

[9.843] WISNER, S.B., ADAMSON, R.B., Combined effects of radiation damage and hydrides on the ductility of Zircaloy-2, Nucl. Eng. Des. **185** (1998) 33–49.

[9.844] WOOD, D.S., WINTON, J., WATKINS, B., Effect of irradiation on the impact properties of hydrided Zircaloy-2 and zirconium-niobium alloy, J. Electrochem. Technol. **4** (1966) 250–258.

[9.845] PICKLES, B.W., Embrittlement of heat-treated Zr-2.5 wt% Nb pressure tubes, Can. Metall. Q. **11** (1972) 139–146.

[9.846] MIN, S.-J., KIM, M.-S., KIM, K.-T., Cooling rate- and hydrogen content-dependent hydride reorientation and mechanical property degradation of Zr-Nb alloy claddings, J. Nucl. Mater. **441** (2013) 306–314.

[9.847] AITCHISON, I., "The effect of orientation of hydride precipitates on the fracture toughness of cold-rolled Zircaloy-2 and 2.5Nb zirconium", Applications-Related Phenomena in Zirconium and Its Alloys, ASTM STP 458 (BAROCH, E.F., Ed.), ASTM International, West Conshohocken, PA (1969) 160–178.

[9.848] DAVIES, P.H., STEARNS, C.P., "Fracture toughness testing of Zircaloy-2 pressure tube material with radial hydrides using direct-current potential drop", Fracture Mechanics, Vol. 17, ASTM STM 905, (UNDERWOOD, J.H., et al., Eds), ASTM International, West Conshohocken, PA (1986) 379–400.

[9.849] COLEMAN, C.E., et al., Minimizing hydride cracking in zirconium alloys, Can. Metall. Q. **24** (1985) 245–250.

[9.850] WALLACE, A.C., SHEK, G.K., LEPIK, O.E., "Effects of hydride morphology on Zr-2.5Nb fracture toughness", Zirconium in the Nuclear Industry: Eighth International Symposium, Proc., ASTM STP 1023, San Diego, 1988 (VAN SWAM, L.F.P., EUCKEN, C.M., Eds), ASTM International, West Conshohocken, PA (1989) 66–88.

[9.851] CHOW, C.K., SIMPSON, L.A., "Analysis of the unstable fracture of a reactor pressure tube using fracture toughness mapping", Case Histories Involving Fatigue and Fracture Mechanics, ASTM STP 918 (HUDSON, C.M., RICH, T.P., Eds), ASTM International, West Conshohocken, PA (1986) 78–101.

[9.852] SIMPSON, L.A., CHOW, C.K., "Effect of metallurgical variables and temperature on the fracture toughness of zirconium alloy pressure tubes", Zirconium in the Nuclear Industry: Seventh International Symposium, Proc. ASTM STP 939, Strasbourg, 1985 (ADAMSON, R.B., VAN SWAM, L.F.P., Eds), ASTM International, West Conshohocken, PA (1987) 579–596.

[9.853] COLEMAN, C.E., et al., "Evaluation of Zircaloy-2 pressure tubes from NPD", Zirconium in the Nuclear Industry: Eighth International Symposium, Proc. ASTM STP 1023, San Diego, 1988 (VAN SWAM, L.F.P., EUCKEN, C.M., Eds), ASTM International, West Conshohocken, PA (1989) 35–49.

[9.854] EDSINGER, K., DAVIES, J.H., ADAMSON, R.B., "Degraded fuel cladding fractography and fracture behavior", Zirconium in the Nuclear Industry: Twelfth International Symposium, Proc. ASTM STP 1354, Toronto, 1998 (SABOL, G.P., MOAN, G.D., Eds), ASTM International, West Conshohocken, PA (2000) 316–339.

[9.855] ERICKSON, W.H., HARDIE, D., The role of hydride precipitate in the fracture of zirconium and its alloys, J. Inst. Met. **93** (1965) 444–446.

[9.856] VELEVA, M., ARSENE, S., RECORD, M.C., BÉCHADE, J.L., BAI, J.B., Hydride embrittlement and irradition effects on the hoop mechanical properties of pressurized water reactor (PWR) and boiling water reactor (BWR) Zircaloy cladding tubes, Part 2: Morphology of hydrides investigated at different magnifications and their interaction with the processes of plastic deformation, Metall. Mater. Trans. A **34** (2003) 567–578.

[9.857] ARSENE, S., BAI, J.B., BOMPARD, P., Hydride embrittlement and irradiation effects on the hoop mechanical properties of pressurized water reactor (PWR) and boiling water reactor (BWR) Zircaloy cladding tubes, Part 3: Mechanical behaviour of hydride in stress-relieved annealed and recrystallized Zircaloys at 20°C and 300°C, Metall. Mater. Trans. A **34** (2003) 553–555.

[9.858] BILBY, B.A., COTTRELL, A.H., SWINDEN, K.H., The spread of plastic yield from a notch, Proc. R. Soc. London. Ser. A Math. Phys. Sci. **272** (1963) 304–314.

[9.859] BILBY, B.A., COTTRELL, A.H., SMITH, E., SWINDEN, K.H., Plastic yielding from sharp notches, Proc. R. Soc. London. Ser. A Math. Phys. Sci. **279** (1964) 1–9.

[9.860] SMITH, E., The Spread of Plasticity from Stress Concentration, Proc. R. Soc. London. Ser. A Math. Phys. Sci. **285** (1965) 46–57.

[9.861] CHAN, K.S., A fracture model for hydride-induced embrittlement, Acta Metall. Mater. **43** (1995) 4325–4335.

[9.862] NILSSON, K.-F., JAKŠIĆ, N., VOKÁL, V., An elasto-plastic fracture mechanics based model for assessment of hydride embrittlement in zircaloy cladding tubes, J. Nucl. Mater. **396** (2010) 71–85.

[9.863] GRANGE, M., BESSON, J., ANDRIEU, E., An anistropic Gurson type model to represent the ductile rupture of hydride Zircaloy-4 sheets, Int. J. Fract. **105** (2000) 273–293.

[9.864] GURSON, A.L., Continuum theory of ductile rupture by void nucleation and growth, Part 1: Yield criteria and flow rules for porous ductile media, J. Eng. Mater. Technol. **99** (1977) 2–15.

[9.865] TVERGAARD, V., NEEDLEMAN, A., Analysis of the cup-cone fracture in a round tensile bar, Acta Metall. **32** (1984) 157–169.

[9.866] ROUSSELIER, G., Ductile fracture models and their potential in local approach of fracture, Nucl. Eng. Des. **105** (1987) 97–111.

[9.867] KESSLER, H.D., SHERMAN, R.G., SULLIVAN, J.F., Hydrogen affects critical properties in commercial titanium, J. Met. **7** (1955) 242–246.

[9.868] WEINSTEIN, D., HOLTZ, F.C., Susceptibility of zirconium and zirconium alloys to delayed failure hydrogen embrittlement, Trans. Am. Soc. Metals **57** (1964) 284–293.

[9.869] ÖSTBERG, G., Some observations on the ductility of zirconium alloys, with special reference to the effect of hydrogen, J. Inst. Met.**93** (1964–65) 223–228.

[9.870] PERRYMAN, E.C.W., Pickering pressure tube cracking experience, Nucl. Energy **17** (1977) 95–105.

[9.871] CAUSEY, A.R., URBANIC, V.F., COLEMAN, C.E., In-reactor oxidation of crevices and cracks in cold-worked Zr-2.5 wt% Nb, J. Nucl. Mater. **71** (1977) 25–35.

[9.872] CHEADLE, B.A., ELLS, C.E., "Crack initiation in cold-worked Zr-2.5 wt. per cent Nb by delayed hydrogen cracking", Hydrogen in Metals: Proceedings of the 2nd International Congress, Paris, 1977, Pergamon Press, Oxford (1977) Paper 3C8.

[9.873] WINTON, J., MURGATROYD, R.A., The effect of variations in composition and heat treatment on the properties of Zr-Nb alloys, J. Electrochem. Technol. **4** (1966) 358–365.

[9.874] DUNN, J.T., JACKMAN, A.H., Replacement of a Cracked Pressure Tube in Bruce GS Unit 2, Report No. AECL-7537, Atomic Energy of Canada Limited, Chalk River, ON (1982).

[9.875] DUNN, J.T., KAKARIA, B.K., GRAHAM, J., JACKMAN, A.H., CANDU-PHW Fuel Channel Replacement Experience, Report No. AECL-7538, Atomic Energy of Canada Limited, Chalk River, ON (1982).

[9.876] CHEADLE, B.A., COLEMAN, C.E., AMBLER, J.F.R., "Prevention of delayed hydride cracking in zirconium alloys", Zirconium in the Nuclear Industry: Seventh International Symposium, Proc. ASTM STP 939, Strasbourg, 1985 (ADAMSON, R.B., VAN SWAM, L.F.P., Eds), ASTM International, West Conshohocken, PA (1987) 224–240.

[9.877] RODGERS, D.K., COLEMAN, C.E., HOSBONS, R.R., "Fracture of a core component in a nuclear reactor", Failure Analysis: Techniques and Applications, ASM International, Materials Park, OH (1992) 159–166.

[9.878] URBANIC, V.F., McDOUGALL, G.M., WHITE, A.J., BAHURMUZ, A.A., "Deuterium ingress at rolled joints in CANDU reactors", Proc. Int. Conf. on Expanded and Rolled Joint Technology, Toronto, 1993, Canadian Nuclear Society, Toronto, ON (1993).

[9.879] PLATONOV, P.A., et al., "The study of cause of cracking in zirconium alloy channel tubes", poster presented at Zirconium in the Nuclear Industry: Eighth International Symposium, Proc. ASTM STP 1023, San Diego, 1988.

[9.880] FIELD, G.J., DUNN, J.T., CHEADLE, B.A., Analysis of the pressure tube failure at Pickering NGS "A" Unit 2 Nuclear Systems Department, Can. Metall. Q. **24** (1985) 181–188.

[9.881] JONSSON, A., HALLSTADIUS, L., GRAPENGIESSER, B., LYSELL, G., "Failure of a barrier rod in Oskarshamn-3", Proc. Int. Topical Mtg on LWR Fuel Performance, Fuel for the 90's, Avignon, 1991, American Nuclear Society, La Grange Park, IL (1991) 371–377.

[9.882] SCHRIRE, D., et al., "Secondary defect behaviour in ABB BWR fuel", Proc. Int. Topical Mtg on LWR Fuel Performance, West Palm Beach, 1994, American Nuclear Society, La Grange Park, IL (1994) 398–409.

[9.883] ARMIJO, J.S., "Performance of failed BWR fuel", Proc. Int. Topical Mtg on LWR Fuel Performance, West Palm Beach, 1994, American Nuclear Society, La Grange Park, IL (1994) 410–422.

[9.884] CHEADLE, B.A., DAVIES, P.H., FLOYD, M.R., GRIFFITHS, M., Axial Splitting of Zircaloy Fuel Cladding: A Review of Occurrences, Relevant Microstructural Features and Potential Mechanical Tests to Measure Failure Resistance, Report No. RC-1792, Atomic Energy of Canada Limited, Chalk River, ON (1997).

[9.885] CLAYTON, J.C., "Internal hydriding in irradiated defected Zircaloy fuel rods", Zirconium in the Nuclear Industry: Eighth International Symposium, Proc. ASTM STP 1023, San Diego, 1988 (VAN SWAM, L.F.P., EUCKEN, C.M., Eds), ASTM International, West Conshohocken, PA (1989) 266–288.

[9.886] LYSELL, G., GRIGORIEV, V., "Characteristics of axial splits in failed BWR fuel rods", Proc. 9th Conf. on Environment Degradation of Materials in Nuclear Power Systems — Water Reactors, Newport Beach, 1999, The Minerals, Metals and Materials Society, Warrendale, PA (1999) 193–199.

[9.887] EFSING, P., PETTERSSON, K., "Delayed hydride cracking in irradiated zircaloy cladding", Zirconium in the Nuclear Industry: Twelfth International Symposium, Proc. ASTM STP 1354, Toronto, 1998 (SABOL, G.P., MOAN, G.D., Eds), ASTM International, West Conshohocken, PA (2000) 340–355.

[9.888] EDSINGER, K., "A review of fuel degradation in BWRs", Proc. Int. Topical Mtg on LWR Fuel Performance, Park City, American Nuclear Society, La Grange Park, IL (2000) 523–540.

[9.889] SHIMADA, S., ETOH, E., HAYASHI, H., TUKUTA, Y., A metallographic and fractographic study of outside-in cracking caused by power ramp tests, J. Nucl. Mater. **327** (2004) 97–113.

[9.890] SAKAMOTO, K., NAKATSUKA, M., HIGUCHI, T., "Simulation of cracking during outside-in type failure of high burn-up fuel cladding tubes", paper presented at Water Reactor Fuel Performance Mtg, Seoul, 2008, Paper 8009.

[9.891] OGATA, K., BABA, T., KAMIMURA, K., ETOH, Y., ITO, K., "Separate effects of factors affecting outside-in cracking of high burnup fuel cladding", paper presented at Water Reactor Fuel Performance Mtg, Seoul, 2008, Paper 8130.

[9.892] OGATA, K., et al., "Conditions to cause cladding failure by hydrogen-induced cracking", Int. Topical Mtg on LWR Fuel Performance, TopFuel 2013, Charlotte, 2013, American Nuclear Society, La Grange Park, IL (2013) 456–461.

[9.893] SAKAMOTO, K., NAKATSUKA, M., HIGUCHI, T., ITO, K., "Role of radial temperature gradient in outside-in type failure of high burn-up fuel cladding tubes during power ramp tests", Proc. Int. Topical Mtg on LWR Fuel Performance, TopFuel 2009, Paris, 2009, Curran, Red Hook, NY (2009) Paper 2076.

[9.894] ALVAREZ HOLSTON, A.-M., et al., "A combined approach to predict the sensitivity of fuel cladding to hydrogen-induced failures during power ramps", Proc. Int. LWR Fuel Performance Mtg, Orlando, 2010, American Nuclear Society, La Grange Park, IL (2010) Paper 127.

[9.895] UNNIKRISHNAN, K., et al., "Observation of delayed hydride cracking in PHWR fuel assembly", Proc. Int. Conf. on CANDU Fuel, Ottawa, 2008, Canadian Nuclear Society, Toronto, ON (2008).

[9.896] SIMPSON, C.J., ELLS, C.E., Delayed hydrogen embrittlement in Zr-2.5wt % Nb, J. Nucl. Mater. **52** (1974) 289–295.

[9.897] COLEMAN, C.E., et al., "Mitigation of harmful effects of welds in zirconium alloy components", Zirconium in the Nuclear Industry: Tenth International Symposium, Proc. ASTM STP 1245, Baltimore, 1993 (GARDE, A.M., BRADLEY, E.R., Eds), ASTM International, West Conshohocken, PA (1994) 264–284.

[9.898] PLATONOV, P.A., et al., “A review of investigation of RBMK fuel channels: Control and protection of rod channels for the 15 years of operation”, poster presented at Zirconium in the Nuclear Industry: 10th Int. Symp., Baltimore, MD, 1993.

[9.899] KUBO, T., et al., In-situ scanning electron microscope observation and finite element analysis of delayed hydride cracking propagation in Zircaloy-2 fuel cladding tubes, J. ASTM Int. **8** (2011) Paper JAI102960.

[9.900] McRAE, G.A., COLEMAN, C.E., LEITCH, B.W., The first step for delayed hydride cracking in zirconium alloys, J. Nucl. Mater. **396** (2010) 130–143.

[9.901] COLEMAN, C.E., et al., Measurement of rates of delayed hydride cracking (DHC) in Zr-2.5 Nb alloys — An IAEA coordinated research project, J. ASTM Int. **5** (2008) Paper JAI101091.

[9.902] KIM, Y.S., Driving force for delayed hydride cracking of zirconium alloys, Met. Mater. Int. **11** (2005) 29–38.

[9.903] BLOMBERG, G., LYSELL, G., SCHRIRE, D., ANGHEL, C., SCHNEIDER, R., “Post-irradiation examination of a failed BWR fuel rod from Forsmark I”, Proc. Int. Topical Mtg on LWR Fuel Performance, TopFuel 2013, Charlotte, 2013, American Nuclear Society, La Grange Park, IL (2013) 433–441.

[9.904] DUTTON, R., NUTTALL, K., PULS, M.P., SIMPSON, L.A., Mechanisms of hydrogen induced delayed cracking in hydride forming materials, Metall. Trans. A **8** (1977) 1553–1562.

[9.905] COLEMAN, C.E., AMBLER, J.F.R., “Susceptibility of zirconium alloys to delayed hydrogen cracking”, Zirconium in the Nuclear Industry: Third International Symposium, Proc. ASTM STP 633, Quebec City, 1976 (LOWE, A.L., Jr., PARRY, G.W., Eds), ASTM International, West Conshohocken, PA (1977) 589–607.

[9.906] COLEMAN, C.E., Acoustic Emission from Zirconium Alloys During Mechanical and Fracture, Report No. AECL-9111, Atomic Energy of Canada Limited, Chalk River, ON (1986).

[9.907] SHEK, G.K., et al., Hydride morphology and striation formation during delayed hydride cracking in Zr-2.5% Nb, J. Nucl. Mater. **231** (1996) 221–230.

[9.908] LIN, G., SKRZYPEK, S., LI, D., EADIE, R.L., Monitoring Crack Advance Using Acoustic Emission and Combined Acoustic Emission and Potential Drop in Zr-2.5% Nb, J. Test. Eval. **26** (1998) 15–25.

[9.909] SHALABI, A.F., MENELEY, D.A., Initiation of delayed hydride cracking in zirconium-2.5 wt% niobium, J. Nucl. Mater. **173** (1990) 313–320.

[9.910] YAN, D., EADIE, R.L., The critical length of the hydride cluster in delayed hydride cracking of Zr-2.5wt% Nb, J. Mater. Sci. **35** (2000) 5667–5672.

[9.911] SHI, S.-Q., LIAO, M., PULS, M.P., Modelling of time-dependent hydride growth at crack tips in zirconium alloys, Model. Simul. Mater. Sci. Eng. **2** (1994) 1065–1078.

[9.912] SHI, S.-Q., PULS, M.P., “Computer modelling of hydride growth and fracture at a crack tip under temperature transients in zirconium alloys”, Proc. Int. Conf. on Modelling and Simulation in Metallurgical Engineering and Materials Science, Beijing, 1996 (YU, Z., XIAO, Z., XIE, X., Eds), Metallurgical Industry Press, Beijing (1996).

[9.913] SHI, S.-Q., Diffusion-controlled hydride growth near crack tip in zirconium under temperature transients, J. Nucl. Mater. **275** (1999) 318–323.

[9.914] LUFRANO, J., SOFRONIS, P., BIRNBAUM, H.K., Modeling of hydrogen transport and elastically accommodated hydride formation near a crack tip, J. Mech. Phys. Solids **44** (1996) 179–205.

[9.915] SIMPSON, L.A., PULS, M.P., The effects of stress, temperature and hydrogen content on hydride-induced crack growth in Zr-2.5 pct Nb, Metall. Trans. A **10** (1979) 1093–1105.

[9.916] COLEMAN, C.E., Susceptibility of Cold-worked Zirconium-2.5 wt% Niobium Alloy to Delayed Hydrogen Cracking, Report No. AECL-5260, Atomic Energy of Canada Limited, Chalk River, ON (1976).

[9.917] HUANG, F.H., MILLS, W.J., Delayed hydride cracking behavior for Zircaloy-2 tubing, Metall. Trans. A **22** (1991) 2049–2060.

[9.918] EFSING, P., PETTERSSON, K., “The influence of temperature and yield strength on delayed hydride cracking in hydrided Zircaloy-2”, Zirconium in the Nuclear Industry: Eleventh International Symposium, Proc. ASTM STP 1295, Garmisch-Partenkirchen, 1995 (BRADLEY, E.R., SABOL, G.P., Eds), ASTM International, West Conshohocken, PA (1996) 394–404.

[9.919] GRIGORIEV, V., JAKOBSSON, R., Delayed hydrogen cracking velocity and J-integral measurements on irradiated BWR cladding, Zirconium in the Nuclear Industry: Fourteenth International Symposium, Proc. ASTM STP 1467, Stockholm, 2004 (RUDLING, P., KAMMENZIND, B., Eds), ASTM International, West Conshohocken, PA (2005) 711–728.

[9.920] KUBO, T., KOBAYASHI, Y., UCHIKOSHI, H., Measurement of delayed hydride cracking propagation rate in the radial direction of Zircaloy-2 cladding tubes, J. Nucl. Mater. **427** (2012) 18–29.

[9.921] SAGAT, S., COLEMAN, C.E., GRIFFITHS, M., WILKINS, B.J.S., “The effect of fluence and irradiation temperature on delayed hydride cracking in Zr-2.5 Nb”, Zirconium in the Nuclear Industry: Tenth International Symposium, Proc. ASTM STP 1245, Baltimore, 1993 (GARDE, A.M., BRADLEY, E.R., Eds), ASTM International, West Conshohocken, PA (1994) 35–61.

[9.922] RODGERS, D.K., et al., In-reactor performance of pressure tubes in CANDU reactors, J. Nucl. Mater. **383** (2008) 22–27.

[9.923] SHI, S.-Q., PULS, M.P., Criteria for fracture initiation at hydrides in zirconium alloys I. Sharp crack tip, J. Nucl. Mater. **208** (1994) 232–242.

[9.924] SHI, S.-Q., PULS, M.P., Dependence of the threshold stress intensity factor on hydrogen concentration during delayed hydride cracking in zirconium alloys, J. Nucl. Mater. **218** (1994) 30–36.

[9.925] YAN, D., EADIE, R.L., Calculation of the delayed hydride cracking velocity vs. K_I curve for Zr-2.5Nb by critical hydride cluster length, J. Mater. Sci. **37** (2002) 5299–5303.

[9.926] SMITH, E., The fracture of hydride material during delayed hydride cracking (DHC) crack growth, Int. J. Press. Vessels Piping **61** (1995) 1–7.

[9.927] WÄPPLING, D., MASSIH, A.R., STÅHLE, P., A model for hydride-induced embrittlement in zirconium-based alloys, J. Nucl. Mater. **249** (1997) 231–238.

[9.928] KIM, Y.S., MATVIENKO, Y.G., CHEONG, Y.M., KIM, S.S., KWON, S.C., A model of the threshold stress intensity factor, K_{IH}, for delayed hydride cracking of Zr-2.5Nb alloy, J. Nucl. Mater. **278** (2000) 251–257.

[9.929] ZHENG, X.J., LUO, L., METZGER, D.R., SAUVE, R.G., A unified model of hydride cracking based on elasto-plastic energy release rate over a finite crack extension, J. Nucl. Mater. **218** (1995) 174–188.

[9.930] ZHENG, X.J., METZGER, D.R., GLINKA, G., DUBEY, R.N., “Modelling of hydride cracking”, Proc. ASME Pressure Vessels and Piping Conference, Montreal, 1996, American Society of Mechanical Engineers, New York (1996) 181–186.

[9.931] COLEMAN, C.E., et al., The effect of microstructure on delayed hydride cracking behavior of Zircaloy-4 fuel cladding — An IAEA coordinated research program, Zirconium in the Nuclear Industry: Sixteenth International Symposium, Proc. ASTM STP 1529, Chengdu, 2010 (LIMBÄCK, M., BARBÉRIS, P., Eds), ASTM International, West Conshohocken, PA (2012) 544–574.

[9.932] AMBLER, J.F.R., COLEMAN, C.E., “Acoustic emission during delayed hydrogen cracking in Zr-2.5 wt% Nb alloy”, Hydrogen in Metals: Proceedings of the 2nd International Congress, Paris, 1977, Pergamon Press, Oxford (1977) Paper 3C10.

[9.933] AMBLER, J.F.R., “Effect of direction of approach to temperature on the delayed hydrogen cracking behavior of cold-worked Zr-2.5Nb”, Zirconium in the Nuclear Industry: Sixth International Symposium, Proc. ASTM STP 824, Vancouver, 1982 (FRANKLIN, D.G., ADAMSON, R.B., Eds), ASTM International, West Conshohocken, PA (1984) 653–674.

[9.934] SHEK, G.K., GRAHAM, D.B., “Effects of loading and thermal maneuvers on delayed hydride cracking in Zr-2.5 Nb alloys”, Zirconium in the Nuclear Industry: Eighth International Symposium, Proc. ASTM STP 1023, San Diego, 1988 (VAN SWAM, L.F.P., EUCKEN, C.M., Eds), ASTM International, West Conshohocken, PA (1989) 89–110.

[9.935] COLEMAN, C.E., SAGAT, S., SHEK, G.K., GRAHAM, D.B., DURAND, M.A., Locating a leaking crack by safe stimulation, Int. J. Press. Vessels Piping **43** (1990) 187–204.

[9.936] YAN, D., SUN, S., EADIE, R.L., SHEK, G.K., SEAHRA, H., The delayed hydride cracking avoidance manoeuvre for Zr-2.5 Nb pressure tube alloy, Int. J. Press. Vessels Piping **77** (2000) 531–538.

[9.937] CIRIMELLO, P., DOMIZZI, G., HADDAD, R., Influence of metallurgical variables on delayed hydride cracking in Zr-Nb pressure tubes, J. Nucl. Mater. **350** (2006) 135–146.

[9.938] SHEK, G.K., METZGER, D.R., “Effect of hydrogen concentration on the threshold stress intensity factor for delayed hydride cracking in Zr-2.5Nb pressure tubes”, Proc. ASME Pressure Vessel and Piping Conference, Baltimore, 2011, American Society of Mechanical Engineers, New York (2011) 1287–1295.

[9.939] RESTA LEVI, M., PULS, M.P., “DHC behaviour of irradiated Zr-2.5Nb pressure tubes up to 365ºC”, Proc. 18th Int. Conf. Structural Mechanics in Reactor Technology, SMiRT 18, Beijing, 2005, International Association for Structural Mechanics in Reactor Technology, Raleigh, NC (2005) Paper G10-3.

[9.940] SMITH, R.R., EADIE, R.L., High temperature limit for delayed hydride cracking, Scr. Metall. **22** (1988) 833–836.

[9.941] SAGAT, S., PULS, M.P., “Temperature limit for delayed hydride cracking in Zr-2.5Nb alloys”, Proc. 17th Int. Conf. Structural Mechanics in Reactor Technology, SMiRT 17, Prague, 2003, International Association for Structural Mechanics in Reactor Technology, Raleigh, NC (2003) Paper G06-4.

[9.942] COLEMAN, C.E., et al., Delayed hydride cracking in Zircaloy-4 fuel cladding — An IAEA coordinated research program, Nucl. Eng. Technol. **41** (2009) 171–178.

[9.943] INTERNATIONAL ATOMIC ENERGY AGENCY, Evaluation of Conditions for Hydrogen Induced Degradation of Zirconium Alloys during Fuel Operation and Storage, IAEA-TECDOC-1781, IAEA, Vienna (2015).

[9.944] MARKELOV, V., GASEV, A., KOTOV, P., NOVIKOV, V., “Temperature dependence of delayed hydride cracking velocity in fuel cladding made from zirconium alloys of different composition”, Trans. Conf. on TopFuel Reactor Fuel Performance, Manchester, 2012, European Nuclear Society, Brussels (2012) 346–355.

[9.945] GRIGORIEV, V., et al., “Experimental studies of DHC of unirradiated and irradiated fuel rod cladding and implications to in-pile operation and dry storage conditions”, Zirconium in the Nuclear Industry: Seventeenth International Symposium, Proc. ASTM STP 1543, Hyderabad, 2013 (COMSTOCK, B., BARBÉRIS, P., Eds), ASTM International, West Conshohocken, PA (2015).

[9.946] SIMPSON, L.A., CANN, C.D., The effect of microstructure on rates of delayed hydride cracking in Zr-2.5% Nb alloy, J. Nucl. Mater. **126** (1984) 70–73.

[9.947] COLEMAN, C.E., SAGAT, S., AMOUZOUVI, K.F., Control of Microstructure to Increase the Tolerance of Zirconium Alloys to Hydride Cracking, Report No. AECL-9524, Atomic Energy of Canada Limited, Chalk River, ON (1987).

[9.948] JOVANOVIĆ, M.J., et al., The effect of annealing on hardness, microstructure and delayed hydride cracking in Zr-2.5Nb pressure tube material, Mater. Charact. **47** (2001) 259–268.

[9.949] OH, J.Y., KIM, I.S., KIM, Y.S., A normalization method for relationship between yield stress and delayed hydride cracking velocity in Zr-2.5Nb alloys, J. Nucl. Sci. Technol. **37** (2000) 595–600.

[9.950] BICKEL, G.A., GRIFFITHS, M., CHAPUT, H., BUYERS, A., COLEMAN, C.E., "Modeling irradiation damage in Zr-2.5Nb and its effects on delayed hydride cracking growth rate", Zirconium in the Nuclear Industry: Seventeenth International Symposium, Proc. ASTM STP 1543, Hyderabad, 2013 (COMSTOCK, R., BARBÉRIS, P., Eds), ASTM International, West Conshohocken, PA (2015), 800–829.

[9.951] PAN, Z.L., et al., Effect of irradiation on the fracture properties of Zr-2.5Nb pressure tubes at the end of design life, J. ASTM International **2** (2005) Paper JAI12436.

[9.952] MILLS, J.W., HUANG, F.H., Delayed hydride cracking behavior for Zircaloy-2 plate, Eng. Fract. Mech. **39** (1991) 241–257.

[9.953] KIM, S.S., KWON, S.C., KIM, Y.S., The effect of texture variation on delayed hydride cracking behavior of Zr-2.5%Nb plate, J. Nucl. Mater. **273** (1999) 52–59.

[9.954] RESTA LEVI, M., SAGAT, S., The Effect of Texture on Delayed Hydride Cracking in Zr-2.5Nb Alloy, Report No. AECL-12045, Atomic Energy of Canada Limited, Chalk River, ON (1999).

[9.955] COLEMAN, C.E., CHEADLE, B.A., CANN, C.D., THEAKER, J.R., "Development of pressure tubes with service life greater than 30 years", Zirconium in the Nuclear Industry: Eleventh International Symposium, Proc. ASTM STP 1295, Garmisch-Partenkirchen, 1995 (BRADLEY, E.R., SABOL, G.P., Eds), ASTM Int., West Conshohocken, PA (1996) 884–898.

[9.956] KIM, S.S., KIM, Y.S., K_{IH} in radial textured Zr-2.5%Nb pressure tube, J. Nucl. Mater. **279** (2000) 286–292.

[9.957] SAGAT, S., CHOW, C.K., PULS, M.P., COLEMAN, C.E., Delayed hydride cracking in zirconium alloys in a temperature gradient, J. Nucl. Mater. **279** (2000) 107–117.

[9.958] SAKAMOTO, K., NAKATSUKA, M., HIGUCHI, T., BARBÉRIS, P., DEAN, S.W., Simulation of outside-in cracking in boiling water reactor fuel cladding tubes under power ramp, J. ASTM Int. **7** (2010) Paper JAI102938.

[9.959] NUTTALL, K., "Some aspects of slow crack growth in hydrided Zr-2.5% Nb alloys", Proc. Effect of Hydrogen on Behavior of Materials (THOMPSON, A.W., BERNSTEIN, I.M., Eds), Metallurgical Society of AIME, New York (1976) 441–452.

[9.960] NUTTALL, K., RAGOWSKI, A.J., Some fractographic aspects of hydrogen-induced delayed cracking in Zr-2.5 wt% Nb alloys, J. Nucl. Mater. **80** (1979) 279–290.

[9.961] AMOUZOUVI, K.F., CLEGG, L.J., Effect of heat treatment on delayed hydride cracking in Zr-2.5 Wt Pct Nb, Metall. Trans. A **18** (1987) 1687–1694.

[9.962] TIFFANY, C.F., MASTERS, J.N., "Applied fracture mechanics", Fracture Toughness Testing and Its Applications, ASTM STP 381 (BROWN, W.F., Jr., Ed.), ASTM International, West Conshohocken, PA (1965) 249–277.

[9.963] COLEMAN, C.E., Delayed Hydride Cracking Considerations Relevant to Spent Nuclear Fuel Storage, Report No. EPRI-1022921, Electric Power Research Institute, Palo Alto, CA (2011).

[9.964] SAGAT, S., SHI, S.-Q., PULS, M.P., Crack initiation criterion at notches in Zr-2.5Nb alloys, Mater. Sci. Eng. A **176** (1994) 237–247.

[9.965] SHI, S.-Q., PULS, M.P., SAGAT, S., Criteria of fracture initiation at hydrides in zirconium alloys II. Shallow notch, J. Nucl. Mater. **208** (1994) 243–250.

[9.966] SCARTH, D.A., SMITH, E., Developments in flaw evaluation for CANDU reactor Zr-Nb pressure tubes, J. Press. Vessel Technol. **123** (2001) 41–48.

[9.967] McKINNON, M.A., STEWART, L., "Spent nuclear fuel integrity during dry storage", Storage of Spent Fuel from Power Reactors, IAEA-TECDOC-1089, IAEA, Vienna (1999) 297–302.

[9.968] COLEMAN, C.E., SIMPSON, L.A., Evaluation of a Leaking Crack in an Irradiated CANDU Pressure Tube, Report No. AECL-9733, Atomic Energy of Canada Limited, Chalk River, ON (1988).

[9.969] MOAN, G.D., et al., Leak-before-break in the pressure tubes of CANDU reactors, Int. J. Press. Vessels Piping **43** (1990) 1–21.

[9.970] PARK, Y.-W., CHUNG, Y.-K., Leak-before-break assessment of CANDU pressure tube considering leak detection capability, Nucl. Eng. Des. **191** (1999) 205–216.

[9.971] WALKER, J.R., A probabilistic approach to leak-before-break in CANDU pressure tubes, Int. J. Press. Vessels Piping **43** (1990) 229–239.

[9.972] PULS, M.P., et al., A probabilistic method for leak-before-break analysis of CANDU reactor pressure tubes, Nucl. Eng. Des. **185** (1998) 241–248.

[9.973] KOIKE, M.H., TAKAHASHI, T., BABA, H., Leak-before-break experiments on heat-treated Zr-2.5 wt% Nb pressure tubes, Int. J. Press. Vessels Piping **43** (1990) 39–56.

[9.974] DUNDULIS, G., JANULIONIS, R., GRYBENAS, A., MAKAREVICIUS, V., Application of "leak before break" assessment for pressure tube in delayed hydride cracking, J. Disaster Res. **5** (2010) 378–384.

[9.975] LANGFORD, W.J., "Metallurgical properties of cold-worked Zircaloy-2 pressure tubes irradiated under CANDU-PHW power reactor conditions", Irradiation Effects on Structural Alloys for Nuclear Reactor Applications, ASTM STP 484 (BEMENT, A.L., Ed.), ASTM International, West Conshohocken, PA (1970) 259–285.

[9.976] LANGFORD, W.J., MOODER, L.E.J., Fracture behaviour of zirconium alloy pressure tubes for Canadian nuclear power reactors, Int. J. Press. Vessels Piping **6** (1978) 275–310.

[9.977] LANGFORD, W.J., MOODER, L.E.J., Metallurgical properties of irradiated cold-worked Zr-2.5 wt% Nb pressure tubes, J. Nucl. Mater. **39** (1971) 292–302.

[9.978] WILKINS, B.J.S., BARRIE, J.N., ZINK, R.J., Slit-burst Testing of Cold-worked Zr-2.5 wt.% Nb Pressure Tubing for CANDU-PHW Reactors, Report No. AECL-6195, Atomic Energy of Canada Limited, Chalk River, ON (1978).

[9.979] COLEMAN, C.E., WILLS, C.A., Regression Analysis of Slit Burst Test Data for Cold-worked Zr-2.5 wt% Nb Pressure, Report No. CRNL-2501, Atomic Energy of Canada Limited, Chalk River, ON (1983).

[9.980] ST LAWRENCE, S., COLEMAN, C.E., "Upper shelf fracture behaviour of Zr-2.5Nb pressure tube material", paper presented at Congr. on Nuclear Materials, Karlsruhe, 2010.

[9.981] RODGERS, D.K., et al., In-reactor performance of pressure tubes in CANDU reactors, J. Nucl. Mater. **383** (2008) 22–27.

[9.982] SIMPSON, L.A., CHOW, C.K., DAVIES, P.H., Standard Test Method for Fracture Toughness of CANDU Pressure Tubes, Report No. COG-89-110-1, Atomic Energy of Canada Limited, Chalk River, ON (1989).

[9.983] DAVIES, P.H., SHEWFELT, R.S.W., "Link between results of small- and large-scale toughness tests on irradiated Zr-2.5Nb pressure tube material", Zirconium in the Nuclear Industry: Eleventh International Symposium, Proc. ASTM STP 1295, Garmisch-Partenkirchen, 1995 (BRADLEY, E.R., SABOL, G.P., Eds), ASTM International West Conshohocken, PA (1996) 492–517.

[9.984] DAVIES, P.H., "Predicting crack instability behaviour of burst tests from small specimens for irradiated Zr-2.5Nb pressure tubes", Fatigue and Fracture Mechanics, Vol. 28, ASTM STP 1321 (UNDERWOOD, J.H., MacDONALD, B.D., MITCHELL, M.R., Eds), ASTM International, West Conshohocken, PA (1997) 535–561.

[9.985] DAVIES, P.H., SHEWFELT, R.S.W., "Size, geometry, and material effects in fracture toughness testing of irradiated Zr-2.5Nb pressure tube material", Zirconium in the Nuclear Industry: Twelfth International Symposium, Proc. ASTM STP 1354, Toronto, 1998 (SABOL, G.P., MOAN, G.D., Eds), ASTM International, West Conshohocken, PA (2000) 356–376.

[9.986] LEITCH, B.W., "Fracture analyses of an internally pressurized tube containing an axial, through-wall crack", Fatigue and Fracture Mechanics, Vol. 29, ASTM STP 1332 (PANONTIN, T.L., SHEPPARD, S.D., Eds), ASTM International, West Conshohocken, PA (1999) 830–850.

[9.987] WALKER, T.J., KASS, J.N., "Variation of zircaloy fracture toughness with irradiation", Proc. Int. Symp. on Zirconium in Nuclear Applications, ASTM STP 551, Portland, 1973 (SCHEMEL, J.H., ROSENBAUM, H.S., Eds), ASTM International, West Conshohocken, PA (1974) 328–354.

[9.988] MAHMOOD, S.T., FARKAS, D.M., ADAMSON, R.B. ETOH, Y., "Post-irradiation characterization of ultra-high-fluence Zircaloy-2 plate", Zirconium in the Nuclear Industry: Twelfth International Symposium, Proc. ASTM STP 1354, Toronto, 1998 (SABOL, G.P., MOAN, G.D., Eds), ASTM International, West Conshohocken, PA (2000) 139–169.

[9.989] ROWE, R.G., HOAGLAND, R.G., "The effect of cold work, thermal treatment, and neutron irradiation on the fracture toughness of Zircaloy-2", Irradiation Effects in Structural Alloys for Thermal and Fast Reactors, ASTM STP 457, San Fransisco, 1968, ASTM International, West Conshohocken, PA (1969) 3–16.

[9.990] HUANG, F.H., Brittle-fracture potential of irradiated Zircaloy-2 pressure tubes, J. Nucl. Mater. **207** (1993) 103–115.

[9.991] KOIKE, M.H., AKIYAMA, T., NAGAMATSU, K., SHIBAHARA, I., "Change of mechanical properties by irradiation and evaluation of the heat-treated Zr-2.5 Nb pressure tube", Zirconium in the Nuclear Industry: Tenth International Symposium, Proc. ASTM STP 1245, Baltimore, 1993 (GARDE, A.M., BRADLEY, E.R., Eds), ASTM International, West Conshohocken, PA (1994) 183–201.

[9.992] CHOW, C.K., NHO, K.H., Effect of thickness on the fracture toughness of irradiated Zr-2.5Nb pressure tubes, J. Nucl. Mater. **246** (1997) 84–87.

[9.993] CHOW, C.K., et al., "Fracture toughness of irradiated Zr-2.5 Nb pressure tubes from CANDU reactors", Zirconium in the Nuclear Industry: Ninth International Symposium, Proc. ASTM STP 1132, Kobe, 1990 (EUCKEN, C.M., GARDE, A.M., Eds), ASTM International, West Conshohocken, PA (1991) 246–275.

[9.994] DAVIES, P.H., HOSBONS, R.R., GRIFFITHS, M., CHOW, C.K., "Correlation between irradiated and unirradiated fracture toughness of Zr-2.5Nb pressure tubes", Zirconium in the Nuclear Industry: Tenth International Symposium, Proc. ASTM STP 1245, Baltimore, 1993 (GARDE, A.M., BRADLEY, E.R., Eds), ASTM International, West Conshohocken, PA (1994) 135–167.

[9.995] HOSBONS, R.R., DAVIES, P.H., GRIFFITHS, M., SAGAT, S., COLEMAN, C.E., "Effect of long-term irradiation on the fracture properties of Zr-2.5Nb pressure tubes", Zirconium in the Nuclear Industry: Twelfth International Symposium, Proc. ASTM STP 1354, Toronto, 1998 (SABOL, G.P., MOAN, G.D., Eds), ASTM International, West Conshohocken, PA (2000) 122–138.

[9.996] AITCHISON, I., DAVIES, P.H., Role of microsegregation in fracture of cold-worked Zr-2.5Nb pressure tubes, J. Nucl. Mater. **203** (1993) 206–220.

[9.997] THEAKER, J.R., et al., "Fabrication of Zr-2.5Nb pressure tubes to minimise the harmful effects of trace elements", Zirconium in the Nuclear Industry: Tenth International Symposium, Proc. ASTM STP 1245, Baltimore, 1993 (GARDE, A.M., BRADLEY, E.R., Eds), ASTM International, West Conshohocken, PA (1994) 221–242.

[9.998] COLEMAN, C.E., THEAKER, J.R., KIDD, K.V., Effect of fabrication variables on irradiation response of crack growth resistance of Zr-2.5Nb, J. ASTM International **1** (2004) Paper JAI12437.

[9.999] COLEMAN, C.E., et al., Mechanical properties of Zr-2.5Nb pressure tubes made from electrolytic powder, J. ASTM Int. **4** (2007) Paper JAI101111.

[9.1000] SMITH, E., DAVIES, P.H., Modelling the fissuring flat-fracture mode of crack growth in Zr-2.5Nb CANDU pressure-tube material, J. Mater. Sci. **30** (1995) 561–567.

[9.1001] SMITH, E., DAVIES, P.H., Modelling the softening within the fracture process zone associated with the fissuring mode of crack growth in Zr-2.5Nb CANDU pressure tube material, J. Mater. Sci. **31** (1996) 835–841.

[9.1002] DAVIES, P.H., HIMBEAULT, D.D., SHEWFELT, R.S.W., HOSBONS, R.R., "Crack growth resistance of irradiated Zr-2.5Nb pressure tube material at low hydrogen levels", Effects of Radiation on Materials: Twentieth International Symposium, Proc. ASTM STP 1405, Williamsburg, 2000 (ROSINSKI, S.T., GROSSBECK, M.L., ALLEN, T.R., KUMAR, A.S., Eds), ASTM International, West Conshohocken, PA (2001) 846–868.

[9.1003] CHOUBEY, R., ALDRIDGE, S.A., THEAKER, J.R., CANN, C.D., COLEMAN, C.E., "Effects of extrusion-billet preheating on the microstructure and properties of Zr-2.5 Nb pressure tube materials", Zirconium in the Nuclear Industry: Eleventh International Symposium, Proc. ASTM STP 1295, Garmisch-Partenkirchen, 1995 (BRADLEY, E.R., SABOL, G.P., Eds), ASTM International, West Conshohocken, PA (1996) 657–675.

[9.1004] MARKELOV, V.A., et al., "Fracture toughness and delayed hydride cracking of Zr-alloys for CANDU and RBMK pressure tubes", Proc. Int. Symp. on Resolution of Problems Encountered in Pressurized Water Reactors, Fontevraud, 2002, Société Française D'Énergie Nucléaire, Paris (2002).

[9.1005] CHOW, C.K., SIMPSON, L.A., "Determination of the fracture toughness of irradiated reactor pressure tubes using curved compact specimens", Fracture Mechanics: Eighteenth Symposium, Proc. ASTM STP 945, Boulder, 1985 (READ, D.T., REED, R.P., Eds), ASTM International, West Conshohocken, PA (1988) 419–439.

[9.1006] URBANIC, V.F., The occurrence of ZrO_2 wedging in cracked Zr-2.5 wt% Nb alloy, Corrosion **33** (1977) 188–189.

[9.1007] YAGNIK, S.K., et al., Round-robin testing of fracture toughness characteristics of thin-walled tubing, J. ASTM Int. **5** (2008) Paper JAI101140.

[9.1008] GRIGORIEV, V., JOSEFSSON, B., ROSBORG, B., "Fracture toughness of zircaloy cladding tubes", Zirconium in the Nuclear Industry: Eleventh International Symposium, Proc. ASTM STP 1295, Garmisch-Partenkirchen, 1995 (BRADLEY, E.R., SABOL, G.P., Eds), ASTM International, West Conshohocken, PA (1996) 431–447.

[9.1009] FUKUDA, T., ITAGAKI, N., KAMIMURA, J., MOZUMI, Y., FURUYA, T., "Fracture toughness of hydrogen-absorbed Zircaloy-2 cladding tube", Proc. TopFuel 2003, Würzburg, 2003, Kerntechnische Gesellschaft, Dusseldorf (2003).

[9.1010] HSU, H.H., CHIEN, K.F., CHU, H.C., KUO, R.C., LIAW, P.K., "An X-specimen test for determination of thin-walled tube fracture toughness", Fatigue and Fracture Mechanics, Vol. 32, ASTM STP 1406, (CHONA, R., Ed.), ASTM International, West Conshohocken, PA (2002) 214–226.

[9.1011] BERTSCH, J., HOFFELNER, W., Crack resistance curves determination of tube cladding material, J. Nucl. Mater. **352** (2006) 116–125.

[9.1012] SAINTE CATHERINE, C., LE BOULCH, D., CARASSOU, S., RAMASUBRAMANIAN, N., LEMAIGNAN, C., An internal conical mandrel technique for fracture toughness measurements on nuclear fuel cladding, J. Test. Eval. **34** (2006) 373–382.

[9.1013] OBERLÄNDER, B.C., IFE Report, IFE/KR/F-2003/134, Kjeller, Norway (2003).

Appendix I

INTERNAL FRICTION AND ANELASTICITY IN ZIRCONIUM

Z. Pan
Atomic Energy of Canada Limited, Ontario, Canada

I.1. INTRODUCTION

When an ideal elastic solid is subjected to a stress below the elastic limit, the corresponding strain is proportional to stress and disappears upon stress removal. In real materials, the strain may lag behind the stress and would gradually change towards an equilibrium value after stress removal. The time dependent stress-strain behaviour is called anelasticity. If a sinusoidal stress is applied to a sample, the realizable vibration strain will take a finite time to develop and thus will lag behind the stress by a phase angle ϕ, causing a hysteresis loop to open up on the stress-strain diagram. The area of this loop represents the dissipated energy (Δw) per unit volume per cycle within the sample. This energy is absorbed by the sample, causing the sample vibration to damp out. The damping is called internal friction. Both ϕ and Δw can be used to define the measure of internal friction as follows:

$$Q^{-1} = \tan\phi = \delta/\pi = (1/2\pi)\Delta w/w \qquad \text{(I.1)}$$

where w is the total elastic energy per unit volume per cycle of the sample under forced vibration and δ is the logarithmic decrement of the decaying vibration amplitude A after removing the driving vibration stress given by:

$$\delta = \ln(A_n / A_{n+1}) \text{, or, average } \overline{\delta} = (1/n)\ln(A_1 / A_{n+1}) \qquad \text{(I.2)}$$

Internal friction in solids results from the stress induced movement of defects (e.g. point defects, dislocations and grain boundaries) or phase transformations. Therefore, measurements of internal friction can be used to study such movements of defects or transformations. This research is called ‘mechanical spectroscopy’, because the measurement of internal friction as a function of frequency or temperature exhibits a spectrum consisting of a series of peaks. This appendix describes progress since the summary in 1971 [I.1], giving examples for three temperature ranges: below room temperature; up to 720 K (450ºC); and above 700 K (430ºC). Detailed descriptions of mechanical spectroscopy and anelasticity can be found in Refs [I.2, I.3].

I.2. IN THE LOW TEMPERATURE RANGE

Ritchie and Fantozzi [I.4], and Benoit [I.5] have analyzed the general features of internal friction in cold worked Zr, as well as other hexagonal closed packed (HCP) metals. Plastically deformed HCP metals exhibit a broad internal friction peak below room temperature. The peak has some characteristics of the relaxation due to stress induced dislocation movement observed in face centred cubic (FCC) metals, which is called dislocation relaxation or Bordoni peak. The internal friction spectrum of HCP metals at low temperature depends on the sample purity. Only in the purest HCP metals does the internal friction spectrum exhibit behaviour similar to that observed in pure FCC metals.

Savino et al. and Bolcich et al. [I.6–I.9] used 99.99 wt% and 99.999 wt% pure Zr to determine the internal friction spectrum in the low temperature range and found three internal friction peaks. Peak P_1 appeared at 90 K (-183ºC, 1 Hz) after cold work and disappeared on heating the sample above 200 K (-73°C). The peak was interpreted as dislocation relaxation, where the movement of dislocations must overcome the Peierls-Nabarro barrier of the Zr lattice. Another peak, P_2, was found at about 150 K (-123ºC, 1 Hz), the height of which depended on the annealing temperature and the amount of cold work, and was attributed to the interaction of point defects with dislocations. Peak P_3 at about 200 K (-73°C, 1 Hz) was unstable.

Miyada-Naborikawa et al. [I.10–I.13] observed the deformation-induced peaks at 80 Hz in 99.99 wt% Zr specimens deformed at 8 K (-265ºC) or 300 K (27ºC), shown in Figs. I.1 and I.2. They de-convoluted the broad peak into five peaks, each of which had a single relaxation time: P_d' (140 K (-133ºC)), P_d (170 K (-103ºC)), P_1 (210 K (-63ºC)), P_2 (230 K (-43ºC)) and P_3 (255 K (-18ºC)). The first four peaks were detected in both deformed and annealed specimens, but P_3 was only seen in cold-rolled specimens. Both peaks P_d' and P_d were attributed to kink-pair generation in <11$\bar{2}$0> screw dislocations moving on the prismatic or pyramidal planes. Peak P_1 was thought to be the reorientation of hydrogen interstitial atoms in the stress field of dislocations. Peak P_2 was attributed to the interaction of dislocations with intrinsic point defects. Peak P_3 was conjectured to be due to the interaction of dislocations with hydrogen atoms. The solubility limit of hydrogen in pure Zr is extremely low (i.e. ~ 0.02 ppm (1.8×10^{-4} at.%) at 273 K (0°C)); any mechanism associated with hydrogen must be confirmed by the dependence of the peak height on hydrogen concentration. Peak P_t, at 280 K (7ºC) in Fig. I.2, was only observed in the specimen deformed at 8 K (–265ºC). Transmission electron microscope (TEM) observations on twins and dislocations [I.12] suggested that peak P_t might be associated with the stress induced movements of twin boundaries.

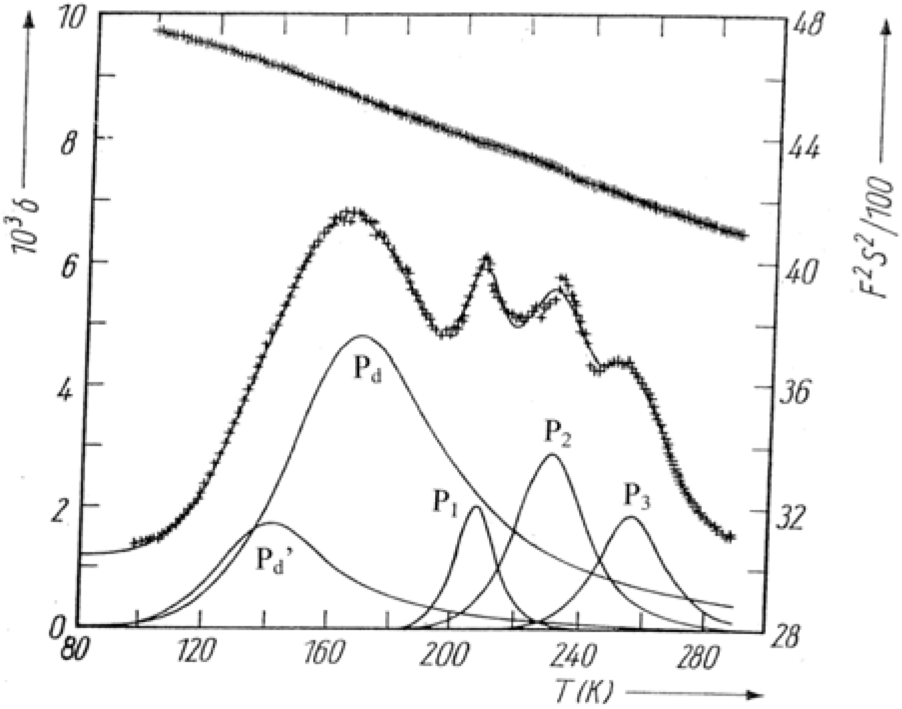

FIG. I.1. Internal friction peaks determined at 80 Hz in a 99.99% Zr specimen cold rolled to 20% at room temperature (from [I.11]), where $F^2S^2/100$ = (Frequency)^2/100 *in units of (Hz)*^{2}*.*

Pichon et al. [I.14] found six internal friction peaks below 400 K (127°C) in 99.999 wt% Zr neutron irradiated with a dose of about 7×10^{22} n/m^2 ($E > 1$ MeV) at 77 K (-196°C) and attributed some of these peaks to the reorientation of radiation induced interstitials, and to the interactions of these defects with dislocations. Doherty et al. [I.15] detected two peaks at 80 K (-193ºC) and 250 K (-23ºC) at 100 kHz in 99.9 wt% Zr and 99.999 wt% Zr and attributed the peaks to dislocation relaxation and to the interaction of dislocations with point defects, respectively. Petit et al. [I.16, I.17] determined a peak at 120 K (-153ºC, 1 Hz) or 220 K (-53ºC, 20 kHz) in 99.9 wt% or 99.99 wt% Zr. Pal-Val et al. [I.18] also determined a peak at 225 K (-48°C, 87 kHz) in deformed Zr. All these peaks below room temperature in pure Zr are complicated by their sensitivity to impurities and the level of cold work, thus these proposed mechanisms require confirmation.

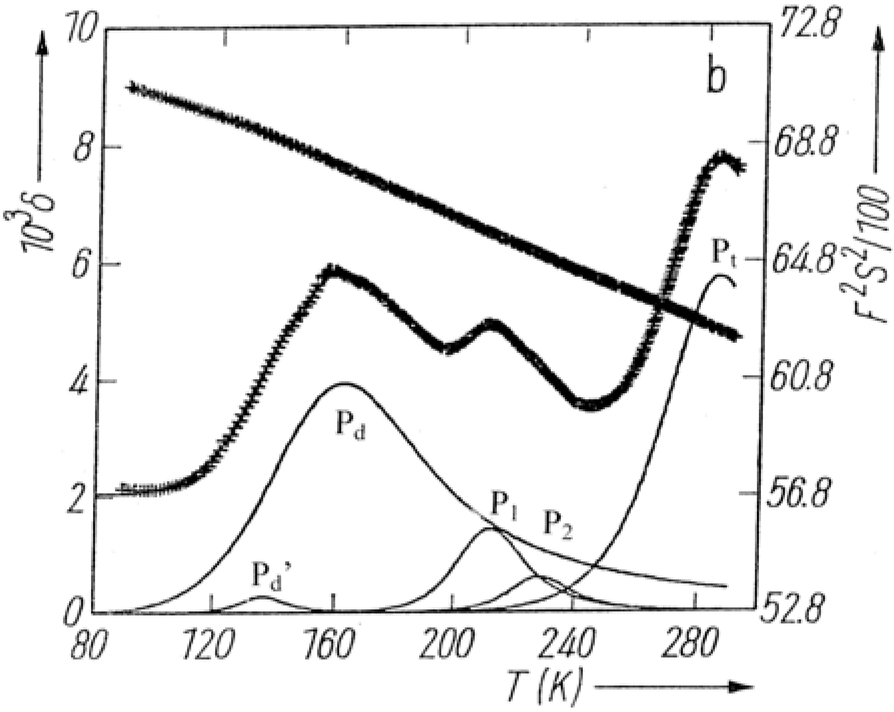

FIG. I.2. Internal friction peaks and modulus determined at 80 Hz in a 99.99% Zr specimen elongated to 17% at 8 K (−265°C) (from [I.13]), where $F^2S^2/100$ = (Frequency)^2/100 in units of (Hz)^2.

I.3. IN THE MID-TEMPERATURE RANGE

Ritchie et al. [I.19–I.21] and Rosinger et al. [I.22] found an internal friction peak at 723 K (450°C, 2.4 Hz) or at 738 K (465°C, 4.5 Hz) in two commercially pure Zr single crystals (Figs I.3 and I.4). A specimen containing 2.8 at.% (5030 ppm) oxygen with an orientation of <hkl0> along the longitudinal dimension was used for flexure vibration (i.e. bending force was perpendicular to the basal plane of the HCP lattice). A second specimen containing 4.0 at.% (7250 ppm) oxygen with an orientation of <0001> was used for torsion vibration (i.e. shear strain on the basal plane). Both specimens contained about 350 ppm metallic impurities. This peak was not found in a third Zr single crystal containing a very low oxygen concentration of 0.07 at.% (125 ppm). Adding praseodymium of 0.097 at.% (1500 ppm) to a crystal containing 2.8 at.% (5030 ppm) oxygen, the peak was depressed [I.22]. The internal friction peak in the two single crystals appeared as a typical relaxation with a single relaxation time. From measurements of the peak temperature shift with frequency, the activation energy was determined as (46 ± 2) kcal/mol (193 kJ/mol) whilst the pre-exponential factor of relaxation time τ_0^{-1} was determined to be 1.1×10^{15} s^{-1}. These results are in reasonable agreement with parameters estimated from Zr polycrystalline samples, where a small peak was found on the low temperature tail of a larger peak due to grain boundary sliding [I.23–I.27]. The well-defined and reproducible internal friction peak can only be observed in single crystal specimens containing interstitial oxygen >1 at.% (1770 ppm).

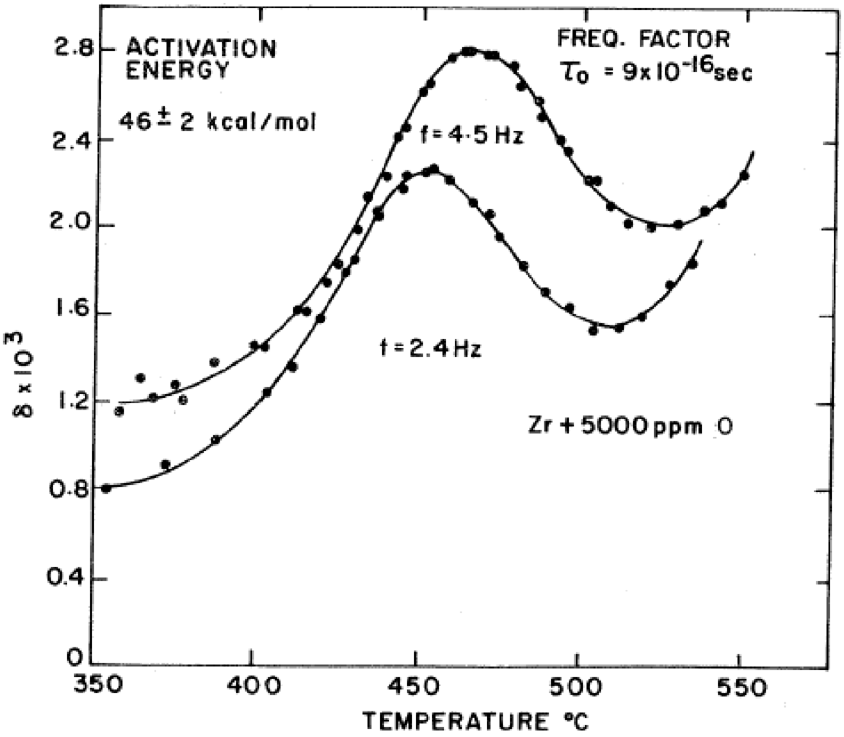

FIG. I.3. Internal friction peak due to stress induced reorientation of interstitial oxygen-substitutional atom pairs determined using a flexure pendulum in a single crystal Zr specimen with orientation <hkl0> (from [I.19]).

Povolo et al. [I.28, I.29] proposed a group theory method to analyse the symmetry of point defects in HCP metals. Browne [I.24] applied the method to interpret the relaxations of substitutional-interstitial (*s-i)* pairs and interstitial-interstitial (*i-i)* pairs in Zr. Following the suggestions from [I.23–I.29], Ritchie et al. [I.19–I.21] theoretically investigated the relaxation mechanism and kinetics of stress induced reorientation of *s-i* and *i-i* pairs in the HCP lattice of Zr. They indicated that when the oxygen concentration was less than 4.0 at.% (7250 ppm), the peak was dominated by the *s-i* relaxation, but with higher concentrations of oxygen, the *i-i* pair relaxation also contributed to the internal friction peak. There are six equivalent nearest neighbour configurations for these *s-i* pairs. If the substitutional atom is fixed and the reorientation of pairs occurs through jumps of the more mobile interstitial oxygen atom, two distinct types of jumps can lead to reorientation. One, w_1, is parallel to the basal plane and the other, w_2, is perpendicular to the basal plane (i.e. c-axis jump). As predicted by Nowick in [I.3, p. 332], only properly oriented single crystals can be used to distinguish the two possibilities of jumps in the reorientation of *s-i* pairs by relaxation measurements. Ritchie's results on the two Zr single crystal specimens have confirmed that both jumps may contribute to the relaxation of interstitial oxygen. Previously, it was assumed that the c-axis jump was the rate controlling process in the volume diffusion of oxygen in α-Zr. Ritchie et al. [I.21] compiled data from internal friction, strain ageing and other measurements relating to oxygen diffusion in α-Zr, spanning a temperature range of 560–1770 K (290–1500°C) and covering fourteen orders of magnitude in the diffusion coefficient. Two equations can be used to fit these data:

$$D = 0.0661 \times 10^{-4} \exp(-44000/RT), \qquad 560\ \mathrm{K} < T \leq 920\ \mathrm{K} \tag{I.3}$$

$$D = 16.5 \times 10^{-4} \exp(-54700/RT), \qquad 920\ \mathrm{K} < T < 1770\ \mathrm{K} \tag{I.4}$$

where the volume diffusion coefficient D is in m^2/s, T is in K and R = 8.314 J/(mol·K). Equation (I.3) is attributed to basal plane jumps of oxygen and Eq. (I.4) describes c-axis jumps of oxygen.

Therefore, both mechanisms of jumps can contribute to the diffusion of oxygen in Zr in different temperature ranges.

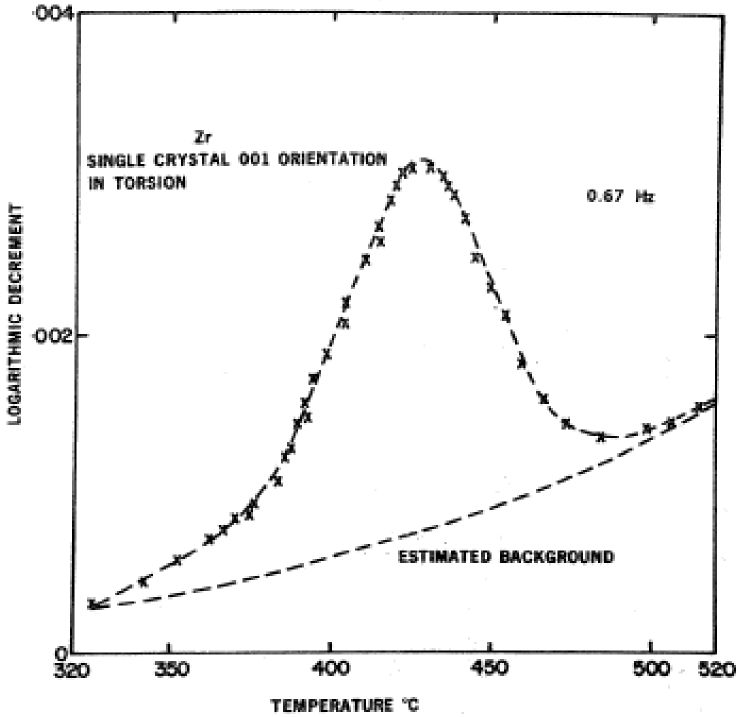

FIG. I.4. Internal friction peak due to stress induced reorientation of interstitial oxygen-substitutional atom pairs determined using a torsion pendulum in a single crystal Zr specimen with orientation <0001> (from [I.21]).

For specimens with low oxygen concentrations, the *s-i* relaxation peak was absent in the mid-temperature range, but other internal friction peaks were observed. Ritchie et al. [I.30–I.33] reported peaks P_0, P_1 and P_2 in a sample of nominal 99.999% Zr (Fig. I.5). Peak P_2 only appeared for the strain-amplitude $\varepsilon \leq 2 \times 10^{-6}$; it was accompanied by peaks P_0 and P_1 if $\varepsilon > 2 \times 10^{-6}$. Peaks P_0, P_1 and P_2 were, respectively, attributed to (a) the thermally assisted unpinning of dislocations from pinning points (mainly oxygen interstitials); (b) impurities diffusing longitudinally along dislocation cores (pipe diffusion); and (c) transverse core diffusion of impurities (dragging perpendicular to dislocation lines). Internal friction and elastic modulus appear amplitude-dependent and time-dependent in the temperature range of these peaks. Ritchie et al. [I.33], Atrens et al. [I.34], and Ritchie et al. [I.35] investigated the non-linear behaviour of internal friction in 99.999% Zr and Marz-grade Zr (99.9%) specimens using a ‘programmed vibration anneal’ to ensure a reproducible starting microstructure. They derived a map of strain amplitude versus temperature and presented various possible relaxation mechanisms in different regions of the map. Ritchie et al. and Povolo et al. [I.36–I.43] discussed the mechanisms of amplitude-dependent and time-dependent internal friction spectra and compared the calculation methods of true or intrinsic damping at a homogeneous strain from measured raw data of internal friction.

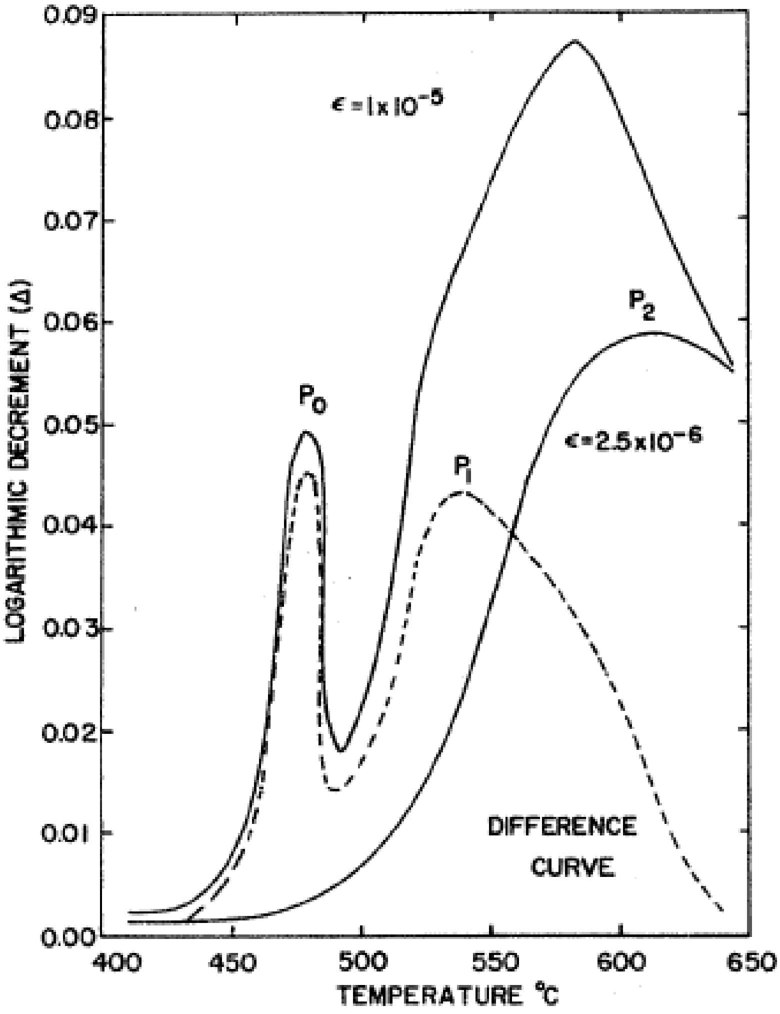

FIG. I.5. Internal friction peaks at higher temperature determined using a flexure pendulum (4 Hz) in a nominally 99.999% pure Zr polycrystalline specimen at different strain amplitudes (from [I.30]).

I.4. IN THE HIGH TEMPERATURE REGION

The internal friction spectrum of polycrystalline Zr in the high temperature range (>670 K (400°C)) can be resolved into five peaks [I.44]: in addition to the peaks P_0, P_1 and P_2, two high temperature peaks P_3 and P_4, were found that were attributed to twinning and grain boundary relaxation, respectively. Bratina et al. [I.45] first found an internal friction peak attributable to grain boundary sliding in Zr. Povolo et al. [I.46–I.48] investigated in detail the internal friction peak due to grain boundary sliding in polycrystalline 99.8% Zr and Zircaloy-4. One peak was present in pure Zr (Fig. I.6), but two peaks were observed in Zircaloy-4, which were attributed to the sliding of particle free grain boundaries and particle bearing grain boundaries, respectively. This latter peak was associated with a change of the grain boundary viscosity due to the segregation of solutes at the grain boundary of Zr alloys. For the grain boundary peak of pure Zr, the activation energy and pre-exponential factor of relaxation time were determined to be 270 kJ/mol and 1.5×10^{-18} s with the peak temperature of 822 K (549°C, 0.67 Hz). Povolo et al. [I.48] analyzed the relaxation parameters of grain boundary sliding in Zr using a continuous-distribution dislocation model for a high angle grain boundary and obtained reasonable agreement with experimental results.

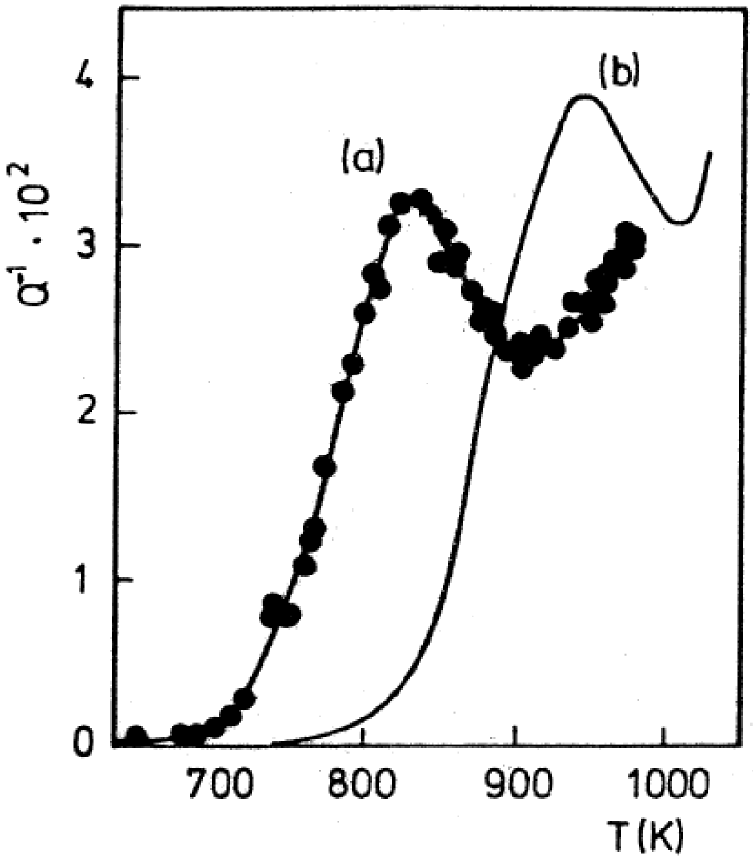

FIG. I.6. Internal friction peak due to grain boundary sliding determined using a pendulum at about 1 Hz for curve (a) and at about 70 Hz for curve (b) during cooling in a pure Zr polycrystalline specimen with an average grain size of 20 μm (from [I.46]).

I.5. HYDROGEN RELATED EFFECTS

The behaviour of hydrogen and hydrides in Zr and Zr alloys has been investigated using internal friction techniques. Reference [I.1] described some internal friction peaks associated with hydrogen in Zr. Ritchie et al. [I.49, and Pan and Puls I.50] detected a low temperature peak at 220 K (-53°C, 40 kHz) in Zr-2.5Nb + 1.34 at.% (150 ppm) H alloy specimens (Fig. I.7). The peak height was increased by a thermal cycle through a higher temperature of 443 K (170°C) and thus the increase was explained as being due to an increase in the density of misfit dislocations induced by hydride re-precipitation. A truncated peak [I.51–I.57] was observed at the phase transformation point of hydride dissolution (during heating) or precipitation (during cooling); the peak height and peak temperature depended on the hydrogen concentration. The peak was accompanied by a distinct change in the slope of the corresponding elastic modulus versus temperature curve. Schiller [I.51] first suggested the method to determine the phase diagram of metal-hydrogen systems by means of the slope change; consequently, it is now used to determine the terminal solid solubility of hydrogen in Zr and Zr alloys [I.56] (Fig. I.8). Numakura et al. [I.52] argued that the misfit dislocations of hydride precipitates were responsible for the precipitation peak.

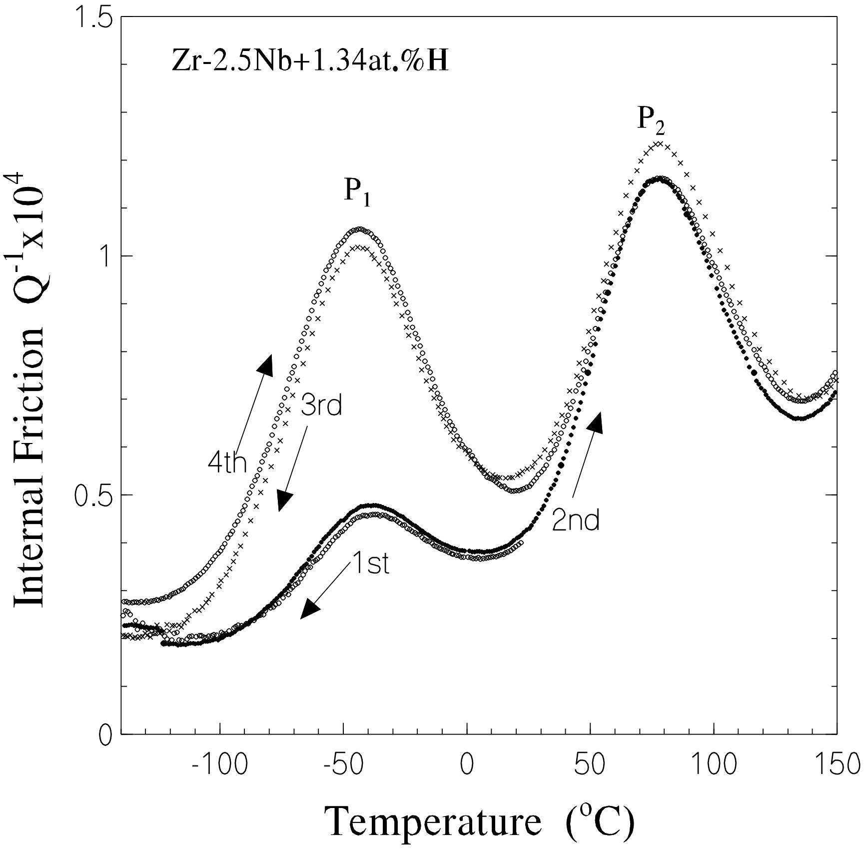

FIG. I.7. The effect of thermal cycles on the low temperature internal friction peak determined using a composite oscillator technique at 40 kHz (from [I.50]), but peaks P_1 and P_2 cannot be the same peaks as the corresponding ones in Figs I.1 and I.2.

Povolo and Bisogni [I.58], Mazzolai et al. [I.59, I.60] and other researchers [I.61–I.63] observed three relaxation peaks associated with hydrogen diffusion in Zr [I.1]. Recently, Wipf et al. [I.64] determined a relaxation peak in solid hydride of $ZrH_{1.9}$ at about 320 K (47°C, 1 kHz) and attributed this peak to a Zener-type relaxation in a concentrated ‘lattice gas’. Originally, the Zener relaxation was attributed to the reorientation of substitutional impurity atom pairs in FCC substitutional alloys (e.g. α-brass [I.3]). Pan and Puls [I.65] investigated this peak (P_2) at 355 K (82 ºC, 40 kHz) in Zr and Zr-2.5Nb alloy containing hydrogen concentrations up to 60 at.% (16 200 ppm) H (i.e. solid hydride of composition $ZrH_{1.5}$). They found that when previous results [I.58–I.63] were included, the height of peak P_2 was proportional to the square of the hydrogen concentration (in at.%) in Zr specimens. This proportionality was thought to be evidence that peak P_2 can be attributed to the stress induced reorientation of interstitial hydrogen atom pairs within the FCC lattice of δ-hydride. The experiments [I.65] also showed that the presence of peak P_3 at 455 K (182ºC, 40 kHz) was dependent on the thermal history of the Zr specimens containing hydrogen. The authors proposed that peak P_3 was associated with the stress induced motion of interstitial hydrogen atoms across the interface between the HCP lattice of α-Zr and the face centred tetragonal (or FCC) lattice of quench induced hydrides.

Sinning [I.66] reviewed various possible relaxation mechanisms associated with the stress induced movement of hydrogen in zirconium and other metals and showed that the internal friction technique is a useful tool to study the hydrogen behaviour not only in crystalline solids but also in quasicrystals and amorphous materials.

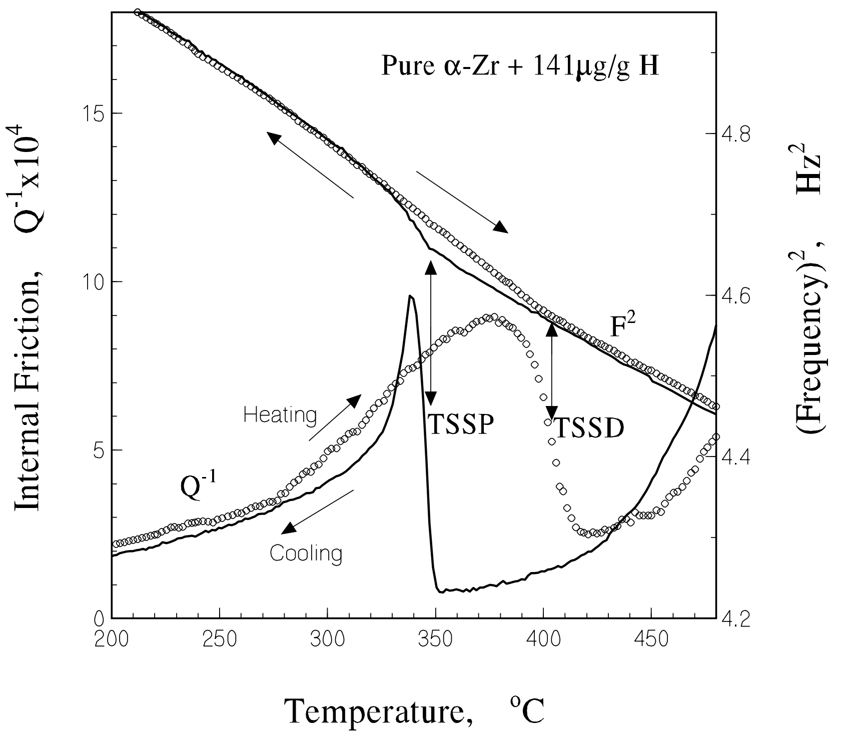

FIG. I.8. Hydride precipitation peak during cooling and dissolution peak during heating and corresponding elastic modulus curves in a pure Zr specimen containing a hydrogen concentration of 141 ppm (1.27 at.%) (from [I.54]); TSSD — terminal solid solubility for dissolution; TSSP — terminal solid solubility for precipitation.

I.6. SUMMARY

Some internal friction phenomena in Zr and Zr alloys are well characterized. For example, the high temperature peak due to the grain boundary relaxation was determined in polycrystalline Zr at 822 K (549°C, 0.67 Hz). In Zr containing oxygen >1 at.% (1770 ppm), the internal friction peak at 723 K (450°C, 2.4 Hz) is attributed to the stress induced reorientation of atomic pairs *i-s* of interstitial oxygen and substitutional impurity atoms. In Zr and Zr alloys containing hydrogen, hydride precipitation (or dissolution) peak during cooling (or heating) is accompanied by a slope change in the temperature dependence of the elastic modulus curves, which may be used to determine the terminal solid solubility of hydrogen in Zr alloys. The reorientation of hydrogen atom pairs can result in an internal friction peak at 355 K (82°C, 40 kHz) in the FCC Zr-hydride. Other internal friction peaks in the low temperature range and amplitude-dependent internal friction at middle temperature range in pure Zr and Zr alloys are not well understood and further research is needed to elucidate their mechanisms.

REFERENCES

[I.1] DOUGLASS, D.L., The Metallurgy of Zirconium, Atomic Energy Review, IAEA, Vienna (1971), section 3.2.

[I.2] SCHALLER, R., FANTOZZI, G., GREMAUD, G. (Eds), Mechanical Spectroscopy Q^{-1} 2001 with Applications to Materials Science, Materials Science Forum 366–368, Trans Tech Publications, Switzerland (2001).

[I.3] NOWICK, A.S., BERRY, B.S., Anelastic Relaxation in Crystalline Solids, Academic Press, New York (1972).

[I.4] RITCHIE, I.G., FANTOZZI, G., “Internal friction due to intrinsic properties of dislocation in metals: Kink relaxations,” Dislocations in Solids, Vol. 9 (NABARRO, F.R.N., Ed.), North-Holland, Amsterdam (1992) 57–134.

[I.5] BENOIT, W., "Dislocation relaxation", Mechanical Spectroscopy Q^{-1} 2001 with Application to Materials Science Materials Science Forum 366–368 (SCHALLER, R., FANTOZZI, G., GREMAUD, G., Eds), Trans Tech Publication Ltd, Switzerland (2001) Chapter 3, 141–177.

[I.6] SAVINO, E.J., BISOGNI, E.A., Low temperature internal friction of cold worked zirconium, J. Phys., Colloq. C2 **32** (1971) 209–213.

[I.7] SAVINO, E.J., BISOGNI, E.A., Low-temperature relaxation processes in cold-worked zirconium, J. Nucl. Mater. **50** (1974) 298–308.

[I.8] BOLCICH, J.C., MONDINO, M., "Internal friction in Zr after deformation", Proc. 3rd European Conf., Internal Friction and Ultrasonic Attenuation in Solids, Manchester, 1980 (SMITH, C.C., Ed.), Pergamon Press, Oxford, UK (1980) 91–96.

[I.9] BOLCICH, J.C., SAVINO, E.J., Low-temperature internal friction in cold-worked zirconium, J. Nucl. Mater. **92** (1980) 357–359.

[I.10] MIYADA-NABORIKAWA, L.T., DE BATIST, R., EERSELS, L., Internal friction in zirconium, J. Phys., Colloq. C5 **42** (1981) 283–288.

[I.11] MIYADA-NABORIKAWA, L.T., DE BATIST, R., Low-temperature internal friction peaks in pure zirconium deformed at 300 K, Phys. Status Solidi A **89** (1985) 191–198.

[I.12] MIYADA-NABORIKAWA, L.T., DE BATIST, R., DELAVIGNETTE, P., Transmission electron microscopy observations of dislocations and twins in polycrystalline zirconium, Phys. Status Solidi A **89** (1985) 521–531.

[I.13] MIYADA-NABORIKAWA, L.T., DE BATIST, R., DELAVIGNETTE, P., Low-temperature relaxation peaks in zirconium deformed at 8 K, Phys. Status Solidi A **90** (1985) 277–283.

[I.14] PICHON, R., BISOGNI, E., MOSEK, P., Frottement interne dans le zirconium irradié aux neutrons à 77 K, Radiat. Eff. **20** (1973) 159–168.

[I.15] DOHERTY, J.E., GIBBONS, D.F., Deformation peaks in α-zirconium, J. Appl. Phys. **42** (1971) 4502–4503.

[I.16] PETIT, J., QUINTARD, M., SOULET, R., DE FOUQUET, J., Étude des pics de frottement intérieur observés après écrouissage sur le titane et le zirconium, dans le domaine des basses temperatures, J. Phys., Colloq. C2 **32** (1971) 215–220.

[I.17] PETIT, J., QUINTARD, M., FERRON, G., Pic de relaxation associé aux interstitiels intrinsiques dans le zirconium deformé à basse temperature, J. Nucl. Mater. **56** (1975) 341–347.

[I.18] PAL-VAL, P.P., HAMERSKY, M., TROJANOVA, Z., LUKAC, P., Internal friction in α-zirconium polycrystals, Phys. Status Solidi A **125** (1991) K13–K16.

[I.19] RITCHIE, I.G., ROSINGER, H.E., ATRENS, A., Anelastic relaxation and the diffusion of oxygen in alpha-zirconium, J. Nucl. Mater. **62** (1976) 1–8.

[I.20] RITCHIE, I.G., ATRENS, A., The diffusion of oxygen in alpha-zirconium, J. Nucl. Mater. **67** (1977) 254–264.

[I.21] RITCHIE, I.G., SPRUNGMANN, K.W., ATRENS, A., ROSINGER, H.E., "Anelastic relaxation peaks in single crystals of zirconium-oxygen alloys," Proc. 6th ICIFUAS, Internal Friction and Ultrasonic Attenuation in Solids (HASIGUTI, R.R., MIKOSHIBA, N., Eds), University of Tokyo Press, Tokyo (1977) 447–451.

[I.22] ROSINGER, H.E., FAULKNER, D., ATRENS, A., RITCHIE, I.G., Effect of praseodymium on the internal friction in a zirconium-oxygen single crystal, J. Nucl. Mater. **62** (1976) 121–122.

[I.23] BROWNE, K.M., Stress induced diffusion of oxygen in alpha-zirconium, Scr. Metall. **5** (1971) 519–523.

[I.24] BROWNE, K.M., Mechanical relaxation and diffusion of interstitial atoms in H.C.P. metals, Acta Metall. **20** (1972) 507–514.

[I.25] GACOUGNOLLE, J.L., SARRAZIN, S., DE FOUQUET, J., Low frequency study of the internal friction spectrum in zirconium and zirconium-hafnium-oxygen solid solutions between 300 and 700°C, J. Phys., Colloq. C2 **32** (1971) 21–24.

[I.26] MISHRA, S., ASUNDI, M.K., Internal friction studies in dilute zirconium alloys, Can. Metall. Q. **11** (1972) 69–77.

[I.27] FULLER, P.G., MILLER, D.R., Internal friction and oxygen pair diffusion in α-zirconium, Met. Sci. (1977) 16–22.

[I.28] POVOLO, F., BISOGNI, E.A., Mechanical relaxation modes of paired point defects in H.C.P. crystals, Acta Metall. **14** (1966) 711–718.

[I.29] POVOLO, F., BISOGNI, E.A., Anelastic behaviour of isolated point defects in crystals of H.C.P. structure, Acta Metall. **15** (1967) 701–706.

[I.30] RITCHIE, I.G., SPRUNGMANN, K.W., Dislocation core diffusion and unpinning in α-Zr, J. Phys., Colloq. C5 **42** (1981) 427–432.

[I.31] RITCHIE, I.G., ATRENS, A., SO, C.B., SPRUNGMANN, K.W., Dislocation relaxation in a random array of solutes, J. Phys., Colloq. C5 **42** (1981) 319–324.

[I.32] RITCHIE, I.G., Core diffusion, unpinning and the Snoek-Köster relaxation, Scr. Metall. **16** (1982) 249–253.

[I.33] RITCHIE, I.G., ATRENS, A., BLAIR, D.G., "Anomalously large amplitude dependent damping and modulus defect in polycrystalline zirconium", Proc. 6th ICIFUAS, Internal Friction and Ultrasonic Attenuation in Solids (HASIGUTI, R.R., MIKOSHIBA, N., Eds), University of Tokyo Press, Tokyo (1977) 639–643.

[I.34] ATRENS, A., RITCHIE, I.G., SPRUNGMANN, K.W., "Time and amplitude dependent damping in a single crystal of zirconium", Proc. 6th ICIFUAS, Internal Friction and Ultrasonic Attenuation in Solids (HASIGUTI, R.R., MIKOSHIBA, N., Eds), University of Tokyo Press, Tokyo (1977) 633–637.

[I.35] RITCHIE, I.G., SPRUNGMANN, K.W., Oscillatory internal friction associated with dislocation core rearrangement of impurity interstitials in zirconium, J. Phys., Colloq. C9 **44** (1983) 613–617.

[I.36] FERNANDEZ, L., POVOLO, F., Amplitude-dependent damping in zirconium, Philos. Mag. **31** (1975) 1081–1097.

[I.37] FERNANDEZ, L., POVOLO, F., Amplitude dependent damping in Zircaloy-4 and zirconium at high temperatures, J. Nucl. Mater. **66** (1977) 79–87.

[I.38] RITCHIE, I.G., ATRENS, A., Comments on amplitude dependent damping in zirconium, Scr. Metall. **9** (1975) 1313–1316.

[I.39] ATRENS, A., RITCHIE, I.G., Comment on analysis of the amplitude dependent damping data in terms of the Granato-Lücke model, Scr. Metall. **10** (1976) 211–214.

[I.40] RITCHIE, I.G., ATRENS, A., WOO, C.H., Estimation of the number of pinning points per network length from an analysis of an amplitude dependent damping peak, Scr. Metall. **10** (1976) 1089–1093.

[I.41] RITCHIE, I.G., ATRENS, A., Further comments on ‘amplitude-dependent damping in zirconium’, Scr. Metall. **11** (1977) 107–108.

[I.42] POVOLO, F., Corrections due to inhomogeneous strains to the internal friction measured in free decay, Scr. Metall. **16** (1982) 885–890.

[I.43] RITCHIE, I.G., WOO, C.H., SPRUNGMANN, K.W., Comments on corrections due to inhomogeneous strains to the internal friction measured in free decay, Scr. Metall. **16** (1982) 891–894.

[I.44] RITCHIE, I.G., SPRUNGMANN, K.W., High Temperature Internal Friction in α-Zr, AECL-6810, Atomic Energy of Canada Limited, Chalk River, ON (1981).

[I.45] BRATINA, W.J., WINEGARD, W.C., Internal friction in zirconium, J. Met. **8** (1956) 186–189.

[I.46] POVOLO, F., MOLINAS, B.J., High-temperature internal friction in polycrystalline zirconium and Zircaloy-4, J. Nucl. Mater. **114** (1983) 85–94.

[I.47] POVOLO, F., MOLINAS, B.J., Hysteresis effects on the high-temperature internal friction of polycrystalline zirconium, J. Mater. Sci. **20** (1985) 3649–3660.

[I.48] POVOLO, F., MOLINAS, B.J., High-temperature internal friction in polycrystalline Zircaloy-4, J. Mater. Sci. **21** (1986) 3539–3547.

[I.49] RITCHIE, I.G., PAN, Z.-L., An internal friction study of Zr-2.5 wt% Nb-H alloys, Philos. Mag. A **63** (1991) 1105–1113.

[I.50] PAN, Z.-L., PULS, M.P., Internal friction peaks associated with hydrides in Zr and Zr-2.5Nb, J. Phys. IV, Colloq. C8 **6** (1996) 31–34.

[I.51] SCHILLER, P., Hydrogen in metals as observed by internal friction, Nuovo Cimento. B **33** (1976) 226–241.

[I.52] NUMAKURA, H., ITO, T., KOIWA, M., Low-frequency internal friction study of Zr-H and Zr-D alloys, J. Less-Com Met. **141** (1988) 285–294.

[I.53] RITCHIE, I.G., SPRUNGMANN, K.W., Hydride precipitation in zirconium studied by low-frequency pendulum techniques, J. Phys., Colloq. C9 **44** (1983) 313–318.

[I.54] RITCHIE, I.G., PAN, Z.-L., Internal friction and Young’s modulus measurements in Zr-2.5Nb alloy doped with hydrogen, M^{3}D Mechanics and Mechanisms of Material Damping, ASTM STP 1169 (WOLFENDEN, A., Ed.), ASTM International, West Conshohocken, PA (1992) 385–395.

[I.55] PAN, Z.-L., PULS, M.P., RITCHIE, I.G., Measurement of hydrogen solubility during isothermal charging in a Zr alloy using internal friction technique, J. Alloys Cmpd. **211/212** (1994) 245–248.

[I.56] PAN, Z.-L., RITCHIE, I.G. PULS, M.P., The terminal solid solubility of hydrogen and deuterium in Zr-2.5Nb alloys, J. Nucl. Mater. **228** (1996) 227–237.

[I.57] PAN, Z.-L., PULS, M.P., Precipitation and dissolution peaks of hydride in Zr-2.5Nb during quasistatic thermal cycles, J. Alloys Cmpd. **310** (2000) 214–218.

[I.58] POVOLO, F., BISOGNI, E.A., Internal friction in zirconium-hydrogen alloys at low temperatures, J. Nucl. Mater. **29** (1969) 82–102.

[I.59] MAZZOLAI, F.M., RYLL-NARDZEWSKI, J., SPEARS, C.J., An investigation of the zirconium-hydrogen system by internal friction, Nuovo Cimento. B **33** (1976) 251–263.

[I.60] MAZZOLAI, F.M., RYLL-NARDZEWSKI, J., An anelastic study of the diffusion coefficient of hydrogen in α-zirconium, J. Less-Com Met. **49** (1976) 323–327.

[I.61] BUNGARDT, K., PREISENDANZ, H., Dämpfung und Schubmodul von Zirkonium und Zirkonium-Wasserstoff-Legierungen, Z. Metallkd. **51** (1960) 280–289.

[I.62] CHANG, R., Phase transformation, twinning and anelastic phenomenon associated with zirconium dihydride, J. Nucl. Mater. **2** (1960) 335–340.

[I.63] PROVENZANO, V., SCHILLER, P., SCHNEIDERS, A., Internal friction study of zirconium alloyed with hydrogen and deuterium, J. Nucl. Mater. **52** (1974) 75–84.

[I.64] WIPF, H., KAPPESSER, B., WERNER, R., Hydrogen diffusion in titanium and zirconium hydrides, J. Alloys Cmpd. **310** (2000) 190–195.

[I.65] PAN, Z.-L., PULS, M.P., Internal friction peaks associated with the behaviour of hydrogen in Zr and Zr-2.5Nb, Mater. Sci. Eng., A **442** (2006) 109–113.

[I.66] SINNING, H.-R., New aspects of mechanical relaxation by hydrogen in metals, Mater. Sci. Eng., A **442** (2006) 99–105.

Appendix II

A HISTORY OF MODELS FOR THE GROWTH RATE OF DELAYED HYDRIDE CRACKING (DHC)

C.E. Coleman
Chalk River Laboratories, Ontario, Canada

G.A. McRae
Carleton University, Ottawa, Canada

The underlying mechanism for crack propagation by DHC described in Section 9.7.6.2 is generally accepted: for cracks to propagate, hydrogen in solid solution must travel to the crack tip, where the hydrogen may precipitate as brittle hydride, which then cracks when the hydride has grown large enough and if the applied stress is high enough. Although cracking is intermittent, its average growth rate will be determined by the growth rate of the hydride, which in turn is controlled by the arrival rate of hydrogen. The process is 'delayed' because of the time required for the hydrogen to travel to the crack tip. This hydrogen movement is the slowest part of the process and is therefore the rate-determining step. The rate of forming the hydride precipitate and the rate of cracking of the hydride are too fast to be rate controlling. Models of the process focus on the 'driving force' that is responsible for moving the hydrogen. Criteria for cracking the hydride itself are based on fracture properties that do not depend on time. The threshold K_I for DHC, K_{IH}, requires these fracture criteria, but once K_{IH} is exceeded but before K_{IC} is attained, the rate of crack propagation depends only on the rate of accumulation of hydrogen. It is this part of the K_I versus the crack growth rate curve, as shown in Fig. 9.191, that is the focus of this discussion.

The delays in cracking are of the same durations as expected if the hydrogen were diffusing and, hence, early models described the hydrogen flux in terms of concentration gradients, through Fick's empirical laws of diffusion. Such a formulation requires a means of forming a concentration gradient to start the process.

In a discussion on hydride cracks at welds, in 1974 Simpson and Ells [II.1] commented that "the 14% volume expansion accompanying the formation of hydride will reduce the magnitude of the tensile stress across the weld notch, and hence favour diffusion of hydrogen to the notch".

In 1977, Dutton and Puls [II.2, II.3] equated the steady state solution for the rate of substance diffusing through the unit length of a cylinder [II.4] to a crack growth rate. Their model assumed cracking was a steady-state process limited by diffusion of hydrogen to the high, local tensile stress region at the crack tip that acts as a hydrogen sink. These authors also invoked the volume increase when a hydride precipitates, postulating :

> "…it is energetically more favourable for hydride to precipitate under the action of the high tensile stress within the hydrogen sink, compared with a position in the matrix, away from the crack. Thus there exists a thermodynamic driving force for hydrides far from the crack (at L) to preferentially dissolve and reprecipitate at the crack tip (at ℓ)".

Thus, their solution reduced to one based on the concentration gradient, which "gives rise to a higher concentration of hydrogen in solution at L, compared with that at ℓ and causes diffusion of hydrogen from L to ℓ". Simpson and Puls echoed this interpretation in 1979 [II.5]: "The principal driving force … is the difference in local hydrogen concentration between hydride platelets close to and remote from the crack-tip". At the time, it was deemed that hydrides had to be present throughout the material to act as a source of hydrogen. In the next iteration in 1982 [II.6], "the driving force for this process [hydrogen diffusion to the crack tip] is provided by the shift in the TSS [terminal solid solubility of hydrogen] caused by the tensile stresses".

When the effect of a temperature gradient was included in the analysis in 2000 by Sagat et al. [II.7], the driving force was also seen to be concentration gradient:

> "It is the difference in hydrostatic stress at the boundaries at L and ℓ that, initially, is responsible for causing hydrogen to diffuse to the crack tip and form a hydride there, but once formed, generates a concentration gradient between crack tip and bulk hydrides which is the driver for the growth of the crack tip hydride".

In 2005, Kim [II.8] considered a situation in which all the hydrogen was in solution at a temperature just above the terminal solid solution for precipitation (TSSP). Kim proposed that

> "the tensile stress applied at the crack tip acts to trigger nucleation of hydrides only at the crack tip, thus lowering the supersaturated hydrogen concentration.… This consequently leads to the development of a difference in the hydrogen concentration … between the crack tip and the bulk.… Therefore, the difference in the hydrogen concentration is a driving force for the DHC allowing the hydrogen to move to the crack tip from the bulk region".

These proposed models all have two things in common: (i) they invoke a volume expansion when hydrides form; and (ii) they maintain that concentration gradients are the driving force leading to the flux of hydrogen to the crack tip that makes DHC possible. If concentration gradients are indeed behind the movement of hydrogen in solution, then the concentration of hydrogen in solution in the bulk, far from the crack tip, must be higher than the concentration of hydrogen in solution at the crack tip. The problem with the flux depending only on the concentration gradient is that there must be some mechanism added to start the process, because before the tensile stress is applied to the crack, the concentration of hydrogen is the same everywhere, yet DHC can still happen. In all of these models, the concentration gradient is formed after precipitation of hydride at the crack tip lowers the hydrogen concentration in solution there for various reasons: hydride precipitation at a crack tip is favoured because of the volume expansion of a hydride; stress modifies the terminal solid solution (TSS); or because applied stress triggers precipitation from supersaturated solution. These interpretations can be collectively called precipitation first models (PFMs), because, in all cases, some precipitation is proposed to happen first to form the concentration gradient that is the driving force for hydrogen movement. Note that a concentration gradient does not have the units of force.

In an elegant series of experiments with interstitial carbon partitioning between different iron alloys, Darken [II.9] showed in 1949 that when the chemical potential gradients were zero, concentration gradients could still exist without any concomitant flux. In 1959 measurements by Yang et al. [II.10] showed that stress changed the electrode potential of pure metals allowing the authors to conclude that "the chemical potential of an interstitial solute tends to increase on compression and decrease on tension". Li et al. [II.10] analysed this suggestion in 1966 by correlating a pressure volume work term with the chemical potential in a metal matrix at the end of particles and at some distance from the particles — the pressure is the hydrostatic stress, and the volume is the partial molar volume of hydrogen in solution. The gradient of the chemical potential leads to a concentration difference in the two locations and an 'equilibrium segregation'. These authors concluded that this effect "may have important implications for hydrogen embrittlement" in metals.

In 1971 Stevens and Dutton [II.11] examined the diffusion of interstitial atoms in gradients of temperature and pressure following the kinetic model of Girifalco [II.12] for diffusion in a temperature gradient. This model is based on the difference in jump frequencies up and down the temperature and pressure gradients. Flux equations predicted that the interstitials would migrate in response to a pressure gradient and, by implication, warned of hydrogen in zirconium diffusing from a location of low tensile stress to one of high tensile stress. Based on this analysis, and by analogy with work on titanium alloys [II.13], Simpson and Ells [II.1] suggested that the rate at which the hydrogen would flow, J, in a uniaxial stress gradient, dσ/dx, would be described by:

$$J = -DC[d(\ln C)/dx - (V_H/3RT).\ d\sigma/dx] \tag{II.1}$$

where:

D = diffusivity of hydrogen in zirconium alloy;
C = concentration of hydrogen;
V_H = volume of transport [1] or partial-molar volume of hydrogen in zirconium;
R = gas constant;

and T = cracking temperature.

At the time, 1974, several of the values of the variables were not well founded and the predicted flux of hydrogen was underestimated.

In the initial models of DHC growth the effect of hydrogen in solution interacting with the stress gradient — the drift term — was considered but was said to be small [II.3]. Once MacEwan et al. [II.14] measured the partial molar volume of hydrogen in solution in zirconium in 1985, the measurements made in 1978 and 1983 by Coleman and Ambler [II.15, II.16] of the critical hydrogen concentration of hydrogen to cause DHC could be interpreted by Eadie and Coleman [II.17] in 1989 as a tiny (rather than large) effect of stress on TSSP. In [II.15] and [II.17] DHC was observed after cooling to close to the terminal solid solution for dissolution (TSSD) so no hydrides were present in the zirconium matrix. In an experiment by Eadie et al. [II.18] in 1992, on material where all the hydrogen was in solution, a hydrogen concentration gradient of 2 ppm/mm was developed in a stress gradient of 100 MPa/mm at around 573 K (300ºC) confirming:

- The value of the partial molar volume;
- That the drift term was important;
- That hydrides are not required in the metal matrix as a source to increase the hydrogen concentration at the crack tip.

The cracking experiments were interpreted as follows [II.19]: The hydrostatic stress at the crack tip results in an elevated concentration of hydrogen in solution due to the interaction of the partial molar volume of hydrogen in solution and the hydrostatic stress. The amplification is large enough at a sharp crack under load for the hydrogen concentration in solution at the crack tip to reach the precipitation solubility limit when the hydrogen concentration in solution far from the crack tip is close to the apparent dissolution solvus concentration. The results of similar experiments to those in Refs [II.15, II.16] by Shi et al. in 1995, and by Schofield et al. in 2002 [II.20, II.21] were interpreted as being due to the same process. Hydrogen embrittlement of steel is explained by a similar time-dependent accumulation of hydrogen at a stress concentration [II.22].

Subsequent papers by Puls and colleagues, using basically the same geometry as in [II.2, II.3], now included in their model the above information acknowledging that the drift term was not small and that hydrides need not necessarily be present in the zirconium alloy matrix [II.23]. The

---

[1] Postulated by analogy with the heat of transport in a temperature gradient.

revised models also included and gave an explanation for why the temperature for the presence of hydrides depended on whether the material was being heated or cooled [II.24, II.25].

In 2004, Shmakov et al. [II.26] published a diffusion model based on the hydrogen moving up the stress gradient to a crack tip and obtained good agreement with values of crack growth rates at temperatures between 433 and 555 K (160 and 282°C).

McRae et al. [II.27], following a similar approach to that of Eadie et al. [II.19] and Shmakov [II.26], showed how a simple model derived from both concentration gradients and hydrostatic stress gradients, providing a gradient in chemical potential, could account for and predict seven distinctly different, independent experimental observation sets of DHC, within the experimental errors. The gradient in chemical potential does have the units of force, and, as indicated by Li et al. [II.10], includes the product of the hydrostatic stress gradient and the partial molar volume of hydrogen in solution in zirconium. Again, only the hydrogen in solution is important; no hydrides are required in the metal matrix, once a critical hydrogen concentration is exceeded. This hydrogen diffuses to the crack tip because of the hydrostatic stress gradient where it accumulates until it reaches TSSP, whereupon hydrides precipitate, grow and, if the conditions are appropriate, crack. The elevated concentration of hydrogen in solution at the crack tip remains at the TSSP value. The drift term continues to move hydrogen to the crack tip, but the concentration cannot exceed TSSP, so hydrogen moving to the crack tip becomes hydride, and steady-state concentrations ensue. The concentration gradient opposes the movement of hydrogen under the influence of the hydrostatic stress gradient. This type of model is called a diffusion first model (DFM):

— The model provides a closed-form steady-state solution to the Nernst-Einstein flux equation (similar to Eq. (II.1)), so that the model is written in terms of a single stress-independent solvus, TSSP, rather than two solvi.

— Only the hydrogen in solution is used, independent of whether hydrides are present or not in the zirconium matrix.

— The model predicts the concentration of hydrogen in solution will be higher at the crack tip than in the bulk, which is opposite to the PFM picture presented previously. In this way, the DFM can be distinguished from the PFMs.

The result is a simple two-term equation describing the crack growth rate by DHC, V_c, that is surprisingly accurate when used to predict a broad range of observations:

$$V_c = w.D\,[C_b - C_P \exp(\sigma_h V_H/RT)] \qquad \text{(II.2)}$$

where:

w = empirical constant;
C_b = concentration of hydrogen in solution in the bulk material;
C_P = TSSP concentration;

and σ_h = hydrostatic stress.

Kim [II.8] proposed his qualitative picture of the DHC process because of perceived shortcomings of the quantitative models based on the amplification of hydrogen concentration at the crack tip because of the gradient in stress. A critique of Kim's dismissal of the quantitative models for DHC has been published by Puls [II.28]. Puls provided an updated version of the original model of Dutton et al., correcting some errors and misunderstandings in the original work, and incorporating new results [II.29]. McRae et al. [II.28] showed that Kim's premise was not correct, and that the stress gradient was sufficient to amplify the hydrogen concentration appropriately. This analysis led to Eq. (II.2), which successfully refuted each of the alleged shortcomings.

The success of DFMs to describe accurately and in a straightforward manner the critical hydrogen concentration for flaw growth by DHC, and the dependence of flaw growth rate on both temperature and temperature history, based on well characterized properties, is powerful support for this approach. This type of model is therefore used in the main text.

REFERENCES

[II.1] SIMPSON, C.J., ELLS, C.E., Delayed hydrogen embrittlement in Zr-2.5wt%Nb, J. Nucl. Mater. **52** (1974) 289–295.

[II.2] DUTTON, R., PULS, M.P., "A theoretical model for hydrogen induced sub-critical crack growth", Effect of Hydrogen on Behaviour of Materials, Proc. Int. Conf. Jackson Lake Lodge, Moran, 1975 (THOMPSON, A.W., BERNSTEIN, I.M., Eds), Metallurgical Society of AIME, New York (1976) 516–528.

[II.3] DUTTON, R., NUTTALL, K., PULS, M.P., SIMPSON, L.A., Mechanisms of hydrogen induced delayed cracking in hydride forming materials, Metall. Trans. A **8** (1977) 1553–1562.

[II.4] CRANK, J., The Mathematics of Diffusion, Clarendon Press, Oxford, UK (1979).

[II.5] SIMPSON, L.A., PULS, M.P., The effects of stress, temperature and hydrogen content on hydride-induced crack growth in Zr-2.5 pct.Nb, Metall. Trans. **10A** (1979) 1093–1105.

[II.6] DUTTON, R., PULS, M.P., SIMPSON, L.A., "Hydride-induced crack growth in zirconium alloys", Fracture Problems and Solutions in the Energy Industry, Proc. 5th Canadian Fracture Conf., Winnipeg, 1981 (SIMPSON, L.A., Ed.), Pergamon Press, Oxford and New York (1982) 13–25.

[II.7] SAGAT, S., CHOW, C.K., PULS, M.P., COLEMAN, C.E., Delayed hydride cracking in zirconium alloys in a temperature gradient, J. Nucl. Mater. **279** (2000) 107–117.

[II.8] KIM, Y.S., Driving force for delayed hydride cracking of zirconium alloys, Met. Mater. Int. **11** (2005) 29–38.

[II.9] DARKEN, L.S., Diffusion of carbon in austenite with a discontinuity in composition, Trans. AIME **180** (1949) 430–438.

[II.10] LI, J.C.M., ORIANI, R.A., DARKEN, L.S., The thermodynamics of stressed solids, Z. Phys. Chem. Neue Folge **49** (1966) 271–290.

[II.11] STEVENS, R.N., DUTTON, R., The Effect of Temperature, Pressure and Concentration Gradients on Diffusion, AECL-3793, Atomic Energy of Canada Limited, Chalk River, ON (1971).

[II.12] GIRIFALCO, L.A., Semiempirical approach to the theory of thermal diffusion in crystals, Phys. Rev. **128** (1962) 2630–2638.

[II.13] WAISMAN, J.L., SINES, G., ROBINSON, L.B., Diffusion of hydrogen in titanium alloys due to composition, temperature, and stress gradients, Metall. Trans. **4** (1973) 291–302.

[II.14] MacEWEN, S.R., COLEMAN, C.E., ELLS, C.E. FABER, J.J.R., Dilation of h.c.p. zirconium by interstitial deuterium, Acta Metall. **33** (1985) 753–757.

[II.15] COLEMAN, C.E., AMBLER, J.F.R., Measurement of effective solvus temperature of hydrogen in Zr-2.5 wt% Nb using acoustic emission, Can. Metall. Q. **17** (1978) 81–84.

[II.16] COLEMAN, C.E., AMBLER, J.F.R., Solubility of hydrogen isotopes in stressed hydride-forming metals, Scr. Metall. **17** (1983) 77–82.

[II.17] EADIE, R.L., COLEMAN, C.E., Effect of stress on hydride precipitation in zirconium-2.5% niobium and on delayed hydride cracking, Scr. Metall. **23** (1989) 1865–1870.

[II.18] EADIE, R.L., TASHIRO, K., HARRINGTON, D., LEGER, M., The determination of the partial molar volume of hydrogen in zirconium in a simple stress gradient using comparative microcalorimetry, Scr. Metall. Mater. **26** (1992) 231–236.

[II.19] EADIE, R.L., MOK, D., SCARTH, D.A., LEGER, M., The hydrostatic stress field around the crack tip in zirconium 2.5% niobium and implications for delayed hydride cracking, Scr. Metall. Mater. **25** (1991) 497–502.

[II.20] SHI, S.-Q., SHEK, G.K., PULS, M.P., Hydrogen concentration limit and critical temperatures for delayed hydride cracking in zirconium alloys, J. Nucl. Mater. **218** (1995) 189–201.

[II.21] SCHOFIELD, J.S., DARBY, E.C., GEE, C.F., “Temperature and hydrogen concentration limits for delayed hydride cracking in irradiated Zircaloy”, Zirconium in the Nuclear Industry: Thirteenth International Symposium, ASTM STP 1423, Annecy, 2001 (MOAN, G.D., RUDLING, P., Eds), ASTM International, West Conshohocken, PA. (2002) 339–357.

[II.22] TROIANO, A.R., The role of hydrogen and other interstitials in the mechanical behaviour of metals, Trans. ASM **52** (1960) 54–80.

[II.23] SHI, S.-Q., LIAO, M., PULS, M.P., Modelling of time-dependent hydride growth at crack tips in zirconium alloys, Modelling Simul. Mater. Sci. Eng. **2** (1994) 1065–1078.

[II.24] PULS, M.P., Elastic and plastic accommodation effects on metal-hydride solubility, Acta Metall. **32** (1984) 1259–1269.

[II.25] PULS, M.P., Effects of crack tip stress states and hydride-matrix interaction stresses on delayed hydride cracking, Metall. Trans. A **21** (1990) 2905–2917.

[II.26] SHMAKOV, A.A., KALIN, B.A., MATVIENK, Y.G., SINGH, R.N., DE, P.K., Diffusion model of delayed hydride cracking in zirconium alloys, Mater. Sci. **40** (2004) 764–771.

[II.27] McRAE, G.A., COLEMAN, C.E., LEITCH, B.W., The first step for delayed hydride cracking in zirconium alloys, J. Nucl. Mater. **396** (2010) 130–143.

[II.28] PULS, M.P., Review of the thermodynamic basis for models of delayed hydride cracking rate in zirconium alloys, J. Nucl. Mater. **393** (2009) 350–367.

[II.29] PULS, M.P., The Effects of Hydrogen and Hydrides on the Integrity of Zirconium Alloy Components: Delayed Hydride Cracking, Engineering Materials, Springer-Verlag, London (2012).

Since the last publication on zirconium by the IAEA in 1971 there has been a need to gather and update relevant information. In an effort to bridge the years-long gap on zirconium, its development and use in industry, and to provide comprehensive information on the material the IAEA initiated a comprehensive project on the metallurgy of zirconium, which resulted in this publication. These volumes cover a wide range of the applications, properties and irradiation behaviour of zirconium.

INTERNATIONAL ATOMIC ENERGY AGENCY
VIENNA